

# A. I. Ch. E. JOURNAL

CHEMICAL ENGINEERING RESEARCH AND DEVELOPMENT /

JUNE 1959

UNIVERSITY  
OF MICHIGAN

JUN 30 1959

ENGINEERING  
LIBRARY

## CONTENTS

- |  |   |
|--|---|
| Mass Transfer at Low Flow Rates in a Packed Column   | V. P. Dorweiler and<br>R. W. Fahien                             |
| Axial Mixing and Extraction Efficiency   | C. A. Sleicher, Jr.   |
| Effect of a Volume Heat Source on Free Convection Heat Transfer  | I. E. Randall and<br>Alexander Sesonske                         |
| Reduced Density Correlation for Hydrogen: Liquid and Gaseous States  | Charles A. Schaefer and<br>George Thodos                        |
| An Improved Equation of State for Gases  | Joseph J. Martin, Rajendra M.<br>Kapoor, and Noel De Nevers     |
| Solubility of Liquids in Compressed Hydrogen, Nitrogen, and Carbon Dioxide   | J. M. Prausnitz and<br>P. R. Benson                             |
| Interfacial Resistance in the Absorption of Oxygen by Water  | S. H. Chiang and H. L. Toor                                     |
| Factors Affecting Density Transients in a Fluidized Bed  | James M. Dotson   |
| Viscous Flow Relative to Arrays of Cylinders   | John Happel   |
| Mass Transfer from a Solid Sphere to Water in Highly Turbulent Flow  | L. R. Steele and<br>C. J. Geankoplis                            |
| Turbulent Flow of Pseudoplastic Polymer Solutions in Straight Cylindrical Tubes  | Robert G. Shaver and<br>Edward W. Merrill                       |
| Turbulent Flow of Non-Newtonian Systems  | D. W. Dodge and A. B. Metzner                                   |
| Characteristics of Transition Flow Between Parallel Plates   | G. A. Whan and R. R. Rothfus                                    |
| Treatment of Thermodynamic Data for Homogeneous Binary Systems   | H. C. Van Ness and<br>R. V. Mrazek                              |
| The Molecular Structure of Liquids   | John S. Dahler  |
| Chromatographic Columns Containing a Large Number of Theoretical Plates  | A. S. Said  |
| Two-dimensional Laminar-Flow Analysis, Utilizing a Doubly Refracting Liquid  | John W. Prados and<br>F. N. Peebles                             |
| Liquid-Side Mass Transfer Coefficients in Packed Towers  | Kakusaburo Onda, Eizô Sada,<br>Yasuhiro Murase                  |
| The Dynamics of Heat Removal from a Continuous Agitated-Tank Reactor   | R. J. Fanning and<br>C. M. Sliepcevich                          |
| Turbulent Liquid Flow Down Vertical Walls  | H. H. Belkin, A. A. MacLeod,<br>C. C. Monrad, and R. R. Rothfus |
| Phase Equilibria in Mixtures of Polar and Nonpolar Compounds: Derived Thermodynamic Quantities for Alcohols and Hydrocarbons | Cline Black   |
| Heat Transfer and Fluid Dynamics in Mercury-Water Spray Columns  | R. D. Pierce, O. E. Dwyer, and<br>J. J. Martin                  |
| Flow Characteristics in Horizontal Fluidized Solids Transport  | Chin-Yung Wen and<br>H. P. Simons                               |
| Effective Diffusivity of Packed Bed  | M. Kimura, K. Ueda, and<br>T. Ofuka                             |

## SPIRAL CONDENSERS ON TOP

Our new Series "G" condensers are designed for installation as the top section of a column or for direct connection to the vapor outlet nozzle of a vessel.

Economy is obvious in the elimination of elaborate supporting structures, large diameter vapor lines and other auxiliaries essential to conventional designs.

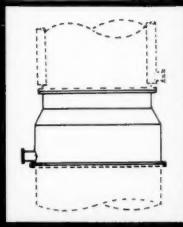
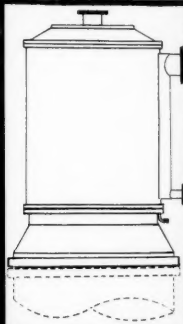
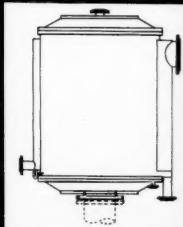
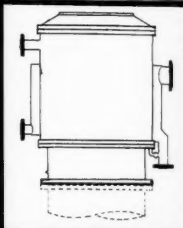
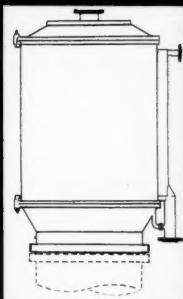
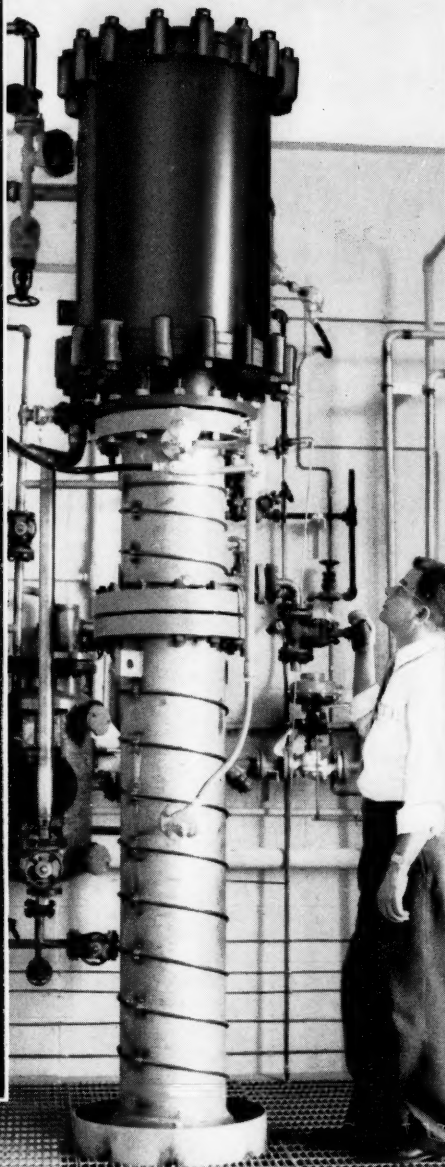
None of the exclusive features of the Spiral condenser have been sacrificed for this direct mounting arrangement. The vapor path can be full counter current spiral flow, combined cross flow-spiral flow or full cross flow. Any combination for maximum or minimum cooling of condensate and noncondensables can be obtained in the in-built after-cooling zone.

The Spiral condenser is unequaled for stripping out soluble gases. The rapid and complete separation of condensate from fixed gases prevents partial re-absorption, and separate outlets are provided for the condensate and the noncondensables.

The Spiral is furnished for either total, partial, reflux, vent or knock-down condensing services in sizes from 15 sq. ft. to 1600 sq. ft. and for design pressures up to 150 p.s.i.g. Large volume condensate retention capacity can be incorporated when desired.

Spirals are fabricated in any material that can be cold formed and welded to ASME Code requirements.

Write for full particulars.



**AMERICAN HEAT RECLAIMING CORPORATION**  
1270 Sixth Avenue, New York, N. Y.



# A.I.Ch.E. JOURNAL

JUNE, 1959 • VOL. 5, NO. 2

The A.I.Ch.E. Journal, an official publication of the American Institute of Chemical Engineers, is devoted in the main to theoretical developments and research in chemical engineering and allied branches of engineering and science. Manuscripts should be submitted to the New York office.

## PUBLISHER

F. J. Van Antwerpen

## EDITOR

Harding Bliss

## MANAGING EDITOR

Sylvia Fourdrinier

## ASSISTANT PUBLISHER

L. T. Dupree

## ADVERTISING MANAGER

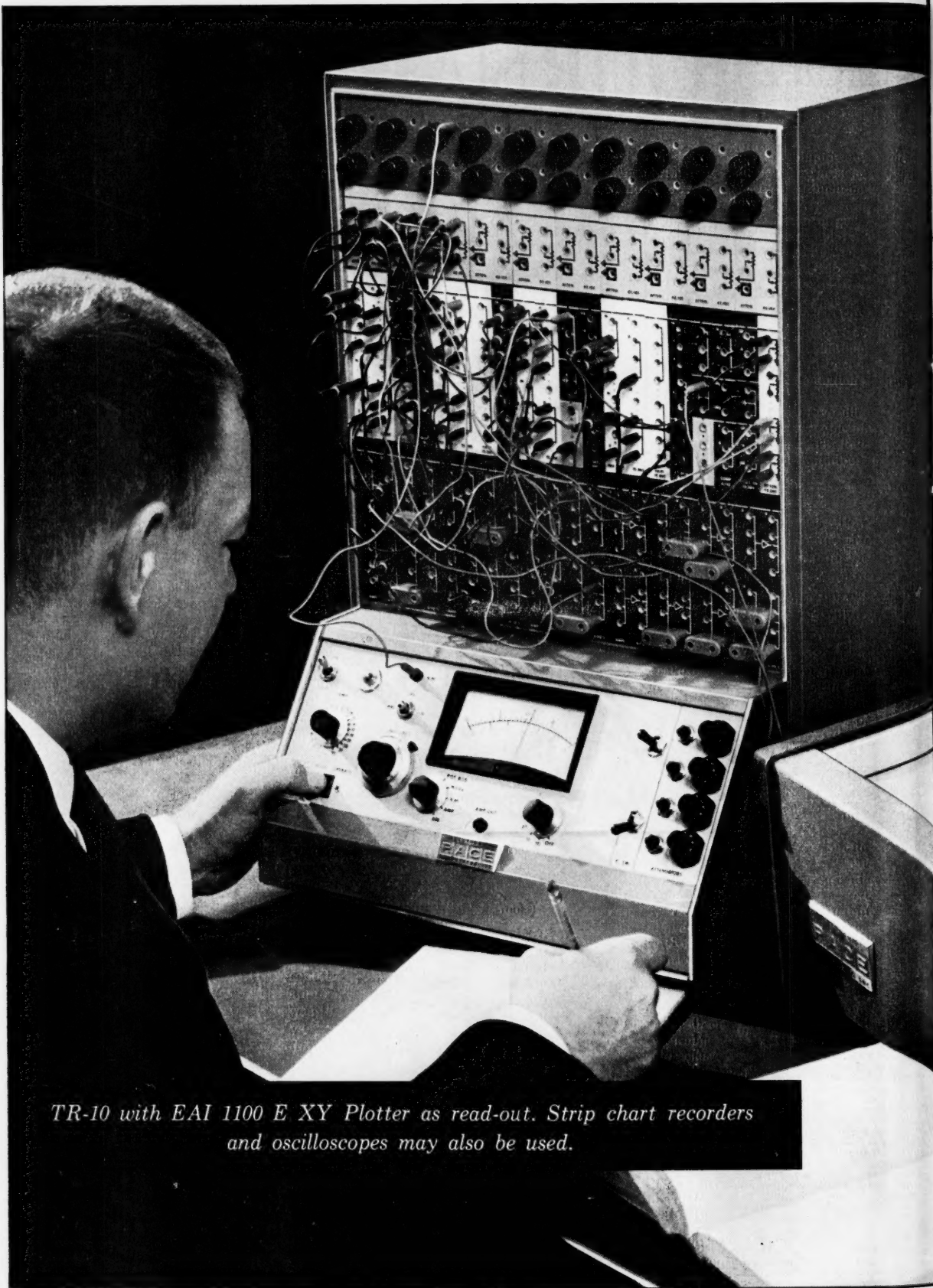
P. A. Jolcivar

## ADVISORY BOARD

C. M. Cooper	R. H. Newton
O. E. Dwyer	R. L. Pigford
W. C. Edmister	E. L. Piret
E. R. Gilliland	J. M. Smith
A. N. Hixson	Theodore Vermeulen
H. F. Johnstone	R. R. White
W. R. Marshall, Jr.	R. H. Wilhelm

Publication Office, Richmond, Virginia. Published quarterly in March, June, September, and December by the American Institute of Chemical Engineers, 25 West 45 Street, New York 36 New York. Manuscripts and other communications should be sent to the New York office. Correspondence with the editor may be addressed to him at Yale University, 225 Prospect Street, New Haven 11, Connecticut. Statements and opinions in the *A.I.Ch.E. Journal* are those of the contributors, and the American Institute of Chemical Engineers assumes no responsibility for them. Subscriptions: one year, member \$4.50, nonmember \$9.00; two years, member \$7.50, nonmember \$15.00; additional yearly postage, Canada 50 cents, Pan American Union \$1.50, other foreign \$2.00 (foreign subscriptions payable in advance). Single copies: \$3.00. Second-class mail privileges authorized at Richmond, Virginia. Copyright 1959 by the American Institute of Chemical Engineers. National headquarters of A.I.Ch.E. is concerned about nondelivery of copies of the *A.I.Ch.E. Journal* and urgently requests subscribers to give prompt notification of any change of address. Sixty days must be allowed for changes to be made in the records.

The Sea and the A. E. C. ....	137
Mass Transfer at Low Flow Rates in a Packed Column <i>V. P. Dorweiler and R. W. Fahien</i> .....	139
Axial Mixing and Extraction Efficiency ..... <i>C. A. Sleicher, Jr.</i>	145
Effect of a Volume Heat Source on Free Convection Heat Transfer ..... <i>I. E. Randall and Alexander Sesonske</i>	150
Reduced Density Correlation for Hydrogen: Liquid and Gaseous States <i>Charles A. Schaefer and George Thodos</i> .....	155
An Improved Equation of State for Gases <i>Joseph J. Martin, Rajendra M. Kapoor, and Noel De Nevers</i> .....	159
Solubility of Liquids in Compressed Hydrogen, Nitrogen, and Carbon Dioxide ..... <i>J. M. Prausnitz and P. R. Benson</i>	161
Interfacial Resistance in the Absorption of Oxygen by Water <i>S. H. Chiang and H. L. Toor</i> .....	165
Factors Affecting Density Transients in a Fluidized Bed ..... <i>James M. Dotson</i>	169
Viscous Flow Relative to Arrays of Cylinders ..... <i>John Happel</i>	174
Mass Transfer from a Solid Sphere to Water in Highly Turbulent Flow ..... <i>L. R. Steele and C. J. Geankoplis</i>	178
Turbulent Flow of Pseudoplastic Polymer Solutions in Straight Cylindrical Tubes ..... <i>Robert G. Shaver and Edward W. Merrill</i>	181
Turbulent Flow of Non-Newtonian Systems .... <i>D. W. Dodge and A. B. Metzner</i>	189
Characteristics of Transition Flow Between Parallel Plates <i>G. A. Whan and R. R. Rothfus</i> .....	204
Treatment of Thermodynamic Data for Homogeneous Binary Systems <i>H. C. Van Ness and R. V. Mrazek</i> .....	209
The Molecular Structure of Liquids ..... <i>John S. Dahler</i>	212
Chromatographic Columns Containing a Large Number of Theoretical Plates ..... <i>A. S. Said</i>	223
Two-dimensional Laminar-Flow Analysis, Utilizing a Doubly Refracting Liquid ..... <i>John W. Prados and F. N. Peebles</i>	225
Liquid-Side Mass Transfer Coefficients in Packed Towers <i>Kakusaburo Onda, Eizô Sada, and Yasuhiro Murase</i> .....	235
The Dynamics of Heat Removal from a Continuous Agitated- Tank Reactor ..... <i>R. J. Fanning and C. M. Sliepcevich</i>	240
Turbulent Liquid Flow Down Vertical Walls <i>H. H. Belkin, A. A. MacLeod, C. C. Monrad, and R. R. Rothfus</i> .....	245
Phase Equilibria in Mixtures of Polar and Nonpolar Compounds: Derived Thermodynamic Quantities for Alcohols and Hydrocarbons .... <i>Cline Black</i>	249
Heat Transfer and Fluid Dynamics in Mercury-Water Spray Columns <i>R. D. Pierce, O. E. Dwyer, and J. J. Martin</i> .....	257
Flow Characteristics in Horizontal Fluidized Solids Transport ..... <i>Chin-Yung Wen and H. P. Simons</i>	263
Effective Diffusivity of Packed Bed ..... <i>M. Kimura, K. Ueda, and T. Ofuka</i>	267
Communications to the Editor	
Physical Interpretation of the Relaxation Method in Heat Conduction ..... <i>John S. Thomsen</i>	268
Heat Transfer ..... <i>Leonard Wender and G. T. Cooper</i>	269
Diffusion in a Pore of Irregular Cross Section— a Simplified Treatment ..... <i>Alan S. Michaels</i>	270
Slot Capacity of Bubble Caps ..... <i>Andrew Pusheng Ting</i>	271
Books .....	273



## *The Sea and the A. E. C.*

It is gradually becoming apparent that the oceans represent the last great frontier on earth. They are the frontier of exploration for man's curiosity and of development for man's needs.

Sea water can be demineralized by vapor compression or multiple-effect evaporation, freezing, electro-dialysis, and extraction. This can be done, thanks to good engineering, with certain of these processes at costs which are now competitive with those of municipal water in many places. As our more usual supplies of fresh water are progressively damaged and made more costly through continuing abuse, fresh water from the sea probably will soon be a recognized source of industrial water. The opportunities for high-quality engineering work and skillful engineers are almost unlimited in this field.

The sea may also be used for growing food. As our world populations skyrocket, as our misuses of land multiply, and as our land becomes more and more enriched in strontium-90, we must sooner or later seek the sea as a place to grow food. While the food grown there may not appeal to man (until some future date when appeal won't make much difference), food for animals could be grown in the sea now.

The sea bottoms are also a great source of raw materials, as the results of the International Geophysical Year have shown. Manganese, cobalt, iron, and copper abound on certain parts of the bottoms of the oceans. It is thought that development of these

deposits may be economically attractive under conditions existing at the present time.

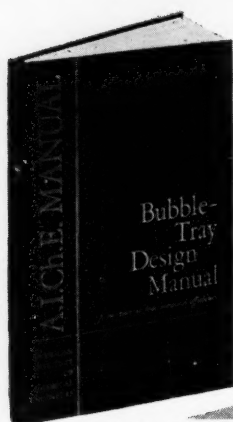
These wonderful prospects, under more normal circumstances, should give us great comfort. The sea offers the solution to three of man's greatest problems—a shortage of water, prospects of famine, and the depletion of our high-grade mineral resources.

However there is a threat to this prospect. For some time the Atomic Energy Commission and its British and French equivalents have been dumping radioactive wastes into the oceans. It is to be assumed that this was done only with low-level wastes and in as safe a manner as possible; however was it safe enough? Our ignorance of the sea is profound. Sea currents, tidal waves, submarine earthquakes, and submarine topography have been explored only to very limited extents. How can anyone say with any confidence what is safe? A broken container would lead to wide dispersion at first, but maybe later some marine organism would concentrate these materials. Furthermore the attitude of the A. E. C. in the matter of fall-out and the level of radioactivity in Minnesota wheat (a six-month delay in reporting the distressing results) does not inspire confidence.

Let us hope that our oceans, the last great frontier on earth and the greatest hope for the alleviation of some of man's problems, will not be contaminated for all time through inadequate knowledge.

H.B.

# Results . . . from a five-year study of bubble-tray efficiencies



An A.I.Ch.E. Technical Manual

## Bubble-Tray Design Manual

*prediction of fractionation efficiency*

by the  
Distillation Subcommittee  
of the Research Committee

*Limited Edition*

### TABLE of CONTENTS

Foreword . . . . .	iii
I. Theory . . . . .	1
II. Methods of Calculating Physical Properties . . . . .	14
III. Research Results . . . . .	25
IV. Efficiency Prediction Method . . . . .	63
V. Methods to Increase Efficiency . . . . .	72
VI. Multicomponent Systems . . . . .	74
VII. Tray Design . . . . .	76
VIII. Fractionation . . . . .	76
IX. Sample Calculations . . . . .	77
Notation . . . . .	83
Literature Cited . . . . .	87
Conversion Factors . . . . .	89
Tables 1 through 6 . . . . .	89
Sponsoring Companies . . . . .	94
Calculation Form Sheets . . . . .	95

1. Enables the engineer to predict efficiencies for commercial bubble trays used in multicomponent fractionation.
2. Contains sample calculations made on plant-scale columns.
3. Includes calculation form sheets for the use of the reader. (Additional sheets may be purchased.)

Available NOW to

Members of A.I.Ch.E. . . . . \$5.00  
Non-members . . . . . \$10.00  
Calculation form sheets . . . . . .25  
(One bound in book but also available for separate purchase)

prices are postpaid

Hard covers, gold stamped, 6 $\frac{1}{8}$ " x 9 $\frac{1}{4}$ ", 94 pages, attractively designed and printed.

Published and sold by

**AMERICAN  
INSTITUTE  
OF  
CHEMICAL  
ENGINEERS**

**AMERICAN INSTITUTE OF CHEMICAL ENGINEERS**  
25 West 45 Street  
New York 36, New York

Enclosed is my check for \_\_\_\_\_ (Add 3% sales tax for delivery in New York City.) Send me \_\_\_\_\_ copies of the **Bubble-Tray Design Manual**.  
Send me \_\_\_\_\_ loose calculation form sheets.

Name

Address

Member ( )

Non-member ( )



# Mass Transfer at Low Flow Rates in a Packed Column

V. P. DORWEILER and R. W. FAHIEN

Iowa State College, Ames, Iowa

Mass transfer in packed columns has been investigated for a variety of column and packing sizes but at flow rates restricted to fully developed turbulent conditions. The present work was undertaken to investigate mass transfer at flow-rate conditions in the transition and laminar regions.

A dual treatment of experimental data required a knowledge of the variation of concentration and velocity with radial position. A tracer-injection technique was employed which consisted in the introduction of a tracer gas into the center of a bulk gas stream and the measurement of the tracer-gas concentration at various radial positions downstream. The velocity distribution for the packed column was determined by means of a five-loop, circular, hot-wire anemometer. The test column was a vertical 4-in. pipe, packed with  $\frac{1}{8}$ -in. spherical, ceramic catalyst-support pellets.

Mass transfer diffusivity and Peclet number were determined from two solutions of the differential-diffusion equation applied in previous investigations. An analytical solution in terms of Bessel functions was used to calculate values of average diffusivity and Peclet number and a seminumerical solution in terms of homogeneous linear-difference equations to calculate values of point diffusivity and Peclet number.

Variation of diffusivity and Peclet number with radial position is shown, average diffusivity and Peclet number being correlated with Reynolds number. The interaction of molecular and eddy mass transfer mechanisms with decreasing mass velocity is illustrated by defining a molecular and an eddy Peclet number and correlating with Reynolds number. Eddy diffusivity is correlated as a function of local flow conditions.

This paper presents a continuation of a previous study of mass transfer in a packed system (1). In the first paper mass transfer was investigated in the turbulent region for a range of column and packing sizes; the present study considered the flow range over which a separation of molecular and eddy mechanisms could be obtained. Consequently the lower velocity streams in the laminar and transition regions were investigated as well as the initial points of the fully developed turbulent region.

The general expression for the rate of mass transfer is

$$N_A = -E \frac{\partial C}{\partial y} \quad (1)$$

Two previous studies of mass transfer in packed systems differed in the approach used in the definition of diffusivity. Bernard (2) considered diffusivity to be independent of position in the system. An average diffusivity was thereby obtained which is an average for all flow conditions throughout the system. The approach used in the previous work (1) was to permit diffusivity and velocity to vary with radial position. A "point" diffusivity was obtained which is a function of position in the system, that is of point flow conditions.

These two mathematical techniques, used to solve the basic differential equation for mass transfer under the different assumptions, were employed in this work, to obtain a wider expression for the mass transfer parameters. The average diffusivity was analyzed for molecular and eddy contributions, and the variable term was analyzed for an expression

relating diffusivity with point flow conditions and radial position. While the packed column is not a general system for the study of mass transfer, the techniques of definition and calculation derived herein are not restricted to this system.

## EQUIPMENT AND PROCEDURE

The general experimental equipment used in this study was described in detail in the previous paper (1). The only new piece of apparatus introduced was a five-loop, circular hot-wire anemometer used to determine the velocity distribution across the packed bed. Figure 1 is a schematic representation of the anemometer. Platinum wire of 0.006-in. diameter was used for the loops. Construction details and calibration procedures are discussed by Schwartz (3).

The experimental procedure to obtain concentration data was essentially that described previously. The technique for velocity determination in the packed system (3) indicated that an optimum position above the bed exists for the measurement of velocities representing the true distribution in the packing. If the loops are located lower than this optimum position, the extreme turbulence of the gas emerging from the packing (radial velocities of the air emerging from restricted flow and returning to empty tube conditions) would cause the anemometer to indicate too high a velocity owing to the cooling by these radially directed velocity components. If the anemometer were higher, a return of the velocities to an empty-tube distribution would be obtained. The anemometer was operated at 1 in. above the bed in this investigation, after this was determined experimentally as an optimum height.

## CALCULATION OF RESULTS

The basic differential equation for mass transfer, which considers diffusion in the

radial direction only and bulk flow in the axial direction, is

$$\frac{\partial}{\partial r} \left( E r \frac{\partial C}{\partial r} \right) = u r \frac{\partial C}{\partial z} \quad (2)$$

Angular symmetry is assumed. The following boundary conditions are imposed:

1. At  $z = 0$ , the plane of the injection tube tip

$$C(r, 0) = C_i, \text{ for } 0 < r < t$$

and

$$C(r, 0) = 0, \text{ for } t < r < r_0$$

2. At the tube wall

$$\frac{\partial C(r_0, z)}{\partial r} = 0$$

3. At the tube center

$$\frac{\partial C(0, z)}{\partial r} = 0$$

## Analytical Solution

On the assumption that  $E$  and  $u$  are independent of position, the solution of Equation (2) presented by Bernard (2) and modified by Kurihara (4) is in the form of an infinite Fourier-Bessel series

$$\frac{C}{C_A} \frac{C_A}{C_M} = 1 + \frac{2}{t} \sum_{n=1}^{\infty} \frac{1}{\beta_n} \frac{J_1(\beta_n t)}{J_0(\beta_n r_0)} J_0(\beta_n r) \exp(-\beta_n^2 z/\alpha) \quad (3)$$

The series converges rapidly for small values of  $C_{\max}/C_{\min}$ ; that is  $z$  is sufficiently great. The reduced form of Equation (3) is

$$\frac{C}{C_A} \frac{C_A}{C_M} = 1 + \frac{2}{t\beta_1} \frac{J_1(\beta_1 t)}{J_0(\beta_1 r_0)} J_0(\beta_1 r) \exp(-\beta_1^2 z/\alpha) \quad (4)$$

Concentration at the column center, where  $r = 0$ , is given by

$$\frac{C_0}{C_A} \frac{C_A}{C_M} = 1 + \frac{2}{t\beta_1} \frac{J_1(\beta_1 t)}{J_0(\beta_1 r_0)} \exp(-\beta_1^2 z/\alpha) \quad (5)$$

By plotting  $C/C_A$  vs.  $J_0(\beta_1 r)$  one can obtain the value of  $C_0/C_A$  analytically. The intercept of such a linear plot is  $C_M/C_A$ . Since all of the other terms of Equation (5) are then known,  $\alpha$  can be calculated. The average Peclet number can also be calculated, since

$$Pe = D_p \frac{V}{E} = D_p \alpha \quad (6)$$

Equation (4) was applied in this investigation by the fitting of the experi-

V. P. Dorweiler is with Standard Oil Company (Indiana), Whiting, Indiana.

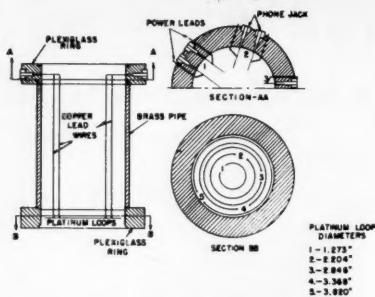


Fig. 1. Hot-wire anemometer.

mental concentration data to a linear relationship with the first-order Bessel function by the least squares procedure. The analytical determination of  $C_M/C_A$  differs from that employed by Bernard, which was a graphical integration of point concentration data on an area-weighted basis. The analytical procedure was preferred, since more dependence on the linear relationship is necessarily involved.

#### Illustration of Analytical Solution

Application of least squares to the experimental concentration data, for a run at a mass velocity of 214 lb./sq. ft./hr., established the following best line:

$$\frac{C}{C_A} = 0.6404 J_0(\beta, r) + 1.086 \quad (7)$$

The value of  $C_M/C_A = 1.086$ , and  $C_0/C_A = 1.726$ . The value of  $C_0/C_M$  then is 1.516. From Equation (4)

$$\begin{aligned} 1.516 &= 1 + \frac{2}{(0.435/2)(1.904)} \\ &\times \frac{J_1(1.904 \times 0.435/2)}{J_0^2(1.904 \times 2.013)} \\ &\times \exp(-1.904^2 \times 30.4/\alpha) \\ &= 1 + 6.003 \exp(-145.459/\alpha) \\ &= 1 + 6.003 \exp(-28.839/Pe) \end{aligned}$$

The  $\alpha$  ratio and Peclet number are

$$\alpha = 44.897 \text{ in.}^{-1}, \text{ and } Pe = 11.74$$

Diffusivity, in terms of the corresponding flow rates, is given as the reciprocal of the  $\alpha$  ratio

$$E/V = 0.0223 \text{ in.}$$

Since  $V$  is based upon superficial column area, any  $E$  calculated from this ratio will also be on a superficial basis; the  $\alpha$  ratio is however a ratio of the true restricted terms

$$\frac{V/\delta}{E/\delta} = \frac{V}{E} = \alpha$$

#### Seminumerical Solution

Under the rigid assumptions that the mass transfer process is a function of local

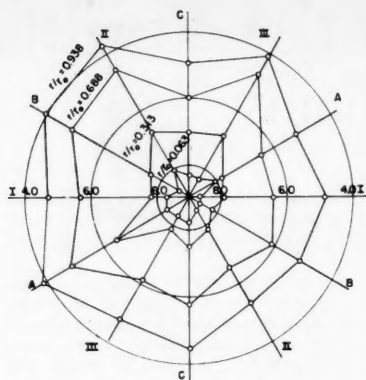


Fig. 2. Variation of concentration with angular position.

flow conditions and that the velocity and diffusivity vary with position in the system, Equation (2) involves functional relations between diffusivity and velocity with radial position. Since the nature of these relations is unknown, an analytical solution is not possible. A seminumerical method was employed in the previous work (1) to solve the equation. Equation (2) was replaced by a system of difference equations written about points over the radius. This system is linear in the eigen functions at each interval about the point and in the eigen value. Solution of Equation (2) is of the form

$$C = \sum_{n=0}^N A_n R_n \exp(-\lambda_n z/r_0^2) \quad (8)$$

A simplification in the solution is possible. Since Equation (8) involves negative exponential terms in  $z$  and  $\lambda$ , and since  $\lambda$  increases with  $n$ , the series converges rapidly for a sufficiently large  $Z$ :

$$C = A_0 R_0 Z_0 + A_1 R_1 Z_1 \quad (9)$$

when one applies boundary conditions 1 to 3 and imposes the orthogonality of the eigen functions, a direct solution for diffusivity is available in the form

$$E_{k+1/2} = \frac{\lambda_1 h^2 \sum_{k=0}^k P_k (C_k - C_M)}{\theta_{k+1/2} (C_k - C_{k+1})} \quad (10)$$

The value of  $\lambda_1$  is given by

$$\lambda_1 = -\frac{r_0^2}{z} \ln Z_1 \quad (11)$$

where

$$Z_1 = \frac{\sum_{k=0}^N P_k (C_k - C_M)^2 \times \sum_{k=0}^t P_k}{\sum_{k=0}^t P_k (C_k - C_M) \times \sum_{k=0}^N C_k P_k} \quad (12)$$

The mean integral concentration is obtained by a volumetric flow rate-weighted average of point concentrations:

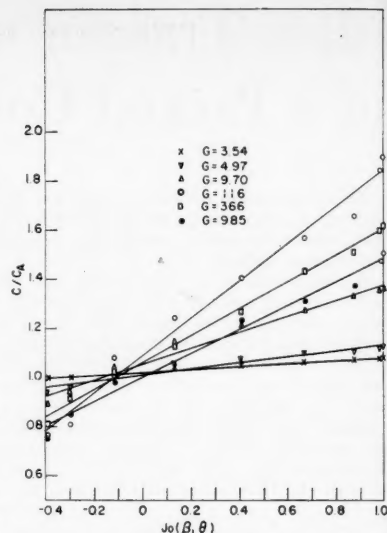


Fig. 3a. Variation of concentration with Bessel function of zero order, Equation (11).

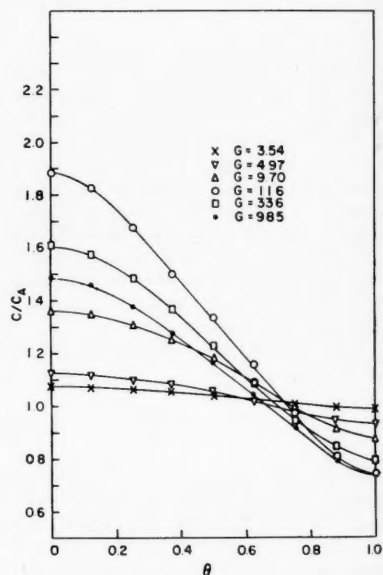


Fig. 3b. Variation of concentration with radial position.

$$C_M = \frac{\int_0^1 C u \theta d\theta}{\int_0^1 u \theta d\theta} = \frac{\sum_{k=0}^N C_k P_k}{\sum_{k=0}^N P_k} \quad (13)$$

#### Illustration of Seminumerical Solution

The seminumerical solution is illustrated in Table 1, which has been subdivided to illustrate better the details involved.

#### RESULTS

Concentration data in the form of  $C/C_A$  ratios were used directly in the

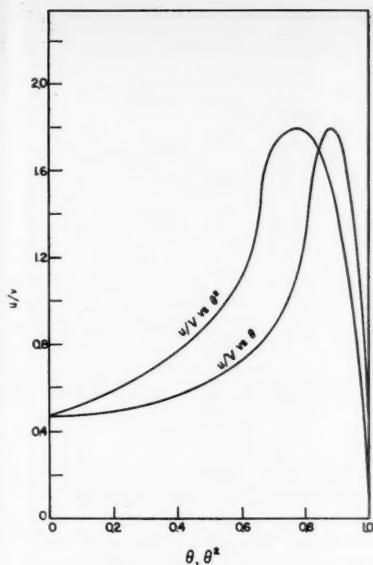


Fig. 4a. Variation of velocity with radial position.

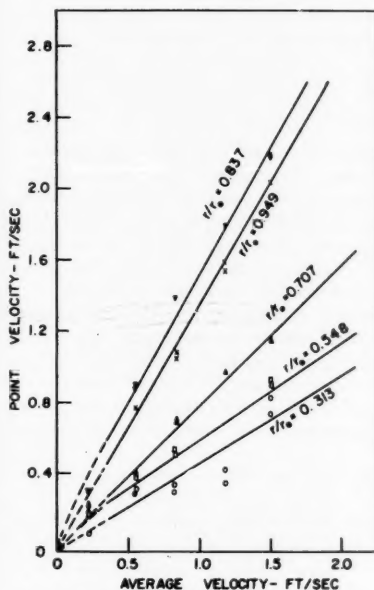


Fig. 4b. Variation of velocity profile with mass velocity.

mathematical analysis, since the analytical solution is of this form, and the numerical solution involves a homogeneous ratio of concentrations. Similarly velocity data in the form of  $u_k/V$  ratios were used directly in the seminumerical solution to yield values of  $E_{k+1/2}/V$  corresponding to the  $\alpha$  ratio.

Figure 2 illustrates the deviation of the test bed from perfect angular symmetry of packing, which was assumed in both solutions. The concentration data used represent the average of six points of radial symmetry, thereby weighting the concentrations throughout the bed.

TABLE I. SEMINUMERICAL SOLUTION

k	e	Calculation of $C_k$		Calculation of Eigen Value				Calculation of Diffusivity and Peclet Number			
		$C_k/C_A$	$u_k/V$	$F_k/V$	$C_k F_k/V$	$\frac{C_k - C_A}{C_A}$	$\frac{F_k(C_k - C_A)}{V C_A}$	$\frac{F_k(C_k - C_A)^2}{V C_A^2}$	$\frac{F_k(C_k - C_A)}{V C_A}$	$\frac{C_k - C_A}{C_A}$	$\frac{E_{k+1/2}}{V}$ (in.)
0	0.000 0.063	1.726	-	0.0074 <sup>a</sup>	0.0128	0.752	0.00557	0.00419	0.00557	0.042	0.0115
1	0.125 0.188	1.684	0.480	0.0600	0.1010	0.710	0.04260	0.03025	0.04817	0.114	0.0122
2	0.250 0.313	1.570	0.506	0.1265	0.1986	0.596	0.07539	0.04494	0.12357	0.141	0.0152
3	0.375 0.438	1.429	0.550	0.2063	0.2947	0.455	0.09384	0.04270	0.21741	0.153	0.0176
4	0.500 0.563	1.276	0.624	0.3120	0.3981	0.302	0.09422	0.02846	0.31163	0.162	0.0185
5	0.625 0.688	1.114	0.749	0.4681	0.5215	0.140	0.06544	0.00918	0.37717	0.147	0.0202
6	0.750 0.813	0.967	1.018	0.7635	0.7383	-0.007	-0.00535	0.00004	0.37183	0.135	0.0183
7	0.875 0.938	0.832	1.805 1.548	1.5794	1.3140	-0.142	-0.22427	0.03185	0.14756	0.060	0.0142
8	1.000	0.772	-	0.755 <sup>b</sup> 0.2488	0.5602 0.1393	-0.202	-0.14658	0.02961 0.22119	0.00098	-	-

$$C_k = \frac{C_k F_k}{\sum F_k} = \frac{0.1393}{0.2488} = 0.557$$

$$\frac{1}{\lambda_1} = \frac{\sum \frac{C_k F_k}{C_A} \frac{F_k(C_k - C_A)}{V C_A}}{\sum \frac{F_k(C_k - C_A)^2}{V C_A^2}} = \frac{0.1393 \times (0.00557 + 0.1152 \times 0.04260)}{0.0074 \times 0.0004 + 0.1152 \times 0.0600} = 13.381$$

$$\lambda_1 = \frac{1}{13.381} \ln \left( \frac{1}{\lambda_1} \right) = \frac{2.013^2}{30.4} \ln 13.381 = 0.3458 \text{ in}$$

$$E_{k+1/2} = \frac{\lambda_1^2}{2} \sum \frac{F_k(C_k - C_A)}{C_A} = \frac{(0.3458)^2}{2} \frac{(1/0.1393)(0.2173)}{(0.1393)(0.155)} = 0.0176 \text{ in.}$$

$$(Pe)_k = \frac{D_0(u_k/V)}{E_{k+1/2}} = \frac{0.262 \text{ in}(1/0.1393)}{(0.0176 \text{ in})} = 8.68$$

<sup>a</sup> $F_0$  is obtained by consideration of an increment of one-half normal width, and must then be equivalent to  $1/2P(h/4)$ , where  $P(h/4)$  is the mean value of  $P$  in the region  $0 < \theta/2 < h/2$ . Since velocity changes negligibly in this region,  $P(h/4) = 1/2P(h/2)$ , and  $F_0 = 1/4P(h/2)$ .

<sup>b</sup>By similar reasoning,  $F_8 = (1/4P)(1/2 \ln 7)$ .

<sup>c</sup>Since  $t$  is non-integral in  $k$ , the summation is performed to the next integral value above  $t$ , and the resulting value linearly proportioned. In this application  $t = 0.1152$ , which is less than one increment; hence, the  $t/n$  fraction is used to proportion the  $F_k(C_k - C_A)/C_A$  term.

Figures 3a, b illustrate the fit of concentration data to the theoretical calculations. Figure 3a represents a plot of Equation (4). The data are seen to scatter seriously at high values of  $C_0/C_A$  corresponding to peak values of Peclet number. The linear relationships shown were established by least squares. Figure 3b represents a plot of Equation (8). These data are smoothed values fitted to the boundary conditions and used in the seminumerical solution. Scatter of data about the smoothed curves was generally much less than that experienced in the linear fitting.

Velocity distribution across the test bed is shown in Figure 4a. This distribution was found to be essentially independent of total flow rate above an average superficial velocity of 0.4 ft./sec., in agreement with the results of Schwartz (3). The plot of point velocity vs. average velocity at constant radial position (Figure 4b) indicates this independence, as well as the deviation from a uniform distribution at low flow rates. Generally the hot-wire anemometer was found to give a sufficiently accurate material balance only at average velocities above 0.2 ft./sec., which prevents the numerical treatment of data below this velocity.

Average diffusivity and Peclet number, determined over a range of mass velocities from 985 to 3.54 lb./sq. ft. (hr.), are shown in Figures 5a, b, plotted against

Reynolds number. The values of average diffusivity and Peclet number are tabulated in Table 2.\*

Point diffusivity and Peclet number are shown as functions of radial position in Figures 6a and b. Point diffusivity was found to be constant at the bed center, to reach a maximum near the column wall, and to decrease at the wall. Point Peclet number was found to be constant at the bed center and to increase as the column wall was approached. An expected decrease of Peclet number at the wall was not detected, since the numerical method yielded an average value at one-half increment away from the wall. Point diffusivity and Peclet number are listed in Tables 3\* and 4\* for eight mass velocities ranging from 985 to 50.2 lb./sq. ft. (hr.)

## DISCUSSION OF RESULTS

The scope of this investigation was chosen to cover an extended range of a Peclet number-Reynolds curve, which includes the initial points of a fully developed turbulent region, the full transition region, and the onset of the laminar region. Of special interest was a study of the interaction of eddy and

\*Tables 2, 3 and 4 are on file with the American Documentation Institute, Auxiliary Publications Photoduplication Service Library of Congress, Washington 25, D. C., and may be ordered as document No. 5871 on remission of \$1.25 for microfilm or \$1.25 for photoprints.

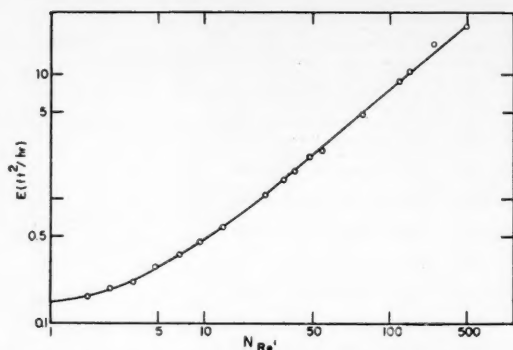


Fig. 5a. Average diffusivity calculated by the analytical method.

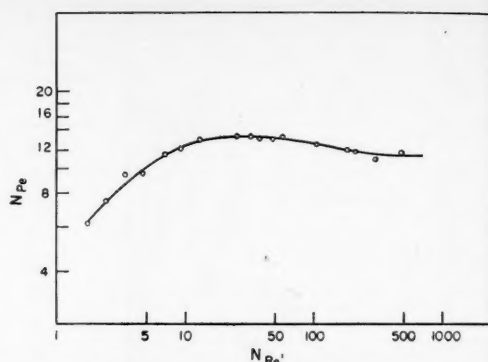


Fig. 5b. Average Peclet number calculated by the analytical method.

molecular mechanisms as the importance of molecular transfer developed.

An inspection of Figure 5b will reveal qualitatively the interaction of eddy and molecular mechanisms. At a Reynolds number above 200 the Peclet number is found to be essentially constant with velocity, as has been demonstrated by Towle and Sherwood (5) and Bernard (2) for empty tubes and in the previous work (1) for packed beds. At a Reynolds number of 200 a break in the curve is observed, corresponding to the departure of eddy diffusivity from a linear relationship with velocity. As Reynolds number (velocity) decreases, the eddy diffusivity decreases more rapidly, with a corresponding increase in Peclet number. With further decrease in Reynolds number the turbulent effects in the bed diminish. Molecular diffusivity, which is independent of velocity, becomes increasingly important, that is of the same order of magnitude as the eddy diffusivity. With further decrease in Reynolds number Peclet number reaches a maximum and then decreases as the eddy diffusivity damps out, ultimately reaching a linear relationship with velocity during completely laminar flow. In Figure 5a diffusivity is seen to assume a limiting value at low Reynolds number. This is presumably the molecular diffusivity. Since this value is determined on a superficial basis,  $\alpha = (V/\delta)/D$ , the limiting value obtained is  $D/\delta$ . When one uses a value of  $\delta = 0.32$  (6), the value of  $D$ , obtained is 0.45 sq. ft./hr., which agrees with the published value of molecular diffusivity for carbon dioxide in air (7).

An over-all correlation of data from this investigation with those reported from other works is presented in Figure 7. An empirical relation developed previously (1) was used to correlate various column and packing sizes.

#### THEORETICAL CONSIDERATIONS

A quantitative explanation of mass transfer in a given system is inherently based upon a knowledge of flow conditions existing within the system. Limita-

tions in the precise definition of the nature of these flow conditions impose severe limitations upon an analogous definition of the mechanism of mass transfer. Virtually all previous studies of the diffusional mechanism have concerned themselves with the consideration of fully developed turbulent systems. In general, application of existing theories of turbulence has aided substantially in the understanding of diffusion in these turbulent systems. Application of the theories of turbulence to a system so complex as a packed bed however must be greatly restricted, since many of the basic physical conditions of empty-tube turbulence do not pertain. While in empty tubes eddy displacements are random in length and subjected generally only to tube-wall restrictions, in packed beds these are controlled by randomly arranged interstitial channels. While the scale of turbulence decreases, the intensity of turbulence is seen to increase. Still further complexities are introduced by the coexistence of laminar and turbulent conditions within individual voids.

The mass transfer mechanism in a packed bed has been described on a theoretical basis with a completely developed state of turbulence (complete mixing within a void and sufficiently high velocities with a correspondingly large number of fluid elements into and out of a void) for a regular packing arrangement assumed. In accordance with the random walk theory (8) Peclet number is given by

$$N_{Pe} = c \frac{1 - R_z}{1 + R_z} \quad (14)$$

with  $R_z = -1$  indicating laminar conditions and  $R_z = 0$  indicating complete mixing. The increase in Peclet number with radial position can be explained on a semitheoretical basis as a result of a change in the correlation coefficient from a value near zero throughout the center portion of the bed to negative values nearer the wall, with  $R_z = -1$  giving an infinite Peclet number. This is a semitheoretical approach, since the derivation of the random walk theory depends upon the existence of complete

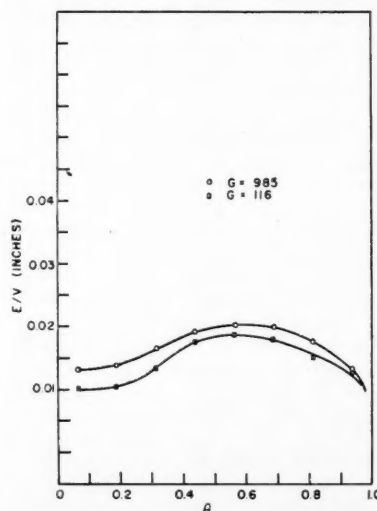


Fig. 6a. Variation of diffusivity with radial position.

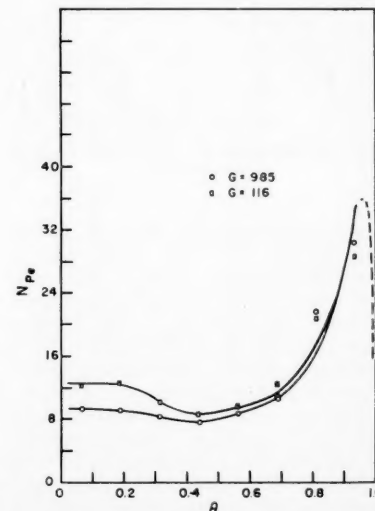


Fig. 6b. Variation of Peclet number with radial position.



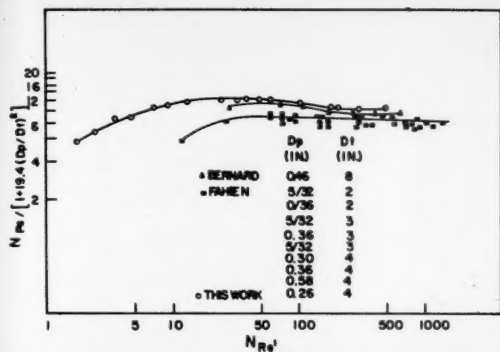


Fig. 7. Correlation of average Peclet number with Reynolds number and  $D_p/D_t$ .

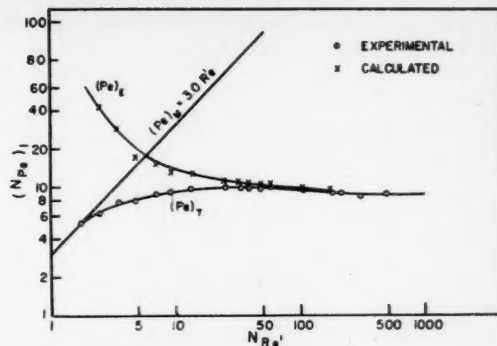


Fig. 8. Correlation of molecular, eddy, and total Peclet numbers with modified Reynolds number.

turbulence, that is, the correlation coefficient being constant at zero.

Bernard (2) used pressure-drop data to determine the nature of turbulence in a packed bed. Since experimental friction-factor-Reynolds-number curves indicated no sharp breaks over the transition region (defined by the break in Peclet-number-Reynolds-number curve) as contrasted with the discontinuity in the empty tube curve, the turbulence existing within the bed is seen to develop gradually over the range of flows. The correlation of pressure-drop and mass transfer data with the packing diameter used as the length parameter seems to indicate that interstitial turbulence is a function of packing sizes.

The continuous nature of the friction-factor-Reynolds-number curves does not indicate the physical significance of the transition point in Peclet-number-Reynolds-number curves. This was postulated by Bernard from the following experimental observations. In liquid systems large eddies with scales up to several particle diameters were observed for flow rates considerably below turbulent values. The pressure drop, which is essentially dependent on flow conditions in the interstices between packing particles, would therefore not reflect the existence of these large eddies, and in turn these large eddies cannot be assumed to cause the interstitial turbulence. When one considers that the Reynolds number point of departure of the transition region from the turbulent region was found to increase in magnitude directly with  $D_p/D_t$  or to remain fixed with a Reynolds number based upon  $D_t$ , the transition region is thought to be created by these large eddies, which apparently are generated under conditions similar to empty-tube conditions. Further at fully developed turbulent conditions the large eddies were no longer present.

These two systems, while in agreement from pressure-drop considerations, are irresolvable in an attempt to define a mass transfer mechanism on the basis of

either. Point diffusivity was found to be proportional to both factors, that is proportional to column diameter near the wall and to pellet diameter near the bed center. Any development of a diffusional mechanism must then consider both processes. Yet any attempt to visualize a mechanism for mass transfer is generally reduced to a consideration of a single void. Perhaps then the most significant approach is to analyze an over-all mechanism, as is suggested by the average data obtained from the analytical solution, and also to analyze a variable mechanism, as is suggested by point data obtained from the numerical solution.

#### Average Diffusivity Data

Since the molecular and the eddy mechanisms are seen to be involved in the over-all process, a parallel transfer is perceivable:

$$E = D_i + E \quad (15)$$

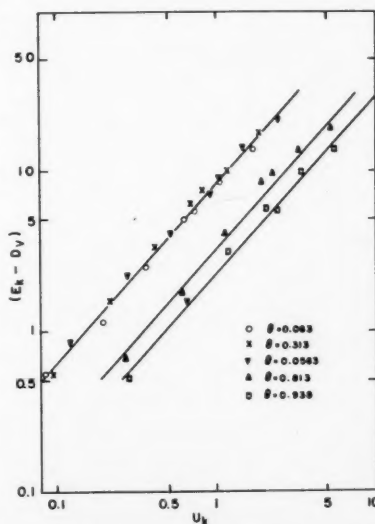


Fig. 9a. Velocity function, Equation (31).

or when one rearranges

$$\frac{1}{E} = \frac{1}{D_i} + \frac{1}{E} \quad (16)$$

and when one divides through by  $D_p V$ ,

$$\frac{1}{(N_{Pe})_T} = \frac{1}{(N_{Pe})_M} + \frac{1}{(N_{Pe})_E} \quad (17)$$

A means of determining the molecular term is now found in the Peclet number defining identity

$$(N_{Pe})_M = N_{Re'} (N_{Sc})_M \quad (18)$$

where

$$N_{Re'} = D_p \frac{\rho(V/\delta)}{\mu} \quad (19-20)$$

and

$$(N_{Sc})_M = \frac{\mu}{D_i \rho}$$

Molecular Peclet number is then given by

$$(N_{Pe})_M = D_p V / D_i \delta \quad (21)$$

When a void fraction of 0.32 (6), with a value of unity for the molecular Schmidt

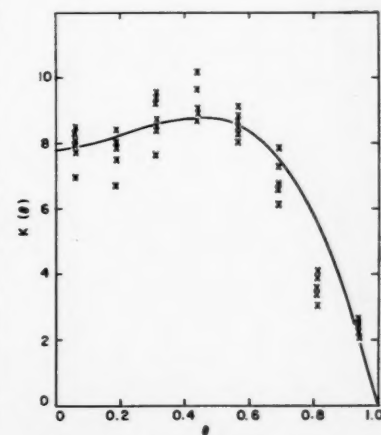


Fig. 9b. Position function, Equation (32).

number, is assumed, the molecular Peclet number is

$$(N_{Pe})_M = 3.13N_{Re'} \quad (22)$$

The eddy Peclet number can then be calculated from Equation (17).

The average Peclet numbers were treated in this manner. The resulting values of eddy and molecular Peclet numbers as well as the total Peclet number are plotted against Reynolds number in Figure 8. Eddy Peclet number is seen to be indistinguishable from total Peclet number for Reynolds numbers above 300, to increase quite gradually from this identity with total Peclet number for Reynolds number between 300 and 30, and to increase sharply at a Reynolds number of about 8. This last point is interpreted as the point of severe damping of turbulence within the bed.

An inspection of Figure 8 reveals that, consistent with the observations of Bernard, an eddy effect is permissible in this gaseous system down to very low values of Reynolds number. Further as Reynolds number tends toward zero, the eddy mechanism is seen to damp out rapidly, thereby allowing an establishment of completely laminar conditions. The lowest measured effective Peclet number was found to be equal to the theoretical molecular Peclet number, which leads to the conclusion that completely laminar conditions were found to exist.

#### Point Diffusivity Data

A second approach to the examination of the mass transfer process involves diffusivity as a function of local flow conditions. The nature of this function can then be determined by the fitting of experimental point data to the proposed expression. From Equation (15) the total diffusivity can be expressed as a molecular term and an eddy term, the former being invariant in the system. Hence

$$E = D_e + Kf(u, \theta) \quad (23)$$

The value assumed for the molecular diffusivity in this system was the limiting value of diffusivity shown in Figure 5a. By plotting  $E_k$ , or  $(E - D_e)_k$ , vs.  $u_k$  at constant radial positions, one obtains the relationship

$$(E - D_e)_k = K_k u_k^{1.12} \quad (24)$$

By plotting  $K_k$  vs.  $\theta$  one gets

$$K_k = 7.80(1 + \theta^{1.7} - 2\theta^{3.4}) \quad (25)$$

Equation (23) then becomes

$$E_k = D_e + 7.80u_k^{1.12}(1 + \theta^{1.7} - 2\theta^{3.4}) \quad (26)$$

Figures 9a, b show the fit of experimental data to the velocity and position functions.

Equation (26) represents the data for the system investigated in this work. The equation is restricted to the system studied, since no general variation of column or packing size was considered, that is the  $D_e/D_i$  parameter. However the general technique of determining velocity and position functions on an empirical basis seems to be a sound approach. Equation (26) can be used to predict diffusivity for the system from a knowledge of the velocity distribution.

The variation of eddy diffusivity with radial position can be interpreted theoretically on the basis of the Prandtl mixing-length definition of diffusivity as the product of deviating velocity and eddy mixing length. Since point velocity and void space, characterizing the deviating velocity and mixing length, both increase near the wall, the diffusivity increases. Near the wall velocity decreases rapidly to zero, while void space increases to unity. The preponderant effect of diminishing velocity decreases diffusivity. Figure 9b however illustrates the residual dependence of diffusivity on void space, since the velocity effect has been isolated from the defining function.

#### CONCLUSIONS

Mass transfer in packed beds can be described as consisting of parallel- and eddy-transfer mechanisms. The molecular contribution is invariant with the physical system and is the sole mechanism operating at very low Reynolds number. The eddy contribution, considered on a point basis, is found to vary with local flow conditions and can be defined on the basis of these flow conditions. From empirical relations eddy diffusivity can be predicted in terms of point velocity, an easily measured operating variable.

The variation of eddy diffusivity can be explained on the basis of velocity and void space variation within the system.

#### ACKNOWLEDGMENT

This paper is based on a master of science thesis by V. P. Dorweiler, presented to Iowa State College in December, 1956. Work was performed in the Ames Laboratory of the U. S. Atomic Energy Commission.

The authors wish to express their appreciation to the Ames Laboratory of the Atomic Energy Commission for the support of this project.

#### NOTATION

$A$  = constant in series solution, area  
 $C$  = concentration, volume % carbon dioxide in air  
 $C_A$  = measured average concentration  
 $C_f$  = concentration of pure carbon dioxide in injection tube  
 $C_M$  = integral average concentration  
 $C_o$  = concentration at column center  
 $D_p$  = pellet diameter, in.

$D_i$  = tube diameter, in.  
 $D_e$  = molecular diffusivity, sq. ft./hr.  
 $E$  = eddy diffusivity, sq. ft./hr.  
 $E$  = total effective diffusivity, sq. ft./hr.  
 $G$  = mass velocity, lb./sq. ft./hr.  
 $h$  = interval size in numerical solution  
 $J_0$  = zero-order Bessel function of first kind  
 $J_1$  = first-order Bessel function of first kind  
 $k$  = number of position of radial point  
 $K$  = position function of eddy diffusivity  
 $K_k$  = constant for given radial position  
 $n$  = index of summation  
 $N$  = total number of intervals in numerical solution  
 $N_{Pe}$  = Peclet number,  $D_p V/E$   
 $N_{Re'}$  = modified Reynolds number,  $D_p G/(\mu/\rho D_e)$   
 $(N_{Sc})_M$  = Schmidt number,  $\mu/\rho D_e/D_M$   
 $P_k$  = weight function in numerical solution =  $u_k \theta_k$   
 $r$  = radial distance from center of bed, with  $r_o$  the tube radius, in.  
 $R$  = eigen function representing the radial variation of concentration  
 $R_z$  = correlation coefficient  
 $t$  = radius of injector tube, in.  
 $u$  = superficial point velocity, ft./sec.  
 $V$  = superficial average velocity, ft./sec.  
 $z$  = height of packed bed above injector tube, in.  
 $Z$  = function representing the axial variation of concentration

#### Greek Letters

$\alpha$  = ratio of  $V/E$ , ft.<sup>-1</sup>  
 $\beta_n r_o$  = roots of  $J_1(\beta_n r_o) = 0$   
 $\delta$  = void fraction  
 $\lambda$  = eigen constant in numerical solution  
 $\rho$  = density, lb./cu. ft.  
 $\theta$  = dimensionless radial position term,  $r/r_o$   
 $\mu$  = absolute viscosity, lb. mass/ft./sec.

#### LITERATURE CITED

1. Fahien, Raymond W. and J. M. Smith, *A.I.Ch.E. Journal*, **1**, 28 (1955).
2. Bernard, R. A., and R. H. Wilhelm, *Chem. Eng. Progr.*, **46**, 233 (1950).
3. Schwartz, Clarence E., and J. M. Smith, *Ind. Eng. Chem.*, **45**, 1209 (1953).
4. Kurihara, Hiroo M., M.S. thesis, Purdue Univ., Lafayette, Indiana (1954).
5. Towle, W. L., and T. K. Sherwood, *Ind. Eng. Chem.*, **31**, 457 (1939).
6. Schaffer, Michael R., M.S. thesis, Purdue Univ., Lafayette, Indiana (1952).
7. Sherwood, T. K., and R. L. Pigford, "Absorption and Extraction," McGraw-Hill, New York (1952).
8. Latinen, George A., Ph.D. thesis, Princeton Univ., Princeton, New Jersey (1954).

Manuscript received January 7, 1958; revision received August 4, 1958; paper accepted August 6, 1958.

# Axial Mixing and Extraction Efficiency

C. A. SLEICHER, JR.

Shell Development Company, Emeryville, California

The effect of back mixing of either phase in an extraction column, which decreases the extraction efficiency, is analyzed theoretically by means of an idealized diffusion model that can be characterized by four dimensionless parameters: a Peclet number of each phase, a mass transfer number, and the usual extraction factor. Calculations for a wide range of these parameters were performed on a digital computer.

The principal results, presented in a table, will be useful in the design and scale up of extraction columns and in the interpretation of experimental results from extractors and from some reactors in which a first-order reaction occurs.

Circulation and back mixing, or axial mixing, in extraction columns reduce the number of theoretical stages (efficiency). If the back mixing is very severe, the column may extract less than would one theoretical stage. Ideally each phase should flow with no axial mixing; that is it should be in plug flow. In practice, however, there is always some axial mixing. For most extraction-column designs, operating conditions that give high rates of interphase mass transfer give appreciable axial mixing. Failure to account for axial mixing may lead to column-height or packing-efficiency correlations that scatter badly or that may give large errors when extrapolated to large packing or column diameter. In this paper the effect of axial mixing on the efficiency of countercurrent extraction columns is analyzed theoretically by means of an idealized diffusion model.

Despite the realization that back mixing decreases extraction efficiency, there was little mention of it in the literature until 1950. In that year Morello and Poffenberger (7) and Geankoplis and Hixson (2) noted the existence of back mixing, especially in spray towers. The significance of the mixing to extraction efficiency, however, was not clearly stated until 1952 (8). Later work (1, 3, 4) included experimental measurements of local mass transfer coefficients and concentration gradients in extraction columns in which there was appreciable back mixing of the continuous phase. All this work was carried out in spray or packed

columns. In 1954 Vermijs and Kramers (12) noted some effects of back mixing in a rotating-disk column. In no case, however, was there any attempt to characterize quantitatively the axial mixing of either phase. Furthermore at the time this work was begun there had not appeared an experimental or theoretical analysis relating efficiency to back mixing.

A recent Atomic Energy Commission report (6) gives some theoretical results for special cases, and a supplement to the report (5), which appeared as this paper was being prepared, contains many numerical results. The equations given in these reports are essentially the same as those given here. Furthermore axial concentration profiles are tabulated in the supplement (5); whereas in this paper only the exit concentrations are tabulated. It was nevertheless thought worthwhile to publish the results given here because a somewhat broader range of parameters was investigated, the interpretation of the assumptions and applicability of the results is different, and the method of solving the equations is quite different. In the A.E.C. report the emphasis is on the use of the analysis for interpretation of experimental results, whereas in this paper emphasis is on the scale-up problem.

## ANALYSIS

The effect of back mixing on efficiency is presented here for continuous, countercurrent extraction with feed and solvent

introduced at opposite ends of the column. The calculation is based on a three-component system and an idealized diffusion model, the eight principal assumptions in the analysis being

1. The back mixing of each phase may be characterized by a constant axial diffusion coefficient.
2. The end conditions usually assumed (13) for models of this type are applicable [Equations (4) through (7)].
3. The mean velocity and concentration of each phase are constant across that part of the column diameter which is occupied by the phase.
4. The solvent and solute-free raffinate are immiscible (or their solubility does not vary with solute concentration and hence height).
5. The volume rates of the solvent and feed phases do not change with height.
6. The distribution coefficient (equilibrium ratio) is constant; that is, it is not a function of concentration.
7. The product of the mass transfer coefficient and the interfacial area per unit tower volume is constant throughout the column.
8. The gradients of solute concentration in each phase are continuous; that is, there are no discontinuities as would occur in a series of discrete well-mixed stages.

Figure 1 shows the notation and the model based on these assumptions. More detailed notation and the notation of Miyauchi (6) are given at the end of the paper. Material balances around each





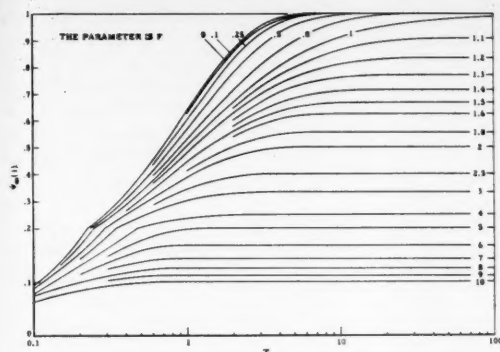


Fig. 3. Extraction with plug flow of each phase (no back mixing,  $P_e = R = \infty$ ).

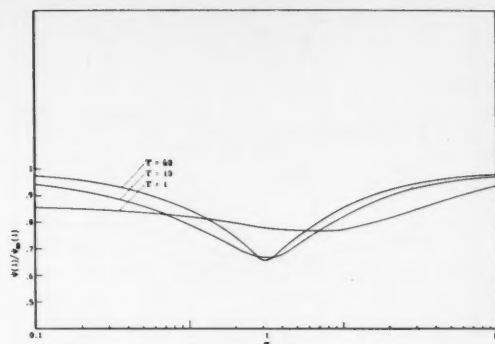


Fig. 4. Change of  $\psi(1)/\psi_\infty(1)$  with  $F$ ,  $P = R = 2$ .

A more complete table has been deposited with the A.D.I.\* In the A.D.I. table the two rather special cases for  $F = 0$  and for  $P = 55$  with  $R = .001$  are at the head of the table, whereas the remaining cases are tabulated in an orderly pattern. The solutions for  $P = R = \infty$  and  $P = R = 0$  have not been tabulated, but they are easily found from Equations (20) and (21). For reference the former is graphed in Figure 3, and the latter is within 1% of the case of  $P = R = .05$ .

The range of  $P$  and  $R$  covered is .05 to 55. The exact solutions for one well-mixed stage ( $P = R = 0$ ) differ from the solutions for  $P = R = .05$  by less than 1%. At high  $P$  however the  $\psi(1)$  for  $R = .05$  and  $R = 0$  differ by more than 1%, and so in this range  $\psi(1)$  was calculated for  $R = .001$  and .0001. These solutions differ by less than 0.1% and therefore probably differ from the solutions for  $R = 0$  by much less than 1%. Solutions for  $R = .001$  are given in the A.D.I. table. At high  $P$  however it is unlikely that  $R$  could be as low as .05. Thus for practical purposes Peclet numbers of .05 and 0 are equivalent. Values of  $P$  and  $R$  that are higher than 55 are not reported, because they could not be calculated without writing another program. Now  $\psi(1)$  varies most strongly with high  $R$  when  $F = 1$  and  $P$  is large. In this region  $\psi(1)$  for  $P = R = 55$  differs from  $\psi_\infty(1)$  by at most 5%. For  $F$  less than .8 or greater than 1.2 the difference is less than 2.4%. Thus solutions for  $P$  and  $R$  of 55 are quite close to the limiting case of  $P$  and  $R$  equal to infinity.

The calculations cover a range of  $T$  between 0.1 and 60. It is rare if ever that  $T$  is less than 0.1. It may occasionally be greater than 60, but the difference in  $\psi(1)$  between  $T = 60$  and  $T = \infty$  is very small. At low  $P$  and  $R$  the difference is a maximum at  $F = 0$ , where it is 1.6%; at high  $P$  and  $R$  the difference is

a maximum at  $F = 1$ , where it is also 1.6%.

The range of  $F$  covered is 0 to 10. Although the case of  $F = 0$  is of little interest in extraction, it is included because it corresponds to a reactor in which rate-controlled, first-order reactions of constituents of one phase are catalyzed by a second immiscible phase. The solutions for  $F = 0.8$  and  $F = 1.2$  were found because of the rather rapid change of  $\psi(1)/\psi_\infty(1)$  with  $F$  near  $F = 1$ , which is illustrated in Figure 4 for  $P = R = 2$  and three values of  $T$ . Because of this behavior it was thought that plots of  $\psi(1)$  vs.  $F$  might show peculiarities in the vicinity of  $F = 1$ , but such is not the case.

The density of parameters within the range discussed above is sufficient to allow interpolation with a precision of 1 or 2%. For interpolation in  $F$  near

Accurate interpolation among the four parameters is often required because extractor height is sensitive to the extraction required. Such interpolation is of course laborious and time consuming. A correlation of the results has therefore been developed in which interpolation in  $F$  only is required. The correlation uses the ratio  $T_p/T$ , where  $T_p$  is that value of  $T$  which will accomplish the given extraction in a column with no axial mixing. Now the ratio  $T_p/T$  is equal to  $L_p/L$ , the ratio of height of a plug-flow column to the actual height, and it will therefore be called column efficiency  $E_c$ . A column efficiency of 0.7 can be interpreted to mean that  $1 - 0.7 = 0.3$  is the fraction of required height that is necessary to overcome the effect of axial mixing. If  $E_c$  is known,  $T_p$  can be calculated and used in Equation (20) to find the extent of extraction  $\psi$ .

The correlating equation for  $E_c$  is

$$E_c = \frac{PR}{PR + T[aP + bR + c\sqrt{PR} - d\sqrt{P+R} + g(P-R)e^{-hT}]} \quad (22)$$

where the constants are the following functions of  $F$  only:

$F$	$a$	$b$	$c$	$d$	$g$	$h$
0.1	0.43	0.15	0.31	0.41	-0.305	0.073
0.2	0.47	0.21	0.485	0.59	-0.29	0.085
0.3	0.495	0.27	0.625	0.73	-0.255	0.094
0.4	0.515	0.32	0.75	0.85	-0.22	0.100
0.6	0.55	0.425	0.975	1.07	-0.15	0.115
0.8	0.58	0.52	1.16	1.25	-0.075	0.125
1.0	0.61	0.61	1.31	1.42	0	0.135
1.5	0.675	0.81	1.61	1.78	0.18	0.155
2.0	0.73	1.00	1.85	2.10	0.35	0.172
3.0	0.80	1.38	2.12	2.45	0.64	0.201
4.0	0.845	2.00	2.25	2.65	0.865	0.225

$F = 1$  it is suggested that plots of  $\psi(1)$  vs.  $F$  be used; for interpolation in  $F$  with  $F$  not near unity and for interpolation in  $T$ ,  $P$ , and  $R$  usually greater precision is obtained from plots of  $\psi(1)/\psi_\infty(1)$  vs. the parameter. Such plots have the added conceptual advantage that  $\psi(1)/\psi_\infty(1)$  is a direct measure of the extent to which back mixing decreases extraction; the ratio may be considered a back mixing efficiency.

This empirical equation gives a maximum error of 10% in  $E_c$  and 1.5% in  $\psi$  in the range  $0.1 \leq F \leq 4$ ,  $2 \leq P$  and  $R \leq 55$ ,  $1 \leq T \leq 60$ . These errors are well within the accuracy justified by the assumptions in the analysis. The equation should not be used outside the tested range of parameters, and in particular it should not be used for Peclet numbers less than about 1 or 2.

Figures 5 and 6 illustrate the behavior of extraction efficiency for certain sets

\*Tabular material has been deposited as document 5875 with the American Documentation Institute, Photoduplication Service, Library of Congress, Washington 25, D. C., and may be obtained for \$1.25 for photoprints or \$1.25 for 35-mm. microfilm.



solvent, feed compositions, and flow rates.

Figure 7 is an example of a kind of plot, derived from the data of Table 1, useful to the design engineer. It shows the height of a column in feet vs. the extent of extraction for three values of  $F$ . In this case  $K/V_F$ ,  $U_F/E_F$ , and  $U_s/E_s$  have been assumed constant at 0.5, 1, and 1 ft.<sup>-1</sup> respectively. Such a chart shows clearly the amount that column height must be increased or feed/solvent ratio decreased to effect a given change in extraction.

#### APPLICABILITY OF THE ANALYSIS

The applicability of the analysis is limited by the assumptions listed earlier. Of these, assumptions 3 through 8 need little comment, except a note that their admissibility must be determined in each case. Assumptions 1 and 2 however merit further discussion.

Assumption 1 is that the extraction process may be represented by a diffusion model. Actually axial mixing in the continuous phase of an extraction column is the result of two effects. The first is true turbulent and molecular diffusion in the axial direction. This type of diffusion can be determined by measuring the concentration upstream from a plane of steady injection of a tracer. Second, axial mixing is caused by non-uniform velocity and subsequent radial mixing, which is sometimes called *Taylor diffusion* after G. I. Taylor's analysis of axial mixing in pipes (9, 10, 11). This type of mixing could not be detected by the preceding experiment, but it can be determined, for example, from the spreading of pulse injection of tracers, that is, by measuring the residence-time distribution. Of course this type of experiment will detect the combined effects of the two causes of axial mixing. Both types of diffusion are deleterious in extraction, because both cause a decrease in the net driving force for mass transfer. In the dispersed phase an analogous situation exists. True dispersed-phase diffusion is caused by actual backflow of some drops in a random manner. However the drops also have a spread in residence-time distribution owing to the fact that some drops move faster than others because of the nonuniformity of drop size and of continuous-phase velocity. In addition the residence-time distribution is affected by drop interactions (coalescence, redispersion), which occur even in a nonstaged column.

There are many extraction situations in which Taylor diffusion predominates over eddy diffusion. This would usually occur for example in both phases of packed and spray columns and in both phases of a rotating-disk column operated at high throughput and low rotor speed. In this analysis true eddy diffusion has been assumed, and the question arises as to the conditions under which an eddy-

diffusion coefficient can be used to represent the effect of Taylor diffusion in extraction. At present this question cannot be answered; it can only be pointed out that the conditions will depend on other factors, such as the rate of coalescence and redispersion of the dispersed phase and the rate of radial mixing of the continuous phase. Because of the variation of mass transfer rate and concentration with drop size, they will also depend on drop-size distribution. The most reasonable approach at present is to use an eddy-diffusion coefficient that is related to the downstream spread of a tracer, for that is at least a measure of axial mixing if not of its effect on extraction.

The choice of boundary conditions, assumption 2 and Equations (3) through (6), is really a consequence of the use of a diffusion model. This point and the diffusion and boundary equations have been discussed in detail by Wehner and Wilhelm (13). An analysis which included Taylor diffusion effects would necessarily employ quite different boundary conditions. As  $P$  and  $R$  increase, however, the solutions become less sensitive to the choice of boundary conditions. For  $P$  and  $R$  above about 10 any reasonable boundary conditions will give solutions nearly equal to those for the boundary conditions (3) through (6).

#### ACKNOWLEDGMENT

The author wishes to thank Doris K. Liddke for programming the calculations and the Shell Development Company for permission to publish this material.

#### NOTATION

The letters in parentheses refer to the notation for the equivalent group or parameter of references 5 and 6.

$A = (1 - A_1)$ , coefficient in Equation (13)  
 $a = (a)$ , interfacial area between phases per unit-tower volume  
 $B = (-A_2)$ , coefficient in Equation (13)  
 $C = (-A_3)$ , coefficient in Equation (13)  
 $D = (-A_4)$ , coefficient in Equation (13)  
 $E_i = (E_i)$ , eddy diffusivity of phase  $j$ ,  $j = f$  or  $s$   
 $e_i$  = superficial eddy diffusivity of phase  $j$ ,  $e_i E_j$   
 $F = (A)$ , extraction factor =  $V_F m/V_s$   
 $K = (K_s)$ , over-all mass transfer coefficient based on area  $a$   
 $L$  = column length  
 $m = (m)$ ,  $x/y$  at equilibrium, distribution coefficient  
 $P = (P_s B)$ ,  $V_s L/E_s = U_s L/E_s$ , Peclet number of feed phase based on column length

$R = (P_s B)$ ,  $V_s L/E_s = U_s L/E_s$ , Peclet number of solvent phase based on column length  
 $T = (N_0)$ ,  $KaL/V_F$ , a mass transfer number sometimes called the number of transfer units  
 $T_p$  = piston-flow, or plug-flow, value  
 $U_i = (u_i)$ , velocity of phase  $j$ ,  $j = f$  or  $s$   
 $V_i = (F_i)$ , superficial velocity of phase  $j$ ,  $e_i V_j$   
 $w = (Z)$ ,  $z/L$ , dimensionless distance from feed end of column  
 $x = (c_s)$ , concentration of solute in feed phase  
 $y = (c_s)$ , concentration of solute in solvent phase  
 $z = (z)$ , distance from feed end

#### Greek Letters

$\Gamma = (1 - Y)$ , dimensionless concentration of solvent phase,  $(y - y_i)V_s/(x_i - my_i)V_f$   
 $\epsilon_i = (\epsilon_i)$ , volume fraction or holdup of phase  $j$ ,  $j = f$  or  $s$   
 $\lambda_n = (\lambda_{n+1})$ , exponent in Equation (13)  
 $\psi = (1 - X)$ , dimensionless concentration of feed phase,  $(x_i - x)/(x_i - my_i)$   
 $\psi_\infty = \psi$  for the case of plug flow ( $P = R = \infty$ )

#### Subscripts

$f = (x)$ , feed phase  
 $i = (\text{superscript } 0 \text{ or } L)$ , inlet of either phase  
 $s = (y)$ , solvent phase

#### LITERATURE CITED

1. Cavens, S. D., and J. E. Ewanchyna, *Can. J. Chem. Eng.*, **113** (October, 1957).
2. Geankoplis, C. J., and A. N. Hixson, *Ind. Eng. Chem.*, **42**, 1141 (1950).
3. Gier, T. E., and J. O. Hougen, *ibid.*, **45**, 1362 (1953).
4. Heertjes, P. M., W. A. Holve, and H. Talsma, *Chem. Eng. Sci.*, **3**, 122 (1954).
5. McMullen, A. K., Terukatsu Miyauchi, and Theodore Vermeulen, *UCRL-3911*, Supplement, U. S. Atomic Energy Comm. (1958).
6. Miyauchi, Terukatsu, *ibid.* (1957).
7. Morello, V. S., and Noland Poffenberger, *Ind. Eng. Chem.*, **42**, 1021 (1950).
8. Newman, M. L., *ibid.*, **44**, 2457 (1952).
9. Taylor, G. I., *Proc. Roy. Soc. (London)*, **A219**, 186 (1953).
10. *Ibid.*, **A223**, 446 (1954).
11. *Ibid.*, **A225**, 473.
12. Vermijs, H. J. A., and H. Kramers, *Chem. Eng. Sci.*, **3**, 55 (1954).
13. Wehner, J. F., and R. H. Wilhelm, *ibid.*, **6**, 89 (1956).

Presented at A.I.Ch.E. Atlantic City Meeting. Manuscript received August 27, 1958; revision received November 10, 1958; paper accepted November 10, 1958.

# Effect of a Volume Heat Source on Free-Convection Heat Transfer

I. E. RANDALL and ALEXANDER SESONSKÉ

Purdue University, Lafayette, Indiana

Heat transfer to a horizontal cylinder from an ordinary fluid containing a volume heat source was studied analytically. The first approach to this problem was to assume that the heat source existed only in the boundary layer surrounding the cylinder. By solving the equations for a vertical flat plate cooling the ambient fluid and applying the results to a horizontal cylinder, one could determine the effect of a volume heat source on the heat transfer coefficient for the cylinder case. The variables studied were volume heat sources from 0 to 300 B.t.u./ $(\text{sec.})(\text{cu. ft.})$  and temperature difference across the boundary layer in the range 20° to 100°F.

In the laminar-flow region a volume heat source was found to increase the heat transfer coefficient for any given temperature difference across the boundary layer. This increase, due to the decrease in boundary-layer thickness caused by the volume heat source, was moderate, being about 20% for a 1½-in. O.D. cylinder with a heat source strength of 100 B.t.u./ $(\text{sec.})(\text{cu. ft.})$  and a temperature difference across the boundary layer of 20°F.

## PROBLEM ANALYSIS

The model considered was a horizontal cylinder immersed in an infinite fluid containing a volume heat source. The cylinder surface temperature was maintained lower than the temperature of the surrounding fluid by having a coolant passed through it, and the volume-generated heat thus removed. Since there was no impressed flow on the bulk fluid body, this cooling took place by free convection.

Free-convection heat transfer problems are generally solved with the simultaneous use of the continuity equation, an energy balance, and the appropriate momentum balances in conjunction with boundary-layer theory. The inclusion of a volume heat source in such a problem, however, complicates the physical picture, since at steady state conditions this heat generated at all points in the fluid will have to be removed, necessitating a temperature gradient. Since the fluid density is a function of temperature, a velocity gradient will also be generated throughout the fluid. Boundary-layer theory though assumes that all the temperature and velocity gradients occur in a layer near the body surface, with the rest of the body isothermal and at constant velocity. Since this is not the case with a volume heat source present, the boundary-layer assumptions are not strictly applicable, and their use constitutes an approximation to the true picture.

Many attempts were made therefore to find a suitable model, one in which the boundary-layer theory need not be

used. The initial step was to investigate boundary conditions for the solution. Utilizing the no slip at the tube wall assumption, the authors established the velocity at the wall as zero. Two thermal-boundary conditions were possible however. Either the heat flux at the wall or the temperature variation of the wall could be specified but not both. For the problem under consideration a constant wall temperature was specified with the remainder of the boundary condition necessary for solution dependent on the model used.

At first the cylinder was assumed to be immersed in an infinite domain, a fluid which extends to infinity in every direction. With a volume heat source present, however, the velocity and temperature profiles theoretically do not become constant and hence would have to be known to infinity. This model was therefore rejected because of boundary-condition difficulties.

A model which appeared promising was one having a concentric, perfectly insulated outer cylinder surrounding the tube. Although with this model zero velocity and zero temperature gradient ( $\partial T/\partial r$ ) could be specified at the outer wall, a solution to the equations could not be obtained because of mathematical difficulties encountered; so this model was dropped.

Concurrent with this analytical study experimental work was being carried out as part of the over-all project. While attempts were being made to circumvent the boundary-layer assumptions, tests showed that the temperature and velocity gradients which were expected through the fluid were negligible relative to the larger gradients in the immediate vicinity

of the tube (1). It therefore appeared that the boundary-layer assumptions were valid, and the boundary-layer approximations could be used.

On this evidence a boundary-layer solution, with the assumption that the heat source was present only in the boundary layer, was attempted. Since Hermann (4) presented an exact analytical solution for free convection heat transfer to air having no volume heat source, a check was available for the iteration technique attempted for solution with an Electrodata digital computer. Hermann's equations were converted to difference form and his results used as initial conditions for the iterations. Thus if the iteration technique were to work, the iterations should have converged immediately to the initial conditions. Once this proof of the technique was completed, Hermann's equations could be altered to include the effect of the volume heat source, and the problem could be solved. The iterations however diverged, indicating the need for a lengthy step-size study. The following approximate solution was therefore attempted.

## THEORETICAL SOLUTION DEVELOPMENT

A common technique in the solution of fluid flow-heat transfer problems involving cylinders is to solve a similar problem for a flat plate and by conformal mapping or some other procedure transform the results to the cylinder. This technique is valid owing to the boundary-layer character of the differential equations underlying the theoretical solutions for both cases (4). The technique is used because boundary-layer problems for the

I. E. Randall is with the Atomics International Division of North American Aviation, Inc., Canoga Park, California.



flat-plate geometry are more readily solvable than the ones for the outside of a cylinder. Thus to find heat transfer coefficients to the cylinder, both with and without heat source, flat-plate solutions could be obtained and then transformed to the cylinder. If however the ratio of the heat transfer coefficients for the flat plate were determined instead, this ratio could be applied directly to the cylinder, if the assumption is made that the transformation will introduce errors of equal relative magnitude to both coefficients. This was the procedure followed for this solution, which is described in detail by Randall (10).

The model used was a vertical plate cooling a surrounding infinite still fluid at a constant temperature everywhere except in the boundary layer. The assumptions made were

1. There are no effects longitudinally along the plate; that is the problem is two-dimensional.
2. There is no velocity component perpendicular to the surface of the plate.
3. The buoyant force is the only driving force for fluid flow.
4. The fluid will not slip at the wall.
5. The fluid velocity is zero at the outer edge of the boundary layer.
6. The surface temperature of the plate is constant all over the plate.
7. The thermal and momentum boundary layers are of equal thickness. This assumption is valid for fluids having a Prandtl number close to 1.0, a condition approached by water in the 300° to 600°F. range.

In addition Eckert's (2) temperature and velocity profiles were assumed in the boundary layer. These profiles are shown in Figure 1. The defining equations for them are

$$\phi = \theta \left(1 - \frac{y}{\delta}\right)^2$$

$$u = \omega \frac{y}{\delta} \left(1 - \frac{y}{\delta}\right)^2$$

The boundary conditions for this problem were

$$\begin{aligned} \text{at } y = 0, \quad u = 0, \quad \phi = \theta \\ \text{at } y = \delta, \quad u = 0, \quad \phi = 0 \end{aligned}$$

The assumed profiles were shown to be in good agreement with the experimental profiles of Schmidt and Beckmann (7).

Two balances were used to obtain the solution, a momentum balance and an energy balance. The momentum balance was obtained by the use of the von Karman approximate method shown in reference 2.

$$\frac{d}{dx} \int_0^\delta u^2 dy$$

$$= g\beta \int_0^\delta \phi dy - \nu \left(\frac{du}{dy}\right)_{y=0} \quad (1)$$

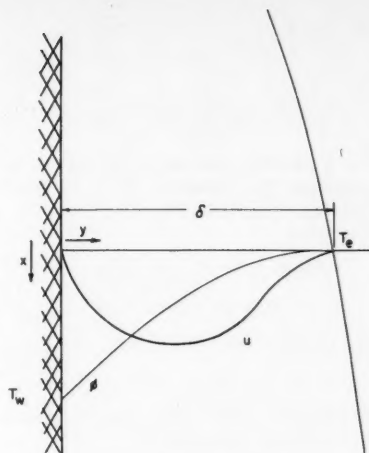


Fig. 1. Assumed velocity and temperature profiles.

In a similar fashion the energy balance was obtained:

$$\begin{aligned} \rho C_p \frac{d}{dx} \int_0^\delta T u dy \\ - \rho C_p \frac{d}{dx} \int_0^\delta T u dy \\ + \int_0^\delta q''' dy + k \left(\frac{dT}{dy}\right)_{y=0} = 0 \end{aligned}$$

Dividing through by  $\rho C_p$  one obtains

$$\frac{d}{dx} \int_0^\delta \phi u dy \quad (2)$$

$$= -\alpha \left(\frac{d\phi}{dy}\right)_{y=0} - \frac{q'''}{\rho C_p} \delta$$

since  $\phi = T_e - T$  and  $\alpha = k/\rho C_p$

The volume heat-source term  $q'''$  can be taken out from under the integral sign, since it is considered uniform throughout the boundary layer and is therefore a constant.

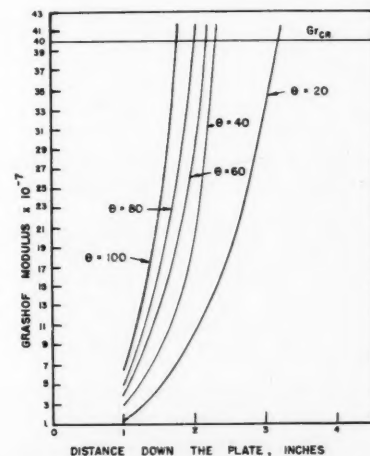


Fig. 2. Variation of Grashof modulus with  $x$  at parametric temperature differences.

The expressions for  $\phi$  and  $u$  were then substituted into Equations (1) and (2) and integrated and differentiated. The resulting equations were

$$\frac{1}{105} \frac{d}{dx} (\omega^2 \delta) = \frac{1}{3} g\beta \theta \delta - \nu \frac{\omega}{\delta} \quad (3)$$

$$\begin{aligned} \frac{1}{30} \theta \frac{d}{dx} (\omega \delta) - \frac{2\alpha\theta}{\delta} \\ + \frac{1}{\rho C_p} q''' \delta = 0 \end{aligned} \quad (4)$$

Next the equations were rendered dimensionless by defining the quantities

$$\begin{aligned} \Delta &= \left(\frac{g\beta\theta}{\nu^2}\right)^{1/3} \delta \\ \Omega &= (g\beta\theta\nu)^{-1/3} \omega \\ X &= \left(\frac{g\beta\theta}{\nu^2}\right)^{1/3} x = (N_{Gr})^{1/3} \\ K &= \left[\frac{\nu^{1/3}}{(g\beta)^{2/3} \theta^{5/3}}\right] \frac{q'''}{\rho C_p} \end{aligned} \quad (5)$$

When one substitutes expressions (5) into Equations (3) and (4), the equations become

$$\frac{1}{105} \frac{d}{dX} (\Omega^2 \Delta) = \frac{1}{3} \Delta - \frac{\Omega}{\Delta} \quad (6)$$

$$\frac{1}{30} \frac{d}{dX} (\Omega \Delta) - \frac{2}{N_{Pr}} \frac{1}{\Delta} + K \Delta = 0 \quad (7)$$

This pair of simultaneous equations was then solved by a variation of the method of Frobenius (8).

$\Omega$  and  $\Delta$  were expanded in the MacLaurin series.

$$\begin{aligned} \Omega(X, N_{Pr}, K) \\ = \sum_{n=0}^{\infty} K^n \Omega_n(X, N_{Pr}) \\ \Delta(X, N_{Pr}, K) \\ = \sum_{n=0}^{\infty} K^n \Delta_n(X, N_{Pr}) \end{aligned} \quad (8)$$

Substituting these series into Equations (6) and (7) and collecting terms of like coefficient, one gets

$$\begin{aligned} K^0 \left[ \frac{1}{105} \frac{d}{dX} (\Omega_0^2 \Delta_0) - \frac{\Delta_0}{3} + \frac{\Omega_0}{\Delta_0} \right] \\ + K^1 \left[ \frac{1}{105} \frac{d}{dX} (\Omega_0^2 \Delta_1 + 2\Omega_0 \Omega_1 \Delta_0) \right. \\ \left. - \frac{1}{3} \Delta_1 \frac{\Omega_1}{\Omega_0} - \frac{\Omega_0 \Delta_1}{\Delta_0^2} \right] \\ + K^2 \left[ \text{many termed expression} \right] \\ + K^3 \left[ \text{many termed expression} \right] + \dots = 0 \end{aligned} \quad (9)$$

$$\begin{aligned}
& K^0 \left[ \frac{1}{30} \frac{d}{dx} (\Omega_0 \Delta_0) - \frac{2}{N_{Pr}} \frac{1}{\Delta_0} \right] \\
& + K^1 \left[ \frac{1}{30} \frac{d}{dx} (\Omega_0 \Delta_2 + \Omega_1 \Delta_1 + \Omega_2 \Delta_0) \right. \\
& \quad \left. - \frac{2}{N_{Pr}} \left[ \frac{\Delta_1^2}{\Delta_0^3} - \frac{\Delta_2}{\Delta_0^2} \right] + \Delta_1 \right] \\
& + K^2 \left[ \text{many termed expression} \right] \\
& + K^3 \left[ \text{many termed expression} \right] + \dots = 0 \quad (10)
\end{aligned}$$

If an entirely general solution were to be obtained for Equations (9) and (10), the quantities in the brackets had to be equal to zero. Therefore if the terms having like coefficients in Equations (9) and (10) were taken together, they formed a set of two simultaneous equations

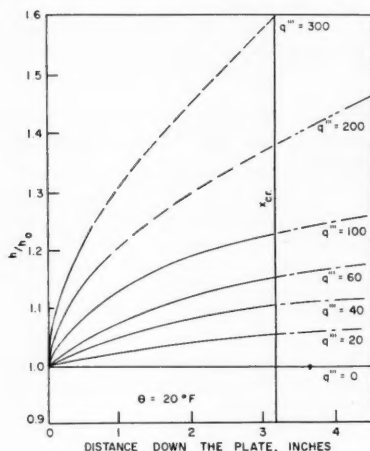


Fig. 3. Variation of  $h/h_0$  with  $x$  for parametric volume heat sources.

tions from which the values of  $\Omega_n$  and  $\Delta_n$  were calculated. For example the terms whose coefficient is  $K^0$  are

$$\begin{cases} \frac{1}{105} \frac{d}{dX} (\Omega_0^2 \Delta_0) - \frac{\Delta_0}{3} + \frac{\Omega_0}{\Delta_0} = 0 \\ \frac{1}{30} \frac{d}{dX} (\Omega_0 \Delta_0) - \frac{2}{N_{Pr}} \frac{1}{\Delta_0} = 0 \end{cases} \quad (11)$$

A solution of the form

$$\begin{cases} \Omega_0 = C_1 X^n \\ \Delta_0 = C_2 X^n \end{cases} \quad (12)$$

was assumed.

When one substituted expressions (12) into (11), the following equations resulted:

$$\begin{aligned}
& \frac{2m+n}{105} C_1^2 C_2 X^{2m+n-1} \\
& - \frac{C_2 X^n}{3} + \frac{C_1}{C_2} X^{m-n} = 0 \quad (13)
\end{aligned}$$

$$\begin{aligned}
& \frac{m+n}{30} C_1 C_2 X^{m+n-1} \\
& - \frac{2}{C_2 N_{Pr}} X^{-n} = 0 \quad (14)
\end{aligned}$$

For a perfectly general solution of these equations the exponents of  $X$  for each equation must be equal.

Therefore

$$2m + n - 1 = n = m - n$$

$$m + n - 1 = -n$$

and  $m$  and  $n$  are

$$m = 1/2; \quad n = 1/4$$

Substituting these values into Equations (13) and (14), one obtains

$$\begin{cases} \frac{1.25}{105} C_1^2 C_2 - \frac{C_2}{3} + \frac{C_1}{C_2} = 0 \\ \frac{0.75}{30} C_1 C_2 - \frac{1}{C_2 N_{Pr}} = 0 \end{cases}$$

The latter equations were solved simultaneously for  $C_1$  and  $C_2$  with the results

$$C_1 = 2[0.143 + 0.150 N_{Pr}]^{-1/2}$$

$$C_2 = 3.94 N_{Pr}^{-1/2} [0.953 + N_{Pr}]^{1/4}$$

Therefore

$$\Omega_0 = 2[0.143 + 0.150 N_{Pr}]^{-1/2} X^{1/2}$$

$$\Delta_0 = 3.94 N_{Pr}^{-1/2} [0.953 + N_{Pr}]^{1/4} X^{1/4}$$

A similar procedure was used to calculate  $\Omega_1$ ,  $\Omega_2$ ,  $\Delta_1$ , and  $\Delta_2$ . From Equations (9) and (10) it should be noted that to calculate values for  $\Omega_n$  and  $\Delta_n$ , the values of  $\Omega_0$  through  $\Omega_{n-1}$  and  $\Delta_0$  through  $\Delta_{n-1}$  must be known.

The results of these calculations were

$$\Omega_n = [g_n(N_{Pr}) X^{n/2}] X^{1/2}$$

$$\Delta_n = [f_n(N_{Pr}) X^{n/2}] X^{1/4}$$

and

$$\Omega = \sum_{n=0}^{\infty} K^n g_n(N_{Pr}) X^{n/2} X^{1/2} \quad (15)$$

$$\Delta_0 = \sum_{n=0}^{\infty} K^n f_n(N_{Pr}) X^{n/2} X^{1/4} \quad (16)$$

Values of  $g_n$  and  $f_n$  were calculated through  $n = 2$ , where the series were truncated.

It should be noted here that the solutions for  $\Omega_0$  and  $\Delta_0$  are quite similar to Eckert's (2) solutions for a vertical flat plate without volume heat source. The remainder of the terms in the respective series must express the effect of this source.

The following derivation was used to obtain the heat transfer coefficients.

Fourier's law states that

$$q = -k \left( \frac{d\phi}{dy} \right)_{y=0} \quad (17)$$

Since  $\phi$  is defined as

$$\phi = \theta \left( 1 - \frac{y}{\delta} \right)^2$$

then

$$\left( \frac{d\phi}{dy} \right)_{y=0} = -\frac{2\theta}{\delta} \quad (18)$$

Therefore

$$q = \frac{2k\theta}{\delta} \quad (19)$$

The heat transfer coefficient is defined by the equation

$$q = h\theta$$

Substituting this in Equation (19) one got

$$h = \frac{2k}{\delta} \quad (20)$$

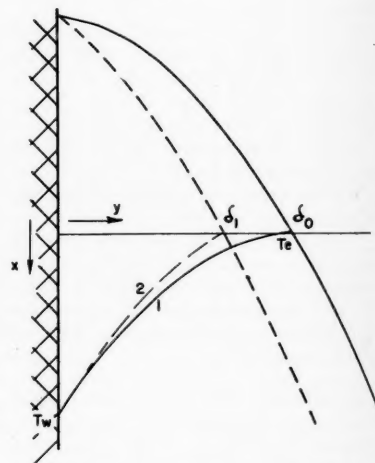


Fig. 4. Effect on the boundary-layer thickness of a volume heat source.

The ratio of the heat transfer coefficient with volume heat source to the coefficient without the heat source is therefore

$$\frac{h}{h_0} = \frac{\frac{2k}{\delta}}{\frac{2k}{\delta_0}} = \frac{\delta_0}{\delta}$$

Since  $\Delta$  is defined as  $[(g\beta\theta)/\nu^2]^{1/3} \delta$ , substituting in the corresponding  $\Delta$ 's one got

$$\frac{h}{h_0} = \frac{\Delta_0 \left[ \frac{g\beta\theta}{\nu^2} \right]^{-1/3}}{\Delta \left[ \frac{g\beta\theta}{\nu^2} \right]^{-1/3}} = \frac{\Delta_0}{\Delta}$$

Therefore

$$\frac{h}{h_0} = \frac{C_2 X^{1/4}}{\sum_{n=0}^{\infty} K^n f_n(N_{Pr}) X^{n/2} X^{1/4}}$$

and

$$\frac{h}{h_0} = \frac{C_2}{\sum_{n=0}^{\infty} K^n f_n(N_{Pr}) X^{n/2}} \quad (21)$$

When one substitutes for  $C_2$  the equivalent function of  $N_{Pr}$ , and notes that  $X = (N_{Gr})^{1/3}$ , Equation (22) is obtained.

$$\frac{h}{h_0} = \frac{3.94 N_{Pr}^{-1/2} [0.953 + N_{Pr}]^{1/4}}{\sum_{n=0}^{\infty} K^n f_n(N_{Pr}) [N_{Gr}]^{n/6}} \quad (22)$$

## RESULTS

The effectiveness of the volume heat source could best be evaluated from the derived equations when one carries out a parametric study. Variables studied were

$$\frac{h}{h_0} = \frac{3.88}{3.88 - 1.78 q''' \theta^{-3/2} x^{1/2} + 0.886 [q''']^2 \theta^{-3} x} \quad (25)$$

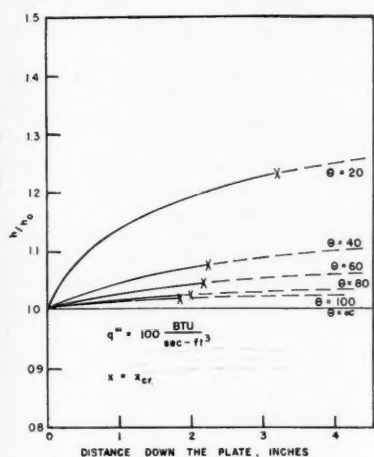


Fig. 5. Variation of  $h/h_0$  with  $x$  for parametric temperature differences.

temperature difference, magnitude of the heat source, and tube size. The parameter study was conducted about a single fluid condition, 1 atm. and 200°F., where a number of properties are fairly constant as a function of temperature. Although a solution of some uranium compound would be necessary to provide the volume heat source, the properties of pure water at these conditions were assumed. The Prandtl number, which was not treated as a variable in this study, was equal to 1.70. With these data expressions (5) yielded

$$\begin{aligned} \Omega &= 3.17 X^{1/2} - 7.25 K X \\ &\quad - 6.17 K^2 X^{3/2} \\ \Delta &= 3.88 X^{1/4} - 12.91 K X^{3/4} \\ &\quad + 46.5 K^2 X^{5/4} \end{aligned}$$

When the numerical values of  $C_2$  and

$f_n$  are substituted into Equation (21), the equation becomes

$$\frac{h}{h_0} = \frac{3.88}{3.88 - 12.91 K X^{1/2} + 46.5 K^2 X} \quad (23)$$

When one uses the physical properties,  $K$  and  $X$  become

$$K = \frac{v^{1/3} q'''}{(g\beta)^{2/3} \theta^{5/3} \rho C_p} = 4.30 \times 10^{-3} \theta^{-5/3} q''' \quad (24)$$

$$X = \left[ \frac{g\beta\theta}{v^2} \right]^{1/3} x = 1023 \theta^{1/3} x$$

On substitution of expressions (24) into Equation (23), one obtained

$$\frac{h}{h_0} = \frac{3.88}{3.88 - 1.78 q''' \theta^{-3/2} x^{1/2} + 0.886 [q''']^2 \theta^{-3} x} \quad (25)$$

When one used Equation (25), two sets of calculations were performed, one for  $\theta$  constant and  $q'''$  as a parameter and the second for  $q'''$  constant and  $\theta$  a parameter.

As a guide in the determination of applicable combinations of  $\theta$  and  $x$ , where the flow in the boundary layer would be laminar as assumed in the derivation, Grashof numbers were calculated. Figure 2 shows the variation of  $N_{Gr}$  with  $x$  for parametric  $\theta$ 's. Eckert and Soehngen (3) found that for a vertical flat plate the incidence of turbulence for free-convection flow is characterized by a critical Grashof number of  $4 \times 10^6$  (Figure 2).

For the first set of calculations, where  $\theta$  is a constant and  $q'''$  a parameter, the values of the temperatures were taken as  $T_w = 190^\circ\text{F}$ . and  $T_e = 210^\circ\text{F}$ . Substituting  $\theta = 20^\circ\text{F}$  into Equation (25) and using parametric values of  $q'''$ , one obtained the curves of  $h/h_0$  vs.  $x$  shown in Figure 3. Turbulence will occur at  $x_{cr} = 3.2$ , beyond which the calculations are not valid. Since maximum was obtained to the left of  $x_{cr}$  for  $q''' = 200$  and  $q''' = 300$ , extrapolated expected results are shown as dotted lines for these two cases.

The physical explanation for the increase in heat transfer coefficient by the inclusion of a volume heat source with a constant  $\theta$  or  $T_e - T_w$  is shown in Figure 4, where curve 1 shows the temperature profile without a heat source. The inclusion of the heat source raises the temperature of the fluid at every point in the boundary layer, resulting in the higher temperature profile, curve 2. Since the heat transfer coefficients are being compared at constant  $T_e - T_w$ ,  $\delta_1$  will be less than  $\delta_0$ , and therefore  $h/h_0 > 1$ .

Figure 5 shows that for constant  $q'''$  an increase in  $\theta$  lowers the curve of  $h/h_0$  vs.  $x$ . This is explained in Figure 6, where curves 1 and 2 and the values  $\delta_0$ ,  $\delta_1$ ,  $T_w$ , and  $T_e$  are the same as in Figure 4. If the wall temperature is now lowered

to  $T_w'$ , curve 3 is the nonheat-source temperature profile. Including the heat source in the boundary layer will raise the temperature profile to curve 4. Since the value of the heat source remains constant at constant  $y$ , the differences between curves 1 and 2 and curves 3 and 4 are the same. The temperature increase between the latter curves is however of smaller relative magnitude to  $\theta$  than in the case of the former curves. Thus curve 4 has the value  $T_e$  at a larger value of  $y$  than does curve 2;  $\delta_0/\delta_1 > \delta_0/\delta_2$ , and  $h/h_0$  is less for the greater  $\theta$ .

## APPLICATION TO CYLINDER

The foregoing analysis for a vertical plate may be applied to a cylinder by the use of the procedure followed by Hermann (4), who established a hydrodynamic and thermal comparison between the two cases for free convection.

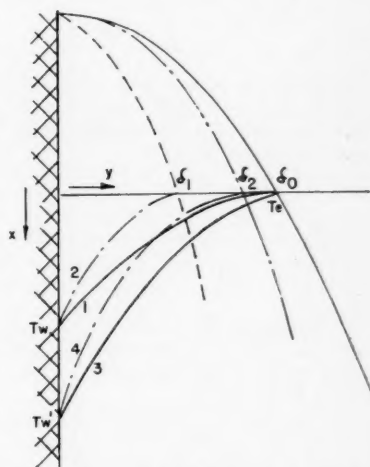


Fig. 6. Effect on the boundary-layer thickness of increasing the temperature difference at a constant heat-source value.

Although differences exist in the behavior of the boundary layer for each case, the differential equations are of similar form, and relations can therefore be set up between the two cases. By the introduction of calculated azimuth functions, Hermann represented cylinder variables in a dimensionless basis similar to those used for plates.

For equivalent hydrodynamic conditions, which he showed to exist when the Grashof number of the plate was equal to that of the cylinder, Hermann developed the following Nusselt number ratio:

$$\frac{N_{Nu}(\text{cylinder})}{N_{Nu}(\text{plate})} = 0.777$$

This is in fair agreement with an experimental ratio for air of 0.87 as given by Jakob (5). Since  $N_{Nu}$  is proportional to  $N_{Gr}^{1/4}$ , these ratios can be rearranged to

yield the plate-height to cylinder-diameter ratio when the heat transfer coefficients are equal. Hermann's ratio yields a height to diameter ratio of 2.76, and Jakob's ratio yields 1.75. For this study a ratio of 2.5 was used as suggested by Eckert (2), which represents a compromise between experimental and analytical results.

In the application of the results it has been assumed that the ratio  $h/h_0$  will remain unchanged for an equivalent cylinder system. For cylinders of practical dimensions the magnitude of the uncertainty in the plate-height to cylinder-diameter ratio has a minor effect on the results.

The average ratio of heat transfer coefficients from 0 to  $x$  on the plate, which is equivalent to the average from 0 to  $2.5 D$ , is

$$\left(\frac{h}{h_0}\right)_{avg} = \frac{\int_0^{2.5D} \frac{h}{h_0} dx}{\int_0^{2.5D} dx} \quad (28)$$

Thus for a  $1/4$ -in. O.D. horizontal cylinder with  $\theta = 20^\circ\text{F}$ . and  $q''' = 60$  B.t.u./ $(\text{sec.})(\text{cu. ft.})$ , by graphical integration of Figure 3

$$\left(\frac{h}{h_0}\right)_{avg} = \frac{\int_0^{0.0521} \left(\frac{h}{h_0}\right) dx}{\int_0^{0.0521} dx} = 1.022$$

The limitation due to the incidence of turbulence will then determine the size of the cylinder that the results can be applied to for any  $\theta$ .

For example for  $\theta = 20^\circ\text{F}$ . the largest cylinder to which the results will apply is 1.28 in. in diameter; for  $\theta = 100^\circ\text{F}$ . the largest cylinder is 0.720 in. in diameter.

#### LIMITATIONS ON RESULTS

The denominator of Equation (25) is an infinite series defined by Equation (8) which was truncated to permit evaluation. A general expression for  $\Delta_n(X, Pr)$  must be determined from the solution of simultaneous equations of like coefficient arising from Equations (9) and (10). Direct analytical solutions for these equations however could not be obtained. Thus a general analytic term for  $\Delta_n(X, Pr)$  and therefore for the series could not be obtained. This eliminated the application of the usual tests for convergence of infinite series.

However it was agreed (6) that the series was similar to one analyzed by Lefschetz and that it would indeed converge. Until the general term is found, though, perhaps numerically, the radius of convergence is indeterminate.

It should be recognized that the truncation used is quite common for an integral solution following the Karmann-Pohl-

hausen approach. Sparrow and Gregg (9) for example discuss convergence of a similar series and conclude that the truncation error is negligible.

#### CONCLUSIONS

1. With a volume heat source present in a fluid being cooled by free convection the heat transfer coefficient will be slightly higher than its value with no heat source present. This is due to the decrease in boundary-layer thickness caused by the inclusion of the volume heat source.

2. For parametric values of the temperature difference across the boundary layer an increase in the value of the volume heat source increases the ratio of the heat transfer coefficients ( $h/h_0$ ) for a given cylinder diameter.

3. For parametric volume heat-source magnitudes an increase in the temperature difference across the boundary layer decreases the ratio of the heat transfer coefficients for a given cylinder diameter.

4. As the cylinder diameter increases, the incidence of turbulence occurs at smaller values of the temperature difference across the boundary layer.

#### ACKNOWLEDGMENT

This work was carried out under the auspices of the United States Atomic Energy Commission, Contract AT(11-1)-432.

The authors are grateful to E. M. Sparrow of the National Aeronautics and Space Administration for many helpful suggestions.

#### NOTATION

- $C$  = constant;  $C_1, C_2$ , etc., constant in the solution of differential equations.  
 $C_p$  = heat capacity at constant pressure, B.t.u./ $(\text{lb.})(^\circ\text{F.})$   
 $D$  = diameter, ft.  
 $f_n$  = algebraic expression  
 $g$  = acceleration due to gravity, ft./sec.<sup>2</sup>  
 $g_n$  = algebraic expression  
 $N_{Gr}$  = Grashof modulus ( $= g\beta\theta x^3/\nu^2$ )  
 $h$  = heat transfer coefficient with volume heat source;  $h_0$ , without volume heat source, B.t.u./ $(\text{sec.})(\text{sq. ft.})(^\circ\text{F.})$   
 $k$  = thermal conductivity, B.t.u./ $(\text{sec.})(\text{sq. ft.})(^\circ\text{F.}/\text{ft.})$   
 $K$  = heat-source function =

$$\left[ \frac{\nu^{1/3}}{(g\beta)^{2/3}\theta^{5/3}} \right] \left[ \frac{q'''}{\rho C_p} \right]$$

dimensionless

$N_{Pr}$  = Prandtl modulus ( $= \nu/\alpha$ ), dimensionless

$q$  = heat flux at a wall, B.t.u./ $(\text{sq. ft.})(\text{sec.})$

- $q'''$  = volume heat source, B.t.u./ $(\text{cu. ft.})(\text{sec.})$   
 $r$  = distance in the radial direction, ft.  
 $r_0$  = outer radius of the cylinder, ft.  
 $T$  = temperature at any point;  $T_w$ , wall temperature;  $T_1$ , reference temperature;  $T_\infty$ , temperature of the environment,  $^\circ\text{F.}$   
 $u$  = velocity in the  $x$  direction, ft./sec.  
 $x$  = distance;  $x_{cr}$ , critical distance for turbulent flow, ft.  
 $X$  = distance function ( $= (g\beta\theta/\nu^2)^{1/3}x$ ), dimensionless  
 $y$  = distance, ft.

#### Greek Letters

- $\alpha$  = Thermal diffusivity ( $= k/\rho C_p$ ), sq. ft./sec.  
 $\beta$  = density coefficient of expansion  $\rho(t) = \rho(t_0)(1 - \beta(t - t_0))$ ,  $1/^\circ\text{F.}$   
 $\delta$  = boundary-layer thickness;  $\delta_0$ , without volume heat source;  $\delta_1$ ,  $\delta_2$ , with volume heat source, ft.  
 $\Delta$  = boundary-layer thickness function ( $= (g\beta\theta/\nu^2)^{1/3}$ ), dimensionless  
 $\Delta_0, \Delta_1, \dots, \Delta_n$  = coefficients of an infinite series  
 $\theta$  = Temperature function ( $T_\infty - T_w$ ); in body force term ( $T - T_1$ ),  $^\circ\text{F.}$   
 $\nu$  = kinematic viscosity, sq. ft./sec.  
 $\rho$  = density, lb./cu. ft.  
 $\phi$  = temperature function ( $T_\infty - T$ ),  $^\circ\text{F.}$ ; angular coordinate in polar coordinate, radians.  
 $\omega$  = proportionality constant, ft./sec.  
 $\Omega$  = proportionality constant function  $= [(g\beta\theta/\nu^2)^{1/3}]$ , dimensionless  
 $\Omega_0, \Omega_1, \dots, \Omega_n$  = coefficients of an infinite series

#### LITERATURE CITED

- DeGuzman, J. P., AECU 3523, U. S. Atomic Energy Comm. Doc. (1958).
- Eckert, E. R. G., "Introduction to the Transfer of Heat and Mass," pp. 66-68, 159-171, McGraw-Hill, New York (1950).
- , E. Soehngen, "Proc. of the General Discussion on Heat Transfer," pp. 321-323, Inst. Mech. Engrs., London (1951).
- Hermann, R., *Natl. Advisory Comm. Aeronaut. Tech. Mem.* 1366 (1954).
- Jakob, Max, "Heat Transfer," Vol. 1, John Wiley, New York (1949).
- McDowell, R. H., W. R. Fuller, and F. W. Carroll, personal communication (June, 1957).
- Schmidt, E., W. Beckmann, *Tech. Mech. u. Thermodynam.*, 1, 1, 341, 391 (1930).
- Sparrow, E. M., personal communication (May, 1957).
- , and J. L. Gregg, *Trans. Am. Soc. Mech. Engrs.*, 78, 435 (1956).
- Randall, I. E., M.S. thesis, Purdue University, Lafayette, Ind. (1957).

Presented at 1958 Nuclear Congress Meeting. Manuscript received January 10, 1958; revision received October 29, 1958; paper accepted October 30, 1958.



# Reduced Density Correlation for Hydrogen: Liquid and Gaseous States

CHARLES A. SCHAEFER and GEORGE THODOS

The Technological Institute, Northwestern University, Evanston, Illinois

The available experimental density data for hydrogen have been compiled to produce a reduced density correlation for the liquid and gaseous states. This investigation has utilized fifty-seven sources of data, extending from the early studies of Amagat (1880) to the recent contributions of Johnston, Keller, and Friedman (1954).

Based on the concept of a reduced density, a correlation for hydrogen has been developed ranging in temperature from the melting point ( $14^{\circ}\text{K.}$ ) to  $3,300^{\circ}\text{K.}$  and in pressure as high as 2,550 atm. This correlation provides continuity between the liquid and gaseous phases; whereas existing equations of state fail to describe the experimental behavior in the transitional region, particularly near the critical point.

Four hundred and eighty-five experimental points covering the entire region were checked to establish the reliability of this correlation, which reproduced the experimental data to within 0.49%.

Present technological practices use generalized reduced-state correlations for the estimation of thermodynamic and transport properties of substances. The validity of this approach has proved satisfactory in the correlation of densities (49), viscosities (71), thermal conductivities (64, 66), and diffusion coefficients (27); more intensive investigations indicate that helium and hydrogen do not conform to this generalized pattern. Nelson and Obert (59) also recognize this inconsistency and suggest the use of a quantum parameter for these light gases.

To correlate the properties of hydrogen and helium one proposal considers adjustment of their critical constants. Newton (60) presents a generalized activity-coefficient chart based on an empirical correction quantity of 8 added to both the critical temperature and critical pressure of hydrogen, helium, and neon. Dodge (26) utilizes this concept to correlate compressibility factors; Morgen and Childs (57) show that this concept is valid in limited ranges of temperature and pressure. Basing their studies on hydrogen PVT data, Maslan and Littman (52) construct a compressibility chart. Data for the inert gases are fitted to this chart by the application of additive corrections to the critical temperature and pressure of argon, neon, and helium.

In viscosity studies Brebach and Thodos (15) present a reduced-state correlation for diatomic gases. To describe

properly the behavior of hydrogen with this correlation it was necessary to adjust progressively the critical temperature and pressure.

Alternatively equations of state have been used to predict generalized behavior. While such equations are of a generalized form, the constants involved and their use have a specific value for each substance. Beattie and Bridgeman (13) point out that simple equations of state derived from theoretical considerations are inaccurate for a wide range of temperature and pressure. Furthermore empirical expansion type of equations require a large number of terms for use over a large range; hence they are inconvenient for use in thermodynamic calculations.

Owing to the anomalous behavior of hydrogen and helium, specific reduced-state correlations are recommended for the estimation of their physical properties. The present investigation concerns a comprehensive literature survey of hydrogen density data and the construction of a reduced-state correlation.

## EXPERIMENTAL BACKGROUND

To obtain sufficient experimental data for the development of the density correlation, a comprehensive literature search has been conducted. Extending from the early work of Amagat (1 to 5) to the recent contributions of Johnston, Keller, and Friedman (33), fifty-seven sources of

experimental density data have been utilized in this study. The data cover the range between  $14^{\circ}$  and  $773^{\circ}\text{K.}$  and pressures as high as 12,580 atm. This range not only includes the gas phase but also extends into the liquid region. Considerable duplication was found to exist at temperature levels from  $200^{\circ}$  to  $450^{\circ}\text{K.}$  In contrast to this situation experimental data above  $773^{\circ}\text{K.}$  were nonexistent.

Despite the fact that Amagat (2) initiated measurements as early as 1880, his work is consistent with data reported later by other investigators. Between the period of 1901 to 1928 considerable experimental work was reported by investigators at the Physical Laboratory of the University of Leiden. This group, headed primarily by Kamerlingh Onnes, produced reliable density data extending from the saturated envelope to the gaseous state. During this period Holborn and Otto reported density data for the gaseous state only, primarily between  $65^{\circ}$  and  $473^{\circ}\text{K.}$  The experimental data of Bridgman (17, 18) extend up to 12,580 atm. but are limited to temperatures of  $303^{\circ}$  and  $338^{\circ}\text{K.}$

The experimental findings of Bartlett *et al.* (8, 9, 10), as well as those of Deming and Shupe (24), permit the extension of these studies to  $773^{\circ}\text{K.}$  The recent contributions of Johnston *et al.* (33, 34) represent a comprehensive coverage of temperature and pressure. These investigators have produced consistent data ranging from the boiling point through the critical point and well into the gaseous region. Much of the foregoing data have been compiled by Woolley, Scott, and Brickwedde (33) in 1948. Their smoothed data are reported in tabular form.

# DEVELOPMENT OF REDUCED-STATE CORRELATION

A reduced-state correlation of density with temperature and pressure requires accurate values for the temperature, pressure, and density at the critical point. For hydrogen the critical values reported by Kobe and Lynn (48) have been accepted; these are  $T_c = 33.3^\circ\text{K}$ ,  $P_c = 12.8 \text{ atm.}$ , and  $\rho_c = 0.0310 \text{ g./cc.}$

The majority of experimental data upon which this correlation has been based are not reported in terms of absolute densities. Rather, experimental densities are presented in terms of Amagat units and Amagat densities, which are values relative to those at standard conditions. The conversion of these values for hydrogen to absolute units, grams per cubic centimeter, has been accomplished by the use of  $M = 2.016 \text{ g./g.-mole}$  and  $V_c = 22,428 \text{ cc./g.-mole}$  at the standard conditions of  $0^\circ\text{C.}$  and  $1 \text{ atm.}$  With these constants the absolute density for hydrogen becomes

$$\rho = 8.9888 \times 10^{-5} d_A$$

$$= 8.9888 \times 10^{-5} \frac{P}{\text{A.U.}} \quad (1)$$

Figure 1 presents a density correlation for hydrogen in which reduced density is a function of reduced temperature and reduced pressure. This correlation presents values resulting from the work of the fifty-seven investigators indicated in this figure. The data are customarily reported isothermally under varying pressures. Hence it was necessary to prepare a cross plot for several of these references. This procedure involved plotting the experimental isotherms on log-log paper with reduced density and reduced pressure as the coordinates. From these cross plots the experimental density correlation was developed by plotting the isothermal data at the pressures indicated in Figure 1.

The saturated envelope was established from the data of Kamerlingh Onnes, Crommelin, and Cath (40) and Mathias, Crommelin, and Kamerlingh Onnes (53). Additional data substantiating and extending this curve to the melting point were obtained from other references (16, 25, 69, 72, 75, 76, 77, 82). The intersections of the isobars and saturated vapor curve were located from the vapor-pressure data of Kamerlingh Onnes and Keesom (45), Cath and Kamerlingh Onnes (19), Keesom, Bijl, and van der Horst (47), and White, Friedman, and Johnston (78).

At pressures above  $P_R = 15$  and temperatures below  $T_R = 6.0$  the only data reported are those of David and Hamann (22). These data enable the interpolation over the region of  $T_R = 2.4$  to  $T_R = 6.0$  and  $P_R = 15$  to  $P_R = 100$ .

As already pointed out, the experimental data are limited to temperatures

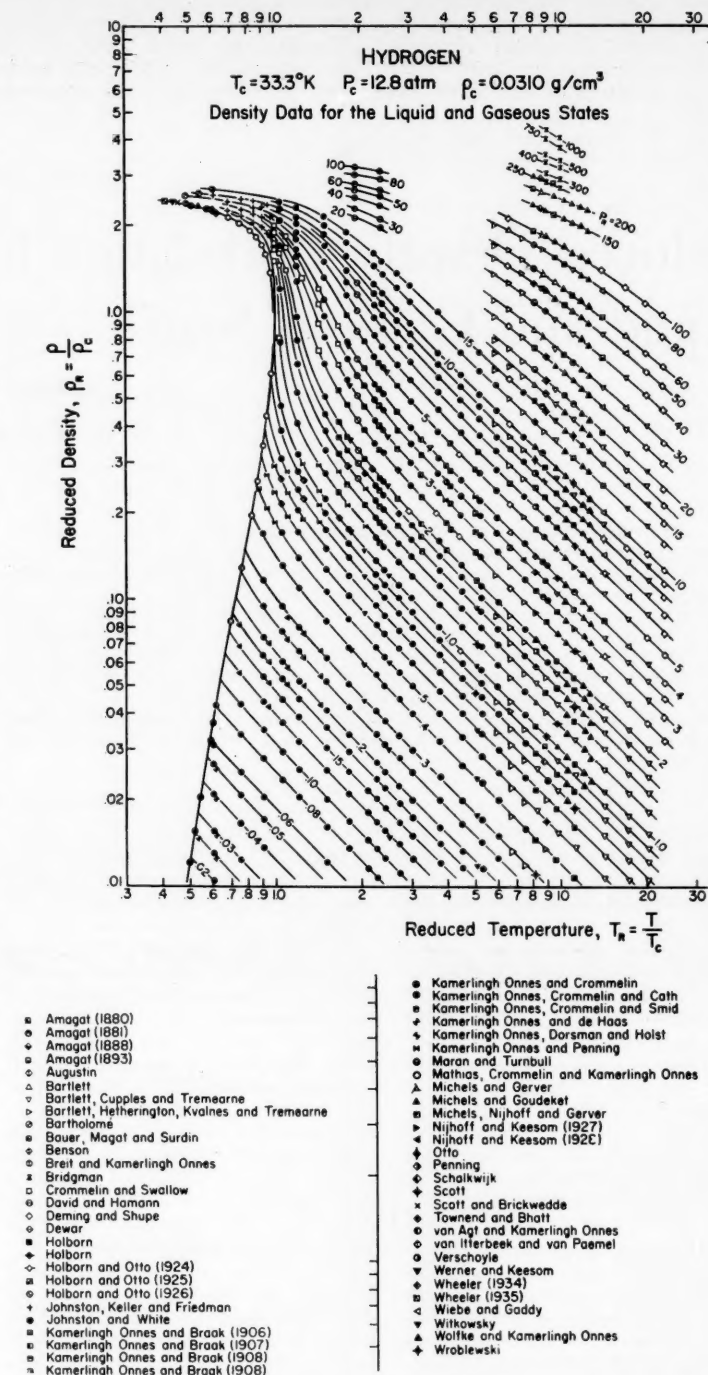


Fig. 1. Correlation of experimental density data for hydrogen.

of less than  $773^\circ\text{K.}$  The extension of this correlation to higher temperatures was accomplished through the application of a compressibility-factor chart. Values in the high-temperature region of the Nelson-Obert chart (58) were plotted against the reduced temperature for different reduced-pressure parameters.

Since in the limit at high reduced temperatures these isobars converge to  $z = 1.00$ , the relationships of this cross plot were readily extrapolated, and the extrapolated values produced linear relationships at high temperatures on the Nelson-Obert chart. By means of these linear compressibility-factor relationships

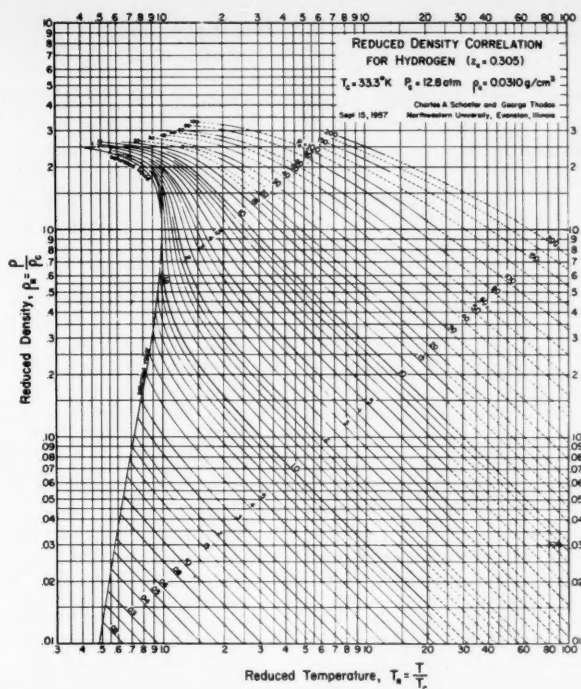


Fig. 2. Reduced-density correlation for hydrogen (logarithmic coordinates).

and the experimental densities at the highest reported temperatures, the isobars of Figure 1 were extended through use of the following equation:

$$\frac{\rho_R}{\rho_{R_1}} = \frac{z_1}{z} \frac{P_R}{P_{R_1}} \frac{T_{R_1}}{T_R} \quad (2)$$

For isobaric conditions,  $P_R = P_{R_1}$ , Equation (2) becomes

$$\rho_R = \frac{z_1}{z} \frac{T_{R_1}}{T_R} \rho_{R_1} \quad (3)$$

Following this approach, the authors calculated reduced densities up to temperatures of  $T_R = 100$  and pressures of  $P_R = 200$  as extensions of the experimentally established isobars.

Bridgman's data (17, 18) appear to be consistent with those of experimenters at lower pressures. Owing to the limited temperature range of his investigations, however, isobars through his data could not be reliably extended.

Figure 2\* presents the final reduced density correlation based on 2,500 experimental density values. The solid lines represent regions covered by experimental points; whereas the dashed lines represent the regions involving the extensions already discussed.

The correlation presented in Figure 2 permits the rapid determination of hydro-

gen densities over extended conditions of temperature and pressure. However the low-temperature liquid region is not readily interpreted, because of the inherent compact nature of reduced-density correlations plotted on logarithmic coordinates. A more expedient representation of the low-temperature liquid region is realized on rectilinear coordinates as presented in Figure 3. As before, the solid lines represent regions covered by experimental points; whereas the dashed

lines represent extensions of data. As already pointed out, the use of rectilinear coordinates limits the extent of the temperature range. The correlation presented in Figure 3 permits the rapid determination of hydrogen densities for the liquid- and dense-phase regions on an expanded scale; Figure 2 shows this region in a compact manner.

## DISCUSSION OF RESULTS

Since the reduced-state correlation of density with temperature and pressure (Figure 2) is based on experimental data, its reliability as a means of determining accurate density values depends upon two factors.

First is the accuracy of the experimental results as reported by the various investigators. The data (11, 44, 51, 85) which were obviously out of line from the general trend of the experimental points were eliminated. Otherwise no discrimination was made in preparing this correlation.

The second factor is the reliability of the correlation to reproduce values consistent with the ones determined experimentally. To determine its reliability a representative sampling of data was taken from each reference source presented in Figure 1. Four hundred and eighty-five values were read from the chart at varying temperatures and pressures so as to cover the entire range indicated by solid lines. The correlation of Figure 2 produced agreement to within 0.49% of the experimental data; it was found to be in best agreement, 0.21%, with the work of Michels *et al.* (54, 55, 56). The deviation from the data of Kamerlingh Onnes *et al.* (35 to 38, 41, 42, 43, 46, 72), Witkowsky (81), and Deming and Shupe (24) was 0.38%. The correlation reproduced the results of Amagat (2, 3, 4, 5), Holborn (23), Holborn

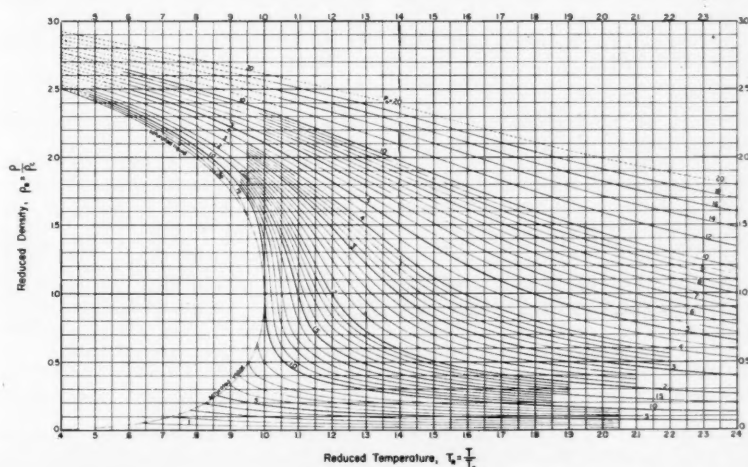


Fig. 3. Reduced-density correlation for hydrogen in the saturated- and dense-phase regions (rectilinear coordinates).

\*An 8 1/2 by 11-in. reproduction of Figure 2, with fine graph lines shown, is available upon request from the authors.



and Otto (29, 31, 32), and Johnston and White (34) to within 0.56%. The greatest deviations, 0.70 and 0.99%, were from the data of Bartlett *et al.* (8, 9, 10) and Crommelin and Swallow (20, 21), respectively. The deviation from the work of Crommelin and Swallow can be explained in part by the low-temperature region investigated. Near the critical point the isobars have a steep slope, and hence the chart is difficult to read.

It is concluded that owing to the comprehensive literature survey Figure 2 is a representative correlation of the available absolute-density values. Furthermore the average deviation of 0.49% indicates that the chart is reliable in producing values consistent with the experimental data.

#### NOTATION

A. U. = Amagat unit  
 $d_A$  = Amagat density  
 $P$  = pressure, atm.  
 $P_R$  = reduced pressure  
 $\rho$  = absolute density  
 $\rho_R$  = reduced density  
 $T_R$  = reduced temperature  
 $z$  = compressibility factor  
 $z_1$  = compressibility factor at the reference point  
 $\rho_R, P_R, T_R$  = reduced states for density, pressure, and temperature at the reference point (highest reported temperature)

#### LITERATURE CITED

- Amagat, E. H., *Ann. chim. et phys.*, **28**, No. 4, 274 (1873).
- Ibid.*, **19**, No. 5, 345 (1880).
- Ibid.*, **22**, No. 5, 353 (1881).
- , *Compt. rend.*, **107**, 522 (1888).
- , *Ann. chim. et phys.*, **29**, No. 6, 68 (1893).
- Augustin, Herbert, *Ann. Physik.*, **46**, No. 4, 419 (1915).
- Bartholomé, E., *Z. physik. Chem. (B)*, **33**, 387 (1936).
- Bartlett, E. P., *J. Am. Chem. Soc.*, **49**, 687 (1927).
- , H. L. Cupples, and T. H. Tremearne, *J. Am. Chem. Soc.*, **50**, 1275 (1928).
- Bartlett, E. P., H. C. Hetherington, H. M. Kvalnes, and T. H. Tremearne, *ibid.*, **52**, 1363 (1930).
- Bassett, James, and R. Dupinay, *Compt. rend.*, **191**, 1295 (1930).
- Bauer, E., M. Magat, and M. Surdin, *J. phys. radium*, **7**, No. 7, 441 (1936).
- Beattie, J. A., and O. C. Bridgman, *Proc. Am. Acad. Arts Sci.*, **63**, 229 (1928).
- Benson, S. W., *J. Phys. & Colloid Chem.*, **52**, 1060 (1948).
- Brebach, W. J., and George Thodos, *Ind. Eng. Chem.*, **50**, 1095 (1958).
- Breit, G., and Heike Kamerlingh Onnes, *Communs. Phys. Lab. Univ. Leiden*, No. 171a (1924).

- Bridgman, P. W., *Rec. trav. chim.*, **42**, 568 (1923).
- , *Proc. Am. Acad. Arts Sci.*, **59**, 173 (1924).
- Cath, P. G., and H. Kamerlingh Onnes, *Communs. Phys. Lab. Univ. Leiden*, No. 152a (1917).
- Crommelin, C. A., and J. C. Swallow, *ibid.*, No. 172a (1924).
- , *Proc. Intern. Congr. Refrig.*, 4th Congr., **1**, 53a (1924).
- David, H. G., and S. D. Hamann, *Trans. Faraday Soc.*, **49**, 711 (1953).
- de Haas, W. J., *Communs. Phys. Lab. Univ. Leiden*, No. 127a (1912).
- Deming, W. E., and L. E. Shupe, *Phys. Rev.*, **40**, 848 (1932).
- Dewar, J., *Proc. Roy. Soc. (London)*, **73A**, 251 (1904).
- Dodge, B. F., "Chemical Engineering Thermodynamics," p. 160, McGraw-Hill, New York (1944).
- Fair, J. R., and B. J. Lerner, *A.I.Ch.E. Journal*, **2**, 13 (1956).
- Holborn, L., *Ann. Physik.*, **63**, No. 4, 674 (1920).
- Holborn, L., and J. Otto, *Z. Physik.*, **23**, 77 (1924).
- Ibid.*, **30**, 320 (1924).
- Ibid.*, **33**, 1 (1925).
- Ibid.*, **38**, 359 (1926).
- Johnston, H. L., W. E. Keller, and A. S. Friedman, *J. Am. Chem. Soc.*, **76**, 1482 (1954).
- Johnston, H. L., and David White, *Trans. Am. Soc. Mech. Engrs.*, **72**, 785 (1950).
- Kamerlingh Onnes, Heike, and C. Braak, *Communs. Phys. Lab. Univ. Leiden*, No. 97a (1906).
- Ibid.*, No. 99a (1907).
- Ibid.*, No. 100a (1908).
- Ibid.*, No. 100b (1908).
- Kamerlingh Onnes, Heike, and C. A. Crommelin, *Communs. Phys. Lab. Univ. Leiden*, No. 137a (1913).
- Kamerlingh Onnes, Heike, C. A. Crommelin, and P. G. Cath, *ibid.*, No. 151c, (1917).
- Kamerlingh Onnes, Heike, C. A. Crommelin, and E. I. Smid, *ibid.*, No. 146b (1914).
- Kamerlingh Onnes, Heike, and W. J. de Haas, *ibid.*, No. 127c (1912).
- Kamerlingh Onnes, Heike, C. Dorsman, and G. Holst, *ibid.*, No. 146a (1915).
- Kamerlingh Onnes, Heike, and H. H. F. Hyndman, *ibid.*, No. 78c (1902).
- Kamerlingh Onnes, Heike, and W. H. Keesom, *ibid.*, No. 137d (1913).
- Kamerlingh Onnes, Heike, and F. M. Penning, *ibid.*, No. 165b (1923).
- Keesom, W. H., A. Bijl, and H. van der Horst, *ibid.*, No. 217a (1931).
- Kobe, K. A., and R. E. Lynn, Jr., *Chem. Revs.*, **52**, 117 (1953).
- Lydersen, A. L., R. A. Greenkorn, and O. A. Hougen, *Wisconsin Univ. Eng. Exp. Sta. Rept. No. 4* (October 1955).
- Maran, S. H., and David Turnbull, *Ind. Eng. Chem.*, **34**, 544 (1942).
- Martinez, J. P., and Heike Kamerlingh Onnes, *Communs. Phys. Lab. Univ. Leiden*, No. 164 (1923).
- Maslan, F. D., and T. M. Littman, *Ind. Eng. Chem.*, **45**, 1566 (1953).
- Mathias, E., C. A. Crommelin, and H. Kamerlingh Onnes, *Communs. Phys. Lab. Univ. Leiden*, No. 154b (1921).

- Michels, A., and A. J. J. Gerver, *Ann. Physik.*, **16**, No. 5, 745 (1933).
- Michels, A., and M. Goudekot, *Physica*, **8**, 347 (1941).
- Michels, A., G. P. Nijhoff, and A. J. J. Gerver, *Ann. Physik.*, **12**, No. 5, 562 (1932).
- Morgen, R. A., and J. H. Childs, *Ind. Eng. Chem.*, **37**, 671 (1945).
- Nelson, L. C., and E. F. Obert, *Trans. Am. Soc. Mech. Engrs.*, **76**, 1057 (1954).
- Nelson, L. C., and E. F. Obert, *A.I.Ch.E. Journal*, **1**, 74 (1955).
- Newton, R. H., *Ind. Eng. Chem.*, **27**, 302 (1935).
- Nijhoff, G. P., and W. H. Keesom, *Communs. Phys. Lab. Univ. Leiden*, No. 188d (1927).
- Ibid.*, No. 188e (1928).
- Otto, J., "Handbuch der Experimentalphysik," **8**(2), 161, Akademische Verlagsgesellschaft M.B.H. Leipzig (1929).
- Owens, E. J., and George Thodos, *A.I.Ch.E. Journal*, **3**, 454 (1957).
- Penning, F. M., *Communs. Phys. Lab. Univ. Leiden*, No. 166 (1923).
- Schaefer, C. A., M.S. thesis, Northwestern Univ., Evanston, Ill. (1957).
- Schalkwijk, J. C., *Communs. Phys. Lab. Univ. Leiden*, No. 70 (1901).
- Scott, G. A., *Proc. Roy. Soc. (London)*, **A125**, 330 (1929).
- Scott, R. B., and F. B. Brickwedde, *J. Research, Natl. Bur. Standards*, **19**, 237, (1937).
- Townend, D. T. A., and L. A. Bhatt, *Proc. Roy. Soc. (London)*, **A134**, 502 (1931).
- Uyehara, Otto, and K. M. Watson, *Natl. Petrol. News*, **36**, R764 (October 4, 1944).
- van Agt, F.P.G.A.J., and Heike Kamerlingh Onnes, *Communs. Phys. Lab. Univ. Leiden*, No. 176b (1925).
- van Itterbeek, A., and O. van Paemel, *Physica*, **8**, 133 (1941).
- Verschoyte, T. H., *Proc. Roy. Soc. (London)*, **A111**, 552 (1926).
- Werner, Waclaw, and W. H. Keesom, *Communs. Phys. Lab. Univ. Leiden*, No. 178a (1925).
- Wheeler, T. S., *Proc. Indian Acad. Sci.*, **A1**, 105 (1934).
- , *Current Sci. (India)*, **3**, 347 (1935).
- White, David, A. S. Friedman, and H. L. Johnston, *J. Am. Chem. Soc.*, **72**, 3927 (1950).
- Wiebe, R., and V. L. Gaddy, *ibid.*, **60**, 2300 (1938).
- Wiebe, R., V. L. Gaddy, and C. Heins, *J. Am. Chem. Soc.*, **53**, 1721 (1931).
- Witkowsky, A. W., *Anz. Akad. Wiss. Krakau*, p. 305 (1905).
- Wolfke, M., and Heike Kamerlingh Onnes, *Communs. Phys. Lab. Univ. Leiden*, No. 171c (1924).
- Woolley, H. W., R. B. Scott, and F. G. Brickwedde, *J. Research Natl. Bur. Standards*, **41**, 379 (1948).
- Wroblewski, Sigmund, *Wien Akad. Ber.*, **97**, 1346 (1888).
- Zlunitsyn, S. A., and W. S. Rudenko, *Zhur. Ekspl. i Teoret. Fiz.*, **16**, 776 (1946).

Manuscript received December 3, 1957; revision received November 13, 1958; paper accepted November 14, 1958.



# An Improved Equation of State for Gases

JOSEPH J. MARTIN, RAJENDRA M. KAPOOR, and NOEL DE NEVERS, University of Michigan, Ann Arbor, Michigan

Based on properties which are characteristic of all gases, modifications are developed for an equation of state previously proposed in this journal (1). A specific application of the modified equation is made for the PVT data on carbon dioxide, and considerable improvement over the original equation is shown for densities in the neighborhood of 1.4 times the critical density. The new equation differs from the old equation only by the presence of the  $A_5$  and  $C_5$  terms, these having originally been taken to be zero.

In an earlier paper the general PVT characteristics of pure gases and liquids were presented by Martin and Hou (1). The hypothesis was advanced that complete representation of the PVT behavior of any pure gas requires a knowledge of the critical temperature, pressure, and volume and of the slope of the vapor-pressure curve at the critical point. Based on this hypothesis an equation of state of the following form was developed:

$$P = \sum_{i=1}^5 \frac{f_i}{(V-b)^i} \quad (1)$$

In this expression the  $f_i$ 's are temperature functions of the kind

$$f_i = A_i + B_i T + C_i \exp(-kT/T_c) \quad (2)$$

Although it was desirable to evaluate all the constants, it did not prove possible at the time; therefore  $A_1$ ,  $C_1$ ,  $B_4$ ,  $C_4$ ,  $A_5$ , and  $C_5$  were set equal to zero, and  $B_1$  was set equal to  $R$  so that proper behavior would be obtained at infinite attenuation (that is, ideal-gas state). The expanded form of the original equation is

$$P = \frac{RT}{V-b} + \frac{A_2 + B_2 T + C_2 \exp(-kT/T_c)}{(V-b)^2} + \frac{A_3 + B_3 T + C_3 \exp(-kT/T_c)}{(V-b)^3} + \frac{A_4}{(V-b)^4} + \frac{B_5 T}{(V-b)^5} \quad (3)$$

and the constants are evaluated from formulas derived from the general PVT characteristics and the basic hypothesis. The derivations of these formulas are presented in the original paper (1).

## THE MODIFICATION

Since its original development six years ago, the equation of state has been applied to a number of compounds. In some cases only the minimum four facts ( $P_c$ ,  $T_c$ ,  $V_c$ , and  $m$ , the slope of the vapor-pressure curve at the critical) were employed to get the equation constants. In other cases the equation was fitted to the actual data by adjusting constants. To understand the new modification, it is desirable to know how the equation is fitted to the data for a given gas. When one refers to an isometric plot such as shown in the accompanying figure, the first step consists in obtaining the temperature functions along the

critical isotherm. In this procedure the data are fitted with extremely high precision at the critical temperature to a density of about 1.5 times the critical density. The critical isometric is then fitted exactly from the critical point to the highest temperature to which it extends as a straight line. For all ordinary substances this is the highest temperature encountered in practical use.\* Next, by means of the Boyle point temperature, the data are fitted at high temperature and low density. By means of the  $T'$  temperature the data are fitted at low temperature and low density.

For densities a little over the critical and temperatures above the critical there was no actual fitting operation even when data were available. Comparison of the equation with the experimental data in this region, which is circled in the figure, showed, however, that the isometrics predicted by the equation curved upward a little too much. This was true for a wide variety of gases. To correct this curvature of the higher density isometrics, recourse was made to two additional properties that are common to all gases. As pointed out in the original paper, the isometrics at about 1.5 to 2.0 times the critical density tend to be straight, just as at the critical density. Mathematically this means that

$$(d^2P/dT^2)_V = 0 \text{ at } V = V_c/n \quad (4)$$

where  $n$  lies between 1.5 and 2.0. The slope of this isometric is from three to eight times the slope of the critical isometric, a condition which may be stated as

$$(dP/dT)_V \text{ (at } V = V_c/n) = y(dP/dT)_V \text{ (at } V = V_c) = ym \quad (5)$$

From Equations (4) and (5) it is possible to evaluate two more constants in the general equation of state. Because the equation as originally developed satisfactorily represents the data at low densities, it was desirable to make modifications which would have little effect on the equation at low densities. New constants therefore were placed in the  $f_5/(V-b)^5$  term, which rapidly approaches zero as  $V$  becomes large. In the original equation  $A_5$  and  $C_5$  were

\*For low-boiling-point gases, such as hydrogen and helium, the critical isometrics curve downward at the highest temperatures. This downward curvature occurs only at high reduced temperatures which are not encountered with ordinary compounds. To fit the data for low-boiling-point gases, it is necessary to add another temperature term to Equation (2).

arbitrarily set equal to zero; in the modified form they have been given finite values determined from relations (4) and (5).

The proposed modification does not affect the formulas for the evaluation of the  $f_i(T_c)$  or the formulas for  $A_2$ ,  $B_2$ ,  $C_2$ , and  $A_1$ ; it does necessitate the formulation of new equations for the constants  $A_3$ ,  $B_3$ ,  $C_3$ ,  $A_4$ ,  $B_4$ , and  $C_4$ . The formulas for these, derived from the conditions previously used to solve for  $A_1$ ,  $B_1$ ,  $C_1$ , and  $B_5$  plus the two new conditions, are outlined as follows:

$$\text{From } (d^2P/dT^2)_V = 0 \text{ at the critical density (6)}$$

$$(d^2P/dT^2)_V = 0 \text{ at } n \text{ times the critical density. (4)}$$

one may obtain by differentiating the proposed equation

$$C_2/(V-b)^2 + C_3/(V-b)^3 + C_4/(V-b)^4 + C_5/(V-b)^5 = 0 \quad (7)$$

at  $V = V_c$  and at  $V = V_c/n$ . Eliminating  $C_4$  and solving for  $C_3$  in terms of  $C_2$  (which is already known), one gets

$$C_3 = \frac{C_2[(V_c-b)^3 - (V_c/n-b)^3]}{(V_c/n-b)^2 - (V_c-b)^2} \quad (8)$$

and

$$C_5 = -C_2(V_c-b)^3 - C_3(V_c-b)^2 \quad (9)$$

The remaining constants to be evaluated are  $A_3$ ,  $B_3$ ,  $A_4$ , and  $B_4$ . The two  $B$ 's are solved for by means of the conditions

$$(dP/dT)_V = m \text{ at } V = V_c \quad (10)$$

and

$$(dP/dT)_V = ym \text{ at } V = V_c/n. \quad (5)$$

Thus

$$m = (dP/dT)_V = \left[ \frac{R}{(V_c-b)} + \frac{B_2}{(V_c-b)^2} + \frac{B_3}{(V_c-b)^3} + \frac{B_4}{(V_c-b)^4} \right] - \left[ \frac{C_2}{(V_c-b)^3} + \frac{C_3}{(V_c-b)^4} + \frac{C_5}{(V_c-b)^5} \right] \frac{k \exp(-kT/T_c)}{T_c} \quad (11)$$

and

$$ym = (dP/dT)_V = \left[ \frac{R}{(V_c/n-b)} + \frac{B_2}{(V_c/n-b)^2} + \frac{B_3}{(V_c/n-b)^3} + \frac{B_4}{(V_c/n-b)^4} \right] - \left[ \frac{C_2}{(V_c/n-b)^3} + \frac{C_3}{(V_c/n-b)^4} + \frac{C_5}{(V_c/n-b)^5} \right]$$

	Original equation	Modified equation
$T_c$	547.5°R.	Same
$P_c$	1069.4 lb./sq. in.	Same
	abs.	Same
$V_c$	0.03454 cu. ft./lb.	Same
$Z_c$	0.27671	Same
$m$	14.0	Same
$\beta$	3.25	Same
$T_h/T_c$	2.3	Same
$T'/T_c$	0.80	Same
$n$	....	1.70
$y$	....	3.50
$b$	0.007495	Same
$A_2$	-8.9273631	Same
$A_3$	0.18907819	0.17948621
$A_4$	$-2.112459 \times 10^{-3}$	Same
$A_5$	....	$7.017835 \times 10^{-6}$
$B_3(R)$	0.24381	Same
$B_2$	$5.262476 \times 10^{-8}$	Same
$B_5$	$-7.04617 \times 10^{-5}$	$-5.770542 \times 10^{-5}$
$B_8$	$1.9565593 \times 10^{-8}$	$1.023511 \times 10^{-8}$
$C_2$	-150.97587	Same
$C_3$	4.0831424*	4.705805
$C_5$	....	$-4.55437 \times 10^{-4}$

Figure 1 is a graph showing the relationship between Reduced Pressure ( $P_r$ ) on the vertical axis and Reduced Temperature ( $T_r$ ) on the horizontal axis. The graph displays several curves representing the equation of state of density for different values of  $P_r$  (0.05, 0.2, 0.4, 0.6, 1.0, 1.5, 2.0). The curves are fitted along critical isotherms. A dashed line indicates the region of modification. The curves are labeled with their respective  $P_r$  values:  $P_r = 0.05$ ,  $P_r = 0.2$ ,  $P_r = 0.4$ ,  $P_r = 0.6$ ,  $P_r = 1.0$ ,  $P_r = 1.5$ , and  $P_r = 2.0$ . The region of modification is indicated by a dashed line and labeled "Region of modification". The curves are fitted along critical isotherms, with labels "Fitted at  $T_r^*$ ", "Fitted along critical isotherm", and "Fitted at Boyle point".

$$\left[ + \frac{C_3}{(V_c/n - b)^3} + \frac{C_5}{(V_c/n - b)^5} \right] \frac{k \exp(-kT/T_c)}{T} \quad (12)$$
$$B_3 = \frac{m(V_c - b)^5 - my(V_c/n - b)^5}{(V_c - b)^2 - (V_c/n - b)^2} - \frac{B_2(V_c - b)^3 + B_2(V_c/n - b)^3}{(V_c - b)^2 - (V_c/n - b)^2} - R[(V_c - b)^2 + (V_c/n - b)^2] \quad (13)$$

$$B_5 = m(V_c - b)^5 - R(V_c - b)^4 - B_2(V_c - b)^3 - B_3(V_c - b)^2 \quad (14)$$

$$A_3 = f_3(T_c) - B_3 T_c - C_3 \exp(-k) \quad (15)$$
$$A_5 = f_5(T_c) - B_5 T_c - C_5 \exp(-k) \quad (16)$$
$$P = \frac{RT}{V-b} + \frac{A_2 + B_2T + C_2 \exp(-kT/T_c)}{(V-b)^2} + \frac{A_3 + B_3T + C_3 \exp(-kT/T_c)}{(V-b)^3} \quad (17)$$

For testing the improvement of the modified equation over the original equation, the highly precise data for carbon dioxide were chosen. In the accompanying table are listed the equation constants calculated for carbon dioxide, both for the original equation and for the modified equation. Using these constants in Equation (3) and (17) the authors computed the pressures for several hundred points at varying temperatures and densities. The computed pressures were compared with the experimental pressures reported by Michels and deGroot (2). The important points which may be drawn from this comparison are

2. At densities greater than 1.3 times the critical density and temperatures above the critical, the original equation predicts pressures which dip below the measured pressures and then rise above them at the highest temperatures. For example, at 1.50 times the critical density the original equation predicts pressures which, over a 180°R. temperature range, go from 1.30% greater than the measured pressure, to 6.32% less, and then to 5.50% greater. The modified equation substantially corrects this error. For the same example at 1.50 times the critical density, pressures are predicted which go uniformly from 0.17% greater than the experimental to 5.25% greater. At this density the proposed equation is more accurate than the original equation (2.02% average error vs. 2.92%).

original equation. The modified equation has a maximum error of 1.68% in this range compared with 5.98% for the original equation and an average error of 0.93% vs. 2.68% for the original equation. In this region the modified equation also has more accurate derivatives of pressure with respect to temperature than the original equation.

The data show that the modified equation represents the experimental data with greater precision than the original equation in the neighborhood of 1.4 times the critical density. The modification makes the equation a more useful tool for thermodynamic calculations which require precise relations between pressure, volume, and temperature.

$$A_1, B_1, C_1, A_2, \dots = \text{characteristic constants in Equation (2)}$$
$$M = \text{slope of reduced vapor pressure curve at critical point } dP_r/dT_r = -mP_c/T_c$$
 $P$  = pressure $R$  = universal gas constant

$T$  = absolute temperature

$T_b$  = Boyle point temperature

$T'$  = absolute temperature for which the slope at  $P = 0$  of the isotherm on the compressibility chart equals the slope of the line joining the critical point and ( $Z = 1, P = 0$ )

$V$  = specific volume or molal volume

$$Z = \text{compressibility factor} = PV/RT$$

$b$  = characteristic constant for each substance

$$f_1, f_2 \dots = \text{temperature functions defined by Equation (2)}$$
$$f_1(T_c), f_2(T_c) \dots = \text{preceding functions}$$

$$\text{evaluated at } T = T_c$$
 $k = \text{constant}$ 

$m$  = slope of the critical isometric on a pressure-temperature diagram

$n$  = reduced density  $> 1.0$  at which  $(d^2P/dT^2)_V = 0$

$y$  = ratio of slope of isometric of reduced density  $n$  to slope of critical isometric

$$\beta = \text{characteristic constant in } V_e - b = \beta V_e / 15 Z_e$$
 $\rho$  = density

### Subscripts

$c$  = value at critical p

 $T_c, P_c$ 

$i$  = summation index

$r$  = reduced property,  $T_r = T/T_c$

1. Martin, J. J., and Y. C. Hou, *A.I.Ch.E. Journal*, **1**, 142 (June, 1955).
2. Michels, A., and S. R. deGroot, *Appl. Sci. Research*, **A**, **1**, 565 (1948).

Manuscript received November 11, 1957; revision received August 22, 1958; paper accepted August 26, 1958.

# Solubility of Liquids in Compressed Hydrogen, Nitrogen, and Carbon Dioxide

J. M. PAUSNITZ and P. R. BENSON

University of California, Berkeley, California

The vapor-phase solubilities of carbon tetrachloride, *iso*-octane, toluene, and *n*-decane were measured in compressed hydrogen, nitrogen, and carbon dioxide at 50° and 75°C. and at various pressures between 20 and 90 atm. The virial equation of state was used to describe the volumetric properties of the vapor mixtures, and the second virial cross coefficients were evaluated from the solubility data. The results indicate that the vapor phase departs from ideality very quickly for these systems as the pressure increases, particularly at pressures greater than 10 atm.

The solubility of a liquid in a gas at low pressure is given by the vapor pressure of the liquid. The mole fraction of the heavier component in the gaseous phase is computed by Raoult's Law:

$$y_1 = \frac{(1 - x_2)P_1^0}{P} \quad (1)$$

At low pressures  $x_2$  is negligible compared with unity, and the solubility is then just the ratio of the vapor pressure to the total pressure. As the total pressure rises, Equation (1) fails, not because of nonidealities in the liquid but because of nonideal mixing in the gaseous phase, which causes the fugacity of the heavier component to be significantly different from its partial pressure. At very high pressures, approaching the critical pressure of the gas-liquid mixture, the non-ideality of the liquid phase also becomes important in determining the vapor-phase solubility of the heavier component. In the intermediate pressure range, however, it is the vapor-phase non-ideality which determines that solubility. This work reports new data on the solubility of liquids in compressed gases and uses them to compute virial coefficients for the vapor-phase mixtures.

## THERMODYNAMIC RELATIONSHIPS

A binary system at temperature  $T$  and total pressure  $P$  consisting of a heavy (liquid) component 1 and a light (gaseous) component 2 will be considered. At equilibrium the distribution of the heavier component between the two phases  $L$  and  $G$  is governed by the Gibbs relation

$$\bar{f}_1^L = \bar{f}_1^G \quad (2)$$

where the bar indicates that component 1 is in solution. The fugacities are related to the mole fractions by

$$\bar{f}_1^L = \gamma_1^L (1 - x_2) P_1^0 \phi_1^0 \cdot \exp \left[ \frac{v_1^{0L} (P - P_1^0)}{RT} \right] \quad (3)$$

$$\bar{f}_1^G = \phi_1 y_1 P \quad (4)$$

P. R. Benson is with North American Aviation, Canoga Park, California.

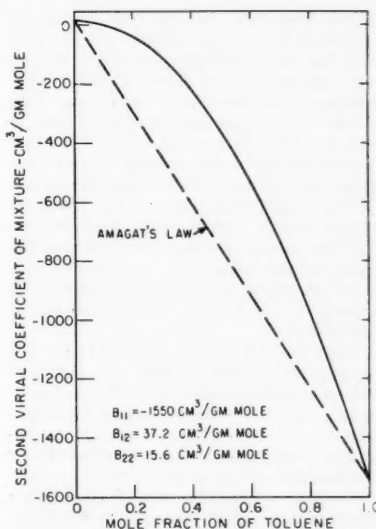


Fig. 1. Second virial coefficient of hydrogen-toluene mixtures at 75°C.

When Equations (3) and (4) are substituted into Equation (2), the vapor-phase solubility is

$$y_1 = \frac{\gamma_1^L (1 - x_2) P_1^0 \phi_1^0}{\phi_1 P} \cdot \exp \left[ \frac{v_1^{0L} (P - P_1^0)}{RT} \right] \quad (5)$$

Solubilities of gases in nonpolar liquids have been correlated by Jolley and Hildebrand (5), and with the help of Henry's Law (and by use of fugacities rather than partial pressures) it is possible to make good estimates of  $x_2$  provided that the total pressure is not extremely large. At such pressures  $x_2$  will be small compared with unity, and thus  $y_1$  is not sensitive to  $x_2$ . Also, when  $x_2$  is small, the liquid phase is ideal with respect to the solvent, and  $\gamma_1^L = 1$ . The problem of computing the vapor-phase solubility therefore reduces to the calculation of the fugacity coefficient, which can be com-

\*If  $x_2$  exceeds about 0.20, a small correction for liquid-phase nonideality may be required. This can be estimated by Hildebrand's equation after an appropriate (empirically determined) solubility parameter for the gaseous component (4) has been assigned.

puted from an equation of state for the gaseous mixture. A particularly convenient equation of state for this purpose is the virial equation; details of this computation are presented elsewhere (8). If the virial equation is terminated after the second virial coefficient, the fugacity coefficient in a binary mixture is given by

$$\ln \phi_1 = \frac{2}{v} [y_1 B_{11} + y_2 B_{12}] - \ln z \quad (6)$$

Numerical values for  $B_{11}$  can be obtained with high accuracy from the recent work of Pitzer and Curl (7), and values of  $B_{12}$  can be estimated for a variety of systems by methods described previously (8, 9). If Amagat's Law is assumed,  $B_{12}$  is the arithmetic average of  $B_{11}$  and  $B_{22}$ , and the fugacity coefficient can be evaluated by the Lewis fugacity rule. This assumption however is a good approximation only at very low pressures (9, 10, 11). If components 1 and 2 are both small molecules of low molecular weight, a simple extension of the two-parameter theory of corresponding states may be used to evaluate  $B_{12}$  (3). Generally however the three-parameter law of corresponding states (6) must be used with suitable semiempirical corrections (9). To illustrate how remote the value of  $B_{12}$  can be from the arithmetic average of  $B_{11}$  and  $B_{22}$ , one should consider mixtures of toluene and hydrogen. The second virial coefficient of the mixture is given by

$$B_m = y_1^2 B_{11} + 2y_1 y_2 B_{12} + y_2^2 B_{22} \quad (7)$$

Figure 1 shows a plot of  $B_m$  vs. composition for this system at 75°C.; the second virial coefficients are based on experimental results reported in this work. In this case  $B_{12}$  does not even fall between the values of  $B_{11}$  and  $B_{22}$  but is larger than either one of them. Hence any type of averaging law seeking to compute  $B_{12}$  from  $B_{11}$  and  $B_{22}$  cannot be successful for this system.

At moderate pressures and temperatures  $y_1 \ll y_2$ . Equation (6) therefore indicates that the fugacity coefficient  $\phi_1$  is very sensitive to the virial coefficient  $B_{12}$ . Measurements of the solubility of liquids in compressed gases, therefore, are particularly useful for obtaining information on the interaction between dissimilar molecules (2, 10). This work presents data for the solubilities of carbon tetrachloride, *iso*-octane (2, 2, 4 trimethyl pentane) toluene, and decane in com-



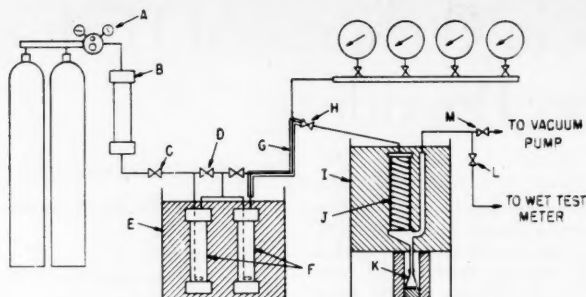


Fig. 2. Schematic diagram of equipment.

pressed nitrogen, hydrogen, and carbon dioxide at 50° and 75°C.

#### EXPERIMENTAL

The solubility of liquids in a compressed gas was measured in a flow system shown schematically in Figure 2.

The gas was fed from two cylinders into a manifold constructed from copper pipe (11/16-in. O.D., 7/16-in. I.D.). The cylinders of gas were used to maintain a steady supply of high-pressure gas.

From the manifold the gas passed through a Victor GD-62B pressure regulator (A), designed for controlled pressures between 0 and 3,600 lb./sq. in. gauge. Before entering the equilibrium cells (F) the gas was dried with silica gel in the drying tube (B), which was constructed from a 9-in. length of 2½-in. double, extra-strong steel pipe, capped at each end, and sealed with O rings.

Two equilibrium cells connected in series were used to assure saturation of the gas, even though experimental evidence indicated that one cell was sufficient. The cells were made with 2½-in. double, extra-strong stainless-steel pipe, type 347, capped and sealed in the same manner as the drying tube with O rings. A detail drawing of an equilibrium cell is given in Figure 3. The liquid was contained within the cells in

Pyrex liners, and the gas was very finely dispersed from a fritted-glass sparger (pore size 14μ) at the bottom of the cells. To prevent entrainment of liquid from the equilibrium cells two layers of 6-mm. glass beads were placed on a Teflon support at the top of the liquid in each cell. The beads caused the finely dispersed gas to form into large bubbles before they broke the surface of the liquid. Any spray from the large bubbles which might have escaped from the cell was trapped by glass-wool plugs at the exits of the cells. The equilibrium cells were immersed in a constant-temperature bath (E), which was controlled to within ±0.05°C.

After leaving the second cell the vapor mixture was led to a Hoke stainless-steel-needle expansion valve (H). This section of tubing and the tubing between the cells was heated with a spiral winding of Nichrome wire and insulated to prevent any condensation of the liquid.

Pressure within the second equilibrium cell was determined from one of the Bourdon-tube pressure gauges, connected to a manifold which was constructed from the same pipe as the gas-cylinder manifold. Full-scale pressures of the four gauges were respectively 160, 600, 1,500, and 2,000 lb./sq. in. gauge. The gauge employed at a given pressure was the one which indicated the pressure between one-third and two-thirds full-scale reading. All gauges were calibrated with an Ashcroft dead-weight gauge tester; pressure measurement accuracy was within ±0.6%.

After expansion the vapor mixture entered the condenser (J) in the refrigerated ethylene glycol-water bath (I), operated at -25° ± 0.1°C. for all liquids except carbon tetrachloride, where -22°C. was used to prevent freezing. In the condenser, the vapor was distributed to six spirals of ¼-in. copper tubing, each approximately 3 ft. long. Condensate from the tubes dripped onto the sloping bottom of the condenser and ran into a ¾-in. copper tube at the lowest point; this tube was joined to a piece of glass tubing which terminated in a standard taper ground-glass joint. A well-insulated 25-ml. flask was connected to this joint to collect the condensate. The gas leaving the condenser passed through a plug of glass wool at the entrance of a vertical section of 1-in. copper tubing. It was assumed that the vapor leaving the condenser was in equilibrium with the condensate. This assumption was checked several times by the adsorption of the remaining trace of condensable vapor from the condenser on activated carbon and the

TABLE 2. EQUILIBRIA IN BINARY SYSTEMS CONTAINING NITROGEN

Component 1	Temperature, °C.	Total pressure, atm.	y <sub>1</sub>
CCl <sub>4</sub>	50	28.4	0.0189
	50	42.8	0.0139
	50	63.9	0.0111
	75	30.6	0.0410
	75	53.9	0.0276
	75	71.7	0.0231
	75	23.5	0.0109
i-C <sub>3</sub> H <sub>8</sub>	50	26.4	0.0101
	50	50.7	0.00686
	50	74.3	0.00608
	50	83.4	0.00611
	75	28.5	0.0230
	75	41.2	0.0178
	75	55.2	0.0150
C <sub>6</sub> H <sub>5</sub> CH <sub>3</sub>	50	22.9	0.00692
	50	34.8	0.00524
	50	47.3	0.00442
	50	60.2	0.00403
	75	21.2	0.0194
	75	37.1	0.0130
	75	51.9	0.0106
n-C <sub>10</sub> H <sub>22</sub>	50	28.4	0.000495
	50	53.9	0.000410
	50	71.9	0.000409
	50	87.7	0.000419
	75	27.1	0.00172
	75	34.4	0.00145
	75	41.7	0.00139

TABLE 3. EQUILIBRIA IN SYSTEMS CONTAINING CARBON DIOXIDE

Component 1	Temperature, °C.	Total pressure, atm.	y <sub>1</sub>
CCl <sub>4</sub>	50	20.2	0.0238
	50	24.8	0.0200
	50	27.2	0.0187
	75	20.2	0.0540
	75	23.6	0.0476
	75	27.2	0.0415
	75	20.5	0.0130
i-C <sub>3</sub> H <sub>8</sub>	50	23.6	0.0119
	50	27.2	0.0109
	75	20.2	0.0311
	75	23.7	0.0272
	75	27.5	0.0245
	75	20.5	0.00822
	75	23.9	0.00760
C <sub>6</sub> H <sub>5</sub> CH <sub>3</sub>	50	27.0	0.00705
	75	20.7	0.0209
	75	24.3	0.0186
	75	27.3	0.0170
	75	20.2	0.000761
	75	24.1	0.000714
	75	29.2	0.000703
n-C <sub>10</sub> H <sub>22</sub>	75	21.6	0.00225
	75	24.1	0.00216
	75	27.3	0.00204

determination of weight increase. The correction calculated in this manner was always the same as the one calculated from the liquid-vapor pressure at the temperature of the condenser, thereby verifying the equilibrium assumption.

From the condenser the flow of gas was measured with a wet-test meter and then vented to the atmosphere. A vacuum pump was connected through a valve at the outlet

TABLE 1. EQUILIBRIA IN BINARY SYSTEMS CONTAINING HYDROGEN

Component 1	Temperature, °C.	Total pressure, atm.	y <sub>1</sub>
CCl <sub>4</sub>	75	39.9	0.0268
	75	54.2	0.0203
	75	69.7	0.0165
	75	69.7	0.0165
i-C <sub>3</sub> H <sub>8</sub>	50	32.9	0.00677
	50	45.2	0.00506
	50	62.0	0.00401
	75	35.3	0.0155
C <sub>6</sub> H <sub>5</sub> CH <sub>3</sub>	75	51.6	0.0108
	75	65.8	0.00869
	50	40.4	0.00343
	50	55.3	0.00262
n-C <sub>10</sub> H <sub>22</sub>	50	62.9	0.00240
	75	42.8	0.00814
	75	52.8	0.00696
	75	55.4	0.00665
	75	69.2	0.00544
	50	30.4	0.000297
	50	41.8	0.000217
	50	50.2	0.000186
	75	32.7	0.000987
	75	45.2	0.000730
	75	55.6	0.000599



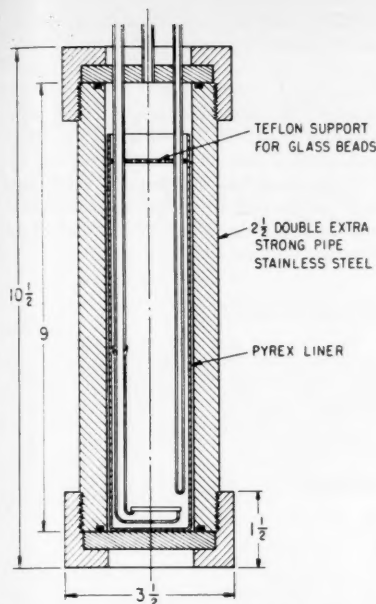


Fig. 3. Equilibrium cell.

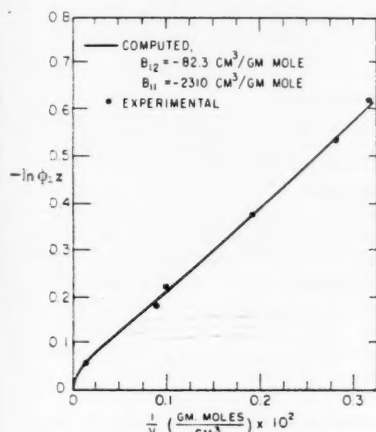


Fig. 4. Phase equilibria for nitrogen-iso-octane at 50°C.

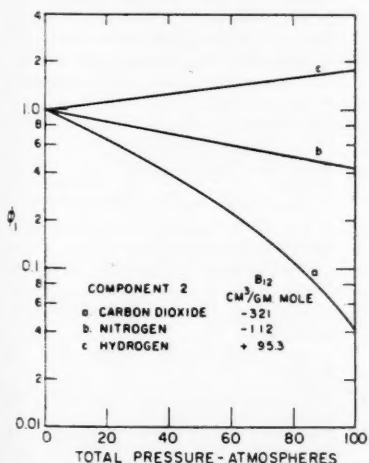


Fig. 5. Fugacity coefficient of decane in hydrogen, nitrogen, and carbon dioxide at 75°C.

of the condenser to permit evacuation of the complete system before all runs.

#### TEMPERATURE CONTROL AND MEASUREMENT

The constant-temperature bath for the equilibrium cells was controlled to  $\pm 0.05^\circ\text{C}$ . The condenser temperature was maintained constant to within  $\pm 0.1^\circ\text{C}$ . by the control of the refrigeration evaporator pressure and by an auxiliary 150-w. heater. Temperatures in the second equilibrium cell and in the condenser were measured with copper-constantan thermocouples which were checked against a National Bureau of Standards calibrated thermometer. Temperature measurement was  $\pm 0.05^\circ\text{C}$ .

#### MATERIALS

The purities of the liquids were: carbon tetrachloride, reagent grade; toluene, reagent grade; iso-octane (2, 2, 4 trimethylpentane); and *n*-decane, practical grade.

Each of the liquids was distilled in an eleven-tray glass column at a reflux ratio of approximately 5 to 1. The column was surrounded by a heated jacket, and a dry nitrogen atmosphere was maintained over the system. The nitrogen was dried by bubbling it through concentrated sulfuric acid and then passing it through a long tube of potassium hydroxide flakes. Drierite was placed in the reboiler to remove any traces of water and to act as boiling chips. The first and last 10% of the liquid charged to the still was discarded, and only the 80% heart cut was used for the experimental determinations.

The gases were passed through a bed of activated charcoal to remove any traces of hydrocarbons and then passed through a bed of silica gel to remove any moisture. The activated charcoal and silica gel were renewed each time the equilibrium cells were opened to change liquids.

#### EXPERIMENTAL PROCEDURE

Details of the experimental procedure are given elsewhere (1). Special care was taken to assure attainment of steady state conditions (3 to 12 hr. depending on the percentage condensible in the gas phase). Initially the gas flow rate was varied to determine the rate at which complete saturation of the gas was assured; final data were taken with gas flow rates in the range 0.005 to 0.020 cu. ft./min. as measured by the wet-test meter. During a run the flow rate was held constant to within 1% or better.

To assure that equilibrium between gas and liquid had been attained, several precautions were taken. First, it was ascertained that changes in the gas flow rate did not affect the results; second, it was shown that the results were independent of the liquid height in the equilibrium cells. Finally runs were made at very low pressure, where the observed results were in excellent agreement with those calculated from ideal-gas behavior.

#### TREATMENT OF DATA

Solubilities of gases in liquids were taken from the literature whenever possible and otherwise estimated from corre-

lations (5). In some cases the data and the estimates were not of very high accuracy, although probably within 5%. However since calculation of the liquid fugacity is insensitive to the gas solubility [Equation (3)], these inaccuracies did not seriously impair computation of  $\phi_1$ . In no case did  $x_2$  exceed 0.30; hence even an error of as much as 10% in  $x_2$  would at most produce a 3% error in  $\bar{f}_1^L$ . Where necessary the Hildebrand equation was used to compute  $\gamma_1^L$ , but in no case did  $\gamma_1^L$  differ from unity by more than 1/2%.

The composition of the vapor phase was calculated from the measured volume of gas and the measured weight of condensate collected, with the necessary correction made for liquid not condensed. Experimental values of the vapor-phase solubility were reproducible to within 1%. For a given gas-liquid pair, vapor-phase compositions were determined for each temperature at a series of pressures, and values of  $\ln \phi_{1z}$  were plotted as a function of  $1/v$  to check the consistency of the data. A typical plot is shown in Figure 4. From Equation (6)

$$\ln \phi_{1z} = \ln \frac{\gamma_1 f_1^L}{y_1^P} + \ln z$$

$$= \frac{2}{v} (y_1 B_{11} + y_2 B_{12}) \quad (8)$$

The compressibility factor and the molar volume of the gaseous mixture were computed by the virial equation with a preliminary estimate for  $B_{12}$ . A value of  $B_{12}$  was then computed from Equation (8). This new value of  $B_{12}$  was then used to reevaluate  $z$  and  $v$ , and still another value of  $B_{12}$  was calculated. In this way it was possible to converge rapidly upon

TABLE 4. SECOND VIRIAL CROSS COEFFICIENTS FOR TWELVE BINARY SYSTEMS

Components	Temperature, $^\circ\text{C}$ .	$B_{12}$ , (cc./g.-mole)
$\text{H}_2, \text{CCl}_4$	75	$34.9 \pm 5.5$
$\text{H}_2, i\text{-C}_8\text{H}_{18}$	50	$37.6 \pm 5.9$
	75	$55.7 \pm 6.0$
$\text{H}_2, \text{C}_6\text{H}_5\text{CH}_3$	50	$19.0 \pm 5.9$
	75	$37.2 \pm 6.0$
$\text{H}_2, n\text{-C}_{10}\text{H}_{22}$	50	$81.2 \pm 6.9$
	75	$95.3 \pm 7.0$
$\text{N}_2, \text{CCl}_4$	50	$-58.5 \pm 5.9$
	75	$-49.6 \pm 5.5$
$\text{N}_2, i\text{-C}_8\text{H}_{18}$	50	$-82.3 \pm 5.7$
	75	$-60.3 \pm 6.5$
$\text{N}_2, \text{C}_6\text{H}_5\text{CH}_3$	50	$-98.1 \pm 6.2$
	75	$-88.1 \pm 7.5$
$\text{N}_2, n\text{-C}_{10}\text{H}_{22}$	50	$-141 \pm 5$
	75	$-112 \pm 7$
$\text{CO}_2, \text{CCl}_4$	50	$-205 \pm 8$
	75	$-163 \pm 9$
$\text{CO}_2, i\text{-C}_8\text{H}_{18}$	50	$-303 \pm 8$
	75	$-252 \pm 9$
$\text{CO}_2, \text{C}_6\text{H}_5\text{CH}_3$	50	$-254 \pm 8$
	75	$-215 \pm 9$
$\text{CO}_2, n\text{-C}_{10}\text{H}_{22}$	50	$-417 \pm 7$
	75	$-321 \pm 8$

a true value for  $B_{12}$ ; usually two or three trials were sufficient.

For each temperature and for each system the coefficient  $B_{12}$  was calculated at several pressures ranging from 20 to 90 atm. At a constant temperature for a given system the values were almost always reproducible to within 5 cc./g.-mole, and the maximum range was 10 cc./g.-mole.

## RESULTS

The solubilities of carbon tetrachloride, iso-octane, toluene, and *n*-decane in compressed hydrogen are given in Table 1; the solubilities in compressed nitrogen in Table 2, and those in compressed carbon dioxide in Table 3. Table 4 gives the second virial cross coefficients for the various binary gas-liquid pairs.

The data show that the vapor phase departs from ideality very quickly for these systems as the pressure increases, particularly at pressures greater than 10 atm. Even at 1 atm. pressure the departure from ideality is a few per cent in some cases. For example, for the system nitrogen and iso-octane the vapor-phase fugacity coefficient of the iso-octane at 1 atm. total pressure and 50°C. is 0.967.

For a given liquid the vapor-phase fugacity coefficient (and hence its vapor-phase solubility) is strongly dependent on the nature of the gaseous component. To illustrate, Figure 5 shows the effect of pressure on the vapor-phase fugacity coefficient of *n*-decane in hydrogen, nitrogen, and carbon dioxide at 75°C.

A comparison between the various methods of calculation of vapor-phase compositions is shown in Figure 6, which shows the vapor-phase concentration of *n*-decane in nitrogen at 50°C. as a function of pressure, calculated from the ideal-gas law, the Lewis fugacity rule, and the virial equation of state, with the second virial cross-coefficient as calculated from vapor-phase solubility data. In this particular case the Lewis fugacity rule introduces as much as a sixfold error over a wide pressure range, and the ideal-gas law introduces a two- to fourfold error in the same pressure range. It appears therefore that as a result of compensating errors the Lewis fugacity rule is actually worse in some cases than the ideal-gas law.

A comparison (Figure 7) was also made between equilibrium ratios  $K$ , as computed from the virial equation of state and as predicted from standard  $K$ -charts for the system nitrogen and iso-octane at 50°C. The error introduced by the use of the standard  $K$ -charts is small at low pressures but rapidly increases as the pressure exceeds 10 atm.

While vapor-phase fugacity coefficients for liquids in nitrogen and carbon dioxide were always less than unity for the systems studied, the fugacity coefficients were greater than unity for the same

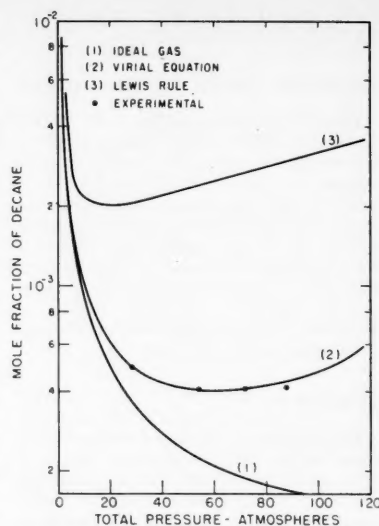


Fig. 6. Vapor-phase solubility of decane in nitrogen at 50°C.

liquids in hydrogen, or at the same temperature and total pressure a liquid is more soluble in nitrogen than in hydrogen and more soluble in carbon dioxide than in nitrogen. This result is not surprising if one remembers that like dissolves like. The difference in physical properties between hydrogen ( $T_c = 33^\circ\text{K.}$ ) and a typical liquid ( $T_c \sim 500^\circ\text{K.}$ ) is certainly larger than that between the physical properties of nitrogen ( $T_c = 126^\circ\text{K.}$ ) or carbon dioxide ( $T_c = 304^\circ\text{K.}$ ) and a typical liquid. In the solubility of liquids in gases one therefore finds a qualitative order quite similar to that found in the solubility of gases in liquids. This selectivity is especially pronounced if the gaseous solvent is slightly above its critical temperature. Thus for example the solubility of naphthalene in ethylene ( $T_c =$

$9.2^\circ\text{C.}$ ) at  $35^\circ\text{C.}$  and 100 atm. is about one thousand times as large as that computed from the ideal-gas-law relation [(Equation (1)), and the solubility in nitrogen at the same temperature and pressure is about two orders of magnitude smaller than that in ethylene (8).

A method of correlating these as well as previously published gas-liquid equilibrium data will be presented in a separate publication.

## ACKNOWLEDGMENT

This research was supported in part by a grant from the Petroleum Research Fund administered by the American Chemical Society. Grateful acknowledgment is hereby made to the donors of this fund.

## NOTATION

- $B$  = second virial coefficient  
 $f$  = fugacity  
 $P$  = pressure  
 $R$  = gas constant  
 $T$  = absolute temperature  
 $v$  = molar volume  
 $x$  = mole fraction in liquid phase  
 $y$  = mole fraction in vapor phase  
 $z$  = compressibility factor

## Greek Letters

- $\gamma^L$  = activity coefficient in liquid phase  
 $\phi$  = fugacity coefficient in vapor phase

## Subscripts

- 1, 2 = components  
 $m$  = mixture

## Superscripts

- $L$  = liquid phase  
 $G$  = gas phase  
 $o$  = pure component

## LITERATURE CITED

- Benson, P. R., M.S. thesis, Univ. Calif., Berkeley (1958).
- Ewald, A. H., W. B. Jepson, and J. S. Rowlinson, *Discussions Faraday Soc. No. 15*, 238 (1953).
- Guggenheim, E. A., and M. L. McGlashan, *Proc. Roy. Soc. (London)*, **A206**, 448 (1951).
- Hildebrand, J. H., and R. L. Scott, "Solubility of Non-Electrolytes," 3 ed., Chap. 15, Reinhold, New York (1950).
- Jolley, J. E., and J. H. Hildebrand, *J. Am. Chem. Soc.*, **80**, 1050 (1958).
- Pitzer, K. S., et al., *J. Am. Chem. Soc.*, **77**, 3427 (1955).
- , and R. F. Curl, *ibid.*, **79**, 2369 (1957).
- Prausnitz, J. M., *A.I.Ch.E. Journal*, **5**, 3 (1959).
- , and R. D. Gunn, *ibid.*, **4**, 4 (1958).
- Reuss, J., and J. J. M. Beenakker, *Physica*, **22**, 869 (1956).
- Van Ness, H. J., *A.I.Ch.E. Journal*, **1**, 100 (1955).

Manuscript received July 23, 1958; revision received September 16, 1958; paper accepted October 2, 1958.

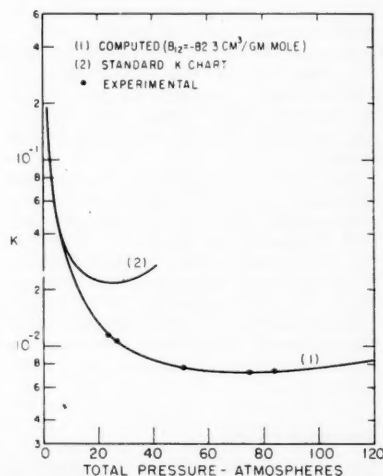


Fig. 7. Equilibrium ratios for iso-octane in nitrogen at 50°C.

# Interfacial Resistance in the Absorption of Oxygen by Water

S. H. CHIANG and H. L. TOOR

Carnegie Institute of Technology, Pittsburgh, Pennsylvania

Transient absorption rates of oxygen into water have been measured by passing a laminar jet through the pure gas for contact times varying from 0.8 to 11.8 msec. The absorption rate is significantly lower than the theoretical value corresponding to no interfacial resistance, if a diffusivity of  $2.20 \times 10^{-5}$  sq. cm./sec. at 22.2°C. is used for comparison. The available evidence indicates that this diffusivity is about correct and that the lowered rate may be caused by an interfacial resistance described by an interfacial transfer coefficient equal to 0.6 cm./sec. This resistance is small enough to be neglected in most gas absorbers.

Interfacial resistance in gas absorption has recently come under intensive study because of its fundamental importance in mass transfer. Higbie (8) in developing his penetration theory for mass transfer demonstrated a possible method of measuring interfacial resistance. Although his technique failed, the principle has proved to be valid. In essence a pure gas is contacted with a liquid which is stationary or in laminar flow, and the rate of absorption is compared with the rate calculated from Fick's second law for unsteady state diffusion. An interfacial resistance may cause the absorption rate to be lower than the theoretical value, but unfortunately a lower rate may also be caused by secondary effects such as a boundary layer or interfacial contamination. Consequently interfacial resistance has turned out to be quite elusive, and, as techniques have been refined, reported interfacial resistances have become smaller and smaller.

In the carbon dioxide-water system, for example, Higbie first found what appeared to be an appreciable interfacial resistance by passing gas bubbles through a water-filled tube. Emmert and Pigford (7) later observed about the same value in short and long wetted-wall columns, but Danckwerts and Kennedy (5), using a rotating drum, obtained more self-consistent data and an appreciably lower resistance.

More recently Cullen and Davidson (2), using a laminar jet, found a negligible interfacial resistance in the same system and showed that the high values which had been reported were most likely due to secondary effects, such as boundary layers and surface contamination. These results were substantiated by a number of other independent studies with different laminar-jet techniques (2, 11, 12, 13).

The foregoing history of an interfacial

resistance is very similar to that of condensation coefficients for pure materials, a very closely related subject; again, as techniques have been refined, the measured condensation coefficients have approached 1 (10), equivalent to the interfacial resistance approaching a very small value.

Oxygen-water has been studied much less extensively than carbon dioxide-water. Emmert and Pigford found a large resistance in a wetted-wall column, but Davidson and Cullen (6), using a wetted sphere, later concluded that interfacial resistance was negligible in this system. Both these studies were made at relatively long contact times, where rate measurements are not very sensitive to an interfacial resistance.

The object of this work is to examine further the oxygen-water system at very short contact times by means of a previously reported laminar-jet technique (12), since it is theoretically possible to observe an interfacial resistance at short times which cannot be observed at longer contact times.

## THEORY AND EXPERIMENT

The simplest mechanism for the transfer across an interface is described by

$$N_A = k_s(C^* - C_i) \quad (1)$$

The interfacial transfer coefficient is then the reciprocal of the interfacial resistance. It can never be infinite, since gas molecules can transfer across the interface only at a finite rate. The upper limit for  $k_s$  can be obtained from the kinetic theory of gases (4):

$$k_s = \frac{\alpha H}{\sqrt{2\pi RTM}} \quad (2)$$

If the condensation coefficient is 1, and there is no other interfacial resistance,  $k_s$  is so large that interfacial resistance is

practically zero, and interfacial equilibrium will be very closely approached during practical mass transfer operations.

However it is possible to conceive of a region of exceptionally high diffusional resistance in the liquid adjacent to the interface, and an equation of the same form as Equation (1) may also be used to describe this transfer (12); therefore presently it is convenient to consider  $k_s$ , defined by Equation (1) with an upper limit set by Equation (2), when  $\alpha = 1$ .

$k_s$  is examined by the passage of a laminar jet through a pure gas for a short distance. The rate of absorption of gas is compared with the rate calculated from Fick's law for unsteady state diffusion into a liquid in rodlike flow, with Equation (1) as the boundary condition at the interface. The solution for the average absorption rate over the jet is (5)

$$\bar{N}_A = \frac{D(C^* - C_0)}{k_s \theta} \left[ e^{k_s \theta / D} \cdot \operatorname{erfc} k_s \sqrt{\frac{\theta}{D}} + 2k_s \sqrt{\frac{\theta}{\pi D}} - 1 \right] \quad (3)$$

and when  $k_s$  is infinite the equation reduces to the well-known form

$$\bar{N}_A = 2(C^* - C_0) \sqrt{\frac{D}{\pi \theta}} \quad (4)$$

The total amount of gas absorbed per unit area in the absence of interfacial resistance is then given by

$$\frac{Q}{A} = 2(C^* - C_0) \sqrt{\frac{D \theta}{\pi}} \quad (5)$$

There are a number of conditions which must be satisfied for these equations to apply (3), the most important being that the jet is in rodlike flow. Since a boundary layer must exist when the jet is formed, it is necessary that the surface of the jet accelerate rapidly to the bulk velocity. If this does not occur, the absorption rate will be lower than these equations predict; if there is a significant boundary-layer effect, the rate will then

S. H. Chiang is with the Linde Company, Tonawanda, New York.

vary with jet length (12). This fact allows hydrodynamic effects to be separated from purely time-dependent effects such as diffusion, interfacial resistance, chemical reactions, etc., and affords a method of checking for self-consistency. Thus it was shown that when carbon dioxide was absorbed by a water jet formed with a very thin sharp-edged orifice plate, the absorption rate per unit area depended only upon contact time and was independent of jet length (12). This indicated that such a jet was essentially in rodlike flow and that the assumptions made in deriving Equations (3) and (4) were satisfied over wide ranges of jet length and velocity. A theoretical analysis of some of the hydrodynamic factors has been presented by Scriven (13).

The present work is based on a technique described previously (12). A laminar jet formed by a thin-orifice plate is passed through 99.5% oxygen saturated with water vapor, and, as the oxygen is absorbed, fresh gas is fed to the absorber from a constant-pressure source. The absorption rate is measured directly by the timing of the motion of a soap film moving in a capillary tube which is in the line connecting the absorber and constant-pressure source.

The absorption rate is quite small because of the relatively low solubility of oxygen in water, and the absorber was insulated to reduce the temperature fluctuations during a run to the order of  $\pm 0.03^\circ\text{C}$ . (The absorber and soap bubble make an excellent thermometer.) The system was in a constant-temperature room held at  $22.2 \pm 0.25^\circ\text{C}$ .

The orifice plates used were 0.01-cm.-thick stainless steel, and the orifices were 0.0914 and 0.0825 cm. in diameter. This type of thin orifice was shown previously to give essentially rodlike flow in the jet (12). The jet was removed from the absorber by being passed into a water-filled 0.11-cm.-diameter hole in a Lucite rod.

The water used was obtained by the

condensation of steam and was titrated for the oxygen content before being used. The inlet concentration averaged about 1% of saturation (relative to pure oxygen at 1 atm.), and the water leaving the system had a concentration very close to the inlet value because of the short contact times used. The nitrogen/oxygen ratio in the feed water was assumed to be the same as the ratio in water in equilibrium with air, and the dissolved nitrogen was treated in Equations (3) and (4) as if it were oxygen; this gave an average inlet concentration of total gas of about 3% of saturation. This treatment can be justified by the following analysis.

Gas-phase resistance is negligible, and if nitrogen interfacial resistance is also small, Equation (4), with suitable physical constants, describes the nitrogen desorption. The nitrogen accumulated in the gas phase during a run is very small, and if the trace of nitrogen present in the gas feed is neglected, the rate of transfer of nitrogen is

$$\bar{N}_A' = -2C_0' \sqrt{\frac{D'}{\pi\theta}} \quad (6)$$

Adding this to Equation (4) for oxygen and taking the two diffusivities as equal, one gets

$$(\bar{N}_A)_{net} = 2(C^* - C_{OT}) \sqrt{\frac{D}{\pi\theta}} \quad (7)$$

where

$$C_{OT} = C_0 + C_0' \quad (8)$$

and since the net rate of absorption of total gas is measured in the experiment, the nitrogen in the feed water can be treated as oxygen.

The jet area and contact time were calculated directly from measurements of jet length, diameter, and water flow rate, and the measured absorption rates were corrected to correspond to a total oxygen pressure of 1 atm. and an oxygen content in the feed water of zero.

Diffusivities have been measured by a number of workers in the temperature range of  $10^\circ$  to  $25^\circ\text{C}$ ., and without

temperature correction they vary from  $1.8 \times 10^{-5}$  to  $2.6 \times 10^{-5}$  sq. cm./sec. These results have been summarized by Davidson and Cullen (6). If the measured temperature dependence of Davidson and Cullen is used to correct the values to a common temperature, three independent measurements (1, 6, 9) yield a diffusivity in the region of  $2.2 \times 10^{-5}$  to  $2.4 \times 10^{-5}$  sq. cm./sec. at  $22.2^\circ\text{C}$ . with eight other values scattered about equally above and below. It appears probable that the correct diffusivity lies in this intermediate region.

## RESULTS

A range of contact time from 0.833 to 11.8 msec. was obtained when the jet length was varied from 0.505 to 6.16 cm. and the water flow rate from 0.737 to 2.688 cc./sec. The average rate of absorption is shown as a function of  $1/\sqrt{\theta}$  in Figure 1, where each point represents the average value of three independent measurements. The original data are available (3). The solid line is the equation for no interfacial resistance [Equation (4)]. The solubility was taken from the International Critical Tables, and the diffusivity used was the lowest probable value,  $2.20 \times 10^{-5}$  sq. cm./sec.

The dotted line in Figure 1 is the best straight line through the data. The results are replotted in Figure 2 to clarify the long contact-time values. Here the amount of gas absorbed is shown as a function of  $\sqrt{\theta}$ , and the theoretical line for no interfacial resistance is Equation (5) with the same physical constants as before.

## DISCUSSION

The data are more scattered than those reported for the absorption of carbon dioxide because of the extremely low flow rates which had to be measured. The maximum deviation among repeated runs was 10%, and the average was less than 5%. A more critical analysis of the data is shown in Figures 3 and 4. In Figure 3 the amount of gas absorbed is plotted against  $\sqrt{\theta}$  for different jet lengths, and the data are fitted by straight lines through the origin. The data are then cross plotted in Figure 4 at a constant contact time, where it is seen that the amount of gas absorbed per unit area is independent of jet length (the maximum deviation from the horizontal line is 5%). This confirms the earlier conclusions that the hydrodynamic effects are negligible in jets formed with a thin-orifice plate and indicates that the data are self-consistent.

Figures 1 and 2 show that the data fall significantly below the theoretical line for no interfacial resistance, when the lowest probable diffusivity is used. The choice of any higher diffusivity would cause an even greater difference between

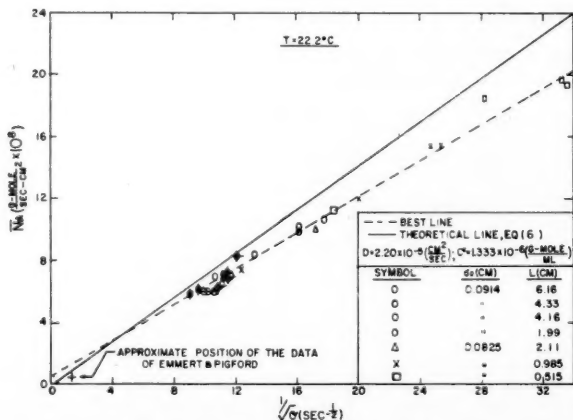


Fig. 1. Rate of oxygen absorption into water.



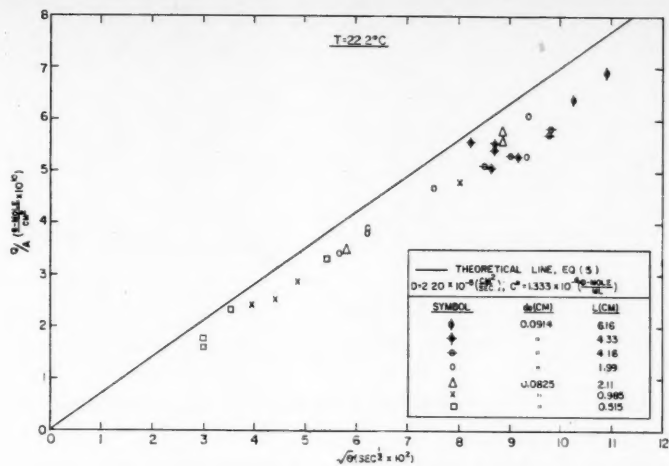


Fig. 2. Amount of oxygen absorbed per unit area.

the theoretical line and the data, and the diffusivity would have to be considerably less than  $2.2 \times 10^{-5}$  for the theoretical line to be included in the 95% confidence limits of the data.

The best straight line through the data (the dotted line in Figure 1) is given by  $\bar{N}_A = 4.83 \times 10^{-9} + 5.77 \times 10^{-9}/\sqrt{\theta}$ , where the standard deviation of the slope is  $8.00 \times 10^{-11}$ . Thus the best straight line intersects the  $y$  axis at  $\bar{N}_A = 4.83 \times 10^{-9}$  and the 95% confidence limits of the intercept are  $7.34 \times 10^{-9}$  and  $2.33 \times 10^{-9}$ ; therefore it is improbable that the data fit a straight line passing through the origin as demanded by the equation for no interfacial resistance [Equation (4)]. Since at long times the rate must approach zero under any circumstances, the nonzero intercept implies that  $\bar{N}_A$  is not a linear function of  $1/\sqrt{\theta}$ . Both these factors, the low rate and nonzero intercept, indicate the presence of an interfacial resistance which causes the rate to be lower than the theoretical and the relationship between  $\bar{N}_A$  and  $1/\sqrt{\theta}$  to be nonlinear, but they are not conclusive.

Figure 5 compares the experimental absorption rates with the theoretical rates for various values of  $k_s$  [Equation (4)], and  $k_s$  of 0.6 cm./sec. appears to give the best fit to the data. If the interfacial resistance is due entirely to a low condensation coefficient, the value of  $k_s$  corresponds to  $\alpha = 1.8 \times 10^{-6}$ .

If a diffusivity of  $2.4 \times 10^{-5}$  sq. cm./sec. is used for comparison, as in Figure 6, none of the constant resistance lines fit the data so well as when the lower diffusivity is used. However the best value of  $k_s$  is not changed much by the change in diffusivity, for it is seen to be in the range of 0.4 to 0.6 cm./sec.

There are two possible means of explaining the results without postulating an interfacial resistance (and in view of the history of the carbon dioxide studies,

perhaps this would be the prudent viewpoint):

1. There may be secondary effects which cause the absorption rate to be lower than the theoretical value and the time dependence to be somewhat different from the theoretical.

2. The diffusivity of oxygen in water may be appreciably lower than expected, and small secondary effects may explain the nonzero intercept.

The first explanation seems unlikely, for a technique very similar to that used here checked the theoretical value quite closely in the carbon dioxide-water system as well as in other systems (12, 3); moreover Figure 4 eliminates the possibility of any significant hydrodynamic effect such as a boundary layer or a stagnant zone at the receiver.

The only other possibility which could account for the lowered rate (aside from a leak in the system, which is ruled out on a number of grounds) is that the nitrogen/oxygen ratio in the entering water was about five times greater than the ratio at equilibrium. This is highly unlikely, for the maximum expected value would be the ratio in air, only 1.5 times greater than the equilibrium value.

Raimondi and Toor's (12) data could be interpreted to indicate a very small boundary-layer effect which would tend to give a positive  $y$ -axis intercept, and this is also possible in this work. Since there may have been some entrainment in the longest jet (6.16 cm.), the best straight line was recalculated without these points, and the lower limit of the 95% confidence level was found to be  $1.76 \times 10^{-9}$ . A small boundary-layer effect might then be used to explain the difference between this value and zero.

Thus if this explanation were used to explain away the nonzero intercept, and the diffusivity were  $1.6 \times 10^{-5}$  instead of  $2.2 \times 10^{-5}$  sq. cm./sec., the data would indicate no interfacial resistance.

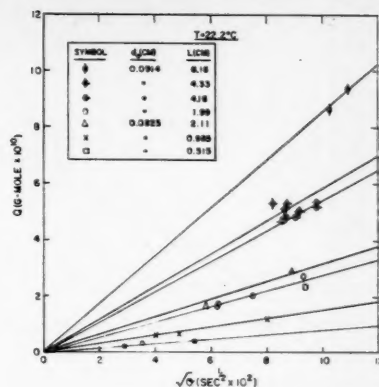


Fig. 3. Amount of oxygen absorbed at different jet lengths vs. square root of contact time.

Some support for this argument can be obtained from Emmert and Pigford (7), who absorbed oxygen in water in a relatively long wetted-wall column. Based on a diffusivity equivalent to  $2.40 \times 10^{-5}$  at 22.2°C. their data were 10 to 20% below the theoretical value for no interfacial resistance. The present data deviate from the theoretical by about the same amount, if this higher value of  $D$  is used in Equation (4). This agreement does not prove that the same interfacial resistance existed in both cases; on the contrary it indicates that either there is no interfacial resistance or the magnitude of the resistance is quite different in the two cases. This is due to the contact times used by Emmert and Pigford being of the order of 0.5 sec., 50 to 500 times larger than used here (see Figure 1), and at this long time an interfacial resistance of the magnitude considered here would be completely obscured by the large diffusional resistance in the liquid.

Figure 5, which contains the theoretical lines for various values of  $k_s$ , shows that at long contact times a curve passing through the present data is almost indistinguishable from the line for no interfacial resistance. Thus if there is an interfacial resistance present, Emmert and Pigford's value is about fifty times greater than the value reported here. The only line which will fit both sets of

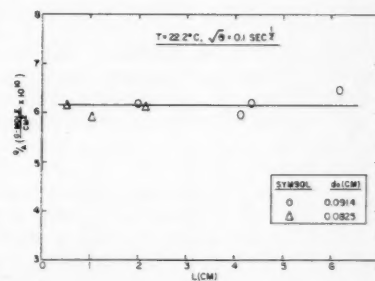


Fig. 4. Comparison of oxygen absorbed per unit area at different jet lengths for same contact time.

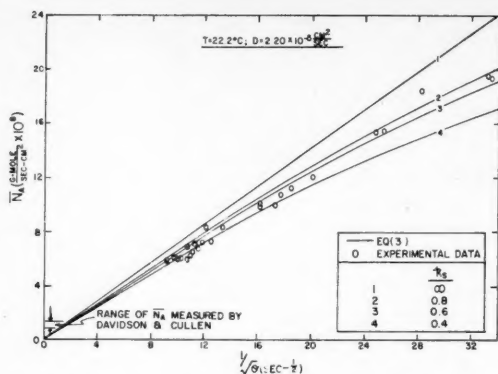


Fig. 5. Comparison of oxygen-absorption data with different interfacial-resistance lines.

data is a straight line through the origin, which corresponds to no interfacial resistance, and  $D = 1.6 \times 10^{-5}$  sq. cm./sec. Unfortunately this check could easily be fortuitous, since Emmert and Pigford's data for carbon dioxide were later shown to be low, quite possibly because of the hindering effect of a surface-active agent. Since the surface-active agent was present in their oxygen measurements also, the interfacial resistance in their system could well have been much greater than the value found in this work, where the interface is clean.

Davidson and Cullen (6) also measured the transient absorption of oxygen in water at relatively long contact times (the order of 0.1 sec.). They used a wetted sphere and reported no interfacial resistance and a diffusivity (by interpolation) of  $2.20 \times 10^{-5}$  sq. cm./sec. at  $22.2^\circ\text{C}$ . This technique was also used with other gases, and the measured diffusivities were shown to check known values quite accurately.

Their absorption rate was in the range  $0.75 \times 10^{-5}$  to  $1.3 \times 10^{-5}$  g.-moles/(sq. cm.)(sec.) (corrected to  $22.2^\circ\text{C}$ .) which, in the absence of a very large interfacial resistance, corresponds to the long contact-time region in this work, where the effect of interfacial resistance is small (Figure 5). However since the flow in their case was quite different from that used here, the diffusion equation for their system was solved approximately with a constant interfacial resistance described by  $k_s = 0.6$  cm./sec. The results showed, as expected, that the interfacial resistance is almost completely obscured by the diffusional resistance and that the convergence of the curves for various values of  $k_s$  at long contact times is essentially the same as shown in Figure 5. At their shortest contact time this interfacial resistance would lower the absorption rate about 2% and at their longest contact time by about 1%; even if this resistance were present, the shape of the rate curve would be practically indistinguishable from the curve for no interfacial resistance.

However the diffusivity calculated by the use of the equation for no interfacial resistance would be 2 to 4% low since the diffusivity appears as the square root in the rate equation; therefore the corrected diffusivity would be about  $2.25 \times 10^{-5}$  sq. cm./sec. This change is insignificant and has negligible effect on the value of  $k_s$  obtained in this work.

Thus the work of Davidson and Cullen and the present work could be considered as one set of transient experiments covering an effective contact time range of 0.8 to about 900 msec. The entire set of experiments is consistent with a diffusivity of  $2.25$  sq. cm./sec. and an interfacial transfer coefficient of  $0.6$  cm./sec.

Since interfacial resistance is in series with a liquid-phase resistance, its effect depends upon the relative magnitude of the two resistances (12). As in packed columns the liquid-side resistance is usually appreciably larger than the interfacial resistance reported in this work, the interfacial resistance could be safely neglected in this case. However if  $k_s$  is a constant, it would limit the maximum possible mass transfer coefficient which could be obtained; even if the liquid- and gas-phase resistances were reduced to zero, the over-all coefficient could not exceed  $0.6$  cm./sec. On the other hand, if the experimental data reported here are in error by about 15%, the maximum possible coefficient is set by Equation (2) with  $\alpha = 1$ , and the maximum over-all coefficient is more than  $10^6$  times greater than the foregoing limit.

#### ACKNOWLEDGMENT

This work was carried out with the financial support of the National Science Foundation.

#### NOTATION

$A$  = surface area, sq. cm.  
 $C_0$  = initial gas concentration in liquid, g.-mole/cc.  
 $C_i$  = interfacial gas concentration in liquid, g.-mole/cc.

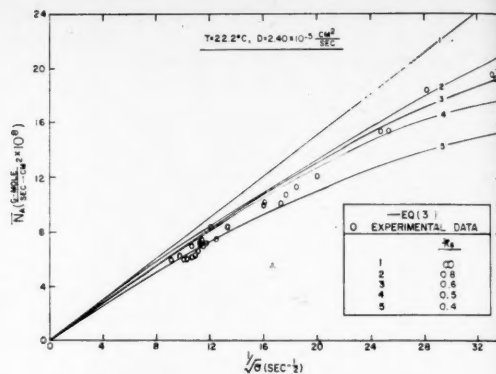


Fig. 6. Comparison of oxygen-absorption data with different interfacial-resistance lines.

$C^*$  = equilibrium gas concentration in liquid, g.-mole/cc.

$D$  = diffusivity of gas in liquid, sq./cm./sec.

$H$  = Henry's law constant erg/g.-mole  
 $k_L$  = interfacial mass transfer coefficient, cm./sec.

$k_s$  = interfacial transfer coefficient

$M$  = molecular weight

$N_A$  = mass transfer rate, g.-mole/(sec.)(sq. cm.)

$\bar{N}_A$  = average mass transfer rate, g.-mole/(sec.)(sq. cm.)

$Q$  = amount of gas absorbed, g.-mole

$R$  = gas constant, erg./(g.)(mole)(°K.)

$T$  = temperature, °K.

$\alpha$  = condensation coefficient

$\theta$  = time, sec.

primes = nitrogen

#### LITERATURE CITED

- Carlson, Tor, *J. Am. Chem. Soc.*, **33**, 1027 (1911).
- Cullen, E. J., and J. F. Davidson, *Trans. Faraday Soc.*, **53**, 113 (1957).
- Chiang, S. H., Ph.D. thesis, Carnegie Institute of Technology, Pittsburgh, Pa. (1958).
- Danckwerts, P. V., *Research (London)*, **2**, 494 (1949).
- Danckwerts, P. V., and A. M. Kennedy, *Trans. Inst. Chem. Engrs. (London)*, Supplement No. 1, **32**, S53 (1954).
- Davidson, J. F., and E. J. Cullen, *ibid.*, **35**, 51 (1957).
- Emmert, R. E., and R. L. Pigford, *Chem. Eng. Progr.*, **50**, 87 (1954).
- Higbie, Ralph, *Trans. Am. Inst. Chem. Engrs.*, **31**, 365 (1935).
- Kolthoff, I. M., and C. S. Miller, *J. Am. Chem. Soc.*, **63**, 1013 (1941).
- Littlewood, Roy, and Eric Rideal, *Trans. Faraday Soc.*, **52**, 1598 (1956).
- Nijssing, R.A.T.A., Thesis, Physische Technologie Der Technische Hogeschool, Delft, Holland (1957).
- Raimondi, Pietro, and Toor, H. L. *A.I.Ch.E. Journal*, **5**, 1 (1959).
- Scriven, E. L., II, Ph.D. thesis, Univ. Del., Newark (1956).

Manuscript received June 3, 1958; revision received October 13, 1958; paper accepted October 13, 1958.

# Factors Affecting Density Transients in a Fluidized Bed

JAMES M. DOTSON

General Electric Company, Waterford, New York

The effects of five operating variables on the uniformity of fluidization in a 4-in.-diameter column were determined by a statistically designed experiment. Density fluctuations inside the bed were measured by a capacitance method. Certain parts of the experiment were repeated in a 24-in.-diameter column for comparison with the 4-in.-column data.

In the 4-in. column gas velocity had by far the greatest effect on uniformity, with uniformity generally decreasing with an increase in gas velocity. This is consistent with the theory that most gas introduced in excess of the rate for incipient fluidization passes through the bed in the form of various-sized bubbles. Better uniformity at the lower bed level indicates that bubbles grow in size as they proceed up the column. An entirely different gas-flow pattern was indicated in the 24-in. column.

Uniform expansion of a fluidized bed with an increase in gas velocity would result in uniform density throughout; this is a condition ideal for maximum solids-gas contact. There are several factors however which favor bubble and agglomerate formation and thus make the bed less than 100% uniform throughout.

If chemical reactions are occurring in the fluidized bed, then uniformity could affect performance through its effect on over-all rate, conversion, or selective reactions if simultaneous reactions can occur. Gas bypassing could result in less over-all contact and conversion. If the reaction mechanism is such that desirable reactions occur at the surface of the solids but undesirable reactions proceed in the gas phase, then bubble formation with its greater gas phase would favor the undesirable reaction. Because of these possible effects of bed uniformity on chemical reactions, the effects of several operating variables on bed uniformity were investigated.

Only a superficial estimate of fluidization uniformity can be made in a transparent or open-top vessel. Quantitative measurements require investigation into the interior of the bed by a measuring device which disturbs the fluidization characteristics to a negligible degree. X-ray absorption (3) and electrical-capacitance techniques (1, 2) have been used for this purpose. Electrical capacitance was selected for this investigation because it is simpler and because it measures a smaller segment of the bed; it is based on the large difference in dielectric constant between gases and

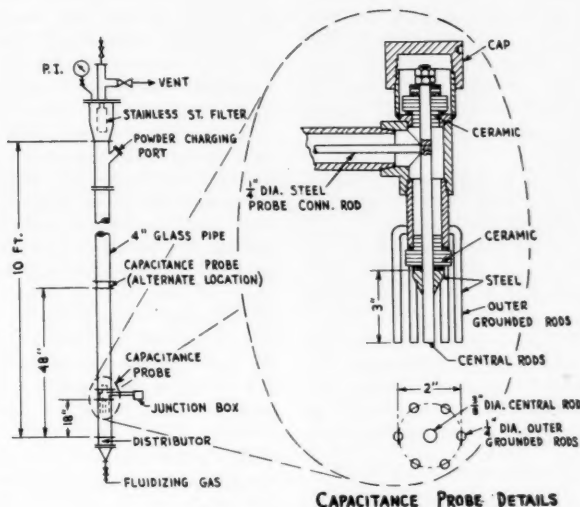


Fig. 1. Four-inch fluidization column.

TABLE I. SCREEN ANALYSES OF SILICON POWER

-60-mesh grind			-200-mesh grind		
Mesh size (U.S.S.)	% retained 4 in. runs	% retained 24 in. runs	Mesh size (U.S.S.)	% retained 4 in. runs	% retained 24 in. runs
50	0	0	50	0	0
70	0.4	0.2	70	0.2	0.2
100	13.3	7.9	100	4.7	0.2
140	17.6	17.3	140	6.7	0.2
200	16.8	18.7	200	5.9	0.4
270	11.8	15.2	270	5.7	10.1
400	16.0	19.7	400	16.7	33.5
-400	24.1	21.0	-400	60.1	55.4
	100.0	100.0		100.0	100.0

James M. Dotson is with the General Electric Company, Waterford, New York.

most solids. The presence of a gas-solid mixture (as in a fluidized bed) between the plates of a capacitor produces an effective dielectric constant which is proportional to the relative quantity of each phase. Thus by measuring the capacitance of an appropriately sized probe placed in the bed, one can calculate densities within the probe plates from known dielectric constants of the two phases or from an empirical calibration of density vs. capacitance over the desired density range.

The application of capacitance methods to measurement of fluidization characteristics is not new. It was developed independently at the Bureau of Mines (1) and at the duPont laboratories (2). New information reported here includes improvements in capacitance measurements and calculations over those reported (1, 2) and the results of a statistical experiment designed to evaluate the independent effects and interactions of six operating variables on uniformity of fluidization in a particular system. A probe was designed to give a minimum interference with fluidization in its immediate vicinity and to measure the density of a finite volume. The new method of calculation accounts for the nonlinearity between density and effective dielectric constant. The ranges in bed height and superficial gas velocity have been greatly extended over those reported (3).

The results of a statistically designed experiment reported here show the effect of particle size, distributor type, bed level, probe height, superficial velocity, and column diameter. The solid phase consisted of a mixture of metallic silicon and copper powder with a weight ratio of 93/7. Inert gas (approximately 85 to 15 volume ratio of nitrogen and carbon dioxide) was the fluidizing gas. These experiments were conducted at atmospheric pressure and ambient temperature.

## APPARATUS AND EXPERIMENTAL PROCEDURES

### Capacitance-Measuring Equipment

The only equipment not commercially available was the probe itself; a sketch is shown in Figure 1. The effective portion of the probe was the volume enclosed

by the six outer grounded rods, which together with the central rod formed a coaxial capacitance cell 2 in. in diameter and 3 in. long.

To compare the uniformity in a 4- and 24-in. column on the same scale, it was necessary to use the same probe size in both columns. It was thought at the time that the maximum bubble size in the 24-in. column was about 3 in. or larger. This probe length was therefore selected, since a completely gas-filled capacitor volume would produce a minimum chart reading. This resulted in a comparatively oversized probe volumetrically in the 4-in. column. It is believed however, on the basis of visual observations, that the seven vertically oriented rods (which occupied only 3% of the column cross-sectional area) had a negligible effect on the fluidization characteristics of the bed in their immediate vicinity and below them. In a separate test, with only the effective portion of the probe (rods) submerged in the bed, the emerging gas bubbles could be observed as they broke the surface in the vicinity of the probe rods. Compared with a probe-free bed no tendency was observed for the gas bubbles to avoid the probe or be broken into smaller bubbles by the probe rods. The author believes that similarly the probe rods

affected the fluidization characteristics to a negligible degree when the probe was completely submerged within the bed.

Other capacitance-metering equipment consisted of a detector and a recorder with 0- to 1.0-ma. full-scale sensitivity, 0.2-sec. full-scale response, 1 in./sec. chart speed.

### Fluidization Columns

The 4-in. column consisted of a 10-ft.-high section of 4-in. I.D. glass pipe, gas distributor at bottom (described below), a 6-in.-diameter disengaging head at the top of the column; and a star-type stainless steel filter mounted in the disengaging head to prevent powder from leaving the column. The capacitance probe was held in place by a metal spacer sandwiched between sections of the glass pipe at heights of 18 or 48 in. above the gas distributor. Figure 1 shows a sketch of this column.

Two distributor types were used: a 1-in.-thick section of porous carbon and an orifice type having one 0.073-in.-diameter hole every 1.8 sq. in., arranged on 1½-in. equilateral triangle centers.

The 24-in. column was constructed of a 24-in. schedule-20 steel pipe and contained eighteen vertically mounted 1½-in. schedule-40 pipes, arranged on 4½-in. triangular centers (central pipe omitted) to simulate a heat transfer coil. Only the orifice type of distributor was used in this column. Hole size and number per unit of cross-sectional

TABLE 2. CAPACITANCE-PROBE EXPERIMENT DESIGN

COLUMN DIAMETER →			4 INCH				24 INCH
PROBE HEIGHT ↓ 18 IN.	POWDER GRIND ↓ -60 MESH -200 MESH	DIST. TYPE →	POROUS CARBON		ORIFICE		ORIFICE
		BED HEIGHT →	5 Ft.	9 Ft.	5 Ft.	9 Ft.	9 Ft.
		RUN NUMBER →	4-7	4-5	4-6	4-12	24-12
			4-11	4-9	4-10	4-14	24-14
48 IN.	-60 MESH		4-4	4-8	4-3	4-2	24-2
	-200 MESH		4-15	4-1	4-13	4-16	24-16
SUPERFICIAL VELOCITY, FPS.			0.05 0.1 0.3 0.5 0.7				0.3 0.5 0.7

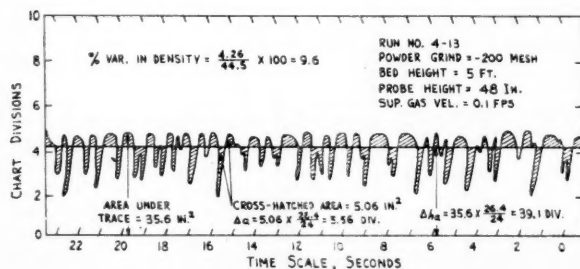


Fig. 2. Typical recorder trace, 4-in. column.

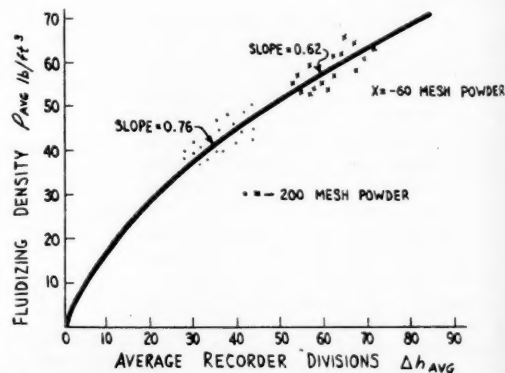


Fig. 3. Fluidization density vs. average recorder deflection.



area were the same as for the 4-in. column; these holes were arranged on 1½-in. square centers.

#### Powder

Two powder grinds (-60 mesh and -200 mesh of commercial silicon metal) were used, each mixed with 7% by weight of copper powder, 80% of which was below 10 μ.

Screen analyses of the silicon are shown in Table 1.

#### EXPERIMENTAL PROCEDURE

Fluidizing gas was started through the empty column at a superficial velocity of 0.1 ft./sec. (0.3 ft./sec. in 24-in. column); the capacitance instrument was checked for zero reading. A weighed quantity of powder was charged to the column to the desired bed height. The recorder chart was started and ran for 24 sec. at this gas velocity; bed height was recorded from a visual average of the fluctuating top of the dense phase in the 4-in. column (by Δ*p* measurements in the 24-in. column). The gas velocity was successively adjusted to 0.3, 0.5, 0.7, and 0.05 ft./sec. with recorder-chart traces taken and bed heights observed at each velocity. Velocities were repeated in the same order. Powder was discharged from the column and reweighed. The capacitance probe was again checked for zero reading with the empty column.

The operating conditions were changed as necessary for the next run, and the procedure was repeated.

The same powder charge for each grind was used for all the 4-in. experiments. The 24-in. runs were also made with the same powder charge for each grind, but these were not the same identical charges used in the 4-in. column.

The statistical design is shown in Table 2. Runs were made in the random order shown.

#### Calculation of Data

Fluidization nonuniformity was calculated in terms of percentage variation in density, defined as (variation in density, lb./cu. ft. × 100)/(average density, lb./cu. ft.). The variation in density represents an integration with respect to time of the irregularity in density above and below the average density. Thus for a perfectly uniform fluidized bed the variations in density above and below the mean and the percentage variation would be zero. The other extreme of 100% variation in density would be represented by the condition of alternately filling the probe volume with all solid and all gas. The values for average density and variation in density were calculated from the recorded values of probe capacitance over a 24-sec. time interval. A typical recorder trace is shown in Figure 2 and will be used to illustrate the method of calculation. The original 24-in. chart length represented a 24-sec. sampling time at a 1-in./sec. chart speed. The average recorder reading was calculated to be 39.1 divisions from a planimeter area of 35.6 sq. in.

between the trace and base line, 24-in. chart length, and a conversion factor of 26.4 divisions/in. Average recorder height was drawn on the chart. Area between average line and trace (cross-hatched area) was determined by planimeter (5.06 sq. in.) and converted to equivalent recorder divisions (5.56 divisions). The average recorder height (Δ*h<sub>a</sub>* = 39.1) was converted to average density of 44.5

seen from Table 3, in which averages of percentage variation in density are presented.

Over the ranges investigated, all variables except bed height had a measurable influence on uniformity of fluidization. The relative effect of each of the primary variables was much greater for some than for others, as may be seen from the sums of squares assignable to each primary variable:

Primary variable	Sums of squares	Percentage of total sums of squares due to primary variables
A. Distributor	31.711	0.6
B. Bed height	5.137	0.1
C. Probe height	1,982.253	39.4
D. Powder grind	57.852	1.2
E. Gas velocity	2,959.505	58.8
Total due to primary variables	5,036.458	100.1
A.B.C.D. (within replicates, d.f. = 1)	4.965	
E. (within replicates, d.f. = 80)	86.889	

lb./cu. ft. by a calibration chart (Figure 3). This is an empirical calibration chart representing a plot of experimentally determined bed densities (bed weight/measured volume) vs. the average recorder reading for all of the 4-in. runs.\* The variation in recorder trace (Δ*a* = 5.56 divisions) was converted to variation in density (Δ*p* = 4.26 lb./cu. ft.) from the slope of the Figure 3 curve (0.76). For simplification in calculation the following conversion factors were used, representing the approximate slopes at the density in question:

-60 mesh = 0.625 lb./cu. ft. per recorder division

-200 mesh = 0.76 lb./cu. ft. per recorder division

Percentage variation in density was then variation in density, lb./cu. ft. × 100 = average density, lb./cu. ft.  

$$\frac{4.26}{44.5} \times 100 = 9.6\%$$

#### Statistical Analysis

The effects of the five operating variables on bed uniformity, plus all interactions, were determined from a statistical analysis of variance. Significant differences between levels were determined by the *t*-test method. Standard statistical methods were used in this analysis (6).

#### EXPERIMENTAL RESULTS AND DISCUSSION—4-IN.-COLUMN DATA

A comparison of the over-all effects of each of the primary variables may be

seen from Table 3, in which averages of percentage variation in density are presented. Over the ranges investigated, all variables except bed height had a measurable influence on uniformity of fluidization. The relative effect of each of the primary variables was much greater for some than for others, as may be seen from the sums of squares assignable to each primary variable:

Gas velocity and probe height had the greatest effects by far, with fluidization uniformity generally being inversely proportional to both of these variables. Powder grind had a detectable but relatively minor effect, with the -200-mesh powder giving better uniformity. The same thing was true of the gas-distributor plate, with the porous type giving slightly better uniformity.

The effects of these variables were far from uniform over the whole experiment, however, as shown by the following table of two- and three-way interactions with superficial velocity, all of which were significant at the 1% level.

Interaction	Sums of squares
1. CE, probe height and superficial velocity	325.8
2. DE, powder size and superficial velocity	209.7
3. BDE, bed height, powder size, and superficial velocity	34.3
4. CDE, probe height, powder size, and superficial velocity	21.3

The only significant two-way interaction exclusive of velocity was between probe height and powder size (interaction CD, with 21.7 sums of squares), which was significant at the 7% level. The direction and magnitude of these interactions with gas velocity may be seen in Figures 4 through 7.\*

These data were interpreted as follows:

1. Most fluidizing gas introduced in excess of the rate necessary for incipient fluidization (approximately 0.02 to 0.05 ft./sec.) passes through the powder bed in the form of bubbles. This was indicated by the plateau bed densities at low superficial velocities (Figure 2) as well as by the very large over-all decrease in

\*Tabular material has been deposited as document 5873 with the American Documentation Institute, Photoduplication Service, Library of Congress, Washington 25, D. C., and may be obtained for \$1.25 for photoprints or \$1.25 for 35-mm. microfilm.

\*See footnote in second column.

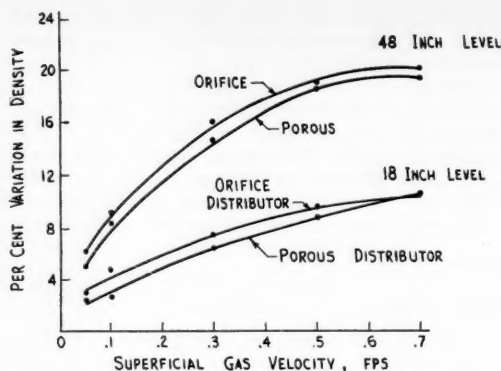


Fig. 4. Interaction among distributor, probe height, and gas velocity in 4-in. column.

TABLE 3. AVERAGE PERCENTAGE VARIATION IN DENSITY FOR PRIMARY VARIABLES—4-IN. COLUMN

Primary variable	Level	Average percentage variation in density	Difference between levels, 1 minus 2
Distributor	A <sub>1</sub> (porous)	9.618	-0.890*
	A <sub>2</sub> (orifice)	10.508	
Bed height, ft.	B <sub>1</sub> (5)	10.242	0.358
	B <sub>2</sub> (9)	9.884	
Probe height, in.	C <sub>1</sub> (18)	6.543	-7.040†
	C <sub>2</sub> (48)	13.583	
Powder grind	D <sub>1</sub> (-60 mesh)	10.664	1.202*
	D <sub>2</sub> (-200 mesh)	9.462	
Velocity, ft./sec.	E <sub>1</sub> (0.05)	4.087	†
	E <sub>2</sub> (0.10)	6.076	
	E <sub>3</sub> (0.30)	11.200	
	E <sub>4</sub> (0.50)	13.942	
	E <sub>5</sub> (0.70)	15.009	

\*Represents the significant difference between levels at 5%; that is, if this experiment could be repeated many times (which it cannot), one would expect a difference this large to result from random fluctuations occasionally (less than 5% of the time).

†Represents the significant difference between levels at 1%.

uniformity with an increase in superficial velocity (Table 3). This two-phase system of gas-solid fluidization has been postulated by numerous investigators (2, 3).

2. Gas bubbles grow in size as they proceed up the column, as indicated by the large decay in uniformity between the 18- and 48-in. levels in the column. This is illustrated by the large difference

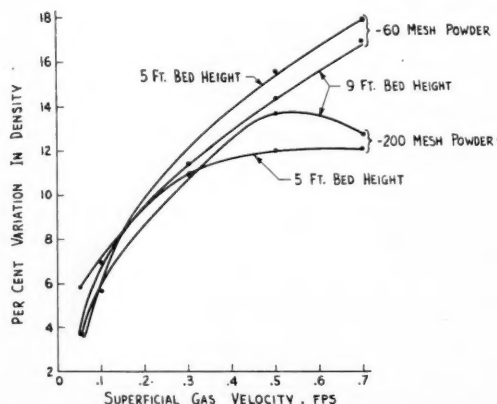


Fig. 5. Interaction among bed height, powder grind, and gas velocity in 4-in. column.

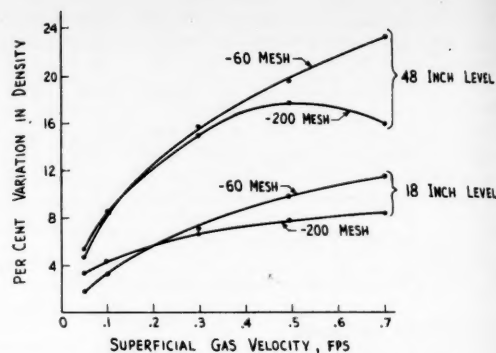


Fig. 6. Interaction among probe height, powder grind, and gas velocity in 4-in. column.

between the 18- and 48-in. average curves in Figure 4. An analogy between bubble coalescence in this and a true liquid-gas system is suggested (4).

3. Generally additional powder in the upper part of the column had no effect on the fluidization characteristics in the lower part of the bed, as indicated by the insignificant over-all bed height effect (Table 3). Under the limited conditions of a high gas velocity and fine powder the uniformity was decreased by the addition of four more feet of powder (lower two curves in Figure 5). However under the conditions of high velocity and coarse powder the additional bed height had the opposite effect on fluidization uniformity. Although these peculiar interactions are presently unexplainable, they are believed to be real, as indicated by a significant difference at the 1% level.

4. There was some evidence of an interaction between the type of distributor, probe height, and gas velocity, as indicated by the three-way interaction between these variables significant at the 10% level. The greatest difference between distributors was found at a 0.1 ft./sec. velocity 18 in. above the distributor. (See plot of interaction Figure 4.) These results tend to confirm those of Grohse (3), who found a porous type of distributor much superior to an orifice

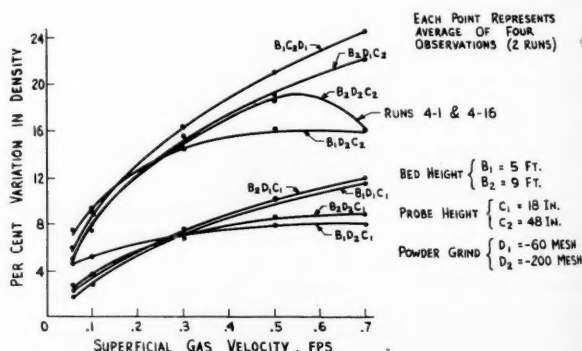


Fig. 7. Interaction among bed height, probe height, powder grind, and gas velocity in 4-in. column.

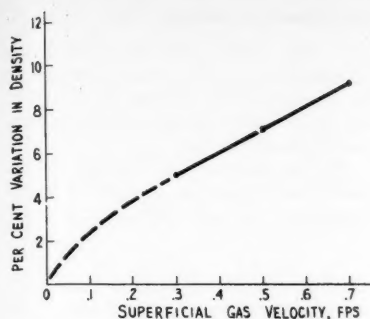


Fig. 8. Variation in density, 24-in. column.

type at most levels in a 15-in.-high bed in the 0.1 ft./sec. velocity region. Morse and Ballou (2) reported that the use of a fine-cloth type of distributor improved the uniformity over no distributor for as much as 16 in. above the distributor but that at higher levels the improvement was negligible. It is concluded that outside the narrow limits of 0- to 18-in. bed levels and possibly at gas velocities up to 0.3 ft./sec. the effect of initially good gas distribution is pretty well lost among other more dominant factors.

5. The interaction between powder size and gas velocity (interaction DE) was very pronounced. At the lower gas velocities better fluidization uniformity was obtained with the -60-mesh powder, but at 0.3 ft./sec. and above this trend was reversed. This tendency toward reversal with increasing gas velocity was found at both probe heights but was most pronounced at the 18-in. level (Figure 6, CDE interaction). The poorer fluidization of the -200-mesh powder at low gas velocities has been attributed to gas channeling through the relatively compact bed. This conclusion was confirmed visually. Gas channels, or in some cases distinct bubble paths, were observed under the conditions of low gas velocity and fine powder in the lower section of the column. At higher gas velocities the gas channels broke up, but the trend toward better uniformity was offset by the formation of large bubbles. Bubble formation was found to be favored by the coarse powder, a confirmation of previous findings (2).

6. With the coarse powder, bubble

TABLE 6. AVERAGE PERCENTAGE VARIATION IN DENSITY FOR PRIMARY VARIABLES—24-IN. COLUMN

Primary variable	Level	Average percentage variation in density	Difference between levels
Probe height, in.	$C_1$ (18)	7.13	0.05
	$C_2$ (48)	7.08	
Powder grind	$D_1$ (-60 mesh)	7.11	0
	$D_2$ (-200 mesh)	7.11	
Velocity, ft./sec.	$E_3$ (0.3)	4.96	2.18*
	$E_4$ (0.5)	7.14	
	$E_5$ (0.7)	9.225	

\*Represents the significant difference (by *t* test) between levels at 5%. The value of the standard error for difference between two means is  $(\sigma_{x_1} - \sigma_{x_2}) = 0.989$ .

growth up the column was found to be accelerated by an increase in gas velocity over the entire range of 0.05 to 0.7 ft./sec. (Figure 6); the same trend was observed for the fine powder up to a velocity of 0.3 ft./sec., but above this velocity bubble growth rate leveled off. An actual increase in uniformity was obtained in some cases by increasing the gas velocity from 0.5 to 0.7 ft./sec. The most general conditions under which a statistically significant decrease was observed were with -200-mesh powder at the 48-in. level, in which the difference in going from 0.5 to 0.7 ft./sec. was 1.6 units. This represents a significant difference, since it is three times the standard error for differences of 0.521 unit. The increase in uniformity in going from 0.5 to 0.7 ft./sec. was even more evident for those runs in which the bed height was 9 ft., used -200-mesh powder, and was at the 48-in. level (runs 4-1 and 4-16). The average of these two runs is shown in Fig. 7 (BCDE interaction). The same trend toward better uniformity was also observed under comparable conditions in the 24-in. column, but the difference between 0.5 and 0.7 ft./sec. was not statistically significant, probably owing to the higher error term in the large column.

At this time no entirely satisfactory explanation can be offered for these unexpected interactions between powder size and gas velocity and for their effect on bubble growth. They may in some way be related to the scale (or eddy size) in turbulent diffusion. This explanation is suggested by a comparison of

these data with those reported by Hanratty, *et al.* (5) in which the Peclet number was observed to go through a minimum value with an increase in Reynolds number. These phenomena were found to be related more specifically to the scale term in the Peclet number and to the fraction voids. In their liquid-solid (particulate) system the minimum density uniformity occurred at approximately 0.7 fraction void; in the gas-solid system discussed here the minimum density uniformity occurred at approximately 0.75 fraction void. The diffusion phenomena of Hanratty were explained as follows: "Eventually, at a fraction void of 0.70, a fluid element may begin to flow past solid particles without the necessity at each level of flowing laterally in order to evade a particle. Beyond the critical fraction void, in dilute beds, the turbulence is particle generated and the eddy diffusivity then is a direct function of particle population. . . ." Similar phenomena may be occurring in the system presented in this paper, in which at a sufficiently high void volume the tendency for bubbles to move laterally is decreased and their chances of colliding and coalescing with other bubbles thereby reduced. If this explanation is valid, then a similar critical velocity might be expected with the coarse powder at some gas velocity above 0.7 ft./sec., the maximum studied here.

#### Twenty-four-Inch Results

The average percentage variations in density for the primary variables studied (probe height, powder grind, and gas velocity) are shown in Table 6.\* These data were interpreted as follows:

1. In comparison with that of the 4-in. column under comparable conditions the indicated fluidization uniformity was about twice as good in the 24-in. column (7.1 vs. 13.8 over-all).

2. Contrary to the findings in the 4-in. column, no indication of bubble growth was found between the 18- and 48-in. levels in the 24-in. column.

3. Generally the effect of gas velocity was similar in both columns (Figure 8).

\*See footnote on page 171.

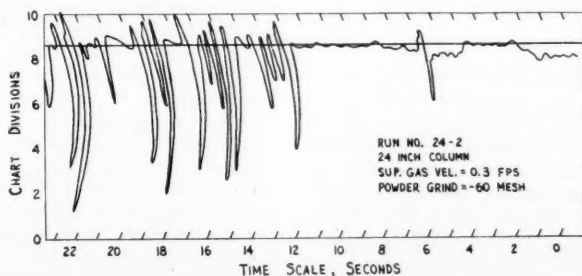


Fig. 9. Typical recorder trace, 24-in. column.

4. Reproducibility of data was very much poorer in the 24-in. column, especially at the lower velocities.

No entirely satisfactory explanation can be offered to account for all these somewhat surprising results. The author expected larger bubbles in the large column and suspects that large bubbles were actually present but that only occasionally would the bubble paths contact the probe. One reason for believing this is the generally poorer reproducibility of the 24-in. data in comparison with the 4-in. data. Figure 9 shows a good example of this phenomenon. For the first part of the trace practically no bubbles were evident. This was followed immediately by a period in which many large bubbles contacted the probe. Since the probe was located in the horizontal center of the bed, it would have been possible for the bubbles periodically to channel around the probe through other vertical paths. Another reason for suspecting the presence of bubbles in the 24-in. column (but generally undetected by the capacitance probe) is the difference between the over-all density (measured by bed volume and powder weight) and local density at the probe. This difference is in the direction one would expect for such an occurrence. An example of the difference in density is as follows:

Run 24-2	
Powder size:	-60 mesh
Probe height:	48 in.
Superficial gas velocity:	0.5 ft./sec.
Over-all density:	47.5 lb./cu. ft.
Local density at probe:	59.1 lb./cu. ft.

These are believed to be real differences in density. The presence of large bubbles or bubble paths in this column was confirmed subsequently by the helium tracer technique, which showed gross gas bypassing. Because of this nonrepresentative sampling in the center of the bed only, the results obtained in the 24-in. column and reported here should not be used as a true indication of the effect of the primary variables throughout the entire bed.

## CONCLUSIONS

### 4-inch Column

1. Over the ranges studied, all operating variables except bed height had a measurable influence on the uniformity of density throughout the bed.

2. Gas velocity through the powder bed had by far the greatest effect on uniformity, with uniformity generally decreasing with an increase in gas velocity. This was interpreted to mean that most gas introduced in excess of the rate for incipient fluidization passes through the bed in the form of various-sized bubbles.

3. Better uniformity at the lower bed level indicates that bubbles grow in size as they proceed up the column.

4. Bubble growth is accelerated by a coarser powder.

5. Fine powder promotes the formation of gas channels or bubble paths at low gas velocities in the lower section of the powder bed.

6. Except in the vicinity immediately above it the type of distributor has relatively little effect on uniformity.

### Twenty-four-inch Column

1. The more uniform density (in comparison with that of the 4-in.) found in the horizontal center of the 24-in. column is not believed to be representative of the entire bed.

2. Gas channels or distinct bubble paths are believed to be present in the column.

## ACKNOWLEDGMENT

The author wishes to thank G. J. Hahn, Statistical Methods Section, General Engineering Laboratory, General Electric Company, for the statistical calculations.

## LITERATURE CITED

- Dotson, James M., *et al.*, *Chem. Eng.* **56**, 128 (October, 1949).
- Morse, R. D., and C. O. Ballou, *Chem. Eng. Progr.*, **47**, 199 (1951).
- Grohse, E. W., *A.I.Ch.E. Journal*, **1**, No. 3, 358 (1955).
- Davidson, Leon, and E. H. Amick, Jr., *A.I.Ch.E. Journal*, **2**, 337 (1956).
- Hanratty, Thomas J., George Latinen, and Richard H. Wilhelm, *A.I.Ch.E. Journal*, **2**, 372 (1956).
- Davies, O. L., "Statistical Methods in Research and Production," Oliver and Boyd, London (1954).

Manuscript received April 14, 1958; revision received August 28, 1958; paper accepted August 31, 1958.

# Viscous Flow Relative to Arrays of Cylinders

JOHN HAPPEL

New York University, New York, New York

The free-surface model, successfully employed to predict sedimentation, resistance to flow, and viscosity in assemblages of spherical particles, has been extended to the case of flow relative to cylinders. It is shown to be in good agreement with existing data on beds of fibers of various types and flow through bundles of heat-exchanger tubes for cases where it can reasonably be expected to apply. Close agreement in the dilute range with the only theoretical treatment for flow parallel to a square array of cylinders provides interesting validation of the model.

The steady slow motion of fluids relative to assemblages of spherical particles has been previously treated mathematically by the use of modification of the unit-cell technique. Results have been reported for sedimentation and resistance to flow (11) as well as for viscosity of suspensions (10). The present development extends this theory to the case of flow relative to groups of cylindrical objects.

The derivations are developed on the basis that two concentric cylinders can serve as the model for fluid moving through an assemblage of cylinders. The inner cylinder consists of one of the rods in the assemblage and the outer cylinder of a fluid envelope with a free surface. The relative volume of fluid to solid in the cell model is taken to be the same as the relative volume of fluid to solid in the assemblage of cylinders. In effect one

assumes that at a distance from the disturbance to fluid motion caused by a cylinder the velocity of flow will not be greatly affected by the exact shape of the outside boundary. The important consideration is that the appropriate boundary condition of no slippage along the walls of the fluid envelope be maintained. The situation is easily visualized in Figure 1, which shows the unit cell in a square array as compared with the model assumed for axial flow. The cross-hatched area occupied by fluid is the same for both the array and model. The dotted line indicates the outside boundary of the fluid envelope at which a condition of no friction is maintained. Employment of appropriate boundary conditions en-



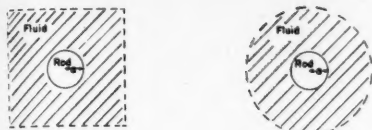


Fig. 1. Free-surface model for axial flow.

ables closed solutions to be obtained for the Navier-Stokes equations by the use of this model.

Two basic cases are considered; in the first case flow is assumed to be parallel to the axis of the cylinder, and in the second, flow is at right angles to the cylinder axis. These results are directly applicable to the cases where fluid is flowing parallel or perpendicular to a bank of cylinders. In the case of random assemblages, where the cylinders are not parallel to each other, it is necessary to employ a weighted average. In the case of flow perpendicular to cylinders the model does not distinguish between crossed or parallel arrangement of the cylinders, and in such random assemblages it is necessary in averaging to give twice the weight to the correlation for flow perpendicular to cylinders as for flow parallel to cylinders.

$$k = \frac{2\epsilon^3}{[1 - \epsilon] \left[ 2 \ln \left( \frac{1}{1 - \epsilon} \right) - 3 + 4(1 - \epsilon) - (1 - \epsilon)^2 \right]} \quad (9)$$

#### FLOW PARALLEL TO CYLINDERS

The basic differential equation to be solved is

$$\frac{d}{dr} r \frac{du}{dr} = \frac{1}{\mu} \frac{dp}{dx} \quad (1)$$

The solution to this equation for constant  $dp/dx$  is

$$u = \frac{1}{4\mu} \frac{dp}{dx} r^2 + A \ln r + B \quad (2)$$

In this case one assumes that fluid is moving through the annular space between the cylinder of radius  $a$  and the fluid envelope of radius  $b$ . (The same result could be obtained if the over-all fluid motion were assumed to be zero and the inner cylinder to be in motion.) These boundary conditions give

$$u = 0 \quad \text{at} \quad r = a \quad (3)$$

$$\frac{du}{dr} = 0 \quad \text{at} \quad r = b$$

whence by substitution in (2),

$$A = -\frac{1}{2\mu} \frac{dp}{dx} b^2 \quad (4)$$

$$B = \frac{1}{4\mu} \frac{dp}{dx} (2b^2 \ln a - a^2)$$

Thus

$$u = -\frac{1}{4\mu} \frac{dp}{dx} \left[ (a^2 - r^2) + 2b^2 \ln \frac{r}{a} \right] \quad (5)$$

The flow rate through the entire annulus of fluid between  $r = a$  and  $r = b$  will be

$$Q = 2\pi \int_a^b ur \, dr = \frac{-\pi}{8\mu} \frac{dp}{dx} \left[ 4a^2b^2 - a^4 - 3b^4 + 4b^4 \ln \frac{b}{a} \right] \quad (6)$$

If  $u_{avg} = Q/\text{area}$  and Darcy's equation for flow through a porous medium is written  $u_{avg} = -(K/\mu) (dp)/(dx)$ ,

$$K = \frac{1}{8b^2} \left( 4a^2b^2 - a^4 - 3b^4 + 4b^4 \ln \frac{b}{a} \right) \quad (7)$$

The well-known Carman-Kozeny (3) equation, derived on the basis of semi-empirical reasoning, also gives an expression for the Darcy constant

$$K = \frac{\epsilon m^2}{k} \quad (8)$$

In the present case  $m = (b^2 - a^2)/2a$ , and thus the Kozeny constant becomes

$$k = \frac{2\epsilon^3}{[1 - \epsilon] \left[ 2 \ln \left( \frac{1}{1 - \epsilon} \right) - 3 + 4(1 - \epsilon) - (1 - \epsilon)^2 \right]} \quad (9)$$

It should be noted that in this case the solution obtained applies to the complete Navier-Stokes equations.\* The inertia terms vanish because there is no change in cross section along the direction of flow, hence no velocity change in the  $x$  direction.

#### FLOW PERPENDICULAR TO CYLINDERS

The inertia terms are omitted from the Navier-Stokes equations to obtain the creeping-motion equations. Expressed in cylindrical coordinates and for two dimensions these are

$$\begin{aligned} \frac{\partial p}{\partial r} &= \mu \left( \nabla^2 v_r - \frac{v_r}{r^2} - \frac{2}{r^2} \frac{\partial v_\theta}{\partial \theta} \right) \\ \frac{1}{r} \frac{\partial p}{\partial \theta} &= \mu \left( \nabla^2 v_\theta - \frac{v_\theta}{r^2} + \frac{2}{r^2} \frac{\partial v_r}{\partial \theta} \right) \\ \frac{\partial v_r}{\partial r} + \frac{v_r}{r} + \frac{1}{r} \frac{\partial v_\theta}{\partial \theta} &= 0 \end{aligned} \quad (10)$$

It is convenient to employ the stream function defined by the relations

$$v_r = \frac{1}{r} \frac{\partial \psi}{\partial \theta} \quad \text{and} \quad v_\theta = -\frac{\partial \psi}{\partial r} \quad (11)$$

\*Sparrow and Loeffler (12a) present an analytical solution for the longitudinal laminar-flow between cylinders arranged in triangular or square array. For large spacings the result is equivalent to Equation (9) above. A similar result for square spacing was also obtained by L. S. Leibenson (11a).

Equations (10) then assume the form of the biharmonic equation

$$\nabla^4 \psi = 0 \quad (12)$$

A suitable general solution of Equation (12) is

$$\psi = \sin \theta \left[ \frac{1}{8} Cr^3 + \frac{1}{2} Dr \left( \ln r - \frac{1}{2} \right) + Er + \frac{F}{r} \right] \quad (13)$$

In this case a solid cylinder of radius  $a$  is assumed to be moving perpendicular to its axis in a fluid cell of radius  $b$ . (The same result would be obtained if one assumed that fluid is moving perpendicular to a stationary cylinder of radius  $a$ .) There is assumed to be no shearing stress on the outside cylindrical fluid surface.

Under these assumptions the boundary conditions are

$$\begin{aligned} u &= U \\ v_r &= U \cos \theta \\ v_\theta &= -U \sin \theta \end{aligned} \quad \left. \begin{aligned} & \\ & \\ & \end{aligned} \right\} \text{at } r = a$$

$$\begin{aligned} v_r &= 0 \\ \frac{\partial v_\theta}{\partial r} + \frac{1}{r} \frac{\partial v_r}{\partial \theta} - \frac{v_\theta}{r} &= 0 \end{aligned} \quad \left. \begin{aligned} & \\ & \end{aligned} \right\} \text{at } r = b \quad (14)$$

These conditions provide four simultaneous equations to establish the values of the four constants. The drag on the solid cylinder  $r = a$  requires the evaluation of only one constant, since (12)

$$W = 2\pi\mu D \quad (15)$$

The constant  $D$  is found to be

$$D = \frac{-2U}{\ln \frac{b}{a} + \frac{a^4}{b^4 + a^4} - \frac{1}{2}} \quad (16)$$

and thus

$$W = \frac{4\pi\mu U}{\ln \frac{b}{a} - \frac{1}{2} \left( \frac{b^4 - a^4}{b^4 + a^4} \right)} \quad (17)$$

If the cylinder remains stationary and fluid passes it, the force associated with a single cylindrical cell may be equated to the pressure gradient

$$\frac{W}{\pi b^2} = \frac{dp}{dx} \quad (18)$$

As previously stated, the Darcy equation may be written  $u_{avg} = U = -(K/\mu) (dp/dx)$ , and the Darcy constant is then found to be

$$K = \frac{b^2}{4} \left[ \ln \frac{b}{a} - \frac{1}{2} \left( \frac{b^4 - a^4}{b^4 + a^4} \right) \right] \quad (19)$$

Similarly on the basis of the Carman-Kozeny theory  $K = (\epsilon m^2/k)$ , and the Kozeny constant becomes

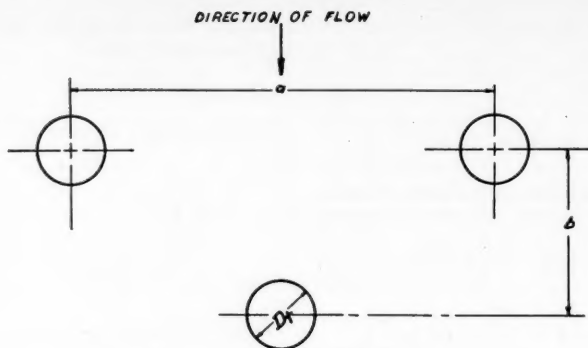


Fig. 2. Tube-layout-definition sketch.

$$k = \frac{2\epsilon^3}{[1 - \epsilon] \left\{ \ln \left( \frac{1}{1 - \epsilon} \right) \left[ \frac{1 - (1 - \epsilon)^2}{1 + (1 - \epsilon)^2} \right] \right\}} \quad (20)$$

## RESULTS AND DISCUSSION

Table 1 gives a comparison of values of the Kozeny constant computed from the above equations and the theoretical value for an assemblage of spherical particles (11) based on the free-surface model. Although the Kozeny constant for spheres lies between those for parallel and perpendicular flow with cylinders for fractional void volumes between 0.4 and 0.8, at higher values of voidage the Kozeny constant for spheres is higher than for both types of cylindrical assemblage. The model does not appear to be applicable to fractional void volumes below about 0.4 to 0.5.

Carman's book (3) gives a comprehensive survey of the available data on fibers for testing the Carman-Kozeny equation. He points out that elongated shapes such as fibers can be readily packed in a uniform manner to give high porosities. Thus Davies (5) studied beds of fibers used for air filters over a range of  $\epsilon = 0.7$  to 0.994 and obtained an empirical relationship from which the

Kozeny constant can be computed. For  $\epsilon < 0.8$  the equation is applicable with  $k \approx 6$ , but thereafter values of  $k$  rapidly increase; at  $\epsilon = 0.9$ ,  $k = 9.7$ , and at  $\epsilon = 0.99$ ,  $k = 38.8$ . This is in good agreement with values in Table 1, since the orientation is neither parallel nor perpendicular to flow. Other data do not show such good agreement, but it is difficult to judge the reliability of this type of information because no exact

$$k = \frac{2\epsilon^3}{[1 - \epsilon] \left[ -3 + 2 \ln \left( \frac{1}{1 - \epsilon} \right) \right]} = \frac{\epsilon^3}{[1 - \epsilon] [-1.5 - \ln(1 - \epsilon)]} \quad (24)$$

data are reported on the fiber arrangement.

Some data, which again show scatter, are available for flow along parallel-oriented fibers. Sullivan (13) has shown that if textile fibers are oriented parallel to one another and normal to the direction of flow,  $k = 6$  when  $\epsilon < 0.85$  and increases at higher porosities. This is in good agreement with Table 1. Sullivan (13) also found that with bundles of fibers combed parallel to the direction of flow,  $k \approx 2.4$  in the range of  $\epsilon = 0.55$  to 0.8, somewhat lower than the values reported in Table 1. He found much lower values of  $k$  for a series of experiments with straight, smooth cylinders of various materials, though again in all these experiments there are questions of degree of randomness of arrangement, uniformity of diameter, and degree of straightness of the fibers.

Of special interest is Emersleben's (7) exact theoretical solution of the Navier-Stokes equations for flow parallel to uniform circular cylinders in a square array. Emersleben represented the square array of circular sections by contours of a constant value of a special Epstein zeta

function (9), which, though it represents them closely above  $\epsilon \approx 0.8$ , becomes a progressively poorer approximation at lower porosities. At  $\epsilon = 0.9$ , the Emersleben equation corresponds to  $k = 6.3$  and compares with a value of  $k = 7.3$  from Table 1; this indicates that in this range there is not much difference in the resistance between a square array and the array presumed by the free-surface model. At lower porosities agreement is poorer, but as porosity is increased, it becomes exceptionally good.

Thus for small values of  $\rho$  Emersleben (8) has shown that the Epstein zeta function he uses can be represented as

$$Z_0(\rho) = -\pi \ln \rho^2 - 8.234 \quad (21)$$

For small values of  $\rho$  the Kozeny constant can also be simply represented (6) as

$$k = \frac{\epsilon^3 \pi}{(1 - \epsilon)} \times \frac{1}{Z_0(\rho)} \quad (22)$$

For example when  $\rho = 0.1$ , which corresponds to  $\epsilon = 0.97$ , Equation (22) gives results for  $k$  about 5% too high.

Noting that  $\rho^2 = (1 - \epsilon)/\pi$ , one finds that Equation (22) reduces to

$$k = \frac{\epsilon^3}{[1 - \epsilon] [-1.476 - \ln(1 - \epsilon)]} \quad (23)$$

Similarly for the free-surface model, as  $(1 - \epsilon)^2 \ll (1 - \epsilon)$ , Equation (9) becomes for dilute systems

$$k = \frac{\epsilon^3}{[1 - \epsilon] [-1.5 - \ln(1 - \epsilon)]} \quad (24)$$

This excellent agreement provides validation for the free-surface model for dilute systems.

At extremely high dilutions the logarithmic term in Equation (23) will be large compared with 1.476, and as  $\epsilon \rightarrow 1$ ,  $k = -1/[(1 - \epsilon) \ln(1 - \epsilon)]$ . Similarly for flow perpendicular to cylinders, Equation (20) reduces to  $k = -2/[(1 - \epsilon) \ln(1 - \epsilon)]$ . Thus in the extreme the resistance in the case of flow perpendicular to cylinders is just double that for axial flow. The analogous expression for flow through assemblages of spheres is  $k = 1/[2(1 - \epsilon)]$ .

As assemblages of uniform-sized cylinders become less porous with  $\epsilon < 0.3$ -0.5, agreement with the values shown in Table 1 becomes poorer. With systematic rather than random arrangement agreement is also poorer. Thus for a square array of cylinders touching each other Sullivan gives an experimental value of  $k = 0.83$  for axial flow. Flow perpendicular to such an array would not be possible; that is  $k \rightarrow \infty$ . It is possible to obtain less porous systems without having cylinders touch each other by the use of different arrangements and the employment of a range of cylinder sizes, but no

TABLE 1. VALUES OF THE KOZENY CONSTANT

Fractional void volume	Flow parallel* to cylinders	Flow perpendicular to cylinders	Flow through assemblage of spheres
0.99	31.10	53.83	71.63
0.90	7.31	11.03	11.34
0.80	5.23	7.46	7.22
0.70	4.42	6.19	5.79
0.60	3.96	5.62	5.11
0.50	3.67	5.38	4.74
0.40	3.44	5.28	4.54

\*For the case of flow parallel to cylinders Sparrow and Loeffler's treatment (12a) indicates that at high fractional void volumes arrangement does not affect permeability. At a fractional void volume of 0.5 they find  $k \approx 3.5$  for equilateral and  $k \approx 2.9$  for square array. Numerical results at lower voidages given by these authors show even greater deviations between equilateral and square arrangement.

data are available for flow resistance for such systems.

Another field of practical interest is the pressure drop through tube banks, such as are employed in heat exchangers. Here again it would be anticipated that the theoretical relationship developed would apply best to a nonsystematic arrangement or to one in which symmetry is maintained around each cylinder, that is the equilateral triangular spacing. One correlation quite generally used is that of Chilton and Genereaux (4) based on viscous flow across banks of tubes in an equilateral arrangement. Mathematically this correlation is similar to the empirical equation of Darcy and the Carman-Kozeny relationship. Thus the Darcy constant as defined above becomes

$$K = \frac{m^2[(a - D_i)/a]}{3.30} \quad (25)$$

The present theoretical treatment gives  $K = \epsilon m^2/k$ , where the value of the Kozeny constant is established from Equation (20) or the values in Table 1 for flow perpendicular to cylinders. If  $b$  is taken as the longitudinal pitch (Figure 2), the fractional void volume for a staggered arrangement will be

$$\epsilon = \frac{ab - \pi D_i^2/4}{ab} \quad (26)$$

Since  $(a - D_i)/a = (ab - D_i b)/ab$ , it is clear that the Chilton and Genereaux method involves the employment of  $b$  instead of  $\pi D_i/4$ . Since  $b$  is always bigger than  $\pi D_i/4$ , this method must result in a smaller constant in the denominator of the expression on the right side of Equation (25) than the Kozeny constant.

Two sets of data with transverse pitches (that is, ratio of  $a/D_i$ ) of 1.25 and 1.59 were employed in the establishment of Equation (25), and thus  $K = 0.061m^2$  and  $0.109m^2$  respectively. For these pitches  $\epsilon = 0.42$  and  $0.64$ , corresponding to values of  $k$  from Table 1 of 5.30 and 5.85, and accordingly values of  $K = 0.079m^2$  and  $0.110m^2$  respectively. Thus the pressure drop predicted by the theoretical relationship is 23% lower than the correlation for 1.25 pitch but is in close agreement at 1.59 pitch.

More recent data by Bergelin *et al.* (1) indicate agreement with the theory in the low Reynolds-number range (below  $N_{Re} \approx 5$ , in this case defined as  $D_i G_m/\mu$ ) for equilateral arrangements. At higher Reynolds numbers the pressure drop is greater than predicted, but substantial deviations do not occur until Reynolds numbers over 100 are reached. Data obtained by Bergelin *et al.* with other types of tube arrangement show greater disagreement, especially with the staggered square-tube distribution. In this

latter case the clearance between tubes in the direction of flow varies substantially, and so the flow pattern is not uniform around the tubes. The present theoretical method does not allow for variations in tube arrangement. Bergelin found that it was possible to bring data for each distribution into line by assuming that the pressure gradient would vary directly with the number of rows. A theoretical analysis on this basis would involve in its simplest form the treatment of resistance to flow through a single row of parallel cylinders, such as has been presented by Tamada and Fujikawa (14).

It may be concluded that the free-surface model presents a simple and uniform method for handling problems in viscous flow through assemblages of cylinders. It is in reasonable agreement with available data for systems involving random or uniform flow of fluids through various fibrous materials and through banks of tubes in equilateral arrangement. This technique should have further application in developing more complicated cases such as those involving simultaneous heat transfer. It should also be useful in providing suitable parameters for the correlation of experimental data.

#### ACKNOWLEDGMENT

This research was supported in part by a grant from The Petroleum Research Fund administered by the American Chemical Society. Grateful acknowledgment is hereby made to the donors of the fund.

#### NOTATION

(consistent absolute units)

- $a$  = radius of cylindrical rod, transverse, pitch (Figure 1)
- $A, B, C, D, E, F$  = constants
- $b$  = radius of cylindrical rod, longitudinal pitch
- $dp/dx$  = pressure gradient
- $D_i$  = outside tube diameter
- $D_v$  = volumetric hydraulic diameter =  $4 \alpha m$
- $G_m$  = mass velocity through minimum cross section
- $k$  = Kozeny constant
- $K$  = Darcy constant
- $m$  = hydraulic radius, (free volume)/(exposed area)
- $p$  = pressure at any location
- $Q$  = flow rate
- $r$  = distance from axis of cylinder
- $u$  = fluid velocity in  $x$  direction, axial in case of flow parallel to cylinders, perpendicular to cylinders in case of cross flow

- $v_r$  = fluid velocity in radial direction
- $v_\theta$  = fluid angular velocity
- $u_{avg}$  = average value of  $u$
- $U$  = cylinder velocity in  $x$  direction
- $W$  = force on cylinder in  $x$  direction
- $x$  = direction of average fluid flow relative to solid cylinder
- $Z_0(\rho)$  = value of the second-order Epstein zeta function with non-vanishing lower parameters along the constant-value contour which most nearly approximates the circle  $\rho^2 = x^2 + y^2$

#### Greek Letters

- $\nabla^4$  = biharmonic operator =  $(\nabla^2)^2$  where  $\nabla^2$  is the Laplace operator
- $\epsilon$  = fractional void volume
- $\theta$  = angular distance
- $\mu$  = viscosity
- $\rho$  = ratio of cylinder radius to distance between cylinder centers in a square lattice
- $\psi$  = stream function

#### LITERATURE CITED

1. Bergelin, O. P., G. A. Brown, H. L. Hull, and F. W. Sullivan, *Trans. Am. Soc. Mech. Engrs.*, **72**, 881 (1950).
2. Boucher, D. F., *Chem. Eng.*, **56**, No. 5, 118 (1949).
3. Carman, P. C., "Flow of Gases Through Porous Media," Academic Press, New York (1956).
4. Chilton, T. H., and R. P. Genereaux, *Trans. Am. Inst. Chem. Engrs.*, **29**, 161 (1933).
5. Davies, C. N., *Discussions Faraday Soc.*, **3**, 127 (1948); *Proc. Inst. Mech. Engrs., London*, **1B**, 185 (1952).
6. Emersleben, Otto, *Anwendungen der Mathematik*, No. 3, Greifswald (1958).
7. ———, *Z. Physik*, **26**, 601 (1925).
8. ———, *Phys. Verhandl.*, **6**, 150 (1955).
9. Epstein, Paul, *Math. Annalen*, **56**, 615 (1903); **63**, 205 (1906).
10. Happel, John, *J. Appl. Phys.*, **28**, 1288 (1957).
11. ———, *A.I.Ch.E. Journal*, **4**, 197 (1958).
- 11a. Leibenson, L. S., *Complete Works*, Vol. 3, Moscow (1955) (in Russian).
12. Slezkin, N. A., "Dynamics of Viscous Incompressible Fluids" (in Russian), Gos. Izdat. Tekh.-Teor. Lit., Moscow (1955).
- 12a. Sparrow, E. M., and A. L. Loeffler, Jr., *A.I.Ch.E. Journal* (to be published).
13. Sullivan, R. R., *J. Appl. Phys.*, **13**, 725 (1942).
14. Tamada, K., and H. Fujikawa, *Quart. J. Mech. & Appl. Math.*, **10**, Part 4, 423 (1957).

Manuscript received May 8, 1958; revision received September 8, 1958; paper accepted September 18, 1958.

# Mass Transfer from a Solid Sphere to Water in Highly Turbulent Flow

L. R. STEELE and C. J. GEANKOPLIS

The Ohio State University, Columbus, Ohio

Mass transfer coefficients from  $\frac{1}{2}$ -in. spheres of benzoic and cinnamic acids and 2-naphthol to water were measured in the high Reynolds number region of 600 to 140,000. Previous data for liquids extended only to a Reynolds number of 11,000. Three separate and approximately parallel lines of  $J_D$  vs. Reynolds number were found for the different solutes, and the shape of the curves was found to be similar to the total-drag-coefficient correlation for spheres.

Experiments with benzoic acid and 2-naphthol showed an effect of driving force and hence flux on the  $J_D$  values. Mass transfer did occur in saturated solutions having zero driving force. When one subtracted the amount of mass transfer at zero driving force from the values at other driving forces, the corrected  $J_D$  values at different driving forces were the same for a given solute. Possible explanations may be the effect of extreme turbulence on crystallization or physical attrition.

The transfer of mass from single spheres to a flowing liquid at low velocity or low Reynolds number has been extensively studied by a number of investigators (4, 5, 7, 8), and a correlation was presented by Garner and Suckling (5). However few data are available above a Reynolds number of 1,000 and none above 11,000. The effect of varying the Schmidt number for a given solute and for different solutes and the effect of mass flux on the mass transfer coefficients have not been studied in the very turbulent region and only sparingly in the low Reynolds number region.

In the present experimental work,  $\frac{1}{2}$ -in. spheres of benzoic and cinnamic acids and 2-naphthol were used, and mass transfer coefficients were measured at a Reynolds number between 600 and 140,000. The effects of mass flux and Schmidt number were also investigated.

## LITERATURE REVIEW AND THEORY

In mass transfer from dissolving solids to flowing liquids the driving force is assumed to be the saturation solubility adjacent to the solid minus the bulk-stream concentration. In most previous investigations (4, 5, 7, 8) the bulk-stream concentration was kept constant at approximately zero. The mass transfer flux and mass transfer coefficient are related by

$$N_A = K_L(C_s - C_L) \quad (1)$$

To reduce the mass flux at a given temperature and Reynolds number  $C_L$  can be increased from the normal zero value.

The dimensionless number of Chilton and Colburn (2) is defined as

$$J_D = \frac{K_L}{V} \left( \frac{\mu}{\rho D_L} \right)^{2/3} \quad (2)$$

The  $J_D$  factor has been correlated against the Reynolds number  $D_p V \rho / \mu$  for spheres.

Linton and Sherwood (7) determined  $J_D$  values for individual benzoic acid spheres for a Reynolds number range of 1,500 to 11,000. The spheres were mounted in the center of the pipe and supported by a metal wire normal to the flow. Data were also obtained for transverse cylinders with cinnamic and benzoic acids, with the  $J_D$  for benzoic acid being approximately 20% higher than for cinnamic acid.

McCune and Wilhelm (8) used a 2-naphthol pellet which was resting on a wire screen, up through which the liquid flowed. Data were obtained for a Reynolds number range of 30 to 500, in which the pellet was essentially immobile on the screen.

Garner and Suckling (5) determined  $J_D$  values for single spheres of adipic and benzoic acids for a Reynolds number range of 30 to 700. The spheres were supported by an axial rod on the downstream side. They correlated their data and those of Garner and Grafton (4) and found that for Reynolds numbers greater than 100 above the natural-convection region

$$J_D = (\text{constant}) N_{Re}^{-0.5} \quad (3)$$

Dryden, Strang, and Withrow (3) found that at Reynolds numbers below 10 in packed beds values of  $J_D$  for benzoic acid were greater than for 2-naphthol.

Goldstein (6) discussed the drag on a sphere and stated that spheres supported

by a cross wire will disturb the flow continuity over the sphere surface and give a total drag up to double that when the sphere is held at the back by an axial spindle. He gives a plot of total drag vs. Reynolds number values up to 4,000,000. At low Reynolds numbers the drag coefficient decreases with increasing Reynolds numbers and levels off in the Reynolds number region of 5,000 to 250,000. Then the drag coefficient suddenly drops over 50% and then increases. Binder (1) discusses the changes in the flow patterns and wakes which cause these unusual changes in the drag coefficient. It would be expected that these phenomena should cause somewhat similar changes in the  $J_D$  vs. Reynolds number plot.

## EXPERIMENTAL METHODS AND RESULTS

### Materials and Spheres

The three different types of solute crystals used were benzoic acid, trans-cinnamic acid, and 2-naphthol. Distilled water was used for all runs. The  $\frac{1}{2}$ -in. spheres were made by casting in plaster-of-Paris molds. An 0.064-in. brass wire  $1\frac{1}{2}$ -in. long was cast into the sphere. This wire was the spindle mount holding the sphere axially from the rear. The wire was inserted for  $\frac{3}{4}$  in. into a larger supporting rod.

The molded sphere was easily removed from the casting and was washed with water and dried in a desiccator before being weighed. After mass transfer the sphere was again dried and weighed. The diameter was measured in four directions before and after a run, and the average was used. The maximum change in diameter during a run was less than 0.8%. Figure 1 shows a typical cinnamic acid sphere after a mass transfer run.

### Apparatus

In the process flow (Figure 2) the distilled water was drawn from storage and pumped

TABLE 1. EXPERIMENTAL SOLUBILITY DATA IN WATER

Solute	Temperature, °C.	$C_s'$ , g./liter
Cinnamic acid	25.0	0.491
Cinnamic acid	34.3	0.700
Cinnamic acid	21.5	0.460
Cinnamic-acid spheres	25.0	0.495
Benzoic acid	25.0	3.38
Benzoic acid	34.3	4.85
Benzoic acid	21.5	3.06
Benzoic-acid spheres	25.0	3.40
2-Naphthol	25.0	0.725
2-Naphthol spheres	25.0	0.740

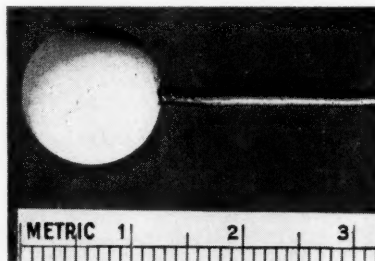


Fig. 1. Cinnamic acid sphere after a run.

L. R. Steele is with Argonne National Laboratories, Lemont, Illinois.



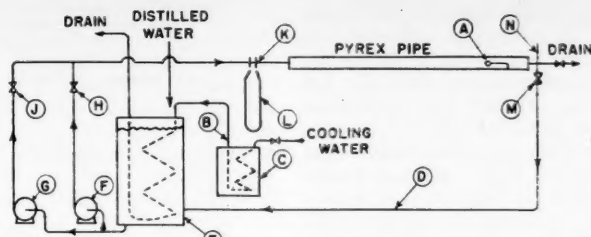


Fig. 2. Process-flow diagram: A = cast sphere, B = cooling-water line, C = ice bath, D = return line, E = stainless steel drum, F = small pump, G = large pump, H = globe valve, J = globe valve, K = orifice, L = manometer, M = recycle valve, N = thermometer.

through an orifice to the 1½-in. I.D. Pyrex test section. The test sphere was mounted 15 in. from the downstream end of the pipe, which was 10 ft. long. The water was recirculated and the temperature controlled. Depending on the type of solute used, runs lasted for as long as 4 to 60 min.

#### Solubility Determinations

The solubilities of the three solutes were experimentally determined (Table 1). An excess of crystals was placed in a glass-stoppered Erlenmeyer flask and covered with a rubber stall. The flask was totally immersed in a constant-temperature bath and agitated for one day by a magnetic stirrer. The clear solution was pipetted and analyzed with a Beckman DK-2 spectrophotometer. The absorption peak was 270 mμ for cinnamic acid, 226 for benzoic, and 225 for 2-naphthol. Knowns were run and results interpolated. Identical results were also obtained with cast spheres instead of crystals.

Data from Table 1 are plotted (Figure 3) and show that the value for 2-naphthol checks those of McCune and Wilhelm (8). The data for benzoic acid check those from Seidell (9, 10). The data for cinnamic acid from Seidell scatter widely. The values used in calculations of  $J_D$  are those taken from the solid lines in the plot.

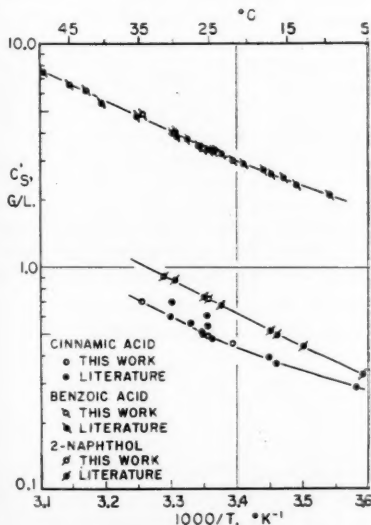


Fig. 3. Solubilities.

#### Diffusivities Used

The available diffusivity data are plotted as Schmidt numbers in Figure 4. Linton and Sherwood (7) give experimental data for benzoic and cinnamic acids from 10° to 25°C. For the range of 25° to 35°C. the Wilke equation (11) was used for extrapolation of the temperature effect. For 2-naphthol the experimental data (8) for 15° to 21°C. were plotted, and a line was drawn through the middle of these three points parallel to the other two lines. In developing his equation Wilke (11) shows a maximum deviation

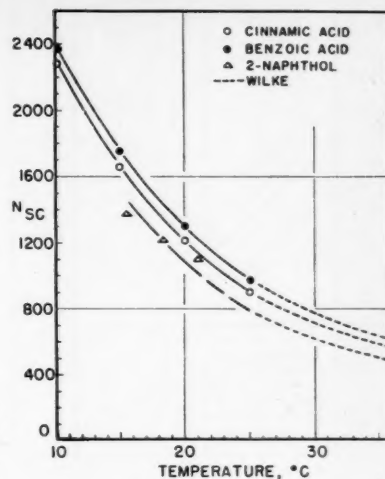


Fig. 4. Schmidt number vs. temperature.

of about 25% and an average of 6%. Values of the three solutes predicted with the Wilke equation had a maximum deviation of less than 25%. The values used to calculate  $J_D$  are those taken from the lines in Figure 4.

TABLE 2. MASS TRANSFER DATA (AXIAL MOUNTING OF SPHERE)\*\*

Solute	$D_p$ , cm.	$V'$ , cm./sec.	Temperature, °C.	$C_s'$ , g./liter	$C_L'$ , g./liter	$K_L/V \times 10^5$	$N_{Sc}$	$J_D \times 10^3$	$N_{Re}$
Cinn.	1.270	640	25.3	0.495	0	5.76	885	5.37	102,000
Cinn.	1.275	106	24.5	0.490	0	7.21	925	6.85	16,900
Benz.	1.267	103	25.0	3.40	0	8.53	970	8.37	16,350
2-Naph.	1.265	141	25.0	0.725	0	4.55	785	3.87	22,400
Cinn.	1.275	308	34.9	0.713	0	9.29	573	6.42	60,400
2-Naph.	1.277	527	25.3	0.725	0	3.94	773	3.31	86,000
2-Naph.	1.270	218	21.1	0.630	0	3.25	1003	3.27	31,800
Benz.†	1.270	249	25.7	3.45	3.01	15.60	940	14.92	40,200
Benz.†	1.260*	128	25.0	3.40	3.40	1.060†	970	1.038†	20,200
Benz.†	1.250	124	25.0	3.40	1.70	9.13	970	8.93	19,400
2-Naph.†	1.274	133	25.0	0.725	0.725	0.213†	785	0.184†	21,200
2-Naph.†	1.257	150	25.3	0.725	0.330	4.93	744	4.15	23,700
Cinn.*	1.277	58.6	24.8	0.495	0	10.27	906	9.45	9,490
2-Naph.*	1.273	58.6	24.9	0.725	0	7.50	790	6.32	9,410
Benz.*	1.273	58.6	25.0	3.40	0	10.84	970	10.45	9,320

\*Cross wire instead of axial spindle.

\*\*Tabular material has been deposited as document 5877 with the American Documentation Institute, Photoduplication Service, Library of Congress, Washington 25, D. C., and may be obtained for \$1.25 for photoprints or \$1.25 for 35-mm. microfilm.

†Reduced flux.

‡Saturated solution; calculated as if  $C_L = 0$ .

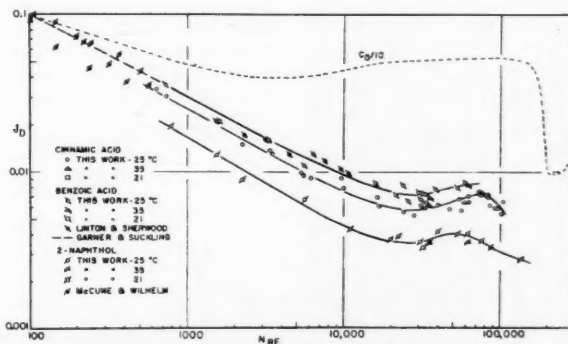


Fig. 5.  $J_D$  vs. Reynolds number.

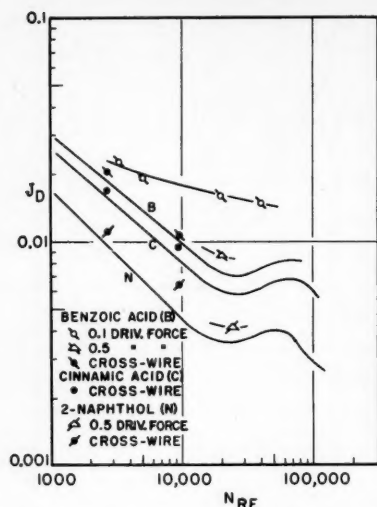


Fig. 6. Effect of flux and type of sphere mounting on  $J_D$ .

#### Calculation of $J_D$

The experimental data were used to calculate  $J_D$  as follows. From weight loss, duration of run, and average diameter,  $N_A$  was calculated. With the solubility data in Figure 3, Figure 4, velocity data, and Equations (1) and (2),  $J_D$  was then calculated. The average velocity in the annular free space between the sphere and the pipe wall was used. The data are given in Table 2.

#### DISCUSSION

##### Correlation of $J_D$ vs. Reynolds Number

The mass transfer data are plotted in Figure 5. There are three distinct lines with the benzoic-acid line being about 25% above the cinnamic and the cinnamic being about 55% above the 2-naphthol line. Linton and Sherwood (7) at Reynolds numbers below 11,000 found the  $J_D$  for benzoic acid to be about 20% above the values for cinnamic acid for cross cylinders. Dryden and coworkers (3) also found  $J_D$  values for benzoic acid to be greater than those for 2-naphthol.

Data of other investigators plotted in Figure 5 were corrected by the use of the average velocity in the annular-free space. The Garner and Suckling line (5) for benzoic acid when extended past a Reynolds number of 700 checks the present benzoic acid correlation. The data of Linton and Sherwood (7) for benzoic acid also check the present work. The 2-naphthol data of McCune and Wilhelm (8) at low Reynolds numbers appear to be somewhat higher than the extrapolation of the 2-naphthol line through the present work; this may be due to their use of a screen before the pellet. The leveling off of the  $J_D$  values at high Reynolds numbers and then the drop are similar to the total drag correlations of Goldstein (6).

At all Reynolds numbers the benzoic acid line is about 80% above the 2-naphthol line. Hence this spread cannot be due to errors in the diffusivity but must be due to other causes. Visual inspection of the spheres showed them to be quite smooth before mass transfer and to have only a slight roughness on the surface after the runs. Several experiments were performed with the same sphere used for several different runs, and no trends were noticed. Also in one case the sphere was artificially roughened before the run, and no effect was apparent.

A detailed analysis of the errors in the determination of  $J_D$  was made for such errors as those which occurred in weighing, orifice calibration, temperature and diameter measurement, etc. The maximum known error was calculated to be  $\pm 10\%$ . In Figure 5 the maximum deviation of the data from each average line is 15% for the cinnamic acid line, and the average deviation is  $\pm 5\%$ . These small errors cannot account for the three different lines found. In the runs for a given solute the temperature was varied from 21° to 35°C., which changed the Schmidt number twofold. All these data fall near the proper line, which confirms the two-thirds exponent for a given solute.

##### Effect of Type of Sphere Mounting

In Figure 6 several runs are plotted in which the sphere was mounted by a cross wire instead of an axial spindle at the rear. These data give  $J_D$  values about 10 to 30% higher. The data of Linton and Sherwood (7) in Figure 5 were also obtained with a cross-wire mount and those of McCune and Wilhelm (8) with a screen which might be termed a multiple cross-wire mount.

##### Flux Effects

It was speculated that the mass flow or flux might interact, or have a coupling effect on the boundary layer, or change the bulk properties which would change  $J_D$ . Benzoic acid, which has the largest solubility, would have the greatest flux, since the driving force is  $(C_s - C_L)$ , where  $C_L$  is zero. To check this the  $C_L$  was made greater than zero in several runs, so that the driving force was reduced to about 10% of the original maximum for benzoic acid. This should have reduced the flux to a value close to that of 2-naphthol. The data in Figure 6 show

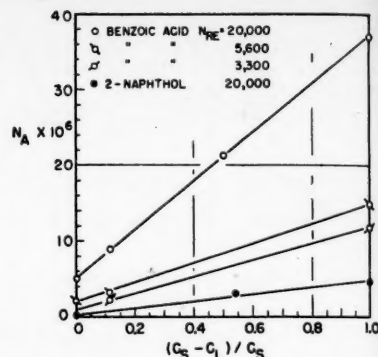


Fig. 7. Effect of driving force on flux.

that the  $J_D$  values are much greater at low flux values than at maximum flux and that the low flux benzoic acid and high flux 2-naphthol lines are not the same. Also at low Reynolds numbers the effect of flux decreases markedly.

Several runs were also made in a saturated solution with the sphere which should give a zero driving force. Some mass transfer did occur in these runs, and the flux data are shown in Figure 7. Subtracting this zero driving-force flux value from the others in Figure 7 one can calculate a corrected  $N_A$  and  $J_D$  for each driving force (Table 3). These corrected values of  $J_D$  are approximately constant and independent of driving force for benzoic acid and 2-naphthol. The corrected values for benzoic acid are not equal to those for 2-naphthol; hence other reasons must be sought for the differences in the  $J_D$  values of the three solutes.

Another way used to attempt to correct the  $J_D$  for driving-force effects for benzoic acid was to assume a pseudo solubility at other temperatures. By trial and error it was found that at an assumed temperature of 29°C. the  $J_D$  values for benzoic acid check for different driving forces. An estimate of the temperature rise at the sphere surface due to friction drag showed an insignificant temperature rise. Hence the significance of this 29°C. temperature is not apparent. For 2-naphthol this pseudotemperature was found to be about 26°C.

An explanation of this mass transfer at saturation or zero driving force could be derived from the concept of equilibrium at saturation and attrition. At

TABLE 3. EFFECT OF ZERO DRIVING-FORCE FLUX AT  $N_{Re} = 20,000$

Solute	Percentage of maximum driving force	$J_D \times 10^3$	$N_A \times 10^6$	$J_D$ corrected $\times 10^3$
Benzoic	100	7.06	37.2	6.08
Benzoic	50	8.93	21.5	6.80
Benzoic	11.5	16.05	9.02	6.84
Benzoic	0	—	5.16	—
2-Naphthol	100	3.77	4.54	3.58
2-Naphthol	54	4.15	3.27	3.85
2-Naphthol	0	—	0.23	—

high turbulence a steady state dynamic equilibrium is present in the saturated solution. The mass flux from the sphere (dissolution) is equal to the mass flux to the sphere (crystallization). The material going to the sphere must crystallize on the surface by the growth of existing crystals and possibly by the formation of new crystals. Some crystals may grow larger than others; this makes the surface more irregular and less densely packed than before. These new, fine crystals could have difficulty in adhering to the surface in the highly turbulent stream. Hence these enlarged, existing crystals or the new crystals could easily be broken off and carried away in the main stream.

This mass transfer at zero driving force could also be due to physical attrition, where eddies tear off or wear away minute particles of the cast solid other than those actually dissolved by true mass transfer. If mass transfer due to this type of attrition is present, it should be an additive effect along with the true dissolution mass transfer. However, as discussed previously, this correction gives constant  $J_D$  values for a given solute (Table 3) but does not give the same values for all solutes. Hence attrition alone is probably not causing these differences. It should be noted that the mass transfer at zero driving force for benzoic acid increases with increasing

Reynolds numbers (Figure 7). Preliminary hardness tests made on the cast spheres indicated that 2-naphthol was the hardest material and benzoic acid the softest.

Further studies should be made in mass transfer from dissolving solids in turbulent fluids on the role of physical properties of the solute such as hardness, crystalline structure, and ability to crystallize.

#### NOTATION

- $C_D$  = total drag coefficient for spheres.  
 $C_s$  = concentration of solute in saturated solution, g./cc.  
 $C_s'$  = concentration of solute in saturated solution, g./liter.  
 $C_L'$  = concentration of solute in solution, g./liter.  
 $C_L$  = concentration of solute in solution, g./cc.  
 $D_L$  = molecular diffusivity, sq. cm./sec.  
 $D_p$  = diameter of sphere, cm.  
 $J_D$  = dimensionless number for mass transfer.  
 $K_L$  = mass transfer coefficient, g./(sq. cm.)(sec.), g./cc.  
 $N_A$  = flux, g./(sq. cm.)(sec.).  
 $N_{Re}$  = Reynolds number =  $D_p V \rho / \mu$   
 $N_{Sc}$  = Schmidt number =  $\mu / \rho D_L$   
 $V'$  = average velocity in pipe, cm./sec.  
 $V$  = average velocity in annular area between pipe and sphere, cm./sec.

- $\mu$  = viscosity, g./(sec.)(cm.)  
 $\rho$  = density, g./cc.

#### LITERATURE CITED

1. Binder, R. C., "Advanced Fluid Dynamics and Fluid Machinery," p. 116, Prentice Hall, New York (1951).
2. Chilton, T. H., and A. P. Colburn, *Ind. Eng. Chem.*, **26**, 1183 (1934).
3. Dryden, C. E., D. A. Strang, and A. E. Withrow, *Chem. Eng. Progr.*, **49**, 191 (1953).
4. Garner, F. H., and R. W. Grafton, *Proc. Roy. Soc. (London)*, **A224**, 64 (1954).
5. Garner, F. H., and R. D. Suckling, *A.I.Ch.E. Journal*, **4**, 114 (1958).
6. Goldstein, Sydney, "Modern Measurements in Fluid Mechanics," p. 16, 491, Clarendon Press, Oxford (1938).
7. Linton, W. H., and T. K. Sherwood, *Chem. Eng. Progr.*, **46**, 258 (1950).
8. McCune, L. K., and R. H. Wilhelm, *Ind. Eng. Chem.*, **41**, 1124 (1949).
9. Seidell, Atherton, "Solubilities of Organic Compounds," 3 ed., Vol. II, D. Van Nostrand, New York (1941).
10. ———, and W. F. Linke, "Solubilities of Inorganic and Organic Compounds," Supplement to 3 ed., D. Van Nostrand, New York (1952).
11. Wilke, C. R., and Pin Chang, *A.I.Ch.E. Journal*, **1**, 264 (1955).

Manuscript received August 27, 1958; revision received November 6, 1958; paper accepted November 6, 1958.

## Turbulent Flow of Pseudoplastic Polymer Solutions in Straight Cylindrical Tubes

ROBERT G. SHAVER and EDWARD W. MERRILL

Massachusetts Institute of Technology, Cambridge, Massachusetts

Experimental studies are described concerning the fluid dynamics, particularly in the turbulent region, of dilute solutions of free-draining, nonassociating, linear polymers; sodium carboxymethylcellulose, ammonium alginate, polyisobutylene, and carboxypoly-methylene, all of which are pseudoplastic. These solutions were run in laminar, transition, and turbulent flow in a pipeline flow apparatus designed to permit measurement of dynamic pressure drop and impact pressure by radial traverse.

Photographic studies with dye injection used at the tube wall and at the tube center showed that turbulent flow of these pseudoplastic fluids has the following characteristics compared to Newtonian fluids: poor over-all radial mixing, thicker nonturbulent layer at the wall, and decreased rate of formation of horseshoe vortices at the wall.

A pseudoplastic fluid generally is defined as one which has a viscosity that decreases reversibly with increasing shear rate, which has no yield value, and which undergoes no time-dependent change in consistency. Dilute solutions of free-draining, essentially nonassociating polymers represent one class of pseudoplastic fluid, perhaps the most common. With

one exception\* the experimental studies described herein were concerned exclusively with this class of pseudoplastic fluid.

The shear-rate-shear-stress relationships of these polymer solutions can be

\*The exception is polyvinyl alcohol (Elvanol), which shows a strong tendency to associate by hydrogen bonding in dilute solution. The associating tendency in the Elvanol solution studies was so great that opalescence was noted, suggesting micelle formation. The results are irrelevant, since the solution behaved as a Newtonian fluid.

correlated in general over a rather broad range of shear rates by the power-law model  $\tau = b(du/dy)^n$  (4, 8, 9, 10).

Since the shear stress in a fluid flowing steadily in a straight cylindrical tube varies linearly from zero at the axis to a maximum  $\tau_w = (\Delta P/L) \cdot (R/2)$  at the wall, the flow equations for pseudoplastics in laminar flow can be derived by assuming the power-law rheology (3, 8). The resultant expressions are friction factor:

$$f = [16b/(D^2 V^{2-n} \rho)] \cdot [2(3 + 1/n)]^{1/n} / 8 \quad (1)$$

Robert G. Shaver is with the Dewey and Almy Chemical Company, Cambridge, Massachusetts.

Poiseuille's law:

$$Q = \pi(\Delta p/2Lb)^{1/s}$$

$$R^{3+1/s} \cdot \pi/(3 + 1/s) \quad (2)$$

Velocity distribution:

$$u/u_{max} = 1 - (1 - y/R)^{1/s+1} \quad (3)$$

Equation (1) is consequently analogous to the relation for a Newtonian fluid:

$$f = 16/N_{Re} \quad (4)$$

when the pseudoplastic Reynolds number is defined as  $(D^2 V^{2-s} \rho / b) \cdot 8[2(3 + 1/s)]^{-s}$ . Previous work (4, 8, 9, 18) has shown that these expressions for the Fanning friction factor and Poiseuille's law agree with experimental data if the fluid can be characterized by a single value of  $s$  over most of the range of shear stress encountered in flow (say, from  $0.25\tau_w$  to  $\tau_w$ ). However data for well-defined turbulent flow of pseudoplastic fluids have heretofore been lacking. Therefore it was the objective of this study to examine the nature of turbulent flow for one class of pseudoplastic fluids. For this purpose dilute solutions of sodium carboxymethylcellulose, ammonium alginate, carboxypolymethylene, and polyisobutylene were prepared, the rheology of which is unequivocally pseudoplastic according to

TABLE I. RHEOLOGICAL CONSTANTS OF FLUIDS

Run	Fluid	Temperature, °F.	Note A Temperature, 200 to 20,000 sec. <sup>-1</sup>		Note B 0.1 to 42 sec. <sup>-1</sup>	
			<i>b</i>	<i>s</i>	<i>b</i>	<i>s</i>
1C-F, A1-7	Water	72 to 73	0.0095	1.00	Same	
B1	1.5% Elvanol	71	0.0254	1.00	Same	
2A, C1	0.18% CMC-70	72	2.09	0.60	0.38	0.86
3A-B, D1	0.30% CMC-70	71	4.80	0.54		
3C, D2-4	0.30% CMC-70, degraded*	71	1.27	0.66		
3D	0.30% CMC-70, degraded*	71	1.05	0.68		
3E-F, D5-7	0.30% CMC-70, degraded*	71	0.505	0.75		
3H, D8	0.30% CMC-70, degraded*	71	0.120	0.85		
4A-C, E1-3	0.41% CMC-70	71	9.20	0.53	1.18	0.83
4D-E, E4-6	0.41% CMC-70, degraded*	71	4.01	0.59		
4F-G, E7	0.41% CMC-70, degraded*	92	3.03	0.62		
5A-B, F1-5	0.35% CMC-70	71	2.22	0.64		
G1	1.0% alginate	76	3.47	0.70		
H1	0.83% alginate	74	2.15	0.73	1.20	0.78
6B-D, I1-4	0.62% alginate	72	1.38	0.74		
J1-2	0.46% alginate	72	0.422	0.82	0.39	0.86
K1-3	0.10% alginate	71	0.0302	0.95		
L1	0.20% alginate	71	0.119	0.84		
M1	0.30% alginate	71	0.189	0.83		
8A-B, N1-4	0.50% CMC-70S	74	7.05	0.54		
9A-B, O1	0.25% CMC-70S	74	2.22	0.61	0.25	1.00
P1	0.12% Carbopol 934	70	0.710	0.78	4.9	0.85
Q2-3	0.52% Vistanex	77	0.644	0.71	0.095	0.98
Q4	0.52% Vistanex, shear degraded	77	0.133	0.82		
R1	Impure cyclohexane	77	0.0108	1.00	Same	

\*Upon aging in the storage vessel, presumably by enzymatic attack. Viscometric tests just before and just after the pipe-line runs showed identical values of  $b$  and  $s$ , thus eliminating degradation by shear as the cause.

Note A: Data from Merrill-Brookfield viscometer. These values of  $s$  used in transition and turbulent flow correlations.

Note B: Data from modified Brookfield Synchroelectric viscometer. These values of  $s$  not applicable to transition and turbulent flow correlations.

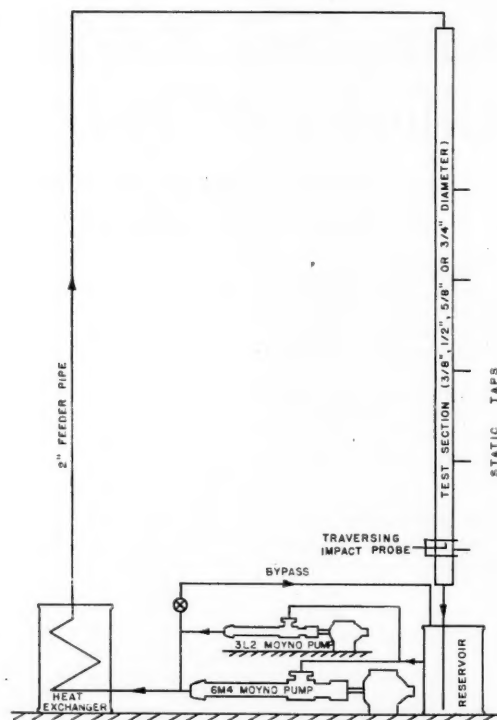


Fig. 1. Schematic diagram of the pipe-line flow apparatus.

the foregoing definition. The solutions were made highly dilute for two reasons, (1) to achieve a sufficiently high level of fluidity, so that turbulent flow might be achieved without inordinately large pumping requirements and (2) to avoid the complications of gel structure, concomitant false yield value, and gross elasticity that all these polymers exhibit in solutions of higher concentration. That gross elasticity in the solutions studied was totally absent cannot be proved rigorously, but qualitative observations that these solutions without exception poured like water without any trace of stringiness strongly suggest that gross elasticity was absent. That gel structure and yield value were absent is quantitatively substantiated by the viscometric data which show curves going to the origin (0, 0) at low shear rates and the total absence of time dependence in the curves over the entire range of shear rates.

#### EXPERIMENTAL APPARATUS AND PROCEDURE

The polymers used in this study were sodium carboxymethylcellulose, CMC-70 and CMC-70S of the Hercules Powder Co.; ammonium alginate, Kelco Co. Superloid; carboxypolymethylene, Goodrich Chemical Co. Carbopol 934; and polyisobutylene, Enjay Co. Vistanex B-100. These commercial polymers were used as received



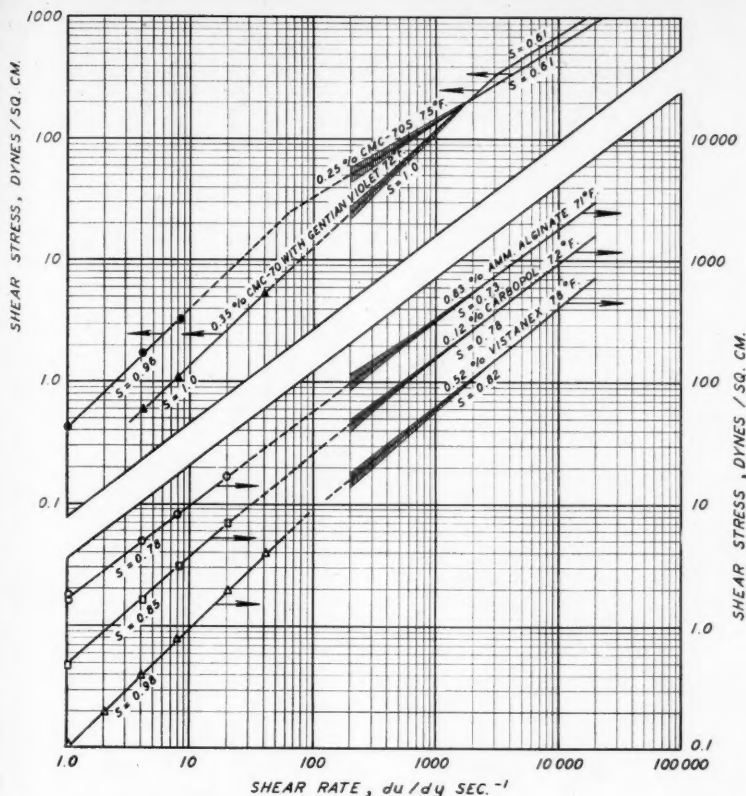


Fig. 2.

carboxymethylcellulose\*, though having some degree of stiffness compared with the others, is nonetheless quite flexible by comparison with a truly rigid polysaccharide such as amylose in aqueous solution.

The rheological (shear-stress-shear-rate) curves were determined over a wide range that exceeded in all but one or two cases the maximum (wall) values achieved in the subsequent pipeline flow experiments, with the Merrill-Brookfield coaxial-cylinder viscometer (5, 7) in the range of 200 to 20,000 (sec.<sup>-1</sup>) (sec.) of shear rate and a Brookfield Synchroelectric viscometer modified with a coaxial-cylinder rotor and stator (2) in the range of 0.1 to 42 sec.<sup>-1</sup>. The salient feature of these two viscometers with respect to the fluids studied is the very small gap between rotor and stator relative to the diameter of the rotors. This permits one to achieve direct measurement of substantially point values of shear stress and corresponding shear rate.

The pipeline flow experimentation in this work was carried out in a recirculating system that could be fitted with smooth-bore test sections varying in diameter from 3/8 in. I.D. to 3/4 in. I.D. These test sections were fitted so that frictional pressure drop might be measured at various locations along the tubes and so that impact pressure might be measured as a function of radial position. This system was pumped by either of two Moyno pumps in parallel which provided essentially pulse-free, positive-displacement pumping up to 40 gal./min. Figure 1 is a schematic diagram of this apparatus.

The impact-pressure traversing mechanism was designed and built to include positive, continuous location of the probe in the tube by means of a micrometer mechanism; detection of wall position by means of an electrical circuit and an insu-

\*As explained in connection with Table 1, the rheology of sodium carboxymethylcellulose under low rates of shear, irrelevant to this study, is unusual.

from the manufacturers and dispersed into solution according to the manufacturers' recommendations. With the exception of the cyclohexane solutions of the Vistanex all were aqueous solutions.

All these polymers in dilute solution are

believed to be essentially nonassociating, free-draining, and random coiling. Sodium

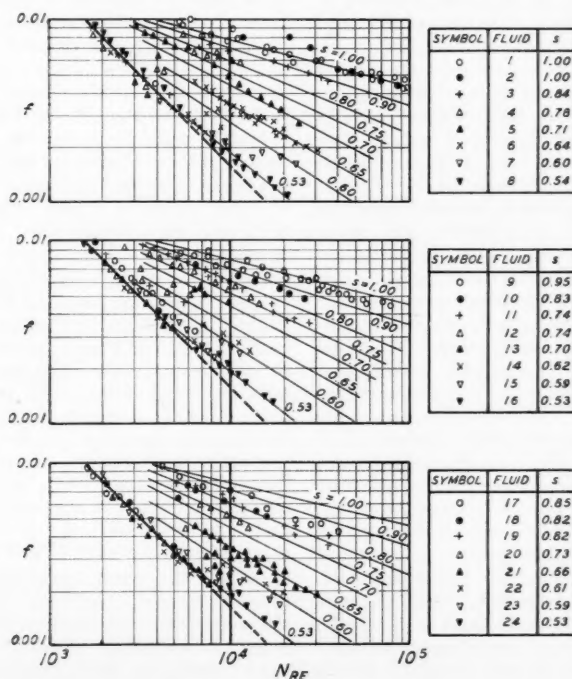
Fig. 3. Friction factor  $f$  vs. Reynolds number. →

$$\frac{D^2 V^2 - \rho}{b} \cdot 8 \left[ \frac{1}{2(3 + 1/s)} \right]^s$$

For various values of  $s$ , in laminar, transition, and turbulent flow

Fluid	Run, Table 1	Fluid	Run, Table 1
1	A 1-7	13	G 1
2	R 1	14	E 7
3	L 1	15	E 5,6
4	P 1	16	E 1
5	Q 2-3	17	D 8
6	F 1-5	18	J 1-2
7	C 1	19	Q 4
8	N 1-4	20	H 1
9	K 1-3	21	D 2-4
10	M 1	22	O 1
11	D 5-7	23	E 4
12	I 1-4	24	E 2,3

Note: The curves  $f$  vs.  $N_{Re}$  at constant  $s$  are identical in the three sections of this figure and are thus drawn to accommodate the data.



SYMBOL	FLUID	s
○	1	1.00
●	2	1.00
+	3	0.84
△	4	0.78
▲	5	0.71
×	6	0.64
▽	7	0.60
▼	8	0.54

SYMBOL	FLUID	s
○	9	0.95
●	10	0.83
+	11	0.74
△	12	0.74
▲	13	0.70
×	14	0.62
▽	15	0.59
▼	16	0.53

SYMBOL	FLUID	s
○	17	0.85
●	18	0.82
+	19	0.82
△	20	0.73
▲	21	0.66
×	22	0.61
▽	23	0.59
▼	24	0.53

lated probe; great structural rigidity in the probe, together with small diameter of the probe tip, accomplished by the nesting of sections of successively smaller-diameter hypodermic tubing, the tip being 0.025 in. O.D. and 0.013 in. I.D.; and minimum disturbance of flow by use of a simple impact tube and a wall tap.

Dye-injection experiments (to be described) consisted of injecting a thin stream of pigmented test fluid at one of several radial positions in a  $\frac{3}{4}$  in. I.D. Lucite tube, the dye stream being observed visually and photographically by means of a short-duration flash. The two main points of injection used were at the axis of, and at the entrance of, the Lucite test section, where an 0.025 in. O.D. hypodermic needle was aligned with the tube axis 185 diam. upstream of the point of observation, and through a wall tap located at, or slightly above, the point of observation. The injection was controlled by a hypodermic syringe compressed by a crank and screw-thread mechanism.

The purposes of these two injection positions were to observe the effect of turbulence on the fluid in the core of the tube and at the boundary of the tube.

## RESULTS

### Rheological Characterization

The power-law expression  $\tau = b(du/dy)^s$  evidently is inapplicable at a shear rate  $du/dy = 0$ , because for all values of  $s < 1.0$  it predicts an infinite value of the slope  $d\tau/d(du/dy)$ , contrary to experimental observation on these fluids. Therefore it is reasonable to expect that if the power-law expression is applied over different ranges of shear rate, the values of  $b$  and  $s$  may have to be adjusted to correlate the data in each range, with  $s \rightarrow 1.0$  as  $(du/dy) \rightarrow 0$ . In the case of each one of the solutions studied, as listed in Table 1, it was found that over the range of shear rate of 200 to 20,000  $\text{sec}^{-1}$  a single value of  $b$  and a single value of  $s$  could be used to correlate the shear-stress-shear-rate data obtained on the Merrill viscometer (lower limit of readability 200  $\text{sec}^{-1}$ ) and that over the range of 0.1 to 42  $\text{sec}^{-1}$ , in which data were obtained from the modified Brookfield Synchroelectric viscometer, the shear-stress-shear-rate relation could be fitted by a single value of  $s$  and single value of  $b$ . The value of  $s$  in the lower shear-rate range was invariably found to be higher than in the higher shear-rate range, substantially so for CMC and polyisobutylene solutions and only slightly so for alginate solutions. Figure 2 shows typical viscometric data as obtained on the Brookfield Synchroelectric viscometer (point readings of shear stress and shear rate) and on the Merrill-Brookfield viscometer. As the latter gives continuous curves on an  $x-y$  recorder, no points are shown for this high-range data. Instead the average of ten or more recorder traces is shown as the solid line, with the maximum and minimum variation shown as the shaded zone. It will be

noted that the zone is broadest at the lower end of the shear-rate range (200  $\text{sec}^{-1}$ ), where the readability is the poorest. Dotted lines in Figure 2 represent the region over which viscometric data is lacking (usually 21 to 200  $\text{sec}^{-1}$ ). It will be noted that over the range of 200 to 1,000  $\text{sec}^{-1}$  the data obtained from the recorder plot are capable of correlation by other values of  $b$  and  $s$  than those given by the straight line. A major question, as yet unanswered, is whether the transition between the low shear-rate range and the high range ( $>200 \text{ sec}^{-1}$ ) is abrupt or gradual. It is reasonable to suppose that it is gradual in the case of alginate and Carbopol solutions. With CMC solutions it may well be abrupt owing to some reversible change in the molecular configuration. By the progressive addition of the dye Gentian violet (pararosaniline chloride) to CMC solution, it was found that two rheological curves with a sharp break point resulted, the lower curve being that of a Newtonian fluid and the upper curve that of a markedly pseudoplastic fluid. The higher the concentration of Gentian violet, the higher was the shear rate necessary to cause transition from Newtonian to

pseudoplastic flow. If the Gentian violet, which is capable of reacting with the  $-\text{COO}^-$  group of the CMC through its group  $-\text{NH}_3^+$ , reinforces some mode of intramolecular association already inherent in CMC that holds the molecule inflexible up to some high level of shear, this abrupt Newtonian-pseudoplastic transition would be one of the phenomena anticipated. One such CMC-Gentian violet curve is shown in Figure 2. In this case the concentration of Gentian violet was sufficiently high to move the transition between Newtonian and pseudoplastic behavior up to about 3,000  $\text{sec}^{-1}$  shear rate. Accordingly the Newtonian nature of the fluid below this transition was detected over a substantial range by the Merrill-Brookfield viscometer, as well as by the Brookfield Synchroelectric viscometer.

Without exception all the transition- and turbulent-regime pipeline flow data have been correlated by using the high-range  $b$  and  $s$  values (range of 200 to 20,000  $\text{sec}^{-1}$ ). The wall shear stresses achieved in these pipeline flow studies varied over a range such that maximum (wall) shear rate was usually in the range of 500 to 20,000  $\text{sec}^{-1}$  and in a

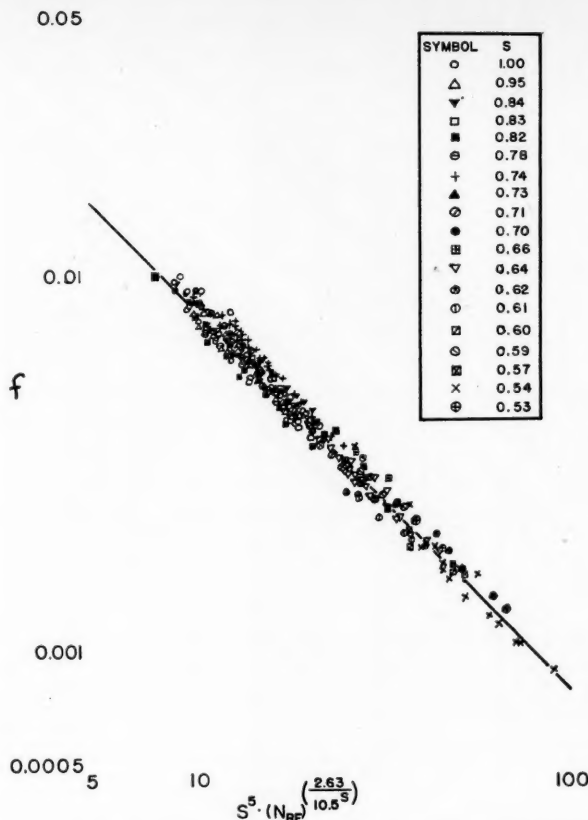
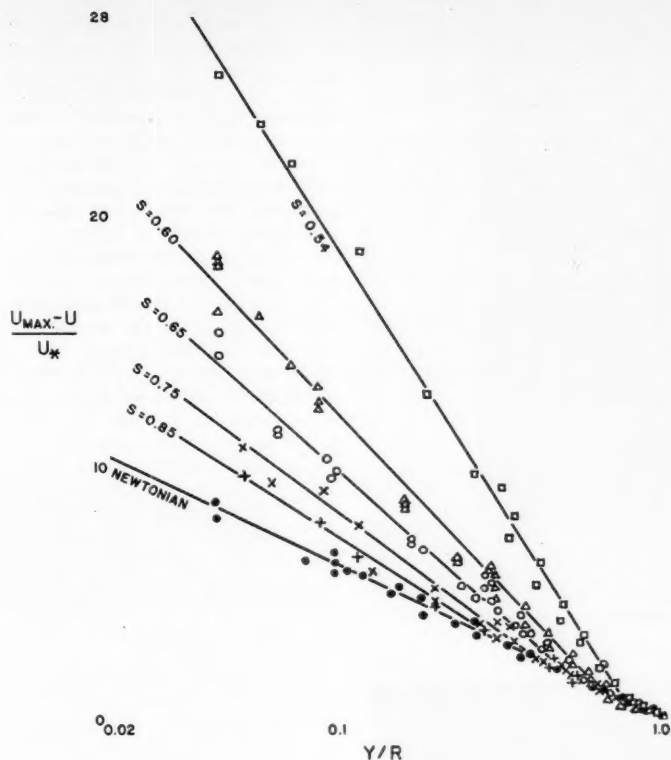


Fig. 4. Empirical correlation of friction factors in pseudoplastic turbulent flow. When the fluid is Newtonian ( $s = 1$ ), the expression reduces to the Blasius equation,  $f = 0.079/(N_{RE})^{1/4}$ .



WHERE  $U_* = \sqrt{\tau_w/\rho}$

- - RUN 8B
- △ - RUNS 4E, F, G & 9B
- - RUNS 5A, B & 3C
- × - RUNS 3E & 6B, D
- +
- - RUNS 1C, D, E, F

Fig. 5. Turbulent velocity profiles for pseudoplastic and Newtonian fluids expressed as velocity deficiencies. The ranges of Reynolds Numbers are: Newtonian; 9,600 to 176,000

$s = 0.85$ ; 17,000  
 $s = 0.75$ ; 7,540 to 10,500  
 $s = 0.65$ ; 8,800 to 14,600  
 $s = 0.60$ ; 8,400 to 14,300  
 $s = 0.54$ ; 8,780

few runs was as high as 40,000 sec.<sup>-1</sup> Under these conditions the volume of fluid contained within an imaginary coaxial cylindrical section, within which the shear rate was 200 sec.<sup>-1</sup> or less, amounted to about one quarter of the total volume in the same section at the lowest values of wall shear stress and a negligible fraction at the highest wall shear stress. That the successful correlation of  $f$  vs.  $N_{Re}$  shown in Figure 4. is based entirely on  $s$  values in the 200 to 20,000 sec.<sup>-1</sup> range suggests that low shear viscometry as a means of predicting the turbulent-flow characteristics of these polymer solutions would be in at least two cases (CMC and Vistanex) totally misleading. Stated in another way, if low shear viscometric data were used

as a basis for predicting the turbulent-flow friction factors of CMC and Vistanex according to the correlations shown in Figure 4, the resulting values of  $f$  would be away out of line and would have to be reported as anomalous. When the high-range viscometric data are used, the predicted  $f$  values are in line with those of alginate and Carbopol and agree well with the experimentally determined values.

#### TURBULENT-FLOW FRICTION FACTORS

In turbulent flow the relationship between the friction factor and the pseudoplastic Reynolds number (Figure 3) was found to consist of a family of curves, each curve depending on  $s$  in

such a way that the friction factor decreased with decreasing  $s$  at a given pseudoplastic Reynolds number.

All the experimental data, which form the basis of Figure 3, are correlated empirically by Equation (5),

$$f = 0.079/(s^5 \cdot N_{Re}^7) \quad (5)$$

where

$$\gamma = 2.63/(10.5)^s \quad (6)$$

In Figure 4 it can be seen that Equation (5) correlates the experimental data in which the rheological behavior ranges from Newtonian to a pseudoplasticity of  $s = 0.53$  with a maximum deviation of +33, to -15%. This correlation cannot be used with fluids having an  $s$  value less than about 0.4, since the predicted friction factor would be less than in laminar flow. In solutions of random coiling, nonassociating high-molecular-weight polymers sufficiently dilute to avoid gel structure and gross elasticity, the value of  $s$  has never been found lower than 0.5 from data obtained on either of the coaxial-cylinder viscometers used in this work. [It is possible to attribute a very low value of  $s$  to a fluid with a yield value, which is really a Bingham plastic, or to a solution of rodlike molecules, for example amylose, but in either of these cases the power-law model  $\tau = b(du/dy)^s$  is at best a very rough approximation of the rheology, which is far better described by other, unrelated equations.]

#### VELOCITY PROFILES AND MIXING LENGTHS

Figure 5 shows the experimentally obtained velocity-profile data for turbulent flow, expressed as velocity deficiencies and collected on one plot. In Newtonian turbulent flow it has been found (1) that this type of correlation brings together the profiles for all conditions of Reynolds number and tube roughness onto a single curve. However it can be seen that this correlation did not bring the pseudoplastic turbulent-velocity profiles onto a single curve but rather presented a series of curves, again depending on the value of  $s$ . In addition it can be seen that there is a region in the vicinity of the center of the tube in which a pseudoplastic curve coincides with the Newtonian, but this region gets progressively smaller as pseudoplasticity is increased. In general it can be said that at a given Reynolds number in turbulent flow in a smooth tube a pseudoplastic polymer solution of the type studied will have a lower friction factor and a less blunt velocity profile than a Newtonian fluid.

In addition it was found that the mixing-length distribution curves calculated from the velocity profiles did not coincide with the classical curves obtained with Newtonian fluids but also deviated

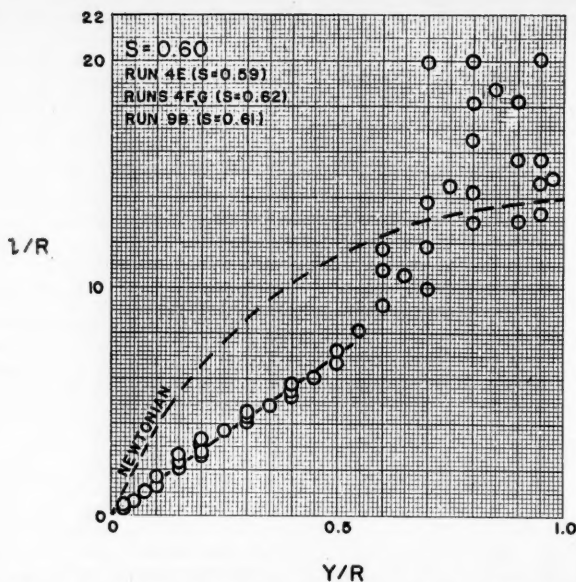
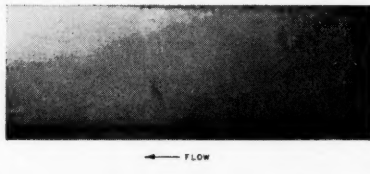


Fig. 6. Typical curve of mixing length distribution for pseudoplastic turbulent flow.



INJECTION 185 DIAMETERS UPSTREAM

Fig. 7. Laminar flow, dye injection at tube center.



INJECTION 1/2 DIAMETER UPSTREAM OF  
EDGE OF PHOTO

Fig. 8. Laminar flow, dye injection at tube wall.

systematically with the value of  $s$ . Figure 6 shows a typical curve of mixing length vs.  $y/R$ . The interdependence of the velocity distribution curve and the distribution of mixing lengths was derived from the velocity distribution curves by the relation

$$l \cdot du/dy = u_* \sqrt{1 - y/R} \quad (7)$$

#### DYE-INJECTION STUDIES

In a series of experiments designed to show something about the nature of the flow, pigmented liquid was injected at various points in a transparent tube and the path of the dye stream was photographed with a high-speed stroboscopic flash\*. It soon became evident that the most informative experiments could be obtained by injecting at two different points, at the entrance of the test section in the center of the tube and at a small, carefully drilled wall tap. Axial injection was intended to show the effect of turbulence on the liquid in the

core of the tube and injection at the wall to show the effect on the fluid in the layer near the wall. The first type of injection was at the portion of the system where the large feed pipe necked down to the smaller test section. As the fluid was being accelerated at that section there was less tendency for flow separation and vortex formation to occur because of the presence of the hypodermic-tubing probe.

As seen in Figure 7, the dye injected at the center of the tube into a stream in laminar flow retains its radial position and identity in both the Newtonian and the pseudoplastic cases, making a straight filament as expected. The presence of the hypodermic probe did not seem to disturb this configuration until the flow increased almost to the transition region. Figure 8 shows that the dye stream injected at the wall retains its unity and runs a straight filament against the tube wall.

The dye stream injected from the axially positioned needle into a Newtonian liquid in turbulent flow as seen by the 40  $\mu$ sec. flash 185 diam. downstream from the point of injection is completely

dispersed across the diameter of the tube (Figure 9). There is no filamental quality left to it, at least on the macroscopic scale. This is in accord with the understanding of Newtonian turbulence as a very rapid, violent mixing action.

Where the dye was injected at the wall, loops of dyed liquid were found emanating from the main body of the wall layer, shown in Figure 11. This effect is in accordance with the observations and calculations reported by Theodorsen (15) concerning horseshoe vortices formed in the vicinity of the wall and traveling toward the center under the influence of the main stream of flow. It indicates that turbulent eddies form at or near the wall and travel radially away from it, thereby mixing fluid from the region of the wall with fluid in the core of the flow. The force that produces the movement toward the center is a lift force generated by the rotating mass intruding into the flowing stream. It exchanges momentum with the fluid through which it is passing by means of normal drag forces and finally loses its identity.

When injected into a highly pseudoplastic CMC solution ( $s = 0.61$ ) in turbulent flow at the center of the tube, the dye stream takes on a strikingly different appearance 185 diam. downstream from the point of injection than it does in Newtonian turbulent flow (Figure 10). To a large extent the dye stream seems to be still intact, although it is highly distorted and grossly distributed across a large portion of the diameter of the tube.

The photographs of the dye stream injected at the center of the tube show that it does not readily lose its identity but rather is pushed aside by the turbulent vortices and does not become part of them. The action has been aptly described by Sherwood (19) as a kneading action.

With respect to the wall-injection study (Figures 11, 12), the smoothly flowing layer near the wall was found to be thicker in these pseudoplastic polymer solutions than in Newtonian liquids in turbulent flow. It was also found that the horseshoe vortices formed in the pseudoplastic liquid are relatively few in number and not at all well developed at this short distance from the point of injection.

On the basis of these observations it is concluded that the formation of horseshoe vortices is highly repressed in pseudoplastic turbulent flow leading to much lower energy dissipation and that the core fluid tends to retain its identity, although being distorted by the vortices that do penetrate it. An explanation appears to lie in the fact that the fluid in the center of the tube, under a low average rate of shear, has as a result a higher viscosity than the fluid near the wall, which is under a high rate of shear. Likewise the fluid in the core of a vortex

\*The pigmented liquid was carbon black dispersed in water. Initially Gentian violet was used. As noted above, this dye reacted with CMC and changed its rheology.



has a higher viscosity than the fluid that surrounds the core, thereby resisting intermingling with the more rapidly moving fluid. The mixing of two liquids of widely differing viscosity, such as water and heavy syrup, might be cited as a crude analogy.

It is apparent from the dye-injection experiments and from the velocity profiles obtained in the turbulent-flow regime that there is no plug flow in the core. That slip at the wall, as suggested as a possibility for some types of fluids (12), is absent in these pseudoplastic polymer solutions under all flow conditions was confirmed because the material balances calculated from the velocity

profiles which assumed zero slip checked with the measured flow rates.

#### FLUCTUATIONS IN PRESSURE

The manometer columns were observed to oscillate over the transition range of most of the fluids tested, giving the impression of periodic lapses into the turbulent form of flow from an unstable laminar form. The oscillations occurred between maxima and minima corresponding clearly to laminar and turbulent forms at the particular Reynolds number, as long as the frequency was low enough for the manometer to register. As the frequency of oscillation became higher,

the maxima and minima of the manometer readings fell between the extrapolated laminar- and turbulent-flow predictions, as would be expected owing to the inertia of the manometric fluid. This phenomenon has been noticed previously (13) and is probably due to the periodic formation of horseshoe vortices, with the consequent distortion of flow, at frequencies low enough to be seen on the manometers.

As the flow rate increased from the transition region into the turbulent region, the manometer oscillations increased in frequency and decreased in amplitude, becoming negligible for fluids of which the  $s$  value is 0.7 or more but persisting in highly pseudoplastic fluids ( $s < 0.7$ ) as a flutter of very small amplitude (less than 1 mm.) and high frequency for a long way into the turbulent region, often up to the maximum obtainable flow rate. These observations suggest that the periodic change between two forms of flow that was observed in the transition region persists into the turbulent region.

A possible explanation for the apparent decrease in the frequency of the formation of vortices is the viscosity gradient present across the radius of a tube that carries a pseudoplastic fluid. If one considers such a fluid flowing in steady laminar flow at a high Reynolds number, the viscosity gradient in it would be defined by the linear shear-stress distribution and the rheological curve of the material. The effect would be to have a minimum viscosity at the wall and a maximum viscosity at the center of the tube. Thus a vortex formed at the wall of the tube in traveling inward toward the center penetrates layers of increasing viscosity. As a consequence of this it seems reasonable to expect that there would be a damping effect on the vortex over and above that imposed by a Newtonian system.

By means of this concept of viscosity gradient two effects observed in pseudoplastic flow can be explained: the persistence of stable laminar flow to abnormally low friction factors (high Reynolds numbers) and the relatively low frequency of formation of turbulent vortices in turbulent flow leading to lower friction factors than Newtonian and to flutter of manometer columns under certain conditions. One could reasonably expect such a viscosity gradient to retard both the point of incipient formation of vortices and the frequency of their formation once this point has been passed.

#### PERIODIC BOUNDARY LAYERS

In view of the foregoing it is interesting to consider the concept of periodic boundary layers as proposed by Richardson (14). Reported experiments were conducted in a pipe fitted with a loose section that could be oscillated in a



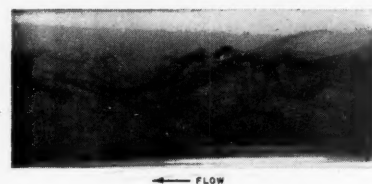
WATER,  $N_{Re} = 3720$   
INJECTION 106 DIAMETERS UPSTREAM

Fig. 9. Newtonian turbulent flow, dye injection at tube center.



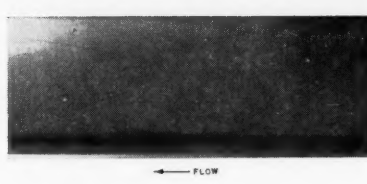
WATER,  $N_{Re} = 3720$   
INJECTION 1/2 DIAMETER UPSTREAM OF  
EDGE OF PHOTO

Fig. 11. Newtonian turbulent flow, dye injection at tube wall.



0.25% CMC-708,  $N_{Re} = 8400$ ,  $S = 0.61$   
INJECTION 106 DIAMETERS UPSTREAM

Fig. 10. Pseudoplastic turbulent flow, dye injection at tube center.



0.25% CMC-708,  $N_{Re} = 12,800$ ,  $S = 0.61$   
INJECTION 1/2 DIAMETER UPSTREAM OF  
EDGE OF PHOTO

Fig. 12. Pseudoplastic turbulent flow, dye injection at tube wall.

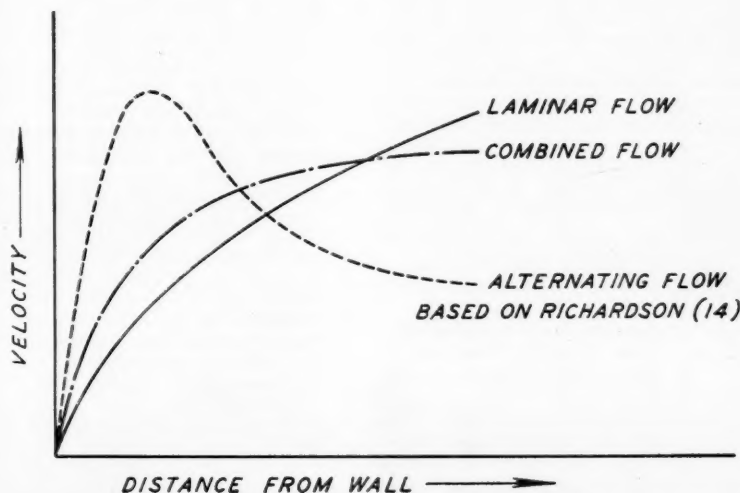


Fig. 13. Conversion of laminar to turbulent profiles.

direction transverse to the flow. When a stable laminar flow was passed through the tube and the loose section oscillated the tube and the loose section oscillated, the resultant velocity profile was the blunt logarithmic type of turbulent flow (14). The effect is ascribed to an alternation between the laminar form of flow and an alternating form the profile of which has a peak near the wall. The turbulent profile is then the time average between the two. (See Figure 13.)

If one ascribes the generation of turbulence to some process resembling the artificially induced one, the decreasing bluntness of pseudoplastic turbulent profiles (compared with the profiles of Newtonian fluids) with increasing pseudoplasticity can be explained in the following manner. Given the laminar form of flow in an unstable region, the vortex formation causes the flow to distort to the alternating form, with a peak near the wall. However the effect of pseudoplasticity, as deduced from other facts, is to reduce the frequency of the occurrence of these vortices. Therefore as pseudoplasticity is increased, progressively less of the alternating form is time averaged with the laminar form, resulting in progressively less blunt turbulent profiles and progressively lower friction factors. Since the laminar profiles become more blunt as pseudoplasticity is increased, it is apparent that the decrease in frequency of alternation must be such as to more than compensate for this effect in the resultant profile.

This concept of the oscillation between two forms of flow in the turbulent region is helpful in that it reasonably explains all the main phenomena observed with the turbulent flow of the pseudoplastic polymer solutions studied:

1. The decrease in friction factors at constant  $N_{Re}$  as pseudoplasticity is increased
2. The progressively less blunt velocity profiles with increasing pseudoplasticity
3. The flutter of the manometer columns in the turbulent region with the highly pseudoplastic liquids
4. The relatively poor mixing of dye stream injected into the center of the tube
5. The thicker calm layer near the wall and fewer horseshoe vortices as seen by wall dye injection.

#### CONCLUSIONS

1. The degree of turbulent agitation in the turbulent flow region is progressively less at comparable Reynolds numbers as pseudoplasticity is increased (measured by decreasing value of  $s$ ).
2. This is attributed to a progressively decreasing frequency of vortex formation at the tube wall.
3. The result of this is lower friction

factors and less blunt velocity profiles in pseudoplastic turbulent flow than in Newtonian turbulent flow.

4. Laminar pseudoplastic velocity profiles are progressively blunter than Newtonian ones, as is predicted by the power model of pseudoplastic rheology.

5. Slip at the wall in these pseudoplastic polymer solutions under all measured flow conditions must be negligible, if it exists at all, to account for the excellent agreement in flow rates calculated by integrating the velocity profiles which assume zero wall slip and by measuring directly. Plug flow of a central core of fluid is shown not to exist by velocity profiles in the laminar regime, photography of axially injected dye streams in turbulent flow.

6. The laminar- and turbulent-flow behavior in tubes of the free-draining, nonassociating polymer solutions studied (despite significantly different features of molecular structure of the several polymers) is well correlated by using the power-law model  $\tau = b(du/dy)^s$  to express the rheology, provided that  $b$  and  $s$  are determined over a range of shear appropriate to the conditions of the fluid at the wall and radially inward to roughly three quarters of the radius of the tube. For the flow conditions reported herein the range of 200 to 20,000  $\text{sec}^{-1}$  of shear rate was appropriate, and the values of  $b$  and  $s$ , found for all solutions to be constant over this range, yielded a satisfactory correlation of the tube-flow data. Viscometric determination in the low range of shear (0.1 to 42  $\text{sec}^{-1}$ ) was shown to be in general of no value.

#### ACKNOWLEDGMENT

The authors wish to thank the Esso Research and Engineering Company for a generous grant under which much of the apparatus was built; Brookfield Engineering Company, Stoughton, Massachusetts, for constructing and donating the two viscometers used in this study; Humble Oil and Refining Company for fellowship support; Dewey and Almy Chemical Company, Division of W. R. Grace and Company, for technical aid, supplies, and a substantial grant under which the Merrill-Brookfield viscometer was developed; and H. H. Carter of the Chemical Engineering Department, Massachusetts Institute of Technology, Cambridge, Massachusetts, for his careful drawings.

#### NOTATION

- $b$  = pseudoplastic rheological constant, (dyne)(sec.)<sup>s</sup>/sq. cm.  
 $d$  = differential operator  
 $D$  = tube diameter, cm.  
 $f$  = Fanning friction factor  
 $l$  = turbulent mixing length, cm.  
 $L$  = length, cm.  
 $N_{Re}$  = pseudoplastic Reynolds number,

$$\left(\frac{D^s V^{2-s} \rho}{b}\right) \cdot 8[2(3 + 1/s)]^{-s}$$

- $P$  = pressure, dynes/sq. cm.  
 $Q$  = volumetric flow rate, cc/sec.  
 $r$  = radius, cm.  
 $R$  = tube radius, cm.  
 $s$  = pseudoplastic rheological exponent  
 $u$  = local velocity, cm./sec.  
 $u_{moz}$  = maximum (axial) velocity in tube, cm./sec.  
 $u_s$  = friction velocity, cm./sec.  
 $V$  = average velocity, cm./sec.  
 $w$  = wall  
 $y$  = distance from wall, cm.  
 $\Delta$  = difference  
 $\gamma$  = exponent to  $N_{Re}$   
 $\mu$  = viscosity, poises  
 $\pi$  = 3.1416  
 $\rho$  = density, g/cc.  
 $\tau$  = shear stress, dynes/sq. cm.  
 $\tau_w$  = wall shear stress, dynes/sq. cm.  
 $du/dy$  = local velocity gradient (shear rate),  $\text{sec}^{-1}$

#### LITERATURE CITED

1. Bakhmeteff, B. A., "The Mechanics of Turbulent Flow," Princeton, Princeton University Press, Princeton, New Jersey (1936).
2. Beerli, G. J., S.B. thesis, Mass. Inst. Technol., Cambridge (1957).
3. Bird, R. B., *A.I.Ch.E. Journal*, 2, 3, 428 (1956).
4. Dadekian, Z. A., and R. C. Engelken, S.B. thesis, Mass. Inst. Technol., Cambridge (1955).
5. Merrill, E. W., *J. Colloid Sci.*, 9, 1, 7 (1954).
6. ———, *Instrument Society of America Journal*, 2, No. 2, 462 (1955).
7. *Ibid.*, 3, No. 4, 124 (1956).
8. ———, *J. Colloid Sci.*, 11, 1 (1956).
9. Metzner, A. B., and J. C. Reed, *A.I.Ch.E. Journal*, 1, 4, 434 (1955).
10. Metzner, A. B., and R. E. Otto, *ibid.* 3, 1, 3 (1957).
11. Mooney, M., *J. Rheol.*, 2, 2, 210 (1931).
12. Oldroyd, J. G., "Proc. Internat. Cong. Rheology, Holland, 1948," North-Holland Publishing Co., Amsterdam Section C, vol. II, p. 130 (1949).
13. Prandtl, L., "Applied Hydro- and Aeromechanics," McGraw-Hill Book Co., Inc., New York (1934).
14. Richardson, E. G., "Dynamics of Real Fluids," Edward Arnold and Co., London (1950).
15. Theodorsen, Theodore, "50 Jahre Grenzschichtforschung," edited by H. Gortler and W. Tollmien, Friedrich Vieweg, Braunschweig, Germany (1955).
16. Toms, B. A., *J. Colloid Sci.*, 4, 511 (1949).
17. Weltmann, R. N., and P. W. Kuhns, *Natl. Advisory Comm. Aeronaut. Tech. Note* 3510 (August, 1955).
18. Weltmann, R. N., *Ind. Eng. Chem.*, 48, 3, 386 (1957).
19. Sherwood, T. K., private communication.

Manuscript received January 7, 1958; revision received July 3, 1958; paper accepted July 10, 1958.

# Turbulent Flow of Non-Newtonian Systems

D. W. DODGE and A. B. METZNER

University of Delaware, Newark, Delaware

A theoretical analysis for turbulent flow of non-Newtonian fluids through smooth round tubes has been performed for the first time and has yielded a completely new concept of the attending relationship between the pressure loss and mean flow rate. In addition, the analysis has permitted the prediction of non-Newtonian turbulent velocity profiles, a topic on which the published literature is entirely silent.

To confirm the theoretical analysis, experimental data were taken on both polymeric gels and solid-liquid suspensions under turbulent-flow conditions. Fluid systems with flow-behavior indexes between 0.3 and 1.0 were studied at Reynolds numbers as high as 35,000. All the fully turbulent experimental data supported the validity of the theoretical analysis. The final resistance-law correlation represents a generalization of von Karman's equation for Newtonian fluids in turbulent flow and is applicable to all non-Newtonians for which the shear rate depends only on shear stress, irrespective of rheological classification. All the turbulent experimental data for the non-Newtonian systems were correlated by this relationship with a mean deviation of 1.9%.

## THEORY

Non-Newtonian fluids are defined as materials which do not conform to a direct proportionality between shear stress and shear rate. Because of this negative definition of non-Newtonian behavior, essentially an infinite number of possible rheological relationships exist for this class of fluids, and as yet no single equation has been proved to describe exactly the shear-stress-shear-rate relationships of all such materials over all ranges of shear rates. If such a general equation could be developed, it seems probable that its complexity would be too great for general engineering utility. Although it is desirable that the following theoretical analysis be universally applicable to all time-dependent, nonelastic fluids, irrespective of any arbitrary rheological classifications such as *Bingham plastic*, *pseudoplastic*, or *dilatant*, this consideration is much too broad to be handled in the initial phases of the development. Therefore a particular rheological model will be selected for use initially, and application of the resulting development to fluids deviating from the assumed model will be considered subsequently.

It has been found experimentally (7, 11, 19, 20) that the relationship between shear stress and shear rate for a great many non-Newtonian fluids, possibly the majority, may be represented closely over wide ranges of shear rate (ten- to one-thousand-fold) by a two-constant power function of the form

$$\tau = K \left( \frac{-du}{dr} \right)^n \quad (1)$$

where  $(-du/dr)$  is the shear rate written for flow within a circular duct. An equation of this type, though empirical, appears to represent the rheological properties for a wide variety of non-Newtonian fluids better than most other proposed equations and certainly better than any other available two-constant equation. For this reason the power-law rheological model will be adopted in the following theoretical analysis. It should be noted that the power-law model includes the special case of Newtonian behavior, namely that case when  $n$  is unity and  $K$  is equal to the Newtonian viscosity. Values of  $n$  between zero and unity characterize pseudoplastic fluids, for which the apparent viscosity [defined by  $\tau/(-du/dr)$ ] decreases with increasing shear rate. Conversely values of  $n$  greater than unity correspond to dilatant fluids, for which the apparent viscosity increases with shear rate. Generally it may be said that  $n$  is an index to the degree of non-Newtonian behavior in that the further  $n$  is removed from unity, above or below, the more pronounced become the non-Newtonian characteristics. On the other hand,  $K$  is related more to the consistency of the system (9, 10).

### Power-Law Fluids

#### Resistance Law

The general method of attack to be used here is similar to that first employed by Millikan (12) for Newtonian fluids. However an additional degree of freedom

represented by the flow-behavior index will be incorporated into the analysis.

According to a concept which has been used successfully with Newtonian fluids, flow in a smooth pipe may be divided into the following three zones:

1. A laminar sublayer lying next to the pipe wall in which the effects of turbulence are negligible

2. A transition zone in which the effects of turbulence and viscous shear are of the same order of magnitude

3. A turbulent core comprising the bulk of the fluid stream. Here the momentum transfer which accompanies the random velocity fluctuations characteristic of turbulent motion, rather than viscous shear, determines the velocity profile. If one assumes the turbulent fluctuations to be independent of viscosity, it follows that the effects of viscosity are negligible in the turbulent core. It will be assumed that the same type of flow division is applicable to non-Newtonian fluids. When one defines  $y$  as the distance of a point within the pipe from the tube wall, the extent of the flow zones will be designated as

laminar sublayer:  $0 \leq y \leq \delta$

transition zone:  $\delta \leq y \leq \lambda$

turbulent core:  $\lambda \leq y \leq R$

For Newtonian fluids it has been shown (5) that the time average velocity at a point within a smooth pipe depends on five independent variables,  $R$ ,  $\rho$ ,  $\tau_w$ ,  $\mu$ , and  $y$ . With non-Newtonian fluids of the power-law type the two flow parameters  $n$  and  $K$  are required to

D. W. Dodge is with E. I. DuPont de Nemours and Company, Inc., Buffalo, New York.

replace the single rheological proportionality constant for Newtonian systems. By analogy to the Newtonian case then it is reasonable to assume that for power-law fluids.

$$u = f(R, \rho, \tau_w, K, n, y) \quad (2)$$

When one applies dimensional analysis, Equation (2) may be written as

$$\frac{u}{u^*} = f_1(Z, \xi, n) \quad (3)$$

where

$$Z = R^n \rho (u^*)^{2-n} / K \quad (4)$$

In the derivation of Equation (3), no assumptions were made regarding the location of the point corresponding to  $u$ , and therefore the equation is valid for all values of  $y$  or  $\xi$ .

Within the laminar sublayer the pipe radius plays no part in determining  $u$ . The effect of  $R$  therefore might be assumed negligible also at slightly greater distances from the wall, as far out as the outer part of the turbulent core. Then within this wall region

$$u = f(\rho, \tau_w, K, n, y)$$

which according to dimensional analysis may be expressed as

$$\frac{u}{u^*} = f_2(Z\xi^n, n) \quad (5)$$

Equation (5) is comparable with Prandtl's wall-velocity law (5) for Newtonian fluids, which agrees well with experimental results. It shall be assumed that this equation is valid in the range  $0 \leq \xi \leq \xi_1$ , where  $\xi_1$  is only slightly greater than  $\lambda/R$ . It is not meant to be implied that the function  $f_2$  will have the same specific form in the laminar sublayer and in the outer part of the turbulent core; generally the forms will be different.

The difference between the velocity at the center line of a tube and the time average velocity at a point elsewhere within the turbulent core has been called the *velocity defect*. From Equation (2) it can be seen that this defect ( $U_m - u$ ) depends at most on  $R, \rho, \tau_w, K, n$ , and  $y$ . However in the core ( $U_m - u$ ) will be determined by the random turbulent fluctuations which have been assumed independent of the apparent viscosity. This assumption has been substantiated for Newtonian fluids. For power-law systems the equivalent assumption is that the velocity defect is independent of  $K$  (but not of  $n$ ), whereby

$$U_m - u = f(\tau_w, \rho, R, y, n)$$

Application of dimensional analysis here yields

$$\frac{U_m - u}{u^*} = f_3(\xi, n) \quad (6)$$

When  $n$  is unity, Equation (6) becomes what is commonly called the *velocity-defect law* for Newtonian fluids, which also has been amply verified by experiments (5).

Equation (6) is strictly applicable only in the turbulent core, that is for  $\lambda/R \leq \xi \leq 1$ . If as an approximation one were to assume that Equation (6) applies over the entire cross section, then it follows that

$$\begin{aligned} V &= \frac{2}{R^2} \int_0^R ur \, dr \\ &= \frac{2}{R^2} \int_0^R U_m r \, dr \\ &\quad - \frac{2u^*}{R^2} \int_0^R f_3(\xi, n) r \, dr \end{aligned}$$

For any specified value of  $n$  this equation becomes

$$V = U_m - u^* \quad (\text{constant})$$

or

$$\frac{U_m - V}{u^*} = P_n \quad (7)$$

Since Equation (7) was derived for any fixed value of  $n$ , it must be expected in general that  $P_n$  will be a function of  $n$ . Experiments with Newtonian fluids have shown that the wall layers are so thin that Equation (7) may be used without appreciable error; it will be assumed that the same is true for the non-Newtonian case. This assumption should be very good for pseudoplastic fluids ( $0 < n < 1$ ) for which a laminar sublayer even thinner than that in the Newtonian case is to be expected, but it may break down for fluids having a value of  $n$  sufficiently above unity to retain an appreciable thickness of the laminar sublayer even under fully turbulent conditions.

The friction factor is defined by

$$f = \tau_w / \frac{\rho V^2}{2} = \frac{D\Delta P}{4L} / \frac{\rho V^2}{2}$$

Therefore

$$\frac{V}{u^*} = \sqrt{\frac{2}{f}} \quad (8)$$

When one writes Equation (3) for the center line of the pipe,

$$\frac{U_m}{u^*} = f_1(Z, 1, n) = F_1(Z, n) \quad (9)$$

by a combination of Equations (7), (8), and (9)

$$\sqrt{\frac{2}{f}} = F_1(Z, n) - P_n \quad (10)$$

Hence an expression for the friction factor may be obtained by finding  $F_1(Z, n)$ .

In the outer part of the turbulent core, where  $(\lambda/R) \leq \xi \leq 1$ , Equations (5)

and (6) are both assumed to be valid. Therefore eliminating  $u/u^*$  from Equations (5) and (6) and replacing  $U_m/u^*$  by Equation (9), one finds for this overlapping region

$$f_2(Z\xi^n, n) = F_1(Z, n) - f_3(\xi, n)$$

It will be noted that  $\xi$  effects the left side of this equation according to  $\xi^n$ , and that the  $F_1$  function on the right side is independent of  $\xi$ . To balance the left side of the equation  $\xi$  must be present in the  $f_3$  function also as  $\xi^n$  rather than  $\xi$ . Hence this equation may be formulated better as

$$f_2(Z\xi^n, n) = F_1(Z, n) - f_3(\xi^n, n) \quad (11)$$

If  $n$  is now eliminated as a variable by considering any fixed value of  $n$ , Equation (11) becomes

$$f_{2n}(Z\xi^n) = F_{1n}(Z) - f_{3n}(\xi^n) \quad (12)$$

When one lets

$$\frac{df_{2n}}{d(Z\xi^n)} = f_{2n}'$$

then

$$\left( \frac{\partial f_{2n}}{\partial Z} \right)_\xi = \frac{df_{2n}}{d(Z\xi^n)} \left( \frac{\partial (Z\xi^n)}{\partial Z} \right)_\xi = f_{2n}' \xi^n$$

and by Equation (12)

$$f_{2n}' \xi^n = \frac{dF_{1n}}{dZ} \quad (13)$$

Similarly

$$\left( \frac{\partial f_{2n}}{\partial \xi^n} \right)_Z = \frac{df_{2n}}{d(Z\xi^n)} \left( \frac{\partial (Z\xi^n)}{\partial \xi^n} \right)_Z = f_{2n}' Z$$

and by Equation (12)

$$f_{2n}' Z = -\frac{df_{3n}}{d\xi^n} \quad (14)$$

From Equation (13) it is seen that  $f_{2n}'$  must have the form  $f(Z)/\xi^n$ , since  $dF_{1n}/dZ$  is independent of  $\xi$ . Furthermore from Equation (14) it is seen that  $f_{2n}'$  must have the form  $f(\xi^n)/Z$ , since  $df_{3n}/d\xi^n$  is independent of  $Z$ . Both these requirements can be satisfied only if

$$f_{2n}' = \frac{A_n}{Z\xi^n} \quad (15)$$

Now by Equations (13) and (15)

$$dF_{1n}(Z) = A_n \frac{dZ}{Z}$$

whereby

$$F_{1n}(Z) = \left( \frac{U_m}{u^*} \right) = A_n \ln Z + B_n \quad (16)$$

By Equations (14) and (15)

$$df_{3n}(\xi^n) = -A_n \frac{d\xi^n}{\xi^n}$$



whereby

$$f_{3n}(\xi^n) = \left( \frac{U_m - u}{u^*} \right) = -A_n \ln \xi^n + E_n \quad (17)$$

The constants of integration in Equations (16) and (17) must be considered as functions of  $n$  unless later proved otherwise. When one combines Equations (12), (16), and (17),

$$f_{2n}(Z\xi^n) = \frac{u}{u^*} = A_n \ln Z\xi^n + B_n - E_n \quad (18)$$

The derivation of Equations (16), (17), and (18) was based on a consideration of the overlapping region  $\lambda/R \leq \xi \leq \xi_1$ , wherein Equations (5) and (6) were equated. As a result it should be expected that these equations can be applied rigorously only to this region. However Equation (16) is independent of  $\xi$  and hence must be truly independent of the location and width of the overlapping region. This can also be seen from the definition of  $F_1(Z, n)$  as given by Equation (9); its applicability cannot be limited to a particular region of  $\xi$ . Considering the original statement of the velocity-defect law, Equation (6), one may modify Equation (17) for all values of  $\xi$  within the turbulent core

$$\frac{U_m - u}{u^*} = -nA_n \ln \xi + g_1(\xi, n) \quad (19)$$

where  $g_1(\xi, n)$  is some unknown function. Equation (19) extends the region of applicability of Equation (17) to the entire turbulent core simply by making it more general. An alternate equation for the velocity profile, valid for the entire turbulent core but not including  $U_m$ , may be formulated from Equations (16) and (19):

$$\frac{u}{u^*} = \frac{U_m}{u^*} - \frac{U_m - u}{u^*} = A_n \ln Z\xi^n + B_n - g_1(\xi, n) \quad (20)$$

If Equation (16) is now substituted into Equation (10), one obtains

$$\sqrt{\frac{2}{f}} = A_n \ln Z + B_n - P_n$$

which by suitable manipulation together with Equations (4) and (8) can be put in the form (3)

$$\sqrt{\frac{1}{f}} = A_{1n} \log [N_{Re}^0(f)^{1-n/2}] + C_n \quad (21)$$

where

$$N_{Re}^0 = D^n V^{2-n} \rho / K \quad (22)$$

$$A_{1n} = 1.628A_n$$

$$C_n = 0.4901A_n \left( 1 + \frac{n}{2} \right) + B_n - P_n$$

$N_{Re}^0$  is not so convenient a Reynolds number for correlation purposes as one proposed by Metzner and Reed (11), the reason being that the use of  $N_{Re}^0$  does not result in a unique relationship between the friction factor and the Reynolds number in the laminar-flow region. Instead a family of curves result with  $n$  as a parameter. The generalized Reynolds number of Metzner and Reed,  $N_{Re}'$ , however does result in a unique relationship in the laminar region for all values of  $n$ , namely the familiar laminar relationship  $f = 16/N_{Re}'$ . The work of Metzner and Reed was based on concepts developed initially by Rabinowitsch (13), who clearly established the fact that for laminar flow through a round tube of any fluid with a shear rate that is a function only of shear stress the relationship between the shear stress at the tube wall  $D\Delta P/4L$  and the quantity  $8V/D$  is unique. Hence the flow characteristics of a fluid are defined just as completely by the laminar  $D\Delta P/4L - 8V/D$  relationship as by the shear-stress-shear-rate relationship, and for pipe-flow situations the former is generally more convenient (10).

In their work Metzner and Reed used the following definitions to define the laminar-flow behavior of non-Newtonian fluids. (These definitions were then used under turbulent-flow conditions as well, just as the viscosity of a Newtonian fluid is defined under laminar conditions but used in both the laminar and turbulent regions.)

$$n' = \frac{d(\log(D\Delta P/4L))}{d(\log(8V/D))} \quad (23)$$

$$\tau_w = \frac{D\Delta P}{4L} = K'(8V/D)^{n'} \quad (24)$$

Equation (23) defines  $n'$ , and Equation (24) defines  $K'$ . Generally Equation (24) does not represent an integration of Equation (23); only when  $n'$  is a constant are the two definitions linked by a simple integration. It will be noted that a marked similarity exists between Equations (1) and (24). The power-law case represents the one situation where  $n'$  and  $K'$  are true constants and are related to the parameters  $n$  and  $K$  by the equations (9, 11)

$$n' = n \quad (25)$$

$$K' = K \left( \frac{3n+1}{4n} \right)^n \quad (26)$$

Hence with constant values of  $n'$  and  $K'$  Equation (24) is simply another statement of the power-law model applied to flow in round tubes.

By use of Equations (25) and (26) it can be shown that for power-law fluids  $N_{Re}^0$  and  $N_{Re}'$  are related by

$$N_{Re}^0 = \frac{1}{8} \left( \frac{6n'+2}{n'} \right)^{n'} N_{Re}' \quad (27)$$

where

$$N_{Re}' = \frac{D^n V^{2-n} \rho}{g_c K' (8)^{n'-1}} \quad (28)$$

Inspection shows that both  $N_{Re}^0$  and  $N_{Re}'$  reduce to the conventional Reynolds number  $DV\rho/\mu$  for the Newtonian case ( $n = n' = 1$ ). If one replaces  $N_{Re}^0$  by  $N_{Re}'$ , Equation (21) becomes

$$\sqrt{\frac{1}{f}} = A_{1n} \log [N_{Re}'(f)^{1-n'/2}] + C_n' \quad (29)$$

where

$$C_n' = A_{1n} \log \left[ \left( \frac{1}{8} \right) \left( \frac{6n'+2}{n'} \right)^{n'} \right] + C_n$$

Equation (29) is the goal which has been sought. Here the form of the equation relating the friction factor and the Reynolds number has been found for the turbulent flow of power-law fluids in a smooth round pipe. It remains for  $A_{1n}$  and  $C_n'$ , two unknown functions of  $n'$ , to be determined experimentally. Two special cases are of particular interest, namely the Newtonian case ( $n' = 1$ ) and the case of ultimate pseudoplasticity ( $n' = 0$ ).

#### Newtonian Case

If Equation (29) is valid as postulated, it should hold for the Newtonian case where  $n'$  is unity. For this situation the equation reduces to

$$\sqrt{\frac{1}{f}} = A \log \left[ \frac{DV\rho}{\mu} \sqrt{f} \right] + C$$

A resistance law of this type was proposed first by von Karman (18) and subsequently by Prandtl (14), both of whom arrived at their conclusion from mixing-length theories. Newtonian data obtained by Nikuradse agreed extremely well with such a relationship and led to the final formula (5, 6, 15)

$$\sqrt{\frac{1}{f}} = 4.0 \log \left[ \frac{DV\rho}{\mu} \sqrt{f} \right] - 0.40 \quad (30)$$

Hence for the Newtonian case ( $n' = 1$ )

$$A_{1n}(1) = 4.0$$

$$C_n'(1) = -0.40$$

It would appear that the von Karman equation, Equation (30), represents a special case of the more general equation derived here for use with Newtonian and non-Newtonian fluids alike.

#### Ultimate Pseudoplastic Case

Velocity profiles may readily be analyzed mathematically for laminar flow of power-law fluids. Typical laminar-velocity-profile plots for several values of  $n'$  have been presented by Metzner (9), reproductions of which are shown in

Figure 1. For Newtonian fluids in laminar flow the velocity profile is parabolic. As  $n'$  decreases toward zero, the laminar-velocity profile becomes progressively flatter, and in the limiting case of  $n' = 0$  it is perfectly flat. On passing from the laminar to the turbulent-flow region the laminar-velocity profile is flattened by a net turbulent momentum transfer from the high- to the low-velocity areas. Hence turbulence leads to the same general effect on the velocity profile as does a decreasing value of  $n'$ . Furthermore when  $n'$  is close to zero, the laminar-velocity profile is so nearly flat that it can be altered only very little on passing from laminar to turbulent flow. In the limiting case of  $n' = 0$ , where the laminar profile is perfectly flat, there can be no distinction between laminar- and turbulent-velocity profiles. The separate friction-factor correlations normally encountered for Newtonian fluids for the laminar- and turbulent-flow regions arise from the change in the relationship between the wall shear rate and the mean velocity, that is the change in the velocity profile which occurs on passing from laminar to turbulent conditions. As the difference between the laminar and turbulent profiles diminishes, so must the difference between the laminar and turbulent friction-factor relationships. In the limit where the two profiles are identical, as represented by the case  $n' = 0$ , the laminar and turbulent friction-factor-Reynolds-number relationships become the same. The same conclusion may also be reached by noting that the apparent viscosity of this fluid is infinite a short distance from the wall, suppressing the turbulence completely. Therefore the turbulent curve for the case of  $n' = 0$  is simply an extension of the laminar-flow line

$$f = 16/N_{Re}' \quad (31)$$

According to Equation (29) a plot of  $\sqrt{1/f}$  vs.  $\log [N_{Re}'(f)^{1-n'/2}]$  at a given value of  $n'$  should be a straight line of slope  $A_{1n}$ . When  $n' = 0$ ,

$$\begin{aligned} \log [N_{Re}'(f)^{1-n'/2}] \\ = \log [N_{Re}'f] = \log 16 \end{aligned}$$

Thus a plot of  $\sqrt{1/f}$  vs.  $\log [N_{Re}'(f)^{1-n'/2}]$  will be a straight line of infinite slope, whereby it is concluded that for an  $n'$  of zero  $A_{1n}(0) = \infty$ . When one considers  $C_n'$  as an intercept, it is further concluded that  $C_n'(0) = -\infty$ .

#### Turbulent-Velocity Profiles

In addition to the results regarding turbulent friction factors the preceding analysis has yielded some significant information about turbulent velocity profiles for non-Newtonian fluids. It has been predicted that turbulent profiles for power-law fluids may be expressed

by Equations (19) or (20), both of which are valid for the entire turbulent core and hence for almost all the fluid stream

$$\begin{aligned} \frac{U_m - u}{u^*} = -n'A_n \ln \xi \\ + g_1(\xi, n') \quad (19) \end{aligned}$$

$$\frac{u}{u^*} = A_n \ln Z\xi^{n'} + B_n - g_1(\xi, n') \quad (20)$$

Before use can be made of these equations, however, it is necessary to appraise the function  $g_1(\xi, n')$ .

First one must consider the turbulent Newtonian case for which the following equations of Prandtl are commonly

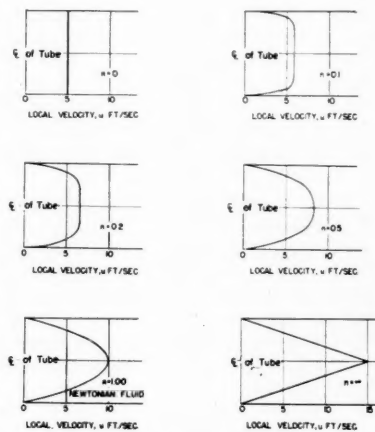


Fig. 1. Laminar velocity profiles for power-law fluids.

accepted as universal velocity distribution laws (15)

$$\frac{U_m - u}{u^*} = -\frac{1}{k} \ln \xi \quad (32)$$

$$\frac{u}{u^*} = \frac{1}{k} \ln Z\xi + B \quad (33)$$

Comparison of Equations (32) and (33) with Equations (19) and (20) shows that the Newtonian equations may be considered as special cases of Equations (19) and (20), where  $A_n(1) = 1/k$  and  $g_1(\xi, 1) = 0$ . Actually these Newtonian equations cannot be exact, since they do not predict a zero slope of the velocity profile at the center line. Hence although the  $g_1(\xi, 1)$  function must be zero at the center line itself, it cannot be precisely zero in the immediate neighborhood thereof. However this discrepancy is so slight and localized that Prandtl's equations represent the experimental data very well, and it can be concluded that the assumption of  $g_1(\xi, 1) = 0$  is an excellent approximation.

Other limits or boundary conditions

may also be placed on the  $g_1$  function. Since the turbulent-velocity profile for fluids with an  $n'$  of zero is perfectly flat, it is required that  $g_1(\xi, 0) = 0$ . Furthermore at the center line of the tube  $\xi = 1$  the velocity defect is zero for all values of  $n'$  by definition, and so  $g_1(1, n') = 0$ . Finally, the preceding analysis showed that in the region  $\lambda/R \leq \xi \leq \xi_1$ ,  $g_1$  is independent of  $\xi$  and is a function of  $n'$  at most. Here  $g_1$  is equal to the integration constant  $E_n$  of Equation (17), which could also be zero.

In view of the several known situations where  $g_1$  is equal to zero, it would appear that at least a reasonable approximation of turbulent-velocity profiles for power-law fluids could be obtained by assuming  $g_1(\xi, n') = 0$ . Therefore subsequent predictions of turbulent-velocity profiles will be based on the assumption that the  $g_1$  function is zero, whereby

$$\begin{aligned} \frac{U_m - u}{u^*} = -n'A_n \ln \xi \\ = -1.415n'A_{1n} \log \xi \quad (34) \end{aligned}$$

$$\frac{u}{u^*} = A_n \ln Z\xi^{n'} + B_n \quad (35)$$

Although such predictions should be considered as approximate at the present time, they represent the first bit of information available in this area and should prove to be of considerable value. Determination of the validity of the assumption regarding the  $g_1$  function must await experimental measurements of non-Newtonian turbulent-velocity profiles.

Equations for the turbulent-velocity profiles of Newtonian systems are frequently expressed in terms of dimensionless parameters. When one modifies and expands these definitions to include all power-law fluids, Equation (35) becomes

$$u^+ = A_n \ln y^+ + B_n \quad (36)$$

where

$$u^+ = u/u^* \quad (37)$$

$$y^+ = Z\xi^n = y^n(u^*)^{2-n}\rho/K \quad (38)$$

These new proposed definitions for  $u^+$  and  $y^+$  reduce to the familiar interpretation for the special case of Newtonian behavior.

Equation (36), like Equations (34) and (35), is assumed to hold throughout the turbulent core only. The laminar sublayer on the other hand is assumed sufficiently thin that the shear stress may be considered constant therein and equal to  $\tau_w$ . Within the laminar sublayer, then, the velocity varies linearly with  $y$ , and

$$\tau = \tau_w = K \left( \frac{-du}{dr} \right)_w = K \left( \frac{u}{y} \right)_w$$

which may be rearranged as

$$u^+ = (y^+)^{1/n} \quad (39)$$

Again the usual Newtonian equation of  $u^+ = y^+$  for the laminar sublayer (5) is simply a special case of the more general expression given by Equation (39).

#### Analysis of Unknown Functions

Since no detailed picture of the actual physical mechanism of turbulence was used in the preceding developments, the theory is not capable of giving complete results. It should be emphasized, however, that this same situation exists at the present time even for the simpler case of turbulent Newtonian flow.

The primary functions of greatest importance here are  $A_{1n}$  and  $C_n'$ . The other functions encountered, namely  $A_n$ ,  $B_n$ ,  $C_n$ , and  $P_n$ , can be related to these. Some such relationships have already been indicated. The function  $P_n$  came about by integration of the general velocity-defect law. Now that a functional form has been proposed for this law, it is possible to evaluate  $P_n$  further. When one employs Equation (34) as the  $f_s$  function, the earlier integration leads to

$$P_n = \frac{U_m - V}{u^*} = \frac{3}{2} n' A_n = \frac{3}{2} \left( \frac{n' A_{1n}}{1.628} \right) \quad (40)$$

The functions  $A_n$ ,  $B_n$ ,  $C_n$ , and  $P_n$  now have all been related to the primary functions  $A_{1n}$  and  $C_n'$ .

Two special cases regarding  $A_{1n}$  and  $C_n'$  have already been mentioned, namely

$$A_{1n}(1) = 4.0 \quad C_n'(1) = -0.40$$

$$A_{1n}(0) = \infty \quad C_n'(0) = -\infty$$

Little more can be said about  $C_n'$  prior to experimental investigation. Several facts concerning  $A_{1n}$ , however, can be established initially. Examining Equation (34) one obviously first observes that  $A_{1n}$  can never be negative, since the velocity defect is always positive and  $\log \xi$  is always negative (or zero). Second the velocity defect should become zero at all  $\xi$  for limiting case of  $n' = 0$ , whereby it is concluded that

$$\lim_{n' \rightarrow 0} (n' A_{1n}) = 0$$

despite the fact that  $A_{1n}(0) = \infty$ . Apparently  $A_{1n}$  approaches infinity more slowly than  $n'$  approaches zero. At the other extreme the velocity defect must remain bounded as  $n'$  increases without limit, a situation that leads to the conclusion

$$\lim_{n' \rightarrow \infty} (A_{1n}) = 0$$

Laminar-velocity profiles for power-law fluids are illustrated in Figure 1. Here

it is shown that as  $n'$  decreases toward zero the velocity profile becomes progressively flatter. All the corresponding turbulent-velocity profiles for finite values of  $n'$  will be considerably flatter owing to the equalizing effect of turbulent momentum transfer. If it is further assumed that this flattening effect does not pass through any maximum or minimum point as  $n'$  decreases toward zero, the turbulent velocity defect at a given  $\xi$ , and hence the product  $n' A_{1n}$ , will decrease with decreasing  $n'$  values. After the known Newtonian point has been selected as a reference, it is possible to place the following restrictions on the  $A_{1n}$  function:

$$A_{1n} < 4.0/n' \quad \text{for } n' < 1$$

$$A_{1n} > 4.0/n' \quad \text{for } n' > 1$$

#### Nonpower-Law Fluids

The developments of the preceding sections have been based on the assumption that the laminar relationship between shear stress and shear rate for the fluid under consideration can be represented by a simple power function. For nonpower-law fluids the property parameters  $n$  and  $K$  or  $n'$  and  $K'$  may still be employed, but in this case they are functions of the shear stress rather than than true constants. The parameters have meaning here only when associated with a specific shear stress.

In a discussion of nonpower-law fluids one fact should be emphasized. The fluid behavior is of interest only in the range of actual shear stresses present in a given flow situation. For a fluid flowing in a pipe or circular duct the shear stress acting on the fluid varies linearly with the radius from zero at the center line to a maximum value given by  $D\Delta P/4L$  at the pipe wall. Hence for a particular flow situation it is entirely irrelevant if the fluid deviates from the power-law behavior only at shear stresses which are higher than this maximum at the pipe wall.

Nonpower-law fluids pose no problem in laminar-flow situations. It has been shown (10, 11) that the laminar relationship  $f = 16/N_{Re}'$  is rigorously valid regardless of whether or not  $n'$  and  $K'$  are constant. When the fluid-property parameters are functions of the shear stress, it is necessary simply to evaluate them at the existing wall shear stress. For turbulent flow the problem on nonconstant fluid property parameters is more complex. However Equation (29) can be validated for the nonpower-law case, if it is possible to select values of the fluid-property parameters such that the equation still defines the relationship between the wall shear stress and the mean velocity. Hence for the nonpower-law case the problem becomes one of establishing the shear stress at which the fluid-property parameters should be

evaluated to avoid or at least minimize any error in the wall shear-rate-mean-velocity relationship. The following analysis is performed in an attempt to find values of the parameters which, when used in Equation (29), will represent a good approximation to the actual, but mathematically more complex, flow situation.

Figure 2 shows a typical Newtonian turbulent-velocity profile (water flowing through a 1-in. pipe at a Reynolds number of 20,000). It will be noted that in the region near the center line the Newtonian profile is quite flat; that is  $(du/dr)$  is very small. Furthermore, according to earlier reasoning, as  $n'$  approaches zero, the velocity profile becomes progressively flatter. This fact indicates that for pseudoplastics at least the mean velocity is relatively insensitive to any variations in  $n'$  in the low shear-stress regions near the center of the tube; in contrast the mean velocity is highly dependent on the high-shear-rate regions near the wall.

To develop this quantitatively one may consider the contribution of the various shear-rate regions to the mean velocity. The contribution of the differential slice illustrated in Figure 2 to the volumetric flow rate is given by

$$dQ = \pi r^2 du$$

This incremental contribution to the volumetric flow rate is attributable to the shear rate occurring at  $r$  and as such is a measure of the dependence of the mean velocity on the shear rate occurring at a shear stress of  $\tau_w(r/R)$ . When one normalizes this point contribution and integrates,

$$\frac{\Delta Q}{Q} = \frac{\Delta V}{V} = \frac{\int_u^{u_m} r^2 du}{\int_0^{u_m} r^2 du}$$

$\Delta V/V$  represents the fraction of  $V$  which would be unaccounted for if the velocity profile were cut off perfectly flat from radius all the way to the center line. Figure 3 is a plot of the fractional-flow contribution  $\Delta V/V$  as a function of  $r/R$  or  $(\tau/\tau_w)$  based on the turbulent Newtonian velocity profile given in Figure 2. Figure 3 dramatically shows that the mean velocity is highly dependent on the shear rates in the very close proximity of the wall and is essentially independent of the shear rates nearer to the center of the tube. For example Figure 3 shows that the shear rates occurring at an  $r/R$  or  $\tau/\tau_w$  less than 0.8 account for only 7% of the mean velocity. Therefore any variation in  $n$  at shear stresses less than  $0.8\tau_w$  would cause an error in only this 7% contribution to the mean velocity. Since the 7% represents the fraction of the mean velocity that would be unaccounted for if the velocity



profile were cut off perfectly flat for all  $r/R$  less than 0.8, a situation far worse than can be anticipated as due to any reasonable variation in  $n'$ , the error in the mean velocity due to a variation of the flow-behavior index in this region would be only a small fraction of this 7% and entirely negligible. On the other hand about 74% of the mean-flow contribution is attributable to the shear rates which occur at shear stresses between  $\tau_w$  and  $0.96\tau_w$ .

These observations lead inescapably to the conclusion that Equation (29) is an excellent approximation for predicting the friction factor for nonpower-law fluids, provided the parameters are evaluated at the existing wall shear stress. Since the turbulent velocity profiles for many pseudoplastic fluids should be flatter than for the Newtonian

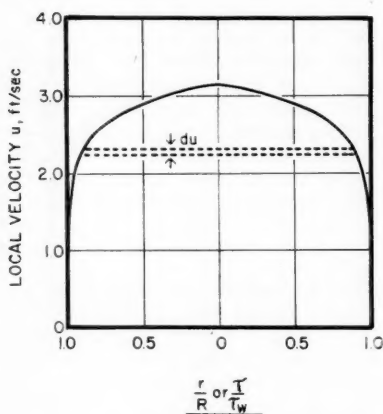


Fig. 2. Newtonian turbulent velocity distribution

( $N_{Re} = 20,000$ ,  $D = 1$  in., water at  $20^\circ\text{C}$ .)

case developed here, the situation depicted by Figure 3 should be even more dramatic in this case. For the limiting case of  $n' = 0$  Figure 3 would be simply two straight lines coinciding with the coordinate axes. Conversely the situation will be less pronounced for dilatant fluids. However even in the dilatant case the mean velocity will be dependent most highly on the wall shear rate, and the same conclusions will probably be valid in most practical cases.

It has now been shown that the friction-factor relationships for both laminar and turbulent flow as given by Equations (31) and (29) respectively are valid for nonpower-law fluids, provided the fluid-property parameters are evaluated at the existing wall shear stress. Unfortunately the wall shear stress is normally the quantity being sought, and hence a trial-and-error procedure is necessitated when one is working with nonpower-law fluids. Equa-

tion (29) would be used repeatedly to calculate the pressure drop until the calculated  $\tau_w$  was identical to the shear stress at which  $n'$  and  $K'$  were evaluated. It should be emphasized, however, that the majority of non-Newtonian fluids can be represented quite well by the power-law model and that the remaining fluids seldom depart radically from this model. Thus in most cases there is a reasonably large region surrounding the existing wall shear stress in which  $n'$  and  $K'$  are nearly constant, and the convergence of the trial-and-error procedure is rapid. A further increase in the rapidity of convergence is provided by the manner in which  $n'$  and  $K'$  change together with shear stress. If the fluid-property parameters vary at all with shear stress, they must vary in opposite directions. For example if  $n'$  increases with increasing shear stress, then  $K'$  must decrease with increasing  $\tau$ . Such a combination of variations tends to cancel their effect on  $N_{Re}'$ , leaving the Reynolds number only weakly dependent on the shear stress at which the parameters are evaluated.

All this discussion has been aimed at extending the power-law friction-factor prediction to include nonpower-law fluids. It is also important to be able to extend the power-law results regarding turbulent-velocity profiles to nonpower-law systems. This should be possible, at least approximately, in the sense that velocity profiles for nonpower-law fluids might be constructed differentially on the basis of the power-law results. The differential form of the velocity-defect law, if no contribution by a  $g_1$  function is assumed, is given by

$$d\left(\frac{U_m - u}{u^*}\right) = -nA_n \frac{d\xi}{\xi}$$

Thus the slope of the velocity-defect plot is a function of  $n$  and  $\xi$ . For power-law fluids ( $nA_n$ ) is a constant independent of  $\xi$ , and this equation may be integrated directly to give Equation (34), the velocity-defect law for power-law fluids. With nonpower-law fluids ( $nA_n$ ) will be a function of the shear stress and hence of  $\xi$ . When one denotes ( $nA_n$ ) by  $f(\xi)$ , the velocity-defect law for nonpower-law fluids may be written as

$$\frac{U_m - u}{u^*} = \int_1^\xi -f(\xi) \frac{d\xi}{\xi}$$

#### Assumption of Strict Similarity

If in place of the velocity-defect law as given by Equation (6), an assumption of strict similarity is made, that is

$$\frac{u}{U_m} = f_3'(\xi, n)$$

one obtains the following equations as the most important results from an

analysis similar to that presented here on the basis of the power-law model (3):

$$\frac{u}{U_m} = \xi^{n'e_n} \quad (41)$$

$$f = \frac{a_n}{(N_{Re}')^{b_n}} \quad (42)$$

$$b_n = \frac{2e_n}{1 + e_n(2 - n')}$$

Equations (41) and (42) are of the same form as the Blasius equations for Newtonian fluids (6). In this case the numerical values of  $a_n$ ,  $b_n$ , and  $e_n$  respectively are approximately 0.079, 0.25, and 1/7 for Reynolds numbers between  $10^4$  and  $10^5$ .

Although the friction-factor correlation suggested by Equation (42) is inferior to

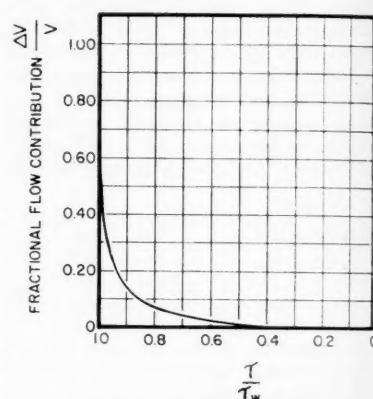


Fig. 3. Newtonian fractional flow contribution

$$\frac{\Delta V}{V} = \frac{\int_u^{U_m} r^2 du}{\int_0^{U_m} r^2 du}$$

that of Equation (29), the former has the advantage of expressing the friction factor explicitly. For certain applications, such as the development of heat and mass transfer analogies, this advantage may well overshadow the accompanying sacrifice in precision, as it has for Newtonian fluids, and result in the practical utilization of Equation (42). The attractiveness of such an approximation is perhaps even more important with non-Newtonian systems.

#### EXPERIMENTAL

The purpose of the experimental phase of this investigation was to test the validity of the proposed theoretical developments and, if found valid, to evaluate the unknown functions  $A_{ln}$  and  $C_n'$  which occur therein. The primary criteria for selection of experimental fluids were that they exhibit a wide range of non-Newtonian characteristics



ted here  
odel (3):  
(41)  
(42)  
e of the  
equations  
his case  
and  $e_n$   
r 0.079,  
numbers

relation  
ferior to

0.2 0

al

mer has  
friction  
ications,  
eat and  
dvantage  
spanning  
Newton-  
practical  
) The  
ximation  
ent with

al phase  
e validity  
lopments  
unknown  
therein.  
of experi-  
it a wide  
eteristics

ne, 1959

under the turbulent experimental conditions. Also it was desirable that fluids representative of both polymeric solutions and solid-liquid suspensions be investigated. Finally the validity of the theoretical analysis could be tested by considering non-power-law as well as power-law fluids. Owing to the viscosity characteristics of dilatant systems and the attending difficulties which arise in handling these fluids under conditions of high shear, the experimental systems were restricted to pseudoplastic

was recycled. The flow rate was measured either by timing a sample collected in a weigh tank or by a Foxboro magnetic flowmeter installed in the recycle line. Test sections of 1/2-, 1-, and 2-in. (nominal) smooth brass pipe were employed. Calming or entrance lengths of about 53 pipe diam. preceded the first pressure tap for each test section, and exit lengths greater than 12 pipe diam. followed the last pressure tap before any type of geometric discontinuity was encountered. Pressure taps were

their dissipation prior to the entry of the test sections. Water was used as the pressure-transmitting medium in the lines connecting the pressure taps to the manometers. Bourdon gauges and two sets of manometers employing fluids of different densities provided pressure-drop measurements over a wide range (0.02 to 160 lb./sq. in.). For each test fluid a few points were taken in the laminar-flow region to check the rheological data and to permit establishment of the point of turbulence

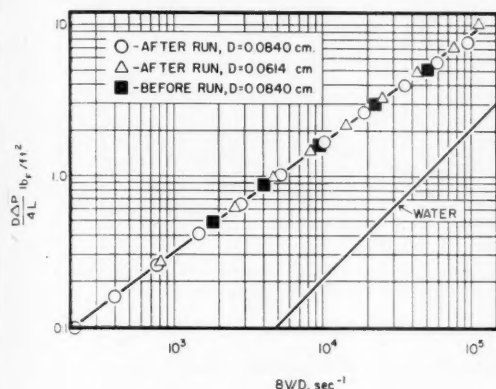


Fig. 4. Flow curve for 0.2% carbopol.

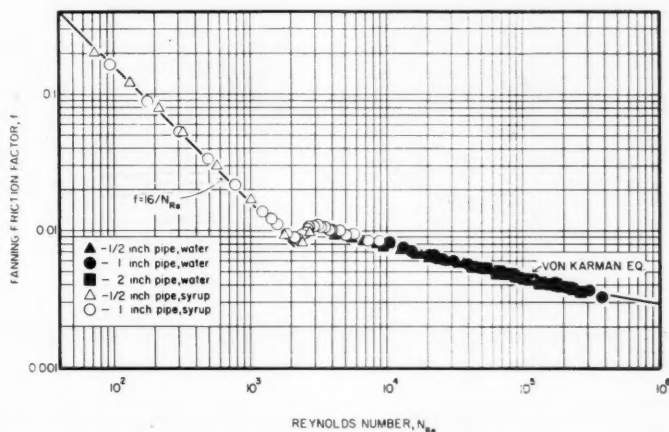


Fig. 5. Friction factor plot of Newtonian data used to check experimental accuracy.

fluids. In view of the far greater industrial importance of pseudoplastic fluids in comparison with dilatant systems, this restriction does not constitute a serious limitation.

Aqueous solutions of Carbopol 934 and sodium carboxymethylcellulose served to represent polymeric solutions, while slurries of Attasol, an attapulgite clay, represented the class of solid-liquid suspensions. Four concentrations of Carbopol, three of Attasol, and two of carboxymethylcellulose (CMC) were studied. In addition, data were taken with two Newtonian fluids, water and a sugar solution, to test the equipment and experimental technique.

Fluid was pumped from an agitated storage tank through one of three horizontal test sections, after which the fluid

formed by small holes carefully drilled through the pipe walls and rounded slightly on the inside by means of a fine file to remove any burrs. To verify uniformity of the pressure gradient each test section was divided evenly into subsections, the 1/2- and 1-in. pipes having three subsections constituting their test sections and the 2-in. pipe having two. The pressure drop could be measured across any of these subsections individually or across the whole of the test sections. To establish further that the pressure-gradient measurements were free from the abnormalities which prevail near an entrance, three pressure taps were located within the calming section of the 1/2-in. pipe. With these it was intended to trace the entrance effects and verify

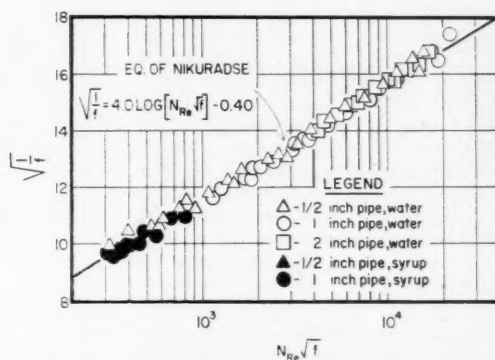


Fig. 6. Turbulent Newtonian data, correlation variables.

inception. After each change in flow rate the manometer lines were flushed clean of any material that had worked its way into them by movement of the manometer legs.

A capillary-tube viscometer, equipped with a constant-temperature bath and suitable for measurements at shear rates in excess of  $(10)^6 \text{ sec}^{-1}$ , was used to establish rheological properties of the fluids under investigation. Viscometric data were normally taken with two different capillary tubes, all of which were first calibrated with National Bureau of Standards' oils. Rheological measurements were made before and after a pipeline run, with special attention being paid to the shear-stress region that was encountered during the pipeline experiments. A detailed description of the apparatus and experimental procedure is available (3).

Typical viscometric data for one of the test fluids are shown in Figure 4. Only two of the non-Newtonian fluids studied truly conformed to the power-law model over the entire range of shear stresses wherein measurements were made. Several additional fluids however approached power-law behavior very closely within restricted regions of shear stress. Generally the polymeric solutions tended more toward power-law behavior than did the clay suspensions.

## Results

The experimental Newtonian results relating the friction factor and Reynolds number are plotted in Figure 5 in the form of a conventional friction-factor diagram. This figure shows that the Newtonian data of this investigation are in excellent agreement with the

established Newtonian relationships for all three flow regions, laminar, transition, and turbulent. Hence it was concluded that the equipment and techniques used in this study were entirely satisfactory, yielding accurate and reliable data. The turbulent Newtonian data are plotted in Figure 6 in terms of the correlating groups of the von Karman equation  $\sqrt{1/f}$  and  $\log [N_{Re} \sqrt{f}]$ . Again the good agreement between the data and the established relationship is evident.

Experimental data taken with the non-Newtonian systems covered the range of variables outlined approximately in Table 1. Figure 7 shows friction-factor data typical of the experimental results for these non-Newtonian systems. Perhaps the most striking feature about Figure 7 is that the turbulent friction-factor data lie below the Newtonian curve and above an extension of the laminar relationship. From the discussions regarding the special cases of Newtonian and ultimate pseudoplastic behavior, it is to be expected that friction factors for all pseudoplastic systems will fall within this general region. Hence, qualitatively at least, Figure 7 supports the earlier theoretical considerations. Second, the friction-factor diagram clearly shows a definite transition region between laminar and turbulent flow which extends over a range of Reynolds numbers comparable to the extent of the Newtonian transition region. According to Figure 7 the onset of turbulence occurred at a Reynolds number slightly larger than the accepted Newtonian value of 2,100.

To test the validity of the theoretically predicted friction-factor correlation, plots of  $\sqrt{1/f}$  vs.  $\log [N_{Re}'(f)^{1-n'/2}]$  are much more informative than the ordinary friction-factor diagrams shown in Figure 7. Figure 8 shows the turbulent data of Figure 7 plotted in terms of the

present data. Of the non-Newtonian fluids tested, four agreed sufficiently well with the power-law model to permit evaluation of the  $A_{1n}$  function in this manner.

The theoretical considerations that  $A_{1n}$  approaches infinity as  $n'$  goes to zero and approaches zero as  $n'$  goes to

data at an  $n'$  of 0.726, it will be noted that separate and slightly different values of  $A_{1n}$  are shown in Figure 9 at this flow-behavior index for each of the three pipe diameters. The individual values of  $A_{1n}$  here were established by the separate consideration of the data obtained from each of the different pipes

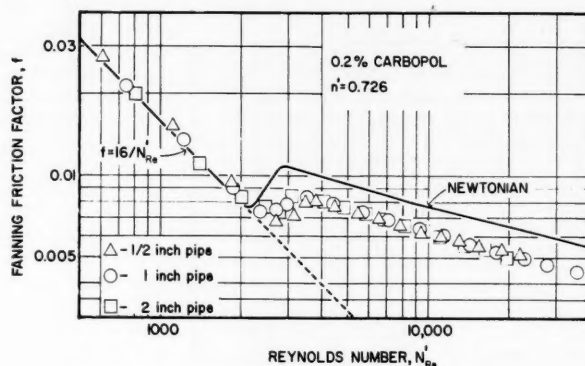


Fig. 7. Typical non-Newtonian friction factor results.

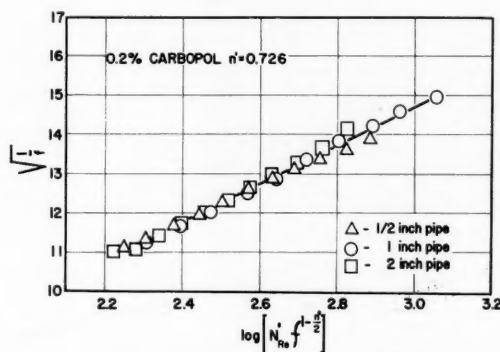


Fig. 8. Turbulent data from Figure 7 plotted in terms of the correlation variables.

TABLE 1. RANGE OF EXPERIMENTAL VARIABLES FOR NON-NEWTONIAN SYSTEMS

Fluid	$N_{Re}'$ Range	$n'$ Range	point values of $n'$ (in 1 in. pipe)		
			$N_{Re}': 5,000$	10,000	20,000
0.5% Carbopol	670-6,000	0.43-0.56	0.54		
0.4% Carbopol	720-11,000	0.51-0.58	0.54	0.57	
0.3% Carbopol	750-19,000	0.62	0.62	0.62	
0.2% Carbopol	610-36,000	0.73	0.73	0.73	0.73
15 % Attasol	540-11,000	0.28-0.44	0.38	0.43	
13 % Attasol	740-22,000	0.26-0.57	0.42	0.49	0.56
11.8% Attasol	830-21,000	0.22-0.68	0.40	0.60	0.68

correlation variables. It is evident that the points do fall on a straight line as predicted, the slope being  $A_{1n}$ . Because of the requirement that  $n'$  be constant throughout the range of experimental measurements, this test could be applied only to the power-law portion of the

infinity suggest that a logarithmic plot of  $A_{1n}$  vs.  $n'$  might be fruitful in determining the form of the  $A_{1n}$  function. Figure 9 is such a logarithmic plot showing all the experimental points of the  $A_{1n}$  function. Although a single correlating line was indicated in Figure 8 for the

and application of least-square techniques thereto. Similarly, by fitting separate least-squares lines through the Newtonian data of Figure 6 for each of the three pipes, slightly different values of  $A_{1n}$  (1) were obtained. It was not the purpose of the present Newtonian data to test the validity of the von Karman equation and its coefficients. Rather it is accepted herein that the coefficients of Equation (30) are reliable for the Newtonian case. However for purposes of comparison with the non-Newtonian measurements it was informative to perform this evaluation of  $A_{1n}$  (1) independently based on the present Newtonian data. Since it is well established for Newtonian fluids that no extraneous diameter effects exist, it is concluded that the indicated non-Newtonian diameter discrepancies in  $A_{1n}$  do not constitute a real effect.

e noted  
different  
Figure 9  
each of  
dividual  
l by the  
ata ob-  
nt pipes

Generally the experimental data for the 1-in. pipe covered a wider range of the correlation variables from which  $A_{1n}$  was determined, and therefore the results for this pipe probably represent better values than for the other two pipes.

The line shown in Figure 9 passing through the data was determined by the method of least squares after placing on it the requirement that it must pass through the point  $A_{1n}(1) = 4.0$ . The equation of this line is given by

$$A_{1n} = \frac{4.0}{(n')^{.75}} \quad (43)$$

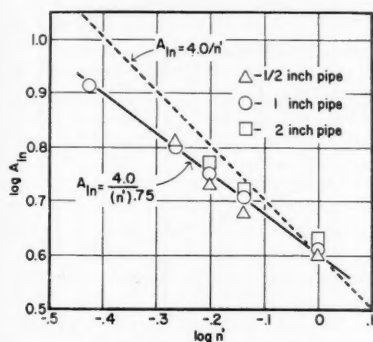


Fig. 9. The  $A_{1n}$  function: variance with the flow behavior index  $n'$ .

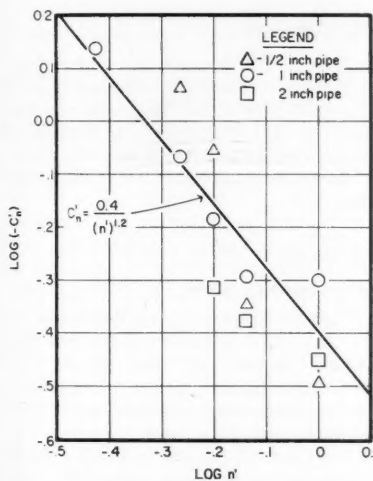


Fig. 10. Dependence of the  $C_n'$  function on  $n'$ .

Besides passing through the known Newtonian point, the expression proposed for the  $A_{1n}$  function satisfies all the theoretical restrictions discussed earlier, namely,

$$\begin{aligned} A_{1n}(n') &\geq 0 \\ A_{1n}(0) &= \infty \\ A_{1n}(\infty) &= 0 \\ n' A_{1n}(0) &= 0 \end{aligned}$$

$$A_{1n} < 4.0/n' \quad (\text{for } n' < 1.0)$$

$$A_{1n} > 4.0/n' \quad (\text{for } n' > 1.0)$$

Hence although the proposed  $A_{1n}$  function must be considered as empirical, it is entirely compatible with all the known theoretical prerequisites.

The  $C_n'$  results calculated by using the  $A_{1n}$  values given by Equation (43) are shown in Figure 10. The wide scatter of the data shown here can be attributed to the inaccuracies encountered in determining  $C_n'$ , a small number, by the subtraction of one large number from another. Although such an operation makes it difficult to obtain accurate values of  $C_n'$ , it should be remembered that by the same token the relationship between the friction factor and Reynolds number is quite insensitive to the  $C_n'$  function. Hence a high degree of precision is not required in this quantity for the purpose of pressure-loss prediction, at least in the  $n'$  range investigated here. Again, the discrepancies between data for the various pipe sizes are about the same for both the Newtonian and non-Newtonian points. Also the differences are not consistent in their direction, and it is concluded that no real additional diameter effect exists.

There is no justification at the present time for placing anything other than a straight line through the data points of

$$C_n' = \frac{-0.40}{(n')^{1.2}} \quad (44)$$

Equation (46) satisfies the Newtonian situation and the one theoretical condition imposed upon  $C_n'$  earlier, namely that  $C_n'$  approach negative infinity as  $n'$  goes to zero.

The final proposed friction-factor correlation is obtained by replacing the general functions  $A_{1n}$  and  $C_n'$  of Equation (29) with their specific forms as given by Equations (43) and (44) respectively.

$$\sqrt{\frac{1}{f}} = \frac{4.0}{(n')^{.75}} \log [N_{Re}'(f)^{1-n'/2}] - \frac{0.40}{(n')^{1.2}} \quad (45)$$

The  $A_{1n}$  and  $C_n'$  functions and Equation (45) were established by using only that portion of the experimental data corresponding to power-law fluids or very close approximations thereof. It is difficult to test the compliance of the data for nonpower-law fluids with the theoretical hypotheses. For example, nonpower-law data cannot be tested by a plot such as Figure 8, since the flow-behavior index is not constant. Even presentation of these data in terms of the familiar friction-factor diagram is of little significance because of the changing values of  $n'$  with Reynolds numbers. Further, if the flow-behavior

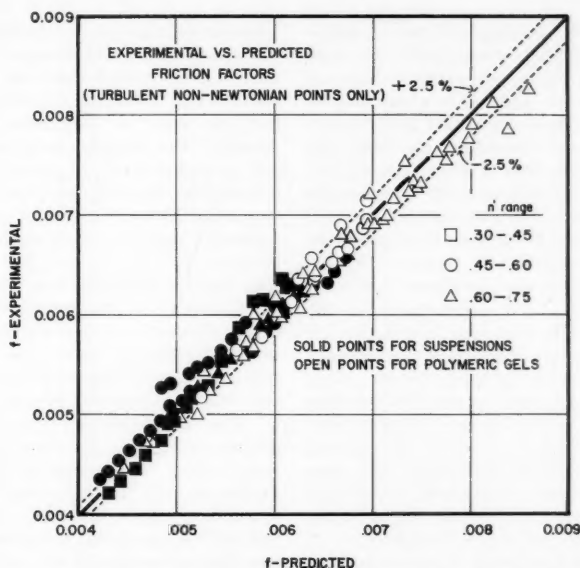


Fig. 11. Comparison of experimental friction factors with those predicted.

Figure 10. The line shown in this figure was located by the method of least squares by incorporating the requirement that it pass through the accepted Newtonian point  $C_n'(1) = -0.40$ . The equation of this line is

index is a function of shear stress, its value at a given Reynolds number will be different for the three pipe sizes, and the friction-factor data for the various pipe diameters would not even coincide. Earlier it was predicted that Equation

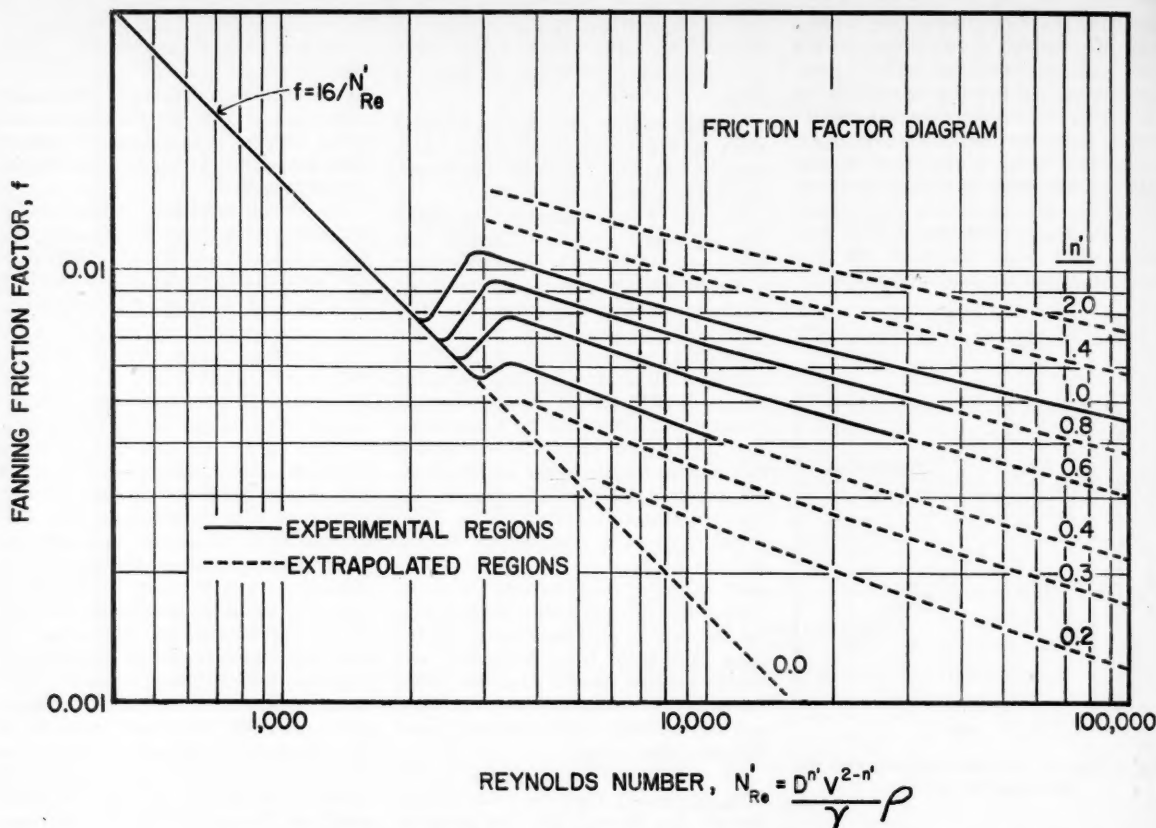


Fig. 12. Final friction factor design chart for Newtonian and non-Newtonian fluids.

(29) or now Equation (45) will be applicable to nonpower-law fluids, provided that the fluid-property parameters are evaluated at the wall shear stress. Perhaps the best way to test this hypothesis and concomitantly to use the nonpower-law data to check the proposed  $A_{1n}$  and  $C_n'$  functions is to compare the experimental friction factor for the nonpower-law fluids with those predicted by Equation (45). By means of experimental Reynolds numbers and the appropriate flow-behavior indexes, Equation (45) has been solved for the friction factor corresponding to each turbulent non-Newtonian test made during this investigation. By including in such a comparison the power-law fluids on which  $A_{1n}$  and  $C_n'$  were based, the accuracy of Equation (45) may be investigated. Figure 11 is a plot of  $f_{\text{expt'l.}}$  vs.  $f_{\text{pred.}}$  showing these results for the non-Newtonian tests only.

Excellent agreement is found between the predicted and experimental friction factors. The points of Figure 11 cover a range of the flow-behavior index from 0.36 to 0.73 and of the Reynolds number from 2,900 to 36,000. (The highest Reynolds numbers correspond also to the highest values of  $n'$ .) Results for the nonpower-law fluids (primarily the clay suspensions) show equal agreement with the predicted friction factors, as do the

power-law fluids on the basis of which the correlating equation was developed. Hence it is proved that, as predicted, Equation (45) is applicable to nonpower-law as well as power-law systems, provided the fluid-property parameters are evaluated at the existing wall shear stress. Also the conformity of the nonpower-law fluids to Equation (45) serves indirectly to support the validity of the proposed  $A_{1n}$  and  $C_n'$  functions. The data of Figure 11 are grouped into three ranges of  $n'$  to illustrate the absence of an effect of the flow-behavior index on the degree of agreement. The 146 points shown in Figure 11 represent all the turbulent non-Newtonian experiments of this investigation. The maximum deviation of an experimental friction factor from the value predicted by Equation (45) is 8.5%, and the mean absolute deviation is 1.9%. Sixty-nine per cent of the deviations lie within the standard deviation of 2.4%, an indication that the deviations of the experimental points from those predicted conform to a statistically normal distribution.

The main objective of this study is the friction-factor-Reynolds-number correlation given by Equation (45). Since this equation cannot be solved for  $f$  explicitly, a graphical presentation of the equation will be found convenient for future use. Figure 12 is a friction-factor plot based

on Equation (45) in the turbulent region. The solid lines of this figure indicate the region in which experimental data were taken, whereas the dashed lines represent modest extrapolations by use of Equation (45).

## DISCUSSION

### Friction-Factor Correlation

The validity of the theoretical relationship developed in this work between the friction factor and the generalized Reynolds number has been established for polymeric solutions, solid-liquid suspensions, power-law, and nonpower-law fluids alike. Equation (45) has been shown to agree very well with the experimental data covering a range of flow-behavior indexes from 0.36 to 1.0. The extrapolations of Figure 12 extend this region of  $n'$  to from 0.2 to 2.0, and it is believed that such moderate extrapolations are entirely permissible. Caution should be observed, however, in extrapolating Equation (45) to values of  $n'$  greatly removed from the experimental range. For very highly dilatant fluids the assumption of a negligible thickness of the laminar sublayer which is incorporated into Equation (7) may fail. On the other hand, when  $n'$  becomes extremely small, for example 0.001, the  $C_n'$  function becomes a significant



part of the quantity  $(1/f)^{1/3}$  and may well require more accurate evaluation than can be obtained by extrapolation according to Equation (44). Actually however it is to be expected that turbulent-flow problems involving flow-behavior indexes outside the range of Figure 12 will be exceedingly rare, and therefore that Figure 12 will be adequate in nearly all practical cases. Extrapolations to Reynolds numbers higher than the experimental range at a given value of  $n'$  should be quite permissible, since all the assumptions involved in the theoretical development of Equation (45) become even more valid as the Reynolds number is increased.

For the non-Newtonian systems studied in this investigation ( $n'$  less than unity) the onset of turbulence always occurred at Reynolds numbers slightly greater than those for Newtonian fluids. Furthermore the data showed some evidence that the Reynolds number corresponding to the onset of turbulence increases slowly with decreasing values of the flow-behavior index. For example with an  $n'$  of 0.726 Figure 7 indicates the start of the transition region at a Reynolds number of about 2,700, whereas for an  $n'$  of 0.38 the onset of turbulence was observed at a Reynolds number of about 3,100. Unfortunately the effect was not clear-cut, since the experimental data close to the onset of turbulence exhibited sufficient scatter to prohibit a precise definition of the transition region. Of necessity the transition-region portions of the friction-factor curves of Figure 12 were located somewhat arbitrarily but in general accordance with the experimental observations.

An interesting point arises regarding the case of ultimate pseudoplasticity ( $n' = 0$ ). It was reasoned earlier that laminar- and turbulent-velocity profiles for this situation would be identical and that as a result the turbulent friction-factor-Reynolds-number correlation would simply be an extension of the laminar relationship. In view of the apparent increase of the critical Reynolds number with decreasing  $n'$ , indicated by the present results, however, a question arises as to whether or not a turbulent-flow condition could ever be attained for this case. With a perfectly flat laminar-velocity profile the flow instability frequently attributed to the influence of a velocity gradient is absent. Everywhere within a tube except at the wall itself the stability parameter of Rouse (14) would be zero, an indication of complete stability. Directly at the tube wall the stability parameter becomes indeterminate. If turbulence were to begin just at the tube wall, which in itself is a questionable notion, it is not clear that propagation would ensue throughout the tube.

An additional non-Newtonian system heretofore unmentioned was studied which did not behave in the same manner

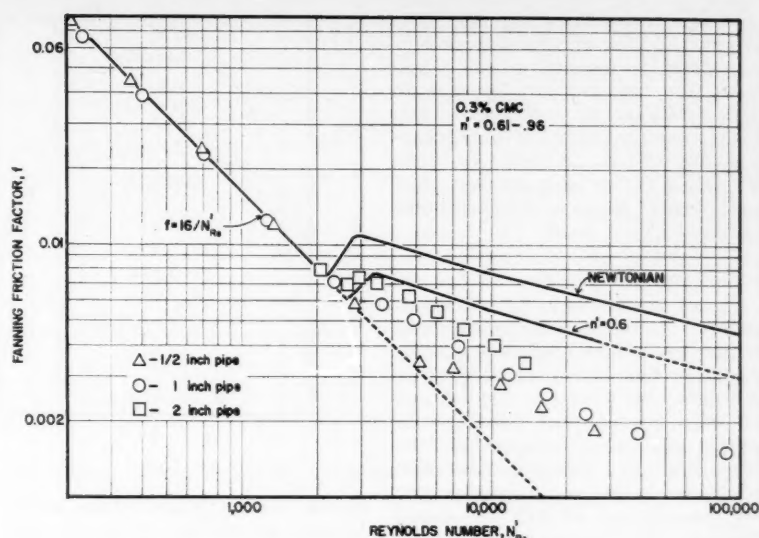


Fig. 13. Friction factor results for anomalous fluid.

as the other experimental fluids. Figure 13 shows a series of friction-factor measurements taken with a 0.3% aqueous solution of carboxymethylcellulose (CMC). The friction factor here follows much more closely an extension of the laminar line than do the data for the other fluids, and a pronounced diameter effect is evident. These observations plus others that will not be pursued here all indicated that the abnormalities manifested by the CMC data are the result of some type of pseudostable laminar- or transitional-flow condition, and that fully developed turbulent-flow was never achieved with these fluids. On the other hand the flow situation obviously deviated from purely laminar motion. It would appear that CMC solutions possess some abnormal ability to suppress the formation and propagation of turbulence. The physical mechanisms responsible for the peculiar behavior of these fluids are not known at the present time, although several possible explanations may be cited (3), of which viscoelasticity appears to be the most probable. That the CMC system represents the abnormal non-Newtonian case seems certain from a consideration of other available turbulent data for a variety of fluid systems (11). In no instance have prior data been reported which resemble the CMC results of this investigation; in all cases a definite break from laminar flow occurred at values of the generalized Reynolds number only slightly greater than 2,100, as in the present study. When one notes that the prior-art data on well-developed turbulent flow are entirely for slurries, it appears that the correlation presented here is of primary value for such systems. Accordingly this correlation is recommended for use with slurries, but it may also be used for polymeric material

provided at least one experimental measurement, under turbulent conditions, is available to determine whether the fluid in question falls into the same category as slurries and the Carbopol (polymeric) solution or into the category of CMC. If such a single measurement is not available, the present design chart may still be used as the best available approximation, since it will always be either correct or, if in error, conservative.

The simplest explanation for the observed difference between the behavior of CMC on the one hand and of Carbopol and slurries on the other is that one or more additional and as yet undefined physical properties are of significance in the case of CMC and other polymer solutions which may later be shown to fall into the same category as CMC. If one were to develop a design chart such as is given in Figure 12 by using CMC solutions of various concentrations, the results would obviously be different from those of Figure 12, even though they might be self-consistent. Since the magnitudes of the unknown but necessary physical properties are not available, such a chart would be of little or no value for use with other fluids; it would obviously be inapplicable to slurries, but more important it would also be inapplicable to other fluids of the general nature of CMC unless they fortuitously possessed exactly the same value of the unknown parameters as does CMC. In view of this rather small probability such a design chart would not be of proved utility except for use with CMC. It is unfortunate that this situation has arisen in another study (16) in which CMC was the only fluid used having a flow-behavior index below 0.70. Since the difference between the friction factors for a Newtonian fluid and one

with an  $n'$  of 0.70 is less than 25% (Figure 12), while Shaver's (16) accuracy was stated to be only  $\pm 12\%$ , it is clear that the one part of Shaver's study which possibly does not contain complications, owing to CMC-like behavior, does not serve to predict the trend of friction factors as a function of  $n'$  with better than order-of-magnitude accuracy.

#### Prior-Art Correlation Methods

Earlier workers have almost unanimously adopted the apparent thesis (although not always stated explicitly) that the shear rates occurring under turbulent conditions are high enough to effect constancy of viscosity and permit correlation of pressure-loss-flow-rate data by standard Newtonian procedures. In essence such studies were not concerned at all with the actual turbulent behavior of non-Newtonian fluids but simply the turbulent behavior of Newtonian systems, which under different circumstances would exhibit non-Newtonian characteristics. The main difference between several approaches proposed in the past has been in defining what value should be used as the constant viscosity. The three primary approaches of the prior art have been based on the use of the viscosity of the dispersion medium (2), a limiting viscosity at infinite shear (1, 21, 22), and a turbulent viscosity established from sample pressure-loss measurements taken on the given fluid under actual turbulent conditions (1, 19).

Portions of the data from the present investigation have been treated according to these prior-art schemes to test the reliability of these three procedures (3). The turbulent viscosities were found to be 1.3 to 5.3 times larger than the limiting viscosities at infinite shear and from three to fourteen times as large as the viscosity of the dispersion medium. Obviously both of the first two design methods are of very limited values. The turbulent viscosities were also found to be variables rather than constants as suggested by the prior art. In fact they varied as much as threefold over a fivefold range of Reynolds numbers.

The most extensive correlation of early data treated all the consistent non-Newtonian data then available in the literature (11). The results were presented as a plot of friction factor vs.  $N_{Re}'$ . This plot showed the end of the stable, laminar flow region occurring at a Reynolds number of 2,100 to 3,000, followed by a broad region extending to  $N_{Re}' = 70,000$ , in which the friction factor was nearly constant. It is very probable that most of the fluids involved were changing from non-Newtonian to Newtonian character at the shear stresses prevalent in the apparent transition region and that this rheological change

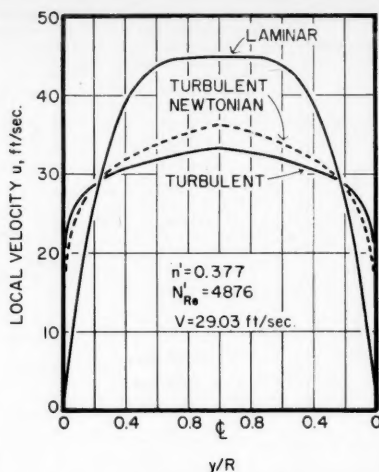


Fig. 14. Typical predicted velocity profiles. All curves are calculated for the same average velocity.

was responsible for the constancy of the friction factor at Reynolds numbers above 2,100 rather than an actual transition phenomenon. The results of the present investigation confirm this premise. Figure 12 illustrates that for fluids with flow-behavior indexes that increase from some low value toward unity, results identical to those observed by Metzner and Reed are to be expected. Thus while their method of correlation represented a considerable improvement over the methods discussed, limitations of the available data prevented development of a truly precise design procedure.

Comprehensive discussions of other (less important) early studies of turbulence in non-Newtonian systems are available in references 3 and 11.

#### Velocity Profiles

If one assumes the  $g_1$  function to be zero, it was predicted from theory that the turbulent-velocity defect for power-law non-Newtonians is given by Equation (34). When Equations (34) and (45) are combined, this predicted velocity-

defect law becomes

$$\frac{U_m - u}{u^*} = 5.66(n')^{0.25} \log \frac{R}{y} \quad (46)$$

The integrated form of the velocity-defect law corresponding to Equation (40) becomes by similar substitution

$$\frac{U_m - V}{u^*} = P_n = 3.686(n')^{0.25} \quad (47)$$

Although Equations (46) and (47) both indicate the flattening influence of a decreasing flow-behavior index on the turbulent-velocity profile, this effect may be appreciated more fully by an examination of the velocity profile itself rather than the velocity defect. Figure 14 shows a predicted turbulent-velocity profile based on a set of conditions representing one of the actual experimental points. Such a profile is readily calculated by using Equations (8), (45), (46), and (47). Included for comparison are the laminar-velocity profile for a fluid having the same properties and a turbulent Newtonian profile corresponding to the same Reynolds number and mean velocity. The pronounced flattening of the laminar profile on transition to the turbulent transfer of momentum is obvious at once. It is worth noting that although pseudoplastic fluids have laminar profiles which are flat relative to the parabolic velocity distribution characteristic of Newtonian laminar motion, the laminar profile for  $n' = 0.377$  is still considerably less flat than the turbulent Newtonian profile.

It has been shown that for power-law fluids the velocity profiles may also be expressed in terms of generalized  $u^+$  and  $y^+$  functions. Equation (36) expresses the relationship between these dimensionless quantities within the turbulent core. When the general  $A_n$  and  $B_n$  functions are replaced with their proposed functional forms, Equation (36) becomes

$$u^+ = \frac{5.66}{(n')^{0.75}} \log y^+ - \frac{0.40}{(n')^{1.2}}$$

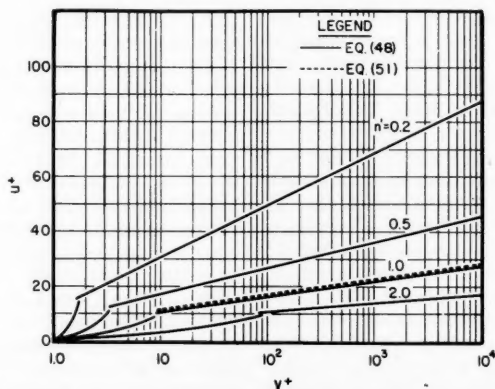


Fig. 15. Generalized ( $u^+ - y^+$ ) velocity profile plot for non-Newtonian as well as Newtonian fluids.

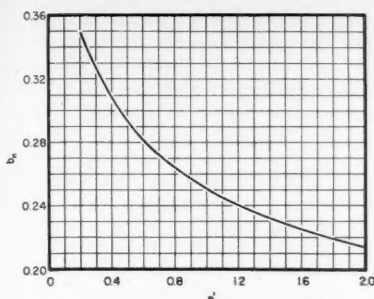


Fig. 16. The  $b_n$  function in the relation

$$f = \frac{a_n}{(N_{Re}')^{b_n}} + \frac{2.458}{(n')^{0.75}} \left[ 1.960 + 1.255n' - 1.628n' \log \left( 3 + \frac{1}{n'} \right) \right] \quad (48)$$

With any given value of  $n'$  Equation (48) simplifies greatly and loses its prodigious appearance. For example for the Newtonian case Equation (48) reduces to

$$u^+ = 5.66 \log y^+ + 5.1 \quad (49)$$

Direct velocity-profile measurements on Newtonian fluids have yielded the equations (15)

$$\frac{U_m - u}{u^+} = 5.75 \log \frac{R}{y} \quad (50)$$

$$u^+ = 5.75 \log y^+ + 5.5 \quad (51)$$

The differences between Equations (49) and (51) and Equations (46) and (48) for the Newtonian case are small. The slight discrepancies in the comparative coefficients arise from the fact that frictional pressure-loss measurements have been used to establish the coefficients in Equations (46) through (49), whereas direct velocity-profile measurements were used in the case of Equations (50) and (51). Any small real differences here are perhaps ascribable to slight inaccuracies encountered during the development, such as the neglect of the laminar sublayer when one is integrating for the mean velocity or the slight inaccuracy of the velocity-defect equation at the center line. Again it is noted that Equations (46) and (48) cannot be perfect, since they do not predict a zero shear rate at the center line of the tube. However in view of the adequacy and widespread acceptance of the corresponding Newtonian Equations (50) and (51), which suffer the same objection, this discrepancy is not considered to constitute a major inconsistency under all conditions. However careful examination of Figure 14 shows that the error introduced appears to increase with decreasing values of  $n'$ ; that is, the region near the center line in which

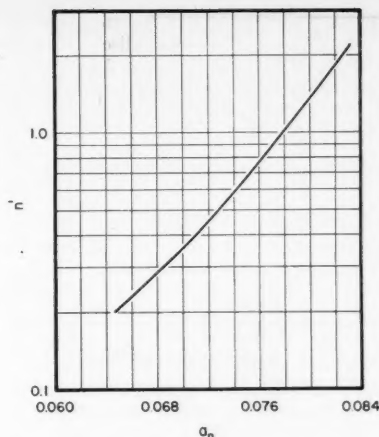


Fig. 17. The  $a_n$  function in the relation

$$f = \frac{a_n}{(N_{Re}')^{b_n}}$$

the turbulent equations predict a steeper profile rather than one which is flatter than the corresponding laminar profile has been increased in breadth for the non-Newtonian case. This makes the theoretically predicted turbulent-velocity profiles for non-Newtonian fluids an extremely tentative proposition until checked by direct experimental measurements. The only available experimental velocity profiles appear to be in the unpublished thesis of Shaver (16). Since it is believed that his data may possibly be influenced by unmeasured complications owing to fluid elasticity or another similar effect, there appear to be no experimental measurements of proved applicability with which the present predictions may be verified or rejected at this time.

Equation (48) is shown plotted for several values of the flow-behavior index in Figure 15. A plot of Equation (51) is also included for comparison. Within the laminar sublayer Equation (39) becomes valid replacing Equation

(36). Curves representing Equation (39) for the corresponding values of  $n'$  are also shown in Figure 15. It is likely that some type of buffer or transition region separates and causes a gradual merging of the laminar sublayer and turbulent core rather than the abrupt transition indicated by the intersections of Figure 15. Velocity-profile measurements with Newtonian fluids have certainly indicated the presence of such a buffer region (5, 15). However the question of the existence and extent of a buffer region with non-Newtonian fluids must await suitable measurements on velocity profiles themselves.

#### Blasius Type of Approximation

It was indicated earlier that Equation (42), a simple expression resembling the equation proposed by Blasius for Newtonian liquids, might be used for non-Newtonian fluids to provide an approximation of the friction factor within a limited range of Reynolds numbers. Figures 16 and 17 post the best values of  $b_n$  and  $a_n$  over the Reynolds number range from 3,000 to 100,000 as obtained by fitting straight lines to the curves of Figure 12. Figure 18 shows the turbulent friction-factor lines predicted by Equation (42), based on the smoothed  $a_n$  and  $b_n$  functions as given in Figures 16 and 17 respectively. For comparison the corresponding curves predicted by Equation (45) are included.

#### Contraction Effects

When a fluid is allowed to flow through a sharp-edged entrance or sudden contraction, a finite length of flow path is required thereafter before a fully developed velocity profile is attained. To trace the extent of entrance or contraction effects a sharp-edged contraction from  $1\frac{1}{2}$ - to  $\frac{1}{2}$ -in. standard pipe was installed at the entrance to the calming section of the  $\frac{1}{2}$ -in. pipe. Three pressure taps were placed in the calming section downstream from the contraction, so

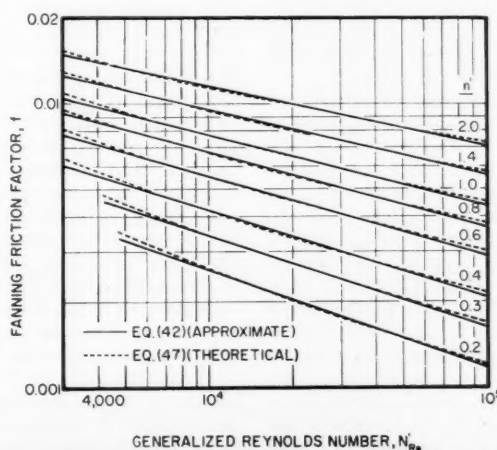


Fig. 18. Comparison of approximate and theoretical equations for the friction factor.



that the pressure gradient might be traced back from the test section to within 5.6 diam. of the point of contraction.

Figure 19 illustrates a typical pressure gradient following the contraction, when laminar flow prevailed. The excessive pressure loss, immediately evident near the contraction, appears to be dissipated completely at about 45 diam. downstream, after which a linear pressure gradient was established. There was some indication that the distance over which the contraction influence was felt increased slightly with increasing velocity or Reynolds numbers, but the data were inadequate to establish any quantitative relationship. In no case however did the laminar entrance length extend appreciably beyond the 53 diam. allowed in this work as a calming section.

Owing to eddy momentum transport it is to be expected that turbulent entrance lengths will be considerably less than for the laminar case at corresponding Reynolds numbers. Experimental data have verified this hypothesis. The entrance lengths under turbulent conditions were so short that their determination was almost impossible. Generally it can be said that all observed turbulent entrance lengths were less than 15 diam. and appeared to be independent of the velocity or Reynolds number. These entrance length results qualitatively agree with similar Newtonian measurements and are of comparable magnitude or somewhat shorter. Since the non-Newtonian velocity profiles for fluids having an  $n'$  of less than unity are always less sharp than in the corresponding Newtonian case, it appears reasonable from a theoretical point of view that a shorter distance should be required to establish the final profile, other factors being constant. It should be noted that entrance lengths determined from excess pressure losses in the region of a contraction are generally smaller than those required to develop completely the velocity profile, since the final velocity distribution is attained earlier in the vicinity of the wall, which determines the pressure gradient, than at the center line of the tube.

By extrapolating the excess pressure curves back to zero length, as is shown in Figure 19, it is possible to arrive at the excess pressure loss which is dissipated within the smaller pipe. Such an excess pressure loss is not equivalent to the total contraction loss, since it does not include the portions of the kinetic energy change and additional fluid friction which take place in the larger pipe prior to the point of contraction. Figure 20 is a plot of the experimentally determined laminar excess pressure losses including kinetic energy effects determined in this manner as a function of the mean velocity. It can be seen that all the data are correlated quite well by a line

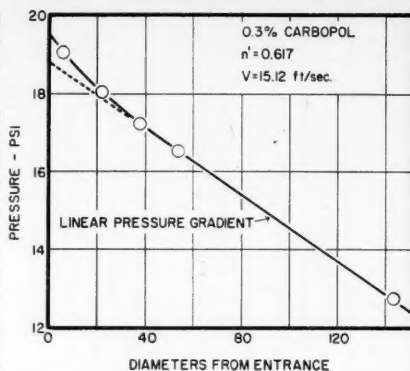


Fig. 19. Typical pressure gradient downstream from an abrupt contraction.

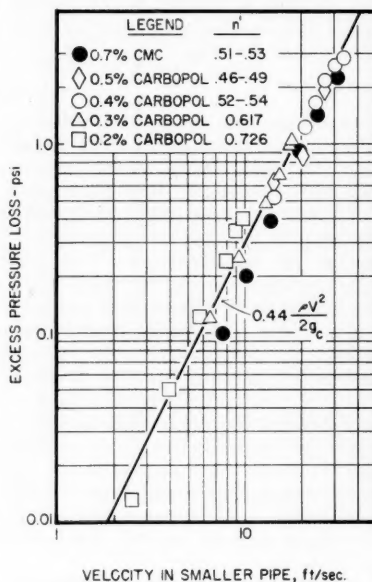


Fig. 20. Laminar contraction losses.

corresponding to 0.44 velocity heads and that no significant effect of the flow-behavior index is apparent. No contraction losses were obtained for the tests corresponding to turbulent conditions, since the accompanying entrance lengths were too short to permit the necessary extrapolation with even a moderate degree of accuracy. However there were very strong indications that turbulent contraction losses correspond to considerably fewer velocity heads than do laminar contraction losses, which is in qualitative agreement with the finding of Weltmann and Keller (21).

McMillen (8) measured laminar-contraction pressure losses in exactly the same manner as was used in the present study and following contractions comparable to those used here. His results showed losses from four to ten velocity heads and indicated that the losses increased with the 1.5 power of the

mean velocity rather than as the square. The large discrepancy between such findings and the others mentioned is obvious and possibly is due to the high viscoelasticity of McMillen's fluid.

When rheological properties were calculated from measurements with the capillary-tube viscometer, an entrance correction of  $1.5 \rho V^2/g_c$  was arbitrarily assumed for lack of more accurately defined procedures. For the vast majority of data this correction was entirely negligible. Only at the highest shear rates did the correction term become appreciable. Employing capillary tubes of several diameters so that the linear velocities were different at the same shear stress made it possible to examine the appropriateness of the assumed entrance correction. Nearly all the data indicated that the correction of  $1.5 \rho V^2/g_c$  was too large. Although the actual entrance losses could not be established precisely from these observations, it appeared that a correction closer to  $1.0 \rho V^2/g_c$  or the Newtonian correction of  $1.12 \rho V^2/g_c$  would have been nearer to the fact for all the fluids of this investigation. Such a conclusion supports the findings of Toms (17) and Weltmann and Keller (21). This capillary correction includes the entire kinetic energy and frictional effects encountered at an essentially infinite reduction in cross section, which certainly should be larger than those at the 2.56:1-diam. reduction employed as the pipeline contraction. Consequently the laminar-contraction losses for the pipeline contraction should be expected to be less than two velocity heads, which again agrees qualitatively with the experimental findings after allowance is made for upstream losses in the pipeline apparatus.

## SUMMARY AND CONCLUSIONS

The present work represents the first theoretical attack in the area of turbulent non-Newtonian flow and has yielded a completely new concept of the attending relationship between the pressure loss and average flow rate based solely on fundamental fluid properties. The turbulent resistance law resulting from this analysis resembles the well-known equation of von Karman for Newtonian fluids but represents a generalization thereof which is applicable to Newtonian and non-Newtonian fluid systems alike, irrespective of any arbitrary rheological classifications. To be rigorous the relationship is restricted to nonelastic, time-independent fluids, which represent the simplest and fortunately the most common case of flow behavior. The latter restriction of time independency however, is of little engineering importance, since it is probable that design calculations with such fluids would be based on the limiting cases of zero and infinite times of shear, representing



start-up and steady state conditions. These limiting cases may be treated individually as if time effects were absent.

The friction-factor relationship given by the theoretical analysis is

$$\sqrt{1/f} = A_{1n} \log [N_{Re}'(f)^{1-n'/2}] + C_n'$$

The  $A_{1n}$  and  $C_n'$  functions required experimental determination, just as in the case of earlier theoretical analyses developed for the simpler special case of Newtonian behavior.

All the fully turbulent experimental data supported the validity of the theoretical analysis. The  $A_{1n}$  and  $C_n'$  functions were established primarily from data taken with polymeric solutions. Subsequent comparison between predicted and experimental friction factors for clay suspensions, however, showed equally good agreement. The final equation

$$\sqrt{1/f} = \frac{4.0}{(n')^{0.75}} \log [N_{Re}'(f)^{1-n'/2}] - \frac{0.4}{(n')^{1.2}}$$

correlated all the turbulent non-Newtonian data for both the slurries and the nonelastic gels (some 146 points) with a mean deviation of 1.9%. Correlation of these data by the empirical prior-art methods showed much poorer agreement and indicated that the prior-art procedures become progressively worse as the intensity of the non-Newtonian characteristics increase. For fluid systems with flow-behavior indexes that are functions of the shear stress it has been shown that  $n'$  should be evaluated at the existing wall shear stress for use in the proposed relationship. A friction-factor expression approximating the theoretical equation for Reynolds numbers less than 100,000, but which expresses the friction factor explicitly, has also been developed.

Transition from laminar to turbulent flow with non-Newtonian systems was found to take place within a Reynolds number range comparable to the extent of the Newtonian transition region. The lower critical Reynolds number corresponding to the onset of turbulence appeared to increase slightly with decreasing values of the flow-behavior index. At  $n'$  equal to 0.38 the onset of turbulence was observed at a Reynolds number of about 3,100.

The theoretical analysis of the present work has permitted the prediction of non-Newtonian turbulent velocity profiles, for which no published literature exists. Although no velocity profiles were actually measured, comparison of this work with the accepted Newtonian relationships indicates that these predictions should be reasonably valid. Generalizations of familiar  $u^+$  and  $y^+$  velocity-profile parameters have been

proposed which extend their utility to non-Newtonian systems.

Pressure-loss measurements taken near a sudden contraction have provided information, although somewhat limited, on the tube lengths over which an entrance effect is observable with non-Newtonian fluids and the magnitude of entrance or contraction losses.

These conclusions are based on data taken with one type of polymeric gel and with slurries. Preliminary measurements on another gel system showed turbulence to be strongly suppressed, perhaps owing to elasticity effects, which have not been considered in the present analysis. The present results may however be used as an approximation for such fluids; while the predicted friction factors may be in error, they will be conservative.

The need for further work lies primarily in characterization of such more complex gels and extension of the present approach to such systems, measurement of velocity profiles to verify the theoretical predictions made herein, and application of this knowledge of the mechanics of turbulence in non-Newtonian systems to problems in areas such as fluid agitation and heat and mass transfer.

#### ACKNOWLEDGMENT

Sincere gratitude is extended to the Texas Company, the United States Army Office of Ordnance Research, and the United States Air Force Bureau of Scientific Research, whose sponsorship made this work possible.

#### NOTATION

- $a_n$  = dimensionless function of flow-behavior index for Blasius type of approximation, defined by Equation (42)
- $A_n$  = dimensionless function of flow-behavior index (constant at any given value of  $n$ )
- $A_{1n}$  = dimensionless function of flow-behavior index
- $b_n$  = dimensionless function of flow-behavior index for Blasius type of approximation, defined by Equation (42)
- $B_n$  = dimensionless function of flow-behavior index
- $C_n$  = dimensionless function of flow-behavior index, defined by Equation (21)
- $C_n'$  = dimensionless function of flow-behavior index, defined by Equation (29)
- $D$  = internal diameter of pipe or tube
- $e_n$  = dimensionless function of flow-behavior index for assumption of strict similarity
- $E_n$  = dimensionless function of flow-behavior index
- $f$  = Fanning friction factor (dimensionless), also used to designate an unspecified function when

followed by series of variables in parentheses

- $g_c$  = dimensional conversion factor, 32.17 (lb.-mass/lb.-force) (ft./sec.<sup>2</sup>)
- $g_1$  = general function of  $\xi$  and the flow-behavior index defined by Equation (19)
- $k$  = turbulent constant appearing in theoretical relationships for Newtonian fluids
- $K$  = fluid consistency index defined by Equation (1)
- $K'$  = fluid consistency index defined by Equation (24)
- $L$  = length of pipe or tube
- $n$  = flow-behavior index (dimensionless), defined by Equation (1)
- $n'$  = flow-behavior index (dimensionless), defined by Equation (23)
- $N_{Re}$  = conventional Reynolds number (dimensionless),  $DV\rho/\mu$
- $N_{Re}'$  = generalized Reynolds number (dimensionless), defined by Equation (28)
- $N_{Re}^o$  = Reynolds number (dimensionless), defined by Equation (22)
- $P_n$  = dimensionless function of flow-behavior index, defined by Equation (7)
- $\Delta P$  = pressure drop,  $\Delta P/L$ , pressure gradient
- $Q$  = volumetric flow rate
- $r$  = radial distance from center of tube
- $R$  = internal radius of pipe or tube
- $u$  = local velocity at  $r$  (or  $y$ )
- $u^*$  = friction or shear velocity, equal to  $\sqrt{\tau_w/\rho}$
- $u^+$  = dimensionless velocity-profile parameter, defined by Equation (37)
- $U_m$  = maximum (center line) linear velocity in tube
- $V$  = mean linear velocity
- $y$  = distance from tube wall, equal to  $(R - r)$
- $y^+$  = dimensionless velocity-profile parameter, defined by Equation (38)
- $Z$  = dimensionless group defined by Equation (4)

#### Greek Letters

- $\delta$  = value of  $y$  at the intersection of the laminar sublayer and transition zone
- $\lambda$  = value of  $y$  at the intersection of the transition zone and the turbulent core
- $\mu$  = viscosity of a Newtonian fluid
- $\xi$  = dimensionless location parameter, equal to  $y/R$
- $\xi_1$  = value of  $\xi$  slightly larger than  $\lambda/R$
- $\rho$  = density
- $\tau$  = shear stress, equal to  $(r \Delta P/2L)$  within round tube
- $\tau_w$  = shear stress at inner wall of tube ( $D \Delta P/4L$ )
- $\gamma$  = grouping of terms forming denominator of the generalized Reynolds number,  $\gamma = g_c K' S'^{-1}$

# LITERATURE CITED

1. Alves, G. E., D. F. Boucher, and R. L. Pigford, *Chem. Eng. Progr.*, **48**, 385 (1952).
2. Caldwell, D. H., and H. E. Babbitt, *Trans. Am. Inst. Chem. Engrs.*, **37**, 237 (1941); *Ind. Eng. Chem.*, **33**, 249 (1941).
3. Dodge, D. W., Ph.D. thesis, Univ. of Delaware, Newark, Delaware (1957).
4. Durand, W. F., "Aerodynamic Theory," III, 127, 142, Julius Springer, Berlin (1935).
5. Hunsaker, J. C., and B. G. Rightmire, "Engineering Applications of Fluid Mechanics," McGraw-Hill, New York (1947).
6. Knudsen, J. G., and D. L. Katz, *Eng. Research Bull.* **37**, Univ. of Mich. Press, Ann Arbor, Michigan (1954).
7. Krieger, I. M., and S. H. Maron, *J. Appl. Phys.*, **23**, 147 (1952).
8. McMillen, E. L., *Chem. Eng. Progr.*, **44**, 537 (1948).
9. Metzner, A. B., "Advances in Chemical Engineering," vol. I, Academic Press, New York (1956).
10. ———, *Ind. Eng. Chem.*, **49**, 1429 (1957).
11. ———, and J. C. Reed, *A.I.Ch.E. Journal*, **1**, 434 (1955).
12. Millikan, C. B., "Proc. Fifth Int. Cong. for Appl. Mechanics," 386, John Wiley and Sons, (1939).
13. Rabinowitsch, B., *Z. physik. Chem.*, **A145**, 1 (1929).
14. Rouse, Hunter, "Elementary Mechanics of Fluids," John Wiley and Sons, Inc., New York (1946).
15. Schlichting, Hermann, "Boundary Layer Theory," McGraw-Hill Book Co., New York (1955).
16. Shaver, R. G., Sc.D. thesis, Mass. Inst. Technol., Cambridge, Massachusetts (1957).
17. Toms, B. A., "Proc. 1st Int. Rheolog. Cong., Holland," II, 135 (1948).
18. von Karman, Th., *Nachr. Ges. Wiss. Gottingen, Math. physik. Kl.*, 58 (1930), and "Proc. of 3rd Int. Cong. of Appl. Mechs., Stockholm, Pt. 1," 85 (1930); also *Natl. Advisory Comm. Aeronaut., Tech. Mem. No. 611*, Washington, D. C. (1931).
19. Ward, H. C., Ph.D. thesis, Georgia Inst. of Technol., Atlanta, Georgia (1952).
20. Weltmann, R. N., *Natl. Advisory Comm. Aeronaut., Tech. Note 3397* (1955); *Ind. Eng. Chem.*, **48**, 386 (1956).
21. ———, and T. A. Keller, *Natl. Advisory Comm. Aeronaut., Tech. Note 3889* (1957).
22. Winding, C. C., G. P. Baumann, and W. L. Kranich, *Chem. Eng. Progr.*, **43**, 527, 613 (1947).

Manuscript received February 4, 1958; revision received July 3, 1958; paper accepted July 7, 1958. Paper presented at A.I.Ch.E. Chicago meeting.

## Characteristics of Transition Flow Between Parallel Plates

G. A. WHAN and R. R. ROTHFUS

Carnegie Institute of Technology, Pittsburgh, Pennsylvania

Measurements of pressure drop and mean local fluid velocities have been made in a smooth rectangular duct of large aspect ratio. Data have been taken on the steady, isothermal flow of water at room temperature in the viscous, transition, and lower turbulent ranges of flow. Impact probes were installed in the center of the stream, where flow between infinitely broad parallel plates was closely approximated. The limits of the transition range are discussed, and mean local fluid velocities are correlated. Comparison is made with transitional behavior in smooth tubes.

The present investigation was undertaken to gain information about the characteristics of steady, isothermal, fluid flow between smooth, parallel, flat plates. Attention was centered on the region of laminar-turbulent transition, although data were obtained in the viscous and lower turbulent ranges as well. The test fluid was water at room temperature flowing at Reynolds numbers between 865 and 40,190. Measurements of temporal mean local fluid velocities were made by means of a calibrated impact probe, and these data were supplemented by corresponding measurements of the pressure drop caused by fluid friction. Forty-six velocity profiles were obtained to furnish a comprehensive

picture of their dependence on the Reynolds number.

Since it was impossible to deal with infinitely broad plates, these were approximated by the long sides of a 0.70- by 14-in. rectangular conduit, 20 ft. in horizontal length, formed from brass plates and equipped with a bell-shaped entrance. The 20:1 aspect ratio of the duct permitted the experimental data to be compared with published information in the fully turbulent range.

Several investigations, such as those of Laufer (3), Skinner (10), and Watten-dorf and Kuethe (13), have been made to determine the velocity distribution for air flowing in fully turbulent motion between parallel plates. More recently Sage and coworkers (2, 4) have obtained several excellent velocity profiles in the lower turbulent region. Their apparatus

was much like that used in the present experiments. Schlinger and Sage (8) have presented a correlation of available velocity data for parallel plates. Using the data of Sage and coworkers as their basis, Rothfus and Monrad (6) have developed a means of correlating parallel-plate velocity profiles with those obtained in smooth tubes under fully turbulent conditions. Rothfus and coworkers (5) have presented simplified methods of calculating velocity profiles and pressure drops based on the Rothfus and Monrad correlation. The fully turbulent range of flow can therefore be handled reasonably well with respect to fluid friction and the distribution of mean local velocities, provided the calming length is sufficient to make entrance effects negligible.

In the fully viscous range of flow the Navier-Stokes equations of motion can

G. A. Whan is at the University of New Mexico, Albuquerque, New Mexico.

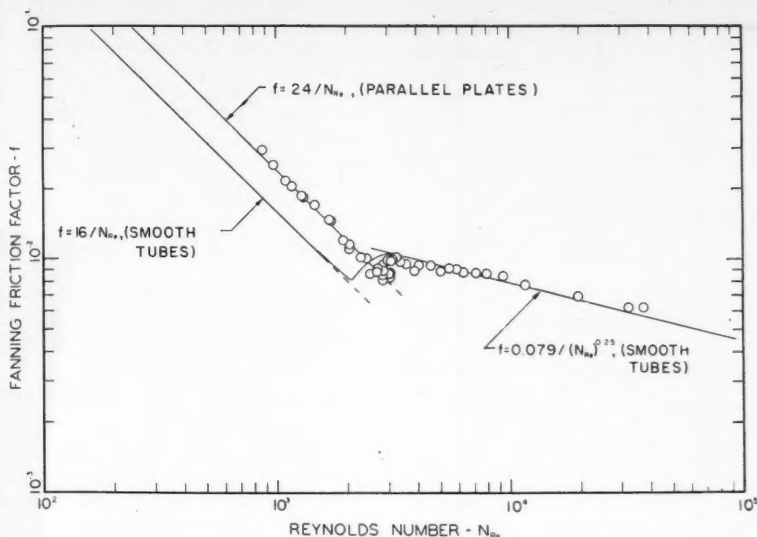


Fig. 1. Fanning friction factors for smooth parallel plates; comparison with smooth-tube correlation is shown.

be integrated without difficulty to obtain the shearing-stress distribution and velocity distribution as well as the pressure loss due to friction (7a). The well-known results of this procedure are summarized in the following equations:

Local shearing stress

$$\tau_{gc} = \frac{\Delta p g_c}{L} (b - y) \quad (1)$$

Local fluid velocity

$$u = \frac{\Delta p g_c}{2\mu L} (2by - y^2) \quad (2)$$

Frictional pressure drop

$$\Delta p = \frac{3\mu VL}{g_c b^2} \quad (3)$$

These equations are based on the assumptions of steady, fully developed viscous motion, zero fluid velocity at the boundaries, constant density and viscosity, and infinitely broad plates.

When one deals with noncircular ducts, it is customary to use a Reynolds number based on the bulk average linear velocity of the fluid and the hydraulic radius of the conduit. For a rectangular duct having a long side of length  $2a$  and a short side of length  $2b$  the Reynolds number is

$$N_{Re} = \frac{4(4ab)V\rho}{2(2a + 2b)\mu} = \frac{4bV\rho}{\left(1 + \frac{b}{a}\right)\mu} \quad (4)$$

As the aspect ratio  $a/b$  increases without limit, thus approaching the case of infinitely broad parallel plates, the Reynolds number becomes

$$(N_{Re})_F = \frac{4bV\rho}{\mu} \quad (5)$$

Regardless of the prevailing type of flow the pressure drop due to fluid friction can be represented by means of the Fanning equation:

$$\Delta p = \frac{2f\rho V^2 L}{g_c D_e} \quad (6)$$

Comparison of Equations (3), (5), and (6) shows immediately that for the case of entirely viscous flow between broad parallel plates

$$f = 24/(N_{Re})_F \quad (7)$$

On the other hand when such flow is fully turbulent, the method of hydraulic radius predicts that

$$f = 0.079/(N_{Re})_F^{0.25} \quad (8)$$

at Reynolds numbers between the upper end of the transition range and 100,000. The latter equation is based on the Blasius friction-factor expression for smooth tubes (1), which correlates tubular data at Reynolds numbers between 4,000 and 100,000.

The conditions of pressure drop and velocity distribution on each side of the transition region can therefore be predicted accurately enough for most purposes. Data taken within the transition range should extrapolate to these limits, and the boundaries of the transition zone should prove to be more or less successfully defined on this basis.

#### EXPERIMENTAL EQUIPMENT

Generally the equipment provided for the flow of water at room temperature from a large constant-head tank to a centrifugal

pump, a surge tank, a bell-shaped entry, a test section, a discharge plenum, and thence back to the supply tank. Part of the discharge from the pump could be recycled directly back to the supply tank to control the flow rate in the test section. The surge tank was protected from pump vibrations by a 1-ft. length of flexible tubing in its feed line. The surge tank and test section were mounted on a heavy angle-iron frame which was cushioned against vibrations from the floor.

The test section was fitted with a smooth tapered entry of sheet brass, constructed of brass plates separated by side blocks; the plates were butt-jointed and braced with machined brass strip and angle iron to preserve exact alignment of their junctions. The test section was 20 ft. long.

Five static pressure taps were situated along the center line of the broad upper side of the test section. The velocity profiles were obtained by means of two impact probes situated on and near the center line of the broad upper side of the duct, a distance of 3 ft. from the discharge end. An aluminum feed mechanism permitted the position of the impact opening to be determined within 0.001 in. The impact probes were formed from stainless steel hypodermic-needle tubing having an 0.058-in. O.D. and an 0.009-in. wall thickness. One of the probes was situated on the center line of the channel and the other 1½ in. off the center line. This permitted verification of the opinion expressed by Sage and his associates that the velocity profile along the broad side of such a duct is essentially flat over the middle 3 in.

The manometers used to measure pressure differences were of the ordinary vertical U-tube type. To magnify the readings monochlorobenzene and monofluorobenzene were used as the manometer fluids, thus yielding multiplications of approximately 10 and 40 respectively.

The temperature of the water flowing in the system was measured at the inlet and outlet ends of the test section by mercury-in-glass thermometers. Since the pumps heated the water slightly, cold tap water was bled into the system from time to time to adjust the temperature. The water temperature was maintained within 0.5°C. of the room temperature to assure essentially isothermal flow.

#### EXPERIMENTAL PROCEDURE

The test section was aligned with the aid of a transit theodolite and leveled to within 0.02 in. over the entire 20 ft. of test length.

Average linear fluid velocities over the middle portion of the conduit were obtained through integration of the experimental velocity profiles in every case. The position of the opening in the impact probe was verified by the determination of both the point of maximum local velocity and the symmetry of the stream. Most of the reported profiles were measured over the upper half of the duct, but at least one point was checked on the other side of the center line in each run. The impact probes were calibrated by the method of Stanton, Marshall, and Bryant (11).

The static pressure differences between successive pairs of taps were obtained, and the pressure gradient over the longest

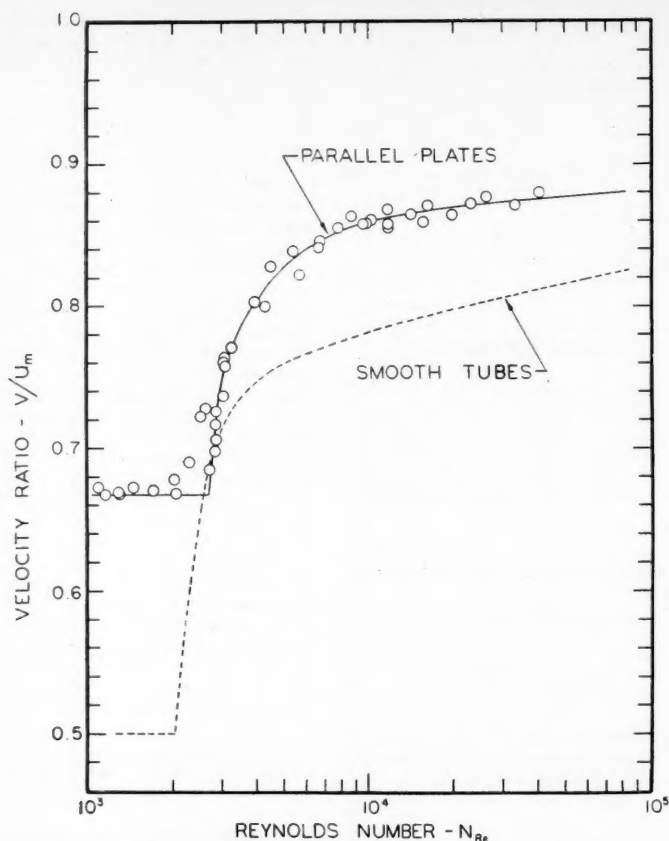


Fig. 2. Effect of Reynolds number on ratio of average to maximum velocity between parallel plates; comparison with smooth-tube correlation is shown.

distance free from entrance effects was used in each case to determine the friction factor.

Velocity measurements were taken after the flow rate had been set and the equipment allowed to run for at least  $\frac{1}{2}$  hr. Fifteen to thirty minutes was typically allowed at each point before the pressure differential across the probe was read. After each profile had been obtained, the maximum point was checked, and at least one point on the opposite side of the center line was measured to verify the symmetry of flow. Room and water temperatures were observed and recorded at the time each point velocity was measured.

#### EXPERIMENTAL RESULTS AND TREATMENT OF DATA

The Fanning friction factors were calculated from the static pressure data by means of Equation (6), with the equivalent diameter taken as four times the half-clearance. The Reynolds number was calculated by means of Equation (5), and the resulting correlation is summarized in Figure 1. For comparison the viscous relationship shown in Equation (7) and the hydraulic-radius prediction shown in Equation (8) are drawn on the same coordinates.

The ratio of average to maximum velocity is shown as a function of Reynolds number in Figure 2. In every case

the maximum velocity is a single experimental point, and the bulk average

velocity is obtained by means of integration under the measured velocity profile.

The data shown in Figures 1 and 2 can be combined to yield consistent values of the friction velocity parameter at the center of the stream. This is readily apparent from the defining equation, namely

$$u_m^+ = \frac{u_m}{u^*} = \left(\frac{u_m}{V}\right)\left(\frac{1}{f/2}\right) \quad (9)$$

In addition the center-line value of the friction distance parameter can also be obtained immediately, since by definition

$$y_m^+ = \frac{bu_*\rho}{\mu} = \frac{1}{4}N_{ReF}\sqrt{f/2} \quad (10)$$

The resulting graph of  $u_m^+$  against  $y_m^+$  is shown in Figure 3. Each point represents a combination of experimental  $V/u_m$  and friction-factor values.

The nature of the velocity profiles in the transition zone between viscous flow and full turbulence is such that a correlation of the  $u^+$ ,  $y^+$  type cannot be used conveniently for interpolation. A correlation of the ratio  $u/u_m$  as a function of Reynolds number at constant values of the distance ratio  $y/b$  however can be interpolated readily. The experimental velocity data were therefore smoothed and correlated as shown in Figure 5. To illustrate the magnitude of agreement between the original data and the final results curves obtained by cross plotting Figure 5 at constant Reynolds numbers are included in Figure 4.

The experimental results summarized in Figures 1, 3, and 5 can be used in the following manner to obtain local velocities

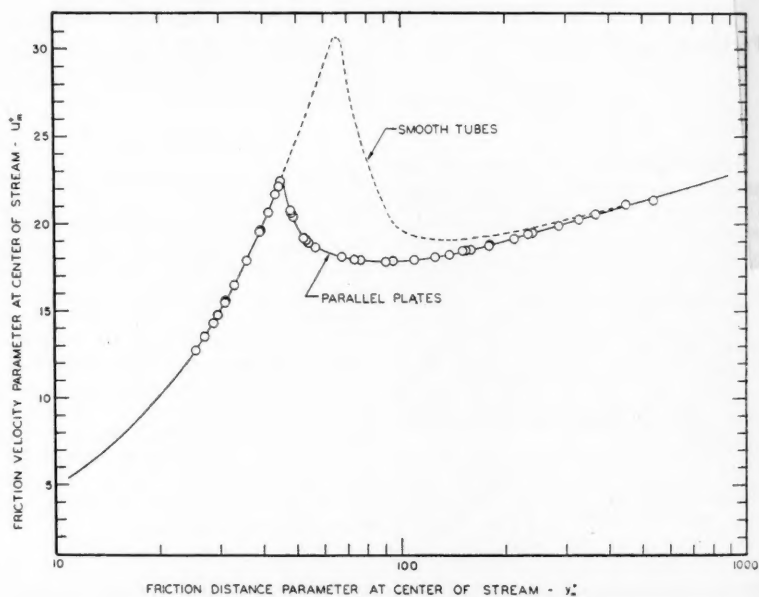


Fig. 3. Relationship between friction-velocity parameter and friction-distance parameter at center of stream flowing between parallel plates; comparison with smooth-tube correlation is shown.



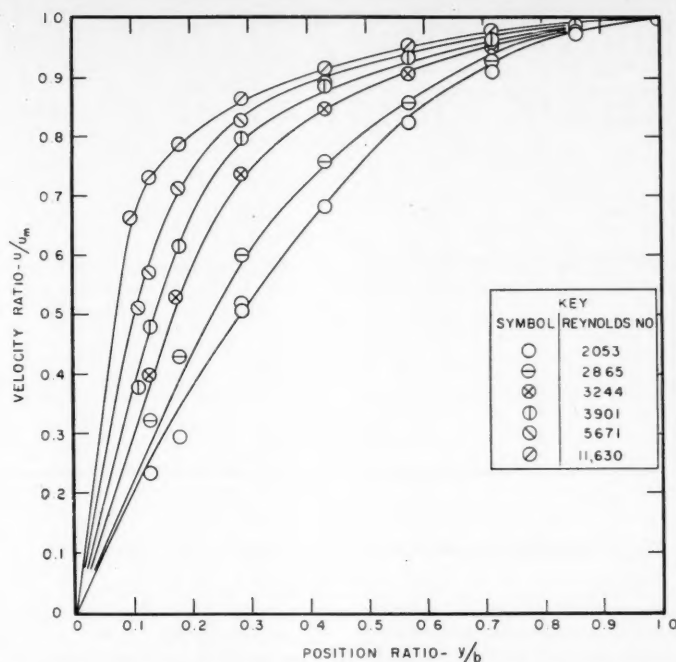


Fig. 4. Velocity profiles for flow between parallel plates. (Solid lines are taken from the smoothed correlation shown in Figure 5. Circles show original data.)

at a given Reynolds number. First the friction factor is read from Figure 1. Second the friction velocity is obtained from the equation  $u_* = V\sqrt{f/2}$ . The parameter  $u_m^+$  is read from Figure 3 at the value of  $y_m^+$  obtained from Equation (10). The center-line velocity is then calculated from the relationship  $u_m = u_m^+ u_*$ , and the local velocity is obtained from the  $u/u_m$  values in Figure 5.

#### DISCUSSION OF RESULTS

The Fanning friction factors show substantial agreement with the theoretical relationship in viscous flow and the hydraulic-radius prediction in full turbulence. Total agreement can hardly be expected, since the test duct is rectangular and unmeasured-edge effects influence the over-all pressure drop to some extent. The data in the fully turbulent range closely reproduce the results of Sage and his associates. The transition range appears to extend from a Reynolds number of 2,700 to about 3,300 with some evidence of persistence as high as 6,000. There is little or no evidence of any departure from the viscous-flow relationship at Reynolds numbers below 2,700. Smooth tubes on the other hand exhibit a small but definite upward divergence from the laminar line in the region between 1,200 and 2,100 Reynolds number. The dip in Figure 1 however has almost the same depth as for smooth tubes, and the minimum point is marked by the same value of the friction factor.

Figure 2 indicates that the center-line

velocity data are consistent with the critical Reynolds number shown by the static pressure data in Figure 1. The scattering of points appears to be unrelated to the direction from which the critical Reynolds number is approached. The smooth-tube line in Figure 2 is based on the data of Senecal and Rothfus (9).

Rothfus and Monrad (6) have shown that coincident velocity profiles occur in smooth tubes and parallel plates when

(1) the flow is fully viscous or fully turbulent, (2) the radius of the tube is equal to the half-clearance between the plates, (3) the skin frictions are equal, and (4) the fluid properties are the same in both conduits. Under such restraints  $u_p^+ = u_p^+$  and  $y_p^+ = y_p^+$ . It follows immediately that the same equalities must hold at the center line of the stream; therefore graphs of  $u_m^+$  against  $y_m^+$  for each configuration should be coincident when drawn on the same set of coordinates.

The parallel-plate data of Figure 3 have been supplemented with a line for smooth tubes which is based for the most part on the experimental results of Senecal and Rothfus (9). It is apparent that the two curves are coincident at  $y_m^+$  values less than 45. The latter value represents the critical Reynolds number of 2,700 for parallel plates by virtue of Equation (10). It is also apparent that the curves merge very gradually at the upper end of the transition zone, and so the point of actual correspondence cannot be stated accurately. At  $y_m^+ = 140$ , however, the deviation is only about 4%, which is within the combined error of the contributory experiments. This point corresponds to a Reynolds number of 8,800 in the parallel-plate case and a Reynolds number of 4,000 in the smooth tube.

Several conclusions can therefore be reached through examining Figure 3. First the degree of correspondence between the velocity profiles for tubes and parallel plates is a weak function of the Reynolds number in the fully turbulent range. Second the correspondence is greatest at high Reynolds numbers. Third from the practical standpoint the method of Rothfus and Monrad can be

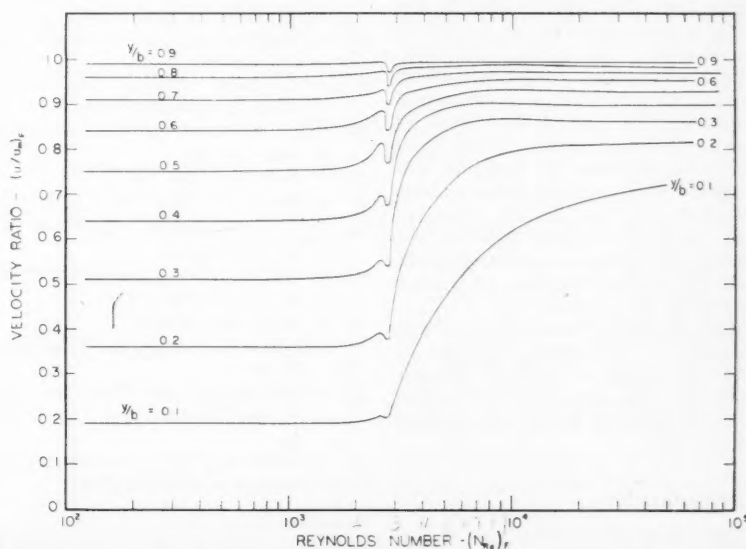


Fig. 5. Correlation of mean local velocities in flow between smooth parallel plates.

used at Reynolds numbers down to the point where the equivalent tube enters transition flow. Fourth the condition of corresponding velocities cannot be used successfully when either conduit is in the transition range. Figure 3 of course deals only with the center line of the stream, but the measured velocity profiles support the stated conclusions.

The behavior of the center-line velocities in the transition range supports the view that local velocities for parallel plates are best correlated in the simple form

$$\frac{u}{u_m} = \phi(N_{Re}, y/b) \quad (11)$$

Figure 5 is a picture of this equation which emphasizes the effect of a Reynolds number on the velocity profile while permitting rather easy interpolation among even values of the distance ratio. For comparison the corresponding correlation for smooth tubes has been prepared from the data of Senecal and Rothfus and is shown in Figure 6.

It is apparent that both parallel plates and smooth tubes exhibit much the same behavior in the transition range. The effect of casting off the first large disturbance eddies at the critical Reynolds number is immediately reflected by the velocity profiles in both cases. It should be noted that the velocity ratios at intermediate values of the distance ratio seem to be more greatly disturbed than those near the wall and near the center of the stream. Once the critical point is passed and the frequency of the disturbance eddies increases with increased Reynolds number, the parallel-plate profile approaches its fully turbulent pattern more gradually than does the smooth-tube profile. The velocity pattern therefore supports the frictional data in showing that the transition zone extends over a longer Reynolds-number range in the case of parallel plates than in the case of smooth tubes.

Figures 5 and 6 can be used as working graphs for the calculation of mean local velocities. They should be viewed as purely empirical except in the fully viscous region, although they are also consistent with accepted notions about fully turbulent flow. In the transition zone, which is the local point of the present investigation, there is no adequate basis for treating the data other than empirically at this time.

The relationship between the friction factors shown in Figure 1 and those for concentric annuli of various diameter ratios has been discussed in a recent paper by Walker, Whan, and Rothfus (12).

#### ACKNOWLEDGMENT

This paper was submitted by G. A. Whan in partial fulfillment of the requirements for the degree of Doctor of Philosophy

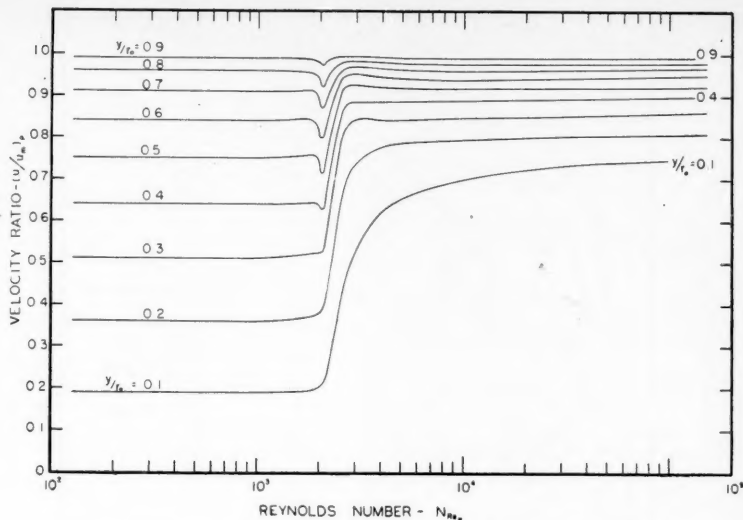


Fig. 6. Correlation of mean local velocities in flow through smooth tubes.

at Carnegie Institute of Technology. Original data and calibrations are presented in the thesis, which is available on inter-library loan from Carnegie Institute of Technology, Pittsburgh 13, Pennsylvania.

#### NOTATION

- $a$  = half of long side of rectangular duct, ft.
- $b$  = half of short side of rectangular duct or half-clearance between infinitely broad parallel plates, ft.
- $D_e$  = equivalent diameter of conduit equal to four times the cross-sectional area divided by the wetted perimeter, ft.
- $f$  = Fanning friction factor, dimensionless
- $g_c$  = conversion factor in Newton's second law of motion equal to 32.2 (lb.-mass)(ft.)/(lb.-force)(sec.<sup>2</sup>)
- $L$  = length of conduit over which  $\Delta p$  is measured, ft.
- $N_{Re}$  = Reynolds number equal to  $D_e V \rho / \mu$ , dimensionless
- $\Delta p$  = pressure drop due to friction, lb.-force/sq. ft.
- $r_0$  = radius of tube, ft.
- $u$  = mean local fluid velocity, ft./sec.
- $u_*$  = friction velocity equal to  $V \sqrt{f/2}$ , ft./sec.
- $u^+$  = friction velocity parameter equal to  $u/u_*$ , dimensionless
- $u_m$  = center-line velocity
- $V$  = bulk average linear fluid velocity, ft./sec.
- $y$  = normal distance from wall to point of measurement in the fluid, ft.
- $y^+$  = friction-distance parameter equal to  $yu_* \rho / \mu$ , dimensionless

#### Greek Letters

- $\mu$  = fluid viscosity, lb.-mass/(sec.)(ft.)
- $\rho$  = fluid density, lb.-mass/cu. ft.

- $\tau$  = mean local shearing stress, lb.-force/sq. ft.
- $\phi$  = function

#### Subscripts:

- $F$  = parallel plates
- $m$  = maximum or center-line value
- $P$  = smooth tubes

#### LITERATURE CITED

1. Blasius, H., *Mitt. Forschungsarb.*, **131**, 1 (1913).
2. Corcoran, W. H., F. Page, Jr., W. G. Schlenger, and B. H. Sage, *Ind. Eng. Chem.*, **44**, 410 (1952).
3. Laufer, John, *Natl. Advisory Comm. Aeronaut. Tech. Note* 2123 (1950).
4. Page, F., Jr., W. H. Corcoran, W. G. Schlenger, and B. H. Sage, *Ind. Eng. Chem.*, **44**, 419 (1952).
5. Rothfus, R. R., D. H. Archer, I. C. Klimas, and K. G. Sikchi, *A.I.Ch.E. Journal*, **3**, 208 (1957).
6. Rothfus, R. R., and C. C. Monrad, *Ind. Eng. Chem.*, **47**, 1144 (1955).
7. Schlichting, Hermann, "Boundary Layer Theory," p. 324, McGraw-Hill, New York (1955).
- 7a. *Ibid.*, p. 60.
8. Schlenger, W. G., and B. H. Sage, *Ind. Eng. Chem.*, **45**, 2636 (1953).
9. Senecal, V. E., and R. R. Rothfus, *Chem. Eng. Progr.*, **49**, 533 (1953).
10. Skinner, G., thesis, Calif. Inst. Tech., Pasadena (1950).
11. Stanton, T. E., D. Marshall, and C. N. Bryant, *Proc. Roy. Soc. (London)*, **A97**, 413 (1920).
12. Walker, J. E., G. A. Whan, and R. R. Rothfus, *A.I.Ch.E. Journal*, **3**, 484 (1957).
13. Wattendorf, F. L., and A. M. Kuethe, *Physics*, **5**, 153 (1934).

Manuscript received April 4, 1958; revision received August 22, 1958; paper accepted August 26, 1958.

# Treatment of Thermodynamic Data for Homogeneous Binary Systems

H. C. VAN NESS and R. V. MRAZEK

Rensselaer Polytechnic Institute, Troy, New York

This paper describes general methods for the treatment of binary data which are both precise and convenient. In particular a new and accurate graphical method of determining partial molal quantities is presented.

The basic equations applicable to homogeneous binary solutions are given in Table 1. In these equations  $G$  represents any molal (or unit mass) property of a homogeneous binary system.  $\Delta G$  represents the property change resulting from mixing the pure components at constant temperature and pressure to form 1 mole (or a unit mass) of the solution. The notation  $\Delta \bar{G}_A$  and  $\Delta \bar{G}_B$  to represent partial property changes resulting from mixing has not been widely used but seems convenient.

The derivation of Equation (5) is given in most advanced thermodynamics texts. Equations (7) and (8) follow directly from Equations (5) and (6) after differentiation at constant temperature and pressure. Equations (7) and (8) represent the form of the Gibbs-Duhem equation valid for systems at constant temperature and pressure. The generality of this equation in its applicability to many different properties has sometimes been overlooked.

Equations (4), (6), and (8) are valid for the excess properties of mixing as well as for the property changes themselves. An excess partial molal property of a component in solution is defined as the difference between the true partial property and the partial property the component would have in an ideal solution at the same temperature, pressure, and composition; that is,

$$\bar{G}_i^E = \bar{G}_i - \bar{G}_i^{ideal}$$

Similarly

$$\Delta \bar{G}_i^E = \Delta \bar{G}_i - \Delta \bar{G}_i^{ideal}$$

and

$$\Delta G^E = \Delta G - \Delta G^{ideal}$$

When the property is volume, internal energy, enthalpy, residual volume, compressibility factor, or heat capacity,  $\bar{G}_i^{ideal} = G_i$  and  $\Delta \bar{G}_i^{ideal} = 0$ . Hence

$$\Delta \bar{G}_i^E = \Delta \bar{G}_i \quad \text{and} \quad \Delta G^E = \Delta G$$

Thus the excess properties do not represent new functions for these quantities.

The excess properties, however, are

H. C. Van Ness is Visiting Fulbright Lecturer at King's College, University of Durham, England, from 1958 to 1959.

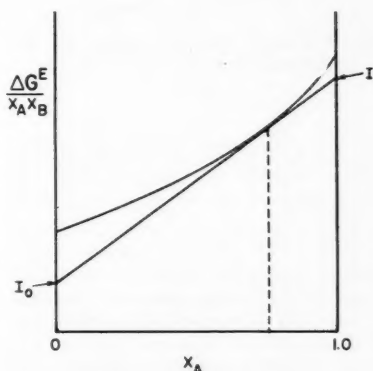


Fig. 1. Graphical procedure for determining partial properties.

distinct quantities for the entropy and free energy. Thus

$$\Delta S^E = \Delta S + R \sum x_i \ln x_i$$

$$\Delta A^E = \Delta A - RT \sum x_i \ln x_i$$

$$\Delta F^E = \Delta F - RT \sum x_i \ln x_i$$

Yet another useful function can be obtained from the Gibbs free energy (4):

$$\frac{\Delta F^E}{RT} = x_A \ln \gamma_A + x_B \ln \gamma_B \quad (9)$$

Comparison of Equation (9) with Equation (4) shows  $\ln \gamma_A$  and  $\ln \gamma_B$  to be related to  $\Delta F^E/RT$  exactly as  $\Delta \bar{G}_A$  and  $\Delta \bar{G}_B$  are related to  $\Delta G$ . Table 2 presents a summary of the functions which are of interest.

The well-known method of tangent

intercepts for the calculation of partial quantities is subject to considerable error because of the inherent uncertainty of the graphical techniques. A new method is presented here which greatly reduces this uncertainty. This method makes use of the plot of  $\Delta G^E/x_A x_B$  vs.  $x_A$ , which has been used increasingly in recent years for the simple presentation of data; its new use is illustrated in Figure 1. The partial properties are shown to be related to the intercepts  $I_0$  and  $I_1$  as follows:

$$I_0 = \frac{\Delta G^E}{x_A x_B} - x_A \frac{d\left(\frac{\Delta G^E}{x_A x_B}\right)}{dx_A}$$

but

$$\frac{d\left(\frac{\Delta G^E}{x_A x_B}\right)}{dx_A} = \frac{\left(\frac{d \Delta G^E}{dx_A}\right)}{x_A x_B} + \left(\frac{\Delta G^E}{x_A x_B}\right) \left(\frac{x_A - x_B}{x_A x_B}\right)$$

Therefore

$$I_0 = \frac{\Delta G^E}{x_A x_B} - x_A \left[ \frac{\left(\frac{d \Delta G^E}{dx_A}\right)}{x_A x_B} + \frac{\Delta G^E}{x_A x_B} \left(\frac{x_A - x_B}{x_A x_B}\right) \right]$$

With a little algebraic manipulation this reduces to

$$I_0 = 2 \left( \frac{\Delta G^E}{x_A x_B} \right)$$

TABLE 1. BASIC EQUATIONS FOR BINARY SYSTEMS AT CONSTANT  $T$  AND  $p$

$x_A + x_B = 1$	(1)
$G = x_A G_A + x_B G_B + \Delta G$	(2)
$G = x_A \bar{G}_A + x_B \bar{G}_B$	(3)
$\Delta G = x_A (\bar{G}_A - G_A) + x_B (\bar{G}_B - G_B)$	(4)
$\Delta G = x_A \Delta \bar{G}_A + x_B \Delta \bar{G}_B$	(5)
$\bar{G}_A = G + (1 - x_A) \left( \frac{dG}{dx_A} \right)$	(6)
$\bar{G}_B = G - x_A \left( \frac{dG}{dx_A} \right)$	(7)
$\Delta \bar{G}_A = \Delta G + (1 - x_A) \left( \frac{d \Delta G}{dx_A} \right)$	(8)
$\Delta \bar{G}_B = \Delta G - x_A \left( \frac{d \Delta G}{dx_A} \right)$	(9)
$\left( \frac{d \bar{G}_B}{dx_A} \right) = - \left( \frac{x_A}{1 - x_A} \right) \left( \frac{d \bar{G}_A}{dx_A} \right)$	(10)
$\left( \frac{d \Delta \bar{G}_B}{dx_A} \right) = - \left( \frac{x_A}{1 - x_A} \right) \left( \frac{d \Delta \bar{G}_A}{dx_A} \right)$	(11)

$$-\frac{1}{x_B^2} \left[ \Delta G^E + x_B \left( \frac{d \Delta G^E}{d x_A} \right) \right]$$

By Equation (6)

$$\Delta G^E + x_B \left( \frac{d \Delta G^E}{d x_A} \right) = \overline{\Delta G_A}^E$$

Thus

$$\overline{\Delta G_A}^E = x_B^2 \left[ 2 \left( \frac{\Delta G^E}{x_A x_B} \right) - I_0 \right] \quad (10)$$

Similarly

$$\overline{\Delta G_B}^E = x_A^2 \left[ 2 \left( \frac{\Delta G^E}{x_A x_B} \right) - I_1 \right] \quad (11)$$

In the limit as  $x_A$  approaches zero,  $x_B$  approaches unity, and  $\Delta G^E/x_A x_B$  approaches  $I_0$ . Thus by Equation (10)

$$\lim_{x_A \rightarrow 0} \overline{\Delta G_A}^E = (1)(2I_0 - I_0) = I_0 \quad (12)$$

In the limit as  $x_A$  approaches unity,  $\Delta G^E/x_A x_B$  approaches  $I_1$ .

By Equation (11)

$$\lim_{x_B \rightarrow 0} \overline{\Delta G_B}^E = (1)(2I_1 - I_1) = I_1 \quad (13)$$

The same derivation could be presented in terms of either  $G$  or  $\Delta G$  as well as  $\Delta G^E$ ; however  $G/x_A x_B$  and  $\Delta G/x_A x_B$  (except for the cases where  $\Delta G = \Delta G^E$ ) approach infinity at both  $x_A = 0$  and  $x_A = 1$ , and the method breaks down. This is not true of  $\Delta G^E/x_A x_B$ , which remains finite. This does not impose a practical limitation on the method, because data can always be easily converted to excess values.

At first thought it might seem that the determination of  $\overline{\Delta G_A}^E$  and  $\overline{\Delta G_B}^E$  by the method just described would be subject to errors of the same order as the usual method of tangent intercepts, because it too requires the graphical determination of the intercepts of tangents drawn to a curve; however this is not the case. The difference lies in the fact that the opposite intercepts come into play in the two cases. On the usual plot of  $\Delta G$  vs.  $x_A$  the intercept at  $x_A = 1$  is used to determine  $\overline{\Delta G_A}$ ; whereas on the plot of  $\Delta G^E/x_A x_B$  the intercept at

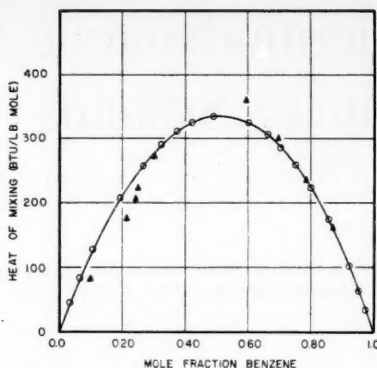


Fig. 2. Integral heat of mixing for the cyclohexane-benzene system: O, (5) Δ, (1)

$x_A = 0$  is employed. This is particularly well exemplified in the determination of the limiting values of  $\overline{\Delta G_A}^E$  at  $x_A = 0$  and  $\overline{\Delta G_B}^E$  at  $x_B = 0$ , that is, the partial properties at infinite dilution. These values are almost impossible to obtain accurately from the usual plot because of the long extrapolations required, but they are simply the intercepts of the curve of  $\Delta G^E/x_A x_B$  vs.  $x_A$  at  $x_A = 0$  and  $x_A = 1$ , as indicated by Equations (12) and (13).

The intercepts of the tangents drawn to the  $\Delta G^E/x_A x_B$  curve are of course subject to the normal errors involved in drawing tangents. However the uncertainty of an intercept increases as the distance of the point of tangency from the intercept increases, and it is clear from Equations (10) and (11) that the greater this distance, the smaller the number by which the intercept is multiplied. Since the multiplying factor  $x^2$  decreases as the uncertainty in  $I$  increases, the uncertainty in the  $\overline{\Delta G}^E$  values remains small.

Another advantage of drawing the  $\Delta G^E/x_A x_B$  plot is that it is a very sensitive indication of the precision of the data. If the data are of poor quality, this is usually obvious from the graph; if the data are reasonably good, this plot provides an excellent means of smoothing

them. In addition this plot shows at a glance whether sufficient data have been taken to allow the determination of partial properties with accuracy over the entire composition range.

These points are well illustrated by the data for the heats of mixing ( $\Delta H = \Delta H^E$ ) of the cyclohexane-benzene system. The data of Schnaible (5, 6) at 25°C. will be compared with those of Brown, Mathieson, and Thynne (1) at 20°C.

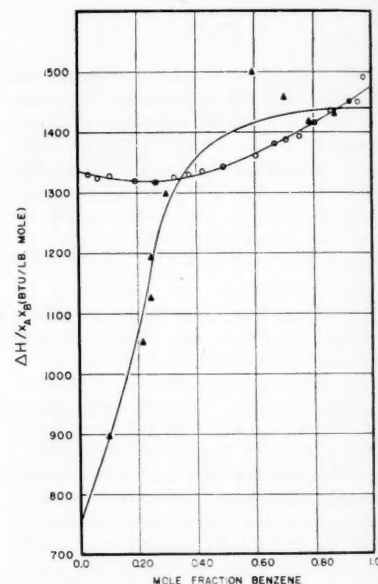


Fig. 3. The cyclohexane-benzene system: O, (5) Δ, (1)

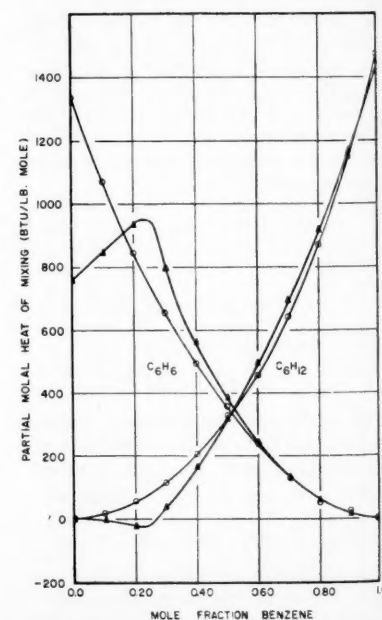


Fig. 4. Partial molal heats of mixing for the cyclohexane-benzene system: O, (5) Δ, (1)

TABLE 2. SUMMARY OF PROPERTIES

Property	$\Delta G$	$\overline{\Delta G_i}$
Volume ( $v$ )	$\Delta v = \Delta v^E$	$\overline{\Delta v_i} = \overline{\Delta v_i}^E$
Residual volume ( $\alpha$ )	$\Delta \alpha = -\Delta v$	
Compressibility factor ( $z$ )	$\Delta z = p \Delta v / RT$	
Internal energy ( $E$ )	$\Delta E = \Delta E^E$	$\overline{\Delta E_i} = \overline{\Delta E_i}^E$
Enthalpy ( $H$ )	$\Delta H = \Delta H^E$	$\overline{\Delta H_i} = \overline{\Delta H_i}^E$
Heat capacity ( $C_p$ or $C_v$ )	$\Delta C_p = \Delta C_p^E$	$\overline{\Delta C_{p,i}} = \overline{\Delta C_{p,i}}^E$
Entropy ( $S$ )	$\Delta S$	$\overline{\Delta S_i}$
Helmholtz free energy ( $A$ )	$\Delta A$	$\overline{\Delta A_i}$
Gibbs free energy ( $F$ )	$\Delta F$	$\overline{\Delta F_i}$
Excess entropy ( $S^E$ )	$\Delta S^E$	$\overline{\Delta S_i}^E$
Excess Helmholtz free energy ( $A^E$ )	$\Delta A^E$	$\overline{\Delta A_i}^E$
Excess Gibbs free energy ( $F^E$ )	$\Delta F^E$	$\overline{\Delta F_i}^E$
Function defined by Equation (9)	$\Delta F^E / RT$	$\ln \gamma_i$



This small temperature difference should have an insignificant effect on the data. Both sets of data are shown on Figure 2, a plot of  $\Delta H$  vs.  $x_{C_2H_6}$ , and on Figure 3, a plot of  $\Delta H/x_{C_2H_6}x_{C_2H_4}$  vs.  $x_{C_2H_6}$ . The data of Schnaible for this uncomplicated system are of obvious superiority, and the sensitivity of Figure 3 in showing inadequacies in the data is evident. Values of  $\Delta H_i$  for both components have been determined from Figure 3 by the method described for both curves shown. The partial molal heats of mixing (also called differential heats of mixing and partial relative enthalpies) so determined are shown in Figure 4.

For highly nonideal systems, for example methanol-benzene, plots of  $\Delta G^E/x_Ax_B$  vs.  $x_A$  may exhibit marked curvature. This curvature reduces the

precision with which slopes can be drawn and makes the extrapolation of the curve to the edges of the diagram uncertain. It is advantageous in such cases to plot the reciprocal function,  $x_Ax_B/\Delta G^E$  vs.  $x_A$ , as this often results in a much more nearly linear curve. The data for the methanol-benzene system plotted both ways are shown in Figure 5. The partial quantities are readily determined from the reciprocal plot by

$$\overline{\Delta G}_A^E = \frac{(x_B)^2 I_0}{\left(\frac{x_A x_B}{\Delta G^E}\right)^2} \quad (14)$$

$$\overline{\Delta G}_B^E = \frac{(x_A)^2 I_1}{\left(\frac{x_A x_B}{\Delta G^E}\right)^2} \quad (15)$$

These equations are derived in a fashion analogous to the derivations of Equations (10) and (11), and all the advantages previously described are retained. Here of course  $I_0$  and  $I_1$  are the intercepts on a plot of  $x_Ax_B/\Delta G^E$  vs.  $x_A$ .

Equations (7) and (8), the Gibbs-Duhem relationships for binary systems at constant temperature and pressure, are applicable to any of the properties listed in Table 2. This form of the Gibbs-Duhem equation is sometimes called the *slope test*, because it relates the slopes of curves of  $\overline{G}_A$  and  $\overline{G}_B$  or  $\overline{\Delta G}_A$  and  $\overline{\Delta G}_B$  vs.  $x_A$  at each value of  $x_A$ . In addition to the slope test there is an *area test*, which is directly applicable to data for  $\overline{\Delta G}_A$  and  $\overline{\Delta G}_B$ . This test has been presented in the literature for the special case of  $\ln \gamma_i$  data only. It is more convenient than the slope test but not so stringent and follows directly from Equation (8), which may be written

$$(1 - x_A) \left( \frac{d \overline{\Delta G}_B}{dx_A} \right) dx_A = x_A \left( - \frac{d \overline{\Delta G}_A}{dx_A} \right) dx_A$$

The two terms of this equation (on the left and right sides) represent the shaded areas shown on Figure 6. Integration from  $x_A = 0$  to  $x_A = 1$  will give the total areas under the two curves, and these must be equal for the area test to be satisfied. This result depends on the fact that the  $\overline{\Delta G}_A$  and  $\overline{\Delta G}_B$  curves start at zero at  $x_A = 1$  and 0 respectively. The mathematical expression for the area test is

$$\int_0^1 \overline{\Delta G}_A dx_A = \int_0^1 \overline{\Delta G}_B dx_A \quad (16)$$

which may also be written

$$\int_0^1 (\overline{\Delta G}_A - \overline{\Delta G}_B) dx_A = 0 \quad (17)$$

The easiest way to compare the two areas of Equation (16) is to determine the average ordinate for each curve by the graphical equivalent of Simpson's rule. It is also possible to plot the differences of the ordinates of the two curves vs.  $x_A$ . According to Equation (17) the area under this curve should be zero. As applied to  $\ln \gamma_i$  values,  $(\overline{\Delta G}_A - \overline{\Delta G}_B)$  becomes  $\ln \gamma_A/\gamma_B$ . This particular plot was proposed independently by Herington (3) and by Redlich and Kister (4).

There would seem to be little point in drawing this latter plot in most cases, because the area test can just as easily be made on the former plot (Figure 6) and examined for at least qualitative agreement with the slope test. It should be noted that the area test will automatically be met when the slope test is satisfied at all values of  $x_A$ . However the reverse is not true. It is entirely possible to have data which satisfy the area test, but not the slope test, and so it is not generally sufficient merely to adjust the curve of  $(\overline{\Delta G}_A - \overline{\Delta G}_B)$  vs.  $x_A$  to achieve zero area. There is no sure method of adjusting an inconsistent set of independently measured  $\overline{\Delta G}_A$  and  $\overline{\Delta G}_B$  values to get correct results.

If the original data are a set of  $\Delta G$  values, the Gibbs-Duhem equation assures thermodynamic consistency for the partial quantities, provided that the calculations are accurate. No objective test for the accuracy of such data is known. The two sets of results presented in Figure 3 illustrate this point. The partial molal heats of mixing calculated from both curves are shown in Figure 4. Both sets of data lead to thermodynamically consistent sets of results, which show merely the excellence of the procedure proposed for the calculation of partial quantities.

The measurements made by Donald and Ridgway (2) of the differential (or partial molal) heats of mixing for the cyclohexane-methylethylketone system provide an excellent example of the testing of data by the Gibbs-Duhem equation.

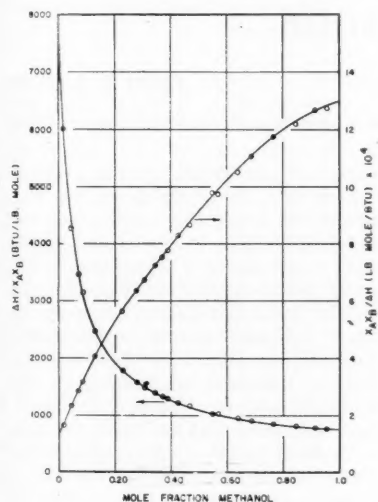


Fig. 5. The methanol-benzene system (5).

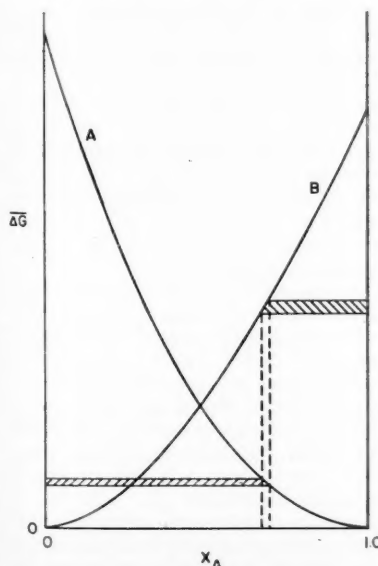


Fig. 6. Area test for thermodynamic consistency.

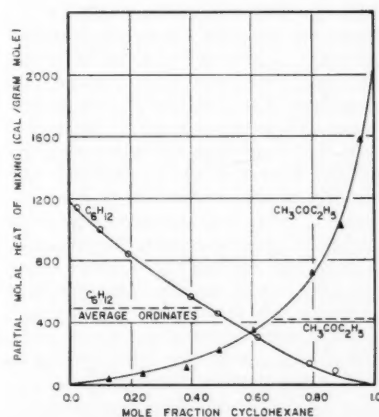


Fig. 7. Independently measured partial molal heats of mixing for the cyclohexane-methylethylketone system as reported by Donald and Ridgway (2).

tion. The independently measured values of  $\Delta \bar{H}_i$  for these components are plotted vs. mole fraction of cyclohexane in Figure 7. The area test shows them to be inconsistent and hence of uncertain accuracy. This test should always be applied to data of this sort.

#### NOTATION

$f_i$  = fugacity of pure  $i$  at the  $T$  and  $p$  of the solution  
 $\bar{f}_i$  = fugacity of component  $i$  in solution  
 $G$  = an extensive property of a binary system on a mole basis

$G_i$  = an extensive property of pure  $i$  on a mole basis  
 $I_0$  = an intercept at  $x_A = 0$   
 $I_1$  = an intercept at  $x_A = 1$   
 $x_i$  = mole fraction of component  $i$  in solution  
 $\gamma_i$  = activity coefficient of component  $i$  in solution =  $\bar{f}_i/x_i f_i$   
 $\Delta$  = designates a property change as a result of mixing at constant  $T$  and  $p$   
 $E$  = an excess property (superscript)  
 $-$  placed over the symbol for an extensive property designates the molal property in solution, that is, the partial molal property

#### LITERATURE CITED

1. Brown, C. P., A. R. Mathieson, and J. C. J. Thynne, *J. Chem. Soc. (London)*, 1230 (1955).
2. Donald, M. B., and Kenneth Ridgway *Chem. Eng. Sci.*, 5, 188 (1956).
3. Herington, E. F. G., *Nature*, 160, 610 (1947).
4. Redlich, Otto, and A. T. Kister, *Ind. Eng. Chem.*, 40, 345 (1948).
5. Schnaible, H. W., Ph.D. thesis, Purdue Univ., Lafayette, Ind. (1955).
6. ———, H. C. Van Ness, and J. M. Smith, *A.I.Ch.E. Journal*, 3, 147 (1957).

Manuscript received April 28, 1958; revision received November 17, 1958; paper accepted November 17, 1958.

# The Molecular Structure of Liquids

JOHN S. DAHLER

Aeronautical Research Laboratory, Wright Air Development Center

This survey presents a rather qualitative description of the present knowledge of liquid structure. The physical picture of this structure, which has been drawn from the interpretation of experimental data will be employed to explain and justify the theoretical methods necessary in the development of a more quantitatively reliable description of the liquid.

Understanding of liquids is much less complete than of the other states of matter. In the case of liquids there would appear to be no obvious element of simplicity comparable to the scarcity of molecular encounters in gases or of the small amplitudes of the thermal motions and high degree of spatial ordering in solids. Despite these difficulties an understanding of the liquid state is gradually emerging, and although knowledge is still far from complete, a qualitative and in some cases almost quantitative explanation of liquid behavior is within reach.

Simple nonassociated liquids of spherical, structureless molecules will be discussed. The interaction of two molecules will in this case depend only upon the distance between their centers. These interactions, together with the thermal motions of the molecules, are responsible for the changes in the physical state of matter that occur when the density and temperature are varied. Indeed it is the object of this survey clearly to describe the roles played by these two factors in the establishment of the detailed molecular structure of liquids.

In principle a precise description of the intermolecular forces can be determined by direct quantum mechanical calculations; however in all but the simplest cases the success of this approach

has been severely limited by mathematical difficulties. Therefore the interactions of most molecular species are actually obtained not from rigorous quantum mechanical arguments but from the semiempirical analysis of experimental data. An excellent account of these methods is included in the recent treatise of Hirschfelder, Curtiss, and Bird (1). Despite the many limitations, such methods give a fairly complete description of the intermolecular forces. Thus it is found that for small separations of the molecules these forces are of a strongly repulsive nature, suggesting the existence of a hard molecular core. When the intermolecular separation increases beyond the diameter of this rigid core, the forces between the two molecules become weakly attractive and tend rapidly to zero.

In liquids one is not usually concerned with the interaction of a single pair of molecules but rather with the potential energy of a molecule due to its simultaneous interactions with several of its neighbors. The total force upon such a molecule is assumed given by the vector sum of its individual and separate interactions with the others. Although the validity of this assumption is certainly suspect, very little information is presently available concerning the affects of nonadditive intermolecular forces upon the behavior of liquids. Moreover it is probably safe to say that the other approximations included in the existing theories of liquids are more serious in their consequences.

#### A DESCRIPTION OF LIQUID STRUCTURE

A precise microscopic description for the state of a liquid would include a

complete specification of the positions and motions for all the molecules. This description is not only complicated, but is wholly lacking in operational significance. One does not experimentally observe the behavior of separate molecules in the liquid but instead observes the heat capacity, thermal conductivity, viscosity, etc. Since these properties bear only a statistical relationship to the molecular-scale description of the liquid, real significance can be associated only with the average or most probable behavior of the molecules and not with a detailed specification of their individual motions. In principle this information can be determined directly from the methods of statistical mechanics; however in practice the success of the statistical approach will depend very largely upon the ability to ascribe a simple and at the same time realistic description to the average behavior of the molecules. Therefore attention is directed toward a qualitative description of liquid structure and the characterization of the molecular-scale processes responsible for the observed macroscopic properties of the liquid.

In the absence of a direct experimental procedure for obtaining this information one must construct a model of the liquid upon the basis of intuitive arguments, its success being judged by its ability to account for the physical properties of the liquid. The rules for constructing this model have changed very little since they were first announced in 1937 by Eyring and Hirschfelder (2).

In the search for a clue to the structure of liquids no single source of information has proved so valuable as the analysis of X-ray diffraction experiments. In these experiments one allows a monochromatic

John S. Dahler is now with the University of Minnesota, Minneapolis, Minnesota.

beam of X rays to fall upon the liquid and then measures the intensity of the scattered radiation as a function of the angle between the primary and secondary beams. The arrangement of the electrons in the liquid somewhat resembles a diffraction grating from which the X rays are scattered or deflected. More correctly this arrangement actually corresponds to two diffraction gratings, one with a spacing characterized by the distribution of the electrons within the individual molecules and another with the coarser spacing provided by the separations between neighboring molecules in the liquid. One may interpret the observed scattering of X rays by the liquid as the superposition of two separate interference patterns, one pertaining to the spatial arrangement of the molecules and the other to their internal electronic structures. Experimentally this decomposition of the diffraction pattern into its component parts can be accomplished by separate measurements upon the dilute vapor and the liquid itself. Thus as the density of the vapor is diminished, there will be a corresponding decrease in the interference of X rays scattered by different molecules. In the limit of infinite molecular dilution this sort of interference is completely absent, and the intensity of the scattered radiation depends upon the internal structure of the particular molecular species present and upon the variable,  $s = (2/\lambda) \sin(\theta/2)$ . Therefore by measurements upon the dilute vapor one can directly obtain that contribution to the diffraction pattern of a liquid which arises from the internal structures of the molecules.

The spatial arrangement or mutual disposition of the molecules may be formally described by the pair distribution function, defined as the probability that the distance between two molecules has the magnitude  $r$ . An alternative interpretation of this function is provided by the observation that  $2\pi n^{(2)}(r)r^2 dr$  gives the number of molecular pairs per unit volume whose separations lie between  $r$  and  $r + dr$ . In terms of this function the intensity of radiation scattered by the liquid can be written as  $J(s) = J_0(s) \cdot E(s)$ , where

$$E(s) = 1 + n^{-1} \int_0^\infty [n^{(2)}(r) - n^2] \frac{\sin(sr)}{sr} 4\pi r^2 dr \quad (1)$$

In the limit of infinite dilution, correlations among the positions of the molecules vanish, and the pair distribution function approaches  $n^2$  as a limit. The factor  $E(s)$  then tends to a value of unity, and the experimental scattering is fully described by  $J_0(s)$ . In liquids  $E(s)$  exhibits considerable departure from unity, an indication that the pair distribution function is no longer given by its

limiting value. This much can be immediately deduced from (1), but a direct evaluation of the pair distribution function from experimental determinations of  $E(s)$  is desired. A way to accomplish this was first suggested by Debye, who found that by Fourier inversion of (1) the pair distribution function could be related to the experimental scattering data according to the relationship

$$n^{(2)}(r) = n^2 + \frac{n}{2\pi^2 r} \quad (2)$$

$$\cdot \int_0^\infty [E(s) - 1] s \sin(sr) ds$$

Therefore by numerical integration of (2) one can construct the pair distribution function from the experimental values of  $E(s)$ . Curves of the radial distribution function  $g(r) = n^{(2)}(r)/n^2$  ob-

shows that the location of the first peak in  $g(r)$  practically coincides with that for the solid. Furthermore the very existence of these pronounced first peaks in  $g(r)$  proves that a certain amount of local or short-range order persists even in the liquid. The broad and rather diffuse appearances of these peaks show that this local order is by no means so well defined as it is in the solid phase. A further distinction between the local structures of liquids and solids is to be found in the actual number of neighbors surrounding a particular molecule. By measuring the areas beneath the various peaks of  $g(r)$ , Eisenstein and Gingrich have calculated the occupancy of the first two shells of neighbors in liquid argon. Their results, obtained by measurements upon the curves of Figure 1, are presented in Table 1.

TABLE 1

°K.	First peak distance, Å	First peak occupancy	Second peak distance, Å	Second peak occupancy
(crystal)	3.82	12	5.4	(6)
84.4	3.79	10.5	5.3	
91.8	3.79	7	4.7	4
144.1	3.8	(4.2)	5.4	
149.3	4.5	6		
(vapor)	4.1	2		

tained in this manner are given in Figure 1. These curves describe the radial disposition of neighbors about a typical molecule in the liquid. The peaks in  $g(r)$  indicate the most probable locations of these neighbors, and the integral  $\int_0^{r_1} 2\pi n^2 g(r) r^2 dr$  gives the number lying within a spherical shell of radii  $r_1$  and  $r_2$  about the central molecule.

The indistinctness of all but the first of these peaks testifies to the absence in liquids of the long-range order or regularity characteristic of crystalline solids. Of course it is just the loss of this long-range order which is associated with the process of melting. The transition from the highly ordered arrangement in the solid to the less rigid, fluid structure of the liquid results from the disrupting effect of the molecular motions, since as the temperature of the solid rises past its melting point, the intermolecular forces responsible for the rigidity of the crystalline lattice must give way before the increasingly violent thermal motions of the molecules. Fusion occurs when the molecules occasionally acquire sufficient thermal energy to overcome the confining field of their neighbors and wander away from their former locations in the crystalline lattice.

Despite the translational freedom acquired upon melting, a molecule in the liquid will still find its motions severely restricted by the presence of neighboring molecules. The density of a solid and its melt usually differ so little that the mean distance between molecules must remain almost unchanged upon fusion. Figure 1

These data illustrate that even near the melting point (84°K.) the occupancy of the shells is somewhat less than in the solid. As the temperature is further elevated, the number of neighbors decreases progressively until, at the critical point (151°K.), the first shell is scarcely half full. Consequently the translational motions of the molecules will be less and less hindered as the temperature of the liquid rises. This accounts for the characteristic increase in the fluidity of liquids, which always accompanies a rise in temperature.

It seems quite unlikely that in liquids the geometrical disposition of the neighboring molecules should retain much evidence of the intricate lattice structure of the solid. In fact one may safely assume that the grosser molecular motions in the liquid will obliterate these finer geometrical features and give rise to a more or less spherically symmetrical distribution of neighbors about the central molecule.

This discussion suggests a cell-like description for the structure of the liquid. Thus for short intervals of time one may picture a molecule as trapped within a sort of shell-like arrangement of its neighbors. The thermal motions of the molecule will then be temporarily limited to oscillations about the center of the cell or cage to which it is confined. Of course the molecules are moving far too rapidly for this local structure to persist over the intervals of time required for the usual performance of experimental observations. The cellular



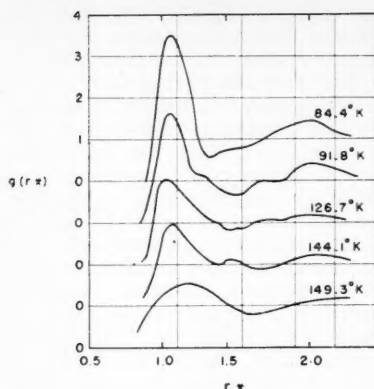


Fig. 1. Experimental curves of the radial distribution function in liquid argon. Curves are functions of the reduced distance  $r^* = r/\sigma$ , where  $\sigma = 3.42$  Å. (33, 34). The vertical traces give the locations of the neighbors in solid argon.

description of liquids is therefore introduced only in the hope of providing a simple explanation for the average motions of the molecules and is not intended as a static description of the liquid structure. Thus the utility of this description will depend upon whether the cellular structure can maintain its identity over periods of time which are significantly longer than the interval between successive collisions of a molecule with its neighbors. (In liquids this interval is about  $10^{-12}$  to  $10^{-14}$  sec.) At first thought it might be imagined that each collision of the central molecule with one of its neighbors would result in the destruction of the local structure. This conclusion must be modified however because of the lagging response of the neighbors to the rapidly changing position of the central molecule. To find the cause for this viscous retardation of the molecular motions one need only observe that each neighbor to a particular molecule is itself surrounded by neighbors of its own. Therefore the dislodgment of a molecule from its position in a shell of neighbors is strongly resisted by the restraining actions of these other molecules. In this way the collective behavior of the molecular motions tends to stabilize briefly the cellular structure of the liquid. A major disruption of this local order will then occur only when a molecule finally accumulates, by repeated collisions with its neighbors, a sufficient excess of kinetic energy to overcome fully their confining influences. On the molecular scale of time mentioned above such a catastrophic event should occur rather infrequently, and even when it does the escaping molecule can proceed but a short distance through the liquid before its excess energy is lost and it once again lies trapped within a new shell of neighboring molecules.

From this discussion one sees that the

wanderings of the molecules, as they move from cell to cell throughout the liquid, closely resemble the random motions of Brownian particles. The validity of this conclusion has been established by the detailed theoretical analysis of Kirkwood (3), who, proceeding from a fundamental statistical approach, was able to show that the average motions of a molecule in the liquid are indeed governed by precisely the same dynamical equations that describe the Brownian motions of colloidal particles. He then demonstrated that this description of the molecular motions can be transformed into a theoretical method of obtaining the transport coefficients in liquids, that is the viscosity, thermal conductivity, and diffusion coefficients. It should be mentioned, that the essential success of this approach lends further support to this simple picture of the molecular-scale processes in liquids.

A simpler and less refined theory of irreversible processes in liquids has been suggested by Eyring (4). In his development the transport coefficients are calculated by a more direct appeal to the cellular structure of the liquid. As a brief illustration of Eyring's scheme the viscous flow resulting from the imposition of an external shear upon the fluid will be considered. In adjusting their motions to this shearing force the molecules must flow past one another. However a particular molecule can join in this flow only if it possesses an energy sufficient to escape from its cell of neighbors. From simple statistical arguments it is known that the probability that a molecule will have this much energy will be proportional to the Boltzmann factor,  $\exp(-E/kT)$ . This factor is in turn proportional to the actual number of molecules participating in the flow and hence to the fluidity of the liquid. Thus the resistance of the liquid to the impressed shear (the viscosity of the liquid) will vary as  $\exp(E/kT)$ . Experimentally it is found that the viscosity of most liquids is well represented by the empirical Andrade equation  $\eta = A \exp(B/T)$ , and so the qualitative realism of Eyring's simple arguments seems assured. The quantitative success of this theory does of course depend upon the accuracy with which one can predict the coefficients occurring in Andrade's equation. Although no truly satisfactory means of performing these calculations have yet been discovered, the qualitative predictions of this theory do offer strong evidence in favor of the cellular description for the liquid.

The remainder of this survey will be devoted to the determination of the thermodynamical behavior of liquids. For this purpose one is more interested in the average arrangements and environments of the molecules than in their grosser motions through the liquid. Thus the brief and rather infrequent transits of

the molecules from one cell to another should have very little influence upon the description of the average arrangement of the molecules in the liquid. To be sure the disorder arising from these random flights is responsible for the rather large entropy of the liquid, but in calculating the internal energy and equation of state one should be able to ignore these gross molecular displacements and limit his attention to the average potential energy of a molecule confined within its shell of neighbors.

## THE THEORY OF LIQUIDS

In the previous section it was illustrated that the extent to which the individual molecules participate in the transfer of momentum, heat, and mass through the liquid will depend upon the average spatial arrangement of neighbors about these molecules. Thus any fundamental approach to transport phenomena should be based upon or include a complete description of the local structure in the liquid. The nonequilibrium conditions giving rise to transport phenomena result in distortions of this molecular structure, thereby introducing complications not present at thermodynamical and mechanical equilibrium. Accordingly it seems practical first to investigate the undistorted structure of a liquid at equilibrium, not only as a first step in the study of transport phenomena but also as a means of calculating the thermodynamical properties and equation of state for the liquid. Thus the remainder of the paper is a summary of the theoretical methods which have been developed to characterize the structure of liquids in equilibrium. These theoretical schemes fall into two categories: the first a direct attempt to calculate the pair distribution function and the other a more intuitive approach based upon previous cellular description of the liquid.

Both the thermal motions of the molecules and their interactions will certainly contribute to the thermodynamical description of the liquid. The effects stemming directly from the thermal motions are however so simple to calculate that one need really be concerned solely with the structural or configurational contributions arising from the molecular interactions. Thus from elementary considerations one knows that the average kinetic energy of a molecule will be  $3kT/2$  and that the thermal motions alone provide a contribution of  $nkT$  to the static pressure of the liquid; the effects of thermal motions upon the other thermodynamical properties can be easily derived.

### The method of the pair distribution function and the superposition principle

From the previous definition of  $n^{(2)}(r)$  it follows that the average potential energy of a molecule is given by



$$n^{-1} \int_0^\infty \varphi(r) n^{(2)}(r) \cdot 2\pi r^2 dr$$

(These arguments are subject to the assumption of pair-additive molecular interactions mentioned in the introductory remarks.) Consequently the thermodynamical internal energy per molecule may be written as

$$u = 3kT/2 + 2\pi n \int_0^\infty \varphi(r) g(r) r^2 dr \quad (3)$$

In a similar manner the virial theorem of mechanics can be transformed into the equation of state

$$p = nkT - \frac{2\pi}{3} n^2 \int_0^\infty g(r) \frac{d\varphi(r)}{dr} r^3 dr \quad (4)$$

These two relationships, together with a similar expression for the chemical potential, provide a complete description of the thermodynamical behavior of the liquid in terms of the radial distribution function and the potential of the intermolecular forces. From this it might be concluded that the experimentally determined curves for  $g(r)$  could be used to calculate the thermodynamical properties of the liquid. In practice this procedure is not too satisfactory, since the experimental measurements fail to possess the high degree of accuracy required for quantitative calculations.

An alternative scheme, involving the theoretical evaluation of  $g(r)$ , is one of the most ambitious and formidable objectives of the theory of liquids. [The requirements placed upon a quantitative theory of the radial distribution function are likely to be quite stringent since calculations based upon (3) and (4) are rather sensitive to minor variations in  $g(r)$ .] The development of such an exact theory has been prevented by enormous mathematical difficulties. Although exact integral equations for the pair distribution

function can be derived, these equations also involve  $n^{(3)}(r_{12}, r_{13}, r_{23})$ , the generalization of the pair distribution function to the case of three molecules; that is,  $n^{(3)}$  is the probability that three molecules will be so located that their separations are given by  $r_{12}$ ,  $r_{13}$ , and  $r_{23}$ . In turn the integral equation for  $n^{(3)}$  includes the distribution function for a set of four molecules, etc., *ad infinitum*. An exact solution of this set of coupled integral equations is of course completely out of the question, and some approximate means of terminating the sequence must be invoked. The only approximation of this sort that has received serious attention is the so-called "superposition principle," which asserts that

$$n^{(3)}(r_{12}, r_{13}, r_{23}) = n^{(2)}(r_{12}) \cdot n^{(2)}(r_{13}) \cdot n^{(2)}(r_{23}) / n^3 \quad (5)$$

When this relationship is substituted into the equation coupling  $n^{(3)}$  and  $n^{(2)}$ , an ordinary integral equation for the pair distribution function is obtained. However owing to the approximations involved in (5) the precise manner in which this substitution is to be effected cannot be uniquely specified. Thus use of the superposition principle has led to two different equations for the pair distribution function, one proposed by Kirkwood (5) and the other by Born, Green, and Yvon (6, 7). The two equations can be solved by numerical methods and their results used for the calculation of the thermodynamical properties of the liquid. The differences in the predictions of the two methods will then provide a crude measure of the error produced by the superposition principle. Extensive calculations based upon these equations have been carried out by Kirkwood and coworkers.

If the distance between molecules 1 and 2 is assigned the value  $r_{12}$ , one may then ask for the probability that a third molecule is so located that its separations from the first two are given by  $r_{13}$  and  $r_{23}$ , respectively. This conditional probability may be constructed from a knowledge of  $n^{(3)}$  and  $n^{(2)}$  and written in the form  $n^{(3)}(r_{12}, r_{13}, r_{23}) / n \cdot n^{(2)}(r_{12})$ . A geometrical illustration of the situation is provided by Figure 2, where the third molecule has been pictured as lying at the center of two concentric spheres of radii  $r_{13}$  and  $r_{23}$ .

According to the superposition principle one should assign equal probabilities to all arrangements of the three molecules, for which the first lies anywhere upon the sphere of radius  $r_{12}$  and the second anywhere upon the sphere of radius  $r_{23}$ . More precisely the conditional probability defined above is assumed to be independent of the value for  $r_{12}$  and given by the product of  $n^{(2)}(r_{13})/n^2$  and  $n^{(2)}(r_{23})$ . This assumption is completely equivalent to replacing the conditional probability by its average over all ar-

rangements of the molecules for which the distances  $r_{13}$  and  $r_{23}$  are held fixed.

In the case of dilute gases this is a valid approximation, and its use leads to correct values for the second and third virial coefficients. Although this correct limiting behavior certainly lends an air of respectability to the approximation, it does not indicate the general validity of the superposition principle. Indeed direct calculations of the thermodynamical properties and equation of state for the liquid based upon this principle provide virtually the only means presently available for testing its validity. A rough estimate of its limit of applicability can be inferred however from the observation that the predicted expressions for the fourth and higher-order virial coefficients are only approximately correct.

Kirkwood, Maun, and Alder (8) have calculated the radial distribution function and the thermodynamical properties for a liquid composed of rigid spheres. Their results for the equation of state are shown in Figure 3, where  $v_0 = \sigma^3/\sqrt{2}$  is the specific volume at closest packing of the spheres. The predictions of the Kirkwood and of the Born, Green, Yvon theories are scarcely distinguishable at the low densities for which the superposition principle is known to be valid; at higher densities the agreement is less satisfactory.

They found that at  $v/v_0 = 1.24$  (or at  $v/v_0 = 1.48$  for the Born, Green, Yvon theory) an abrupt change occurred in the analytical behavior of the radial distribution function. Kirkwood, Maun, and Alder interpreted this transition as evidence of a high-density limit of stability for the liquid phase. If this conclusion is correct, then for higher densities a crystalline phase should be more stable than the liquid. During the past few years there has been wide-spread disagreement concerning the physical significance of these results and the capability of a fluid of rigid spheres to crystallize. On the one side it has been argued that the phase transition predicted by the theory is of no real significance and occurs only because of the approximate nature of the superposition principle. However recent evidence indicates that such a transition really does occur. Thus by employing the Monte Carlo method (to be described later in the text) Wood and Jacobson (9) have experimentally confirmed the existence of a high-density phase transition in a fluid of rigid spheres. Their results, which are substantiated by the independent researches of Alder and Wainwright (10), indicate that there is a sharp discontinuity in the isotherms at a reduced volume of about  $v/v_0 = 1.5$  (see Figure 4).

Calculations based upon a more realistic choice for the intermolecular forces have been performed by Kirkwood, Levinson, and Alder (11), who assumed that the interaction energy was given by

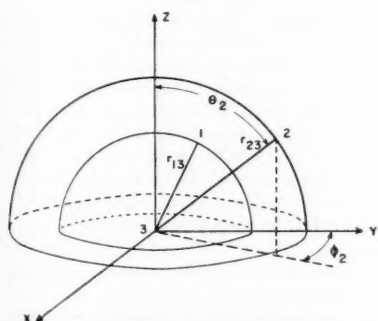


Fig. 2. A geometrical representation of the spatial configuration for three molecules. Molecule 3 has been chosen to lie at the origin of a Cartesian coordinate frame; the other two molecules are located on the surface of two spheres of radii  $r_{13}$  and  $r_{23}$ .

$$\varphi(r) = 4\epsilon[(\sigma/r)^{12} - (\sigma/r)^6]; r \geq \sigma \quad (6)$$

$$+\infty; r < \sigma$$

which for separations greater than the hard-core diameter reduces to the familiar Lennard-Jones 12-6 law. In Figure 5 the results of their calculations are compared with the experimentally determined radial distribution function in liquid argon.

In Figure 6 the experimentally determined equation of state for argon is compared with the theoretical predictions of Kirkwood, Levinson, and Alder. Although the agreement at low density is fairly good, it becomes very unsatisfactory at high densities. This behavior may well reflect the inadequacy of the superposition principle.

The qualitative successes of these calculations lead to the conclusion that, despite its many limitations, the principle of superposition gives a surprisingly realistic picture of the local molecular arrangement in liquids. This provides ample incentive for further investigations directed toward the discovery of an approximation which would retain the qualitative realism of the superposition principle and, at the same time, admit a higher degree of quantitative success. Although progress along these lines has been limited, the recent studies of Mazur and Oppenheim (12) may well result in such a discovery.

From this discussion one sees that the method of the radial distribution function is a formal mathematical approach to the theory of liquids, deriving little benefit from the qualitative considerations presented at the beginning of this survey. This suggests that in the absence of a thoroughly satisfactory theory of the radial distribution function efforts should be directed toward the development of a theory based upon a more direct appeal to an intuitive model for the liquid. This conclusion undoubtedly accounts for the numerous attempts in recent years to work improvements upon the so-called "cell" or "free-volume" theories of the liquid phase.

#### The cell theory of liquids

The cell theory of liquids stems from the pioneering studies of Eyring and

$$U_N = 3NkT/2 + \int_V \int_V \cdots \int_V \Phi_N \cdot W_N d\tau_1 d\tau_2 \cdots d\tau_N / \int_V \int_V \cdots \int_V W_N d\tau_1 \cdots d\tau_N \quad (7)$$

$$= 3NkT/2 + kT^2(\partial \ln Q_N / \partial T)_V$$

Hirschfelder. Their investigations together with those of Lennard-Jones and Devonshire revealed that a fairly satisfactory theory could be developed from the simple and qualitative picture of liquid structure presented earlier in

this survey. However these early studies were based almost solely upon intuitive reasoning, and so it was not until 1950 that a rigorous mathematical justification of the cell theory was established. This important achievement by Kirkwood (13) has been instrumental in reviving interest in the cell theory of liquids. Thus during the past 6 or 7 years there have been several significant advances in the development of this method.

Since the modern adaptations of the cell method are all little more than elaborations upon Kirkwood's original approach, a brief review of his analysis will be given. To establish the relationship between this theoretical development and the previous qualitative arguments it becomes necessary to transform the intuitive description of liquid structure into a mathematical representation. As a first step in this direction a more quantitative description of the probability of a particular arrangement of the molecules in the liquid is established by associating with each molecular configuration the corresponding value for

$$\Phi_N = \frac{1}{2} \sum_{i=1}^N \sum_{j \neq i=1}^N \varphi(r_{ij})$$

the total potential energy of the  $N$  molecules. The probability of a molecular configuration will then be proportional to the Boltzmann factor  $W_N = \exp(-\Phi_N/kT)$  that is associated with that particular spatial arrangement. Hence the most probable dispositions of the molecules are those for which the total potential energy lies near its minimum value.

Now it is a further consequence of the statistical mechanics that each molecular configuration contributes to the thermodynamical description of the liquid only in proportion to its probability of occurrence. Thus the average potential energy will be given by

$$\frac{\int_V \int_V \cdots \int_V \Phi_N \cdot W_N d\tau_1 d\tau_2 \cdots d\tau_N}{\int_V \int_V \cdots \int_V W_N d\tau_1 d\tau_2 \cdots d\tau_N}$$

It then follows that the thermodynamical internal energy may be written as

$$Q_N = \frac{1}{N!} \int_V \int_V \cdots \int_V W_N \cdot d\tau_1 d\tau_2 \cdots d\tau_N \quad (8)$$

is the so-called "configuration integral."

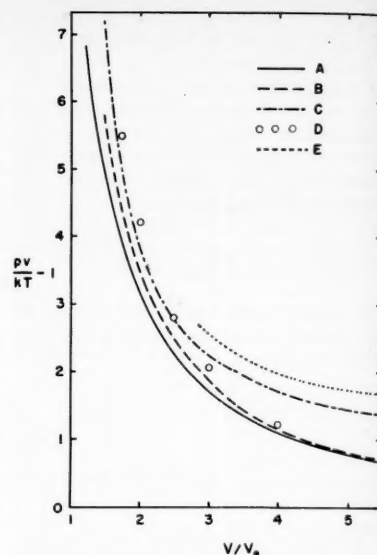


Fig. 3. Equation of state for rigid spheres: A, Kirkwood theory; B, Born, Green, Yvon theory; C, Lennard-Jones and Devonshire cell theory; D, Monte Carlo; E, cell-cluster theory (double-cell approximation).

By similar considerations it can be established that the other thermodynamical properties are functions of this same configuration integral; for instance the Helmholtz free energy or the work function is related to  $Q_N$  in the manner

$$A_N = 3NkT/2 \ln(h^2/2\pi mkT) - kT \ln Q_N \quad (9)$$

From this relationship one sees that the equation of state has the form

$$p = -(\partial A_N / \partial V)_T = kT(\partial \ln Q_N / \partial V)_T \quad (10)$$

These results illustrate the importance of  $Q_N$  in determining the thermodynamical properties of the liquid. If one should succeed in calculating this configuration integral, he would then possess a completely rigorous theory of the liquid. (Of course this would also be true if an exact value for the pair distribution function discussed previously could have been obtained.) Actually to perform the  $3N$ -fold integration of Equation (8) is of course an impossible task, and one must therefore content himself with an approximate evaluation of this complicated integral. It is in the performance of this approximate calculation that the previous qualitative description of liquid structure can be of immense value. Thus one may hope to characterize intuitively those molecular arrangements that will make significant contributions to the configuration integral and to disregard those of minor importance.

Were the liquid frozen, then, since each molecule would be constrained to lie near

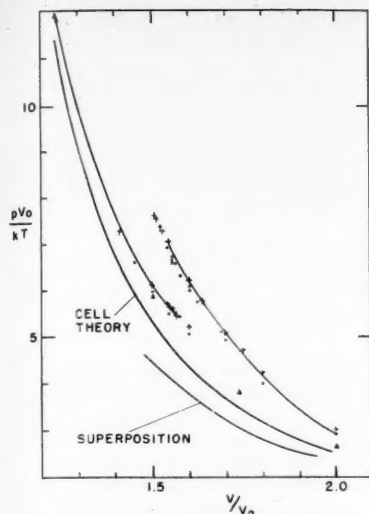


Fig. 4. Equation of state for rigid spheres. The unlabeled solid curve represents Alder and Wainwright's 108-molecule results; +, their 32 molecule results. ● and ▲ respectively represent the Wood and Jacobson and the Rosenbluth and Rosenbluth Monte Carlo results.

a particular site of the crystalline lattice, the volume of the system could be divided into  $N$  identical cells so arranged that the center of each is located at a site of the lattice. As the crystal is permitted to melt, one should expect that the local structure will retain a portion of its original identity, although to be sure the arrangement of neighboring molecules will lose much of its former rigidity. The more statistically favored arrangements of the molecules will certainly be those for which each cell is occupied by a single molecule. However one cannot completely exclude those configurations for which one or more cells are multiply occupied. It is the essence of Kirkwood's method to order these various arrangements according to their relative importance in determining the average structure of the liquid.

If the  $N$  cells are labeled  $\Delta_1, \Delta_2, \dots, \Delta_N$ , each integration involved in Equation (8) can be written as a sum of integrals extending over the individual cells; for example

$$\int_V d\tau_i = \sum_{h_i=1}^N \int_{\Delta_{h_i}} d\tau_i$$

The configuration integral may then be written as the sum of  $N^N$  terms corresponding to the  $N^N$  different ways of placing  $N$  molecules in  $N$  cells.

$$Q_N = (N!)^{-1} \sum_{h_1=1}^N \sum_{h_2=1}^N \dots \sum_{h_N=1}^N \int_{\Delta_{h_1}} \int_{\Delta_{h_2}} \dots \int_{\Delta_{h_N}} W_N \cdot d\tau_1 d\tau_2 \dots d\tau_N \quad (11)$$

Each term in this multiple summation may be characterized by the number of molecules assigned to the individual cells. Thus a typical term is labeled  $Q_N(m_1, m_2, \dots, m_N)$ . Since the total number of molecules is  $N$ , each set of occupation numbers  $\{m\} = (m_1, m_2, \dots, m_N)$  will be subject to the condition  $N = \sum_i m_i$ . Furthermore because the molecules are indistinguishable from one another, there will generally be several terms in (11), each of which corresponds to the same set of occupation numbers. In fact it is not difficult to show that for a given set  $m_1, m_2, \dots, m_N$  there will be precisely  $N!/\prod_i m_i!$  equivalent terms in (11). Consequently one may rewrite this expression

$$Q_N = \frac{\sum_{\{m\}} Q_N(m_1, m_2, \dots, m_N)}{(\prod_i m_i!)} \quad (12)$$

$$= \bar{\sigma}^N Q_N^{(1)}$$

where

$$Q_N^{(1)} = Q_N(1, 1, \dots, 1) \quad (13)$$

and

$$\bar{\sigma}^N = \sum_{\{m\}} (\prod_i m_i!)^{-1} \cdot Q_N(m_1, m_2, \dots, m_N)/Q_N^{(1)} \quad (14)$$

The function  $Q_N^{(1)}$  describes the most important contribution to the configuration integral, namely the molecular arrangement for which each cell is singly occupied. The term  $\bar{\sigma}^N$  represents the effects due to the other less probable configurations of the molecules. At very high densities the repulsive forces between the molecules eliminate the possibility of multiply occupied cells, and so only the configuration  $\{m\} = (1, 1, \dots, 1)$  can contribute to the summation in (14). In this limit  $\bar{\sigma}$  becomes equal to unity. On the other hand in the limit of infinite dilution the cells grow so large that all occupancies occur with equal probability. Furthermore in this limit each of the

entropy. It is therefore quite obvious that  $\bar{\sigma}$  provides an index to the degree of order present in the system. Since it was this same molecular disorder which was previously associated with the Brownian motions of the molecules, it follows that  $\bar{\sigma}$  will also describe the ease with which the molecules move from cell to cell within the liquid.

$\bar{\sigma}$  is a slowly varying function of density, rising monotonically from a value of unity in the crystal to a value  $e \doteq 2.7$  at infinite molecular dilution; moreover,  $\bar{\sigma}$  probably will have an equally weak dependence upon the temperature. Therefore this function should be of little importance in determining the equation of state or the internal energy of the liquid. [From Equations (7) and (10) one sees that  $p$  and  $U_N$  depend only upon the derivatives of  $\bar{\sigma}$  with respect to density and temperature.] One may thus conclude that it is  $Q_N^{(1)}$  which will be principally responsible for these properties of the liquid. This conclusion provides a theoretical justification for the previous characterization of the most probable molecular arrangements in the liquid. Except in the calculation of the entropy one may confine his attention to those configurations for which each cell is singly occupied. It is only when the entropy is calculated that the possibility of multiply occupied cells must be considered. At liquid densities one is almost certain that there will be little contribution to the summation in (14) from cells that are more than doubly occupied. Owing to this simplification the calculation of  $\bar{\sigma}$  for liquids is by no means an impossible task. Although no truly adequate calculations have yet been performed, the exploratory work of Pople (14) has been very useful in obtaining a qualitative estimate for the behavior of  $\bar{\sigma}$ . By employing several approximations he found that for a liquid composed of rigid sphere molecules this factor depends upon density in the manner shown by Table 2.

TABLE 2. THE DENSITY DEPENDENCE OF THE DISORDER PARAMETER IN A LIQUID OF RIGID SPHERES

$v/v_0$	1.000	4.887	7.761	10.0	15.0	20.0	$+\infty$
$\bar{\sigma}$	(1.000)	1.04	1.34	1.57	1.86	1.99	(2.414)

$Q_N(m_1, m_2, \dots, m_N)$  separately approaches a value of  $v^N$ . Therefore

$$\bar{\sigma}^N = \sum_{\{m\}} (\prod_i m_i!)^{-1} = e^N$$

and  $\bar{\sigma}$  has the limiting value of  $e$ .

The contribution of  $\bar{\sigma}$  to the entropy of the liquid is given by  $Nk \ln \bar{\sigma}$ . In the limit of high density the molecules are rigidly confined within their cells, and this entropy contribution vanishes. At infinite dilution, however, the molecules are completely free to lie anywhere within their container, and  $\bar{\sigma}$  makes a contribution of  $Nk = R$  e.u./mole to the

It should be mentioned that in place of the correct value  $e \doteq 2.7$  these calculations predict a low density limit of  $\bar{\sigma} \doteq 2.414$ . This error is not very significant however and simply reflects the neglect of cells which are occupied by three or more molecules. It is much more interesting to see that  $\bar{\sigma}$  remains very near unity until the specific volume becomes about five times that for the close-packed lattice. Thus Pople concluded that the entropy contribution  $Nk \ln \bar{\sigma}$  will be practically zero for the liquid. It seems quite probable that a similar behavior would be observed for more realis-



tic choices of the intermolecular forces. In the absence of any contrary proof one may accept this conclusion and assume that  $\bar{\sigma}$  maintains an almost constant value of unity throughout the entire range of liquid densities.

To calculate  $Q_N^{(1)}$  one must carry out the integration of Equation (8) subject to the condition that each cell contains but one molecule. To perform this calculation exactly would be almost as difficult as the direct evaluation of the configuration integral itself. However one is guided by symmetry arguments and intuitive reasoning to envision a rather simple picture of the situation. Since each molecule is subject to precisely the same environmental conditions, a description of the situation within one particular cell should be equally applicable to any other. Although this is not meant to imply that the positions of molecules in adjacent cells are independent of one another, it does suggest the probability distribution may be chosen to be the same in each cell of the liquid. The simplest but by no means the only way in which this statement can be mathematically formulated is to assume that the probability distribution function inside the  $i$ th cell depends only upon the coordinates of the molecule confined within it. Thus Kirkwood suggested that the probability distribution function within a cell be represented by a function which depends only upon the vector displacement of a molecule from the center of its cell. Since each molecule lies within a single cell, this function must satisfy the normalization condition  $\int_{\Delta} s(\mathbf{r}) d\tau = 1$ . This assumption closely resembles the superposition principle. Thus the probability for the indicated configuration of molecules 1 and 2 should be proportional to  $\kappa^{(2)}(r_{12})$ ; however this probability is taken to be  $s(\mathbf{r}_1) \cdot s(\mathbf{r}_2)$ . As in the case of the superposition principle the adequacy of such an approximation can be judged only by its success in accounting for the observed physical properties of the liquid.

In accordance with this approximation the average potential energy of molecule 1 due to its interactions with all the others is

$$\Phi(\mathbf{r}_1) = \sum_{j=1}^N \int_{\Delta_j} s(\mathbf{r}_j) \varphi(r_{1j}) d\tau_j \quad (15)$$

Furthermore all the thermodynamical properties can be expressed as integrals of  $s(\mathbf{r})$ , that is as functionals of  $s(\mathbf{r})$ . For instance the configurational contributions to the entropy and internal energy are

$$S_N^{(1)} = -Nk \int_{\Delta} s(\mathbf{r}) \ln s(\mathbf{r}) d\tau \quad (16)$$

$$\begin{aligned} U_N^{(1)} &= (N/2) \int_{\Delta} s(\mathbf{r}) \Phi(\mathbf{r}) d\tau \\ &= (N/2) \cdot U_0(v, T) \end{aligned} \quad (17)$$

where terms involving  $\bar{\sigma}$  have not been included.

To calculate the values of these thermodynamical properties one must first prescribe the function  $s(r)$ . The better the choice of this function, the better will be the resulting description of the liquid. However since correlations among the

positions of the molecules have been neglected, no choice of this function can ever give an exact description of the molecular arrangement characterizing the equilibrium state of the liquid. Thus each function  $s(\mathbf{r})$  must necessarily describe a nonequilibrium state of the system, and from the principles of thermodynamics one knows that the degree to which a particular state of the system departs from equilibrium is reflected by the corresponding value for the Helmholtz free energy. The nearer the system lies to thermodynamical equilibrium, the lower will be the associated value of this free energy. Therefore the optimum choice for the distribution function should be that for which the Helmholtz free energy is a minimum. When this minimization is actually carried out, one finds that the optimum function is given by the solution to the integral equation,

$$s(\mathbf{r}) = v_f^{-1} \cdot \exp(-\psi(\mathbf{r})/kT) \quad (18)$$

where  $\psi(\mathbf{r}) = \Phi(\mathbf{r}) - U_0(v, T)$  and  $v_f$  is defined by

$$v_f = \int_{\Delta} \exp(-\psi(\mathbf{r})/kT) d\tau \quad (19)$$

Until very recently solutions for the integral Equation (18) had been demonstrated in only two instances: for rigid spheres and for molecules bound to one another by harmonic forces. In the case of rigid spheres, each of diameter  $\sigma$ , if the lattice chosen for the calculations is taken to be the face-centered cubic arrangement, the unit cells will be dodecahedrons of  $v$ , and the distance between neighboring sites will be  $d_0$ , where  $d_0^3 = \sqrt{2}v$ . Wood (15) has shown that the solution to the integral equation may then be written as

$$\begin{aligned} s(\mathbf{r}) &= v_f^{-1}, \text{ if } \mathbf{r} \text{ lies within } \Delta' \\ &0, \text{ if } \mathbf{r} \text{ lies outside } \Delta' \end{aligned} \quad (20)$$

where  $\Delta'$  is a dodecahedron of altitude  $(d_0 - \sigma/2)$ .  $V_f$  is then just the volume of this smaller dodecahedron, and the equation of state is given by

$$pv/kT = (1 - \sigma/d_0)^{-1} \quad (21)$$

This equation of state has been plotted in Figure 3, where it is compared with

that derived by the method of the pair distribution function. Although the shapes of the curves are similar in the two cases, the cell theory predicts larger values for the compressibility factor  $pv/kT$ .

If the molecular interactions are of the harmonic type  $\varphi(r) = A + Br^2$ , the solution to (18) is

$$s(\mathbf{r}_1) = \frac{\exp\left(-B \sum_{j=1}^N (\mathbf{r}_{1j} - \mathbf{r}_1)^2/kT\right)}{\int_{\Delta} \exp\left(-B \sum_{j=1}^N (\mathbf{r}_{1j} - \mathbf{r}_1)^2/kT\right) d\tau_1} \quad (22)$$

This distribution function is a Gaussian of the type which is associated with the situation in crystalline solids, and thus despite its relative simplicity it should be of little significance in the studies of the liquid. To obtain results of some consequence Equation (18) must be solved for a more realistic choice of the interaction potential.

In accordance with the Kirkwood version of the cell theory a molecule will be surrounded by its neighbors in the manner illustrated by Figure 7a; that is, this method implies that the local geometrical structure in the liquid is the same as that in a crystal. However it has been mentioned previously that there is no evidence for such a lattice structure in liquids, and in fact the previous qualitative arguments suggest that the average arrangement of the neighbors would form an almost spherical shell about a molecule. Thus the large amplitudes of the thermal motions in a liquid would smear the arrangement of neighbors into a structure resembling that of Figure 7b.

On the basis of this argument there would seem to be an excellent physical justification for suppressing the dependence of  $s(\mathbf{r})$  and  $\Phi(\mathbf{r})$  upon the lattice geometry. Accordingly it is reasonable to assume that the cell-distribution function depends only upon the value of the radial coordinate  $r = |\mathbf{r}|$ . Furthermore the physical description of the situation strongly suggests that the average potential field within a cell should be defined as the angle-averaged value of  $\Phi(\mathbf{r})$ , that is by the function

$$\Phi(r) = (4\pi)^{-1} \int_0^{2\pi} \int_0^\pi \Phi(\mathbf{r}) \sin \theta d\theta d\phi \quad (23)$$

Other definitions for the average cell potential have been considered by Dahler, Hirschfelder, and Thacher (16).

Employing the same arguments as before, one finds that the optimum spherically symmetrized cell-distribution function is given by the solution of the integral equation

$$s(r) = \bar{v}_f^{-1} \exp(-\psi(r)/kT) \quad (24)$$

where  $\psi(r)$  is completely analogous to  $\psi(\mathbf{r})$ , and the spherical free volume is



$$\bar{v}_f = 4\pi \int_0^{r_0} \exp(-\psi(r)/kT) r^2 dr \quad (25)$$

The volume of this spherical cell is usually somewhat less than the specific volume, since otherwise adjacent cells will overlap one another. In accordance with these definitions (23) is given explicitly by

$$\Phi(r_1) = \pi \sum_{n=1}^{\infty} c_n \int_0^{\pi} \int_0^{\pi} \int_0^{r_0} s(r_n) \varphi(r_{1n}) r_n^2 \sin \theta_1 \sin \theta_n dr_n d\theta_1 d\theta_n \quad (26)$$

Figure 8 provides an illustration of the coordinates involved in these multiple integrations.

For rigid spheres the solution to this new integral equation retains the form given by (20), where  $\Delta'$  is here a sphere of radius  $(d_0 - \sigma)/2$ . Although the value for the free volume is larger by a factor of 1.35 than in previous considerations, the equation of state is unchanged.

For the harmonic interaction  $\varphi(r) = A' + B'(r - a)^2$  the cell-distribution function is given by the simple Gaussian  $s(r) = \bar{v}_f^{-1} \exp(-Cr^2/kT)$ , where

$$\bar{v}_f = 4\pi \int_0^{r_0} \exp(-Cr^2/kT) r^2 dr$$

and  $C$  depends only upon  $d_0$ ,  $a$ , and  $B$ . All the thermodynamical properties may therefore be expressed in terms of the tabulated incomplete gamma function.

For a more realistic choice of the intermolecular forces Equation (24) must be solved by numerical methods. At the time of this writing extensive calculations based upon the Lennard-Jones 12-6

$$s(r)_{LDJ} = \exp(-\Phi(r)_{LDJ}/kT) / 4\pi \int_0^{r_0} \exp(-\Phi(x)_{LDJ}/kT) x^2 dx \quad (28)$$

interaction [Equation (6)] are nearing completion (17). To simplify these calculations it has been assumed that one may neglect the second and further removed shells of neighbors in determining the cell distribution function. The effect of this approximation is to confine the motions of the molecules to the vicinity of their lattice sites somewhat more than would otherwise be the case. The validity of this last assertion is confirmed by the observation that the second and further removed neighbors always lie separated from the central molecule by distances in excess of the range for the repulsive interactions. Although this same assumption can not be employed in the calculation of the internal energy and of the equation of state, the contributions to these quantities that arise from the second and further removed shells do not depend so critically upon the exact form of  $s(r)$ . Therefore one is presumably justified in using less rigorous methods to evaluate these contributions (32, 17).

These calculations have revealed that the theoretical isotherms for  $pv/kT$  vs.  $v$  consistently lie below the experimental curves, and although the differences between theory and experiment are considerably lessened by the introduction of holes or empty cells, the final results are by no means so satisfactory as one should like. It is believed that a thorough analysis and interpretation of these results will lead to a better understanding of the cell theories and suggest means for their improvement.

Early theories based upon the cell model involved no such elaborate calculations as those outlined above. Instead they employed various approximations to estimate the behavior of the cell distribution function and of the potential field within a cell. An outstanding feature of Kirkwood's approach is the relationship it reveals between these approximations and the solutions to the integral Equation (24). For instance the method of Lennard-Jones and Devonshire (18) corresponds to a very unsymmetrical approximation in which the neighbors are treated on a different par from the molecules within the cells. Thus in their calculation of the cell potential the neighbors were assumed to lie upon the surface of a spherical shell of radius  $d_0 = |R_{12}|$ , and so Equation (26) was replaced by the approximate expression

$$\Phi(r_1)_{LJD} = (c_1/2) \int_0^{\pi} \varphi(\sqrt{(r_1 - R_{12})^2}) \sin \theta_1 d\theta_1 \quad (27)$$

Inserting this approximation into Equations (24) and (25), one obtains the Lennard-Jones and Devonshire estimate for the cell distribution function,

This may be considered as the first step in an iterative solution to Equation (24). The next step in this procedure would be to recalculate the cell potential by inserting  $s(r)_{LJD}$  into Equation (26) and thereby obtaining a second approximation to the cell distribution function. Higher-order approximations are simply obtained by successive repetitions of this process. In fact it is just this sort of scheme which has been employed in the numerical solution of the integral equation (17).

Despite the approximate nature of the Lennard-Jones and Devonshire method it has been remarkably successful in predicting the qualitative behavior of liquids. For rigid spheres the  $LJD$  cell distribution function is of the form given by Equation (20). However the free volume is now much larger than in either of the previous calculations, being eight times greater than the value predicted by the exact solution of Equation (24). The equation of state is unaffected by this difference and given by (21). In their

original presentation Lennard-Jones and Devonshire applied this method to the 12-6 interaction, and a considerable extension of their calculations has since been conducted by Wentorf, Buehler, Hirschfelder, and Curtiss (19). The equation of state is included in Figure 6, but another, more useful illustration is provided by Figure 10. Generally it is found that at very high densities the Lennard-Jones and Devonshire theory is more successful than that of the superposition principle; however at low densities the cell model becomes physically unrealistic and the predictions of this theory become very unsatisfactory. It is just at these low densities that the method of the superposition principle has proved most successful, and so the two schemes have a sort of complementary relationship to one another.

As yet no theory has been devised which is truly applicable over the entire range of liquid and vapor densities. Although numerous extensions of the cell method have been proposed in an effort to achieve such a theory, the results have not been outstanding. Nevertheless these schemes have been very instructive in providing a superior theoretical description of the liquid itself. Most significant among these advances is the development of the so-called "hole theory." From the evidence provided by the experimentally determined radial-distribution function one knows that the number of nearest neighbors to a molecule is progressively lessened as the density of the liquid decreases. However the average distance from the central molecule to these neighbors changes very little with variations in the density. When this information is compared with the picture provided by the cell theory of Kirkwood, attention may be confined in the range of liquid densities to those configurations for which each cell is singly occupied. As the density of the liquid is decreased, the size of these cells and hence the distance from the central molecule to its neighbors steadily increases. However the actual number of neighbors remains unaltered and is taken to the coordination number of the crystalline lattice. Thus in contrast to the experimental evidence of Figure 1 (and Table 1) the cell theory predicts that with decreasing density the curves of  $g(r)$  should exhibit a progressive radial displacement and that the area under the first peak (and all the others) should remain unaltered.\*

To correct this unrealistic behavior Eyring and Cernuschi (20) introduced "holes," or unoccupied cells, into their description of the liquid. According to their model, an expansion of the liquid produces an increase in the number of these holes but leaves the volume of an

\*The precise mathematical relationship between  $g(r)$  and the cell-distribution function has recently been established (21). Calculations based upon this relationship are in agreement with the qualitative description of the situation presented in this paper.

individual cell almost unaltered. Thus the volume of a cell is taken to be  $w = V/L = xv$ , where  $x = N/L$ . If one employs the spherical approximation previously discussed, the radius of a cell will be  $r_0' = (x)^{1/3}r_0$ .

Thus while the cell theory depends upon the production of multiply occupied cells to account for the increased disorder at low densities, the hole theory explains this disorder in terms of an increased number of cells. There is of course an intrinsic disorder associated with the  $L!/N!(L-N)!$  different ways in which the  $N$  molecules may be distributed among the  $L \geq N$  cells. In the absence of holes only one such arrangement is possible, but with increasing dilution more holes appear and the number of possible arrangements approaches a limiting value of unity in the crystal (no holes) to a value of  $e^N$  in the limit of infinite dilution (infinite number of holes). Although this is precisely the behavior of the function  $\bar{\sigma}^N$ , occurring in the theory of Kirkwood, there is certainly no reason for these two quantities to be equal over the entire density range.

Mayer and Careri (22) have shown how this hole model of the liquid can be combined with Kirkwood's method of determining the cell-distribution function. Using their approach one can derive an integral equation for the cell distribution function that has precisely the same form as Equation (24). Of course this function, the cell potential, and the free volume will now exhibit a parametric dependence upon the number of holes present in the liquid. The analytical nature of this dependence is very simple however, and the results of this hole theory are obtained from Equations (24), (25), and (26) by replacing the absolute temperature by  $T/\gamma$  and the specific volume by the cell volume  $w = xv$ . Thus at first it would appear that the introduction of holes necessitates no calculations beyond those already involved in the ordinary cell theory. Actually several complications arise. The dependence of  $\gamma$  upon the number of holes must be determined. If the holes and molecules were distributed randomly among the cells, then  $\gamma$  would be equal to  $x = N/L$ . However this is not the case, since just as in a binary solution there will be different *a priori* probabilities for the cells neighboring a molecule to be occupied by other molecules or by holes. This same problem is encountered in the study of all physical systems which exhibit so-called "order-disorder phenomena," and although no exact solution of this problem has yet been found, several satisfactory approxi-

mation schemes are available (23, 24, 25).

There remains only the problem of choosing the correct number of holes.

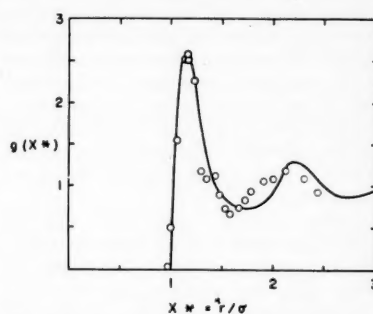


Fig. 5. A comparison of experimental and theoretical radial distribution functions for liquid argon at 91.8°K. and 1.8 atm. The experimental values are those of Eisenstein and Gingrich.

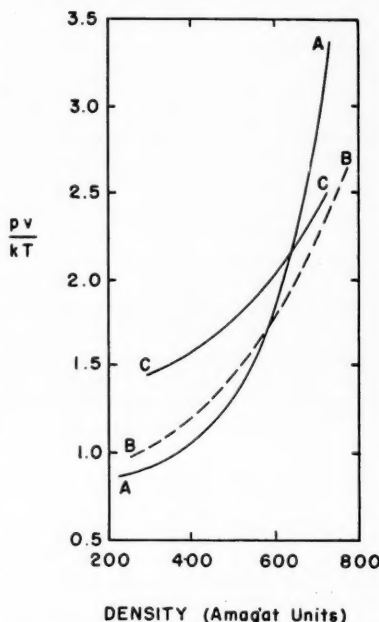


Fig. 6. A comparison of experimental and theoretical equations of state for argon at 273°K.: A, experimental values of (35); B, radial distribution function method; C, cell theory (11).

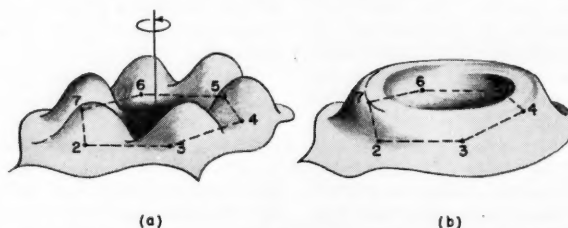


Fig. 7. A schematic representation of the distribution of neighbors about a cell in a two-dimensional hexagonal lattice. The location of the central site is labeled by 1; those of the neighbors by 2, 3, . . . 7. These contours illustrate the arrangement of the neighboring molecules in (a) the crystalline form and (b) the smeared or angle-averaged approximation.

\*From Stirling's approximation  $m! \approx (m/e)^m$  it follows that  $L!/N!(L-N)! \approx (1 + 1/y)^N y$ , where  $y = (1-x)/x$  and  $x = N/L$ . Then since  $\lim_{y \rightarrow \infty} (1 + 1/y)^y = e$ , the validity of this assertion is established.

led to  
e distri-  
e opti-  
rticular  
ensity)  
mholtz  
imum  
- TS  
inter-  
entropy,  
onically  
ed into  
try out  
accom-  
nations  
volume  
in very  
Levine,  
recently  
to be  
e opti-  
is new  
rgy re-  
theory  
nations  
as and  
on the  
ed in a  
  
in the  
method  
scheme  
ons of  
taken  
ion of  
aboring  
ctively  
them.  
er cell  
ce and  
al cell  
density  
by the  
r pars-  
s, and  
reedom  
arance.  
a very  
or the  
at ac-  
  
eory is  
obably  
cts of  
sed of  
itation

will not be too serious, since the theory is constructed in such a manner that the larger clusters are significant only when the molecular disorder becomes quite pronounced. In fact clusters of two cells should introduce corrections comparable to those arising from the doubly occupied cells in Kirkwood's theory. There are however great differences between the usual cell theory and deBoer's formulation of the cell-cluster method. For example when clusters of two or more cells are neglected, his theory reduces directly to that of Lennard-Jones and Devonshire. Thus the double-cell contributions provide the only means by which this method can improve upon a rather crude first approximation, that is the Lennard-Jones and Devonshire theory. Although these double cells do provide an adequate estimate of the entropy of the liquid (27, 28), they are by no means so successful in explaining the equation of state. Thus from Figure 3 one sees that the inclusion of double cells actually leads to an equation of state for rigid spheres which is less satisfactory than that of the simple *LJD* method. (It will subsequently be shown that the *Monte Carlo* isotherm of Figure 3 is the most realistic.) This suggests that the principal drawback of the cell-cluster theory is its reliance upon a rather unrealistic first approximation. Thus one really should employ the best possible cell theory as a starting point for the cluster method. One step along this path has been taken by Dahler and Cohen (29), who generalized the cell-cluster theory to include the possibility of holes. However a more general theory would include Mayer and Careri's method of the cell distribution function (for a liquid with holes) as its first approximation and then describe the molecular disorder in terms of deBoer's clusters. Although such a development has been demonstrated, no numerical tests have yet been conducted. This lack of numerical verification really characterizes the present status of all developments based upon the cluster method. During the next few years calculations based upon these schemes should gradually become available, and then a truly comprehensive appraisal of the cluster theory will be possible.

This survey has touched upon a variety of theories for the liquid state, but, except for the calculations based upon the superposition principle and those using the Lennard-Jones and Devonshire approximation, none have been subjected to an adequate numerical test. Although the hole and cell-cluster methods hold considerable promise, their true worth will depend upon their ability to predict the thermodynamical behavior of the liquid. Within the next few years great activity is expected in the performance of numerical calculations designed to provide tests for these theories. [The investigations of (17) constitute such an

endeavor.] However all the schemes discussed contain two sources of error: the mathematical approximations involved in the calculation of the configuration integral and the physical assumption

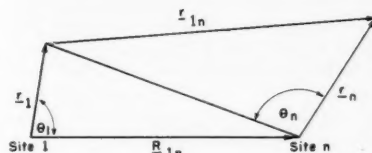


Fig. 8. Coordinates involved in the calculation of the cell potential-energy field. (For a face-centered cubic lattice  $|R_{1n}| = n d_{0.}$ )

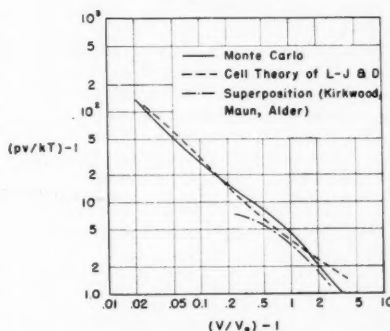


Fig. 9. A log-log plot of  $(pv/kT) - 1$  vs.  $(v/v_0) - 1$  for hard spheres.  $v_0 = \sigma^3/\sqrt{2}$  is the volume per molecule at the closest possible packing. The solid line is the result of the Monte Carlo method as compared with the Lennard-Jones and Devonshire theory (dashed line) and the superposition theory of Kirkwood (dot-dashed line).

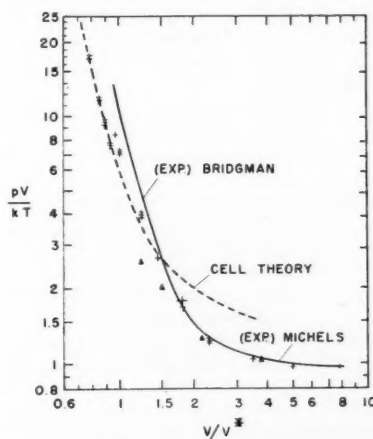


Fig. 10. Compressibility factor vs. reduced volume. The horizontal bars represent the positions of the Monte Carlo average values. The vertical extent of these symbols indicates the uncertainty due to the approximate treatment of second and/or further removed neighbors. The solid curves represent the measurements of (35, 36) on argon. The triangles indicate results obtained by the superposition method.

that the interactions among the molecules may be represented by various empirical laws such as that of the Lennard-Jones 12-6 potential. Therefore in comparing these theories with experimental measurements one is always confronted with uncertainty about the origin of the observed discrepancies. Of course this uncertainty could be resolved if one could perform experiments upon a liquid composed of rigid spheres or of molecules which actually interact according to the 12-6 law. Such experiments can indeed be performed by a numerical procedure known as the *Monte Carlo* method. For an accurate and detailed description of this method one should refer to the original papers on the subject. However it is possible to illustrate the more essential elements of the procedure by considering the situation in a fluid of rigid spheres. For this purpose one can consider a box containing a collection of  $N$  billiard balls numbered 1, 2,  $\dots$ ,  $N$ . A computing machine is then instructed to move the first from its original position to a new location within the box. The magnitude and direction of this displacement are chosen by the machine in a random manner, hence the name *Monte Carlo*. If the molecule is prevented from lying in its new position by the presence of another, the machine is then told to replace it in its original location; otherwise the move is allowed. In either event the machine then plays this same game with a second molecule and so on, until each has been considered. If this process is repeated a sufficient number of times, the spatial distribution of the molecules within the box approaches that of thermodynamical equilibrium (30). Thus using a sample of 256 spheres Rosenbluth and Rosenbluth (31) ascertained that equilibrium was established after each molecule had been moved a total of one hundred times. By examining the surrounding of each molecule they were then able to construct the radial-distribution function as the average description of the molecular environments. Once  $g(r)$  had been determined at a particular density and temperature, the corresponding values for the compressibility factor, internal energy, and other thermodynamical properties could be calculated from the equations given earlier. Thus by repeating the Monte Carlo calculations at a number of densities Rosenbluth and Rosenbluth were able to construct the equation of state shown in Figures 3 and 9. At high densities the predictions of the *LJD* method agree rather well with these results. In this same region there is a great disparity between the Monte Carlo calculations and those based upon the superposition principle. At low densities however the situation is reversed and the superposition theory becomes more satisfactory than that of Lennard-Jones and Devonshire.



Although these initial investigations gave no evidence of a discontinuous phase transition from solid to liquid, the radial-distribution function did exhibit a "clear evolution with increasing volume from a crystalline structure to a liquid type structure with the transition being completely at about  $v/v_0 = 1.5$ ." It was also found that the lattice breakdown at  $v/v_0 = 1.5$  marked the density at which molecules were first observed to slip past one another and escape from their immediate neighbors in the liquid, that is the onset of fluid behavior. Recently this problem has been reexamined by Alder and Wainwright (10) and by Wood and Jacobson (9), who find that for densities near  $v/v_0 = 1.5$  the configuration states of the fluid described by  $g(r)$  may be separated into two different classes, one characterized by a relatively free diffusion of the molecules and another for which diffusion is very restricted. Transitions between these two classes rarely occur; for example during calculation periods (IBM 704) as long as 10 to 30 hr. only zero to three such transitions may be observed. This behavior leads to the conclusion that over a narrow range of densities near  $v/v_0 = 1.5$  the radial-distribution function is double valued, a conclusion which implies the coexistence of two distinct physical phases. By adopting this interpretation of their results Wood and Jacobson were able to construct the discontinuous isotherm shown in Figure 4. Therefore the existence of the phase transformation theoretically predicted by Kirkwood, Maun, and Alder has been confirmed by the Monte Carlo experiments. Since most theories of crystallization rely heavily upon the presence of attractive intermolecular forces, an explanation of the results for rigid spheres would seem to require the discovery of an alternative mechanism for this process; no such mechanism has yet received wide acceptance.

The Monte Carlo method is of course applicable to cases other than those of rigid spheres. Thus Wood and Parker (32) have recently used this technique to study the thermodynamical behavior of a fluid whose molecules interact according to the Lennard-Jones 12-6 law.\* They find that at low densities (Figure 10) there is excellent agreement between the Monte Carlo calculations and the predictions of the superposition method. For higher densities this agreement is less satisfactory however, and instead it is the theory of Lennard-Jones and Devonshire which more closely resembles the Monte Carlo results.

It is significant that at high densities neither theory nor the Monte Carlo

method agrees very well with the few experimental  $p$ - $v$ - $T$  data that are presently available. (The existing data are for Argon.) Although this fact may simply evidence the inadequacy of the 12-6 potential, it could also reflect the existence of nonadditive molecular interactions in the real fluid. However this is all merely speculation, and before any definite conclusions can be drawn one must probably await the accumulation of more accurate experimental information at high densities.

#### NOTATION

$A, B$	= coefficients
$dr_i$	= differential element of volume for $i$ th molecule
$E$	= energy
$g(r)$	= radial distribution function
$h$	= Planck's constant
$J_0(s)$	= intensity of X radiation
$L$	= total number of cells
$m$	= mass of molecule
$m_i$	= number of molecules lying in $i$ th cell
$n$	= number density of molecules
$n^{(2)}(r)$	= pair distribution factor
$r$	= vector displacement
$r_0$	= radius of spherical cell to which molecule is confined
$R_{ij}$	= vector directed from $i$ th to $j$ th lattice sites
$s$	= cell distribution function
$s(r)$	= probability distribution function within a cell
$v$	= specific volume
$v_f$	= free volume
$V$	= total volume of liquid

#### Subscript

$n$	= any one of $c_n$ molecules lying in the $n$ th shell of neighbors to the central molecule
-----	---

#### Greek Letters

$\gamma$	= fraction of occupied cells neighboring an occupied cell
$\Delta'$	= dodecahedron of altitude $(d_0 - \sigma)/2$
$\theta, \phi$	= polar angles of vector $r$
$\lambda$	= wavelength of impinging X rays
$\sigma$	= hard-core diameter
$\bar{\sigma}$	= disorder parameter
$\theta$	= angle between primary and secondary beams
$\phi(r)$	= interaction energy of two molecules separated by a distance $r$

#### LITERATURE CITED

- Hirschfelder, J. O., C. F. Curtiss, and R. B. Bird, "Molecular Theory of Gases and Liquids," John Wiley, New York (1954).
- Eyring, Henry, and J. O. Hirschfelder, *J. Phys. Chem.*, **41**, 249 (1937); J. O. Hirschfelder, *J. Chem. Ed.*, **16**, 540 (1939).
- Kirkwood, J. G., *J. Chem. Phys.*, **14**, 180 (1946).

- Eyring, Henry, *ibid.*, **4**, 283 (1936); see also J. F. Kincaid, Henry Eyring, and A. E. Stearn, *Chem. Revs.*, **28**, 301 (1941).
- Kirkwood, J. G., *J. Chem. Phys.*, **3**, 300 (1935).
- Born, Max, and H. S. Green, *Proc. Roy. Soc. (London)*, **A188**, 10 (1946).
- Yvon, J., *Actualités scientifiques et industrielles*, Hermann & Co., Paris (1935).
- Kirkwood, J. G., E. K. Maun, and B. J. Adler, *J. Chem. Phys.*, **18**, 1040 (1950).
- Wood, W. W., and J. D. Jacobson, *ibid.*, **27**, 1207 (1957).
- Alder, B. J., and T. E. Wainwright, *ibid.*, **27**, 1208 (1957).
- Kirkwood, J. G., V. A. Lewinson, and B. J. Adler, *ibid.*, **20**, 929 (1952).
- Oppenheim, Irwin, and Peter Mazur, *Physica*, **23**, 197, 216 (1957).
- Kirkwood, J. G., *J. Chem. Phys.*, **18**, 380 (1950).
- Pople, J. A., *Phil. Mag.*, **42**, 459 (1951).
- Wood, W. W., *J. Chem. Phys.*, **20**, 1334 (1952).
- Dahler, J. S., J. O. Hirschfelder, and H. C. Thacher, Jr., *ibid.*, **25**, 249 (1956).
- Dahler, J. S., and J. O. Hirschfelder, *J. Chem. Phys.*, to be published.
- Lennard-Jones, J. E., and A. F. Devonshire, *Proc. Roy. Soc. (London)*, **A163**, 53 (1937).
- Wentrof, R. H., R. J. Buehler, J. O. Hirschfelder, and C. F. Curtiss, *J. Chem. Phys.*, **18**, 1481 (1950).
- Cernuschi, F., and Henry Eyring, *ibid.*, **7**, 547 (1939).
- Dahler, J. S., *ibid.*, **29**, 1082 (1958).
- Mayer, J. E., and Giorgio Careri, *ibid.*, **20**, 1001 (1952); also see J. E. Mayer, *Ann. Rev. Phys. Chem.*, **1**, 175 (1950).
- Hill, T. L., "Statistical mechanics," chap. 7, McGraw-Hill, New York (1956).
- Hijmans, Jaap, and Jan deBoer, *Physica*, **21**, 471, 485, 499 (1955); also see Michio Kurata, Ryoichi Kikuchi, and Tatsuro Watari, *J. Chem. Phys.*, **21**, 434 (1953).
- Levine, H. B., J. E. Mayer, and H. Aroeste, *ibid.*, **26**, 201, 207 (1957).
- deBoer, Jan, *Physica*, **20**, 655 (1954).
- Salsburg, Z. W., E. G. D. Cohen, Jan deBoer, *ibid.*, **21**, 137 (1955).
- Salsburg, Z. W., B. C. Rethmeier, and E. G. D. Cohen, *ibid.*, **23**, 407 (1957).
- Dahler, J. S., and E. G. D. Cohen, *ibid.*, to be published.
- Metropolis, Nicholas, M. N. Rosenbluth, A. W. Rosenbluth, A. H. Teller, and Edward Teller, *J. Chem. Phys.*, **21**, 1087 (1953).
- Rosenbluth, M. N., and A. W. Rosenbluth, *ibid.*, **22**, 881 (1954).
- Wood, W. W., and F. R. Parker, *ibid.*, **27**, 720 (1957).
- deBoer, Jan, *Repts. Progr. in Phys.*, **12**, 305 (1949).
- Eisenstein, A., and N. S. Gingrich, *Phys. Rev.*, **62**, 261 (1942).
- Michels, A., Hub. Wijkers, and Hk. Wijkers, *Physica*, **15**, 627 (1949).
- Bridgman, P. W., *Proc. Am. Acad. Arts Sci.*, **70**, 1 (1935).

Presented at A.I.Ch.E. Philadelphia meeting. Manuscript received June 24, 1958; revision received August 28, 1958; paper accepted August 30, 1958.



# Chromatographic Columns Containing a Large Number of Theoretical Plates

A. S. SAID

College of Physicians and Surgeons, Columbia University, New York

To obtain numerical answers for the concentration distribution of solute on a chromatographic column or in the effluent, tables and charts of the Poisson distribution are used. Their use however is limited to a small number of theoretical plates. The transformation of the Poisson to the normal distribution enables the calculations to be performed for any number of theoretical plates through the use of the normal distribution tables.

Equations derived previously for columns containing a large number of plates and employing elaborate mathematical procedures and approximations have been simply deduced by applying a limit property of the Poisson distribution to the exact equations.

A relationship between the Poisson and normal distribution is derived, and charts are drawn which allow the rapid evaluation of the Poisson in terms of the normal values.

In accordance with the plate theory of chromatography a chromatographic column is assumed to be equivalent to a certain number of theoretical plates with the eluent passing continuously, without mixing, through these plates, while equilibrium is established between the solute on any plate in the column and the solute in the eluent passing through the plate. The results expressing the concentrations of solute at different parts of the column and in the effluent are in the forms of Poisson or Poisson-summation distributions (4). For the purpose of numerical calculations tables (3) and charts (1) are available which list the values of  $\phi_n^u$  and  $P_n^u$  for different values of the solution parameter and the column parameter, but the use of these tables and charts is limited to columns containing not more than 200 theoretical plates. In practice however chromatographic columns may contain many thousands of theoretical plates.

Fortunately, for large values of  $u$  and  $n$  the Poisson distribution can be approximated by the normal distribution, and the larger the values of  $u$  and  $n$ , the better is the approximation. It is true for the Poisson-summation distribution  $P_n^u$  that if one transforms to the variable  $t$  and then allows  $u$  to tend to infinity,  $P_n^u$  approaches the normal distribution  $A(t)$ , where

$$A(t) = \frac{1}{\sqrt{2\pi}} \int_{-\infty}^t e^{-z^2/2} dt$$

In other words

$$\lim_{u \rightarrow \infty} P_n^u = A(t) \quad (1)$$

Since the maximum of the zone occurs at  $u \cong n$ , values of  $u$  of practical interest when  $n$  is large, also should be large and in the neighborhood of  $n$ .

Applying this limit property of the Poisson distribution to the case of eluting an originally uniform zone, one finds that the concentration distribution or elution equation

$$R_n = P_{n-M}^u - P_n^u$$

reduces to

$$R_n = A(t') - A(t) \quad (2)$$

where

$$t = (u - n)/\sqrt{u}$$

and

$$t' = \{u - (n - M)\}/\sqrt{u}$$

and for the deposition of a zone at the top of a column the equation

$$R_n = P_n^u$$

reduces to

$$R_n = A(t) \quad (3)$$

Equations (2) and (3) were derived by Glueckauf (2), who set up the elution process as a partial-differential equation and then, by assuming a large number of theoretical plates, was able to reduce that equation to one of a standard form leading to a solution in the form of a normal distribution through a series of approximations and elaborate mathematical manipulations.

The advantage of deducing these

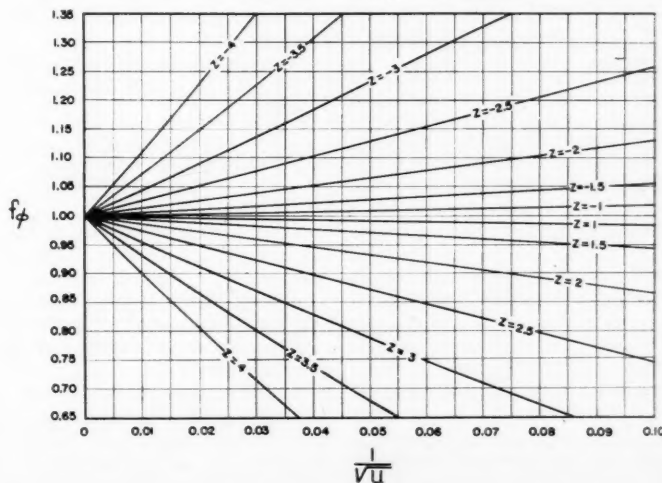


Fig. 1. Plot of Equation (4).

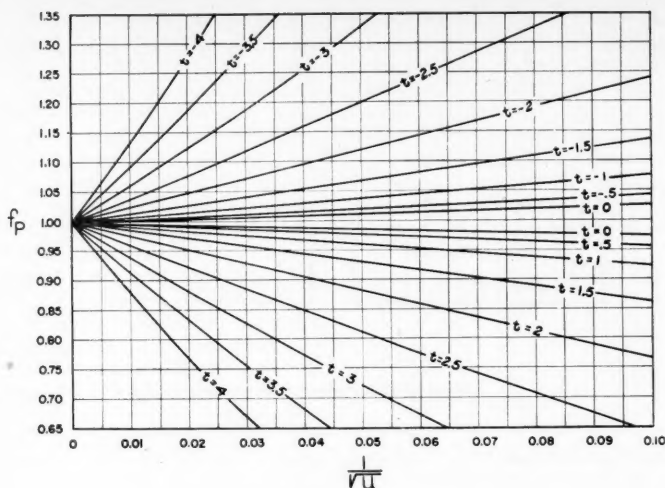


Fig. 2. Plot of Equation (5).

relationships from the exact Poisson solution is clear, since aside from the simplicity of the derivation one can also test the validity of the approximation and determine the limits of the applicability of Equations (2) and (3).

Since the Poisson and normal distributions approach each other rather slowly and at different rates for different regions, these approximations are only valid for very large values of  $n$  and values of  $|(u - n)/\sqrt{u}| < 2$ . On the other hand when the column contains a small or moderately large number of plates, or when one is dealing with regions far from the peak of the zone, as in the case of calculating the impurities owing to one band in another, the Poisson distribution can be replaced by the normal distribution only after the inclusion of a correction factor.

It is shown in the Appendix\* that  $\phi_n^u$  can be rearranged and rewritten in the form

$$\phi_n^u = \frac{1}{\sqrt{2\pi u}} e^{-z^2/2} \left[ 1 + \frac{1}{\sqrt{u}} f_1(z) + \frac{1}{u} f_2(z) + \dots + \frac{1}{u^{r/2}} f_r(z) + \dots \right]$$

For values of  $u > 100$  this series converges rapidly, and one can neglect terms containing  $f_3(z)$  upward and

$$\phi_n^u = f_\phi \frac{1}{\sqrt{2\pi u}} e^{-z^2/2}$$

where

$$z = \frac{u - n - \frac{1}{2}}{\sqrt{u}}$$

\*Tabular material has been deposited as document 5876 with the American Documentation Institute, Photoduplication Service, Library of Congress, Washington 25, D. C., and may be obtained for \$2.50 for photoprints or \$1.75 for 35-mm. microfilm.

$$f_0 = 1 + \frac{1}{\sqrt{u}} f_1(z) + \frac{1}{u} f_2(z) \quad (4)$$

$$f_1(z) = -\frac{z^3}{6}$$

and

$$f_2(z) = \frac{z^5}{72} - \frac{z^4}{12} + \frac{1}{24}$$

Equating  $f_2(z)$  to zero, one finds that  $f_\phi$  is equal to  $1 + 1/\sqrt{u} f_1(z)$  at values of  $z = \pm 0.87, \pm 2.43$ . Actually for values of  $|z|$  lying between 0 and 2.5  $f_\phi$  can be represented almost accurately by the straight line having the equation

$$y = 1 + \frac{1}{\sqrt{u}} f_1(z)$$

when  $f_\phi$  is plotted vs.  $1/\sqrt{u}$  with  $z$  as the parameter.

For values of  $z$  greater than 2.5 the deviation from the straight line equation becomes appreciable and increases rapidly with  $z$ .

It is also shown in the Appendix that  $P_n^u$  can be accurately represented by the relation

$$P_n^u = A(t) \left[ 1 + \frac{t^2 + 2 E(t)}{6\sqrt{u} A(t)} \cdot \left\{ 1 - \frac{t(t^2 - 3)}{12\sqrt{u}} \right\} \right]$$

Instead of a correction factor, defined in this case as simply the ratio between  $A(t)$  and  $P_n^u$ , a more useful definition will be used, namely

$$f_P = \frac{P_n^u}{A(t)} \quad \text{for } t < 0$$

$$= \frac{1 - P_n^u}{1 - A(t)} \quad \text{for } t > 0$$

$$\begin{aligned} \therefore f_P &= 1 + \frac{t^2 + 2 E(t)}{6\sqrt{u} A(t)} \\ &\cdot \left\{ 1 - \frac{t(t^2 - 3)}{12\sqrt{u}} \right\} \quad \text{for } t < 0 \\ &= 1 - \frac{t^2 + 2 E(t)}{6\sqrt{u} [1 - A(t)]} \\ &\cdot \left\{ 1 - \frac{t(t^2 - 3)}{12\sqrt{u}} \right\} \quad \text{for } t > 0 \end{aligned} \quad (5)$$

Equating the last term to zero and solving for  $t$  one finds that  $f_P$  is equal to the first two terms for  $t = 0, \pm\sqrt{3}$ . Actually  $f_P$  can be represented almost accurately for values of  $t$  lying between 0 and 2 by the first two terms only, and a plot of  $f_P$  vs.  $1/\sqrt{u}$  with  $t$  held constant is a straight line. For values of  $t$  greater than 2 deviations from the straight line equation become appreciable and increase rapidly with  $t$ . Figures 1 and 2, respectively, plot  $f_\phi$  vs.  $1/\sqrt{u}$  with  $z$  as the parameter and  $f_P$  vs.  $1/\sqrt{u}$  with  $t$  as the parameter.

#### NOTATION

$A(t)$  = area under the normal distribution curve of error between  $-\infty$  and  $t$

$$= 1/\sqrt{2\pi} \int_{-\infty}^t e^{-x^2/2}$$

$$E(t) = 1/\sqrt{2\pi} e^{-t^2/2}$$

$f_P$  = Poisson-summation correction factor

$f_1(z)$  = function of  $z$

$f_\phi$  = Poisson correction factor

$n$  = theoretical plate number or column parameter

$r$  = positive integer

$R_n$  = concentration ratio of solute in eluent at plate  $n$

$t$  =  $(u - n)/\sqrt{u}$

$u$  = solution parameter

$x$  = variable

$$z = (u - n - \frac{1}{2})/\sqrt{u} = t - \frac{1}{2\sqrt{u}}$$

$$\phi_n^u = e^{-u} \frac{u^n}{n!}$$

$$P_n^u = \sum_{r=n}^{\infty} \phi_r^u$$

#### LITERATURE CITED

1. Campbell, G. A., *Bell System Tech. J.* (Jan., 1923).
2. Glueckauf, E., *Trans. Faraday Soc.*, 51, 34 (1955).
3. Molina, E. C., "The Poisson Exponential Limit," Van Nostrand, New York (1942).
4. Said, A. S., *A.I.Ch.E. Journal*, 2, 477 (1956).

Manuscript received September 19, 1957; revision received May 5, 1958; paper accepted May 7, 1958.

# Two-dimensional Laminar-Flow Analysis, Utilizing a Doubly Refracting Liquid

JOHN W. PRADOS and F. N. PEEBLES

University of Tennessee, Knoxville, Tennessee

An experimental technique for the determination of velocity distributions in two-dimensional laminar flow is described. The method utilizes the optical interference patterns observed in flowing doubly refracting liquids when viewed by transmitted polarized light. The fluid shear-stress distribution may be determined from these interference patterns by methods similar to those employed in solid photoelasticity. Methods are presented for the calculation of velocity distributions from the observed stress distributions. Experiments are described in which the technique was applied to determine velocity profiles in parallel-walled, converging and diverging channels and for flow about a cylindrical obstacle. The doubly-refracting liquids employed were aqueous solutions of an organic dye. Independent experimental checks were obtained in most instances, and these are in satisfactory agreement with the calculated results.

For many years the photoelastic technique has been a powerful tool for experimental stress analysis in solids. This technique is based on the fact that certain substances become temporarily doubly refracting (that is, anisotropic to the passage of light) when subjected to shearing stresses. When a doubly refracting substance is viewed by transmitted light between two polarizing plates, visible interference patterns are produced, which are related to the material dimensions and properties and to the shearing stresses in the specimen. The method has been used extensively in the analysis of two-dimensional stress systems, and special techniques permit the analysis of certain three-dimensional systems. A complete and readable treatment of photoelastic theory and practice is given by Frocht (8).

An analogous phenomenon in liquids was reported by J. C. Maxwell in 1873 (16) and has been the subject of extensive investigation since. General reviews of this work have been presented by Cerf and Scheraga (5), Peebles, Prados, and Honeycutt (19), Edsall (7), and others. In liquids the phenomenon has been called *streaming birefringence*, *streaming double refraction*, or *flow double refraction*. The last name is preferred by the present authors.

By far the largest portion of the investigations on flow double refraction has concerned its application to the study of molecular size and shape. However, as early as 1923, Humphry (13) showed the possibility of using doubly refracting liquids as tools for the visual analysis of flow.

F. N. Peebles is with Union Carbide Nuclear Company, Oak Ridge, Tennessee.

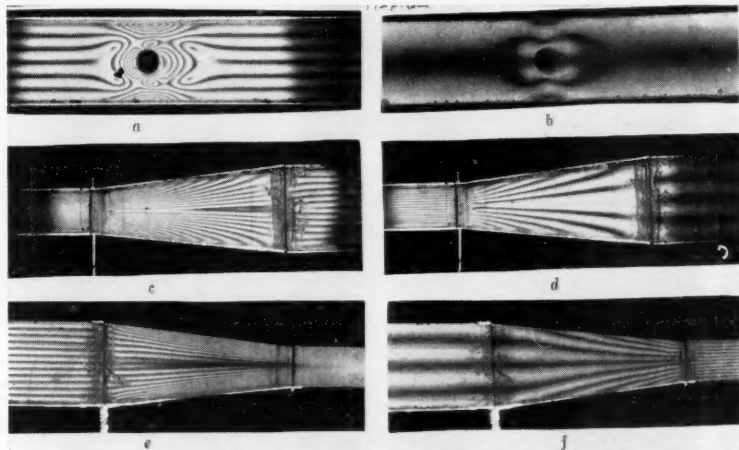


Fig. 1. Typical light interference patterns produced by flow double refraction in aqueous milling yellow solutions.

- Flow about a cylindrical obstacle at an intermediate flow rate, circularly polarized light.
- Flow about a cylindrical obstacle at a low flow rate, plane polarized light.
- Flow in a diverging channel at a high flow rate, circularly polarized light.
- Flow in a diverging channel at a low flow rate, circularly polarized light.
- Flow in a converging channel at a high flow rate, plane polarized light.
- Flow in a converging channel at a low flow rate, plane polarized light.

Visible interference patterns are observed when a doubly refracting liquid is caused to flow through a transparent channel between polarizing plates and viewed by transmitted light. These patterns are composed of alternate light and dark bands which appear stationary in steady laminar flow but take on a random eddying motion in turbulent flow. The bands are of two types: isochromatics which are related to the magnitude of the maximum shearing stress in the liquid, and isoclinics, which are related

to the direction of the maximum shearing stress. Peebles and Prados (20) have shown the conditions necessary to produce light interference (and hence a dark band) for both the isochromatic and isoclinic cases. The two types of bands may be distinguished by the observation of a given flow situation in both plane and circularly polarized light. The isochromatics alone appear in circularly polarized light, while both isochromatics and isoclinics appear in plane polarized light.

The intensity of the doubly refracting behavior is expressed in terms of the amount of double refraction, a measure of the relative velocities of light rays vibrating in different directions in the anisotropic medium. It can be shown that an isochromatic band appears whenever the amount of double refraction and fluid depth along the light path are such that the light transmitted through the liquid undergoes a relative retardation equal to an integral number of wave lengths. The amount of double refraction is a single-valued, increasing function of shear stress for a given doubly refracting liquid. Hence for a given depth of a given liquid there is a fixed value of shear stress associated with each isochromatic band in the interference pattern. This makes possible a quantitative determination of the shear-stress distribution from the interference patterns in a doubly refracting liquid, provided the liquid has first been calibrated by the determination of the relationship between shear stress and amount of double refraction. The method of calibration described by Peebles and Prados (20) consists of subjecting the liquid to known shear stresses, viewing it in polarized light, and observing the formation of the isochromatic bands. A similar procedure yields the relationship between isoclinic bands and stress directions. This relationship is expressed in terms of the extinction angle, which relates the stress direction necessary for light extinction to the axis of polarization of the incident light.

Flow double refraction provides an excellent qualitative way to study laminar, turbulent, or transition (unstable)

flows. Regions of local turbulence, vortices, boundary layers, and the like are clearly defined. Stroboscopic illumination is useful in observing turbulent flow behavior. However attempts to use the technique for quantitative determination of velocity profiles have proved successful only for the case of two-dimensional laminar flow. Photographs of typical two-dimensional laminar-flow situations are shown in Figure 1.

#### PREVIOUS INVESTIGATIONS

Prior applications of the technique of flow double refraction to the analysis of fluid motion have been relatively few in comparison with the large volume of literature dealing with flow double refraction in general. It is felt that some mention of these studies and the doubly refracting liquids employed is in order at the present time.

The earliest such application appears to have been due to Humphry (13) in 1923. Using a colloidal sol of vanadium pentoxide in water, he was able to demonstrate qualitatively the difference between laminar and turbulent flow. Further qualitative studies along these lines were the work of Leaf (14) in 1945, who employed doubly refracting bentonite sols in a locomotive fire box design, and the recent visual studies of Binnie (3, 4) and Lindgren (15) on the transition from laminar to turbulent flow in tubes. The last two investigators used aqueous sols of benzopurpurin and bentonite respectively.

Attempts to obtain quantitative measurements of velocity profiles with flow double refraction were first made by Alcock and Sadron (1) in 1936. Their doubly refracting liquid was sesame oil, which is highly viscous and has a low optical sensitivity but is more stable over periods of time than the colloids previously employed.

By far the most extensive of the quantitative investigations were those reported by Hauser and Dewey (6, 10, 11) between 1940 and 1942. Using bentonite sols they made quantitative and qualitative studies of velocity profiles in two-dimensional laminar flow. However in the analysis of their results two questionable assumptions were made: that the isoclinics were related to streamline direction rather than shear-

stress direction and that the isochromatics were a function of the velocity gradient normal to the streamlines rather than the shearing stress in the liquid. Some calculations presented by Rosenberg (22) and experimental observations made during the present investigation do not support these assumptions.

Weller *et al.* (28, 29) in 1943 carried out some studies similar to those of Hauser and Dewey using a solution of ethyl cellulose in a commercial solvent, Methyl Cellosolve, instead of bentonite. Ullyott (26) in 1947 described work similar to that of Hauser and Dewey and of Weller but made no attempt to interpret his results quantitatively.

A careful study of fluid-flow analysis by the double-refraction technique was presented in 1952 by Rosenberg (22), who showed that the direction of maximum shear stress in fluids and the direction of the streamlines are not coincident except for the case of parallel streamlines and suggested a method for the analysis of a general two-dimensional flow situation in which the streamlines are not parallel. No experimental measurements were reported by Rosenberg, nor did he carry out any actual flow analyses, but some of his suggestions have been extended and incorporated into the present work.

Recent investigations of interest are those of Wayland (27) and of Thurston and Hargrove (24). Wayland studied the flow in the annular space between fixed and rotating cylinders and reported quantitative results for the laminar-flow region; he employed bentonite sols and pure ethyl cinnamate as doubly refracting liquids. Wayland was also able to demonstrate a correlation between the amount of double refraction in pure ethyl cinnamate and the shear stress for turbulent flow. It should be noted that his doubly-refracting liquid had an optical sensitivity considerably lower than that of the liquids employed in the present investigation, and so isochromatics as such did not appear. Instead a compensator was used to measure the amount of double refraction. Such a technique would be essential for studies of turbulent flow, since under such conditions the fringes break up into swirling regions of light and dark and no longer have a fixed location. The studies of Thurston and Hargrove are concerned with the pulsating flow of fluids through circular orifices. Their work utilizes

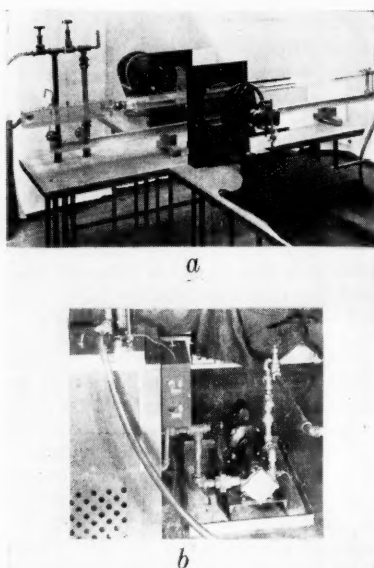


Fig. 2. Photographs of the flow facility: a. flow test channel, calming box and optical components, b. pump and constant-temperature bath.

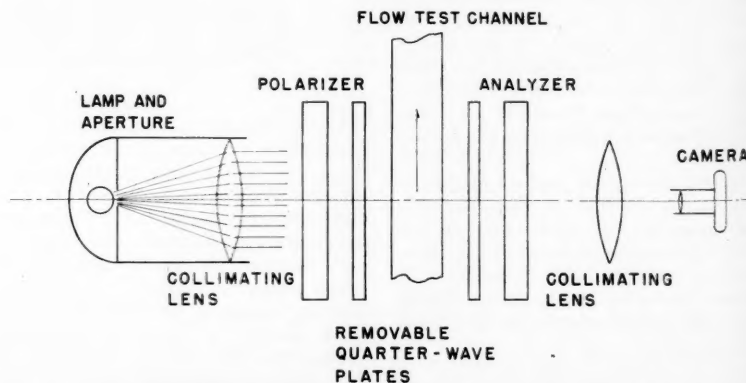


Fig. 3. Schematic representation of the optical system.



omatics  
radient  
than the  
calcula-  
(2) and  
ing the  
t these

ried out  
ser and  
close in  
losolve,  
in 1947  
Hauser  
ade no  
quantita-

ysis by  
as pre-  
, who  
maximum  
tion of  
except  
es and  
is of a  
tion in  
lel. No  
reported  
ut any  
is sug-  
incorpo-

est are  
on and  
he flow  
ed and  
titative  
on; he  
ethyl  
liquids.  
trate a  
double  
and the  
ould be  
id had  
lower  
in the  
omatics  
ompen-  
out of  
would  
at flow,  
fringes  
ght and  
ocation.  
ove are  
of fluids  
utilizes

MERA  
+ - -  
+ - -  
+ - -

an aqueous solution of milling yellow dye as the working fluid and is apparently the first recorded attempt to apply the technique of flow double refraction to unsteady or pulsating flow.

#### METHOD OF APPROACH

It was felt that the flow double refraction method offered unique advantages for the analysis of complex two-dimensional laminar-flow situations, and the present work was undertaken in an attempt to overcome some of the previous difficulties and place the analysis of results on a sounder basis. Specifically the objectives were twofold: the development of mathematical techniques for flow analysis from double refraction measurements based on more general assumptions than those previously employed, and the application of these techniques to the experimental analysis of a number of two-dimensional laminar-flow situations. It was also desired to check the experimental results by independent means wherever possible.

To achieve these objectives a mathematical analysis was made to relate desired flow parameters to quantities which could be obtained from flow double refraction measurements. Next an experimental study was carried out for three types of two-dimensional laminar flow: flow between parallel plates, where the streamlines are straight and parallel; flow in convergent and divergent channels, where the streamlines are straight but not parallel; and flow about a cylindrical obstacle, where the streamlines are neither straight nor parallel. The results were interpreted in the light of the mathematical analysis, and use was also made of some suggestions by Rosenberg (22)

which enable one to avoid the questionable assumptions of former investigators.

The doubly refracting liquid used in the present study was an aqueous solution of a commercially available organic dye, milling yellow. Stable, satisfactory working solutions of this dye can be prepared with viscosities not over twenty times that of water. They exhibit marked flow double refraction in concentrations as low as 1.2% dye by weight. Their use in flow studies was first reported by Peebles, Garber, and Jury (18).

#### MATHEMATICAL RESULTS

It should be emphasized here that the present study is based on the assumption that the amount of double refraction at a point in a doubly refracting liquid in two-dimensional laminar flow is a single-valued function of the maximum shear stress at that point. This has been well justified experimentally in the case of photoelastic solids, but previous investigations involving doubly refracting liquids have not been of such a nature as to confirm or deny the concept. It was further assumed that the extinction angle was a single-valued function of the maximum shear stress at any point in a two-dimensional laminar-flow field.

To carry out a flow analysis under these assumptions it is necessary to have two relationships: that between the maximum shear stress and the velocity gradient normal to the streamlines of flow and that between the direction of action of the maximum shear stress and the direction of the streamlines. These expressions are developed in the Appendix\* and are

$$\frac{\partial V}{\partial n} = \frac{V}{r} \pm \sqrt{E^2 - \frac{4V^2}{r'^2}} \quad (1)$$

\*Tabular material has been deposited as document 5872 with the American Documentation Institute, Photoduplication Service, Library of Congress, Washington 25, D. C., and may be obtained for \$2.50 for photoprints or \$1.75 for 35-mm. microfilm.

$$\theta = \phi - \frac{1}{2} \arctan \left( \frac{D}{G} \right) \quad (2)$$

Equation (2) shows that the streamline directions coincide with the direction of maximum rate of deformation only for cases where the rate of dilation is zero; that is, the normal curves to the streamlines are straight lines, an indication that the streamlines are parallel and that no convergence or divergence of flow is occurring. If one takes only principal values for the arctangent, it is seen that the maximum difference in these directions which can occur is  $\pi/4$  radians and will be manifested in situations where the rate of pure shear  $[(\partial V/\partial n) - (V/r)]$  is zero but the rate of dilation  $-(2V/r')$  is not. Such a situation would be found along the center line of a symmetrical convergent or divergent channel.

Equation (2) indicates that if the isoclinic positions are determined by the maximum rate of deformation, as results of the present study suggest, they will be of little use in determining the streamline patterns in cases where convergence or divergence of the flows occurs. Hence Equation (1) can be used to determine the velocity distribution only for cases where the streamline pattern is known from the channel configuration, where it is known that no divergence or convergence of flow occurs and the streamline patterns can be developed from the isoclinics, or where the streamline patterns can be obtained from some source other than double refraction measurements. The use of Equation (1) in some specific situations will be illustrated.

#### CALCULATION OF VELOCITY DISTRIBUTIONS FOR SPECIFIED CASES

##### Case I: Parallel Straight Streamlines

For laminar flow between flat plates the streamlines are straight and parallel. This situation is approximated experimentally by flow in a straight rectangular channel of high aspect ratio (ratio of

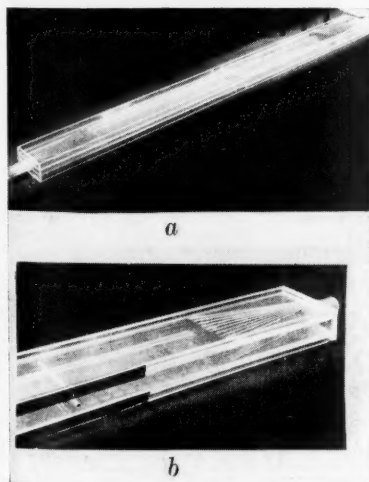


Fig. 4. Photographs of the flow test channel: a. flow test channel before installation of the cylindrical obstacle, b. deep end of channel showing flow diffuser vanes and cylindrical obstacle installed.

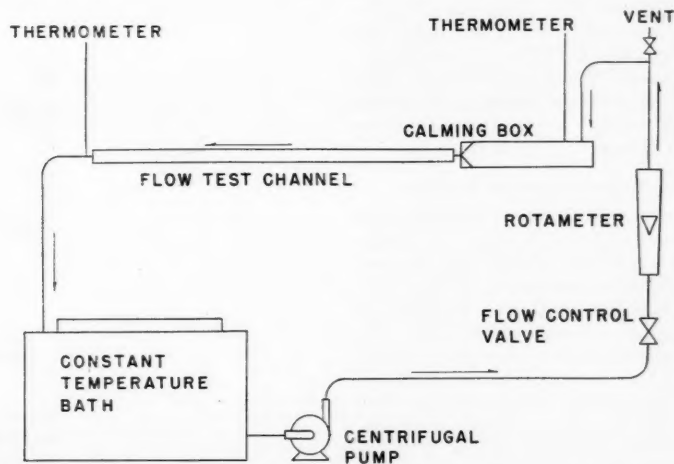


Fig. 5. Schematic representation of the fluid circulating system.

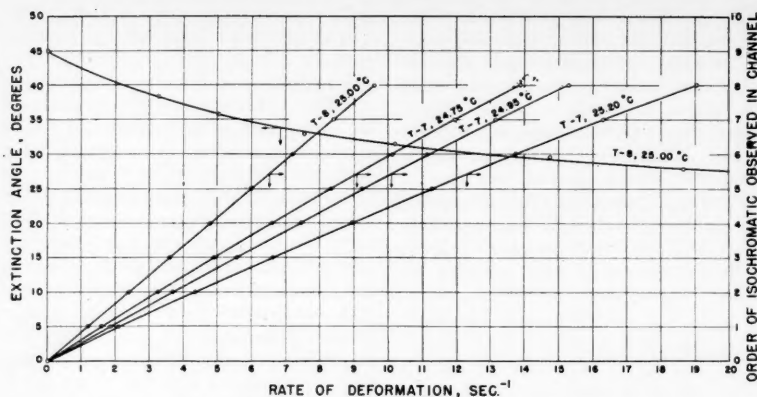


Fig. 6. Optical calibration curves for test solutions T-7 and T-8.

width to depth). In this case the terms  $V/r$  and  $V/r'$  vanish and the streamlines are determined by the channel walls. Equation (1) reduces to

$$\frac{dV}{dn} = \pm E \quad (3)$$

From isochromatic patterns  $E$  may be specified throughout the field of flow. Equation (3) can then be integrated numerically or graphically along a stream normal to obtain the velocity distribution. Necessary boundary conditions are provided by the fact that  $V = 0$  at the channel walls.

#### Case II: Parallel Curved Streamlines

For the case of parallel but curved streamlines  $V/r' = 0$  and  $\theta = \phi$ . Hence the isoclinic patterns may be used to obtain the streamlines throughout the flow field. A graphical or numerical method will be needed to determine their radius of curvature at each point. Equation (1) becomes

$$\frac{\partial V}{\partial n} = \pm E + \frac{V}{r} \quad (4)$$

Having calculated  $r$  from the isoclinics and determined  $E$  from the isochromatics for each point in the field, one may integrate Equation (4) numerically to obtain the velocity distribution. Integration is performed along a streamline normal, subject to the boundary conditions of zero velocity at the walls.

#### Case III: Nonparallel Straight Streamlines

Flow between the two nonparallel walls provides a situation in which the streamlines are straight but not parallel, and the dilation component of the flow does not vanish. A good approximation to this case in practice is found in a symmetrical convergent (divergent) section joining two rectangular channels of the same width but different depths. One considers that the streamlines are radial lines emanating from the line at which the nonparallel walls would converge, if extended.

In the present case Equation (1) reduces to

$$\frac{\partial V}{\partial n} = \pm \sqrt{E^2 - \frac{4V^2}{r'^2}} \quad (5)$$

which must be integrated numerically along a normal curve (here the arc of a circle whose center is the point of convergence of the walls).  $E$  is obtained from the isochromatics and  $r'$  from the channel configuration. The usual boundary conditions of zero velocity at the walls are used, and a check is provided in the fact that  $\partial V/\partial n$  should vanish at the center of the channel for a symmetrical situation.

#### Case IV: General Two-Dimensional Flow with Known Streamlines

Situations may arise in which the streamlines are neither straight nor parallel but are known throughout the flow field from some source other than double-refraction measurements. One can obtain  $r$  and  $r'$  by a graphical or numeri-

cal method throughout the field and then apply Equation (1) directly. Numerical integration is performed along a streamline normal, subject to the zero-velocity conditions at the walls.

#### Case V: General Two-Dimensional Laminar Flow with Unknown Streamlines

Where the streamline distribution is unknown, Equation (1) is not suitable for calculation of velocity distributions. However a method of analyzing such cases has been proposed by Rosenberg (22). The analysis requires introduction of the Stokes stream function, which when inserted into the laminar-flow relationships yields the following equation:

$$\frac{\partial^2 \Psi}{\partial x^2} - \frac{\partial^2 \Psi}{\partial y^2} = E \cos 2\theta \quad (6)$$

An important property of the stream function should be noted at this point; the difference in  $\Psi$  values between two points in the field of flow is numerically equal to the volumetric flow rate across any curve connecting the points. Two direct consequences of this property are that curves of constant stream-function values are the streamlines themselves and that the stream function is constant along any solid boundary. Furthermore for the case of unidirectional flow the value of  $\Psi$  may be obtained across a flow channel by direct integration.

Hence if one considers a situation in which the flow starts out as unidirec-

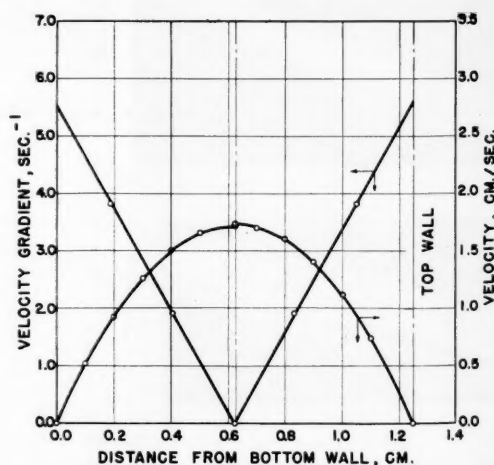
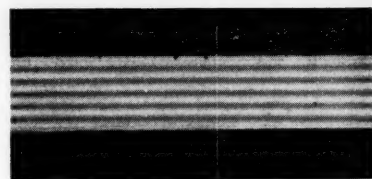


Fig. 7. Flow pattern photograph and plots of velocity gradient and velocity vs. distance for a straight channel of 10:1 aspect ratio; channel depth 1.250 cm., solution calibration T-7, 25.00°C.; measured discharge 18.1 cc./sec.; calculated discharge 18.1 cc./sec.

and then  
numerical  
stream-  
velocity

ar Flow

tion is  
ble for  
utions.  
g such  
enberg  
duction  
which  
ow re-  
uation:

(6)

stream  
point;  
en two  
erically  
across  
Two  
erty are  
unction  
es and  
nstant  
ermore  
ow the  
a flow

tion in  
indirec-

tional in a straight channel, he may assign an arbitrary value to  $\Psi$  along one of the channel boundaries and calculate the distribution of  $\Psi$  across to the other by integration. Having the value of  $\Psi$  along both channel boundaries and across the channel at some distance upstream from the region of interest, one has the necessary boundary conditions to begin a numerical solution of the second-order partial-differential equation (6). The values of  $E$  and  $\theta$  may be obtained throughout the field of flow from the isochromatic and isoclinic patterns, respectively.

Numerical solution of Equation (6) requires that it first be placed in finite difference form. If one assumes that the flow field is divided up into a square grid of equal spacing in both  $x$  and  $y$  directions, the following difference equation results:

$$\Psi(x+h, y) + \Psi(x-h, y) - \Psi(x, y+h) - \Psi(x, y-h) = h^2 E \cos 2\theta \quad (7)$$

One may start from the known values of  $\Psi$  along the boundaries and employ a simple iteration procedure to obtain  $\Psi$  at each corner of the grid of spacing  $h$ . Graphical interpolation may be applied to determine curves of constant  $\Psi$  (streamlines), and numerical differentiation will yield the velocity components if desired.

## APPARATUS

The experimental apparatus consisted of three major subsystems: the optical system, the flow test channel, and the fluid circulation system. Figure 2 shows over-all views of the equipment.

The optical system consisted of an Exakta 35-mm. single-lens reflex camera and standard polariscope components. The polariscope components were a light-source assembly consisting of interchangeable sodium vapor and tungsten lamps and a collimating lens, two polarizing plates mounted on ball-bearing rollers so that their axes of polarization might be varied at will, two quarter-wave plates mounted on sliding tracks to permit ready insertion in or removal from the light path, and a two-section optical bench. A 10-in. field of view was provided by this system. All optical components were mounted on two rigid tables, between which was placed a third table containing the flow test channel. The camera mount was a heavy platform fitted with a vertical rod and an adjustable clamp which held an adapter screwed into the tripod fitting of the camera; the arrangement of these components can be seen in Figures 2a and 3.

Photographs of the flow-test channel are shown in Figure 4. The channel was made of  $\frac{3}{8}$ -in.-thick Plexiglas and provided a rectangular cross section for flow. The aspect ratio (ratio of width to depth) was kept high in order to approximate more closely a two-dimensional flow situation. Flow patterns were observed through the wide dimension of the channel as indicated in Figure 2.  $\lambda$

The channel consisted of two sections of uniform rectangular cross section, one measuring 12.41 by 2.545 cm., the other 12.49 by 1.250 cm. These were joined by a straight-walled converging section. The converging section was symmetrical about the center line of the two uniform sections, and the converging walls made an angle of 5 deg. and 58 min. with the horizontal. Diffuser vanes were provided at each end of the system to spread the flow across the wide dimension and aid in rapid establishment of the two-dimensional velocity profiles. The channel was mounted on an aluminum rail and attached to an upstream calming box and downstream return line with short sections of rubber radiator hose. The hose was secured with circular clamps, and the entire assembly could be moved back and forth along the rail.

This test channel provided an opportunity for observing flow in uniform channels of different aspect ratios (5:1 and 10:1) and in straight convergent and divergent sections. In addition a 0.718-cm. O.D. cylindrical rod was inserted in the 2.545-cm.-deep section about midway along its length. The rod was mounted perpendicular to the side walls of the channel and extended all the way across the flow path, thereby permitting a study of the two-dimensional flow about a cylindrical obstacle. These details may be observed in Figure 4.

The prime fluid-circulation system components were an Aminco 16-gal. constant-temperature bath and a  $\frac{3}{4}$ -hp. centrifugal pump. Flow lines were standard 1-in. brass pipe, and 1-in. O.D.,  $\frac{3}{4}$ -in. I.D. Tygon hose. A rotameter was used for flow-rate measurements, and a precision thermometer

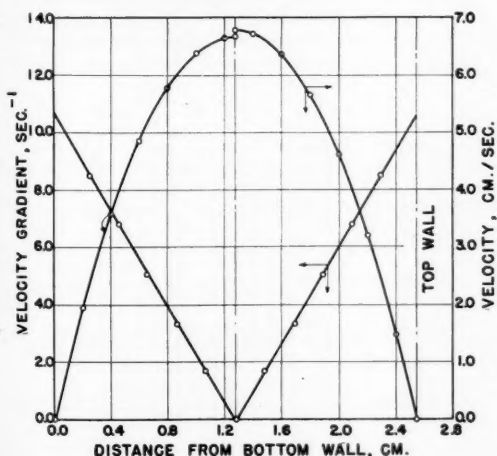
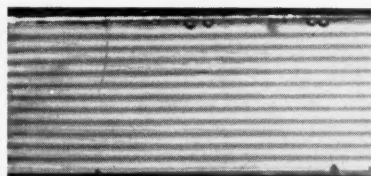


Fig. 8. Flow pattern photograph and plots of velocity gradient and velocity vs. distance for a straight channel of 5:1 aspect ratio: channel depth 2.546 cm.; solution calibration T-7, 24.80°C.; measured discharge 143.3 cc./sec.; calculated discharge 142.1 cc./sec.

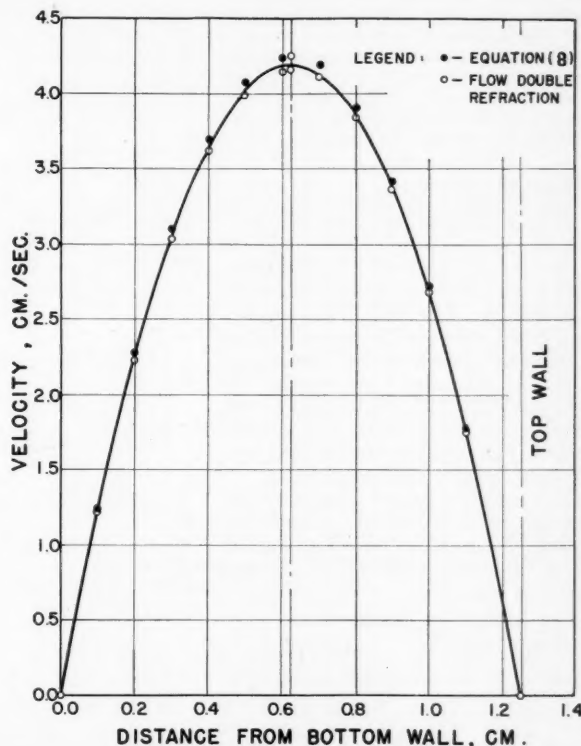
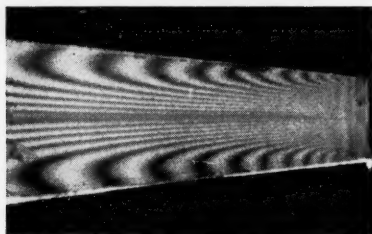


Fig. 9. Comparison of velocity profiles calculated from Equation (8) and obtained from flow double refraction measurements.



of considerable importance to the final photographic results, since each negative was enlarged to approximately 200 times its original area. Photographs were obtained for flow in shallow and deep straight-channel sections, in the converging and diverging sections, and about the cylindrical obstacle.

Most of the photographs of the iso-

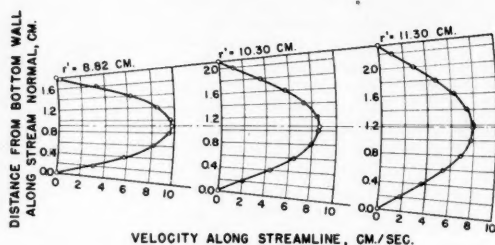
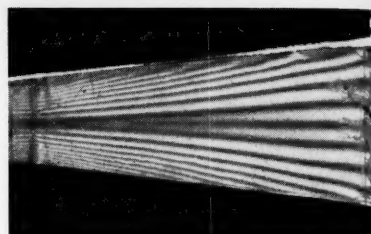


Fig. 10. Photograph and developed profiles for flow in a diverging channel: solution calibration T-7, 24.85°C.; measured discharge 134.6 cc./sec.; calculated discharge  $r' = 8.81$  cm.,  $r' = 10.31$  cm.,  $r' = 11.31$  cm.,  $Q = 136.4$  cc./sec.,  $Q = 138.7$  cc./sec.,  $Q = 139.7$  cc./sec.

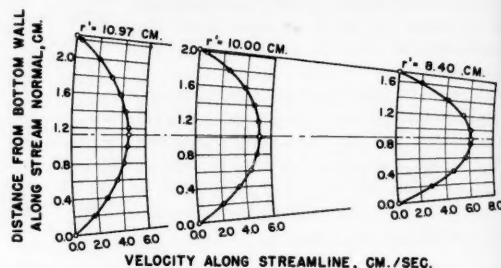


Fig. 11. Photograph and developed velocity profiles for flow in a converging channel: solution calibration T-7, 24.90°C.; measured discharge 81.2 cc./sec.; calculated discharge  $r' = 8.40$  cm.,  $r' = 10.00$  cm.,  $r' = 10.97$  cm.,  $Q = 91.5$  cc./sec.,  $Q = 91.9$  cc./sec.,  $Q = 88.8$  cc./sec.

reading to 0.05°C. was mounted in the calming box just upstream from the flow channel. The arrangement is shown schematically in Figure 5.

The dye solutions themselves were prepared from commercial lots of milling yellow NGS powder. The manner of preparation and optical calibration is described by Peebles and Prados. Viscous properties of the solutions were determined in a variable-head capillary viscometer similar in principle to that described by Maron, Krieger, and Sisko (17). A complete description of the viscometry technique used in the present investigation is given by Havewala (12).

#### EXPERIMENTAL WORK

Photographs were made of the interference patterns over a wide range of flow rates for the available geometries, that is, straight channel flow, converging and diverging flow, and flow about the cylindrical obstacle. The optical components were carefully aligned before each run, and the fluid temperature was maintained at  $25.00 \pm 0.15^\circ\text{C}$ . in the calming box just upstream from the test section. Flow rate and temperature were recorded for each photograph taken.

The optimum exposure time and lens aperture were obtained by trial and error for each film used. The following appeared to give the best results for the isochromatic photographs.

Film	Exposure time, sec.	Lens stop
Tri-X	1.0	Between 11 and 16
Plus X	4.0	Between 11 and 16
Micro File	12.0	8

The Microdol developer used produced a photograph of fine grain, which was

chromatic patterns were made with circularly polarized, monochromatic light, that is, with quarter-wave plates in place and the sodium vapor lamp in use. Some isochromatic patterns, particularly in the convergent and divergent sections, were photographed with monochromatic plane-polarized light by sliding the quarter-wave plates out of the light path. In all cases the axis of polarization of the polarizer was vertical and that of the analyzer was horizontal.

In photographing the isoclinic patterns it was necessary to use white light, so that the black isoclinics might be distinguished from the colored isochromatics. Plane-polarized light of various orientations was provided by rotating the polarizer and analyzer together, keeping them crossed all the while. Isoclinic

photographs were made for flow about a cylindrical obstacle at various orientations of polarizer and analyzer, but at a single flow rate and fluid temperature. The polarizer and analyzer were rotated together in a counterclockwise direction (looking toward the light source). Photographs were made at rotations of 0, 15, 30, 45, 60, 75, 90, and  $-15$  deg. The  $-15$ - and  $75$ -deg. patterns were identical, as were the 0- and 90-deg. patterns.

Because of marked changes over a period of 2 weeks in the optical response of the solutions while they remained in the flow system, samples were withdrawn on each day that photographs were made. These were stored in glass bottles for later calibration. Previous tests had shown that milling yellow solutions stored in glass bottles underwent no measurable

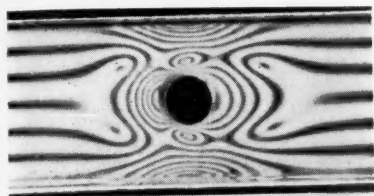
8	-3.59	-3.59	-3.61	-3.72	-4.05	-4.62	-6.09	-8.19	-9.80	-9.90	-8.33	-6.27	-4.99	-4.30	-3.62	-3.67	-3.60	-3.59	-3.59
7	-1.900	-1.900	-1.900	-1.900	-1.900	-1.900	-1.900	-1.900	-1.900	-1.900	-1.900	-1.900	-1.900	-1.900	-1.900	-1.900	-1.900	-1.900	-1.900
6	-0.62	-0.62	-0.58	-0.50	-0.50	-0.51	-0.51	-0.55	-0.59	-0.60	-0.63	-0.67	-0.70	-0.72	-0.72	-0.72	-0.72	-0.72	-0.72
5	-1.731	-1.731	-1.733	-1.728	-1.710	-1.688	-1.658	-1.626	-1.593	-1.567	-1.530	-1.499	-1.462	-1.420	-1.370	-1.320	-1.270	-1.230	-1.193
4	-1.72	-1.72	-1.62	-1.51	-1.19	-0.980	0.30	0.60	0.68	0.16	0.50	0.76	0.62	-0.06	-1.00	-1.38	-1.55	-1.70	-1.72
3	-1.299	-1.299	-1.296	-1.293	-1.273	-1.256	-0.943	-0.751	-0.349	-0.441	-0.769	-0.687	-0.965	-1.179	-1.250	-1.277	-1.298	-1.296	-1.299
2	-0.62	-0.62	-0.63	-0.64	0.74	0.99	2.04	2.56	3.00	3.58	3.70	3.97	1.37	0.76	0.67	-0.01	-0.71	-0.79	-0.82
1	-0.690	-0.690	-0.692	-0.690	-0.683	-0.508	-0.443	-0.329	-0.049	-0.072	-0.150	-0.332	-0.457	-0.504	-0.643	-0.679	-0.686	-0.692	-0.690
0	0	0	0	0	0	0	0	0	0	0	0	0	0	0	0	0	0	0	0
8	0.62	0.62	0.61	0.64	-0.83	-0.97	-2.04	-2.56	-3.00	-3.58	-3.70	-3.97	-1.37	-0.76	-0.67	-0.01	-0.71	-0.79	-0.82
7	0.690	0.690	0.692	0.690	0.683	0.508	0.443	0.329	0.049	0.072	0.150	0.332	0.457	0.504	0.643	0.679	0.686	0.692	0.690
6	1.731	1.731	1.733	1.728	1.710	1.688	1.658	1.626	1.593	1.567	1.530	1.499	1.462	1.420	1.370	1.320	1.270	1.230	1.193
5	1.72	1.72	1.62	1.51	1.19	0.980	0.30	0.60	0.68	0.16	0.50	0.76	0.62	-0.06	-1.00	-1.38	-1.55	-1.70	-1.72
4	1.299	1.299	1.296	1.293	1.273	1.256	0.943	0.751	0.349	0.441	0.769	0.687	0.965	1.179	1.250	1.277	1.298	1.296	1.299
3	0.62	0.62	0.63	0.64	-0.74	-0.99	-2.04	-2.56	-3.00	-3.58	-3.70	-3.97	-1.37	-0.76	-0.67	-0.01	-0.71	-0.79	-0.82
2	0.690	0.690	0.692	0.690	0.683	0.508	0.443	0.329	0.049	0.072	0.150	0.332	0.457	0.504	0.643	0.679	0.686	0.692	0.690
1	1.731	1.731	1.733	1.728	1.710	1.688	1.658	1.626	1.593	1.567	1.530	1.499	1.462	1.420	1.370	1.320	1.270	1.230	1.193
0	1.72	1.72	1.62	1.51	1.19	0.980	0.30	0.60	0.68	0.16	0.50	0.76	0.62	-0.06	-1.00	-1.38	-1.55	-1.70	-1.72
8	0.62	0.62	0.61	0.64	-0.83	-0.97	-2.04	-2.56	-3.00	-3.58	-3.70	-3.97	-1.37	-0.76	-0.67	-0.01	-0.71	-0.79	-0.82
7	0.690	0.690	0.692	0.690	0.683	0.508	0.443	0.329	0.049	0.072	0.150	0.332	0.457	0.504	0.643	0.679	0.686	0.692	0.690
6	1.731	1.731	1.733	1.728	1.710	1.688	1.658	1.626	1.593	1.567	1.530	1.499	1.462	1.420	1.370	1.320	1.270	1.230	1.193
5	1.72	1.72	1.62	1.51	1.19	0.980	0.30	0.60	0.68	0.16	0.50	0.76	0.62	-0.06	-1.00	-1.38	-1.55	-1.70	-1.72
4	1.299	1.299	1.296	1.293	1.273	1.256	0.943	0.751	0.349	0.441	0.769	0.687	0.965	1.179	1.250	1.277	1.298	1.296	1.299
3	0.62	0.62	0.63	0.64	-0.74	-0.99	-2.04	-2.56	-3.00	-3.58	-3.70	-3.97	-1.37	-0.76	-0.67	-0.01	-0.71	-0.79	-0.82
2	0.690	0.690	0.692	0.690	0.683	0.508	0.443	0.329	0.049	0.072	0.150	0.332	0.457	0.504	0.643	0.679	0.686	0.692	0.690
1	1.731	1.731	1.733	1.728	1.710	1.688	1.658	1.626	1.593	1.567	1.530	1.499	1.462	1.420	1.370	1.320	1.270	1.230	1.193
0	1.72	1.72	1.62	1.51	1.19	0.980	0.30	0.60	0.68	0.16	0.50	0.76	0.62	-0.06	-1.00	-1.38	-1.55	-1.70	-1.72

Fig. 12. Tabulation of values of the x component of the rate of deformation and the stream function at the corners of the coordinate grid.

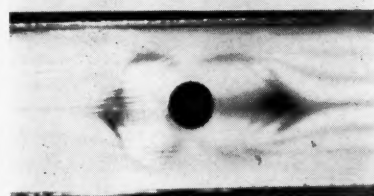


change in optical or viscous properties during periods of at least 3 months. In the present study all calibrations were performed within 3 weeks after the photographs were made. Optical calibration curves for the test solutions used are presented in Figure 6.

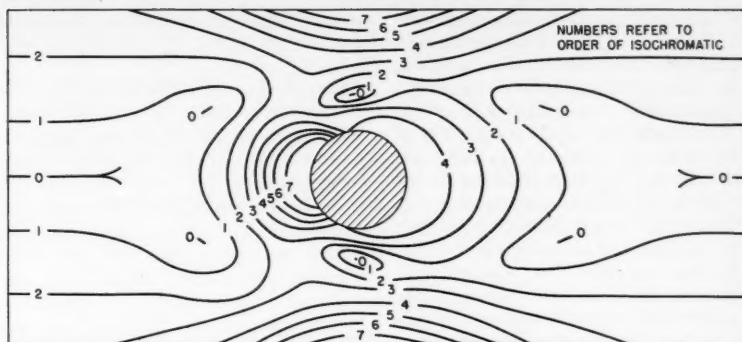
The positions of isochromatic and isoclinic bands were obtained from accurate measurements made from enlargements



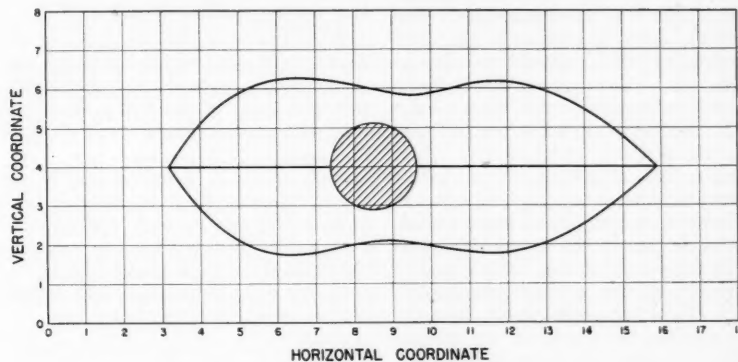
a



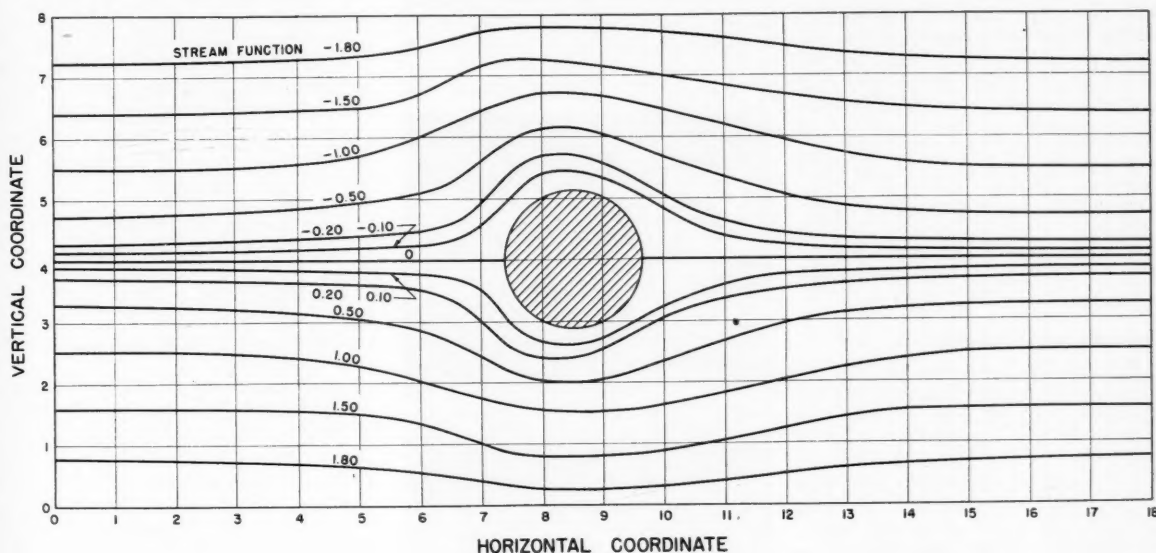
b



(c)



(d)



(e)

Fig. 13. Steps in the development of streamlines about a cylinder: a. isochromatic photograph; b. isoclinic photograph, 0, 90; c. isochromatic tracing; d. isoclinic traced from b; e. developed streamlines about cylinder.

of the flow-pattern photographs. Distance-scale ratios were determined with the known distance from top to bottom of the channel used as a reference. A detailed description of the methods used in the measurements is given by Prados (21).

#### FLOW ANALYSIS FROM PHOTOGRAPHIC MEASUREMENTS

The procedures used to analyze the photographic measurements follow. As these differed for the three types of flow studied, each will be discussed separately.

#### Straight Parallel Flow

The measurements taken from the photographs of straight parallel flow gave the location of each isochromatic along a vertical line from the top to the bottom of the flow channel. From the optical calibration curve for the test liquid a

0.00	-3.59
0.01	-1.800
0.02	-2.62
0.03	-1.731
0.04	-1.72
0.05	-1.299
0.06	-0.82
0.07	-0.690
0.08	0
0.09	0
0.10	0.02
0.11	0.690
0.12	1.70
0.13	1.294
0.14	2.62
0.15	1.738
0.16	3.61
0.17	1.893
0.18	18

rate of deformation was associated with each isochromatic, and hence the rate of deformation could be plotted vs. distance across the channel. Such photographs and plots are shown in Figures 7 and 8.

For straight parallel flow the rates of deformation and velocity gradient are equal. Hence graphical integration of the curve of rate of deformation vs. distance was used to obtain a similar curve of values of velocity vs. distance across the channel. This unidirectional velocity-distribution curve was then integrated to yield the total discharge through the channel. The results of these calculations for the cases illustrated in Figures 7 and 8 are tabulated in Tables 1 and 2.\*

In addition the velocity distribution in the 10:1 aspect-ratio channel was compared with that calculated from viscous information. The results of the viscosity determinations showed that the test solutions used behaved as Newtonian fluids with viscosities of 17.1 and 26.5 centipoises at rates of deformation from 2 to 12 reciprocal sec. (the range of interest of the present investigation). Peebles *et al.* (19) have found that at shear stresses above 20 dynes/sq. cm. milling yellow solutions exhibit marked pseudoplasticity. They have also shown however that at low shear stresses the viscous behavior should become Newtonian, which is in accordance with experimental observation. Hence the formula for velocity distribution of a Newtonian fluid flowing between two parallel plates

$$u = \frac{3Q}{4ab} \left[ 1 - \left( \frac{y}{a} \right)^2 \right] \quad (8)$$

was assumed to hold for the high-aspect-ratio channel and was used to calculate the velocity profile.

Agreement between velocities calculated from Equation (8) and the flow double refraction measurements was excellent. A comparison of the two is shown in Figure 9.

#### Converging and Diverging Flow

Photographic measurements of convergent and divergent flow gave the isochromatic positions along circular arcs centered at the hypothetical point of convergence of the nonparallel channel walls. The rate of deformation along such an arc could be obtained from the optical calibration curve of the test liquid, but here the velocity gradient was no longer equal to the rate of deformation. The velocity profile could be obtained however by direct numerical integration of Equation (5) subject to the boundary conditions of zero velocity at the walls. Integration was carried out by the method of Runge and Kutta as given by Scarborough (23). The results of such integrations at three locations along a divergent channel are shown graphically in Figure 10 and are tabulated in Table 3\*.

\*See footnote p. 227.

Similar results for flow in a convergent channel are given in Figure 11 and Table 4.\*

Since flow across a closed curve in two dimensions is equal to the velocity component normal to the curve multiplied by the length of curve, the discharge through a converging or diverging channel of high aspect ratio can be calculated from the expression

$$Q = b \int_0^N V dn \quad (9)$$

Discharges calculated from Equation (9) are given in Figures 10 and 11.

#### Flow About a Cylindrical Obstacle

From the measured positions of the isochromatic and isoclinic bands one may determine the maximum rate of deformation and angle made by this maximum rate with the horizontal from the flow photographs. These values were found at each corner of a square grid of 144 points, 18 units along the channel by 8 units across the channel. The value of the component of deformation acting in the positive  $x$  direction was found from the following relationship, which follows directly from Equation (34) (see Appendix)\*.

$$E_{xy} = E \cos 2\theta \quad (10)$$

The needed quantities were obtained

\*See footnote in column 1.

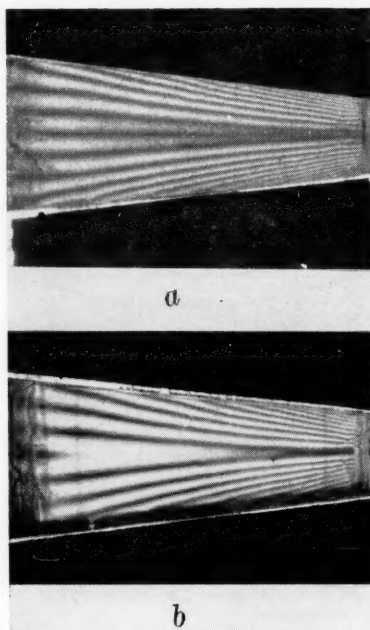


Fig. 14. Flow patterns produced in a converging channel from plane and circularly polarized light at comparable flow rates: a. plane polarized light, circularly polarized light.

from the extinction angle, isoclinic angle, and isochromatic fringes. The values of  $E_{xy}$  obtained at the corners of the grid are tabulated in Figure 12. The values were then used in the numerical integration of Equation (6), which was integrated in difference form [Equation (7)] and required as boundary conditions the values of  $\Psi$  along the top and bottom of the channel and along two adjacent vertical grid lines upstream and two downstream from the obstacle. These values were obtained as follows.

For undisturbed unidirectional flow the stream function can be calculated across the channel from

$$u = \frac{-d\Psi}{dy}; \quad (11)$$

$$\Psi(y) = \Psi(0) - \int_0^y u dy$$

Since  $\Psi$  may be specified with reference to an arbitrary constant only, the value of  $\Psi$  was chosen as zero at the center of the channel, and other values of  $\Psi$  out to the top and bottom walls were calculated from Equation (11). Then use was made of the fact that  $\Psi$  is constant along streamlines and solid boundaries. This immediately specified  $\Psi$  along the top and bottom of the channel and from symmetry considerations along the center line of the channel and the cylinder boundary as well.

The nature of Equation (7) necessitated iteration which started along both upstream and downstream edges of the grid and worked toward the middle. The results of the iteration process are shown in tabular form in Figure 12. Graphic interpolation was used to determine curves along which  $\Psi$  has a constant value. These are the streamlines of flow about the obstacle. The photographs and curves of Figure 13 illustrate the steps in the development of these streamlines from the flow photographs. Calculation procedures and intermediate results are given by Prados (21).

Unfortunately the results of the calculation could not be checked by calculating the discharge, since the flow through the channel was already fixed by fixing the values of the stream function along the boundaries. A number of theoretical results for flow of a viscous fluid about a cylinder were examined, but they were all developed either for the case of unbounded flow (2) or for a Reynolds number of the order of 0.1 (25). The Reynolds number obtained for the present situation was 3.81, calculated by

$$N_{Re} = \frac{dU\rho}{\mu} \quad (12)$$

The viscous drag coefficient for flow about the cylinder was calculated as illustrated in the Appendix. Again checking was hampered by the lack of avail-

able measurements in the literature for flow about a cylinder in a closely bounded channel. The value of the viscous drag coefficient of 1.83 obtained from double-refraction measurements was compared with the experimental value of 2.0 given by Goldstein (9) for flow in an unbounded channel at the same Reynolds number. The value of 1.86 calculated from the expression of Bairstow *et al.* (2) for flow in a bounded channel at Reynolds numbers less than 0.1 gave better agreement.

#### SUMMARY OF RESULTS AND DISCUSSION

Tables 5 and 6\* summarize the agreement obtained between measured and calculated flow rates for the straight channels, converging channel, and diverging channel. Original data, from which these and all other results reported in this paper are compiled, are given by Prados (21). For the straight channels the agreement between measured and calculated flow rates was within +7.3, -9.6%, with a mean square deviation of 4.22%. For the convergent and divergent flows agreement was within +13.2, -11.2%, with a mean square deviation of 7.75%. Twenty-six straight-channel runs and fourteen converging and diverging runs were analyzed. Only one calculation was made for the flow about the cylinder.

An examination of the interference patterns in a convergent or divergent channel by means of both plane- and circularly polarized light as shown in Figure 14 yields some extremely interesting results in support of the present analysis. As can be seen from Figure 14b, the pattern given by circularly polarized light has no zero-order isochromatic along the center of the channel. If the amount of double refraction were dependent only upon the rate of pure shear, as has been suggested by some investigators (6, 7, 19, 29), including the authors, there would certainly be a zero-order isochromatic along the center of the channel, for here the rate of pure shear vanishes. On the other hand the rate of dilation does not vanish, and hence the total rate of deformation is not zero. Therefore the nonappearance of the zero-order isochromatic tends to support the conclusion that the amount of double refraction is a function of the total rate of deformation (or the maximum shear stress) for the doubly refracting liquids employed in the present study.

Figure 14a made in plane-polarized light does show a dark band along the center line of the channel. This might lead one to suppose that it is, indeed, a zero-order isochromatic. However since the isochromatic must appear in circularly polarized light as well as in plane-polarized light, one must conclude that this band is an isoclinic. When one recalls Equation (2) and notes that  $G$  vanishes

at the center of the convergent channel while  $D$  does not, it is seen that here

$$\theta = \phi \pm \frac{\pi}{4} \quad (13)$$

with the sign determined by whether the rate of shear approaches zero from above or below the center line of the channel. Equation (13) states that the plane of maximum shear stress makes an angle of 45 deg. with the horizontal streamlines at the center of the convergent and divergent channels. The total maximum rate of deformation is quite low, however, and the extinction angle is approximately 45 deg. Hence an isoclinic appears along the channel center line. If the optical orientation of the doubly refracting liquid were determined by the streamlines, other circumstances would occur. The horizontal streamline makes an angle of 90 deg. with the vertical plane of polarization of the incident light; the extinction angle is 45 deg., and hence no isoclinic would appear. Since the isoclinic does appear, it may be concluded that the optical orientation of the doubly refracting milling yellow solutions is determined by the direction of the maximum shear stress (or rate of deformation) rather than the streamline direction.

Since the method of treating the data from the double-refraction measurements involved two integrations, it would be expected that any random errors in the measurements of the fringe locations themselves would tend to be averaged out and their effect minimized. There were several possible sources of error however which would not be so affected: misalignment of optical components due to the optical bench being made in two sections rather than one, difference between the temperature indicated by the thermometer upstream from the test section and the actual temperature in the test section itself, personal errors in reading the rotameter or thermometer, and nonparallelism of the channel walls. The effect of errors from these sources is very difficult to estimate. An additional source of error was introduced into the converging and diverging flow calculations by the graphical determination of the radius of curvature of the stream normal.

Because of the lack of an adequate method of checking results it is difficult to assess the validity of the streamline patterns developed about the cylindrical obstacle. The pattern as shown in Figure 13 satisfies one's intuitive notion as to how such a flow should look. The wider separation of the streamlines on the downstream side suggests the existence of a stable pair of vortices directly behind the cylinder. To demonstrate these from flow double-refraction measurements, it would be necessary to refine the coordinate grid considerably, near the cylinder. Unfortunately the isochromatic

patterns are quite faint and distorted in this region, and it is doubtful that any consistent results could be obtained even if the grid were refined.

To obtain any precise indication of flow next to an obstacle of this nature it will probably be necessary to modify the details of channel construction somewhat. As pointed out by Frocht (8) for the case of photoelastic solids, the production of sharp, accurate double-refraction patterns next to solid boundaries requires that all corners be square and surfaces parallel within very close tolerances. In spite of extreme care exercised in the construction of the Plexiglas channels it is doubtful that the required tolerances could be attained, and there was no convenient way to check this internally after the channel had been assembled. Another difficulty arose in the fixing of the cylindrical obstacle in the channel itself. To prevent leaks a rather tight fit was required, and some small amounts of residual stress were set up in the Plexiglas about the cylinder mount. Since Plexiglas is doubly refracting when stressed, this resulted in further distortion of the interference pattern in the immediate vicinity of the cylinder.

Another possible source of error, therefore, was double refraction in the Plexiglas channel walls. However, it is not believed that this would seriously affect the present results, since with the fluid at rest the flow channel appeared uniformly dark, indicating that no appreciable double refraction was occurring along the light path. A faint lightening of the field was observable within  $\frac{1}{16}$  in. of the cylindrical obstacle, but its effect was confined to a region in which no fringes could be clearly observed.

In addition to these sources of error the isoclinic patterns were somewhat diffuse, and it was difficult to locate accurately the center line of a given isoclinic curve for tracing (see Figure 13). This may again have been due in part to nonparallelism of the channel walls or to a slight misalignment of the optical components.

In view of these difficulties it is rather encouraging to note the fairly close agreement in stream-function values at the meeting point for calculations started upstream and downstream from the cylinder (see Figure 12). The agreement, within 2%, of the drag coefficients calculated from flow double refraction and the theoretical formula of Bairstow (2) is also encouraging, although there is considerable uncertainty as to the effect produced by the use of Bairstow's formula at a Reynolds number of 3.81, which is considerably higher than the maximum value of 0.1 for which it was derived.

It is hoped that eventually a more accurate check on these results can be made by the determination of the streamline patterns for flow about a cylindrical obstacle by some method other than

\*See footnote p. 227.



from flow double-refraction measurements. Direct injection of a dark-dye or a stream of tiny air bubbles would enable one to trace out the streamline pattern and compare it with that obtained in the present work as shown in Figure 13.

## CONCLUSIONS AND RECOMMENDATIONS

From the results of the investigation, the following conclusions have been drawn.

1. The experimental quantities furnished by the flow double-refraction technique may be analyzed to yield the streamline and velocity distribution in a two-dimensional laminar-flow situation.

2. The results of such analyses are quantitatively accurate within  $\pm 10\%$  for flow with straight, parallel streamlines and within  $\pm 15\%$  for flow with straight, nonparallel streamlines.

3. Quantitative results may be obtained for a general two-dimensional flow situation involving neither straight nor parallel streamlines. Absolute determination of the limits of error on these results will require further experimental effort.

It is therefore felt that this technique will be of real use in the analysis of complex laminar-flow situations which can be idealized to two dimensions. The technique should be especially valuable in those situations where a measuring probe is undesirable, as in the narrow laminar boundary layers formed next to solid objects in a turbulent stream.

## ACKNOWLEDGMENT

The authors wish to thank the Office of Naval Research for its support of the major portion of this investigation. Additional support from the Engineering Experiment Station and Department of Chemical Engineering of the University of Tennessee is also gratefully acknowledged.

## NOTATION

$a$  = distance from center to top or bottom of rectangular channel  
 $b$  = width of rectangular channel  
 $C_{Df}$  = viscous drag coefficient for circular cylinder  
 $d$  = diameter of cylindrical obstacle  
 $D$  = rate of dilation in a viscous fluid  
 $D_f$  = viscous drag force, exerted in the direction of flow, on a unit length of circular cylinder with axis normal to the flow  
 $E$  = maximum rate of deformation at a point in a viscous fluid  
 $E_\xi$  = rate of deformation in a viscous fluid along a plane oriented at an angle  $\xi$  to the horizontal  
 $E_{xy}$  = rate of deformation in a viscous fluid along a horizontal plane

$f$  = focal length of camera lens  
 $g_c$  = force-mass unit conversion constant  
 $G$  = rate of pure shear in a viscous fluid  
 $h$  = incremental distance in  $x$  and  $y$  coordinates for iterative solution of partial differential equation in difference form  
 $n$  = stream normal coordinate, distance along a curve normal to a set of streamlines  
 $N$  = total distance from wall to wall of channel taken along a stream normal  
 $N_{Re}$  = Reynolds number  
 $Q$  = volumetric discharge through flow channel  
 $r$  = radius of curvature of a streamline  
 $r'$  = radius of curvature normal to a set of streamlines  
 $s$  = streamline coordinate, distance along streamline  
 $t$  = time  
 $u$  = fluid velocity component in  $x$  direction  
 $U$  = mean flow velocity of fluid in a channel, that is, the ratio of volumetric discharge to channel cross-sectional area  
 $v$  = fluid velocity component in  $y$  direction  
 $V$  = fluid velocity along a streamline  
 $x$  = horizontal coordinate-rectangular Cartesian system  
 $y$  = vertical coordinate-rectangular Cartesian system

## Greek Letters

$\beta$  = polar angle inside circular cylinder  
 $\theta$  = angle made by direction of maximum shear stress with the horizontal in a moving viscous fluid  
 $\mu$  = fluid viscosity  
 $\xi$  = angle measured from horizontal made by an arbitrary direction in a moving viscous fluid  
 $\pi$  = ratio of circumference to the diameter of a circle  
 $\rho$  = fluid density  
 $\sigma_x$  = normal stress exerted in  $x$  direction in a moving viscous fluid  
 $\sigma_y$  = normal stress exerted in  $y$  direction in a moving viscous fluid  
 $\tau$  = maximum shear stress at a point in a moving viscous fluid  
 $\tau_\xi$  = shear stress in a moving viscous fluid, acting on a plane oriented at angle  $\xi$  to the horizontal  
 $\tau_{xy}$  = shear stress acting in positive  $x$  direction on a surface facing in positive  $y$  direction in a moving viscous fluid  
 $\phi$  = angle made by a streamline with the horizontal  
 $\Psi$  = Stokes stream function

## LITERATURE CITED

- Alcock, E. D., and C. L. Sadron, *Physics* **6**, 92 (1935).
- Baird, L., B. M. Cave, and E. D. Lang, *Proc. Roy. Soc. (London)*, **A100**, 394 (1922).
- Binnie, A. M., *Proc. Phys. Soc. (London)*, **57**, 390 (1945).
- Binnie, A. M., and J. S. Fowler, *Proc. Roy. Soc. (London)*, **A192**, 32 (1947).
- Cerf, Roger, and H. A. Scheraga, *Chem. Rev.* **51**, 185 (1952).
- Dewey, D. R., Ph.D. dissertation, Mass. Inst. of Technol., Cambridge (1941).
- Edsall, J. T., "Advances in Colloid Science," Vol. I, p. 269, Interscience, New York (1942).
- Frucht, M. M., "Photoelasticity," Vol. I, John Wiley, New York (1941).
- Goldstein, Sydney, "Modern Developments in Fluid Dynamics," Vol. I, The Clarendon Press, Oxford (1938).
- Hauser, E. A., and D. R. Dewey, *Ind. Eng. Chem.*, **31**, 786 (1939).
- , *J. Phys. Chem.*, **46**, 212 (1942).
- Havewala, J. B., Bachelor's thesis, Univ. Tenn., Knoxville (1957).
- Humphry, R. H., *Proc. Phys. Soc. (London)*, **35**, 217 (1923).
- Leaf, Walter, *Mech. Eng.*, **67**, 586 (1945).
- Lindgren, E. R., *Arkiv. Fysik.*, **7**, 293 (1954).
- Maxwell, J. C., *Proc. Roy. Soc. (London)*, **22**, 46 (1873).
- Maron, S. H., I. M. Krieger, and A. W. Sisko, *J. Appl. Phys.*, **25**, 971 (1954).
- Peebles, F. N., H. J. Garber, and S. H. Jury, *Proc. Third Midwestern Conf. on Fluid Mechanics*, Univ. Minnesota Press, Minneapolis (1953).
- Peebles, F. N., J. W. Prados, and E. H. Honeycutt, Jr., *Prog. Rep.* 1 and 3 under Contract Number Nonr-811(04), Eng. Expt. Sta. Univ. Tenn., Knoxville (1954).
- Peebles, F. N., and J. W. Prados, paper in preparation.
- Prados, J. W., Ph.D. thesis, Univ. Tenn., Knoxville (1957). Available on 35-mm. microfilm through University Microfilms, 313 N. First St., Ann Arbor Michigan, at a cost of \$2.35.
- Rosenberg, Benjamin, *Rept.* 617, Navy Dept., David W. Taylor Model Basin, Washington 7, D. C., (1952).
- Scarborough, J. B., "Numerical Mathematical Analysis," 3 ed., The Johns Hopkins Press, Baltimore (1955).
- Thurston, G. B., and L. E. Hargrove, *Tech. Rept.* 1 and 4, Contr. DA-23-072-ORD-583, Office of Ordnance Research and the Research Foundation, Okla. Agr. Mech. Coll., Stillwater (1957).
- Tomotiko, S. and T. Aoi, *Quart. J. Mech. and Appl. Math.*, **3**, 140 (1950).
- Ulliyott, Philip, *Trans. ASME*, **69**, 245 (1947).
- Wayland, Harold, *J. Appl. Phys.*, **26**, 1197 (1955).
- Weller, R., *J. Appl. Mech.*, **14**, 103 (1947).
- Weller, R., D. J. Middlehurst, and R. Steiner, *Natl. Advisory Comm. Aeronaut. Tech. Note* 841 (1942).

Manuscript received January 23, 1958; revision received July 24, 1958; paper accepted October 1, 1958.



# Liquid-Side Mass Transfer Coefficients in Packed Towers

KAKUSABURO ONDA, EIZO SADA, and YASUHIRO MURASE

University of Nagoya, Nagoya, Japan

The physical absorption of gas by water in a tower packed with Raschig rings has been investigated. The liquid-side mass transfer coefficient which was separated by dividing the capacity coefficient by the wetted surface area is discussed from the standpoints of the two-film and penetration theories. A new and simpler dimensionless group is presented which correlates about 90% of the data reported, including the author's own, within an accuracy of  $\pm 20\%$ .

The relation of the liquid-side mass transfer coefficient to packed-tower performance and physical properties of the system is important from the standpoint of packed-tower designs and interesting from the viewpoint of the mechanism of mass transfer.

Many investigators (7, 15, 20, 22) have been studying the relation since Sherwood's (16) experimental equation was reported, but up to the present time the results seem to be far from satisfactory.

In this paper physical gas absorption by water in a tower packed with Raschig rings is described, and  $k_L$  is discussed. The relation of  $k_L$ , which covers about 90% of the data reported, including the authors', within a 20% accuracy, was obtained.

## EXPERIMENTS AND RESULTS

The absorption of pure carbon dioxide by water was studied. To ascertain the exponent of the Schmidt number, the absorption of pure hydrogen was also studied. Because the degree of purity of the gas was more than 99%, the gas-side resistance was regarded as negligible in comparison with the liquid-side resistance. Figure 1 is the flow sheet of the equipment. The packed tower consists of a single glass cylinder

about 80 cm. (2.6 ft.) long, with an inside diameter of 6.0 cm. (2.4 in.), packed to a height of 30 cm. (1 ft.) with 6- (1/4-in.), 8- (1/2-in.) and 10-mm. (2/5-in.) ceramic Raschig rings. The wet packing method was used to pack Raschig rings. Tap water was introduced from the head tank into the tower through the thermostat.

The distributor was constructed as follows: Seven glass tubes with an inside diameter of 4 mm. (1/8 in.) were arranged in a position of an equilateral triangle. The lower end of each distributor tube was set as closely as possible on the top of the packing to avoid upper end effects.

The mass velocity of the liquid was ascertained by the measurement of the quantity of water flowing from the tower bottom per unit time. The temperatures at the top and bottom of the tower were almost the same and were maintained at  $25 \pm 1^\circ\text{C}$ .

To measure the end effect samples were taken from the lower tower end and the funnel which was placed immediately below the support plate of the packing.

For carbon dioxide a sample of 50 cc. was introduced into 0.2N barium hydroxide solution and then back titrated with 0.1N hydrogen chloride solution. The end effect for 6-, 8-, and 10-mm. Raschig rings was equivalent to a packing height of 3.6, 3.5, and 3.1 cm. respectively.

For hydrogen a sample of 500 cc. was withdrawn by Swanson and Hulett's method (21) and analyzed by the explosion method.

As stated above, the gas used was of more than 99% purity, and therefore the gas-side resistance could be assumed to be negligible. The liquid-side capacity coefficient can consequently be computed from

$$k_L a = \{L/(\rho Z)\} \{\ln(C_s - C_1)/(C_s - C_2)\} \quad (1)$$

The saturated concentration  $C_s$  at  $25^\circ\text{C}$ . was taken from the International Critical Tables\*.

The results for carbon dioxide are shown in Figures 2, 3, and 4. In these cases it is known by previous reports (11, 16, 24) that the gas velocity has no relation to the liquid-side capacity coefficient under its loading point, and here it was about  $50 \sim 150 \text{ kg.}/(\text{sq. m.})(\text{hr.})$  [ $11 \sim 31 \text{ lb.}/(\text{sq. ft.})(\text{hr.})$ ].

To test the dumped packing method the tower was repacked with 6-mm. Raschig ring, and the capacity coefficient was measured. The reproducibility was good (Figure 2).

The capacity coefficient increases linearly with the increase of liquid velocity; that is,

$$k_L a = c' L^{m''} \quad (2)$$

where for 6-, 8-, and 10-mm. Raschig rings  $c'$  and  $m''$  were almost the same;  $c' = 0.047$ , and  $m'' = 0.72$ . These results agree with those of previous investigators (16, 25).

The results for hydrogen will be described later.

## DERIVATION OF THE EQUATION OF $k_L$

It is obvious that  $k_L$  and  $a$  depend on packed-tower performances and physical

\*Tabular material has been deposited as document 5874 with the American Documentation Institute, Photoduplication Service, Library of Congress, Washington 25, D. C., and may be obtained for \$2.50 for photoprints or \$1.75 for 35-mm. microfilm.

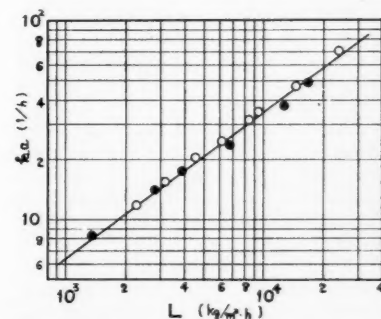


Fig. 2. Relation of  $k_L a$  vs.  $L$  in carbon dioxide absorption by water; ● 6-mm. ceramic Raschig ring repacked.

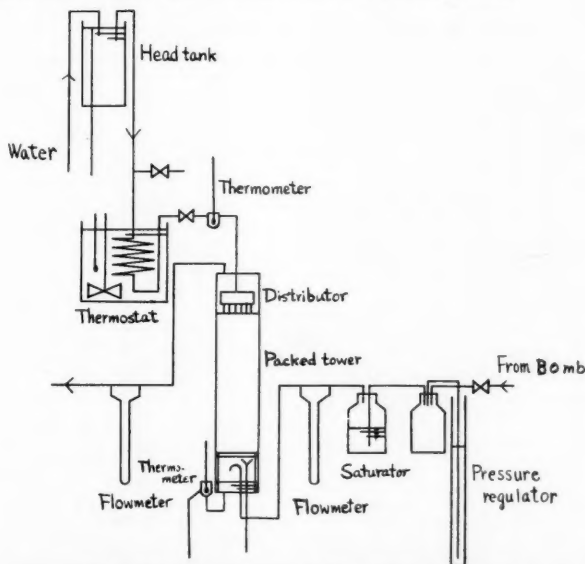


Fig. 1. Schematic diagram of the absorption system.

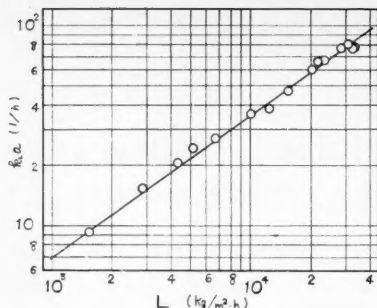


Fig. 3. Relation of  $k_L a$  vs.  $L$  in carbon dioxide absorption by water, 8-mm. ceramic Raschig ring.

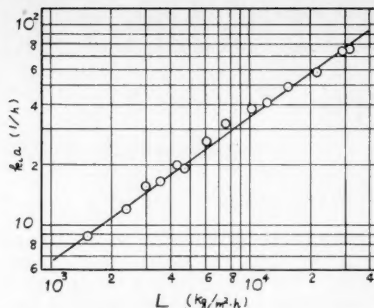


Fig. 4. Relation of  $k_L a$  vs.  $L$  in carbon dioxide absorption by water, 10-mm. ceramic Raschig ring.

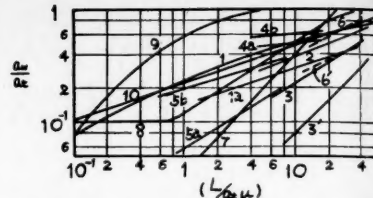


Fig. 5. Relation of  $a_w/a_t$  vs.  $L/a_t \mu$  by various investigators: 1. Fujita and Sakuma (3), 1a. Niwa and Hashimoto (12), 2. Sherwood and Pigford (18), 3 and 3' Shulman and DeGouff (19), 4a, 4b, 5a, 5b Weisman and Bonilla (26), 6 and 6' Mayo, Hunter and Nash (10), 7. Pratt (14), 8. Grimley (4), 9. van Krevelen, et. al. (22), and 10. Hikita and Kataoka (6)

properties of fluids in different ways, because the mass transfer coefficient depends on the diffusion coefficient and film thickness or contact time, but the contact area does not.

To separate  $k_L$  from  $k_L a$  it is necessary to evaluate  $a$ , but at present  $a$  is a very obscure value. For this reason it was assumed that  $a$  is proportional to  $a_w$ . If it is possible within a reasonable error to correlate  $k_L$  separated by  $a_w$  instead of by  $a$ , it will be more convenient. The replacement of  $a$  by  $a_w$  means that  $a = k_a a_w$ . This assumption has been used throughout the paper to separate  $k_L$  from  $k_L a$  and has proved its usefulness within reasonable error, at least for Raschig rings and water. Many investigators have presented the formulas for  $a_w$  (Figure 5). Among these formulas Fujita's (3) was selected because its form is more reasonable, and its validity for water has been confirmed by Hikita (6). Fujita's formula is

$$a_w/a_t = 1 - 1.02e^{-0.278(L/a+\mu)^{0.4}} \quad (3)$$

The total surface area for Raschig ring was computed from  $a_t = 4.7/D_p$  derived from Figure 6.

#### Derivation of the formula from the standpoint of two-film theory

##### Basic concept of $k_L$

From the dimensional analysis and the analogy of the heat transfer the following equation was proposed for the gas absorption in packed towers:

$$Nu' = \frac{k_L [L']}{D_L} = c(Re)^m (Sc)^n \quad (4)$$

For this dimension of length previous investigators have proposed various lengths, for example, the tower diameter (7) and the diameter of a sphere having the same surface area as a packing (20), and have eliminated  $L'$  by Galilei's number (15, 22). The correlations with various variables however are not always good.

This dimensionless group was interpreted as follows. According to the two-film theory the mass transfer coefficient for the liquid film, is equal to  $D_L/x$ ; consequently  $k_L/D_L$  should be a reciprocal of the effective film thickness. If the

dimension of length in the modified Nusselt number is chosen as a length related to  $x$ , the dimensionless group  $(k_L [L']/D_L)$  will be more reasonable.

From this principle, operating holdup

divided by wetted surface area was first chosen as  $L'$ , and the modified Nusselt number became

$$Nu' = k_L h / (D_L a_w) \quad (5)$$

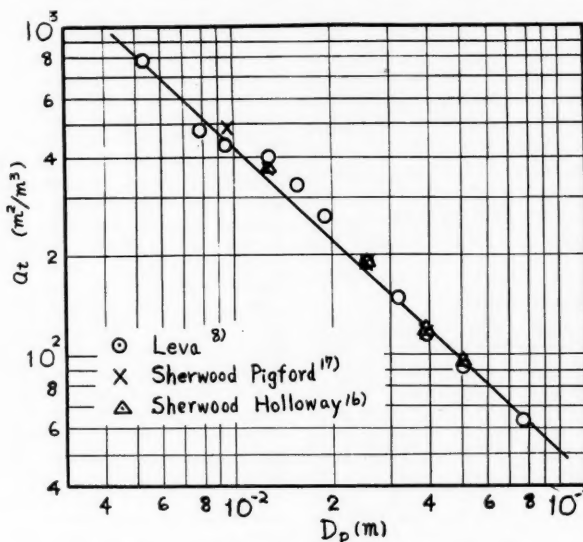


Fig. 6. Estimation of  $a_t$  vs.  $D_p$  by various investigators.

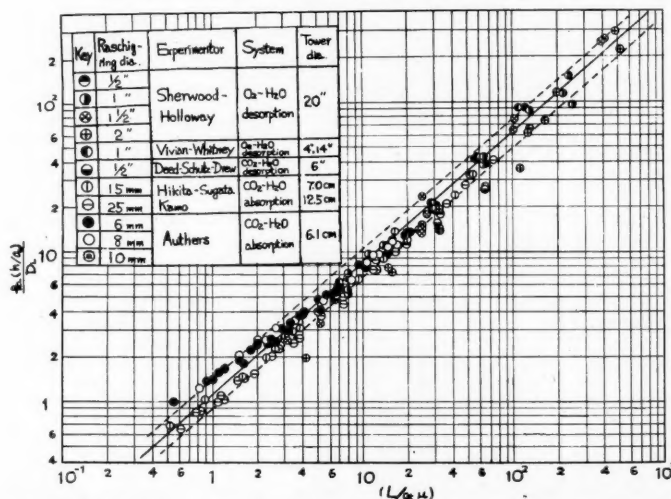


Fig. 7. Relation of  $k_L(h/a_w)/D_L$  vs.  $L/(a_t \mu)$ ; two broken lines indicate the region of  $\pm 20\%$  error.

$a_i \mu$  by  
a and  
to (12),  
and 3'  
5a, 5b  
Mayo,  
t (14),  
et. al.  
ka (6)

as first  
Nusselt

(5)

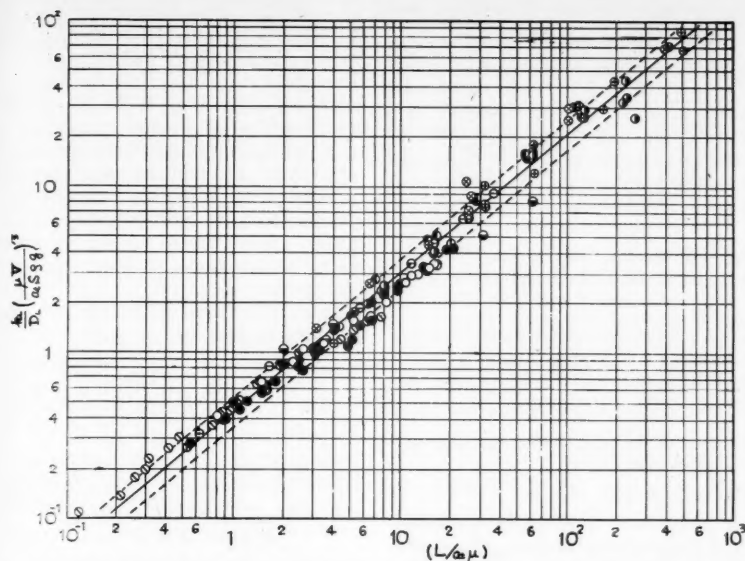


Fig. 8. Relation of  $k_L(\mu V/\rho g a_i S)^{1/3}/D_L$  vs.  $L/(a_i \mu)$ . Keys are the same as those in Figure 7. Two broken lines indicate the region of  $\pm 20\%$  error.

The operating holdup was calculated from the experimental equation of Ôtake (13) and  $a_w$  was calculated from Fujita's formula (3) as described above. Ôtake's equation is

$$h = 1.295(D_p L/\mu)^{0.676} \cdot (D_p^3 \rho^2/\mu^2)^{-0.44} (a_i D_p) \quad (6)$$

This equation is only partially correct, and moreover it is very inconvenient to

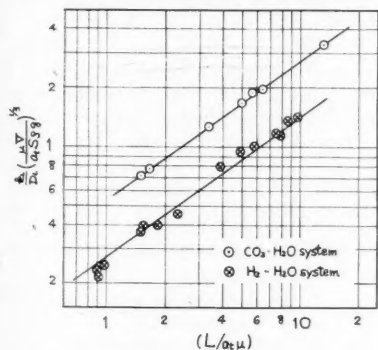


Fig. 9. Relation of  $k_L(\mu V/\rho g a_i S)^{1/3}/D_L$  vs.  $L/(a_i \mu)$  in the absorption system of carbon dioxide-water and hydrogen-water at 25°C.; tower diameter is 6 cm. and packed with 6-mm. Raschig ring to the height of 30 cm.

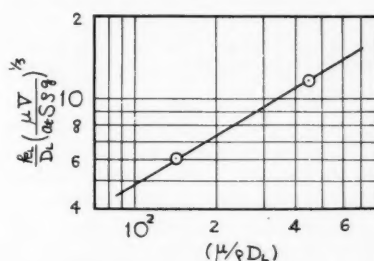


Fig. 10. Relation of  $k_L(\mu V/\rho g a_i S)^{1/3}/D_L$  vs.  $\mu/(\rho D_L)$  for the data in Figure 9 at constant  $N_{Re} = 3$ .

Name	Packing height	Tower diameter, in.
Sherwood-Holloway	6 ~ 49 in.	20
Vivian-Whitney	2 ~ 8 ft.	4 and 14
Hikita et al.	30 cm. (1 ft.)	2.8 and 5 (7 and 12.5 cm.)
The authors	30 cm. (1 ft.)	2.4 (6 cm.)

Name	Liquid velocity	Gas velocity
Sherwood-Holloway	250 ~ 32,000 lb./ (sq. ft.) (hr.)	36 ~ 1,320 lb./ (sq. ft.) (hr.)
Vivian-Whitney	970 ~ 16,000 lb./ (sq. ft.) (hr.)	60 ~ 120 lb./ (sq. ft.) (hr.)
Hikita et al.	380 ~ 70,000 kg./ (sq. m.) (hr.)	20 ~ 80 kg./ (sq. m.) (hr.)
	78 ~ 14,300 lb./ (sq. ft.) (hr.)	4 ~ 16 lb./ (sq. ft.) (hr.)
The authors	1,500 ~ 35,000 kg./ (sq. m.) (hr.)	50 ~ 150 kg./ (sq. m.) (hr.)
	310 ~ 7,200 lb./ (sq. ft.) (hr.)	11 ~ 31 lb./ (sq. ft.) (hr.)

calculate  $h$  and  $a_w$  from their experimental equations at every point.

To avoid such inconvenience, the depth

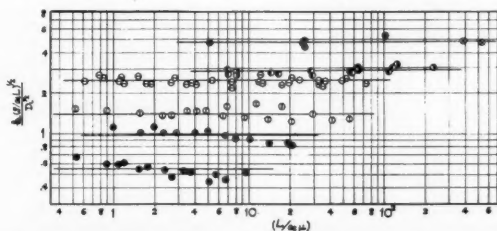


Fig. 11. Relation of  $k_L(\rho/a_i L)^{1/2}/D_L^{1/2}$  vs.  $L/(a_i \mu)$ ; keys are the same as those in Figure 7.

of the thin water layer flowing over packings was considered. Generally, the depth of thin layer flowing down over a plain plate inclining  $\theta'$  toward the horizontal plane is derived theoretically as

$$D = [3\mu V/(B\rho g \sin \theta')]^{1/3}$$

The breadth of the plate may be considered as  $a_w SZ (\sin \theta'')/Z$ , because  $a_w SZ \sin \theta''$  is the perpendicular projection of the total wetted surface area in the tower.

The following formula is gained:

$$D = [3\mu V/a_w \rho g S (\sin \theta') (\sin \theta'')]^{1/3}$$

Putting  $a_i$  instead of  $a_w$  and omitting  $(\sin \theta') (\sin \theta'')$ , one gains the following modified Nusselt number:

$$Nu' = k_L [\mu V/(a_i \rho g S)]^{1/3}/D_L \quad (7)$$

where  $D_L$  for carbon dioxide is calculated by the formula of Wilke and Chang (27). When one uses  $a_i$  instead of  $a_w$  and omits  $(\sin \theta') (\sin \theta'')$ , a hypothetical depth of viscous flow over packings is taken in the same way as if  $L/a_i \mu$  were used as the Reynolds number of a liquid. If  $a_w$  can be replaced by  $a_i$  to correlate  $k_L$  within reasonable error, it will be much more convenient, and this paper will have proved its effectiveness. By this replacement one could correlate  $k_L$  in the same equation, as described later.

Dependence of Equations (5) and (7) on Reynolds number

The modified Nusselt number in Equation (5),  $k_L h/(D_L a_w)$  vs.  $L/(a_i \mu)$ , is plotted in Figure 7 for the authors' experimental data as well as those of Sherwood-Holloway (16), Vivian-Whitney (24) and Hikita et al. (5). The ranges of the conditions are as follows:

The agreement of the data in the  $\pm 20\%$  error region however is rather poor; moreover it is most inconvenient to calculate  $h$  and  $a_w$  from experimental Equations (3) and (6), as mentioned above.

From Equation (7)  $k_L [\mu V/(\rho g a_i S)]^{1/3}/D_L$  vs.  $L/(a_i \mu)$  is plotted in Figure 8 with the same data used as in Figure 7. In Figure 8 the agreement of the data is fair, and the values are easy to calculate. The straight line in Figure 8 represents

$$k_L [\mu V/(\rho g a_i S)]^{1/3}/D_L = 0.44 [L/(a_i \mu)]^{0.82} \quad (8)$$

$\pm 20\%$

### Dependence of Equation (7) on the Schmidt number

The exponent of the Schmidt number in Equation (4) has been discussed frequently by many investigators. Some of them (11, 16, 20, 25) suggest  $n = 1/2$ , but others (7, 22) support the value  $n = 1/3$ . To decide which exponent is right, the absorption of hydrogen by water was carried out in the same apparatus as described above with 6-mm. Raschig rings.

$D_L$  for hydrogen, a correction of the value used in Perry's Hand Book, was selected; that is,  $D_L = 6.30 \times 10^{-5}$  sq. cm./sec. at 25°C.  $N_{Sc} = 143$ . The experimental data are plotted in Figure 9; the ordinate  $k_L[\mu V/(\rho g a_i S)]^{1/3}/D_L$ , and the abscissa is  $L/(a_i \mu)$ .

The data for carbon dioxide and hydrogen in Figure 9 were calculated from the value at the tower end, because for hydrogen it was very difficult at a low Reynolds number to take the sample of 500 cc. from the funnel placed immediately below the support plate.

From Figure 9 the values of  $k_L[\mu V/(\rho g a_i S)]^{1/3}/D_L$  vs. Schmidt number at  $N_{Re} = 3$  were plotted in Figure 10. (As the two lines in Figure 9 are almost parallel, the value of the Reynolds number is indifferent.) The slope of the line in Figure 10 is 0.58; it is clear that the exponent of  $N_{Sc} = 1/2$  is preferable.

### Results

The correlation of  $k_L$  for the Reynolds and Schmidt numbers becomes

$$k_L[\mu V/(\rho g a_i S)]^{1/3}/D_L = 0.021[L/(a_i \mu)]^{0.82} \cdot [\mu/(\rho D_L)]^{1/2} \quad (9)$$

Dividing both sides of Equation (9) by  $(Re)^{1/2}$ , one obtains

$$k_L[\mu^2/(\rho^2 g)]^{1/3}/D_L = 0.021[L/(a_i \mu)]^{0.49} \cdot [\mu/(\rho D_L)]^{1/2} \quad (10)$$

The left-hand side of Equation (10) is the modified Sherwood number named by Krevelen (22).

By dividing both sides of Equation (10) by the Schmidt number, one obtains

$$k_L[\rho/(\mu g)]^{1/3} = 0.021[L/(a_i \mu)]^{0.49} \cdot [\mu/(\rho D_L)]^{-1/2} \quad (11)$$

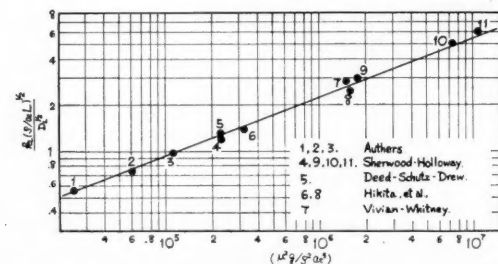


Fig. 12. Relation of  $k_L(\rho/a_i L)^{1/2}/D_L^{1/2}$  vs. (Galilei) for the data in Figure 11 at constant Reynolds.

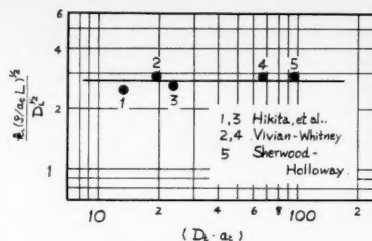


Fig. 13. Relation of  $k_L(\rho/a_i L)^{1/2}/D_L^{1/2}$  vs.  $(D_i a_i)$  at constant (Galilei) ( $D_p = 1$  in.).

The exponent of the Reynolds number in Equations (10) and (11) is in accord with that of wetted-wall (1, 9) and liquid-rod (23) experiments.

### Derivation of the formula from the standpoint of the penetration theory

#### Basic concept of $k_L$

In the packed tower, where the two fluids flow countercurrently, the model of the two-film theory can hardly be understood, even though the interface of the fluids is modified as an effective one.

The penetration theory or its modification, the surface renewal theory, seems to be preferable to the two-film theory. By Higbie's penetration theory  $k_L$  can be described as

$$k_L = 2[D_L/(\pi \theta)]^{1/2} \quad (12)$$

Using an idea similar to that described in the two-film theory one can consider the following dimensionless formula:

$$k_L[T]^{1/2}/D_L^{1/2} = [\text{Dimensionless}] \quad (13)$$

If  $T$  is taken to have a closer connection with  $\theta$  in Equation (13), a more reasonable dimensionless group can be obtained. However since the phenomena in the packed tower is very complex, a simplified model can hardly be presented; therefore the dimensional analysis has been used.

It may be considered reasonable that the time during which the elementary surface of the liquid is exposed to the gas depends upon the operating conditions, the physical properties of the liquid, and the characteristics of the tower and packings; it can be assumed as

$$\theta = f(\rho, \mu, g, D_i, a_i, L) \quad (14)$$

By dimensional analysis various combinations of dimensionless groups were obtained, and from the many results reported the next relation was selected.

$$(1/\theta)[\rho/(a_i L)] = c'[L/(a_i \mu)]^m \cdot [\rho^2 g/(\mu^2 a_i^3)]^n (D_i a_i)^p \quad (15)$$

The first term of the right-hand side of Equation (15) is the Reynolds number based on the total area of packings in unit volume, and the second term is Galilei's number. This latter number was introduced in Equation (15) by the consideration of the dependence of gravity acceleration. The third term refers to dimensions of tower diameter and packing piece.

From Equations (13) and (15) the following is obtained:

$$k_L[\rho/(a_i L)]^{1/2}/D_L^{1/2} = c[L/(a_i \mu)]^m [\rho^2 g/(\mu^2 a_i^3)]^n \cdot (D_i a_i)^p \quad (16)$$

The constants and the exponents of Equation (16) will now be determined from the experimental data and the results reported by others.

### Dependence of Equation (16) on the Reynolds number

The exponent of the Reynolds number in Equation (16) was determined by the authors' experimental data and those of Sherwood-Holloway (16), Deed-Schutz-Drew (2), Vivian-Whitney (24), and Hikita et al. (5) given in Figure 11. The range of the Reynolds number is from 0.5 to 500, and it is found that the exponent  $m = 0$ . In Figure 11 some of the experimental data are omitted to avoid confusion. (All data of each experiment are plotted in Figure 14.)

### Dependence of Equation (16) on Galilei's number

To determine the exponent of Galilei's number the values of  $k_L[\rho/(a_i L)]^{1/2}/D_L^{1/2}$  at constant Reynolds number were plotted against each Galilei's number (Figure 12). From the slope of the plotted line the exponent of Galilei's number = 0.38. The range of Galilei's number is from  $2.5 \times 10^4$  to  $1.1 \times 10^7$ .

### Dependence of Equation (16) on the tower diameter

From the data of Sherwood-Holloway (16) (tower diameter 20 in.), Vivian-Whitney (24) (tower diameter 14 and 4 in.), and Hikita et al. (5) (tower diameter 12.5 and 7 cm.) the values of  $k_L[\rho/(a_i L)]^{1/2}/D_L^{1/2}$  for 1-in. Raschig ring

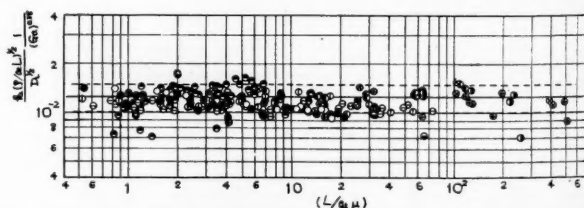


Fig. 14. Relation of  $k_L(\rho/a_i L)^{1/2}/(D_L^{1/2} Ga^{0.38})$  vs.  $L/(a_i \mu)$  for the data reported which is thought to be purely physical; keys are the same as those in Figure 7.



are plotted against the values of  $(D_t a_i)$  in Figure 13. From this figure it is clear that the exponent of  $(D_t a_i)$ ,  $p$ , equals 0.

### Results

All results are given in Figure 14, where almost all the data of each experiment reported are plotted; over 90% of the results lie within a  $\pm 20\%$  error.

From the results discussed above Equation (16) becomes

$$k_L[\rho/(a_i L)]^{1/2}/D_L^{1/2} = 0.013[\rho^2 g/(\mu^2 a_i^3)]^{0.38} \quad (17)$$

The left-hand side of Equation (16) is the result of the use of  $\rho/(a_i L)$  as the dimension of time in Equation (13), but the meaning of  $\rho/(a_i L)$  can be considered as  $L/\rho = u$ , and  $a_i = 4.7/D_p$ ; then  $\rho/(a_i L) \propto D_p/u$ ; that is,  $\rho/(a_i L)$  is proportional to the apparent mean residence time over a packing.

### RESULTS FROM THE TWO THEORIES

The exponent of Galilei's number in Equation (17) may be assumed to be  $1/3$ ; then Equation (17) becomes

$$k_L[\rho/(\mu g)]^{1/3} = 0.013[L/(a_i \mu)]^{1/2} \cdot [\mu/(D_L \rho)]^{-1/2} \quad (18)$$

The coincidence of Equation (11) and Equation (18) is most satisfactory, and the correlation of  $k_L$  from both theories becomes

$$k_L[\rho/(\mu g)]^{1/3} = c[L/(a_i \mu)]^{1/2} \cdot [\mu/(\rho D_L)]^{-1/2} \quad (19)$$

$c = 0.01 \sim 0.02$

The agreement of  $\pm 20\%$  in Figure 14 corresponds to a value of  $c$  of 0.013.

The exponent of the Reynolds number in Equation (19) is in accord with those found in the experiments by wetted wall (1, 9) and by liquid rod (23), and this seems to have an interesting significance for the investigation of the mechanism of gas absorption in packed towers; moreover these coincidences indicate that the assumption made in this paper: ( $a = ka_w$ ) is not only convenient but also reasonable. Here the proportionally constant  $k$  is independent of  $L$  and  $G$ . If  $a$  were a function of  $G$  under its loading point, it is most natural that  $k_L a$  would also be a function of  $G$ , but all the data reported prove that  $k_L a$  is independent of  $G$  (11, 16, 24).

### SUMMARY

1. The absorption of carbon dioxide and hydrogen by water in the tower packed with Raschig rings was investigated.

2. It was proved within an accuracy of  $\pm 20\%$  that  $k_L$  is a function of the total surface area, as shown in Equations (11) and (18).

3. From the standpoint of the two-film theory a new modified Nusselt number is presented which takes the apparent mean depth of liquid as a

dimension of length, and this number covers about 90% of the data reported, including the authors', within an accuracy of  $\pm 20\%$ .

4. From the standpoint of the penetration theory a new and simpler dimensionless formula is presented in Equation (17) which was applicable within an accuracy of  $\pm 20\%$  to almost all the data reported, as shown in Figure 14.

5. From both theories it is found that  $k_L$  depends on the Reynolds and Schmidt numbers, as shown in Equation (19).

The exponent of the Reynolds number is in accord with that found in the experiments by wetted wall and liquid rod; it is believed reasonable that  $a$  is proportional to  $a_w$ , where the proportional constant is independent of  $L$  and  $G$  within an accuracy of  $\pm 20\%$ , at least for Raschig rings and water.

### ACKNOWLEDGMENT

The authors are indebted to S. Hatta of Tokyo University for his encouragement and also to T. Andô for hydrogen-absorption experiments carried out as a part of his Bachelor of Science work and to F. Ôtsubo for experiments on carbon dioxide absorption. Thanks also go to Mrs. M. L. Mayland for her careful review of the English text.

### NOTATION

$a$	= effective surface area of packings, sq. m./cu. m.
$a_i$	= total surface area of packings, sq. m./cu. m.
$a_w$	= wetted surface area of packings, sq. m./cu. m.
$B$	= breadth of a plate, m.
$c, c'$	= a constant
$C_1, C_2, C_s$	= concentration of liquid at the entrance, the exit of the tower, and at the saturation, respectively, kg./m <sup>3</sup> .
$D$	= depth of thin layer of viscous flow, m.
$D_L$	= diffusional coefficient of solute gas, sq. m./hr.
$D_p$	= nominal diameter of a packing, m.
$D_t$	= diameter of the tower, m.
$G$	= mass flow rate of gas, kg./ (sq. m.)(hr.)
$g$	= gravity acceleration, m./hr. <sup>2</sup>
$h$	= operating holdup.
$k$	= proportional constant independent of gas and liquid velocity
$k_L$	= liquid-side mass transfer coefficient, m./hr.
$L$	= mass flow rate of liquid, kg./ (sq. m.)(hr.)
$L'$	= length, m.
$m, m'$	= exponent of the Reynolds number
$m''$	= exponent of liquid velocity
$n, n'$	= exponent of the Schmidt number
$Nu'$	= modified Nusselt number, $k_L[L]/D_L$
$p, p'$	= exponent of $(D_t a_i)$
$S$	= sectional area of empty tower, sq. m.
$T$	= time, hr.

$u$	= mean linear velocity in the tower, m./hr.
$V$	= volumetric flow rate of liquid, cu. m./hr.
$x$	= effective film thickness, m.
$Z$	= height of packing layer, m.

### Greek Letters

$\mu$	= viscosity of liquid, kg./ (m.)(hr.)
$\rho$	= density of liquid, kg./cu. m.
$\theta$	= time during which an element of the liquid surface is exposed to the gas, hr.
$\theta', \theta''$	= inclination angle of a plate to the horizontal
$\pi$	= ratio of circumference of a circle to its diameter

### LITERATURE CITED

- Brötz, W., *Chem.-Ing.-Tech.*, **26**, 470 (1954).
- Deed, D. W., P. W. Schutz, and T. B. Drew, *Ind. Eng. Chem.*, **39**, 766 (1947).
- Fujita, S., et al., *Chem. Eng. (Japan)*, **18**, 64 (1954).
- Grimley, S. S., *Trans. Inst. Chem. Engrs. (London)*, **23**, 233 (1945).
- Hikita, H., et al., *Chem. Eng. (Japan)*, **20**, 113 (1956).
- Hikita, H., and T. Kataoka, *ibid.*, **20**, 528 (1956).
- Kling, G., *Chem.-Ing.-Tech.*, **25**, 577 (1953).
- Leva, Max, "Tower Packing and Packed Tower Design," p. 7, United States Stoneware Co. (1953).
- Lyn, S., J. R. Straatemeier, and H. Kramers, *Chem. Eng. Sci.*, **4**, 49 (1955).
- Mayo, F., T. O. Hunter, and A. W. Nash, *J. Soc. Chem. Ind.*, **54**, 375T (1935).
- Molstad, M. C., et al., *Trans. Am. Inst. Chem. Engrs.*, **38**, 410 (1942).
- Niwa, Hashimoto, thesis, Tokyo Inst. Technol., Tokyo, Japan (1952).
- Ôtake, T., and K. Okada, *Chem. Eng. (Japan)*, **17**, 176 (1953).
- Pratt, H. R. C., *Ind. Chemist*, **26**, 291 (1950).
- Ramm, W. M., "Absorptionsprozesse in der chemischen Technik," p. 229 (1953).
- Sherwood, T. K., and F. A. L. Holloway, *Trans. Am. Inst. Chem. Engrs.*, **36**, 39 (1940).
- Sherwood, T. K., and R. L. Pigford, "Absorption and Extraction," p. 226, McGraw-Hill, New York (1952).
- Ibid.*, p. 228 (1952).
- Shulman, H. L., and J. J. DeGouff, *Ind. Eng. Chem.*, **44**, 1915 (1952).
- Shulman, H. L., et al., *A.I.Ch.E. Journal*, **1**, 253 (1955).
- Swanson, A. A., and G. A. Hulett, *J. Am. Chem. Soc.*, **37**, 2490 (1915).
- van Krevelen, D. W., and P. J. Hof-tijzer, *Chem. Eng. Progr.*, **44**, 529 (1948).
- Vielstich, W., *Chem.-Ing.-Tech.*, **28**, 543 (1956).
- Vivian, J. E., and R. P. Whitney, *Chem. Eng. Progr.*, **43**, 691 (1947).
- Ibid.*, **44**, 529 (1948).
- Weisman, J., and C. F. Bonilla, *Ind. Eng. Chem.*, **42**, 1099 (1950).
- Wilke, C. R., and Pin Chang, *A.I.Ch.E. Journal*, **1**, 264 (1955).

Manuscript received December 11, 1957; revision received May 19, 1958; paper accepted October 6, 1958.

# The Dynamics of Heat Removal from a Continuous Agitated-Tank Reactor

R. J. FANNING and C. M. SLIEPCEVICH

University of Oklahoma, Norman, Oklahoma

The present investigation is concerned with the dynamic characteristics of a 12-in. diameter continuous agitated-tank reactor vessel. Response of the vessel effluent temperature to a change in coolant flow rate through an internal cooling surface is the subject of theoretical and experimental study. Experimental data were obtained through the use of frequency and transient response techniques. Studies were made for the passage of vessel-charge fluids with widely differing physical properties. Also data were taken for various conditions of fluid turbulence both inside and outside the internal heat transfer coils. Experimental and theoretical results are graphically compared. Recommendations are presented for the development of theoretical dynamic relationships.

Systems-engineering techniques are becoming increasingly important in chemical-process development and control. The first step required is a theoretical analysis of the process in question from the standpoint of unsteady state behavior. For all but the simplest of processes such analyses generally yield differential equations describing the dynamic behavior of the given process. One method of profiting from these equations is by electronic simulation. The equations, along with those describing controller action, are programmed into an analogue computer, to simulate the process with its attendant controls. Changes in the response of desired output variables may be observed for different controller settings, flow rates, feed concentrations, equipment sizes, etc. As such simulation techniques become more highly developed, the quantity of chemical-process pilot-plant data customarily necessary may be greatly reduced. For certain types of problems a complete elimination of pilot-plant data can be expected. In addition, information vital to advanced process-control methods is made available.

In the development of equations suitable for analogue-computer programming a number of simplifying assumptions and approximations are generally needed. The validity of certain equations employed may then be open to question. The object of the present investigation is to carry out a theoretical study of the dynamics of heat removal from a continuous agitated-tank reactor. The theoretical equations developed differ because of the various assumptions made in their derivation. Experimental data are then taken to confirm the equation most desirable for a particular set of process conditions. If enough information of this type is made available by further experimentation, process simulation will proceed

at a faster rate, with more assurance of accuracy in the final results.

Many reactors of the batch or agitated-tank type are jacketed, with the inner tank walls serving as a heat-exchange surface. Newer designs have utilized the advantages of internal heat transfer surface together with proper agitation and baffling to provide favorable flow patterns and more effective heat transfer. The present equipment is designed along such lines with helical coils as the internal heat-exchange surface. Since most reactions carried out in continuous, agitated-tank type of units are exothermic, this paper is devoted only to the dynamics of equipment heat removal. The dynamics of the given system are characterized by the comparison of experimental frequency-response data with theoretically derived transfer functions.

## REVIEW OF PREVIOUS WORK

The literature relative to the analysis of process-control equipment by the use of servo-theory techniques is not abundant, because the interest of chemical engineers in this field is recent. Virtually all work with frequency-response methods in process equipment has been reported since 1953. Perhaps the earliest account of frequency-response analysis of a chemical unit operation was presented by Stanton and Hoyt on the dynamics of a fractionating column (8). In the heat transfer field McKnight and Worley described the analysis of a plate heat exchanger by frequency-response methods (6). Cohen and Johnson, as well as Mozley, investigated the dynamics of concentric-pipe heat exchangers (3, 7). Williams and Young investigated the closed-loop dynamics of a multipass commercial type of heat exchanger with attendant control system by means of electronic simulation (9).

No complete work is available relative to the particular type of equipment under investigation. Mason presents an early mathematical study of the transients involved in a continuous-flow, steam-

heated kettle (5). The transfer-function concept was not then in common use, and all solutions were carried out by classical means. Aris and Amundson, as well as Bilous, Block, and Piret, presented recent studies of the dynamics of a continuous agitated-tank reactor (1, 2). In these papers a number of theoretical transfer functions were derived and studied by plotting on a Nyquist diagram. Both articles were theoretical, and no experimental data were taken.

The present work differs from most of the previous efforts on continuous tank type of systems, as emphasis is placed upon experimental data. The investigation consists of a theoretical analysis with accompanying experimental confirmation of the dynamics of a continuous, agitated-tank reactor during removal of sensible heat. The experiments were made with oil and water used as charge fluids and water used as the cooling medium. In all cases the output variable was taken as the tank fluid temperature, while the input or forcing variable was cooling-water flow rate.

## DESCRIPTION OF EQUIPMENT AND EXPERIMENTAL METHODS

### Process Equipment

In the dynamic analysis of a type of equipment or process the object is to obtain a valid relationship between the desired input variable, the output variable which it affects, and time. Such a relationship is usually referred to as the *open-loop* or *process-transfer* function and is essential to a complete understanding of the feedback loop later installed to control the output variable in question. Usually the process-transfer function is defined in terms of the Laplacian complex variable instead of time. Compatibility with modern servo-control theory is thereby assured.

Figure 1 shows a schematic flow diagram of the apparatus used in the investigation. Hot feed is pumped to the agitated tank. Effluent passes by means of a siphoning effect into the discharge barrel for reuse during subsequent runs. Water coolant flows into the bottom of the tank, through helical coils, then to discharge. The coolant flow rate may be forced in a periodic manner by a sine-wave generator mounted on the discharge side of the coolant stream. Both feed and coolant streams are measured accurately by calibrated rotameters.

With the exception of the sine-wave

R. J. Fanning is with the Continental Oil Company, Ponca City, Oklahoma.

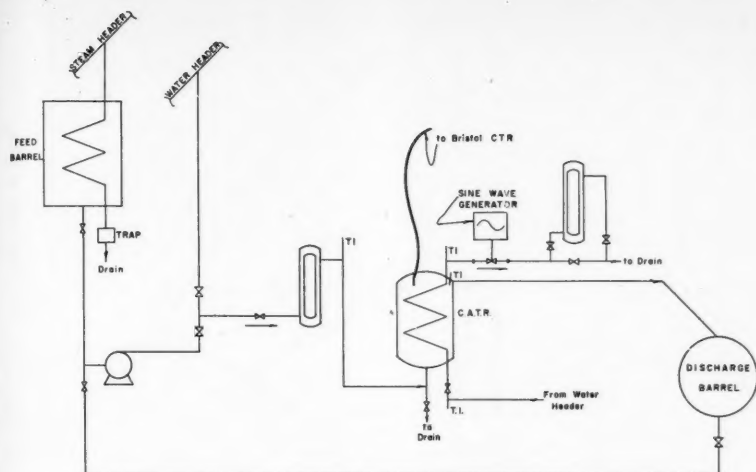


Fig. 1. Flow diagram of equipment.

generator all equipment is quite conventional. The tank reactor vessel is a stainless steel cylinder 12 in. in diameter and 15 in. high. It is provided with a turbine type of impeller with 4-in. diameter blades. Agitator speeds are continuously adjustable from 70 to 1,750 rev./min. Tank baffling consists of 1-in. stainless steel strips extending the height of the tank and spot welded 90 deg. apart. The tank is heavily insulated on top and bottom with plywood and on the sides with 2-in. fiber glass. The helical heat transfer coil, 5 in. in diameter, is constructed from 5/8 in., type-L copper tubing. The output variable, which is the instantaneous temperature within the tank, was recorded continuously by means of a Bristol model-560 recording potentiometer with a strip chart.

#### Sine-Wave Generator

To obtain frequency-response data some method must be at hand to force the desired process variable in a sinusoidal manner. For a change in liquid flow rate such a periodic movement may be accomplished with reasonable accuracy by the use of a stop watch and flow-indicating device. However beyond a frequency of about 1.5 cycles/min., hand methods result in too much wave distortion. Some relatively simple, inexpensive device had to be developed which would permit oscillations up to 5 cycles/min. or higher if necessary. The most satisfactory arrangement consisted of a linear motor control valve with the stem driven by a small, geared-down induction motor.

The basic portion of the sine-wave generator consists of a 1/2-in. research control valve. The trim is stainless steel, and the valve body is bronze with a 150 lb./sq. in. gauge working pressure. Trim bevel is such that the valve is linear through the lower 80% of stem travel. Extensive test data taken at constant pressure drop show this to be true (4). In the construction of the generator the top half of the diaphragm body was removed together with diaphragm and spring. The cast-aluminum housing, which had served as the lower half of the diaphragm body was then used to support the device which imparted a harmonic translational

motion to the valve stem. This device is made up of a rotational power source and Scotch yoke together with connecting gears. The driver consists of a Merkle-Korff SG-10 induction motor attached to a gear reduction housing. Motor gear-train output speed is 1 rev./min. and maximum output torque is 10 lb.-in. Appropriate gear sets connect the motor-output drive to the Scotch-yoke drive. The arrangements of gears are such that yoke-drive speeds of 0.1, 0.25, 0.5, 1.0, 2.5, and 5 cycles/min. are obtainable. The range can easily be increased by exchange with a motor of higher speed. The free end of the valve stem is screwed into the Scotch-yoke drive block and secured by lock nut. Variable, periodic motion is thereby imparted to the valve stem. Since the valve trim is linear, as proved by test, throughout the bottom

portion of its movement, a sine wave of fluid flow passes through the valve body. A variable amplitude of stem movement, and therefore fluid flow rate, is obtained by the installation of yoke-drive throws of varying radii. Throughout most of this work a peak-to-valley stem travel of 1/8 in. was used. The valve-plug location for steady state operation is continuously adjustable.

#### EXPERIMENTAL

The determination of steady state process gains were of key importance in this investigation. Such transient curves give a good indication of system order and amount of deviation from linearity and provide a basis for standardizing magnitude ratios. A step increase in coolant flow rate yielded a negative gain transient; a step decrease yielded the positive transient. The magnitude ratio may be mathematically defined as

Magnitude ratio

$$= \frac{\left( \frac{\Delta \theta}{\Delta W_w} \right)_{F=F}}{\left( \frac{\Delta \theta}{\Delta W_w} \right)_{F=0}} \quad (1)$$

This equation may be easily simplified when it is considered that  $\Delta W_w$  for a given response spectrum was a fixed quantity at all frequencies. Thus the equation may be effectively reduced to

Magnitude ratio

$$= \frac{(\Delta \theta)_{F=F}}{(\Delta \theta)_{F=0}} \quad (1a)$$

The numerator of this expression represents the average total distance between

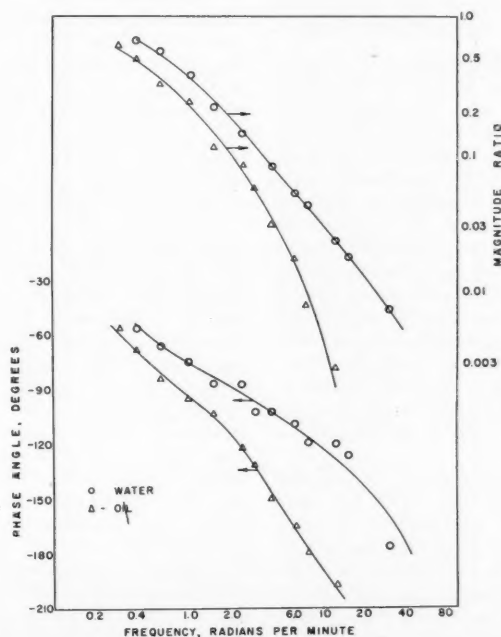


Fig. 2. Bode diagram comparing oil and water frequency-response curves.

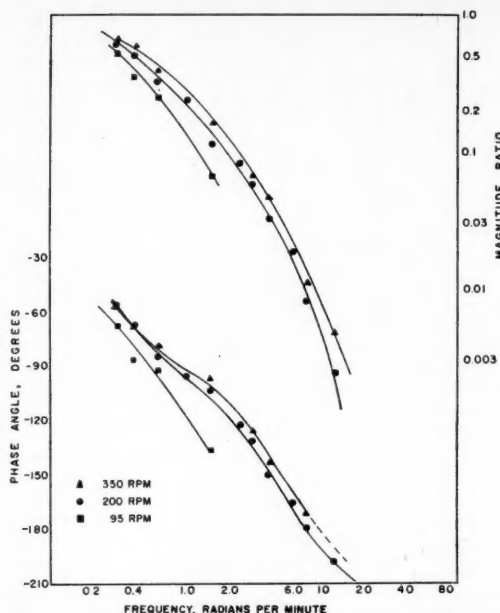


Fig. 3. Effect of tank-fluid conditions on frequency-response curves.

peaks and valleys of the output wave at any frequency  $F$ . The denominator represents the numerical sum of the positive and negative steady state process gains. Although this method of analyzing frequency-response data (magnitude ratio, phase angle, frequency) differs somewhat from procedures used previously, it has proved to be satisfactory. Phase angles were established by averaging the time in degrees between corresponding points on input and output waves.

#### VARIOUS EFFECTS ON SYSTEM DYNAMICS

The bulk of experimental work to date on the dynamics of process equipment has considered only one given set of process parameters. It may be intuitively deduced that the dynamics of heat removal for the given equipment would vary appreciably depending on the type of material processed. The amount of deviation between water and oil is shown by the attenuation and phase-lag curves in Figure 2. The oil used was a special low-viscosity-index material with a viscosity at room temperature comparable to S.A.E. 10 oil. It is seen that the dynamic-response characteristics of a given piece of equipment may be altered significantly according to the type of material being processed.

The effect, if measurable, of different conditions of tank-fluid turbulence upon system response was studied. Oil was selected as the process fluid because of its heavy outside controlling film. Agitator speeds of magnitudes that would yield Reynolds numbers for mixing equal numerical distances apart were selected for experimental parameters. Figure 3 shows the results of such frequency-re-

sponse determinations. It is seen that the two higher agitator speeds yield curves which are quite close; however there is a decided drop in response for the lower speed. As a rule of thumb it may then be stated that, beyond Reynolds numbers of about 2,800 the effect on response of this equipment type is relatively small.

In addition to the effect of fluid conditions existing in the tank itself, it was also desirable to determine the change in equipment-response characteristics brought about by different fluid-flow conditions within the cooling coils. With the existing system it was not possible to maintain other parameters constant while varying flow conditions within the coils from laminar to turbulent types; however the deviations were relatively small. For the laminar flow response data, cooling-coil Reynolds numbers varied from 1,690 to 339, respectively, at the peaks and valleys of the input waves. Because of conduit configuration completely laminar flow probably did not exist over this entire range. The turbulent-flow response data were taken with coolant-flow Reynolds numbers which varied from 3,494 to 2,025. The average tank-fluid temperature was approximately  $15^\circ$  lower for the turbulent-flow response data. Because of its less dominant outside fluid film, water was selected as the process fluid. The results of this experimentation are summarized by the curves shown in Figure 4. As may be expected, equipment response is somewhat faster during conditions of turbulent flow within the cooling coils, all other variables remaining essentially constant. However the amount of change is not great.

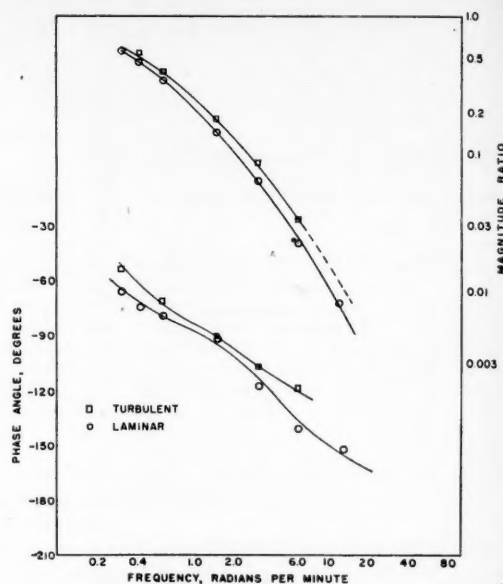


Fig. 4. Effect of coolant-flow conditions on frequency-response curves.

#### DERIVATION OF THEORETICAL TRANSFER FUNCTIONS

As indicated by Figure 1, hot reactor feed is continuously pumped through the system, while a portion of its heat is removed by cooling water flowing through internal coils. It is desirable to study the dynamics of heat removal as a result of a change in coolant rate of flow (or bulk velocity). Throughout all runs the temperature signal was produced from a bare thermocouple junction, thus obviating any considerations regarding thermocouple-well lags. The true-temperature history of the cooling water must be represented by a partial-differential equation, as its temperature changes with time as well as length traversed. Using the method of finite differences applied to an unsteady state heat balance over a small coil section, one can obtain the following partial, nonlinear differential equation:

$$\frac{\partial \theta_w}{\partial t} + \frac{\partial \theta_w}{\partial X} V + \frac{1}{T_1} \theta_w = \frac{1}{T_1} \theta \quad (2)$$

To obtain the transfer function desired,  $\theta/W_w(\omega)$ , the partial derivative  $\partial \theta_w / \partial X$  must be assigned a constant value, since in this case the forcing function is the coolant velocity. Another approach consists of the definition of a single cooling-water temperature in the following manner:

$$\bar{\theta}_w \triangleq \frac{\theta_{w_i} + \theta_{w_o}}{2}$$

or

$$\theta_{w_o} = 2\bar{\theta}_w - \theta_{w_i} \quad (3)$$

The defining differential equation is then reduced to the linear, ordinary type. The key assumptions considered in developing the first of two theoretical derivations are as follows:



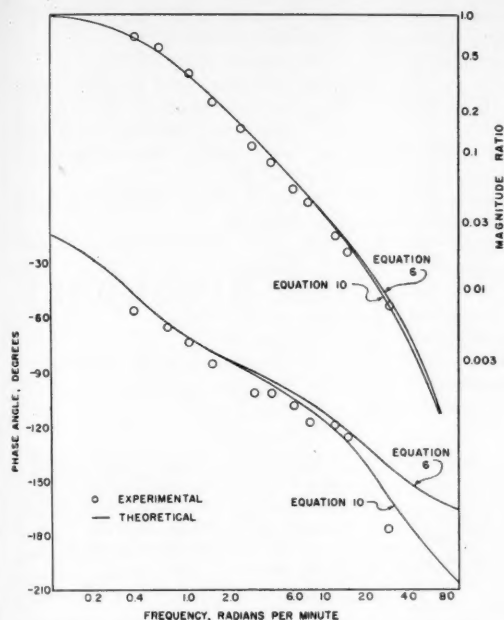


Fig. 5. Experiment and theoretical Bode diagrams, water.

1. All metal capacitances are ignored as negligible in affecting the dynamics of heat removal. The two capacitances taken into account are those of the vessel fluid and the cooling-water holdup.

2. An over-all heat transfer coefficient is employed. Its value is assumed to be constant during the sinusoidal fluctuation of cooling-water flow rate and equal numerically to its value at mean steady state conditions.

$$\frac{\theta}{W_w}(j\omega) = \frac{2K_1/T_6}{(j\omega)^2 + (T_4 + T_7/T_4T_7)j\omega + 1/T_4T_7 - 1/T_3T_6} \quad (6)$$

Again by a dynamic heat balance over the cooling water with a coolant temperature as defined by Equation (3) used, the following relationship is obtained by finite difference techniques:

$$\frac{d\bar{\theta}_w}{dt} + \frac{\bar{\theta}_w}{T_4} - \frac{1}{T_3} \theta = 2K_1W_w \quad (4)$$

where

$$T_2 = \frac{C_w}{\bar{W}_w c_p}, \quad T_3 = \frac{C_w}{UA_a},$$

$$\frac{1}{T_4} = \frac{2}{T_2} + \frac{1}{T_3}, \quad K_1 = \frac{\theta_w c_p}{C_w}$$

By similar methods of dynamic heat balance the following expression is derived for the tank fluid:

$$\frac{d\theta}{dt} + \frac{1}{T_7} \theta = \frac{1}{T_6} \bar{\theta}_w \quad (5)$$

where

$$T_5 = \frac{C_f}{\bar{W}_f c_p}, \quad T_6 = \frac{C_f}{UA_a},$$

$$\frac{1}{T_7} = \frac{1}{T_5} + \frac{1}{T_6}$$

Equations (4) and (5) are then transformed by the Laplace transformation with the condition that all variables are at zero variation from steady state conditions at  $t = 0^+$ . After the solution simultaneously and substitution of  $j\omega$  for the Laplacian complex variable the final form of the first theoretical transfer function is obtained as

Completion of this mathematical operation has required the assumption of essentially linear-system characteristics for small excursions of the forcing and output variables about their mean steady state values. The treatment has produced a relatively simple second-order transfer function with a limiting phase lag of  $-180$  deg. Comparison with experimental results will indicate whether or not the assumptions made in its derivation are justifiable.

The second derivation differs from the first in that individual film coefficients are considered along with another capacitance. The key assumptions are as follows:

1. The internal metal heat transfer coil offers sufficient lag so as to affect control dynamics at the medium and higher frequencies. All other metal capacitances are neglected.

2. The outer film coefficient of heat transfer remains constant during dynamical operation and equal numerically to its value at mean steady state conditions.

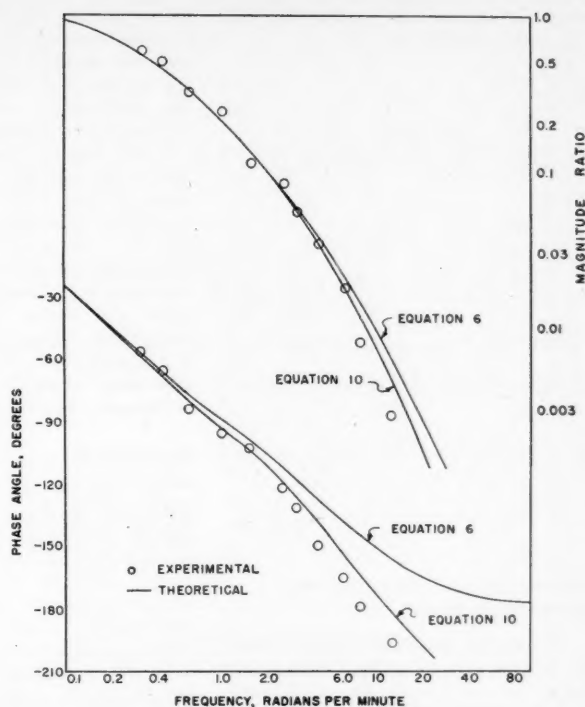


Fig. 6. Experimental and theoretical Bode diagrams, oil.

3. The inside film coefficient of heat transfer remains constant during sinusoidal fluctuations of flow rate and equal numerically to its value at steady state conditions.

When one applied the assumptions as outlined, together with a cooling-water temperature as defined by Equation (3), the following differential equations were derived when dynamic balances were made over the cooling water, heat transfer coils, and tank fluid:

Cooling water

$$\frac{d\bar{\theta}_w}{dt} + \frac{1}{T_{12}} \bar{\theta}_w - \frac{1}{T_8} \theta = 2K_1W_w \quad (7)$$

Coils

$$\frac{d\theta_c}{dt} + \frac{1}{T_{13}} \theta_c = \frac{1}{T_9} \bar{\theta} + \frac{1}{T_{10}} \bar{\theta}_w \quad (8)$$

Tank fluid

$$\frac{d\theta}{dt} + \frac{1}{T_{11}} \theta = \frac{1}{T_{11}} \theta_c \quad (9)$$

New time constants are defined by

$$T_8 = \frac{C_w}{h_i A_i}, \quad T_9 = \frac{C_c}{h_o A_o},$$

$$T_{10} = \frac{C_c}{h_i A_i}, \quad T_{11} = \frac{C_f}{h_o A_o}$$

$$\frac{1}{T_{12}} = \frac{2}{T_2} + \frac{1}{T_8}, \quad \frac{1}{T_{13}} = \frac{1}{T_9} + \frac{1}{T_{10}}$$

Equations (7), (8), and (9) are transformed as before and solved simultane-

ously for the required transfer function. The final equation is

$$\frac{\theta}{W_w} (j\omega) \quad (10)$$

$$= \frac{2K_2 K_3 / T_{11}}{A(j\omega)^3 + B(j\omega)^2 + C(j\omega) + D}$$

where

$$K_2 = \frac{T_{13}}{T_{11}}, \quad K_3 = \frac{T_{13}}{T_9},$$

$$\frac{1}{T_{14}} = \frac{1}{T_5} + \frac{1}{T_{11}}$$

$$A = T_{13}$$

$$B = \frac{T_{13}T_{12} + T_{14}(T_{13} + T_{12})}{T_{12}T_{14}}$$

$$C = \frac{T_{12} + T_{13} + T_{14}}{T_{12}T_{14}} - \left( \frac{K_2}{T_8} + \frac{K_3}{T_{11}} \right)$$

$$D = \frac{1}{T_{12}T_{14}} - \left( \frac{K_3}{T_{12}T_{11}} + \frac{K_2}{T_8T_{14}} \right)$$

#### COMPARISON OF THEORETICAL AND EXPERIMENTAL RESULTS

To prevent misinterpretation caused by meager and widespread data in the comparison of theory and experiment, about twice as many frequencies were tested as was normally the case. Detailed, original, numerical data are available for all runs (4). The sinusoidal value of the output temperature was examined very carefully, especially for phase-lag angles. As a rule a sharper contrast exists in theoretical phase-lag curves as compared with magnitude-ratio curves. All data were taken at an agitator speed of 200 rev./min. and with turbulent-flow conditions existing within the coils.

The theoretical curves are referred to by equation number in Figures 5 and 6. These response curves are for water and oil, respectively. Experimental points are denoted as before with small circles. With water as the process fluid both theoretical lag curves show pronounced leveling tendencies at  $-90$  deg. before continuing on to their respective limiting phase angles of  $-180$  and  $-270$  deg. Such behavior indicates a dominant first-order response at the low and medium frequencies; however the experimental attenuation and phase-lag data show a definite multiorder response at the higher frequencies.

In contrast Equation (10) for oil as the process fluid is practically a straight line up to a lag of  $-120$  deg. Here it curves downward and approaches its limiting-phase angle. Theoretical Equation (6), describing phase-lag loci for oil, reacts in somewhat the same manner except for a slight leveling tendency at  $-90$  deg. and a limiting-phase angle of  $-180$ . From the theoretical and experimental investigation it may be concluded that the response of tank-fluid temperature to a change in coolant flow rate is definitely of higher order. Within limits

of engineering accuracy a second-order transfer function [Equation (6)] represents the response for water over most of the frequency spectrum; however for oil the third-order expression [Equation (10)] is definitely recommended.

At the higher frequencies the original data were carefully examined for resonance as predicted by the theoretical descriptive equations for a concentric-pipe heat exchanger in the paper by Cohen and Johnson (3); no evidence of resonance was detectable, probably because the output variable, tank-fluid temperature, represents the condition of a completely lumped medium. An authoritative discussion of the phenomenon of resonance may be found in reference 3.

#### CONCLUSIONS

The dynamics of heat removal in a continuous agitated tank has been examined theoretically and comparison made with experimental response data. In all cases the forcing variable was coolant flow rate rather than coolant temperature, a fact which is of more interest from a practical control standpoint. The importance of fluid conditions, both inside and outside the heat transfer boundary, has been demonstrated graphically. The Reynolds number for mixing has been established at which response for the given system is significantly affected. Equations which are suitable for ease in adaptation to an analogue computer have been derived which compare favorably with experiment.

Experimental data have shown that little error is introduced by considering all coefficients of heat transfer as constants at mean steady state conditions. Numerical values for the various film coefficients have been calculated from existing correlations developed from data taken during steady state conditions. These are shown to be adequate for the case of transient operation.

Some of the more recent types of continuous agitated-tank reactor-control systems remove heats of reaction by the use of the latent heat of vaporization of a volatile coolant. Of considerable interest would be the development of transfer functions relating reactor-fluid temperature to coolant back pressure, since the latter is normally the variable manipulated in effecting temperature control. Together with information now available, the basis would thus be laid for a comprehensive study of continuous tank types of systems which would include a theoretical and experimental investigation devoted to open-loop dynamics for the case of an autothermic source within the reactor fluid.

#### NOTATION

$A$  = surface area, sq. ft.  
 $C$  = heat capacitance,  $(M)(c_p)$ , B.t.u./°F.

$c_p$  = specific heat, B.t.u./(lb.)(°F.)  
 $d$  = tube diameter, ft.  
 $F$  = frequency, cycles/min.  
 $h$  = individual heat transfer coefficient as obtained from established correlations for similar equipment, B.t.u./(min.)(sq. ft.)(°F.)  
 $h_o$  = outer film coefficient of heat transfer  
 $h_i$  = inside film coefficient of heat transfer  
 $j$  =  $\sqrt{-1}$   
 $L[f(t)]$  =  $\int_0^\infty f(t)e^{-st} dt$   
 $M$  = mass, lb.  
 $s$  = Laplacian complex variable  
 $T$  = time constant, min.  
 $T_1$  =  $A_p C_p / U \pi d$   
 $t$  = time, min.  
 $U$  = over-all heat transfer coefficient, B.t.u./(min.)(sq. ft.)(°F.)  
 $V$  = coolant bulk velocity, ft./sec.  
 $W$  = fluid flow rate, lb./min.  
 $X$  = distance in direction of flow

#### Greek Letters

$\Delta$  = small change in process variable around the steady state  
 $\theta, \theta_c, \theta_w$  = vessel-effluent temperature, coil temperature, and coolant temperature, respectively  
 $\omega$  = imposed frequency, radians/min.  
 $\rho$  = density, lb./cu. ft.

#### Subscripts

$a$  = average area  
 $c$  = coils  
 $f$  = process fluid  
 $i$  = inside area  
 $o$  = outside area  
 $s$  = sectional area  
 $w$  = coolant  
 $w_i$  = coolant in  
 $w_o$  = coolant out

#### LITERATURE CITED

1. Aris, Rutherford, and N. R. Amundson, *Chem. Eng. Progr.*, **53**, 227 (1957).
2. Bilous, Oleg, H. D. Block, and E. L. Piret, *A.I.Ch.E. Journal*, **2**, 249 (1957).
3. Cohen, W. C., and E. F. Johnson, *Ind. Eng. Chem.*, **48**, 1031 (1956).
4. Fanning, R. J., Ph.D. thesis, Univ. of Oklahoma, Norman (1958).
5. Mason, C. E., *Trans. Am. Soc. Mech. Engrs.*, **60**, 327 (1938).
6. McKnight, G. W., and C. W. Worley, *Natl. Instrument Soc. Am.*, Paper 53-6-1 (1953).
7. Mozley, J. M., *Ind. Eng. Chem.*, **48**, 1035 (1956).
8. Stanton, B. D., and P. R. Hoyt, *Texas Agr. and Mech. Coll. Symposium on Instrumentation* (January, 1953).
9. Williams, T. J., and J. M. Young, *Petrol. Refiner*, **36**, 229 (1957).

Manuscript received June 16, 1958; revision received October 14, 1958; paper accepted October 15, 1958.

# Turbulent Liquid Flow Down Vertical Walls

H. H. BELKIN, A. A. MacLEOD, C. C. MONRAD, and R. R. ROTHFUS

Carnegie Institute of Technology, Pittsburgh, Pennsylvania

Photographic methods have been used to study the behavior of water flowing freely down vertical surfaces under the influence of gravity at Reynolds numbers between 200 and 30,000. The physical appearances of the liquid layers in transitional and fully turbulent flow have been noted. Layer thicknesses have been obtained from high-speed photographs and correlated with liquid Reynolds numbers, the range of experimental data thus being extended into the fully turbulent region. A simple basis of comparison with flow between parallel plates has been developed.

The free flow of liquids down vertical walls has been studied by a number of investigators. Almost all the experimental data on liquid depth however have been taken in the region of viscous flow. It is the purpose of this paper to report data which extend thickness measurements into the fully turbulent range. The present experiments utilize water at ordinary room temperature and cover a range of liquid-phase Reynolds numbers from 200 to 30,000.

Kirkbride measured the thicknesses of falling liquid films by means of direct contact with a micrometer (8). Fallah, Hunter, and Nash obtained average thicknesses from measurements of liquid holdup on vertical walls (3). Friedman and Miller also used a drainage method (4). Grimley measured average layer thicknesses by means of the electrical resistance of the liquid and checked his results through an optical shadow method (5). Dukler and Bergelin used a technique involving electrical capacitance and reached an upper Reynolds number of 3,000 (2). Chew used a photometric method to determine thicknesses for flow down mirrored glass plates (1). Kamei and his associates used a modified holdup technique and obtained a few points in the lower turbulent range as well as many in the viscous range (7). Jackson measured thicknesses by means of a radioactive tracer method and reported results

for Reynolds numbers up to 5,600 (6). In total some sixteen investigators using various experimental methods have reported 504 thickness measurements, almost all of which lie in the Reynolds number range between 1 and 5,000. The present paper reports 85 additional points, mostly in the fully turbulent range.

Friedman and Miller injected a dye on the surface of a falling liquid layer and timed its descent to obtain the surface velocity. Grimley measured the velocities of colloidal particles suspended in falling liquid layers by means of a traveling microscope. In both cases the investigators concluded that the surface velocity exceeds its theoretical value over most of the viscous flow range. This behavior seems to be associated with surface waves which have their inception at very low Reynolds numbers. Jackson has shown that waves first appear near the top of the vertical surface when the velocity of wave generation equals the average velocity of the liquid layer, or in other words when the Froude number is unity. The corresponding Reynolds number has been observed to be in the vicinity of 12 to 25. The waves persist at higher Reynolds numbers and pass through a point of maximum amplitude at a Reynolds number of 100 to 200. Grimley has observed that the amplitude then decreases slowly until an almost smooth surface is again attained at a Reynolds number of about 1,000. Regardless of these complications however observers generally agree that the liquid-layer thickness approximates the theoretical relationship for flat-plate flow throughout the viscous or pseudoviscous flow range.

assumed to flow steadily down a flat, vertical surface at the rate of  $\Gamma$  mass units per unit time and unit breadth of the surface. The shearing force at the interface between the liquid and its bounding gas was taken to be zero, and the density of the gas was assumed negligible. Nusselt's equation for the layer thickness can be written in the form

$$y_0 g^{1/3} \rho^{2/3} \mu^{-1/3} = 0.909 \left( \frac{4\Gamma}{\mu} \right)^{1/3} \quad (1)$$

where  $4\Gamma/\mu$  is the bulk Reynolds number of the liquid layer, and  $y_0 g^{1/3} \rho^{2/3} \mu^{-2/3}$  or  $y_0 g^{1/3} \nu^{-2/3}$  is a dimensionless thickness parameter. Although strictly speaking Equation (1) applies only to flow down a flat surface, the layer thickness is normally small enough for any curvature of the surface to be neglected. Similar equations can be developed for cases in which the curvature must be considered.

Dukler and Bergelin have presented an expression for the liquid-layer thickness in fully turbulent flow based on the generalized velocity distribution for smooth tubes. Reasonably good agreement with experimental data was demonstrated in the very low turbulent range. Extensions of essentially the same method to cases involving shearing forces at the gas-liquid interface in condensers have recently been presented by Rohsenow and his associates (10).

Conflicting effects of surface tension have been reported by several investigators. The influence of surface waves on layer thickness, the mechanism of their formation and movement, and the changes in local velocities occasioned by their passing are not well understood. Jackson

H. M. Belkin is at present with the Creole Petroleum Corporation, Caracas, Venezuela, and A. A. MacLeod is with E. I. duPont de Nemours and Company, Inc., Wilmington, Delaware.

The original data and additional photographs appear in two theses available on interlibrary loan from Carnegie Institute of Technology, Pittsburgh 13, Pennsylvania. The silhouette method is described in the D.Sc. thesis by A. A. MacLeod; the direct lighting method is presented in the Ph.D. thesis by H. M. Belkin.

The classical expression for the liquid-layer thickness in fully viscous flow was developed by Nusselt (9) on the basis of several assumptions. A liquid of constant viscosity and density was

however has offered a qualitative description of wave motion and a quantitative treatment of the relationship between surface velocity and the Froude number.

#### EXPERIMENTAL METHOD

The data reported in this paper were obtained in two pieces of apparatus designed along similar lines. In both cases distilled water was made to fall freely down the outer surface of a smooth, vertical rod after being extruded from an annular orifice at the top of the test section. The rod diameters were 0.934 and 0.935 in. In both pieces of equipment several orifices having different clearances were used, depending on the flow rate of the liquid layer. In both cases the water was recycled, and its temperature was maintained within 0.1°C. of the room temperature by partial bypassing through a cooler. Flow rates were measured by rotameters. The test sections were mounted in heavy frameworks to minimize vibrations, and the overhead supply tanks were well baffled to dampen pulsations of the flow.

The thickness of the water layer was determined at various flow rates by comparing high-speed photographs of the liquid with pictures of the dry rod. In one apparatus the illumination from a 10,000-volt spark of 5  $\mu$ sec. duration produced a silhouette of the wetted rod. In the other apparatus the light of a 10,000-volt, 50- $\mu$ sec. spark directly illuminated the water layer so that qualitative information about its physical appearance might be obtained in addition to the thickness data. A spark of short duration was necessary to eliminate blurring of the photographs owing to rapid local movements in the liquid layer. The cameras were centered on a point about 3 ft. from the annular entrance in most of the runs, although checks were made at other levels as well. Three pictures were obtained at each flow rate. No attempt was made to measure the effect of the falling liquid layer on the otherwise quiet room air surrounding the rods.

The meaning of the term *liquid layer thickness* varies somewhat in the published literature, depending on the particular method of measurement being reported. In the present case the meaning can be indicated by developing the working equation. If a side-view or elevation photograph of the dry rod and a corresponding photograph of the wetted rod are carefully taken from the same position with the same camera and then enlarged to the same length, the diameter of the dry rod in the picture bears the same proportional relationship to the actual diameter of the dry rod as the average liquid-layer thickness in the picture does to the actual average liquid-layer thickness. The dry rod in the

picture has a projected area equal to the product  $L' d'$ . Likewise the wetted rod in the picture has a projected area equal to the product  $L' (d' + 2y_b')$ . The difference in measured areas ( $A_2 - A_1$ ) is therefore simply  $2y_b' L'$ . Thus by

the tracings were obtained by means of a polar planimeter. By this method the error in, for example, a 24-sq.-in. area was about 0.02 sq. in. when averaged over three pictures. Such an error might have resulted in an uncertainty of from

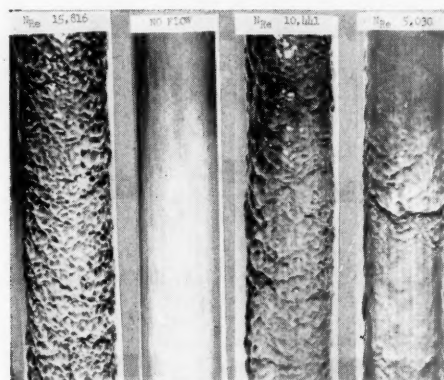


Fig. 1. Photographs of directly lighted vertical rod and falling liquid layers at several Reynolds numbers.

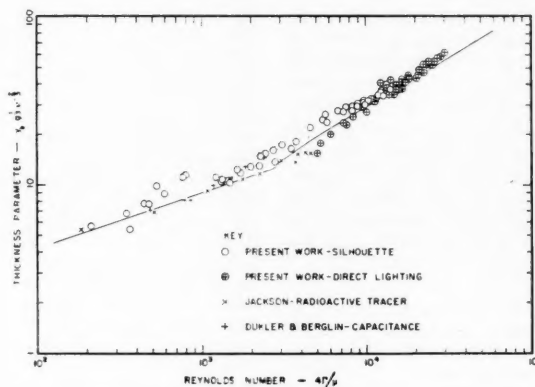


Fig. 2. Effect of Reynolds number on liquid-layer thickness with zero shear at the gas-liquid interface.

virtue of the proportional relationship originally cited it follows that

$$\frac{y_b}{d} = \frac{y_b'}{d'} = \frac{A_2 - A_1}{2L'} \frac{L'}{A'} \\ = \frac{A_2 - A_1}{2A_1} \quad (2)$$

The actual diameter of the dry rod can be measured very accurately with a micrometer. It is apparent therefore that the accuracy and precision with which the thickness is determined must depend on the magnitudes of  $A_1$  and  $A_2$  as well as on the method of measurement. In the present work the enlarged images of the dry and wetted rod were traced on large sheets of paper, and the areas of

0.001 to 0.003 in. in the actual thickness, depending on the degree to which the original photograph was enlarged. It was noted however that a given operator tended to be consistently high or low in his readings. This acted strongly to reduce the actual error in the thickness computed by means of Equation (2).

The photographic method has the advantages of leaving the liquid undisturbed and being independent of elusive factors which influence the drainage type of measurements. On the other hand the photographs tend to indicate too high a value of the thickness because the troughs of the surface waves at the boundary of the image are sometimes masked by the crests of waves closer to the camera. It is possible for such an



effect to make the reported thicknesses as much as 5 to 10% too high.

## EXPERIMENTAL RESULTS AND DISCUSSION

### Physical Appearance

Figure 1 shows typical photographs obtained with direct lighting at zero flow and three different Reynolds numbers in the lower turbulent range. There is evidence of discrete disturbance eddies at 5,030 Reynolds number. This suggests the persistence of transitional flow, since similar formations have been observed in tubes running full of liquid throughout the change from viscous to turbulent flow. On the other hand the appearance of the photographs at the higher Reynolds numbers suggests that full turbulence has been attained. Additional photographs not shown here indicate more intense turbulence but the same over-all type of flow at Reynolds numbers between 16,000 and 30,000. The technique of direct lighting was used only at Reynolds numbers above 5,030.

There was no special significance in the fact that the silhouette method was used at lower flow rates than the technique of direct lighting. The center of attention on the Reynolds number scale just happened to be different at the particular time each method was utilized. The upper limit of the tests was fixed by the supply and discharge capacities of the equipment rather than by any sudden change in the behavior of the liquid layer, such as separation from the surface. The capacities were limited by factors associated with some contemplated diffusion studies in the same equipment.

Silhouettes were obtained down to a Reynolds number of about 200. It was observed that ripples in the liquid layer increased in number but decreased in amplitude as the Reynolds number was increased in the pseudoviscous range. At a Reynolds number of about 1,000 however heavier waves appeared. These increased in number and amplitude with further increase in Reynolds number, until at about 3,000 Reynolds number they covered the surface of the liquid completely. At still higher Reynolds numbers the waves continued to increase in amplitude and tended to move in groups.

In both cases the pictures showed that sinusoidal waves with their clearly defined troughs and crests, as determined by Grimley and Dukler and Bergelin, give way to a random distribution of shallow troughs and sharp crests in the fully turbulent region. No definite patterns of wave length or frequency could be established, but the turbulent waves had nearly the trochoidal form of waves generated by wind on large bodies of water. A trochoid is the curve generated by a point on a circle which rolls along

the underside of a straight line. The pictures made it easy to visualize that a profile cutting across the indentation between adjacent crests might closely resemble such a form.

### Liquid-Layer Thickness

Figure 2 summarizes the experimental results of the thickness determinations. The points selectively tabulated by Dukler and Bergelin and by Jackson in their respective papers are also included for the purposes of comparison.

It is apparent that the data do not make it possible to fix the exact Reynolds number at which the advent of turbulence begins to affect the thickness parameter. The present data obtained by the silhouette technique approximate those of Dukler and Bergelin. On the other hand the results of the direct-lighting technique are in close agreement with Jackson's data. It cannot be said whether the differences are due to experimental errors or are caused by actual alterations in the stable flow at a given Reynolds number.

Some factors in the design and performance of the equipment are relevant to the discussion of critical Reynolds number. The liquid was put on the dry rod by means of annular orifices. The outer portions of the liquid layer were therefore accelerated after application in any case, but the over-all acceleration depended on how closely the orifice clearance matched the final average thickness of the freely falling liquid. Gross accelerations appeared to be confined to the top 6 to 12 in. of the test section. The photographs of the liquid layer were normally taken 36 to 40 in. from the top. In addition a few pictures were taken at 62 in. and analyzed in the usual way. Coincident linear variations of thickness with mass flow rate through a given orifice were obtained at both distances. Thus the values of the thickness parameter shown in Figure 2 should apply at all points on the vertical surface below the region of gross acceleration.

On the other hand it was observed that when the liquid level in the supply tank directly above the test section was permitted to become low, changes occurred in the liquid layer. The surface appeared to have additional wave fronts superimposed on the smaller waves in the falling layer. Furthermore the liquid thickness was found to be greater at low tank levels than might be predicted from data obtained at higher levels with the same orifice. Consequently the tank levels were held at a more or less constant height by utilizing several orifice sizes over the desired range of flow rates. The Reynolds number region covered by a given orifice was permitted to overlap its neighbors in order to check the reproducibility of the liquid-layer thicknesses. No appreciable effect of changing orifice sizes was evident. Such information is merely comparative how-

ever and does not necessarily mean that the measured thicknesses were entirely free of tank-level effects or persistent entrance disturbances. Therefore the spread of the data in Figure 2 occurs for reasons that cannot be pinpointed by means of the present experimental data. Other investigators however seem to have encountered the same order of uncertainty in fixing the critical Reynolds number on the basis of thickness measurements.

### Correlation of Thickness Data

The thickness parameter ( $y_b g^{1/2} \nu^{-2/3}$ ) is related to the Reynolds number ( $4\Gamma/\mu$ ) as shown in Figure 2. Examination of the viscous or pseudoviscous region leads to the conclusion, expressed by numerous investigators, that the experimental data closely follow Equation (1). In other words the thickness of the liquid layer can be predicted with sufficient accuracy by treating the fluid as if it were flowing in viscous motion between two parallel flat plates separated by a clearance equal to twice the thickness of the actual falling layer. The data indicate that such thicknesses occur regardless of the many complicating factors introduced by the presence of a free surface at the gas-liquid interface.

It might reasonably be postulated therefore that transitional and fully turbulent liquid layers can also be handled with sufficient accuracy in the manner of flow between parallel plates. While such an approach is neither particularly new nor different, some recent friction data for parallel plates reported by Walker, Whan, and Rothfus (11) permit a straightforward analysis to be made.

If the curvature of the vertical surface and the shearing force at the gas-liquid interface can both be neglected, the skin friction at the solid surface must be

$$\tau_o g_c = \rho g y_b \quad (3)$$

by virtue of a simple force balance on the liquid. Therefore the Fanning friction factor can be written

$$f = \frac{2\tau_o g_c}{\rho V^2} = \frac{2g y_b}{V^2} \quad (4)$$

The Reynolds number for flow between parallel plates is commonly taken to be

$$N_{Re} = \frac{4y_b V}{\nu} \quad (5)$$

and so through the combination of Equations (4) and (5)

$$N_{Re} \sqrt{f} = \frac{4\sqrt{2} y_b^{1/2} g^{1/2}}{\nu} \quad (6)$$

or

$$y_b g^{1/2} \nu^{-2/3} = 0.315 (N_{Re} \sqrt{f})^{3/2} \quad (7)$$

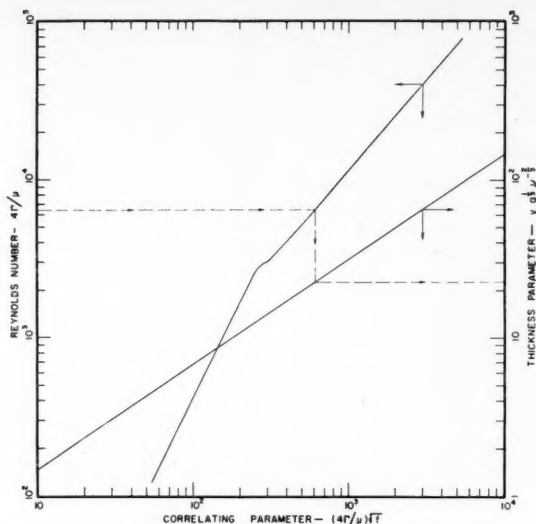


Fig. 3. Relationship between the Reynolds number and liquid-layer thickness predicted from parallel-plate friction data.

Since Equation (7) is developed solely from a force balance and definitions, it is independent of the stable type of flow in the liquid layer. The success with which it can be used to predict liquid-layer thickness at a given Reynolds number depends on the accuracy of two assumptions. First it is assumed that the liquid behaves as it would if the gas-liquid interface were not present; that is, the thickness of the liquid layer remains independent of actual interfacial conditions. Second it is assumed that the actual liquid layer attains its critical Reynolds number at the same value as for flow between parallel plates and that the effect of laminar-turbulent transition on the friction factor is the same in both cases. If the assumptions are met satisfactorily, Equation (7) should be equally valid at all Reynolds numbers.

Accordingly the friction data of Walker, Whan, and Rothfus were used to prepare a logarithmic graph of the Reynolds number against the product  $(N_{Re}\sqrt{f})$ . Equation (7) was then plotted on the same set of coordinates as shown in Figure 3. The solid line in Figure 2 was constructed directly from the corresponding values of thickness parameter and Reynolds number appearing in Figure 3. It can be seen that the experimental data are well represented by the parallel-plate correlation. The critical Reynolds number of 2,700 obtained in the friction experiments appears to be a reasonably satisfactory value for the falling liquid layer as well.

It should be emphasized that Figure 2 does not prove the hydrodynamic equivalence of parallel-plate flow and free flow down a vertical surface. In

fact, it implies nothing about the mechanics of the liquid motion but simply indicates that the parallel-plate relationship seems to be a satisfactory basis for interpolating and extrapolating liquid-layer thicknesses over a long range of Reynolds numbers.

It is interesting to note the relationship between the Fanning friction factor for parallel plates and the Froude number of the liquid layer. Jackson used the Froude number in the form

$$N_{Fr} = V/(gy_b)^{1/2} \quad (8)$$

as a criterion for wave inception. When Equations (4) and (8) are combined, the Froude number can be expressed in terms of the Fanning friction factor as

$$N_{Fr} = \sqrt{2/f} \quad (9)$$

Consequently Equation (7) can equally well be written in the form

$$y_b g^{1/2} \nu^{-1/2} = 0.397(N_{Re}/N_{Fr})^{1/2} \quad (10)$$

Once again the last equation is independent of the type of flow existing in the liquid layer, since it is simply another form of Equation (7).

The Reynolds number and Froude number are related through Equation (9) in the simple case under consideration. Therefore when the Froude number is equal to unity, the condition for wave inception according to Jackson, the Fanning friction factor must be 2.0. For viscous flow between parallel plates,  $f = 24/N_{Re}$ , and so the Reynolds number at wave inception is 12. As might be expected, this result is in close agreement with Jackson's observations in the region very near the top of his test section.

#### NOTATION

- $A_1$  = projected area of dry rod in picture, sq. ft.
- $A_2$  = projected area of wetted rod in picture, sq. ft.
- $d$  = actual diameter of dry rod, ft.
- $d'$  = diameter of dry rod in picture, ft.
- $f$  = Fanning friction factor =  $\frac{2T_0 g_c}{\rho V^2}$   
dimensionless
- $g$  = acceleration due to gravity, ft./sec.<sup>2</sup>
- $g_c$  = conversion factor in Newton's second law of motion = 32.2 (lb.-mass)(ft.)/(lb.-force)(sec.<sup>2</sup>)
- $L'$  = length of picture, ft.
- $N_{Fr}$  = Froude number =  $V/(gy_b)^{1/2}$ , dimensionless
- $N_{Re}$  = Reynolds number =  $4\Gamma/\mu$ , dimensionless
- $V$  = bulk average linear fluid velocity, ft./sec.
- $y_b$  = actual thickness of falling liquid layer, ft.
- $y_b'$  = liquid layer thickness in picture, ft.

#### Greek Letters

- $\Gamma$  = mass flow rate of liquid per unit breadth of vertical surface, lb.-mass/(sec.)(ft.)
- $\mu$  = viscosity of liquid, lb.-mass/(sec.)(ft.)
- $\rho$  = density of liquid, lb.-mass/cu. ft.
- $\tau_0$  = skin friction at solid surface, lb.-force/sq. ft.
- $\nu$  = kinematic viscosity of liquid, sq. ft./sec.

#### LITERATURE CITED

1. Chew J. N., Ph.D. thesis, Univ. Texas, Austin (1953).
2. Dukler, A. E., and O. P. Bergelin, *Chem. Eng. Progr.*, **48**, 557 (1952).
3. Fallah, R., T. G. Hunter, and A. W. Nash, *J. Soc. Chem. Ind. (London)*, **53**, 369T (1934).
4. Friedman, S. J., and C. O. Miller, *Ind. Eng. Chem.*, **33**, 885 (1941).
5. Grimley, S. S., *Trans. Inst. Chem. Eng. (London)*, **23**, 228 (1945).
6. Jackson, M. L., *A.I.Ch.E. Journal*, **1**, 231 (1955).
7. Kamei, S., J. Oishi, H. Iijima, M. Kawamura, and M. Itai, *Chem. Eng. (Japan)*, **18**, 545, (1954).
8. Kirkbride, C. G., *Trans. Am. Inst. Chem. Engrs.*, **30**, 170 (1933).
9. Nusselt, W., *Z. Ver. deut. Ing.*, **60**, 541, 569 (1916).
10. Rohsenow, W. M., J. H. Webber, and A. T. Ling, *Trans. Am. Soc. Mech. Engrs.*, **78**, 1637 (1956).
11. Walker, J. E., G. L. Whan, and R. R. Rothfus, *A.I.Ch.E. Journal*, **3**, 484 (1957).

Manuscript received May 5, 1958; revision received August 4, 1958; paper accepted May 6, 1958. Paper presented at A.I.Ch.E. Salt Lake City meeting.

# Phase Equilibria in Mixtures of Polar and Nonpolar Compounds

## Derived Thermodynamic Quantities for Alcohols and Hydrocarbons

CLINE BLACK

Shell Development Company, Emeryville, California

The properties of vapor mixtures and liquid solutions which determine phase equilibria are of special importance in separation processes. They include the vapor-phase imperfections; the liquid-phase activity coefficients; and the excess heat, entropy, and free energy of mixing.

Correlation of these properties in nonpolar mixtures is relatively simple, but in mixtures of polar and nonpolar compounds the molecular interactions lead to more complex relations. Semiempirical relations reported earlier (3, 4) have been used to calculate the vapor imperfections and to correlate the liquid-phase activity coefficients.

Temperature variations of the activity coefficients can reflect the true heat and entropy effects in solution if sufficient vapor-liquid equilibria are available for a careful and consistent treatment. This is illustrated with binary mixtures of benzene and the *n*-aliphatic alcohols, methanol to pentanol. The results are compared with calorimetric data available in the literature.

The consistent set of cross-correlated coefficients provides a basis for calculating both isothermal and isobaric vapor-liquid equilibria at various conditions for the binaries and for certain ternary and multicomponent mixtures without any additional data.

Most industrial petroleum and chemical processes involve separations in which the products of interest are separated from the undesirable components. Many of these separation schemes depend directly or indirectly on the phase equilibria in the mixtures. Consequently the properties of vapor mixtures and liquid solutions which determine the phase equilibria are of special importance. These include the vapor-phase imperfections; the liquid-phase activity coefficients; and the excess heat, entropy, and free energy of mixing.

Correlation of these properties in nonpolar mixtures is relatively simple, but molecular interactions in mixtures of polar and nonpolar compounds are more complex and lead to more involved algebraic relations.

Even though the excess free energy of mixing does not appear highly sensitive to change in temperature, the heat of mixing depends directly on these changes. Correlations which incorporate temperature variations of the activity coefficients

can reflect the true heat and entropy effects in solution if sufficient vapor-liquid equilibria are available for a careful and consistent treatment. This is illustrated with binary mixtures of benzene and the *n*-aliphatic alcohols, methanol to *n*-pentanol. These represent some of the more complex cases, as interassociation between unlike molecules as well as dissociation of the alcohol polymers takes place upon mixing.

From the cross-correlated results both isothermal and isobaric equilibria can be predicted at any prescribed condition in the range of the correlations. This is illustrated for ten alcohol-hydrocarbon binaries and for some ternary and multicomponent mixtures of the components. The more extensive tabulations are available through the American Documentation Institute.\*

\*Tabular material has been deposited as document 5912 with the American Documentation Institute, Photoduplication Service, Library of Congress, Washington 25, D. C., and may be obtained for \$2.50 for photoprints or \$1.75 for 35-mm. microfilm.

### CORRELATION OF VAPOR-LIQUID EQUILIBRIA

Complete vapor-liquid equilibria provide the relation between the liquid composition, the vapor composition, and the total pressure or boiling temperature of the solution. It is conventional to correlate such data through the activity coefficients in the liquid and the imperfections in the vapors.

Activity coefficients have been calculated from vapor-liquid equilibria according to

$$\log \gamma_i = \log (Y_i P / x_i P_i^0) + \log \theta_i \quad (1)$$

The latter includes the influences of both vapor imperfections and pressure on the liquid phase.

These coefficients were derived from a special approximation (3) in which the nonpolar and polar parts of the energies of attraction of the pure components are combined separately for representing mixtures. If *b*<sub>i</sub> and *a*<sub>i</sub> are van der Waals' covolume and cohesive energy constants,

TABLE 1. CONSTANTS FOR POLAR AND NONPOLAR COMPOUNDS

	$T_c, ^\circ\text{K.}$	$P_c, \text{atm.}$	$E'$	$m$	$\chi$
Methanol	513.3	78.7	0.120	4.75	51.2
Ethanol	516.3	63.1	0.089	4.75	75.9
Isopropanol	508.2	53.0	0.080	4.75	95.2
<i>n</i> -Propanol	536.88	50.0	0.080	4.75	96.17
<i>n</i> -Butanol	560.0	48.4	0.075	4.75	119.61
<i>n</i> -Pentanol	586.1	44.0	0.072	4.75	143.4
Benzene	561.66	47.7	0	—	116.1
Toluene	594.0	41.6	0	—	141.7
Methyleyclohexane	571.1	34.5	0	—	167.9
<i>n</i> -Heptane	540.2	27.0	0	—	189.0

TABLE 2. COEFFICIENTS FOR THE MODIFIED VAN LAAR-TYPE OF EQUATIONS  
ALCOHOL-BENZENE SYSTEMS

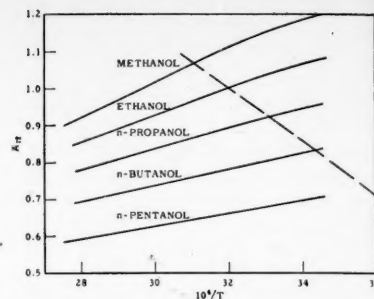
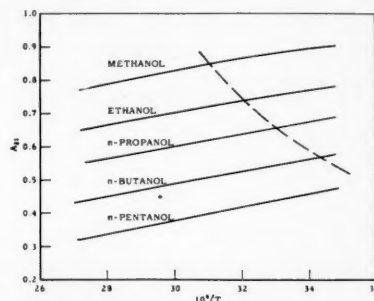
Methanol-benzene	$t, ^\circ\text{C.}$	$A_{12}$	$A_{21}$	$c_{12}$	Type of data	Source of original data
	20	1.1900	0.8950	0.1470	Isothermal	(20)
	35	1.1304	0.8713	0.1320	Isothermal	(24)
	40	1.1083	0.8623	0.1262	Isothermal	(19)
	55	1.0400	0.8350	0.1090	Isothermal	(24)
	(59)	1.0226	0.8275	0.1050	Isobaric	(33)
Ethanol-benzene						
	20	1.0700	0.7715	0.1142	Constant pressure data	(21)
	45	0.9800	0.7250	0.0980	Isothermal	(6)
	(68)	0.9015	0.6870	0.0831	Isobaric, 760 mm. Hg	(8), (31)
Isopropanol-benzene						
	25	0.9370	0.6670	0.0841	Isothermal	(22)
<i>n</i> -Propanol-benzene						
	(27.8)	0.9290	0.6610	0.0832	Isobaric, 100 mm. Hg	(5)
	40	0.8930	0.6370	0.0785	Isothermal	(19)
	(48.8)	0.8680	0.6200	0.0754	Isobaric, 275 mm. Hg	(5)
	(76.1)	0.7980	0.5740	0.0659	Isobaric, 750 and 760 mm. Hg	(31), (5)
<i>n</i> -Butanol-benzene						
	25	0.8155	0.5550	0.0625	Isothermal	(1)
	(83.6)	0.6950	0.4500	0.0500	Isobaric, 760 mm. Hg	(32)
<i>n</i> -Pentanol-benzene						
	(89)	0.5850	0.3305	0.0340	Isobaric, 760 mm. Hg	(32)

TABLE 3. COEFFICIENTS FOR THE MODIFIED VAN LAAR EQUATIONS  
ALCOHOL-TOLUENE SYSTEMS

Methanol-toluene	$t, ^\circ\text{C.}$	$A_{12}$	$A_{21}$	$c_{12}$	Type of data	Reference
	(64.44)	0.9700	0.9290	0.1000	Isobaric, 760 mm. Hg	(2)
Ethanol-toluene						
	35	1.0620	0.7990	0.1048	Isothermal	(15)
	55	0.9880	0.7630	0.0911	Isothermal	(15)

TABLE 4. COEFFICIENTS FOR THE MODIFIED VAN LAAR EQUATIONS  
ETHANOL-SATURATED C<sub>7</sub> HYDROCARBONS

Ethanol-methyleyclohexane	$t, ^\circ\text{C.}$	$A_{12}$	$A_{21}$	$c_{12}$	Type of data	Reference
	35	1.205	1.060	0.185	Isothermal	(16)
	55	1.140	1.010	0.165	Isothermal	(16)
Ethanol- <i>n</i> -heptane	$t, ^\circ\text{C.}$	$A_{12}$	$A_{21}$	$c_{12}$	Type of data	Reference
	30	1.271	1.238	0.280	Isothermal	(28)
	(37.5)	1.242	1.206	0.264	Isobaric, 180 mm. Hg	(14)
	50	1.200	1.154	0.240	Isothermal	(28)
	(55)	1.184	1.136	0.230	Isobaric, 400 mm. Hg	(14)
	70	1.138	1.081	0.205	Isothermal	(28)
					Isobaric, 750 mm. Hg	(14)

Fig. 1. Coefficient  $A_{12}$  in the modified van Laar equations—alcohols (1) with benzene (2).Fig. 2. Coefficient  $A_{21}$  in the modified van Laar equation—alcohols (1) with benzene (2).

respectively, the molal cohesive energy is represented by  $a_i \xi_i^0$ . It is assumed that the vapor mixtures can be predicted from the properties of the individual components. The corresponding rigorous expression for  $\theta_i$  becomes

$$\log \theta_i = [(P - P_i^0)/2.3RT] \\ + [b_i - V_i' - a_i \xi_i^0/RT] \\ + (P/2 \cdot 3R^2T^2)[(\sum G_{ii}Y_i)^2 \\ + (\sum \tilde{G}_{ii}Y_i)^2] \quad (2)$$

For nonpolar compounds the attraction coefficients are predicted from the critical temperature and pressure. Polar compounds require individual coefficients which can be determined from a minimum of vapor-density data. Such coefficients have been given earlier (3) for methanol and ethanol. Coefficients for the higher alcohols have been estimated from the carbon number with the aid of the empirical equation

$$E' = 0.06 + 0.06/n_e \quad (3)$$

derived from available vapor-density data (10, 11, 12, 17, 18, 23) for the low-molecular-weight alcohols. These coefficients together with the critical constants are given in Table 1.

The constants  $\chi_i$  given also in Table 1 are used to estimate the approximate molal-liquid volumes of the components



in solution according to the empirical equation

$$V' = \chi / (1.70897 - 0.74575T_r - 0.26048T_r^{0.5}) \quad (4)$$

Since the contribution of  $V'$  in Equation (2) is relatively small, Equation (4) is an adequate approximation. As the temperature approaches the critical value, Equation (4) predicts molal volumes lower than those of the pure components. At low reduced temperatures the values are nearly the same.

The activity coefficients have been correlated as described earlier (4) with the aid of the two plots

$$(\log \gamma_1)^{0.5} \text{ vs. } (\log \gamma_2)^{0.5} \quad (5)$$

and

$$\log (\gamma_1/\gamma_2) \text{ vs. } x_i \quad (6)$$

The data have been represented with the aid of the modified van Laar type of equations (4), which for binary systems are given according to

$$\left. \begin{aligned} \log \gamma_1 &= a_{12}^2 / (1 + a_{12}^2 x_1 / a_{21}^2 x_2)^2 + E_1 \\ \log \gamma_2 &= a_{21}^2 / (1 + a_{21}^2 x_2 / a_{12}^2 x_1)^2 + E_2 \\ E_i &= c_{ij} x_i (x_i - x_j) \cdot [3(x_i - x_j)(1 - x_i) + 2x_j] \end{aligned} \right\} \quad (7)$$

A summary of the coefficients derived in this way for binary systems consisting of an alcohol and benzene are given in Table 2, together with the source of the experimental data used.

The influence of temperature on the coefficients is shown in Figures 1, 2, and 3, in which  $A_{12}$ ,  $A_{21}$ , and  $c_{12}$  are plotted vs. the temperature. The coefficient  $A_{12}$  is the logarithm of the activity coefficient of component 1, the alcohol, at infinite dilution in liquid 2, benzene. The consistent change in  $A_{12}$  as the carbon number of the alcohol varies from 1 to 5 is evident in Figure 1. Similar consistent changes are noted in the logarithm of the activity coefficient of component 2 at infinite dilution  $A_{21}$  and in  $c_{12}$  in Figures 2 and 3, respectively.

Increasing the temperature causes a decrease in  $A_{12}$ ,  $A_{21}$ , and  $c_{12}$ . The shape of the curves in Figures 1, 2, and 3 for methanol and benzene are quite well established from the isothermal data of Niimi (20) at 20°C., of Scatchard and coworkers (24, 26) at 35° and 55°C. with single points at 25° and 45°C., and of

Lee (19) at 40°C. and the isobaric data of Williams and coworkers (33).

Below about 50°C. for methanol-benzene, as noted in Figure 1, the curve of  $A_{12}$  vs.  $1/T$  begins to deviate appreciably from a linear relation. With ethanol and benzene a similar curvature is noted below about 40°C., as indicated by the dashed line. For *n*-propanol this occurs at a still lower temperature,

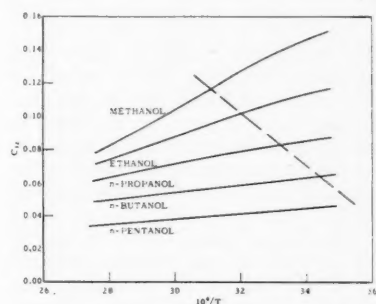


Fig. 3. Coefficient  $c_{12}$  in the modified van Laar equation—alcohols (1) with benzene (2).

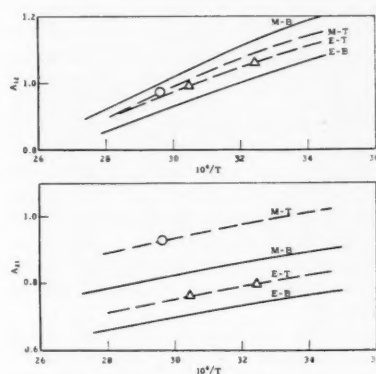


Fig. 4. Influence of temperature on  $A_{12}$  and  $A_{21}$  for methanol-toluene and ethanol-toluene, based on curves for methanol-benzene and ethanol-benzene.

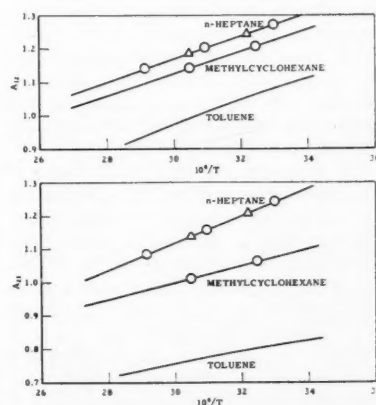


Fig. 5. Influence of hydrocarbon type on  $A_{12}$  and  $A_{21}$  ethanol (1) with hydrocarbons (2).

probably below about 30°C. This is undoubtedly due to an increased inter-association (13) between the alcohol and benzene as the temperature decreases. For alcohols with four or more carbons the data do not establish the shape of  $A_{12}$  vs.  $1/T$  as well, but it appears from the available data that in the temperature region of 20° to 70°C. the relation is nearly linear and the molal heats of mixing at given composition are practically independent of temperature. These same observations and conclusions are evident also in Figures 2 and 3.

The coefficients  $A_{12}$ ,  $A_{21}$ , and  $c_{12}$  decrease as the carbon number increases going from methanol to *n*-pentanol. A nearly linear change is noted if cross plots at constant temperature are prepared from Figures 1, 2, and 3. The coefficients for *n*-pentanol-benzene at temperatures below 89°C. were obtained from such cross plots.

Available vapor-liquid equilibrium data are not sufficient to establish the shape of the curves  $A_{12}$ ,  $A_{21}$ , and  $c_{12}$  vs.  $1/T$  for methanol and toluene. Indeed only the isobaric data at 760 mm. Hg are known (2), which help to establish the three coefficients near 64°C. For ethanol and toluene data at only 35 and 55°C. are known (15). But these two systems can be predicted from these meager data, Table 3, and the established curves for methanol-benzene and ethanol-benzene. As shown in Figure 4, the dashed curves for the toluene systems are drawn in through the data to have shapes similar to the corresponding benzene systems shown as full lines. This is nearly equivalent to the assumption of equal heats of mixing for the toluene and benzene systems with a given alcohol and will be discussed later.

The influence of hydrocarbon type on the coefficients  $A_{12}$ ,  $A_{21}$ , and  $c_{12}$  is illustrated with the systems ethanol-methylcyclohexane and ethanol-*n*-heptane, which will be compared with ethanol-toluene. The coefficients derived for the modified van Laar type of equations and the data sources for these saturated hydrocarbons with ethanol are given in Table 4. The coefficients are given in Figures 5 and 6 for binary mixtures of ethanol in *n*-heptane, methylcyclohexane, and toluene.

#### EXCESS FREE ENERGIES, HEATS, AND ENTROPIES OF MIXING

The heat of mixing and the excess entropy of mixing have been calculated from the excess free energy of mixing and the variation of the activity coefficients with temperature at constant composition. The modified van Laar equations (4) for binary systems [Equations (7)] have been used to calculate  $\log \gamma_i$ 's at given compositions. The excess free energy per mole is calculated at any given composition according to

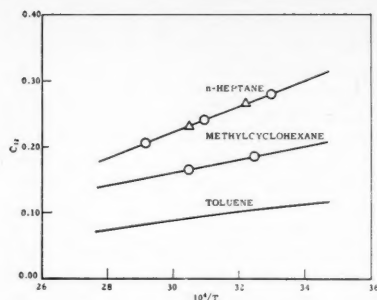


Fig. 6. Influence of hydrocarbon type on  $c_{12}$  ethanol with hydrocarbons.

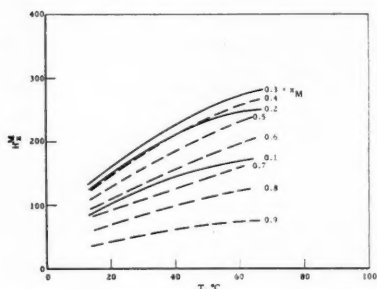


Fig. 7. Influence of temperature on  $H_x^M$  at constant composition methanol with benzene.

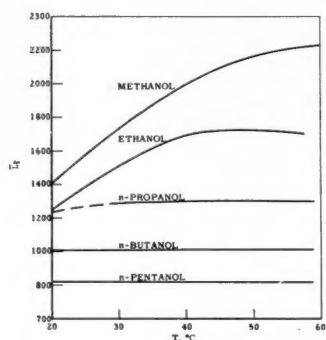


Fig. 8. Differential heat of mixing of alcohol at infinite dilution in benzene vs. temperature.

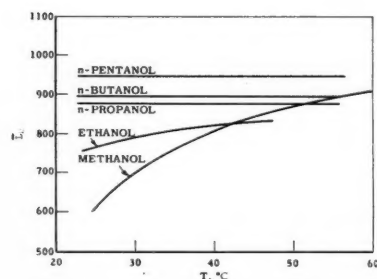


Fig. 9. Differential heat of mixing of benzene at infinite dilution in alcohols vs. temperature.

$$F_x^E = 2.303RT(\sum x_i \log \gamma_i)_x \quad (8)$$

The differential heat of mixing per mole is calculated from the change of  $\log \gamma_i$  with temperature at given composition with the aid of

$$\bar{L}_{ix} = 2.303R(\Delta \log \gamma_i)_x / \Delta(1/T) \quad (9)$$

and the integral heat of mixing per mole is calculated by

$$H_x^M = \sum x_i \bar{L}_{ix} \quad (10)$$

The temperature intervals have been selected so that the results reflect the proper rate of change in the nonlinear regions of  $\log \gamma_i$  vs.  $1/T$ . The heats of mixing calculated for each temperature interval have been considered to correspond to the temperature of the average  $1/T$ 's.

The heats of mixing derived at constant composition at three different temperatures are plotted vs. temperature in Figure 7 for methanol-benzene mixtures. In the range of the data, 20° to 60°C., the heat of mixing increases as the temperature increases; it probably reaches a maximum at a somewhat higher temperature, and at a still higher temperature level it will probably decrease as the temperature is increased. This behavior is to be expected if the temperature coefficient of interassociation (13) between unlike molecules is sufficiently greater than the temperature coefficient of association of the methanol molecules. In addition to the ordinary heat effects resulting from nonpolar forces association gives rise to positive heat of mixing or heat absorbed, and interassociation results in negative heat of mixing or heat evolved.

Similar calculations have been made for methanol-toluene, ethanol-benzene, *n*-propanol-benzene, *n*-butanol-benzene, *n*-pentanol-benzene, ethanol-toluene, ethanol-methylcyclohexane, and ethanol-*n*-heptane. The differential heats of mixing at infinite dilution for each component are given in Table 5 for these systems. For the lower alcohols in mixtures with benzene or toluene the differential heat of mixing increases as the temperature increases in the range considered; for the higher alcohols the differential heats of mixing are practically independent of temperature.

In Figure 8 the differential heats of mixing for the alcohols at infinite dilution in benzene are plotted vs. temperature. As the carbon number increases, the differential heat of mixing of the alcohol at infinite dilution  $\bar{L}_1$  decreases at a given temperature. For mixtures with methanol and ethanol the differential heat of mixing  $\bar{L}_1$  increases as temperature increases, levels off, and probably goes through a very flat maximum. This is probably true with the higher alcohols, with the maximum occurring at successively lower temperatures.

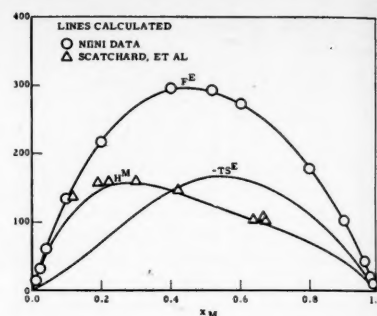


Fig. 10. Excess free energy, heat, and entropy of mixing, cal./g. mole methanol-benzene at 20°C.

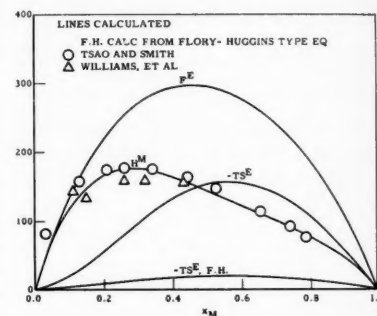


Fig. 11. Excess free energy, heat, and entropy of mixing, cal./g. mole methanol-benzene at 25°C.

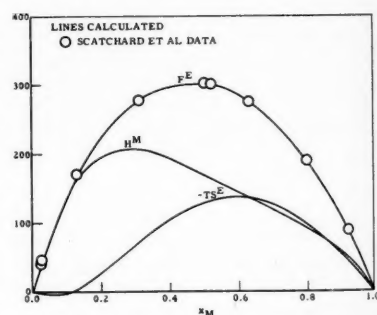


Fig. 12. Excess free energy, heat, and entropy of mixing, cal./g. mole methanol-benzene at 35°C.

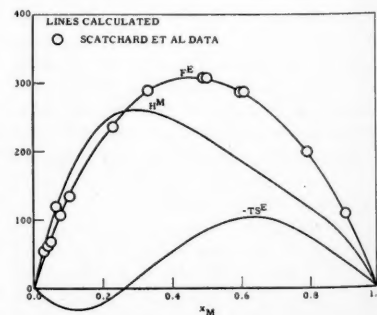


Fig. 13. Excess free energy, heat, and entropy of mixing, cal./g. mole methanol-benzene at 55°C.

The differential heat of mixing  $\bar{L}_2$  for benzene at infinite dilution in the homologous series of alcohols from methanol to *n*-pentanol is plotted vs. temperature in Figure 9. In the low-temperature region the differential heat

of mixing for benzene increases in going from methanol to *n*-pentanol. At a higher temperature level where interassociation has less influence this may not be entirely true.

Integral heats of mixing taken from

TABLE 5. DIFFERENTIAL HEATS OF MIXING AT INFINITE DILUTION DERIVED FROM VAPOR-LIQUID EQUILIBRIA

System	$t$ , °C.	$\bar{L}_1$	$\bar{L}_2$
Methanol-benzene	27.3	1,642	653
	44.7	2,091	840
	62.3	2,233	921
Ethanol-benzene	27.3	1,440	777
	39.9	1,695	821
	56.1	1,695	821
Propanol-benzene	38	1,288	865
Butanol-benzene	50	1,000	872
Pentanol-benzene	36.5	817	943
Methanol-toluene	27.3	1,405	840
	42.3	1,853	866
	57.1	2,035	966
Ethanol-toluene	27.3	1,441	799
	44.7	1,712	833
Ethanol-methylcyclohexane	55	1,504	1,157
Ethanol- <i>n</i> -heptane	55	1,573	1,852

(Nearly constant 30° to 60°C.)  
(Nearly constant 20° to 60°C.)  
(Nearly constant 20° to 60°C.)

(Nearly constant 30° to 70°C.)

TABLE 6. HEATS OF MIXING FOR METHANOL-BENZENE  
 $H^M$ , cal./g. mole at  $x_m = 0.3$

$t$ , °C.	From V-L equil.	Exptl.*	Reference for calorimetric data
15	140	139	Schmidt (27)
20	158	159	Scatchard, <i>et al.</i> (25)
20	158	190-195	Wolfe, <i>et al.</i> (34)
23	167	150	Washburn and Lightbody (30)
25	176	156	Williams, <i>et al.</i> (33)
25	176	175	Tsao and Smith (29)

\*Calorimetric data.

TABLE 7. APPROXIMATE HEATS OF MIXING FOR BINARY SYSTEMS OF ALCOHOLS AND HYDROCARBONS DERIVED FROM VAPOR-LIQUID EQUILIBRIA

Systems	$T$ , °C.	$H^M$ , cal./g. mole								
		0.10	0.20	0.30	0.40	0.50	0.60	0.70	0.80	0.90*
Methanol-benzene	25	115	165	176	163	142	121	101	77	48
	55	164	242	262	248	220	186	151	118	71
Ethanol-benzene	25	105	165	189	191	181	163	138	107	62
	55	130	197	223	222	206	181	153	116	68
Propanol-benzene	55	105	170	206	219	216	200	172	131	75
Butanol-benzene	55	86	147	187	207	212	201	174	134	76
	20									
Pentanol-benzene	to 60	76		182		220		188		83
Methanol-toluene	25	108	155	174	173	163	145	122	92	55
	55	152	230	259	253	232		170	132	
Ethanol-toluene	25	107	167	193	196	188	171	145	110	63
	55	131	200	227	227	211	187	156	119	69
Ethanol-methylcyclohexane	55	117	180	208	216	212	200	180	147	92
Ethanol- <i>n</i> -heptane	55	116	171	193	202	208	215	216	197	136

\*Column headings 0.10, 0.20, . . . 0.90 refer to the mole fractions of alcohol in the liquid for each binary.

TABLE 8. MAXIMUM HEATS OF MIXING

$t$ , °C.	Maximum $H^M$ at any composition, cal./g. mole			
	From V-L equil.	Exptl.*	Reference	
Ethanol-benzene	23	185	182	(30)
<i>n</i> -Propanol-benzene	20 to 60	219	—	
	15		232	(27)
<i>n</i> -Pentanol-benzene	20	220	223	(7)
Methanol-toluene	23	167	159	(30)
Ethanol-toluene	23	195	183	(30)

\*Calorimetric

Figure 7 for methanol-benzene mixtures at a mole fraction of 0.3 for methanol are compared in Table 6 with calorimetric values reported by several investigators (25, 27, 29, 30, 33, 34).

The results derived from vapor-liquid equilibrium data are in substantial agreement with the calorimetric measurements of Schmidt (27), Scatchard, *et al.* (25), and Tsao and Smith (29). The results of Williams, *et al.* (33), and of Washburn and Lightbody (30) are slightly lower than the derived values, and those of Wolfe, *et al.* (34), are somewhat higher than any of the others. No values were calculated at temperatures as low as 15°C., but an extrapolation to 15°C. in Figure 7 gives results in good agreement with those of Schmidt.

The excess entropy of mixing has been calculated from the excess free energy and the heat of mixing at fixed composition according to

$$-TS_x^E = F_x^E - H_x^M \quad (11)$$

The three quantities at 20°C. are shown graphically in Figure 10 for mixtures of methanol and benzene. The excess free energy calculated from the data of Niimi (20) are shown also. The calorimetric heats of mixing of Scatchard, *et al.* (25), are also compared with the derived results in Figure 10.

The three derived thermodynamic quantities  $F_x^E$ ,  $H_x^M$ , and  $-TS_x^E$  at 25°C. are plotted in Figure 11, where the heats of mixing are compared with the calorimetric data of Tsao and Smith (29) and Williams, Rosenberg, and Rothenberg (7) for methanol-benzene. Since the latter data were given graphically, only the points in the region of the maximum are shown for this source. The entropies predicted from the Flory-Huggins relation when applied to these mixtures are much too low. (See the curve marked F.H. in Figure 11.)

For mixtures of methanol and benzene the integral heat of mixing increases as temperature increases up to about 60° or 80°C. In the same region the excess free energy increases only slightly. The excess entropy of mixing is negative and changes to smaller negative values as the temperature increases. The three quantities  $F_x^E$ ,  $H_x^M$ , and  $-TS_x^E$  are given in Figures 12 and 13 for 35° and 55°C., respectively. At low concentrations of methanol the entropy has already become positive at 35°C. (Figure 12), and this positive region increases as temperature increases further (Figure 13).

Figure 14 shows values of  $F_x^E$ ,  $H_x^M$ , and  $-TS_x^E$  for methanol-toluene mixtures derived from the modified van Laar equations with coefficients represented by the curves in Figure 4. It will be remembered that only isobaric data at 760 mm. Hg were available to establish the coefficients at 64.44°C., and the temperature influence was obtained by drawing in the curves with shapes similar to the

corresponding benzene systems. The calorimetric values for the heat of mixing of Tsao and Smith (29) are shown also in Figure 14.

Although the symmetry of the derived results is not in perfect agreement with the data, the magnitude of the values is about right. A comparison of Figures 14 and 11 shows both the maximum heat of mixing and the maximum excess entropy of mixing to be very nearly equal for toluene and benzene mixtures with methanol. The slightly different symmetry of the heat and entropy curves vs.  $x^M$  in the two systems furnishes a higher maximum in the excess free-energy curve for toluene. The data of Tsao and Smith show the heats of mixing for toluene and benzene in methanol to be practically the same at 25°C. The derived heats of mixing at 55°C. are a little higher for mixtures of toluene and methanol than for mixtures of benzene and methanol. These differences may not be real but may be only a reflection of the approximate nature of the slopes of the toluene-methanol curves as established in Figure 4.

Integral heats of mixing derived from the vapor-liquid equilibria and its variation with temperature are given in Table 7 for a few systems at one or two temperatures. For temperatures up to about 60° to 80°C. the heat of mixing of methanol and benzene increases as temperature increases. This limit appears to occur at successively lower temperatures as one goes from methanol to *n*-pentanol in the homologous series. For *n*-pentanol-benzene mixtures the limit is probably below 20°C.

The maximum heat of mixing at any composition has been plotted vs. temperature in Figure 15 for the five alcohols, methanol to *n*-pentanol, in mixtures with benzene. At low temperatures, for example at 25°C., the maximum heat of mixing increases as the carbon number of the alcohol increases. That butanol falls just below propanol and pentanol is not significant. Within the accuracy of the calculations the maximum  $H^M$  at any composition can be considered the same for benzene in *n*-propanol, *n*-butanol, and *n*-pentanol, but in ethanol and methanol the differences are significant.

The derived maximum heat of mixing at any composition is compared with available calorimetric data for five systems in Table 8. As with methanol-benzene mixtures in Table 6, the derived results for methanol-toluene are also slightly higher than the measured values of Washburn and Lightbody (30). Even so, the deviations of the derived from the experimental values are less than 7% for each of the systems.

The influence of hydrocarbon type on the three quantities  $F^E$ ,  $H^M$ , and  $-TS^E$  is shown in Figure 16 for mixtures of ethanol with *n*-heptane, methylcyclohexane, and toluene at 55°C. The excess

free energy decreases in the order *n*-heptane, methylcyclohexane, toluene. The maximum heat of mixing at any composition is nearly the same for the three binaries, but the symmetry of the systems is different. It will be noted also that the maximum heat of mixing is about the same for these systems as for systems composed of benzene with any alcohol from ethanol to *n*-pentanol at the same temperature. Both the magnitude and the symmetry of the excess entropy of mixing vs.  $x_E$  are different for the three

systems. The excess entropy is negative and decreases to smaller negative values going from heptane to methylcyclohexane to toluene at concentrations of ethanol less than about 60% mole. At low concentrations of ethanol  $TS^E$  becomes slightly positive in mixtures with toluene.

#### DERIVED VAPOR-LIQUID EQUILIBRIA

Having correlated the activity coefficients as a function of composition and confirmed the validity of their temperature dependence by comparing calculated and observed heats of mixing, one can now use the cross-correlated coefficients to predict thermodynamically consistent sets of vapor-liquid equilibria. This has been done for both isothermal and isobaric conditions.

The procedure for isothermal calculations is to start with known liquid compositions, calculate the activity coeffi-

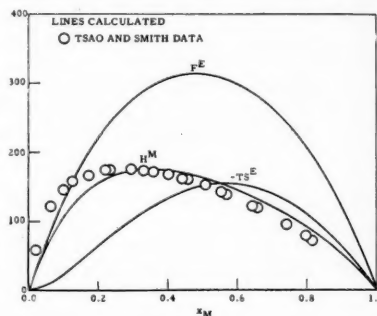


Fig. 14. Excess free energy, heat and entropy of mixing, cal./g. mole methanol-toluene at 25°C.

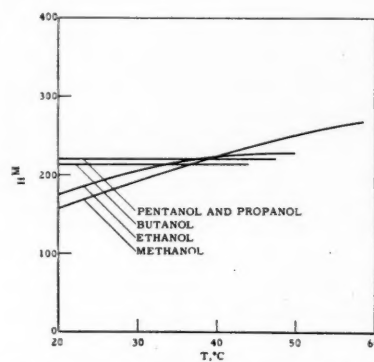


Fig. 15. Maximum heats of mixing, cal./g. mole alcohol-benzene mixtures.

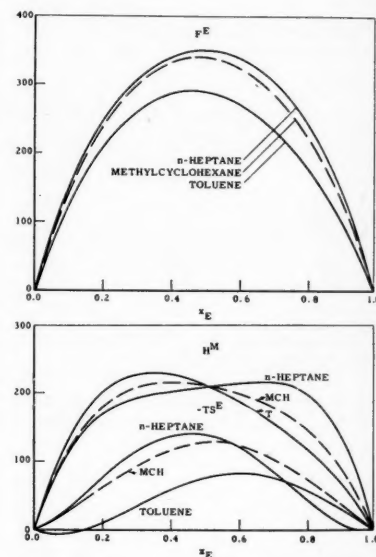


Fig. 16. Influence of hydrocarbon type on  $F^E$ ,  $H^M$ ,  $-TS^E$  ethanol-hydrocarbons.

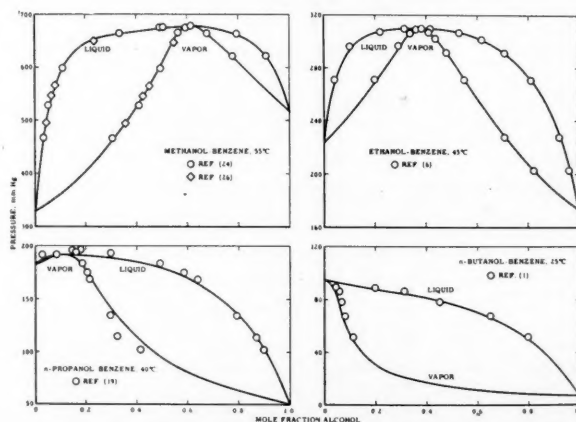


Fig. 17. Comparison of calculated and experimental vapor-liquid equilibria. (Lines are calculated.)



cients according to Equations (7), then use these to calculate the total pressure according to  $P = \Sigma(\gamma_i x_i P_i^0 / \theta_i)$ . The vapor composition is calculated as  $Y_i = \gamma_i x_i P_i^0 / \theta_i P$ . A trial calculation is used to establish final values for  $\theta_i$ 's starting with  $Y_i$ 's calculated with the assumption that  $\theta_i$  is unity.

Isobaric calculations are carried out by first making two isothermal calculations from which the boiling point at any liquid composition and prescribed total pressure is found by interpolating or extrapolating  $\log P$  vs.  $1/T$ . Vapor-liquid equilibria are then calculated at each composition for which the boiling point was established.

Isenthalpic vapor-liquid equilibria calculated with the aid of the cross-correlated coefficients, Tables 2, 3, and 4, provide

calculated results which can be compared directly with the original experimental values. One example for each of the eight binaries for which isothermal data are available is given in Figures 17 and 18.

In Figure 17 calculated and experimental vapor-liquid equilibria are compared for methanol-benzene at 55°C., ethanol-benzene at 45°C., *n*-propanol-benzene at 40°C., and *n*-butanol-benzene at 25°C. The excellent agreement is verification of the validity of Equations (2) and (7). The binaries represented best are the high-quality data of Scatchard and coworkers (24, 26) and of Brown and Smith (6).

Calculated and experimental results are compared in Figure 18 for ethanol-toluene at 55°C., ethanol-methylcyclohexane at 55°C., ethanol-*n*-heptane at 30°C., and isopropanol-benzene at 25°C. The high-quality data of Kretschmer and coworkers (15, 16) for the first two binaries are reproduced quite accurately by the calculations. The two sets of experimental data for ethanol-*n*-heptane are not in very good agreement with each other. For the binary isopropanol-benzene the coefficients used were those taken from the cross plots for the normal alcohols. The small deviations of the calculated from the observed results may be partly due to the effect of branching.

A few calculated isobaric vapor-liquid equilibria are compared with experimental data in Figure 19. For methanol-benzene at 760 mm. Hg the experimental data of Williams and coworkers (33) scatter markedly. The author's calculated results are in substantial agreement with the earlier calculations of Wood (35), as noted in the figure. Results calculated for ethanol-benzene at 760 mm. Hg are in good agreement with the experimental data of Wehe (31) and in rough agreement with the data of Drickamer and coworkers (8). Calculated results are in fair agreement with the data of Wehe (32) for *n*-butanol-benzene at 760 mm. Hg and the data of Arnold quoted by Wehe (32) for *n*-pentanol-benzene at the same pressure.

A basic advantage of the algebraic representation is realized when the data have been cross correlated as shown in Figures 1 to 4. Over the temperature range covered, isothermal vapor-liquid equilibria can be calculated with an accuracy sufficient for most practical purposes. In addition isobaric data at any desired pressure in the range of the correlations can also be derived. Incomplete data can be supplemented by calculations to furnish complete vapor-liquid equilibria; for example, Figure 20 shows four systems with incomplete experimental data which have been supplemented by calculations to furnish complete vapor-liquid equilibria.

In Figure 20 complete vapor-liquid equilibria calculated for ethanol-benzene at 20°C. are compared with the experi-

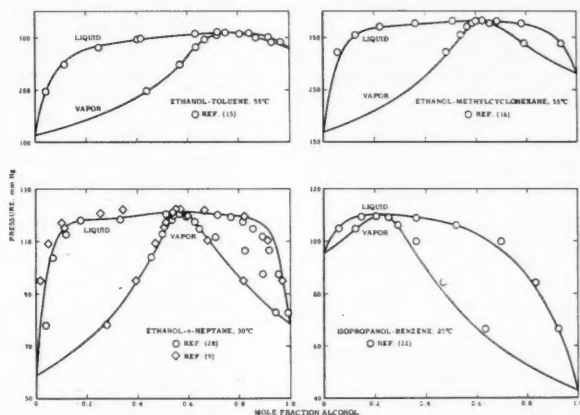


Fig. 18. Comparison of calculated and experimental vapor-liquid equilibria. (Lines are calculated.)

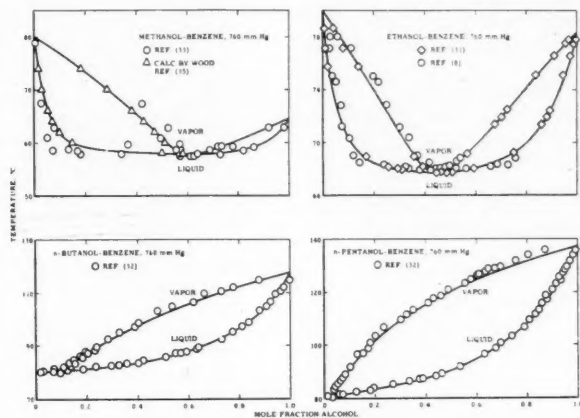


Fig. 19. Comparison of calculated and experimental vapor-liquid equilibria. (Lines are calculated.)

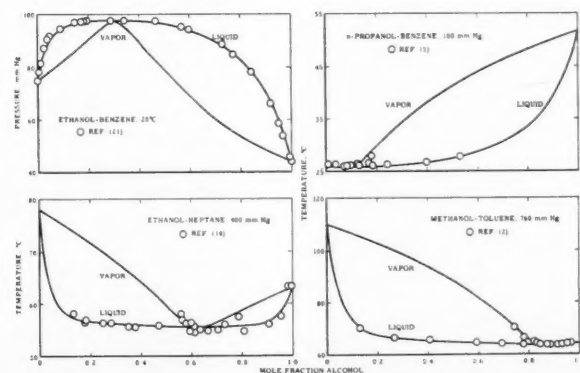


Fig. 20. Supplementing and extending experimental vapor-liquid equilibria. (Lines are calculated.)

mental total pressures of Niini (21). The partially complete data of Britton, *et al.* (5), for *n*-propanol-benzene at 100 mm. Hg and of Katz and Newman (14) for ethanol-*n*-heptane at 400 mm. Hg are compared with complete results provided from calculations. The nearly complete results of Benedict, *et al.* (2), are compared with vapor-liquid equilibria calculated for methanol-toluene at 760 mm. Hg.

As indicated in Figure 4 and confirmed in Figure 14, the estimated effect of temperature on the coefficients  $A_{12}$ ,  $A_{21}$ , and  $c_{12}$  is about right for methanol-toluene. When one knows this, it is possible to calculate vapor-liquid equilibria at other temperatures and pressures. Accordingly vapor-liquid equilibria for this system at 9, 14.7, and 19.7 lb./sq. in. abs. have been predicted. Similarly vapor-liquid equilibria have been calculated for several isothermal and isobaric conditions for each of the alcohol-hydrocarbon binaries described here.\*

Another advantage the cross-correlated coefficients provide is a means of predicting, with no additional data, the ternary or multicomponent vapor-liquid equilibria and heats of mixing in some of the mixtures. These are mixtures in which two of the three components in each ternary are of the same class, for example methanol and ethanol in ternary mixtures with benzene and benzene in multicomponent mixtures with the five alcohols. Ternary systems in which each of the three components is of a different class require data on all three binaries to calculate the ternary equilibria, for example, *n*-heptane-benzene-ethanol.

Accordingly, with the aid of Equations (12), (26), and (27) of reference (4), vapor-liquid equilibria have been calculated for benzene in three- to six-component mixtures with the normal chain alcohols methanol to *n*-pentanol. A simple ternary example, benzene-*n*-pentanol-ethanol at 14.7 lb./sq. in. abs. is given.\*

In summary it has been shown that the modified van Laar type of equation provides an adequate representation of the effect of composition on the activity coefficient for binary mixtures of benzene and alcohols. Consequently these equations also furnish good values for the excess free energies. A cross correlation of the coefficients for these equations as a function of  $1/T$  has been used to predict heats of mixing in good agreement with calorimetric data. From the excess free energies and the heats of mixing the excess entropy of solution has been obtained.

The consistent set of cross-correlated coefficients provides the basis for calculating both isothermal and isobaric vapor-liquid equilibria at various conditions for each of the binaries and for certain ternary and multicomponent mixtures without any additional data.

The influences of carbon number of the alcohol and hydrocarbon type furnish a starting point for further extension of the results.

#### ACKNOWLEDGMENT

The author wishes to thank Emily King and Helen Taylor for assistance in making some of the calculations.

#### NOTATION

- $a_i$  = van der Waals' attraction constant for component  $i$   
 $b_i$  = van der Waals' covolume for component  $i$   
 $a_{ij}^2$  =  $A_{ij} - c_{ij}$  coefficients in Equations (7)  
 $A_{ij}$  = common logarithm of the activity coefficient for component  $i$  at infinite dilution in liquid  $j$   
 $c_{ij}$  = coefficients in Equations (7)  
 $E'$  and  $m$  = individual coefficients for calculating the molecular attraction coefficient for polar compounds  
 $F_x^E$  = excess free energy/mole at composition  $x$   
 $\bar{L}_{ix}$  = differential heat of mixing/mole at composition  $x$   
 $H_x^M$  = integral heat of mixing/mole at composition  $x$   
 $n_c$  = carbon number  
 $P$  = total pressure  
 $P_i^0$  = vapor pressure of pure component  $i$   
 $R$  = universal gas constant  
 $S_x^E$  = excess entropy of mixing/mole at composition  $x$   
 $T$  = absolute temperature  
 $t$  = boiling temperature  
 $V_i'$  = approximation for molal volume of component  $i$  in liquid phase  
 $x_i$  = mole fraction component  $i$  in liquid phase  
 $x_E$  = mole fraction ethanol  
 $Y_i$  = mole fraction component  $i$  in vapor phase

#### Greek Letters

- $\gamma_i$  = liquid phase activity coefficient for component  $i$   
 $\theta_i$  = imperfection-pressure coefficient  
 $\xi^0$  = limiting value at zero pressure of the molecular attraction coefficient  $\xi$   
 $\xi^{*0}$  = nonpolar part of  $\xi^0$   
 $\xi^0$  = polar part of  $\xi^0$   
 $\xi_i$  = attraction coefficient  
 $G_{ii} = (a_i \xi_i^{*0})^{0.5} - (a_i \xi_i^0)^{0.5}$  and  
 $\bar{G}_{ii} = (a_i \bar{\xi}_i^0)^{0.5} - (a_i \bar{\xi}_i^0)^{0.5}$ , differences in the square roots of the nonpolar and polar parts, respectively, of the molal cohesive energies for components  $i$  and  $j$   
 $\chi_i$  = constant in Equation (4)

#### LITERATURE CITED

- Allen, B. B., S. P. Lingo, and W. A. Felsing, *J. Phys. Chem.*, **43**, 425 (1939).

- Benedict, Manson, C. A. Johnson, E. Solomon, and L. C. Rubin, *Trans. Am. Inst. Chem. Engrs.*, **41**, 371 (1949).
- Black, Cline, *Ind. Eng. Chem.*, **50**, 391 (1958).
- Ibid.*, p. 403.
- Britton, E. C., H. S. Nutting, and L. H. Horsley, *Anal. Chem.*, **19**, 601 (1947).
- Brown, I., and F. Smith, *Australian J. Chem.*, **7**, 264 (1954).
- Chalela, D. A., H. H. Steinhauser, and J. O. Hougen, *Ind. Eng. Chem. Data Series*, **2**, 66 (1957).
- Drickamer, H. G., G. G. Brown, and R. R. White, *Trans. Am. Inst. Chem. Engrs.*, **41**, 555 (1945).
- Ferguson, J. B., M. Freed, and A. C. Morris, *J. Phys. Chem.*, **37**, 87 (1933).
- Flock, E. G., D. C. Ginnings, and W. B. Holton, *J. Research Natl. Bur. Standards*, **6**, 881 (1931).
- Halford, J. O., *J. Chem. Phys.*, **17**, 111 (1949).
- Ingle, J. D., and H. P. Cady, *J. Phys. Chem.*, **42**, 397 (1938).
- Jones, L. H., and R. H. Badger, *J. Am. Chem. Soc.*, **73**, 3132 (1951).
- Katz, Kurt, and Morris Newman, *Ind. Eng. Chem.*, **48**, 137 (1956).
- Kretschmer, C. B., and Richard Wiebe, *J. Am. Chem. Soc.*, **71**, 1793 (1949).
- , *Ibid.*, p. 3176.
- , *Ibid.*, **76**, 2579 (1954).
- Lambert, J. D., G. A. H. Roberts, J. S. Rowlinson, and V. J. Wilkinson, *Proc. Roy. Soc. (London)*, **A196**, 113 (1949).
- Lee, Siang Chah, *J. Phys. Chem.*, **35**, 3558 (1931).
- Niini, A., *Ann. Acad. Sci. Fennicae*, **A55**, No. 8, 1 (1940).
- , *Suomalainen Tiedekat. Toimituksia A. 55* (1940).
- Olsen, A. L., and E. R. Washburn, *J. Phys. Chem.*, **41**, 457 (1937).
- Rowlinson, J. S., *Trans. Faraday Soc.*, **45**, 974 (1949).
- Scatchard, George, S. E. Wood, and J. H. Moche, *J. Am. Chem. Soc.*, **68**, 1957 (1946).
- Scatchard, George, L. B. Ticknor, J. R. Goates, and E. R. McCartney, *ibid.*, **74**, 3721 (1952).
- Scatchard, George, and L. B. Ticknor, *ibid.*, p. 3724.
- Schmidt, G. C., *Z. physik. Chem.*, **121**, 221 (1925).
- Smyth, C. P., and E. W. Engel, *J. Am. Chem. Soc.*, **51**, 2260 (1929).
- Tsao, C. C., and J. M. Smith, *Chem. Eng. Progr. Symposium Ser. 7*, **49**, 107 (1953).
- Washburn, E. R., and A. Lightbody, *J. Phys. Chem.*, **34**, 2701 (1930).
- Wehe, A. H., *A.I.Ch.E. Journal*, **1**, 24 (1955).
- , *ibid.*; refers to private communication from T. H. Arnold.
- Williams, G. C., S. Rosenberg, and H. A. Rothenberg, *Ind. Eng. Chem.*, **40**, 1273 (1948).
- Wolfe, K. L., H. Behlke, and K. Wehage, *Z. physik. Chem.*, **B28**, 1 (1935).
- Wood, S. E., *Ind. Eng. Chem.*, **42**, 660 (1950).

Manuscript received June 23, 1958; revision received October 31, 1958; paper accepted November 26, 1958. Paper presented at A.I.Ch.E. Salt Lake City meeting.

\*See footnote p. 249.

# Heat Transfer and Fluid Dynamics in Mercury-Water Spray Columns

R. D. PIERCE, O. E. DWYER, and J. J. MARTIN

University of Michigan, Ann Arbor, Michigan

Heat transfer and fluid dynamics were studied in columns in which hot mercury was sprayed into a rising stream of water. Volumetric and area heat transfer coefficients are presented which were found to be lower than those reported for heat transfer from fixed spheres.

It was observed that considerable water bypassed the stream of drops, while some surrounding the drops flowed downward. This behavior resulted in water temperatures at the base of the column which were considerably higher than the inlet water temperatures. Consequently the outlet mercury temperature did not approach the inlet water temperature as a limit. The very unconventional flow pattern of the water was unexpected and is believed to be an important factor in spray-column heat transfer and mass transfer kinetics.

Direct heat exchange between two immiscible liquids, in the absence of a separating wall, has the apparent advantage of rapid heat exchange and the possibilities of high-power densities and simple heat-exchanger design. If these should prove real, this kind of heat exchange would be attractive for liquid-fueled nuclear reactors. It was from this stand-

study was to investigate the promise of direct liquid-liquid heat transfer for application to the LMFR.

This initial experimental work was simplified by the selection of mercury and water as representatives for bismuth and salt and by the employment of simple spray-column contactors. Heat transfer and fluid dynamics data obtained

of course the physical properties of the organic phases were far different from those of liquid metals. A more nearly similar experiment involves the transfer of heat between metal spheres and fluids. Kramers(5) studied the transfer of heat from isolated steel spheres to flowing air, water, and oils. His data were correlated by the equation

$$N_{Nu} = 2.0 + 1.3(N_{Pr})^{0.15} + 0.66(N_{Pr})^{0.31}(N_{Re})^{0.80}$$

Williams (9) made an extensive study of the existing data for heat and mass transfer from single, stationary spheres and recommended the equation

$$N_{Nu} = 0.37(N_{Re})^{0.6}(N_{Pr})^{0.33}$$

for heat transfer over a range of Reynolds

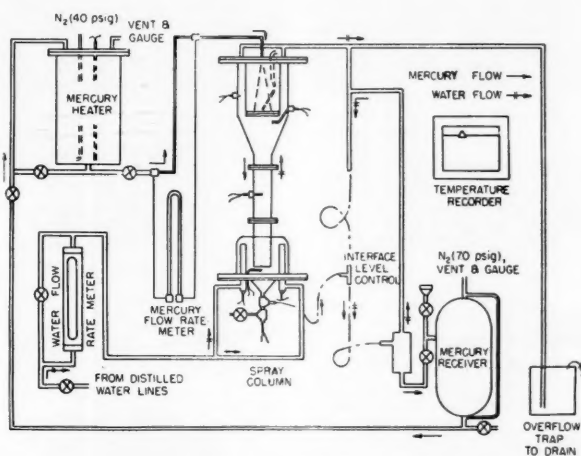


Fig. 1. Flow diagram.

point that the experimental work described in this article was undertaken.

It was suggested by workers at the Brookhaven National Laboratory some years ago that the liquid-metal-fuel reactor under development there might be cooled by the contacting of the molten uranium-bismuth fuel with a fused salt mixture. The purpose of this present

under such conditions can be used to indicate the potentialities of direct heat exchange in more complex equipment.

Heated mercury droplets were sprayed into the top of the columns, and water was introduced at the bottom. Columns of two different lengths and two different diameters and with several different spray nozzles were used.

Some heat transfer studies on spray columns dispersing organic solvents and water have been reported (1, 3, 8), but

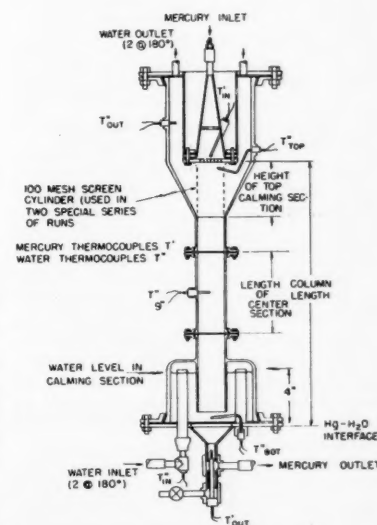


Fig. 2. Spray column.

R. D. Pierce is at Argonne National Laboratory, Lemont, Illinois, and O. E. Dwyer at Brookhaven National Laboratory, Upton, New York.

numbers between  $2 \times 10^2$  and  $2 \times 10^5$ . Ranz (7) correlated a collection of data for both heat and mass transfer from single spheres over the Reynolds number range 1 to  $10^5$ . He found that the heat transfer results under these conditions could be represented by

$$N_{Nu} = 2.0 + 0.60(N_{Pr})^{1/3}(N_{Re})^{1/2}$$

#### EXPERIMENTAL EQUIPMENT

Figure 1 is a flow sheet of the experimental equipment. Distilled water flowed upward through the column, while pre-heated mercury was sprayed from the top of the column and drained continuously from the bottom. In a single run 500 lb. of mercury could be passed through the column.

The columns used in this study, which are similar in design to the column used by Blanding and Elgin (2), are detailed in Figure 2. Six different columns were used, but the same steel end assemblies were used with each. The columns were fabricated from 1- and 2-in. I.D. Pyrex pipe. The enlarged ends of the columns were 6 in. I.D. to accommodate the end assemblies. The chief dimensions of the various columns are listed in Table 1.

Mercury, flowing at constant head from a pressurized header, entered the columns through a spray nozzle. The designs of the twelve fluorothene face plates which were used on this nozzle are listed in Table 2. The entire nozzle assembly was enclosed in a 4-in. cylinder which thermally isolated the nozzle from the water. The volume between the conical section and the cylinder was filled with asbestos insulation.

Mercury was collected at the bottom of the column in a conical pot, near the top of which the mercury-water interface was maintained. The pot and the fittings below it were also insulated.

Water entered the bottom calming section of the column through two vertical  $\frac{1}{2}$ -in. pipes on opposite sides of the column. The water level in this section was maintained at the ends of these pipes. Water from the calming section flowed under a weir and then upward through the column, around the mercury nozzle, and out through two  $\frac{1}{2}$ -in. pipes located on opposite sides of the annulus. In a few runs a cylinder made of 100-mesh stainless steel screening was placed at the top of the column as shown by the dotted lines in Figure 2.

#### MEASUREMENTS

##### Temperatures

Temperatures were measured with 30-gauge copper-constantan thermocouples. The probes for these thermocouples were pieces of  $\frac{1}{8}$ -in. O.D. stainless steel tubing, sealed at their inner ends. The thermocouple junctions, which extended about  $\frac{1}{8}$  in. beyond the insulation, were mounted in the tips of the probes with about  $\frac{1}{8}$  in. of soft solder.

The thermocouples were checked against a standard thermometer before being placed in the equipment; however several were also calibrated in place, since they were in electrical contact with the equip-

ment. All thermocouples were connected to a 16-point Brown Electronik Recorder with a range of  $60^\circ$  to  $220^\circ\text{F}$ .

Figure 2 shows the locations of the thermocouples in the column. Mercury thermocouples were located inside the nozzle and below the collecting pot. Inlet water temperatures were measured in both inlet pipes, the thermocouple that measured the temperature of the water at the bottom of the column being located  $\frac{1}{2}$  in. above the mercury interface and midway between the center line and the wall of the column. The water temperature at the top of the column was measured with a thermocouple located outside the stream of mercury drops and 1 in. below the mercury nozzle, with another thermocouple approximately 2 in. above the face of the mercury nozzle. Water temperatures were also measured in

the middle of the center sections, when they were used. The three thermocouples which entered the column through the glass walls extended through rubber stoppers; the others entered the column through packing glands or drilled pipe plugs.

A differential-thermocouple pair was used to measure the difference in temperature between the mercury and water at the bottom of the column. A Rubicon high-precision potentiometer was used with this pair. When the flow of mercury was suddenly stopped, the differential couples indicated that the temperature difference could be determined from the Brown recorder readings with an uncertainty of only  $0.1^\circ\text{F}$ . However under normal operating conditions the water-temperature variations were such that satisfactory readings could not be obtained with the differential thermo-

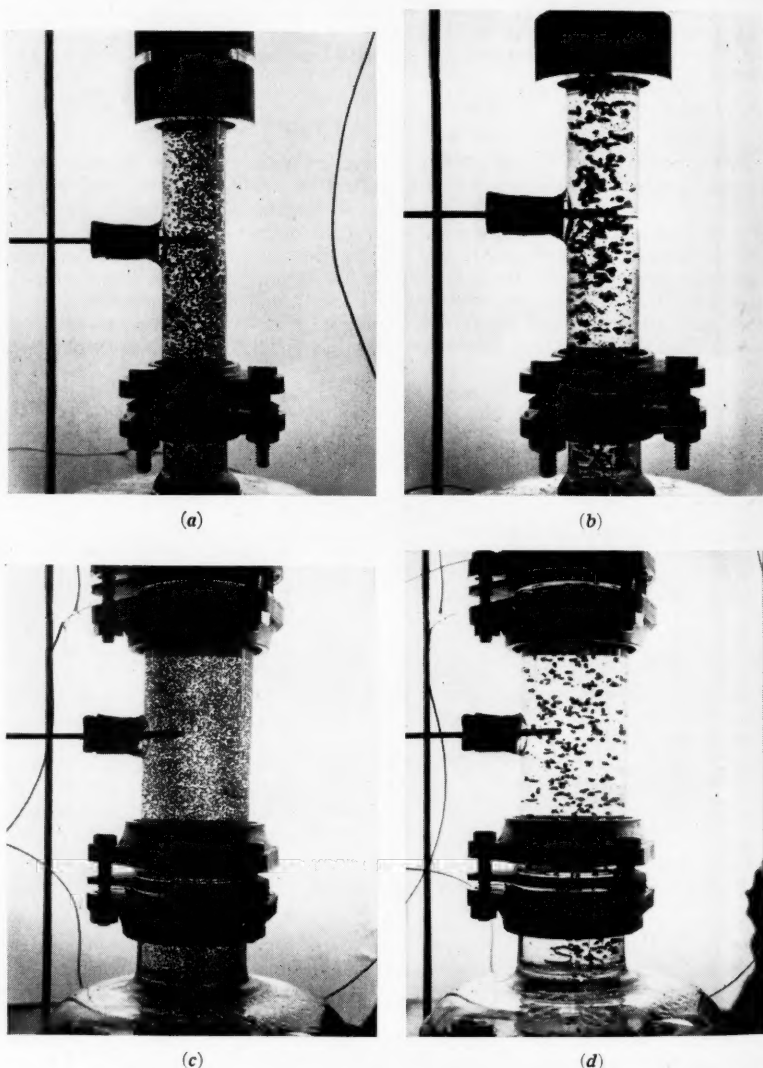
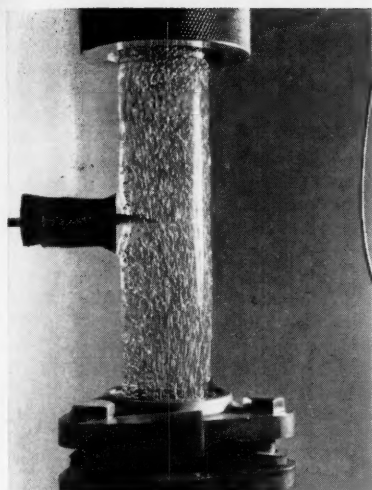
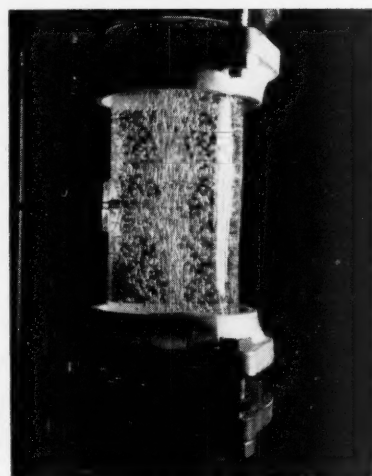


Fig. 3. Photographs of center section of column showing relative drop sizes for different nozzle designs: (a) average drop size 0.042 in., column 1 in. in diameter by 19.4 in. long, nozzle 21 holes by 0.031 in. in diameter; (b) average drop size 0.115 in., column 1 in. in diameter by 19.4 in. long, nozzle 5 holes by 0.089 in. in diameter; (c) average drop size 0.027 in., column 2 in. in diameter by 19.4 in. long, nozzle 29 holes by 0.032 in. in diameter; (d) average drop size 0.10 in., column 2 in. in diameter by 19.4 in. long, nozzle 9 holes by 0.070 in. in diameter.





(a)



(b)

Fig. 4. Photographs of center section of column showing streaks due to velocity effect: (a) average drop size 0.042 in., column 1 in. in diameter by 19.4 in. long nozzle 21 holes by 0.031 in. in diameter; (b) average drop size 0.027 in., column 2 in. in diameter by 19.4 in. long, nozzle 29 holes by 0.032 in. in diameter.

couples and the manually operated potentiometer. Since the 16-point recorder could also be used to indicate continuously, but not record, any one of the points, the water temperature was often determined from periodic observations of the indicated temperature. Each day before the equipment was operated, the readings of the two thermocouples at the bottom of the column were checked to see that they were the same.

#### Water Flow Rate

The water flow rate was measured with a Fischer and Porter Flowrator, having a range of 0.06 to 0.6 gal./min. The Flowrator calibration was checked periodically and found to be accurate to within 1%. The water flow rate did not fluctuate more than 0.01 gal./min. at a flow rate of 0.6 gal./min.

#### Mercury Flow Rate

Mercury flow rates were indicated by an orifice flowmeter which was used to set and maintain a steady flow; however the time-volume relationship for the mercury collected in the receiver was used to determine the actual flow rate. Over the range used, the volume of the receiver was known to within 1%. Because of movement of mercury in the tank, temperature variations in the mercury, and uncertainties in reading the level indicator, the flow rates were estimated to be uncertain by approximately 2%.

#### Drop Sizes

Figures 3a through 3d are prints of a few of the photographs which were used to determine drop size. Mercury drops were photographed at a minimum of four mercury rates in each column and with each nozzle. These pictures were not taken during actual heat transfer runs but were made under similar temperature conditions.

Owing to distortion by the curved walls of the columns only vertical dimensions of the drop images were measured. The measurements were made on images which had been projected to about thirty times actual size. Between thirty and ninety measurements were made from each picture, depending on the total number of drops and the variation in their sizes. Under some conditions a number of very small drops were observed in the columns. These drops, which usually represented less than 1% of the mercury in the column and which appeared to remain fluidized, were not measured.

The maximum variation of apparent drop size with distance from the camera was 5% with the 2-in. columns and 3% with the 1-in. columns. This effect tends to be self-compensating when average dimensions are determined. Drop-size measurements were limited by the sharpness of the images. This caused an uncertainty of about 10% for the smallest drops and about 5% for the larger ones. The drop sizes produced by the five- and the one-hole nozzles are uncertain because of the irregular shapes of the larger drops.

#### Drop Velocities

Drop velocities also were obtained from photographs. The pictures were taken at an exposure time of  $0.0033 \pm 0.0001$  sec. The drop images were elongated as a result of their motion. A small light reflection or high light was produced on one side of each drop, and the vertical length of these high lights was measured to determine drop velocities. Sample pictures are shown in Figure 4.

The velocity pictures were taken during special runs which duplicated the temperature conditions encountered during the heat transfer runs. These pictures were taken in the 19  $\frac{3}{8}$ -in. columns only, but the results are assumed to apply equally well to the shorter columns. A minimum of four mercury rates were photographed with each nozzle. Between 100 and 250 measurements were made from each picture depending on the number of drops in the column. These measurements were taken from images projected to about thirty times actual size. The shutter speed was checked after every

TABLE 1. SPRAY-COLUMN DIMENSIONS

Diameter, in.	Length, in.	Length of center section, in.	Height of top calming section, in.
1	13 $\frac{1}{4}$	omitted	3 $\frac{3}{4}$
1 (Special)	13 $\frac{1}{4}$	omitted	3 $\frac{3}{4}$ (with 1 in. diam. 100 mesh screen cylinder)
1	19 $\frac{3}{8}$	6	3 $\frac{3}{4}$
2	13 $\frac{1}{4}$	omitted	2 $\frac{3}{4}$
2	19 $\frac{3}{8}$	6	2 $\frac{3}{4}$
2 (Special)	19 $\frac{3}{8}$	omitted	6

TABLE 2. MERCURY-NOZZLE DETAILS (FLUOROTHENE PLATES,  $\frac{1}{4}$  IN. THICK AND 4 IN. DIAM.)

Number of holes	Diameter of holes, in.	Layout of holes, in.
With 1-in.-diameter columns		
73	0.0225	3/32 sq. pitch
21	0.031	3/16 sq. pitch
21	0.042	3/16 sq. pitch
16	0.046	3/16 sq. pitch
12	0.055	$\frac{1}{4}$ sq. pitch
9	0.063	$\frac{1}{4}$ sq. pitch
5	0.089	5/16 sq. pitch
1	0.189	centered
With 2-in.-diameter columns		
113	0.016	5/32 sq. pitch
29	0.032	$\frac{1}{4}$ sq. pitch
64	0.046	3/16 sq. pitch
9	0.070	$\frac{1}{2}$ sq. pitch

series with the aid of a photoelectric cell and a cathode-ray oscilloscope.

The lengths of the high lights could not be measured more accurately than by about  $\pm 7\%$ , because the edges of the images were not sharp. Variations in the distance between the camera and the drops made the magnification factors uncertain by as much as 5% for isolated drops, but this effect could be considered to cancel itself when average velocities were determined.

#### Water-Phase Movement

To study movements of the water phase during the operation of the columns, the authors injected dye in the water at one of four different locations: in the inlet water ahead of the column, in the outlet water at the position normally occupied by the outlet water thermocouple, in the top calming section, and in the middle of the column. A Fastex motion picture camera was used to record some of the observations. Most of the motion pictures were taken at a film speed of 1,500 frames/sec.

#### EXPERIMENTAL RESULTS

##### Heat Transfer Data

Typical temperature data are shown on Figure 5, the complete experimental data being presented in reference 6.

Temperatures were recorded after

steady state conditions had been attained. The temperature profiles indicated on Figure 5 are qualitative, because the mercury temperature was determined only at inlet and outlet conditions and the water temperature only at the column ends except in the longer columns. The marked discontinuity in the temperature of the water entering the column was noted in all the runs.

#### Heat Transfer Calculations

Logarithmic-mean volumetric heat transfer coefficients were calculated by

$$Ua = \frac{q_{Hg}}{V \Delta T_{LM}} \quad (1)$$

where

$$\Delta T_{LM} = \frac{(T_{Hg})_{IN} - (T_{H_2O})_{TOP} - (T_{Hg})_{OUT} + (T_{H_2O})_{BOT}}{\ln \frac{(T_{Hg})_{IN} - (T_{H_2O})_{TOP}}{(T_{Hg})_{OUT} - (T_{H_2O})_{BOT}}}$$

Drop-velocity and drop-size data were used to determine mercury holdup,  $H$ , and area factors,  $a$ . The volumetric holdup is defined by

$$H = \frac{R}{\rho_{Hg} \bar{v}_H} \quad (2)$$

The following expression was used simultaneously with Equation (2) to determine  $\bar{v}_H$  and  $H$ :

$$\bar{v}_H = \bar{v}_0 - \frac{W}{1 - H} \quad (3)$$

Equation (3) says that the relative velocity of the mercury droplets throughout the column is independent of the water flow rate. This is not necessarily true, but since the water-velocity term in Equation (3) was usually less than one tenth as large as  $\bar{v}_0$ , the effect on  $\bar{v}_H$  should be small.

Area factors were determined from mercury holdup by Equation (5)

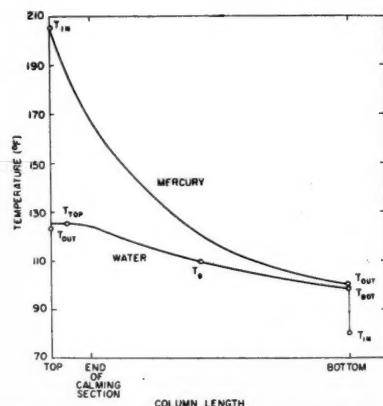


Fig. 5. Apparent temperature profiles in column.

$$a = \frac{\sum_{n=1}^{n=N} n\pi d^2}{V} \quad (4)$$

$$= \frac{H}{\left(\frac{\pi d^3}{6}\right)} \left(\frac{\pi d^2}{\pi d^2}\right) = \frac{6H}{(d^3)} \quad (5)$$

Heat transfer coefficients on an area basis were determined by the division of the volumetric coefficients by the factor  $a$ .

#### DISCUSSION OF RESULTS

##### Heat Transfer

Three quantities,  $q$ ,  $V$ , and  $\Delta T$ , were used in the calculation of the volumetric

heat transfer coefficients. The heat rate was calculated from the mercury data. This value could not be checked with the water data because of heat losses from the system. The water energy gain averaged about 7% lower than the energy loss for the mercury, but at the highest water temperatures the water heat values ran between 15 and 20% low. The greatest possibility of error in the values of  $q_{Hg}$  is that the mercury passing through the outside holes in the nozzles might have been cooler than the mercury at the center where the temperature was measured. Since the nozzle assembly was insulated and heat transfer data were taken at steady state, the errors in the heat term are probably small.

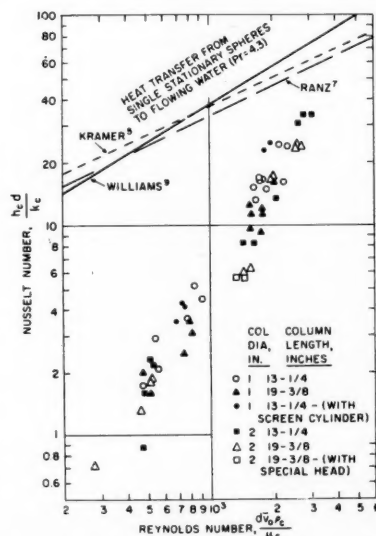


Fig. 6. Nusselt number vs. Reynolds number.

The temperature potential  $\Delta T_{LM}$  is the most uncertain quantity. The temperature difference at the bottom of the column  $\Delta T_{BOT}$  was difficult to measure because fluctuations in  $(T_{H_2O})_{BOT}$  were large compared with  $\Delta T_{BOT}$ . The mean deviation in  $\Delta T_{BOT}$  for most runs was about 50%. Under some conditions the mean deviation was greater than 100%, but generally no coefficients were determined from these runs.

The use of logarithmic mean temperature difference is valid only when the integral  $\int (dq/\Delta T)$  is equal to  $q/\Delta T_{LM}$ . This quality exists when  $\Delta T$  is a linear function of  $q$ . In these experiments the mercury temperature is linear with the heat transferred. Since water temperatures are affected by recirculation and heat losses, their relationship to  $q$  is not necessarily linear, but they appear to be approximately linear with the heat transferred. If both the mercury and water temperatures are linear with  $q$ , the temperature difference is also linear with  $q$ .

The accuracy of the area heat transfer coefficients is also dependent upon the drop velocity and drop size as well as the heat transfer data. Examination of the photographs indicated that drop sizes and velocities for the same operating condition agreed to within 10%. Since the area factors are inversely proportional to velocity and drop diameter [Equations (2) and (5)], a given percentage error in either  $\bar{v}_H$  or  $d$  would result in the same percentage error in the heat transfer coefficient.

If the resistance to heat transfer is assumed to be principally in the water phase, the variables affecting the heat transfer coefficient can be treated by dimensional analysis. Equation (6) relates the variables which are assumed to affect the heat transfer coefficients

$$N_{Nu} = f\left(N_{Re}, N_{Pr}, \frac{D}{d}, \frac{L}{d}, H, \phi\right) \quad (6)$$

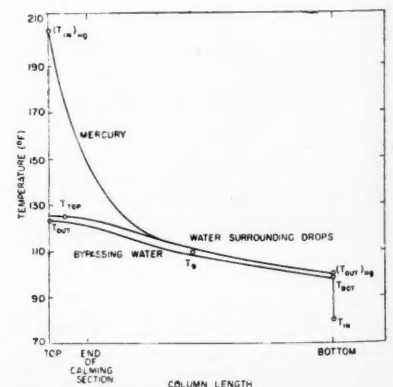


Fig. 7. Probable temperature profiles in column.

TABLE 3. SAMPLE RESULTS

Hg flow rate, lb. (min.)(sq. ft.)	H <sub>2</sub> O flow rate, gal. (min.)(sq. ft.)	$\bar{d}^2/\bar{d}^2$ , in.	$v_{01}$ , ft./sec.	$Pr$	$Re$	$\phi$ $\times 10^{-4}$	H, vol. %	$a$ , sq. ft./cu. ft.	$Ua \times 10^{-3}$ , B.t.u. (hr.)(cu. ft.)(°F.)	$U$ ( $= h_{H_2O}$ ), B.t.u. (hr.)(sq. ft.)(°F.)	$Nu$
Column: 1 in. diam. $\times$ 13- $\frac{1}{4}$ in. long Nozzle: 21 holes $\times$ 0.031 in. diam.											
2,000	54.8	0.045	1.65	4.4	830	43.1	2.51	38.5	19.3	502	5.2
3,500	36.6	0.043	1.6	3.7	950	49.5	4.43	71.8	31.5	439	4.3
3,500	54.8	0.043	1.6	3.9	900	44.6	4.54	73.7	33.8	459	4.5
3,500	73.2	0.043	1.6	4.0	880	42.4	4.67	75.7	35.6	470	4.6
3,500	91.4	0.043	1.6	4.3	810	36.7	4.80	77.8	35.6	458	4.5
3,500	109.8	0.043	1.6	4.7	750	32.4	4.93	80.0	40.3	504	6.9
5,000	54.8	0.040	1.55	3.8	770	35.8	7.08	121.4	48.3	399	3.6
(Special runs using 100 mesh screen cylinder in column)											
2,000	54.8	0.045	1.65	5.1	730	33.2	2.51	38.5	16.0	416	4.3
3,500	54.8	0.043	1.55	4.8	750	31.3	4.54	73.7	29.8	405	4.2
5,000	54.8	0.040	1.55	4.4	680	27.6	7.08	121.4	46.7	386	3.5
Column: 1 in. diam. $\times$ 13- $\frac{1}{4}$ in. long Nozzle: 9 holes $\times$ 0.063 in. diam.											
3,500	36.6	0.094	2.1	3.7	2230	507	3.43	25.8	30.1	1170	24.8
3,500	54.8	0.094	2.1	3.9	2110	455	3.50	26.3	30.0	1140	24.2
3,500	73.2	0.094	2.1	3.9	2110	455	3.57	26.8	31.2	1160	24.6
3,500	91.4	0.094	2.1	3.8	2170	480	3.65	27.4	31.4	1150	24.4
3,500	109.8	0.094	2.1	4.0	2060	433	3.73	28.0	32.1	1150	24.4
5,500	54.8	0.094	2.1	3.6	2330	550	5.50	41.3	47.2	1110	23.8
(Special runs using mesh screen cylinder in column)											
3,500	54.8	0.094	2.1	4.7	1800	333	3.50	26.3	28.2	1070	22.8
4,500	54.8	0.094	2.1	4.3	1930	486	4.50	33.8	39.0	1160	24.7
Columns: 1 in. diam. $\times$ 19- $\frac{3}{8}$ in. long Nozzle: 21 holes $\times$ 0.031 in. diam.											
2,000	54.8	0.045	1.65	4.7	780	37.9	2.51	38.5	13.5	347	3.6
3,500	54.8	0.043	1.6	4.4	810	36.5	4.54	73.7	23.3	316	3.1
5,000	54.8	0.040	1.55	4.1	740	32.4	7.09	121.4	33.4	275	2.5
Column: 2 in. diam. $\times$ 13- $\frac{1}{4}$ in. long Nozzle: 29 holes $\times$ 0.032 in. diam.											
900	18.4	0.048	2.6	4.4	1420	49.2	0.73	10.7	8.13	762	8.3
1,400	18.4	0.048	2.6	3.9	1600	62.4	1.14	16.7	12.65	760	8.3
Column: 2 in. diam. $\times$ 19- $\frac{3}{8}$ in. long Nozzle: 29 holes $\times$ 0.032 in. diam.											
900	18.4	0.048	2.6	4.4	1440	51.2	0.73	10.7	5.9	553	6.0
1,400	18.4	0.048	2.6	4.0	1560	58.7	1.14	16.7	9.8	587	6.4
Column: 2 in. diam. $\times$ 19- $\frac{3}{8}$ in. long (with special top head) Nozzle: 29 holes $\times$ 0.032 in. diam.											
900	18.4	0.048	2.6	4.8	1310	42.0	0.73	10.7	5.6	523	5.7
1,400	18.4	0.048	2.6	4.4	1440	50.0	1.14	10.7	8.7	521	5.7

Some values of the dimensionless groups in Equation (6) are listed in Table 3. The physical properties of water at a temperature midway between  $T_{TOP}$  and  $T_{BOT}$  were used to evaluate these groups. The mean slip velocity could not be measured but was assumed to be equal to the average drop velocity at zero water rate. The nature of the relationship between the dimensionless groups of Equation (6) could not be determined, however, because the drop diameter, which appears in nearly all the groups, was the only variable which could be independently controlled.

Reynolds and Nusselt numbers from all the columns and nozzles are plotted in Figure 6 along with the correlations of Kramers (4), Ranz (6), and Williams (8) for heat transfer from single stationary spheres. The Prandtl number for the three correlation lines in the figure was

4.3, while that for the data points varied from about 3.7 to 5.0. The data on this plot indicate that the heat transfer coefficients for the 19-in. columns are about 20% lower than those in the 13-in. columns. The effects of column diameter, height of top calming section, and mixing in the top section on these coefficients appear slight.

Heat transfer results at varying water rates (Table 3) indicate that both volumetric and area heat transfer coefficients increase only slightly with increased water rates.

#### Water-Phase Dynamics

For nearly every heat transfer run the temperature difference  $[(T_{H_2O})_{BOT} - (T_{H_2O})_{IN}]$  was much greater than the temperature difference  $[(T_{H_2O})_{OUT} - (T_{H_2O})_{BOT}]$ , which indicates that the heat transfer coefficients were a relatively

minor factor influencing the total heat transferred to the incoming water.

The unexpectedly high values of  $(T_{H_2O})_{BOT}$  were not due to the fact that

TABLE 4. MAXIMUM WATER VELOCITY IN THE CENTER SECTION OF THE 1-IN.-DIAMETER  $\times$  19- $\frac{3}{8}$ -IN.-LONG SPRAY COLUMN

Net Water Flow Rate: 0.12 cu. ft./(sq. ft.)(sec.) 54.8 gal./(min.)(sq. ft.)			
Drop size, in.	Mercury rate, lb./(sq. ft.)(min.)	Velocity, ft./sec.	
		Up	Down
0.042	2,600	1.6	0.2
0.042	4,600	2.5	0.3
0.042	5,700	2.0	1.6
0.092	2,600	1.8	0.4
0.092	4,600	2.0	0.6
0.092	5,700	2.0	2.0

the thermocouple measuring the temperature of the water at the bottom of the column was overheated by contact with the falling mercury. This was demonstrated by the variation of the location of the thermocouple.

The effects of column diameter and variation in height of top calming section on the heat transfer coefficients were negligible. The data taken in the 1-in. column with the 100-mesh screen cylinder below the mercury nozzle showed larger temperature discontinuities than data taken without the screen. Probably the increase in the temperature  $T_{BOT}$  was an indirect result of an increase in the water temperature under the mercury nozzle caused by the reduced circulation in this region. Since the thermocouple which measured  $T_{TOP}$  was located just outside the screen, the true top water temperature was probably slightly higher than that measured. The location of this thermocouple, outside the mercury stream, was shown to be satisfactory when the screen was not present but was not verified for the runs with the screen.

The sharp rise in water temperature at the water inlet was caused by the mixing produced by turbulence in and internal recirculation of the water phase. This was evident in both the motion pictures and in the drop velocity pictures. The principal upward flow of water bypassed the falling mercury drops. This rising stream of water continually shifted around the column but generally passed along one side opposite the flowing mercury. Thus two countercurrent streams of water flowed in the columns. Table 4 lists maximum upward and downward water velocities determined from six of the motion pictures. All the water in the columns was observed to undergo considerable recirculation during the flow of mercury. Even water near the inlet and outlet water pipes recirculated to and from the vicinity of the drops. The pictures of dye movements showed relatively little mixing between the rising and falling streams of water. Since horizontal mixing appears slight, an appreciable resistance to heat transfer might exist between water flowing concurrently with the mercury drops and that bypassing them. Three heat transfer observations indicated that this resistance might be important in the mercury-water columns:

1. Over-all heat transfer coefficients decreased with increased column length. This would result if the heat transfer resistance between the countercurrent water streams was relatively large, so that a large portion of the total heat transfer occurred at the ends of the columns where the contact was more complete.

2. Variation in volumetric heat transfer coefficients with drop size is less than would be expected as a result of the increased mercury surface area.

3. Temperature discontinuities which were observed in the 13- and 19-in. columns were almost identical. If heat transfer to the bypassing water were an important mechanism in these experiments, the mercury temperature profile presented on Figure 5 would not be correct, because the mercury temperature would drop more rapidly. The average water-temperature profile would be the same, because it was average water temperatures that were measured. Figure 7 may more nearly represent the true temperature profiles, which were obtained by assuming the double water profiles shown and estimating the mercury profile from the heat transfer data for fixed spheres.

## CONCLUSIONS

Extremely rapid heat transfer was experienced between the dispersed phases in the mercury-water columns. The major transfer resistance was within the bulk of the water phase. Heat transfer results did not vary appreciably with minor changes in column design nor between 1- and 2-in.-diam. columns, but the column efficiencies decreased markedly with increased column length.

This study has illustrated that flow patterns can greatly limit the efficiency of liquid-liquid spray columns. The columns were found to operate with a stream of water flowing with the falling mercury drops and with the principal upward flow of water bypassing the drops. This flow pattern produced a discontinuous rise in the temperature of the water entering the columns. The sharp change in water temperature prevented the outlet mercury temperatures from approaching the inlet water temperatures as a limit. Similar phenomena have been observed recently in organic-water, mass transfer systems (4), but the effect has been overlooked in most spray column studies.

## ACKNOWLEDGMENT

This paper is based on work supported by the U. S. Atomic Energy Commission and carried out by R. D. Pierce, the principal investigator, as a thesis for the Doctor of Philosophy degree from the University of Michigan, Ann Arbor, Michigan.

## NOTATION

$a$  = surface area of drops per unit column volume, sq. ft./cu. ft.  
 $c$  = specific heat, B.t.u./lb. (°F.)  
 $D$  = diameter of column, ft.  
 $d$  = diameter of drop or particle, ft.  
 $f$  = operator signifying function of, dimensionless  
 $g$  = acceleration due to force of gravity, ft./sec.<sup>2</sup>  
 $H$  = volumetric fraction holdup of

discontinuous phase, cu. ft./cu. ft.

$h$  = heat transfer coefficient, B.t.u./hr. (sq. ft./°F.)  
 $k$  = thermal conductivity, B.t.u./hr. sq. ft. (°F./ft.)  
 $L$  = column length, ft.  
 $N$  = number of drops entering column per unit time, sec.<sup>-1</sup>  
 $N_{Nu}$  = Nusselt number,  $h_c d / k_c$ , dimensionless  
 $n$  = number of particular drop in column or number of drops in the column, dimensionless  
 $N_{Pr}$  = Prandtl number,  $(c_p \mu / k)_c$ , dimensionless  
 $q$  = rate of heat transfer, B.t.u./hr.  
 $R$  = mass rate of flow mercury per unit area, lb./sq. ft. (sec.)  
 $N_{Re}$  = Reynolds number,  $d v \rho_c / \mu_c$ , dimensionless  
 $S$  = inside sectional area of empty column, sq. ft.  
 $T$  = Temperature, °F.  
 $U$  = overall heat transfer coefficient, B.t.u./hr. (sq. ft./°F.)  
 $V$  = effective column volume, cu. ft.  
 $v$  = velocity, ft./sec.  
 $W$  = volume rate of flow of water per unit area, cu. ft./sq. ft. (sec.)  
 $\mu$  = coefficient of viscosity, lb./ft. (sec.)  
 $\rho$  = density, lb./cu. ft.  
 $\phi$  =  $d^3 g \rho_c (\rho_d - \rho_c) / \mu_c^2$ , dimensionless  
 Bar over a symbol = arithmetic average value

## Subscripts

$BOT$  = bottom of column  
 $c$  = continuous phase  
 $d$  = dispersed phase  
 $H$  = holdup  
 $LM$  = logarithmic mean value  
 $n$  = particular drop  
 $o$  = zero water flow rate  
 $s$  = slip or contact velocity  
 $T$  = total

## LITERATURE CITED

1. Allen, H. D., W. A. Kline, E. A. Lawrence, C. J. Arrowsmith, and C. Marsel *Chem. Eng. Progr.*, **43**, 459 (1947).
2. Blanding, F. H., and J. C. Elgin, *Trans. Amer. Inst. Chem. Eng.*, **38**, 305 (1942).
3. Garwin, Leo, and B. D. Smith, *Chem. Eng. Progr.*, **49**, 591 (1953).
4. Geankoplis, C. J., P. L. Wells, and E. L. Hawk, *Ind. Eng. Chem.*, **43**, 1848 (1951).
5. Kramers, H., *Physica*, **12**, 2-3 61 (1946).
6. Pierce, R. D., Ph.D. thesis, Univ. of Mich., Ann Arbor (1954).
7. Ranz, W. E., *Chem. Eng. Progr.*, **48**, 247 (1942).
8. Rosenthal, Howard, master's thesis, New York Univ., New York (1949).
9. Williams, G. G., Ph.D. thesis, Mass. Inst. of Tech., Cambridge (1942).

Presented at A.I.Ch.E. Detroit Meeting, Manuscript received October, 1953; revision received October 17, 1958; paper accepted October 18, 1958.



# Flow Characteristics in Horizontal Fluidized Solids Transport

CHIN-YUNG WEN and H. P. SIMONS

West Virginia University, Morgantown, West Virginia

The flow characteristics of dense solid-gas mixtures transported through horizontal pipes were studied with glass beads and coal powders of various sizes (0.0028 to 0.0297 in.) in 1/2-, 3/4- and 1-in. glass pipes and a 1/4-in. steel pipe. Fluidized-bed feeders were utilized, thus permitting solid-gas ratios considerably higher (range 80 to 750) than those possible with conventional pneumatic transport. When such high solid-gas ratios are used, the flow of mixtures in transport lines is characterized by a large amount of slippage between gas and solids. The flow pattern is discussed on the basis of visual observation through glass pipes.

A simple and interesting velocity relationship was noted, namely that the average gas velocity is about twice as large as the average solid-particle velocity. The solid-particle velocities and solid loadings in the pipe line were found to be primary factors affecting pressure drops, and the particle sizes and shapes, on the other hand, exerted a very slight effect on the pressure drops. This is apparently due to the fact that the solids move predominantly in the bottom of the pipes as agglomerated masses rather than as individually suspended particles. A pressure-drop correlation for the dense solid-gas mixtures is proposed, and applications and limitations of the correlation are shown.

Although pneumatic conveying of granular solids has been practiced for many years, the use of fluidized-bed feeders is a relatively recent development. Characterized by high solid-gas ratio mixtures at comparatively high pipe-line capacities (1, 2, 11), this use permits an operation at much lower cost than conventional pneumatic conveying (11). The technique has found many interesting applications, and like many other chemical engineering developments it is in extensive use even though its exact nature—in this case the nature of the flow—is not completely understood. Recent studies have recognized the importance of particle velocity, density, and rheological behavior of solid-gas systems; however the difficulty of accurately measuring these quantities has precluded the establishment of a clear picture of the mutual relations in solid-gas flow phenomena. It is the purpose of the present investigation to study the flow patterns of dense solid-gas systems, particularly the interrelationship of solid and gas velocities, solid-gas ratio, and pressure drop in horizontal transport lines.

In earlier works the study of solid-gas flow was limited to the pneumatic conveying of a few specific materials of relatively large particle size. Gästerstadt (7) found that the specific pressure drop was related to the solid-gas ratio, and Cramp and Priestley (6) developed an empirical relationship for determining the pressure drop for pneumatic conveying in the vertical duct. Wood and Bailey (16) reported that at high solid-gas ratios the system became non-homogeneous, with greatly differing flow characteristics from the lean solid-gas flow. The pressure-drop data for both horizontal and vertical pneumatic transport lines were correlated by Vogt and White (15) by dimensionless groups. Belden and Kassel (3) expressed total pressure drop as the sum of the static and friction

terms which had previously been combined into one term by Vogt and White. Their findings indicate that the pressure drop is nearly independent of tube-diameter-particle-diameter ratio. Hariu and Molstad (8) were able to report average particle velocity, slip velocity, and solids static pressure by means of a dispersed-solids-density calculation. Particle velocities have been studied in lean phase flow by Khudyakov and Chukhanov (10), Uspenskii (14), Clark, *et al.* (5), Mehta (12), and Hinkle (9). However most of these studies are not directly applicable to dense-phase transport. Since the particles in dense solid-gas systems tend to precipitate and move along the bottom of the pipes, it is apparent that the flow pattern must be greatly different from pneumatic transport, in which most of the particles are carried in suspension. Using fluidized-bed feeders, Albright, *et al.* (1, 2), measured pressure drops for powdered-coal systems at comparatively high solid loadings. Koble, *et al.* (11), and Carney (4) reported pressure-drop data for dense-phase solids transport as well. Their correlations were however tentative, and no generalization for prediction of the pressure-drop or solid-delivery rate resulted.

## EXPERIMENTAL

Figure 1 is a diagram of the experimental unit. Solids charged to the hopper could be added continuously to the fluidizer by means of valve 3. When a suitable quantity of solids had been charged into the column (until a bed height of approximately 2.5 ft. was attained), air was introduced through the conical adaptor to the bottom of the fluidizer column, and the solid particles were fluidized. The plug valves (4) were opened, and the solid particles allowed to flow through the pipe. With steady state conditions attained, the solids were collected in the receiver (2) and the time was noted for collection. The carrier air, separated from the solids at the receiver (2), was measured by a dry test meter. The pressure drop for transport across the pipe section

was recorded by the Foxboro type of differential pressure recorder. At the end of the run the two plug valves (4), one at the entrance and the other at the exit end of the pipe, were closed simultaneously, the solids holdup in the pipe being discharged by the blowing of air through the test section, and the collected solids were weighed. The fluidized-solids level in the fluidizer was maintained as constant as possible during the operation by the continuous addition of solids from the hopper. Preliminary tests indicated that the solids flow rate remained constant within the limits of experimental error throughout the entire period of the run. The solids flow rate as well as solid-gas ratio were varied by changing the pressure in the fluidizer and the fluidizing air rate. Since the pressure drops in such dense solids-gas flow fluctuated, in some cases considerably, the integrated average pressure drops were evaluated by a planimeter and the charts from the differential-pressure recorder for the entire period of the run. Flow data\* were collected for a total of approximately 200 runs with glass beads of 0.011-, 0.0058- and 0.0028-in. diameter and coal powder of 0.0297-, 0.0197-, and 0.0044-in. diameter, flowing through 0.5-, 0.75-, and 1.0-in. I.D. glass pipes and 0.364-in. I.D. steel pipe. The glass beads were essentially spherical. The average diameter of the coal particles was determined by screen analysis; the solid particles were periodically inspected under the microscope, and no appreciable attrition was observed. The densities of the glass beads and coal powders were 156 and 81 lb./cu. ft. respectively.

## MODE OF FLOW

Visual observation of the behavior of solids motion in a glass pipe indicated that there may be four modes of flow by which the solid particles travel. Since the solid particles are quite uniformly dispersed throughout the fluidized bed before they are introduced into the pipe, the particles in the early section of the transport line, immediately adjacent to the fluidizer, appear to be evenly distributed (Figure 2a). The particles are accelerated to their terminal velocities in this section and thereafter will tend to settle in the bottom portion of the pipe, forming dunes as shown in Figure 2b. Because of particle settling, solids holdup in this section of the pipe will be larger

\*Tabular material has been deposited as document 5913 with the American Documentation Institute, Photoduplication Service, Library of Congress, Washington 25, D. C., and may be obtained for \$2.50 for photoprints or \$1.75 for 35-mm. microfilm.

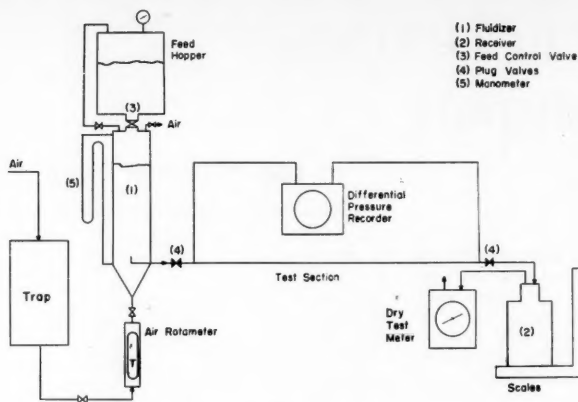


Fig. 1. Schematic diagram of equipment.

than in the early section, and consequently the average particle velocity in such moving dunes is less than when the particles are in true suspension. Solids flow takes place by way of moving from one dune to the next, undergoing deceleration and acceleration alternatively. The distance between the dunes, which depends on the solids flow rate as well as gas flow rate, varies from several inches to several feet. In high velocity flow the dunes either do not form or appear only at the exit end of the pipe. For most runs made in 1-in. glass pipe, the length of the pipe through which no precipitation of the particles occurred was approximately 3 ft. In low-velocity flow the dunes are formed more readily, and length and height of the dunes are correspondingly larger. As the solid loadings increase, the dunes grow, sometimes almost to the same height of the pipe diameter, and small ripples will appear traveling along the top of the thick solid layer, the greater portion of which is practically stationary. This is shown in Figure 2d. Further increase of solid loadings will eventually result in complete blockage of the transport line.

Sometimes, depending on the nature of solids and solid-gas ratio, intermittent flow of gas and solids in alternate slugs will occur, rather than dune formation (Figure 2c). The pressure drops over the transport line are then unstable, a condition which is reflected in considerable fluctuation on the manometer.

#### AVERAGE SOLID AND GAS VELOCITY

Under such irregularities in flow, particle velocities must be expected to vary considerably across the pipe cross section. Moreover the velocities also change from one point to the next along the pipe, even after the particles have left the supposed acceleration region. Consequently it is only logical to express the particle velocity as the average velocity of all the particles for the entire length



Fig. 2a. High velocity flow or near inlet section.

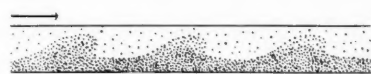


Fig. 2b. Segregation of particles and dunes formation.



Fig. 2c. Intermittent flow of gas and solids in alternate slugs.



Fig. 2d. Low velocity flow; solid ripples travel along the top of stationary solid layer.

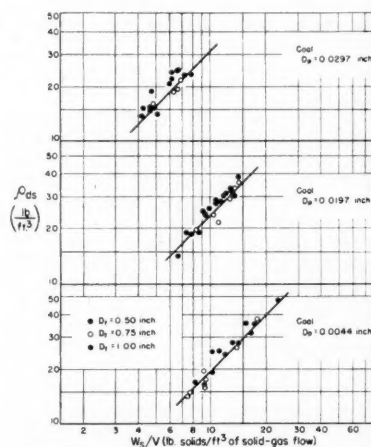


Fig. 3. Dispersed solid density and apparent over-all solid-gas mixture density.

of transport line under consideration. From the equation of continuity

$$G_s = \rho_{ds} U_s \quad (1)$$

where the dispersed solid density may be calculated from the experimental measurement of the solid holdup in the transport lines. If  $W_s$  is the weight of solids retained in the pipe line of length  $L$ , then  $\rho_{ds} = W_s/(\pi D_i^2/4)L$ . If the solid mass velocity, is known, the average particle velocity can be evaluated from Equation (1).

The relationships between the dispersed solid density and the apparent over-all solid-gas mixture density for coal particles and glass beads are shown in Figures 3 and 4. The apparent over-all solid-gas mixture density was obtained by dividing the weight of solid collected by the total volume of solid-gas flow. Figures 3 and 4 indicate considerable slippage between gas and solid in the dense solid-gas flow. Had there been very little or no slippage between the gas and the solids,  $\rho_{ds}$  would be nearly equal to  $W_s/V$ . For coal particles as well as glass beads

$$\rho_{ds} = k(W_s/V) \quad (2)$$

where  $k$ , varies between two and three, corresponding to particle diameters of 0.0044 to 0.0297 in. an indication that  $\rho_{ds}$  depends only slightly on particle diameter. The effect of solids mass velocity on particle velocity is shown in Figures 5 and 6. By means of a cross plot at a constant particle velocity the solids mass velocity can be shown to vary with the minus 0.7 power of the pipe diameter. Based on this relation, an empirical correlation between particle velocity and solid particle densities is presented in Figure 7. While it has been demonstrated that the particle velocity depends on solid mass velocity, pipe diameter of transport line, and the solid particle density, no consistent effect of solid-gas ratio has been found. Since the correlation is not dimensionless, it must be borne in mind that not all the effects of either solid or fluid upon particle velocity have been considered; however the correlation presented in Figure 7 serves to predict the approximate particle velocity of which direct measurement is not practicable.

The average linear gas velocity in transport line can be found similarly from the continuity equation for the gas,

$$G_a = \rho_{da} U_a \quad (3)$$

The dispersed gas density  $\rho_{da}$  is obtained from  $\rho_{da} = W_a/(\pi D_i^2/4)L = (1 - \rho_{ds}/\rho_s) \rho_a$ . Previous workers evaluated the gas velocity based on the empty pipe, but this is an approximation which holds only where the volume occupied by the solid in the lines is negligible. In the dense solid-gas flow system the solids occupy a large portion of the total flow space; the linear gas velocity therefore is

ration.

(1)

may be  
meas-  
trans-  
solids  
with  $L$ ,  
solid  
average  
from

persed  
ver-all  
articles  
ures 3  
l-gas-  
viding  
e total  
and 4  
between  
s flow.  
ppage  
would  
coal

(2)

three.  
ers of  
a that  
particle  
mass  
own in  
ss plot  
solids  
y with  
meter.  
corred  
solid  
figure 7.  
at the  
mass  
rt line,  
o con-  
s been  
s not  
mind  
solid or  
been  
en pre-  
ct the  
which  
able.  
ity in  
imilarly  
ne gas,

(3)

obtained  
 $\rho_{ds}/\rho_g$   
he gas  
e, but  
holds  
by the  
in the  
solids  
al flow  
fore is

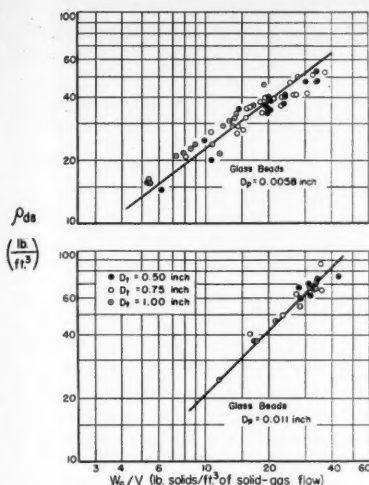


Fig. 4. Dispersed solid density and apparent over-all solid-gas mixture density.

much greater than the superficial gas velocity.

The extent of slippage between gas and solid is shown in Figure 8, in which the solid velocity is plotted against the gas velocity. An arithmetic average of entrance and exit gas velocity was used in the plot, owing to the expansion of the gas in the transport line. Figure 8 indicates the gas velocity to be approximately twice as large as the solid velocity independent of particle sizes. Thus

$$U_s \cong 2U_g \quad (4)$$

The data of Høiri and Molstad (8) in vertical transport, which resemble the dense solid-gas flow, are also included for comparison. It is interesting to note that

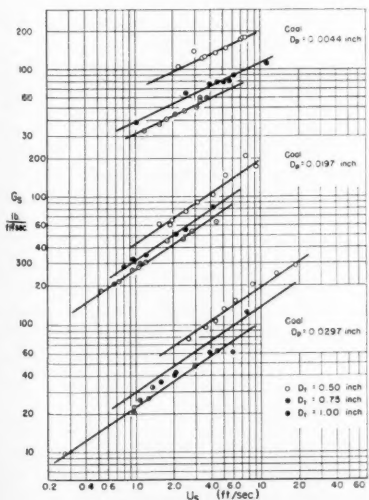


Fig. 5. Solids mass velocity and particle velocity

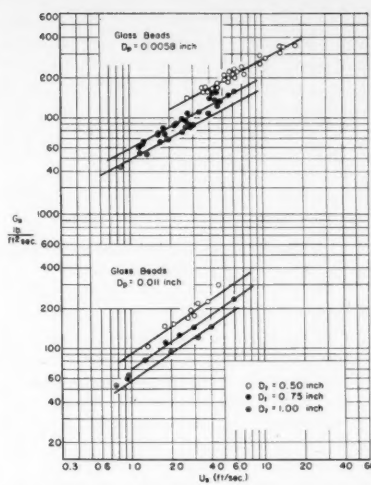


Fig. 6. Solids mass velocity and particle velocity.

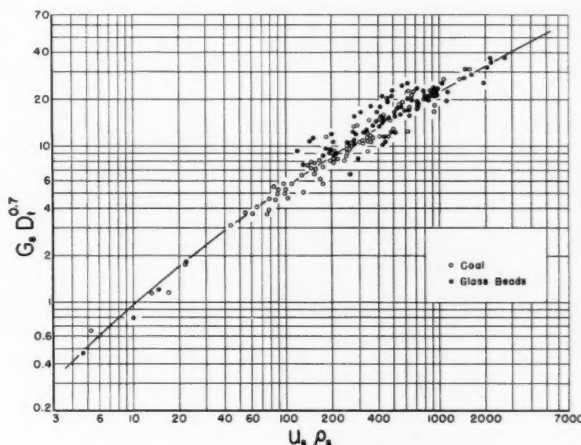


Fig. 7. Solids mass velocity and particle velocity.

such a simple relationship exists between velocity of gas and solid in seemingly a very complex system. Since it is difficult to obtain accurate velocity data, the trend indicated appears to be significant.

#### PRESSURE DROP

For horizontal transport the total pressure drop may be expressed as

$$\Delta P_t = \Delta P_{aa} + \Delta P_{as} + \Delta P_d + \Delta P_f \quad (5)$$

When the solid particles reach the terminal velocity

$$\Delta P_t = \Delta P_d + \Delta P_f \quad (6)$$

$\Delta P_d$  may be evaluated by the equation

$$\Delta P_d = G_s \Delta U/g \quad (7)$$

and is related to drag coefficient according to

$$\Delta P_d = \frac{C_d A_b \rho_s \Delta U^2}{2g(\pi D_t^2/4)} \quad (8)$$

Using the modification of the Fanning friction factor, one can express  $\Delta P_f$  by

$$\Delta P_f = \frac{2f U_s^2 \rho_{as} L}{g D_t} \quad (9)$$

Since no significant difference in pressure drop was observed between the first and second 10-ft. test sections of the pipe, the solid particles were considered to have left the initial acceleration region. The values of  $\Delta P_f$  and  $\Delta P_d$  are calculated. The results indicate that for a 10-ft. section  $\Delta P_d$  is in no case larger than 1.0% of the total pressure drop. If the transport line is long, therefore, the total pressure drop in dense solid-gas mixture can be estimated as equal to  $\Delta P_f$ , the friction of solid particles against particles themselves and against the gas.

The pressure drop is correlated empirically by two dimensionless groups to the particle velocity (Figure 9). The trend can be represented by

$$\left(\frac{\Delta P_t}{L \rho_{as}}\right) \left(\frac{D_t}{D_p}\right)^{1/4} = 2.5 U_s^{0.43} \quad (10)$$

The effect of particle diameter or shape on the pressure drop is again proved to be very small in comparison with the solid dispersed density or solid loadings as well as particle velocity in the transport line. As previously pointed out, this is due to the fact that the solid particles travel predominantly in the bottom of the pipes as agglomerated masses, and thus the effect of diameter and shape practically vanishes. The effect of pipe diameter is not apparent from the equation, since  $\rho_{as}$  is also the function of pipe diameter. Mitlin (13) also reported that the pressure drop is practically independent of particle size and is governed

chiefly by weight of material in the line.

Since air was the only fluid employed, the correlation is not dimensionless, and it should be noted that not all the effects on the pressure drop are taken into consideration in Equation (10). With Equation (4) used, the solid-gas-ratio data reported by Koble (11) and Carney (4) for the ratios above 80 were recalculated and are shown on the same plot (Figure 9) for comparison. Both investigators employed a 1/4-in. pipe. Their results seem to agree within experimental error with the proposed correlation.

The deviation between the values reported by previous investigators is due probably to the method of pressure-drop measurement in the transport line. While some measured the static pressure difference between the fluidizer and the receiver, others determined the pressure drops through taps directly attached to the line. In addition to the inaccuracies caused by the entrance and exit losses in the former method of pressure-drop measurement, both methods may possibly be inflicted with inconsistencies due to particle acceleration. Hinkle (9) re-

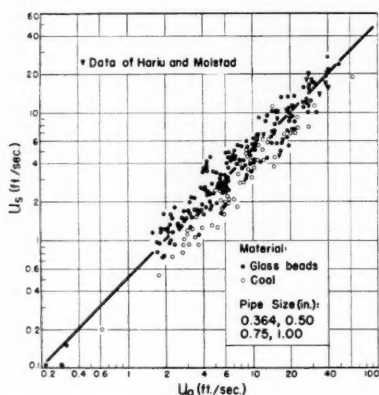


Fig. 8. Solid particle velocity vs. gas linear velocity.

ported that pressure drop due to particle acceleration was a significant fraction of the total pressure drop in the pneumatic conveying system. However in dense solid-gas flow of the type considered, the length of pipe necessary to reach terminal particle velocity, owing to the considerably large frictions exerted between the particles as well as with pipe walls, is probably much less than that expected in lean solid-gas flow, such as in pneumatic conveying. In fact, owing to the segregation of the solid particles in the bottom of the pipe at the downstream end of the transport line, the particles are subjected to repeated positive and negative acceleration, and therefore it is very difficult to determine over what length of pipe the particles are being accelerated or decelerated. Another source of error is the considerable static electricity generated

while the solid particles are passed through pipes. The dryness of the carrier gas seems to affect this considerably, and proper grounding is necessary to minimize static effects, especially when a very dry gas and solid particles having poor electrical conductivity are used.

#### APPLICATION

The following illustrates the application of the developed correlation.

##### Problem

Coal powder ( $D_p = 0.005$  in. and  $\rho_s = 81$  lb./cu. ft.) is to be transported from a fluidized bed to a gasification reactor through a horizontal pipe of 1-in. I.D. and 10-ft. length for manufacturing synthesis gas. For a solid flow rate of 785 lb./hr., estimate the amount of air required to transport the solid, the line pressure drop,

The solid-gas ratio is

$$R = G_s/G_a = 40/0.206 = 194 \text{ lb. solid/lb. air}$$

The pressure drop is evaluated from Equation (10):

$$\Delta P_t = 2.5 \times (1.85)^{0.45} \times 10 \times 21.6 \times (0.005)^{0.25} = 189 \text{ lb./sq. ft./10 ft.}$$

#### CONCLUSION

The flow characteristics of dense solid-gas mixtures, introduced from a fluidized bed feeder into horizontal transfer lines, differ considerably from flow of lean solid-gas suspensions. It was observed that the solid particles tend to segregate in the bottom sector of the conveying pipe and travel as agglomerated masses. Particle size and shape

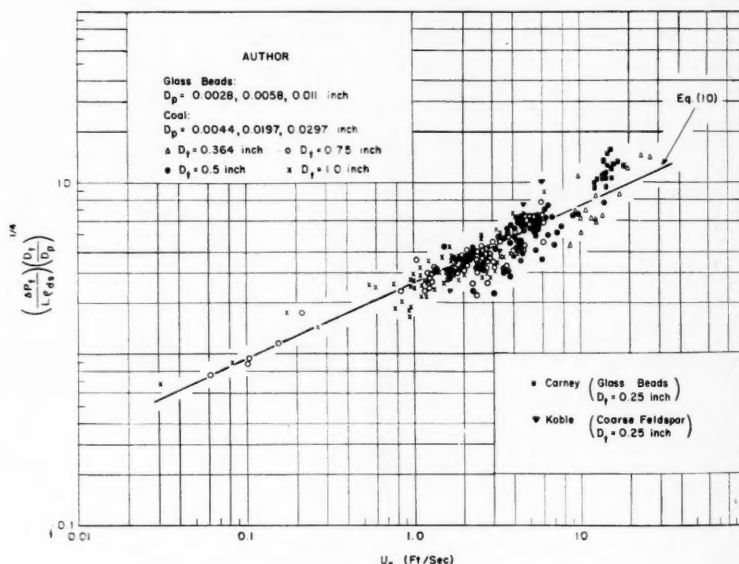


Fig. 9. Pressure-drop correlation.

the average solid particle velocity, and the average slip velocity.

##### Solution

The average solid-particle velocity can be obtained from Figure 7.

$$\begin{aligned} \text{Since } G_s &= 785 \times 144 \times 4/(3600 \times 3.14) = 40 \text{ lb./sq. ft.-sec.} \\ G_s D_p^{0.7} &= 40 \times 0.176 = 7.04 \\ \rho_s U_s &= 150 \text{ lb./cu. ft.} \\ U_s &= 150/81 = 1.85 \text{ ft./sec.} \\ U_a &= 2 \times 1.85 = 3.70 \text{ ft./sec.} \end{aligned}$$

The average slip velocity is therefore

$$\begin{aligned} \Delta U &= U_a - U_s = 1.85 \text{ ft./sec.} \\ \rho_{da} &= G_s/U_s = 40/1.85 = 21.6 \text{ lb./cu. ft.} \\ \rho_{da} &= (1 - \rho_{da}/\rho_s)\rho_a = (1 - 21.6/81) \\ &= 0.076 = 0.0557 \text{ lb./cu. ft.} \end{aligned}$$

The gas mass velocity is

$$G_a = \rho_{da} U_a = 0.0557 \times 3.70 = 0.206 \text{ lb./sq. ft.-sec. or 4.04 lb./hr.}$$

seem to have only a very slight effect on flow characteristics. Large slippages between gas and solid particles in transport line were observed, and a simple relationship that the average gas velocity is about twice as large as the average solid-particle velocity was noted. Empirical correlations for predicting the solid-particle velocity and pressure drop in horizontal line are proposed. The length of pipe required for the solid particles to attain the terminal velocity is difficult to evaluate correctly, since the solids are subjected to repeated positive and negative acceleration.

Although several points have been clarified by the results of the present investigation, the understanding of the problem of dense solid-gas transport is far from complete because of the complexity of the solids flow pattern. Hence



much additional work is required before a conclusive generalization is in sight.

## NOTATION

$A_b$  = cross-sectional area of agglomerated mass of flow in pipe ( $L^2$ )  
 $C_d$  = drag coefficient (no dimension)  
 $D_p$  = average particle diameter ( $L$ )  
 $D_i$  = pipe diameter ( $L$ )  
 $f$  = friction factor (no dimension)  
 $g$  = gravitational acceleration ( $L\theta^{-2}$ )  
 $G_a$  = gas mass velocity in pipes ( $ML^{-2}\theta^{-1}$ )  
 $G_s$  = solid mass velocity in pipes ( $ML^{-2}\theta^{-1}$ )  
 $k$  = constant for a given particle size  
 $L$  = length of the transport line ( $L$ )  
 $R$  = solids to gas ratio (no dimension)  
 $U_a$  = average linear velocity of gas ( $L\theta^{-1}$ )  
 $U_s$  = average linear velocity of solid particles ( $L\theta^{-1}$ )  
 $V$  = total volume of solid and gas collected in the receiver ( $L^3$ )  
 $W_a$  = weight of gas ( $M$ )  
 $W_s$  = weight of solid ( $M$ )

## Greek Letters

$\Delta P_{aa}$  = pressure drop due to acceleration of gas ( $FL^{-2}$ )  
 $\Delta P_{as}$  = pressure drop due to acceleration of solid particles ( $FL^{-2}$ )  
 $\Delta P_d$  = pressure drop due to body drag ( $FL^{-2}$ )  
 $\Delta P_f$  = pressure drop due to friction ( $FL^{-2}$ )  
 $\Delta P_t$  = total pressure drop ( $FL^{-2}$ )  
 $\Delta U$  = slip velocity between gas and solid particles ( $L\theta^{-1}$ )  
 $\rho_a$  = density of gas ( $ML^{-3}$ )  
 $\rho_{da}$  = dispersed gas density ( $ML^{-3}$ )  
 $\rho_{ds}$  = dispersed solid density ( $ML^{-3}$ )  
 $\rho_s$  = solid particle density ( $ML^{-3}$ )

## LITERATURE CITED

1. Albright, C. W., J. H. Holden, H. P. Simons, and L. D. Schmidt, *Ind. Eng. Chem.*, **43**, 1837 (1951).
2. ———, *Chem. Eng.*, **56**, 108 (1949).
3. Belden, D. H., and L. S. Kassel, *Ind. Eng. Chem.*, **41**, 1174 (1949).
4. Carney, W. J., Ph.D. thesis, West Virginia Univ., Morgantown (1954).
5. Clark, R. H., D. E. Charles, J. F. Richardson, and D. M. Newitt, *Trans.*

*Inst. Chem. Engrs. (London)*, **30**, 209 (1952).

6. Cramp, William, and A. Priestley, *Engineer*, **137**, 34 (1924).
7. Gästerstadt, J., *Ver. Deut. Ing. Forschungsarbeiten*, No. 265, 1 (1924).
8. Hariu, O. H., and M. C. Molstad, *Ind. Eng. Chem.*, **41**, 1148 (1949).
9. Hinkle, B. L., Ph.D. thesis, Georgia Inst. Technol., Atlanta (1953).
10. Khudyakov, G. N., and Z. F. Chukhanov, *Doklady Akad. Nauk., U.S.S.R.*, **78**, 681 (1951).
11. Koble, R. A., P. R. Jones, and W. A. Koehler, *Am. Ceram. Soc. Bull.*, **32**, 367 (1953).
12. Mehta, N. C., Ph.D. thesis, Purdue Univ., Lafayette, Indiana (1955).
13. Mitlin, L., Ph.D. thesis, Univ. of London, England (1954).
14. Uspenskii, V. A., *Za Ekon. Topliva*, **8**, No. 3, 26 (1951).
15. Vogt, E. G., and R. R. White, *Ind. Eng. Chem.*, **40**, 1731 (1948).
16. Wood, S. A., and A. J. Bailey, *Proc. Inst. Mech. Engrs.*, **142**, 173 (1939).

Manuscript received September 5, 1956; revision received November 17, 1956; paper accepted November 17, 1956. Paper presented at A.I.Ch.E. Montreal meeting.

# Effective Diffusivity of Packed Bed

M. KIMURA, K. UEDA, and T. OFUKA

Yamaguchi University, Yamaguchi Pref., Japan

From time to time, A.I.Ch.E. Journal presents translations of certain technical articles written by our Japanese colleagues in their own language. These translations are made by Kenzi Etani, who received his B.S. in chemical engineering in 1953 at the Tokyo Institute of Technology and his M.S. in 1955 at M.I.T. He is associated with Stone & Webster and is an associate member of American Institute of Chemical Engineers. He is also a member of the Society of Chemical Engineers, Japan, and the Japan Oil Chemists' Society. His offer to help break down the language barrier is acknowledged.

Abstracts, notation, literature cited, tables, and figure captions not published here appear in English in the original paper. No figures will be reproduced in these translations.

The following article was published in *Chemical Engineering (Japan)*, **21**, pages 17-25 (1957).

The purpose of this experiment was to obtain the relation between effective diffusivity and fractional voids under nonflowing conditions. The results were compared with electric conductivity.

## APPARATUS AND EXPERIMENT

The apparatus used in this experiment is shown in Figure 1. The diameters of the tubes were 3.50 and 3.05 cm. The height of the packed bed was changed from 5 to 15 cm. All apparatus was kept at the constant temperature of  $40 \pm 0.2^\circ\text{C}$ . in a constant-temperature bath. Air having the same temperature was introduced at the top of the packed bed at the constant velocity of 55 cc./sec. Packing materials used were lead shot, ordinary sand, and crushed calcite. Diffusing materials used were benzene and water.

After the equipment had been immersed for 30 to 60 min. in the constant-temperature bath, air was introduced. Prior to the introduction of air, water or benzene diffuses upward and reaches the saturated state. This diffusion is expressed by the following basic equation:

$$\frac{\partial p}{\partial \theta} = \frac{De}{\epsilon} \frac{\partial^2 p}{\partial x^2} \quad (1)$$

$$\left. \begin{aligned} p &= p_s & x &= 0 & \theta &= \theta \\ \partial p / \partial x &= 0 & x &= X & \theta &= \theta \\ p &= p_s & x &= X & \theta &= \infty \\ p &= 0 & x &= X & \theta &= 0 \end{aligned} \right\} \quad (2)$$

If one assumes that packing material is located above the liquid, the relationship

between the concentration gradient at the liquid surface and time would be

$$\left[ \frac{\partial(p/p_s)}{\partial x} \right]_{x=0} = -\frac{2}{x} \left[ e^{-(\pi/2)^2 \tau} + e^{-9(\pi/2)^2 \tau} + e^{-25(\pi/2)^2 \tau} + \dots \right] \quad (3)$$

where

$$\tau = De\theta/\epsilon X^2$$

Figure 2 illustrates the calculated results when  $D_e = 0.03$  sq. cm./sec.,  $X = 8, 12$ , and  $16$  cm., and  $\epsilon = 0.5$ . It is shown also that 5, 11.5, and 20 min. are required to reach a saturated state at a liquid surface for three different bed depths.

The time necessary for reaching the saturated state after the introduction of air would be solved under the following conditions:

$$\left. \begin{aligned} p &= p_s & x &= x & \theta &= 0 \\ p &= p_s & x &= 0 & \theta &= \theta \\ p &= p_s & x &= X & \theta &= 0 \\ p &= 0 & x &= X & \theta &< 0 \end{aligned} \right\} \quad (4)$$

This solution was obtained by Lee and others (8) and is given as follows:

$$\left[ \frac{\partial(p/p_s)}{\partial x} \right]_{x=\bar{x}, \theta=\theta} = 1 - 2e^{-\pi^2 \tau} \quad (5)$$

$$\left[ \frac{\partial(p/p_s)}{\partial x} \right]_{x=\bar{x}, \theta=\infty} = 1 - 2e^{-4\pi^2 \tau} - 2e^{-9\pi^2 \tau} + 2e^{-16\pi^2 \tau} - 2e^{-25\pi^2 \tau}$$

The conclusions are shown in Figure 3. When air is introduced, the saturated state should be reached in a shorter time. To eliminate errors in vaporization of diffusing material during weighing and during saturation in the apparatus before the experiment is started, the following procedure was used.

Benzene or water was weighed after air had been introduced for 30 to 40 min. and again after 5 or 6 hr. The rate of diffusion was determined from the weight at the shorter period minus the weight at the longer period.

#### EXPERIMENTAL RESULTS

Diffusion takes place through the air, screen, packed bed, and turbulent air layer (Figure 4). If one calls the effective diffusivities of these layers  $D_f$ ,  $D_s$ ,  $D_e$ , and  $D_i$ , and the partial pressure of the air above the liquid in the container and at the top of the packed bed  $P_{a0}$  and  $P_{a1}$ , the following equation is derived:

$$N = \frac{\pi}{RT} \ln \frac{P_{a1}}{P_{a0}} \left/ \left[ \frac{\Delta X_s}{D_f} + \frac{\Delta X_e}{D_s} + \frac{\Delta X_e}{D_e} + \frac{\Delta X_i}{D_i} \right] \right. \quad (6)$$

With the total length  $\Delta X_{ap}$  and apparent diffusivity  $D_{ap}$  based on partial pressures  $P_{a0}$  and  $P_{a1}$  considered,

$$N = \frac{D_{ap}\pi}{RT \Delta X_{ap}} \ln \frac{P_{a1}}{P_{a0}} \quad (7)$$

From Equation (6) and (7)

$$\Delta X_{ap}/D_{ap} = \Delta X_s/D_f + \Delta X_e/D_s + \Delta X_e/D_e + \Delta X_i/D_i \quad (8)$$

$$1/D_{ap} = [\Delta X_s/D_f + \Delta X_e/D_s + \Delta X_i/D_i - (\Delta X_s + \Delta X_e + \Delta X_i)/D_e] / \Delta X_{ap} + 1/D_e \quad (9)$$

$D_{ap}$  was obtained experimentally. Since the depth of bed was changed and other conditions were kept constant,  $1/D_e$  was obtained at  $\Delta X_{ap}$  equals 0 in the plot of  $1/D_{ap}$  and  $1/\Delta X_{ap}$ .

Liquid-level change during experimentation was so small that the effect was neglected. The same fractional void was maintained throughout the experiments.

No effect due to the shape of packing materials was found. Crushed calcite and sand were previously screened into three groups: 6 to 8, 8 to 10, and 10 to 14 mesh.

Figures 5, 6, and 7 give the results.

#### EXPERIMENTS ON ELECTRIC CONDUCTIVITY

In the study of thermal diffusion the temperature gradient can be estimated from the electric-voltage gradient. It was assumed that diffusion through packing materials was similar to the case of electric conduction. Thus effective diffusivity obtained in this experiment was compared with electric conductivity, a bridge being employed to determine electric resistance. Electric conductivity of the solution in the packing material voids was determined. When shot lead was used as a packing material, electric resistance was so small that it could not be measured. No effect due to height was found. (See Figure 8.) The concentration of this solution was so high that surface electric conductivity on  $\zeta$  potential was neglected.

#### EXPERIMENTAL RESULTS

Wyllie studied the relationship between voids and electric conductivity in the packing bed, for example glass beads, sand (16) and ion exchange resin (11).

Electricity was conducted three ways: from packing material to solution, through packing material, and through solution. In the case of a nonconductor, the fractional area of fluid  $c$  equals the ratio of specific electric conductivity of the packed bed to that of the fluid itself; that is,  $k_e/k_f$ . The relationship between  $k_e/k_f$  and fractional void  $\epsilon$  is shown in Figure 10. Wyllie (16) mentioned that the following equations can be used: Archie's equation (1)

$$F = \epsilon^{-1.3} \quad (10)$$

Slawinski's equation (13)

$$F = (1.3219 - 0.3219\epsilon)^{2/3} \quad (11)$$

where  $F$  equals  $1/c$ . When the fractional void is small, Equation (10) can be applied, and when it is large, Equation (11) can be used. From Equations (10) and (11)

$$c = \epsilon^{1.3} \quad (12)$$

$$c = \epsilon / (1.3219 - 0.3219\epsilon)^2 \quad (13)$$

Equations (12) and (13) are shown in Figure 10.

In the case of diffusion  $c$  is considered to equal the ratio of effective diffusivity  $D_e$  to diffusivity  $D_f$  without packing. The ratio  $D_e/D_f$  vs. fractional void  $\epsilon$  is shown in Figure 11, in which data obtained by Piret and others (9) are also plotted. These experimental results show that the relationship between effective diffusivity and the fractional void in the packed bed will coincide with that of electric conductivity and fractional voids.

## COMMUNICATIONS TO THE EDITOR

### Physical Interpretation of the Relaxation Method in Heat Conduction

JOHN S. THOMSEN

The Johns Hopkins University, Baltimore, Maryland

The use of the relaxation method for numerical solutions of engineering problems was pioneered by Southwell (1). It was introduced to the field of steady state heat conduction by Emmons (2)

and further developed by Dusenberre (3). (See also references 4 to 7.) The essential requirement that the relaxation procedure must converge to give an exact solution of the difference equations was

demonstrated by Southwell (1) and more rigorously by Temple (10), both using the terminology of elastic-stress problems.

When the convergence proof is stated in thermal terms, it becomes apparent that this method is related to Prigogine's theorem on the minimum production of entropy (8). The one-dimensional problem of a slab with constant surface temperatures, which is divided into  $N$  layers for computational purposes, will be considered. For this system the theorem reduces to the assertion that for fixed values of temperatures  $t_0$  and  $t_N$  all other

$t_i$  assume such values as to minimize the production of entropy in the system.

The rate of entropy production per unit volume is  $-(q''/T^2) \text{ grad } T$  (8), where  $q''$  is the heat flux and  $T$  the absolute temperature. Hence one may approximate  $\phi$ , the entropy production per unit area, by

$$\phi = - \sum_{i=1}^N \frac{q_{i-1,i}}{T_i^2} \left( \frac{T_i - T_{i-1}}{\Delta x} \right) \Delta x \quad (1)$$

$$= \frac{k}{\Delta x} \sum_{i=1}^N \left( \frac{t_i - t_{i-1}}{T_i} \right)^2$$

where  $k$  is the thermal conductivity,  $\Delta x$  the thickness of each layer, and  $t$  the temperature in degrees centigrade or Fahrenheit. Assuming that  $|t_N - t_0| \ll T_0$ , one may write

$$\Phi \equiv \frac{(\Delta x) T^2 \phi}{k} \cong \sum_{i=1}^N (t_i - t_{i-1})^2 \quad (2)$$

The problem now reduces to minimizing  $\Phi$ .

If one differentiates with respect to  $t_i$  and chooses a new value  $t_i^*$  to minimize  $\Phi$  with respect to this variable, one finds

$$t_i^* = \frac{t_{i+1} + t_{i-1}}{2} \quad (3)$$

Corresponding to  $t_i^*$  is a new  $\Phi^*$  such that [with the help of Equation (3)]

$$\Phi - \Phi^* = (t_{i+1} - t_i)^2$$

$$+ (t_i - t_{i-1})^2 - (t_{i+1} - t_i^*)^2$$

$$- (t_i^* - t_{i-1})^2$$

$$= -2(t_i - t_i^*)$$

$$\cdot [t_{i+1} + t_{i-1} - (t_i + t_i^*)]$$

$$= (-2t_i + t_{i+1} + t_{i-1})$$

$$\cdot \left( \frac{t_{i+1} + t_{i-1}}{2} - t_i \right)$$

$$\therefore \Phi^* - \Phi = -\frac{r_i^2}{2} \quad (4)$$

where

$$r_i \equiv t_{i+1} + t_{i-1} - 2t_i \quad (5)$$

To minimize  $\Phi$  one may now choose the point with the greatest  $r_i$  (or one of such points if the  $r_i$ 's are equal for several  $i$ ) and apply Equation (3); new  $r_i$ 's may then be computed and the process repeated. One now notes that the  $r_i$ 's are identical with the residuals in the relaxation method and that this procedure is identical with the basic one-dimensional relaxation procedure.

To show that this process converges to the desired solution one first notes that  $\Phi$ , as defined by Equation (2), is positive definite and hence has a lower bound of zero. Furthermore Equation (4) shows that  $\Phi$  must decrease in each step of the process. It follows that  $\Phi$  must approach a unique limit  $\Phi_{\min}$ . Hence for any prescribed  $\epsilon^2/2$ ,  $\epsilon > 0$  there must be a stage in the relaxation process after which  $\Phi - \Phi^* < \epsilon^2/2$ . It follows from Equation (4) that  $|r_i| < \epsilon$ , which completes the convergence proof. The analysis is

readily extended to two or three dimensions.

When the temperature difference is not small compared with the absolute temperature, the interpretation is somewhat more complicated, although the steady state solution is still a state of minimum entropy production. In any case the relaxation procedure may also be considered as a minimization of the thermal dissipation function defined by Biot (9).

#### LITERATURE CITED

1. Southwell, R. V., "Relaxation Methods in Engineering Science," Oxford Univ. Press, especially pp. 102 to 105 (1940).
2. Emmons, H. W., *Trans. Am. Soc. Mech. Engrs.*, **65**, 607 (1943).
3. Dusenberre, G. M., "Numerical Analysis of Heat Flow," McGraw-Hill, New York, Chap. 3 to 10 (1949).
4. Schneider, P. J., "Conduction Heat Transfer," Addison-Wesley, Cambridge, Chap. 7 (1955).
5. Grinter, L. E., ed., "Numerical Analysis in Engineering," Macmillan, New York, pp. 49, 104, 188 (1949).
6. Booth, Andrew D., "Numerical Methods," Butterworth's Scientific Publications, London, pp. 110 to 141 (1955).
7. Liebmann, G., *Brit. J. Appl. Phys.*, **6**, 129 (1955).
8. de Groot, S. R., "Thermodynamics of Irreversible Processes," North Holland Publishing Company, Amsterdam, pp. 39 to 41, 195 to 207 (1952).
9. Biot, M. A., *Cornell Aeronaut. Lab. Rept. SA-987-S-3* (May 1956).
10. Temple, G., *Proc. Roy. Soc. (London)*, **A169**, 476 (1939).

## Heat Transfer

LEONARD WENDER and G. T. COOPER

The comments of Leva and Wen\* concerning the exclusion of the data of Van Heerden, et al., in working up the external surface correlation are appreciated. However, we wish to make the following comments.

While these data were not treated because of a lack of bed density (or

fraction solids) values, we were of course aware that methods were available for estimating these quantities and that these methods need to be used for applying the correlation. However it was not felt that the large amount of time required for estimating bed voidages for the many Van Heerden runs could be justified, at the expense of working on the other data used, because of the limited usefulness of the Van Heerden data. While it is true

that they represent a careful study of many variables and cover a wide range, all the work was done at a single and very low value (1.18) of  $L_H/D_T$ . Since the later studies of Van Heerden (cited in our paper) appear to show a strong and complex  $L_H$  effect in the region of low  $L_H/D_T$ , it was felt that conclusions resulting from the use of these data would be less profitable than those resulting from the study of data at higher  $L_H/D_T$

\*A.I.Ch.E. Journal, **5**, No. 1, 7M (1959).

values and data at low and varying  $L_H/D_T$  (Dow and Jakob). Furthermore the Van Heerden study was the only one in the external surface study that had only part of the bed in contact with the heat transfer surface, and there was thus an apparatus geometry difference between that study and all the others used.

The Van Heerden data should be studied however, and we have been gradually working them up since the publication of our paper. Our calculations confirm the deviations cited by Leva and Wen and point up the complexity of the

low  $L_H/D_T$  region in the case of external surface. Our paper points out that the external surface correlation is uncertain in the low  $L_H/D_T$  region, and it is hoped that further studies will enable us to improve it in this region.

As to the differences in slope between curves of Van Heerden data and the external surface correlation curve, mentioned by Leva and Wen, we believe these to be caused not by an improper incorporation of the functional relationship between fluid mass velocity and bed expansion but by the uncertainty of

the slope of the correlation curve in the low Reynolds number region resulting from the very small number of points in that region.

The differences in form between our external and internal surface correlations are indeed substantial but were found necessary in our empirical study. However it may still be hoped that more work in this field by others will yet produce a definitive correlation, theoretically based and covering in a single expression both external and internal surface operation.

## Diffusion in a Pore of Irregular Cross Section—a Simplified Treatment

ALAN S. MICHAELS

Massachusetts Institute of Technology, Cambridge, Massachusetts

In a recent issue of this journal Petersen\* developed an expression for the convergence factor for diffusion through a pore whose cross section varied periodically along its length in a hyperbolic fashion, from which he demonstrated how the effective diffusivity in such a pore varied with the ratio of maximum to minimum cross-sectional area. This writer has had occasion to grapple with this same problem; by means of a very elementary analysis of the diffusion process and with the aid of some simplifying assumptions, he has developed a relation between the effective diffusivity and pore geometry that is in remarkably close agreement with Petersen's far more elegant analysis.

Consider two cylindrical capillaries, one of radius  $r_1$  and length  $l_1$  and the other of radius  $r_2$  and length  $l_2$ , which are connected in series. An irregular pore may be considered as composed of any number of these characteristic units in series. Since the diffusional resistance offered by any one of these units is the same as any other, it is possible by characterizing the unit to characterize thereby the entire pore.

A component is assumed to be diffusing through this unit at steady state. If entrance and exit effects at the juncture of the two capillaries are neglected, the flux  $N$  through the two capillaries can be represented by

$$N = D(\pi r_1^2) \left( \frac{c_i - c'}{l_1} \right) = D(\pi r_2^2) \left( \frac{c' - c_o}{l_2} \right) \quad (1)$$

\*Petersen, E. E., *A.I.Ch.E. Journal*, 4, 343 (1958).

If one defines two dimensionless ratios  $L = l_1/l_2$  and  $R = r_1/r_2$ , Equation (1) can be solved for  $c'$  and the flux expressed in terms of the inlet and outlet concentration:

$$N = D \left( \frac{\pi r_1^2}{l_1} \right) (c_i - c_o) \left[ \frac{L}{R^2 + L} \right] \quad (2)$$

An equivalent uniform cylindrical pore can be defined as one with an average volume per unit length that is the same as that of the irregular pore\*; that is,

$$\pi r_e^2 (l_1 + l_2) = \pi r_1^2 l_1 + \pi r_2^2 l_2^2 \quad (3)$$

The flux through the irregular pore can be equated to that through the equivalent pore, if an effective diffusivity is substituted for the diffusion coefficient.

$$N = D_e (\pi r_e^2) \frac{c_i - c_o}{l_1 + l_2} \quad (4)$$

Substituting Equation (3) into (4) and equating the resulting relation to Equation (2), one finds that

$$D/D_e = \left[ 1 + \frac{L}{(L+1)^2} \left( \frac{R^2 - 1}{R} \right)^2 \right] \quad (5)$$

Equation (5) permits calculation of the convergence factor  $D_e/D$  as a function of

\*Alternatively an equivalent cylindrical pore can be defined as one with a surface area per unit volume equal to that of the real pore; in this case the volume of the equivalent pore per unit length will be less than that of the real pore, and a number of equivalent pores in parallel must be selected such that the total pore volume per unit length is the same as that of the real pore. Since the diffusional flux through a uniform cylindrical pore is directly proportional to its cross-sectional area, these two definitions of the equivalent pore yield the same algebraic solution.

$R$  and  $L$ . The parameter  $R$  alone (or more correctly,  $R^2$ ) appears in Petersen's derivation, since his assumed hyperbolic variation of pore cross section with length makes  $(L)$  and  $(R)$  interdependent.

In Figure 1 ( $D_e/D$ ) is plotted as a function of  $R$  for various values of  $L$ . The dotted line on the graph represents Petersen's correlation. It will be noted that the two correlations are in rather close agreement for values of  $R$  up to about five, irrespective of the value of  $L$ . At higher values of  $R$  however they diverge appreciably. In view of the fact that with Petersen's hyperbolic construction of the pore the fraction of the pore length containing the bulges increases with the ratio of maximum to minimum pore diameter (that is,  $L$  increases with  $R$ ), the observed divergence of the two correlations at high values of  $R$  is to be expected.

In the absence of specific microscopic information about pore geometry, it is convenient to assume some arbitrary relation between  $L$  and  $R$  in order to express the convergence factor in terms of a single geometric parameter. One not unreasonable assumption is that the length of a bulge or constriction is proportional to its diameter, that is, that  $L = R$ . In this case Equation (5) becomes

$$D_e/D = \left[ 1 + \frac{(R-1)^2}{R} \right]^{-1} \quad (6)$$

Equation (6) yields values of the convergence factor which are about 30% lower (at higher values of  $R$ ) than Petersen's. In view of the simplifying assumptions employed in the present development this agreement is surprising. If Equation (5) is solved for the case



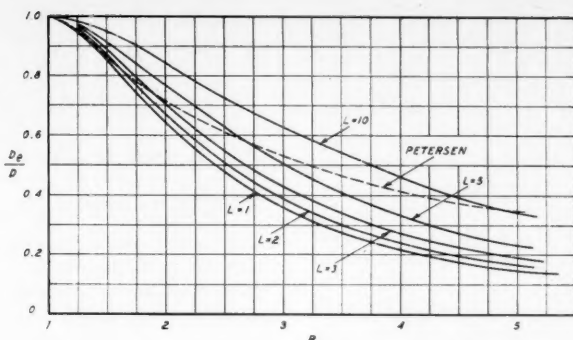


Fig. 1.

where  $L = 2R$ , the values are virtually identical with Petersen's.

Equation (5) has certain unusual properties which merit comment. The function  $L/(L+1)^2$  is relatively insensitive to the value of  $L$ , varying only about threefold as  $L$  increases from 1 to 10; this means that the convergence factor is much more sensitive to the degree of change of pore cross section (or  $R$ ) than it is to the relative lengths of the bulges or constrictions. Also  $L/(L+1)^2$  is a maximum at  $L = 1$  and has the same value for  $1/L$  as it does for  $L$ ; that is to say, the convergence factor will be the same whether the pore con-

strictions occupy a given fraction of the pore length of the pore bulges occupy that fraction, and it will be smallest when the bulges and constrictions occupy equal fractions of the pore length.

Failure to consider entrance and exit effects in the preceding derivation amounts to assuming that all flux lines are parallel to the pore walls at all points. Clearly however there will be parts of the pore where this is not the case, and thus a certain fraction of the pore volume will not contribute to the flux. Consequently the convergence factor calculated from Equation (5) will be greater than the true convergence factor for the corres-

ponding irregular pore, or, conversely, pore dimensional ratios calculated from a measured convergence factor via Equation (5) will always be larger than the actual values. It should however be pointed out that the actual diffusional flow process through a porous solid is an impressively complex matter involving convergence effects, flow splitting, and multidirectional flow paths, of which the individual contributions to the flow resistance are unknown. One may lump all these effects into either a tortuosity factor or a convergence factor; both are calculational conveniences, but in the absence of a detailed knowledge of the geometry of a porous solid, neither throws any direct light on the flow mechanism. In view, therefore, of the limitations attendant upon employing any parallel capillary model to describe a random porous medium, further refinement of the irregular pore model hardly seems profitable.

#### NOTATION

- $c_i$  = constant upstream concentration  
 $c_o$  = constant downstream concentration  
 $D$  = diffusion coefficient  
 $D_e$  = effective diffusivity  
 $L$  = ratio of length of pore bulges to pore constrictions  
 $R$  = ratio of maximum to minimum pore diameter

## Slot Capacity of Bubble Caps

ANDREW PUSHENG TING

Chemical Construction Corporation, New York, New York

In setting up their differential equations Rogers and Thiele (1) overlooked the directional property of the differential slot height and did not put in a necessary minus sign. Later they reversed the integration limits without changing the sign. The final equation for rectangular slots happens to be correct, because the slot width does not vary with the slot height, and two negatives make a positive. However their equations for trapezoidal and triangular slots are incorrect; the capacities of trapezoidal and tri-

angular slots are underestimated by 14.3 and 50%, respectively.

#### DERIVATION OF EQUATION

For the convenience of comparison the notation used here is the same as that used by Bolles (2), except that the slot-height variable and the slot opening start from the top of a slot, as illustrated in Figure 1.

#### Trapezoidal slots

Application of the orifice equation to a

differential element of slot area gives the vapor velocity through the differential area

$$u = K_s \sqrt{2g \left( \frac{\rho_L - \rho_V}{\rho_V} \right) \frac{h}{12}} \quad (1)$$

The vapor flow rate through the differential area is given by

$$dV_s = u dA$$

$$= K_s \sqrt{2g \left( \frac{\rho_L - \rho_V}{\rho_V} \right) \frac{h}{12}} \frac{w dh}{144} \quad (2)$$

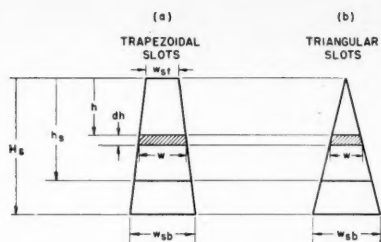


Fig. 1. Slot-opening formula-derivation diagram.

The width of the differential area may be obtained as

$$w = w_{st} + (w_{sb} - w_{st}) \frac{h}{H_s} \quad (3)$$

Combining, rearranging, and integrating Equations (2) and (3) one obtains

$$V_s = \frac{K_s}{144} \sqrt{\frac{2g}{12} \left( \frac{\rho_L - \rho_V}{\rho_V} \right)} \left[ w_{st} \int_0^{h_s} h^{1/2} dh + \frac{w_{sb} - w_{st}}{H_s} \int_0^{h_s} h^{3/2} dh \right] \quad (4)$$

Introducing  $K_s = 0.51$  and applying to the whole tray one gets

$$V = 0.00820 N_c N_s \sqrt{\frac{\rho_L - \rho_V}{\rho_V}} \left[ \frac{2}{3} w_{st} h_s^{3/2} + \frac{5}{2} \left( \frac{w_{sb} - w_{st}}{H_s} \right) h_s^{5/2} \right] \quad (5)$$

The total slot area per tray may be expressed as

$$A_s = N_c N_s H_s (w_{sb} + w_{st}) / (2 \times 144) \quad (6)$$

Combining

$$R_s = w_{st} / w_{sb}$$

with Equations (5) and (6) one gets

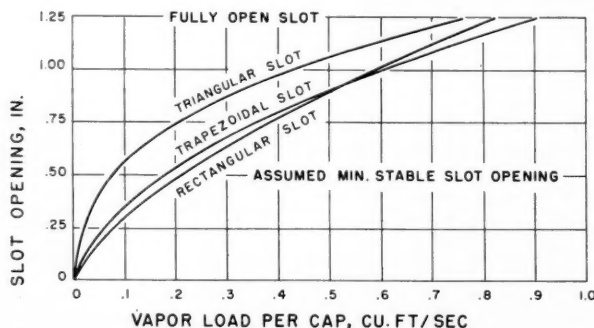


Fig. 2. Performance comparison for common slot shapes with 4-in. bubble caps with 1.25-in. slot height used; system is benzene at atmospheric pressure.

$$V = 2.36 \frac{A_s}{H_s} \sqrt{\frac{\rho_L - \rho_V}{\rho_V}} \left[ \frac{2}{3} \left( \frac{R_s}{1 + R_s} \right) h_s^{3/2} + \frac{5}{2} \left( \frac{1 - R_s}{1 + R_s} \right) \frac{h_s^{5/2}}{H_s} \right] \quad (7)$$

Maximum slot capacity is obtained by the substitution of  $H_s$  for  $h_s$ , which results in

$$V_m = 236 A_s \left[ \frac{2}{3} \left( \frac{R_s}{1 + R_s} \right) + \frac{5}{2} \left( \frac{1 - R_s}{1 + R_s} \right) \right] \sqrt{H_s \left( \frac{\rho_L - \rho_V}{\rho_V} \right)} \quad (8)$$

#### Rectangular slots

This is an extreme case of trapezoidal slots of which  $R_s = 1$ . From Equations (7) and (8)

$$V = 0.787 \frac{A_s}{H_s} \sqrt{\frac{\rho_L - \rho_V}{\rho_V}} h_s^{3/2} \quad (9)$$

and

$$V_m = 0.787 A_s \sqrt{H_s \left( \frac{\rho_L - \rho_V}{\rho_V} \right)} \quad (10)$$

#### Triangular slots

This is another extreme case of trapezoidal slots of which  $R_s = 0$ . From Equations (7) and (8)

$$V = 0.944 \frac{A_s}{H_s} \sqrt{\frac{\rho_L - \rho_V}{\rho_V}} h_s^{5/2} \quad (11)$$

and

$$V_m = 0.944 A_s \sqrt{H_s \left( \frac{\rho_L - \rho_V}{\rho_V} \right)} \quad (12)$$

#### COMPARISON OF TOTAL VAPOR LOAD

##### Rectangular slots ( $R_s = 1$ )

In this case Rogers-Thiele equations are correct and agree with the author's Equations (7) and (8).

##### Trapezoidal slots (for the case $R_s = 0.5$ )

The Rogers-Thiele equation is

$$V_{mR} = 0.734 A_s \sqrt{H_s \left( \frac{\rho_L - \rho_V}{\rho_V} \right)}$$

The author's equation is

$$V_{mT} = 0.839 A_s \sqrt{H_s \left( \frac{\rho_L - \rho_V}{\rho_V} \right)}$$

$$V_{mT} / V_{mR} = 0.839 / 0.734 = 1.143$$

The correct vapor capacity calculated from the author's equation is 14.3% higher than that calculated from the Rogers-Thiele equation.

##### Triangular slots ( $R_s = 0$ )

Similarly

$$V_{mT} / V_{mR} = 0.944 / 0.630 = 1.500$$

The corrected vapor capacity calculated from the author's equation is 50.0% higher than that calculated from the Rogers-Thiele equation.

#### SELECTION OF SLOT DESIGN

To provide a basis for the selection of slot shapes the performance of bubble caps with different slot shapes is compared. This comparison is based on 4-in. caps, used by Bolles in his comparison, with a slot height of 1.25 in. The mean slot width is held constant at 0.25 in. to maintain equal area per slot. The slot designs of the three different 4-in. caps are as follows:

Slot	$R_s$	Number of slots per cap	Slot area per cap sq. in.
Rectangular	1	25	7.82
Trapezoidal	0.5	26	8.12
Triangular	0	19	5.94

The author, as Bolles did, chose the distillation of benzene at atmospheric pressure to compare the slot performance of these bubble caps. In this system the temperature is 176°F., and liquid density equals 50.5 lb./cu. ft.

The calculation of the slot performance was based on the correct equations given in this paper. The calculated slot openings for various vapor loads are presented in Figure 2. This chart shows that the cap with trapezoidal slots provides the greatest capacity at maximum slot opening.

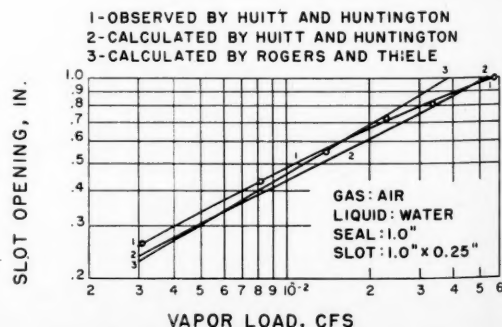


Fig. 3. Calculated and observed slot opening.

ing of the three types. This bears out the popular preference of trapezoidal slots. In either capacity or flexibility trapezoidal slots are better than rectangular slots. This is in disagreement with Bolles' study based upon Rogers-Thiele equations which indicated that the cap with rectangular slots would provide the greatest capacity at maximum slot opening.

It is to be noted that triangular slots are not as undesirable as the Rogers-Thiele equations would show. The maximum capacity of the cap with triangular slots is actually not much lower than that of rectangular or even trapezoidal slots. On the other hand if a column is to be designed to meet the widest range of operation in throughput, caps with triangular slots actually are the best choice and the most stable of the three types (when one assumes a minimum stable slot opening of 0.5 in.). Caps with triangular slots probably can be operated at a throughput of 9.8% of maximum capacity, while caps with rectangular slots probably cannot be operated satisfactorily under 25% of maximum capacity. Since the maximum slot capacity of cap with triangular slots is actually as high as 85 and 93% of the maximum capacity of caps with trapezoidal and rectangular slots respectively, it properly deserves more attention in future applications.

can be used in general for all types of slots.

# CONCLUSION

Slot capacities of trapezoidal and triangular slots in a bubble cap column calculated by Rogers-Thiele equations are underestimated by 14.3 and 50.0%, respectively.

The correct equations given in this paper show that:

1. Caps with trapezoidal slots are better than caps with rectangular slots in either capacity or flexibility.
2. Caps with trapezoidal slots are the best for distillation columns of high vapor/liquid ratios, and caps with triangular slots the best for columns of low vapor/liquid ratios.
3. Triangular slots provide the highest flexibility. Although the maximum capacity of caps with triangular slots is somewhat lower than that of caps with the other two types of slots, it is much higher than indicated by Rogers-Thiele equation; therefore it deserves more attention in the future, especially for distillation and absorption columns with high liquid loadings or widely variable vapor loadings. These occur for instance in batch columns in which fine chemicals

calculated from the author's equation, cu. ft./sec.

- $V_s$  = vapor load per slot, cu. ft./sec.  
 $w$  = slot width, in.  
 $w_{sb}$  = slot width at bottom, in.  
 $w_{st}$  = slot width at top, in.  
 $\rho_L$  = liquid density, lb./cu. ft.  
 $\rho_V$  = vapor density, lb./cu. ft.

# LITERATURE CITED

1. Rogers, M. C., and E. W. Thiele, *Ind. Eng. Chem.*, **26**, 524 (1934).
2. Bolles, W. L., *Petrol. Processing*, 64 (Feb., 1956).
3. Huitt, J. L., and R. L. Huntington, *Petrol. Refiner*, **30**, June, 131, Aug., 111, Oct., 153 (1951).
4. Simkin, D. J., C. P. Strand, and R. B. Olney, *Chem. Eng. Progr.*, **50**, 565 (1954).
5. Griswold, J., D.Sc. thesis, Mass. Inst. Technol., Cambridge (1931).

# BOOKS

**Management for Engineers**, Roger C. Heimer. McGraw-Hill Book Company, Inc., New York (1958). 453 pages. \$6.75.

The purpose of this textbook is to acquaint "the young engineer with the business firm's decision-making process." It is written with the premise that the reader has little knowledge of the workings of a business firm.

For the novice in the business world Chapter 2, "The Legal Forms of Business Organization," and Chapter 3, which analyzes the finances of a mythical business firm, should be particularly helpful. The major portion of the book is concerned with daily operational problems: profit, cost, interest, depreciation, insurance, and inventory.

A basic understanding of organizational structure and operation will be gleaned from the last four chapters, which deal with over-all managerial problems, and really differentiate this book from the usual economics textbook. The young engineer should find these chapters most helpful in understanding managerial decisions.

The best use of this book would be as a supplement to the usual undergraduate economics course.

J. M. RUDER

**Engineering Materials Handbook**. Charles L. Mantell, Editor. McGraw-Hill Book Company, Inc., New York (1957). 1936 pages. \$21.50.

The field of engineering materials is a broad one, and it seems almost impossible that any one book could cover the whole subject completely. The "Engineering Materials Handbook" does, however, cover the field with a remarkable degree of

## Slot of 4-in. cap

## Maximum capacity/cap

## Minimum capacity/cap

	cfs	% trapezoidal	cfs	% maximum
Triangular	.765	84.5	.075	9.80
Trapezoidal ( $R_s = 0.5$ )	.905	100	.176	19.46
Rectangular	.825	91.2	.208	25.2

# DISCUSSION

Huitt and Huntington (3) compared their observed slot openings of a rectangular slot with their equation and also with Rogers-Thiele equation. Figure 3 shows that both equations agree with their data fairly well. However vapor loads predicted by the Huitt-Huntington equation are about 20% higher than their observed values, except when the slot is fully open. Rogers-Thiele equation is on the conservative side when the slot is more than 60% open. Therefore the latter equation is preferable in design calculations to the first. In this comparison a slot orifice coefficient of 0.51 was used. This confirms that 0.51 is a proper and conservative coefficient for rectangular slots.

Simkin *et al.* (4) used the Rogers-Thiele equation with the coefficient modified to fit the experimental data of Griswold (5) for trapezoidal slots. They proposed to use 0.70 in Rogers-Thiele equation instead of 0.51 for trapezoidal slots. This bears out the finding of this paper that Rogers-Thiele equation for trapezoidal slots is about 14% too low. Therefore if equations in this paper are used in design, the same coefficient of 0.51

in small quantities are produced and in which products are often switched from one to another.

# NOTATION

- $A$  = slot area, sq. ft.  
 $A_s$  = total slot area per tray, sq. ft.  
 $g$  = acceleration of gravity, 32.2 ft./sec./sec.  
 $h$  = slot opening variable, in.  
 $h_s$  = slot opening, in.  
 $H_s$  = slot height, in.  
 $K_s$  = slot orifice coefficient  
 $N_c$  = number of caps per tray  
 $N_s$  = number of slots per cap  
 $R_s$  = trapezoidal slot shape factor,  $w_{st}/w_{sb}$   
 $u$  = vapor velocity through an element of slot area, ft./sec.  
 $V$  = total vapor load per tray, cu. ft./sec.  
 $V_m$  = maximum vapor load per tray, cu. ft./sec.  
 $V_{mR}$  = Maximum vapor load per tray calculated from Rogers and Thiele's equation, cu. ft./sec.  
 $V_{mT}$  = maximum vapor load per tray,

# A.I.Ch.E. SPRING PUBLICATIONS NEW NUMBERS IN THE SYMPOSIUM SERIES\*

(Available May 1)

21. **COMPUTER TECHNIQUES IN CHEMICAL ENGINEERING:** 12 papers, primarily on digital-computer techniques in use in the chemical industry.  
\$3.00 to members \$4.00 to nonmembers
- 22 and 23 **NUCLEAR ENGINEERING—Parts V and VI:** In all, 63 papers on the chemical engineering aspects of the nuclear field. Most of the A.I.Ch.E.-sponsored papers presented at the 1958 Nuclear Congress are included in Part VI.  
\$3.50 each to members \$4.50 each to nonmembers
24. **ADSORPTION, DIALYSIS, AND ION EXCHANGE:** Detailed discussion of the use of these operations in fractionation and other operations, with emphasis on the chemical engineering viewpoint.  
\$3.50 to members \$4.50 to nonmembers
25. **REACTION KINETICS AND UNIT OPERATIONS:** 23 surveys of the basic fields in chemical engineering, covering the most recent developments and future trends.  
\$3.50 to members \$4.50 to nonmembers
26. **CHEMICAL ENGINEERING EDUCATION—ACADEMIC AND INDUSTRIAL:** Discussions of new curricular developments in colleges and universities and of industrially sponsored training programs.  
\$3.00 to members \$4.00 to nonmembers

\*Books will be sent to subscribers as they are released. Anyone wishing to place a standing order to receive Monograph and Symposium Series volumes as they are issued is asked to check the box in the coupon below.

†Available in June, 1959

A.I.Ch.E.  
25 West 45 Street  
New York 36, New York

Please send me the following books (check enclosed ☐, bill me ☐);  
Add 3% sales tax for delivery in New York City

- |  |  |
|--|--|
| <input type="checkbox"/> 21 Computer Techniques    | <input type="checkbox"/> 24 Adsorption, Dialysis, Ion Exchange |
| <input type="checkbox"/> 22 Nuclear Engineering V  | <input type="checkbox"/> 25 Reaction Kinetics, Unit Operations |
| <input type="checkbox"/> 23 Nuclear Engineering VI | <input type="checkbox"/> 26 Chemical Engineering Education     |

(Name)

(Address)

☐ Member

☐ Nonmember

completeness, especially in the field of metallic materials.

In forty-three well-organized sections, metals, organic and inorganic materials, and the cause and prevention of failures in materials are treated. To make specific data readily available, technical tables, design information, structural characteristics, and tabular data have been carefully prepared, and the references at the end of each section enable the reader to find any information not embraced in the handbook. The reliability of the information presented is achieved by coordinating the work of more than 150 specialists under the direction of Professor Mantell who is chairman of the Department of Chemical Engineering at the Newark College of Engineering.

To make the book of practical value to an engineer concerned with materials, emphasis is placed on the fabricated forms of materials, their physical and mechanical properties, their advantages, limitations, competition with one another, protection against deterioration, and their ability to withstand use and abuse.

Approximately half of the book concerns metals, and the reviewer feels that the properties of the individual metals are thoroughly covered. The section on steel and its heat treatment is especially well done. However, it is the reviewer's opinion that too little space is given to the difficulties that arise in the fabrication of materials into commercial shapes.

It is in the second half of the book that the reviewer has the idea that the editor has spread himself too thin in a desire to take in the whole field of materials. In devoting reasonably complete attention to such materials as brick, clay, textiles, stone, and concrete, the editor has not allowed enough space for complete coverage to such newer subjects as materials for nuclear reactors, rockets, and guided missiles. While textiles, stone, etc., are of interest to some engineers, it is the reviewer's opinion that chemical and metallurgical engineers would have profited more had the treatment of the newer materials, such as high temperature ceramics, been more inclusive.

Nevertheless, the reviewer feels that the handbook is a good one and would be of practical value to any engineer faced with a problem of the choice of materials, particularly if the choice is to be made in the metallic field.

A. S. TETELMAN  
Yale University

*Modern Mathematics for the Engineer*, E. F. Beckenbach, et al, University of California Engineering Extension Series, McGraw-Hill Book Company, Inc., New York (1958), 514 pages, \$7.50.

This book is described as a broad survey of the applications of advanced mathematics to the expanding modern technology. The basic idea behind the volume is quite sound; indeed, an intimate association with a large number of the theories of advanced mathematics has become a practical necessity for those attempting to keep abreast of the literature in practically any scientific field.

*Modern Mathematics for the Engineer* is



divided into three major sections: Mathematical Models, Probabilistic Problems, and Computational Considerations. These sections are further divided into individual chapters dealing with the more specific problems which might be expected to be encountered, such as linear and nonlinear oscillations, the calculus of variations, hyperbolic partial-differential equations, and boundary-value problems in elliptic partial-differential equations in the first section; the theory of prediction, the theory of games, dynamic programming, and Monte Carlo methods in the section on Probabilistic Problems; and matrices and engineering, functional transformations, nonlinear methods, relaxation methods, and high-speed computing devices in the last section.

From an inspection of this partial list of contents, it can be seen that the authors have not lacked for broadness in their approach to the applications of modern mathematical techniques for the engineer. Many volumes have been written on individual chapters in this book, and in many cases it has been necessary for the authors to assume a fairly complete knowledge of the contents of these volumes in presenting the material. Such is to be expected in any advanced textbook or reference work, although to the engineer whose education and experience has not left him well acquainted with the workings of advanced mathematical methods, the quantity of knowledge necessary for the rewarding pursuit of this book may seem overwhelming. Owing to the nature of the lectures from which the material included in the book is taken, one cannot consider it a textbook in the normal sense of the word.

From the point of view of the practicing engineer, the last section, on Computational Considerations, is probably the most interesting and useful, particularly the chapters dealing with the uses of matrices, relaxation methods, high-speed computers, and methods of steep descent. Unfortunately, the entire subject of functional transformations and associated methods is discussed in some fourteen pages, which is entirely inadequate for methods of such importance. Although many excellent discussions of the subject appear elsewhere, it would seem that the book under consideration here would benefit from the additional scope and balance between the various topics provided by further treatment of this subject.

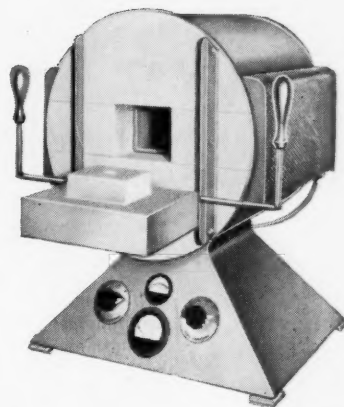
The discussions of the various probabilistic problems and methods are quite interesting and bear close inspection because of the increasing importance of these methods in the solution of a multitude of problems.

In general, it can be said that a book representing such a wide diversification of topics and a variety of authors as this one is quite likely to suffer from sheer magnitude of effort. *Modern Mathematics for the Engineer* represents a successful attempt to minimize these difficulties, however; even the casual reader will be able to gain some understanding of the variety of problems which can be solved with these techniques and, consequently, to develop the interest necessary for the learning of the material. For those more fully acquainted with the various topics encountered in consideration of advanced mathematics, the book would best be described as a valuable reference



## Hevi-Duty "G-07-PT" FURNACE temperatures to 2600° F.

This furnace is designed for high-temperature work where accurate control and uniformity are important. Controls, which provide 48 temperature gradients, and an indicating pyrometer are located in the pyramid base. For greatest uniformity in the heating chamber, three heating elements are installed over and three are beneath the refractory muffle.



Write for Bulletin 957 for full details.

Type	Watts	Chamber			Price
		W.	L.	H.	
G-07-PT	3500	4"	7"	2 3/4"	\$585.00

\*Operating voltage either 115 or 230 A.C. only.

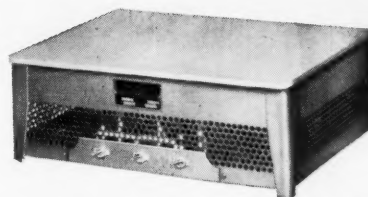
## FOR GENERAL AND SPECIALIZED LABORATORY APPLICATIONS

## "Multiple Unit" HOT PLATE Temperatures to 750° F.

7 Standard sizes, sturdily built to industrial standards. Long life heating units radiate directly to the steel top plate assuring fast heat up and an even heat over the entire top surface.

Three switch heat control offers high, medium and low heats.

Write for Bulletin 835 for complete details.



Type Number	Size in inches	Location of switches on this edge	Shipping Weight: lbs.	Watts	PRICE
12	12x12	12"	35	1200	\$ 55.00
20	12x18	12"	55	1800	70.00
22	18x12	18"	55	1800	70.00
30	18x24	18"	110	3600	102.00
32	24x18	24"	110	3600	102.00
40	6 1/2 x 18	18"	28	1200	50.00
44"	4 1/2 x 24	24"	30	600	50.00

Each Hot Plate operates on 115 or 230 volts.

\*Maximum Temperature 450° F.



## LABORATORY FURNACES



• ELECTRIC EXCLUSIVE

work for the most important of the applications of mathematics for the contemporary engineer.

JOHN B. BUTT

**Elements of Gasdynamics**, H. W. Liepmann and A. Roshko, John Wiley & Sons, 439 pages. \$11.00.

*Elements of Gasdynamics*, by Liepmann and Roshko, is an excellent book. The material covered may be ascertained from the chapter headings which read: (1) Concepts from Thermodynamics; (2) One Dimensional Gasdynamics; (3) One Dimensional Wave Motion; (4) Waves in Supersonic Flow; (5) Flow in Ducts and Wind Tunnels; (6) Methods of Measurement; (7) The Equations of Frictionless Flow; (8) Small-Perturbation Theory; (9) Bodies of Revolution. Slender Body Theory; (10) The Similarity Rules of High Speed Flow; (11) Transonic Flow; (12) The Method of Characteristics; (13) Effects of Viscosity and Conductivity; (14) Concepts from Gas Kinetics.

There are very few criticisms which need to be made. It is unfortunate that the authors chose to use the symbols  $F$  and  $G$  for the Helmholtz and Gibbs free energy rather than  $A$  and  $G$ . The use of  $F$  for the Helmholtz free energy will cause much confusion, since most Americans use  $F$  for the Gibbs free energy and the majority of the tables of thermodynamic data adhere to this convention. This reviewer would have liked to have seen a somewhat more extended discussion of the second law of thermodynamics and of the principles

of irreversible thermodynamics, especially since the latter is used in one form or another extensively throughout the text. The treatment of the Clausius-Clapeyron equation is very poor and unconvincing. The usual thermodynamic derivations are superior to the quasi-molecular one given by the authors. Also the treatment of imperfect gases is superficial, and the relationship between thermodynamic properties and gas imperfection is very incomplete. These criticisms are not meant to imply that the thermodynamics chapter is poor but rather to indicate some places where improvement is possible. The remainder of the book, especially the sections dealing with the hydrodynamics of compressible fluid flow, is admirably clear.

The final chapter on the kinetic theory of gases is short but complements well the rest of the text. This reviewer was very pleased to see a brief discussion of the properties of Couette flow in the Knudsen region. The development of missiles which fly in regions of the upper atmosphere where the mean free path is of the order of the dimensions of the flying object makes this pressure range of great importance.

*Elements of Gasdynamics* is to be recommended to all students interested in gasdynamics and its applications. The book will also be of interest to physical chemists who will find a wide realm of irreversible phenomena which await exploration.

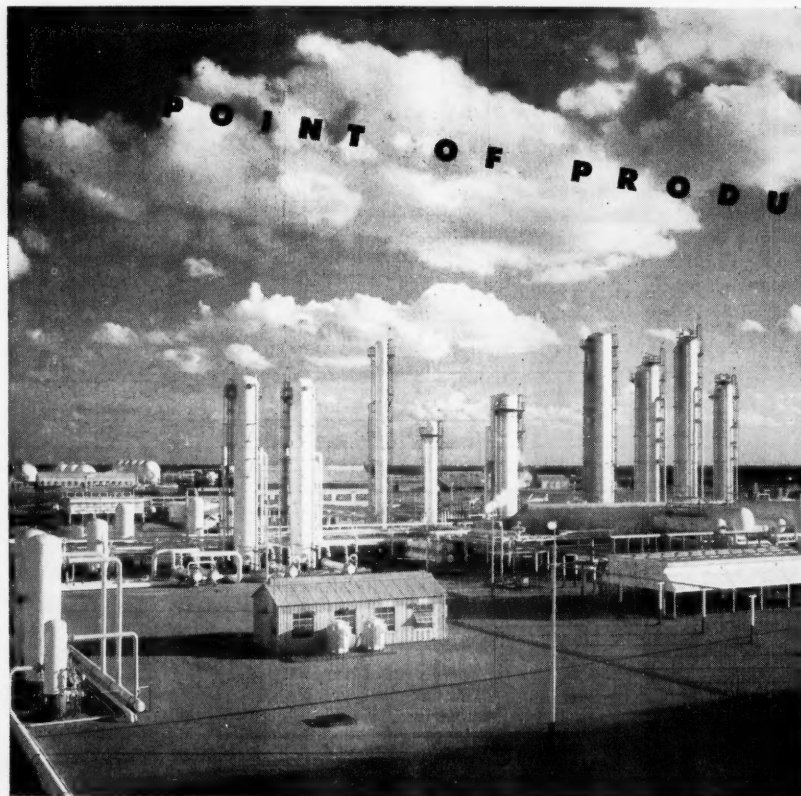
STUART A. RICE  
Junior Fellow  
Society of Fellows  
Harvard University

## INDEX OF ADVERTISERS

Academic Press .....	6J
American Heat Reclaiming Corp. ....	Inside Front Cover
Emco Corporation, The ....	Inside Back Cover
Electronic Associates, Inc. ....	4 & 5J
Hevi-Duty Electric Co. ....	7J
Kellogg Co., The M. W. ...	Outside Back Cover
Stearns-Roger Mfg. Co. ....	8J

## Advertising Offices

<b>New York 36</b> —Paul A. Jolcuvar, Adv. Sales Mgr., Carl G. Lassen, Asst. Adv. Sales Mgr., Donald J. Stroop, Dist. Mgr., Robert S. Bugbee, Dist. Mgr.; 25 W. 45th St., COlumbus 5-7330.
<b>Philadelphia</b> —Lee W. Swift, Jr., Dist. Mgr.; Pleasant Valley Apts., Camden Ave., Moorestown, N. J.
<b>Chicago 4</b> —Martin J. Crowley, Jr., Dist. Mgr.; Robert Kliesch, Dist. Mgr.; 53 West Jackson Blv., Room 504, HArrison 7-3760.
<b>Cleveland 15</b> —Harry L. Gebauer, Dist. Mgr., 1501 Euclid Ave., SUperior 1-3315.
<b>Pasadena 1, Calif.</b> —Richard P. McKey, Dist. Mgr., 465 East Union St., RYan 1-0685.
<b>Dallas 18</b> —Richard E. Hoierman, Dist. Mgr., 9006 Capri Drive, DIamond 8-1229.
<b>Birmingham 9, Ala.</b> —Fred W. Smith, Dist. Mgr., 1201 Forest View Lane, VEsthaven, TRemont 1-5762.



When your next design, engineering or construction project is assigned, call on Stearns-Roger for one reliable source. Upon completion the plant is at the point of production to run far into the future, efficiently, economically.

Engineers, Constructors,  
Manufacturers to INDUSTRY

**Stearns-Roger**  
THE STEARNS-ROGER MFG. CO. - DENVER, COLORADO

DENVER  
EL PASO  
HOUSTON  
SALT LAKE CITY

Stearns-Roger Engineering Co., Ltd. Calgary

.....6J

. Inside

t Cover

k Cover

4 & 5J

.....7J

k Cover

.....8J

v. Sales

. Sales

Robert

St., CO-

t. Mgr.;

Moore-

st. Mgr.;

Jackson

st. Mgr.,

ay, Dist.

585.

st. Mgr.,

h, Dist.

esthaven,

bring or

call on

source.

at the

into the

. Calgary

e, 1959